24th INTERNATIONAL CONGRESS ON ACOUSTICS

ICA 2022

October 24(Mon) - 28(Fri), 2022 | Gyeongju, Korea

PROCEEDINGS



Hosted by The Acoustical Society of Korea | ICA



ICA 2022

24th INTERNATIONAL CONGRESS ON ACOUSTICS

October 24(Mon) - 28(Fri), 2022 | Gyeongju, Korea

A16: NUMERICAL, COMPUTATIONAL AND THEORETICAL ACOUSTICS

PROCEEDINGS of the
24th International Congress on Acoustics

October 24 to 28, 2022 in Gyeongju, Korea

ABS-0829

Computational study of ultrasonic flow meter by lattice Boltzmann method

Hyungkeun CHUNG[1]; Young J. MOON[2]*; Shang-yoon HWANG[3]; Yong-min KIM[4]; Joo-hyun KIM[5]

[1,2] School of Mechanical Engineering, Korea University, Korea, Rep. of

[3,4,5] HSCMT Co., LTD, Korea, Rep. of

ABSTRACT

In this study, computational analysis of ultrasonic flowmeter was performed with regularized lattice Boltzmann method (RLBM). Because RLBM has the advantage of having explicit properties, parallel computing using general-purpose computing on the graphics processing unit (GPGPU) can significantly reduce computational time. A grid-convergence test was first conducted to find the minimum grid resolution required for ultrasonic wave calculation using RLBM. Based on the time-transit method, computational analyses of ultrasound flow meter were performed for various conditions of uniform velocity flow, wall-bounded shear flow, and grid-generated turbulent flow. The present computational method yields an error of about 3-5% for uniform velocity and wall-bounded shear flow conditions. However, in the grid-generated turbulent condition, the error is larger than in the previous cases. The computational results seem to indicate that the time difference of ultrasound arrival was highly influenced by the interaction of ultrasound waves with complex flow such as turbulence.

Keywords: Ultrasonic flow meter, Ultrasound, Lattice Boltzmann method (LBM), GPGPU

1. INTRODUCTION

Ultrasonic flow meter is a device that can measure the flow rate inside the pipe with ultrasonic waves. It is frequently used because of its versatile applications to various fluids with a known speed of sound. In a time-transit ultrasonic flow meter, the velocity of flow is obtained with the time difference between two ultrasonic waves traveling in opposite directions. There have been attempts to analyze ultrasound flow meter computationally. Computational analysis enables us to quantify and visualize the interaction between geometry of the flow meter, flow inside of the tube, and ultrasonic wave. However, ultrasound computation requires high resolution of the mesh, which leads to excessive computational power and calculation time (1). For instance, it is commonly known that around 20 meshes per single wavelength of ultrasound are required to resolve acoustic waves in a field domain. Therefore, resolving 0.5MHz ultrasound in a full-scale ultrasonic flow meter with a diameter of 50mm would require 333 mesh points lengthwise, and thus approximately 3.6×10^7 mesh points in a cubic domain.

In this study, we propose the lattice Boltzmann method (LBM) for calculating ultrasonic waves in a full-scale ultrasonic flow meter. LBM has advantages over traditional computational methods in that it uses a distribution function based on the discretized Boltzmann equation to solve for physical quantities, while adopting an explicit solution procedure. The explicit properties of LBM enable methods to be applied in parallel structures using general-purpose computing in graphics processing units (GPGPUs). The parallelization of the GPU allows simulating ultrasound propagation in the flow meter on a mesh grid size of approximately 1×10^8 in about 10 minutes.

The objectives of this study are to conduct computations for ultrasonic flow meter using LBM and

[1] ryu02129@korea.ac.kr
[2] yjmoon@korea.ac.kr; *corresponding author
[3] envata@naver.com
[4] ieeekim@naver.com
[5] jhkim@hscmt.co.kr

to validate the accuracy of the present computational methods in a full-scale flow meter with uniform velocity flow and wall-bounded shear flow. In addition, it examines the accuracy of the present time-transit method with grid-generated turbulent flow.

2. NUMERICAL METHODS

2.1 Lattice Boltzmann Method (LBM)

Lattice Boltzmann Method (LBM) solves physical quantities such as density and velocity explicitly with a distribution function f (2).

$$f_i(x + c_i\Delta t,\ t + \Delta t) = f_i(x,\ t) + \Omega_i(x,\ t) \tag{1}$$

The most basic LBM method is the Bhatnagar-Gross-Krook (BGK) model with its collision operator Ω shown as follows.

$$\Omega_i(x,\ t) = -\frac{(f_i - f_i^{eq})}{\tau}\Delta t\ , \qquad f_i^{eq} = w_i\rho\left(1 + \frac{u \cdot c_i}{c_s^2} + \frac{(u \cdot c_i)^2}{2c_s^4} - \frac{u \cdot u}{2c_s^2}\right) \tag{2,3}$$

The distribution ideally converges to the equilibrium distribution function f_i^{eq} at a rate determined by the relaxation time τ. The equilibrium function f_i^{eq} is determined by the weight w_i regarding direction, density ρ, velocity u, lattice velocity c_i, and lattice speed of sound $c_s = \sqrt{1/3}$. The calculation consists of a collision and streaming process of distributions through discrete time steps. The time step dt is defined by the speed of sound in lattice unit dv and the unit lattice length dx ($dt = dx/dv$, $dv = 1500 \times \sqrt{3}$ (m/s · lattice speed)). Density and velocity are updated after streaming as follows.

$$\rho = \sum_i f_i\ , \qquad \rho u = \sum_i c_i f_i \tag{4,5}$$

For the grid structure model, the current work selected D3Q19 structure, which uses 19 directions (direction counts denoted as i) to depict the 3D grid domain.

2.2 Regularized Lattice Boltzmann Method (RLBM)

The original LBM using the Bhatnagar-Gross-Krook (BGK) model is unstable in high Reynolds numbers. Therefore, various measures have been proposed to improve stability of the method. One of these measures is the Regularized LBM (RLBM) (3). The RLBM introduces a regularization process to reduce the discrepancy between the non-equilibrium part of distribution function $f_i^{neq} = f_i - f_i^{eq}$ and the first order term of f_i, $f_i^{(1)}$. The regularization process uses the non-equilibrium momentum flux tensor Π^{neq} to obtain $f_i^{(1)}$ and the resulting distribution function after collision f_i^{out}. RLBM reduces the instability to the extent that it can be used to compute ultrasound using LBM.

$$f_i^{(1)} = \frac{w_i}{2c_s^4} Q_{i\alpha\beta}\Pi_{i\alpha\beta}^{neq}\ , \qquad f_i^{\text{out}} = f_i^{eq} + \left(1 - \frac{1}{\tau}\right) f_i^{(1)} \tag{6,7}$$

2.3 Immersed Boundary Lattice Boltzmann Method (IB-LBM)

To simulate boundary of the geometry, the current work selects IB-LBM, which is easy to implement with only a CAD geometry export (STL file format in current work) required. IB-LBM utilizes Lagrangian geometry to impose its velocity on the Eulerian field with a velocity correction. The correction procedure is conducted after the update of density and velocity in the normal LBM procedure. As a way for the velocity correction, multi direct-forcing method proposed by Kang (4) and modified version of direct-forcing method by Li (5) was used in this study. Density and velocity at the position of Lagrangian nodes are interpolated by the surrounding Eulerian nodes, using the discretized Dirac delta function (denoted $D(x_E - x_L)$).

$$\rho_L = \sum_i \rho_E\, D(x_E - x_L)(\Delta x)^d\ , \qquad (\rho u)_L = \sum_i (\rho u)_E\, D(x_E - x_L)(\Delta x)^d \tag{8,9}$$

These interpolated properties are used to obtain the external force needed from Lagrangian points to Eulerian points to impose wanted velocity from the boundary, where u_s denotes the supposed fluid velocity at a given Lagrangian point.

$$\rho_L u_s = (\rho u)_L + \frac{\Delta t}{2} F_s \tag{10}$$

The external force is then spread out again using the Dirac delta function to be used in velocity correction using the momentum equation for the LBM, where Δs is the length between the Lagrangian points in 2D and area in 3D.

$$F_E = \sum_i F_s \, D(x_E - x_L)\Delta s \quad , \qquad \rho u = \sum_i c_i f_i + \frac{\Delta t}{2} F_E \tag{11,12}$$

The modified velocity is used again to re-modify the velocity for a predefined number of iterations. This iterative procedure is intended to improve accuracy compared to the single-iteration direct forcing. Multi direct-forcing method uses explicit measures to impose a velocity close to that of a given geometry in the field, which is relatively inexpensive compared to implicit methods that require computing inverse matrices of enormous size at every time step. The calculated external force is further used as an external force term using Guo's forcing scheme (6).

3. A SIMPLE HARMONIC ULTRASOUND SOURCE

3.1 Computational Setup

To simulate ultrasonic acoustic wave in water with LBM, appropriate level of grid resolution is necessary to provide reliable results. A grid-convergence test with ultrasonic wave of 0.5MHz is conducted with maximum amplitude of 1Pa to investigate optimal and yet minimal resolution for simulation. A cubic domain of 3mm is used, and three levels of resolution are tested: 10, 15, 20 grid lengths per single wavelength. The acoustic pressure profile in the center plane is then expressed in logarithmic scale to check for its attenuation rate. The attenuation rate should be -1 log (Pa)/log (m) according to the inverse square law.

3.2 Grid-convergence test results

Figure 1 shows the computed three-dimensional acoustic pressure at the center plane of a test case with 20 grids per wavelength. In each test case, four crests are compared with a dotted line with an inclination of -1 log (Pa)/log (m) and these results are presented in Figure 2. The first case with 10 grids per wavelength clearly shows that it does not match the correct attenuation rate. The second case of 15 grids per wavelength shows a huge improvement, but the magnitude of the last crest is slightly off the line indicating that the minimal resolution is close to this second test case. The last case of 20 grids per wavelength matches perfectly with the line of the correct attenuation rate. Therefore, it can be concluded that the minimal resolution for simulating 0.5MHz is between 15 to 20 grid lengths per single wavelength.



Figure 1 – Acoustic pressure distribution of center plane depicted in 3D

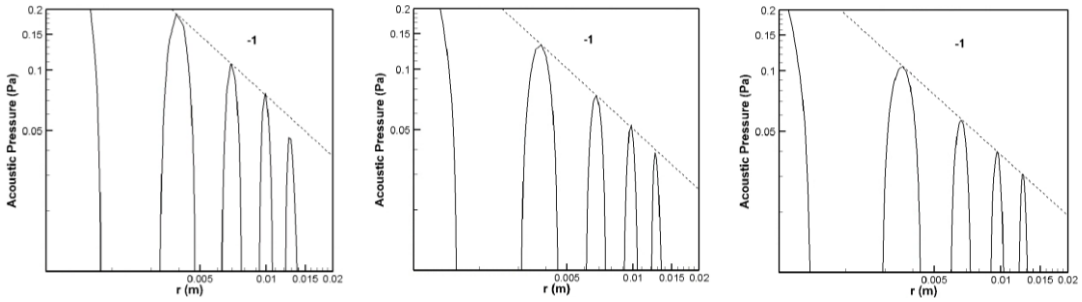


Figure 2 – Acoustic pressure (Pa) versus radius (m) in logarithmic scale. (Left) Resolution of 10 grids per wavelength. (Middle) Resolution of 15 grids per wavelength. (Right) Resolution of 20 grids per wavelength.

4. COMPUTATION OF ULTRASONIC FLOW METER

4.1 Computational Setup

In ultrasonic flowmeters, ultrasonic pulses are generated from one actuator to the other receiver. A pulse is then generated in reverse to measure the time difference of arrival between the two cases. The time difference obtained with two simulations is then used to calculate the flow velocity. Computational simulations are performed in a parallel multi-GPU platform to measure the difference in pulse arrival times for various flow conditions in an ultrasonic flow meter.

In the present computation, the diameters of the flowmeter and actuator are 53.5mm and 16mm, respectively. And physical properties of water such as kinematic viscosity (1.2×10^{-6} m^2/s) and speed of sound (1500 m/s) are used. A computational domain of $54.08 \times 75.84 \times 96$ (mm) is used with a grid size of $339 \times 475 \times 601$ to simulate a full-scale ultrasonic flow meter. In computations, ultrasound wave of 0.5MHz is simulated with 18.75 grids per wavelength.

The actuator is simulated using the IB-LBM, where the actuator moves according to the frequency of the ultrasound. The travelling distance of the pulse is 81mm, and the angle of the actuator and receiver with respect to the axial direction is 40°. Three consecutive pulses are generated at the actuator to obtain time differences more consistently, and a sponge layer is used to avoid any reflections of waves from the inlet and outlet boundaries. In the present computational analyses, four flow conditions are tested: quiescent, uniform velocity, wall-bounded shear, and grid-generated turbulence.

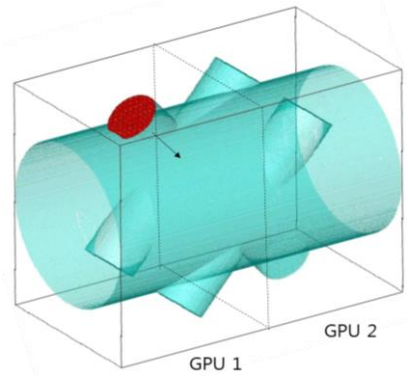


Figure 3 – Computational domain of ultrasonic flow meter simulation. Actuator is colored in red

4.2 Quiescent Flow

Ultrasound simulation in a quiescent condition is conducted to serve as a reference. Figure 4 shows ultrasound waves at different instances at 6.15×10^{-6} s, 2.46×10^{-5} s, and 5.54×10^{-6} s. It shows ultrasound wave propagations, reflections from the side walls, and scattering of waves in the flow meter. Any reflection of waves at the inlet and outlet boundaries are avoided by the sponge layer boundary condition applied to the inlet and outlet boundaries.

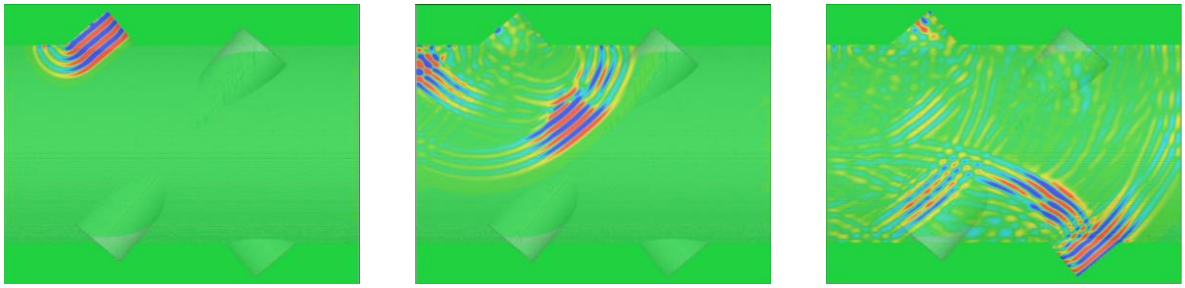


Figure 4 –Ultrasound waves at different instances (at 6.15×10^{-6} s, 2.46×10^{-5} s, 5.54×10^{-6} s)

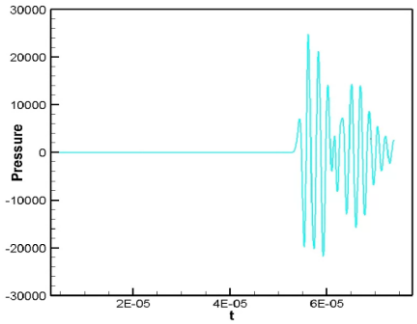


Figure 5 – Pressure probed at the center of the receiver, versus time

Figure 5 shows the pressure probed at the center of the receiver over time. The first three pulses in the figure are the initially generated pulses and the following pulses are produced by reflections from the side wall. Note that the wavefronts of the three first generated pulses are not affected by any geometric disturbances before reaching the receiver.

4.3 Uniform Velocity Flow

A uniform velocity flow of 0.5m/s is tested to verify the accuracy of the ultrasound simulation by measuring the time difference of pulse arrival between opposite directions. Due to the structure of the cavities, there is some pressure and velocity disturbance in the flow, as shown in Figure 6 (left). Since the velocity is not uniform along the path of the ultrasound waves, it is necessary to find the reference average velocity in the direction of wave travel. The reference average velocity along the pathway of the wave is obtained as 0.445m/s by integrating the velocity profile shown in Figure 6 (right).

Figure 7 shows the pressure probed at the center of the receiver, which clearly shows a phase shift created by two ultrasound waves travelling in the opposite directions. The calculated time difference is 2.0×10^{-8}(s), from which the velocity is obtained as 0.432m/s. The computational result is consistent with the physical relationship between the time difference and the flow velocity calculated from the transit time, and an error between the computed and averaged velocities is 2.92%. It clearly shows that the cavity effect is negligible except for the decrease in mean velocity. This also proves that the current grid resolution setting is applicable to simulate the ultrasound wave of 0.5MHz.

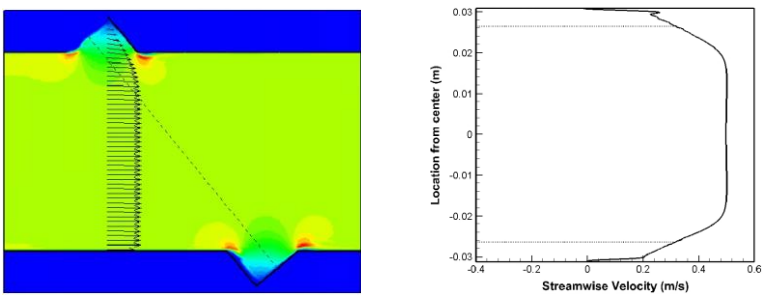


Figure 6 – (Left) Velocity profile on the center plane of the flow meter. The dotted line indicates the centerline of the path. (Right) Streamwise direction velocity (m/s) on the centerline of the path, versus vertical distance (m) across the flow meter. The location of cavity is indicated by dotted lines.

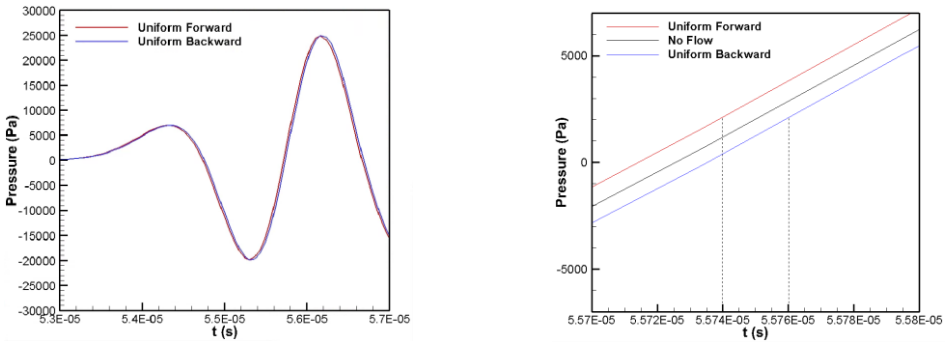


Figure 7 – Pressure probed at the center of the receiver, versus time. The time difference between the two cases is 2.0×10^{-8}(s).

4.4 Wall-bounded Shear Flow

A wall-bounded shear flow is computed with the same procedure. In this case, the imposed flow velocity is maximum at the centerline, which is 0.245m/s. This case is to investigate the effect of continuously varying flow velocity on the transit time of ultrasound (see Figure 8 (left)). The average velocity along the path is obtained as 0.130m/s by integrating the velocity profile shown in Figure 8 (right). Figure 9 shows the pressure probed at the center of the receiver and clearly shows a phase shift created by two waves traveling in opposite directions. The calculated time difference is 0.63×10^{-8}(s), from which the velocity is obtained as 0.136m/s. The error between the computed and the reference velocities is found to be 4.62%. The slightly increased error compared to the previous case indicates that the non-uniform velocity along the path interferes with propagation of the ultrasonic waves. Note, however, that the interaction between the non-uniform flow and the ultrasound wave is not so significant, and this is due to the fact that the flow is symmetric about the centerline so that the downstream and the upstream propagating waves have the same time-shifting delay effect.

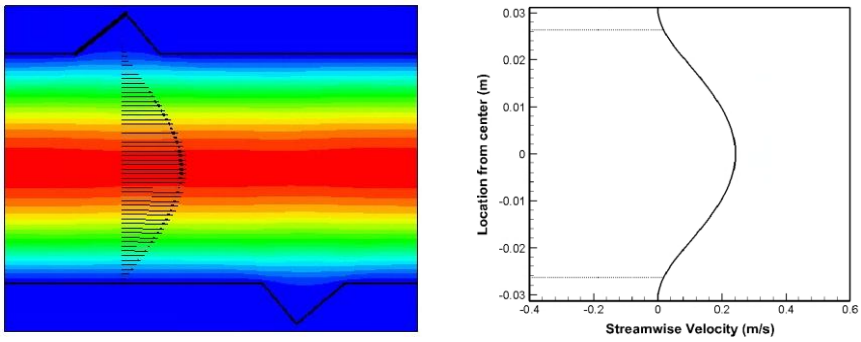


Figure 8 – (Left) Velocity profile on the center plane of the flow meter. (Right) Streamwise direction velocity (m/s) on the centerline of the path, versus vertical distance (m) across the flow meter. The location of cavity is indicated by dotted lines.

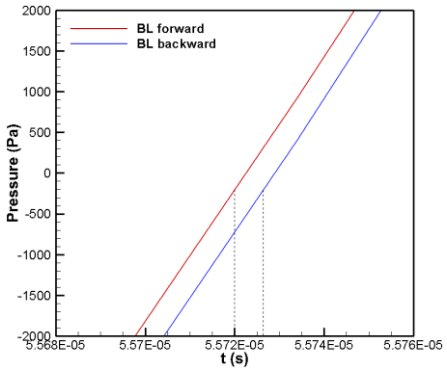


Figure 9 – Pressure probed at the center of the receiver, versus time. The time difference between the two cases is 0.63×10^{-8}(s).

4.5 Grid-generated Turbulent Flow

A grid-generated turbulent flow is computed to investigate the effect of turbulence generated by structural disturbances on ultrasound waves. The diameter of a cylindrical grid structure is 5mm and the distance between the grid structures is 5.6mm. The undisturbed velocity is 0.14m/s and the Reynolds number of the flow is 583 based on the grid diameter. Figure 10 (top left) shows the grid turbulence generated by the grid structure inside the flow meter.

Figure 10 (top right, bottom) clearly shows that the velocity field is highly three-dimensional and non-uniform in both the streamwise and cross-sectional directions, which is strongly affected by the grid turbulence. Table 1 shows the average velocities of seven different cross-sectional slices of planes (indicated by dotted lines on Figure 10 (top right)). Note that the average velocity of a cross-sectional slice is obtained with velocities along the three different paths. The reference average velocity is found to be 0.132m/s, that is, the average of the velocities in Table 1. Note also that this average velocity is different from the reference velocity of 0.14m/s.

As shown in Figure 11, the measured time difference from the pulses is 0.73×10^{-8}(s), from which the velocity is obtained as 0.158m/s. The difference between the computed and the average velocities is 19.7% and that between the computed and reference velocities is 12.9%. Both are larger than in the previous cases for several reasons. One of the reasons is that ultrasound propagation is influenced by the complex flow of turbulence, in which the wavefront of the ultrasonic wave is distorted by the three-dimensional turbulence. Furthermore, the downstream and upstream propagations of ultrasound wave are noticeably different due to the random nature of the turbulent eddies.

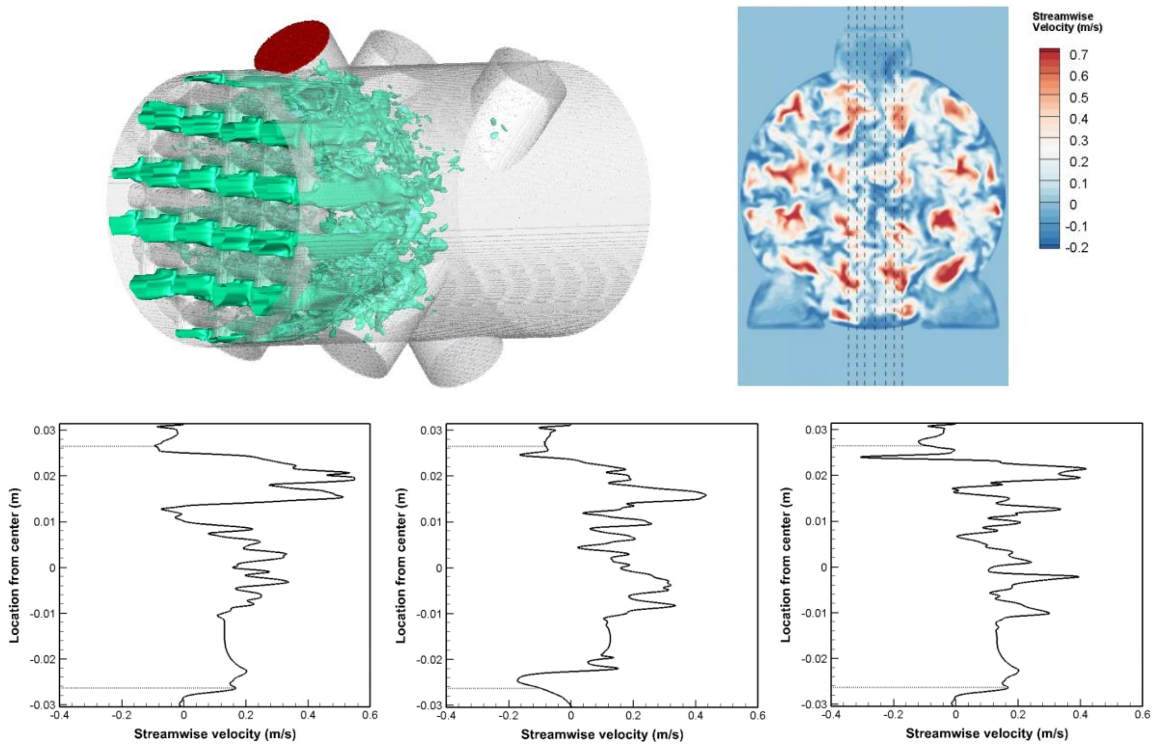


Figure 10 – (Top left) Velocity iso-magnitude surfaces of the grid turbulences. (Top Right) Streamwise velocity profile on a perpendicularly sliced plane at the actuator. (Bottom) Streamwise direction velocities (m/s) along the centerline of the path, versus vertical distance (m) at three cross-sectional slices of planes; -0.0048(m), 0(m) and 0.0048(m). The location of cavity is indicated by a dotted line.

Table 1 – Average velocities from seven different cross-sectional slices of planes

Slice Location, m	-0.0056	-0.0048	-0.0032	0	0.0032	0.0048	0.0056
Average Velocity, m/s	0.155	0.165	0.133	0.0954	0.121	0.124	0.128

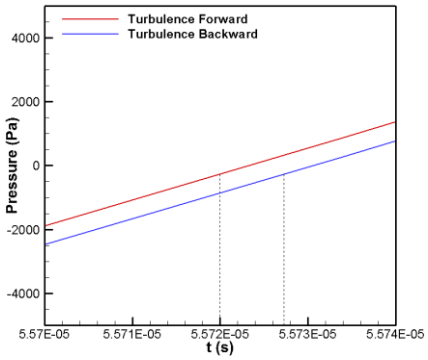


Figure 11 – Pressure probed at the center of the receiver, versus time. The time difference between the two cases is 0.73×10^{-8}(s)

5. CONCLUSIONS

In this computational study, the RLBM computation of ultrasound wave in water was validated by grid-convergence tests. The grid-convergence test shows that at least 15-20 grid points per single wavelength of ultrasound are required to properly simulate the ultrasound waves. The computational results of the ultrasound flow meter show 3~5% error for uniform velocity and wall-bounded shear conditions. On the other hand, the grid-generated turbulent flow condition shows an error of 19.7% between the computed velocity and the velocity averaged in both the wave path direction and cross-sectional direction. The error is 12.9% if the reference velocity of undisturbed flow is used. The relatively large error is due to the fact that grid-generated turbulent flow is fully three-dimensional and velocity field is superimposed with fluctuations of turbulent eddies. The results seem to indicate that the time difference of ultrasound arrival was highly influenced by the interaction of ultrasound waves with complex flow such as turbulence.

ACKNOWLEDGEMENTS

This work was supported by the HSCMT Co., LTD, Korea, Rep. of through the grant (Q2116131).

REFERENCES

1. COMSOL Multiphysics. Ultrasound Flowmeter with Generic Time-of-Flight Configuration.
2. Kruger T, Kusumaatmaja H, Kuzmain A, Shardt O, Silva G, Viggen EM. The Lattice Boltzmann Method., Springer; 2017.
3. Latt J, Chopard B. Lattice Boltzmann Method with regularized non-equilibrium distribution functions. Physical Review Letters. 2005;72.
4. Kang SK, Hassan YA. A comparative study of direct-forcing immersed boundary-lattice Boltzmann methods for stationary complex boundaries. Int. J. Numer. Meth. Fluid; 2011;66.
5. Li Z, Favier J, D 'Ortona U, Poncet S. An immersed boundary-lattice Boltzmann method for single- and multi-component fluid flows. Journal of Computational Physics, Elsevier, 2016;304.
6. Guo Z, Zheng C, Shi B. Discrete lattice effects on the forcing term in the lattice Boltzmann method. Physical Review Letters. 2002;65.

ICA 2022
24th INTERNATIONAL CONGRESS ON ACOUSTICS
October 24(Mon) - 28(Fri), 2022 Gyeongju, Korea

PROCEEDINGS of the
24th International Congress on Acoustics

October 24 to 28, 2022 in Gyeongju, Korea

ABS-0325

Vibro-acoustic shape optimization for radiation problems: Application to compact loudspeakers

Peter Risby Andersen[(1)], Vicente Cutanda Henríquez[(2)], Niels Aage[(3)], Seongyeol Goo [(4)], Junghwan Kook[(5)]

[(1)]Audio Research, GN Audio A/S & Jabra, Denmark, prandersen@jabra.com

[(2)]Centre for Acoustic-Mechanical Micro Systems, Department of Electrical and Photonics Engineering, Technical University of Denmark, Denmark, vcuhe@dtu.dk

[(3)]Centre for Acoustic-Mechanical Micro Systems, Department of Civil and Mechanical Engineering, Technical University of Denmark, Denmark, naage@mek.dtu.dk

[(4)]Innovative SMR System Development Division, Korea Atomic Energy Research Institute, Republic of Korea, ksy1124@kaeri.re.kr

[(5)]Audio Research, GN Audio A/S & Jabra, Denmark, jkook@jabra.com

ABSTRACT

Shape optimization is a promising tool for improving and guiding the design of computationally large-sized vibro-acoustic devices such as compact loudspeaker systems and hearing aids. Typically, such devices are subject to unwanted structural vibrations that can degrade the acoustic performance, i.e., contributing with destructive and constructive interference or creating feedback problems. Numerical-based shape optimization can potentially help engineers to limit or control these vibrational effects. This work presents i) a method to perform gradient-based vibro-acoustic shape optimization and ii) an investigation of the impact of different cost function formulations. The shape optimization framework is based on a coupled vibro-acoustic Finite Element and Boundary Element utilizing a Free Form Deformation parametrization approach. The framework will be used to control the acoustic radiation characteristics of vibrating structures, having the design of compact loudspeakers in mind. When performing shape optimization, a difficult task is to formulate appropriate cost functions that can create well-performing designs in a broadband frequency range. Therefore, the work will discuss different cost function definitions, mainly focusing on manipulating the directivity performance of the acoustic radiation from vibrating structures.

Keywords: loudspeakers, shape optimization, boundary element method, free form deformation

1 INTRODUCTION

This work presents the application of shape optimization for the design of vibro-acoustic devices, with the focus on the design of compact loudspeaker systems such as speakerphones. Speakerphones are communication devices used for online conference meetings typically with multiple participants in a single meeting room. They consist of a loudspeaker system used to radiate sound to the meeting participants and several microphones to pickup speech signals. It is often a requirement that speakerphones should be portable. Hence, it is desirable to make them light and compact. Therefore, their cabinets are typically constructed from e.g. thin plastic materials. A potential shortcoming of this is that not only will the loudspeaker unit vibrate, the cabinet can also vibrate and create unwanted interference in the acoustic signal. Also, microphones mounted on the cabinet might vibrate and therefore deteriorate the voice pickup performance.

Shape optimization based on a full vibro-acoustic discription of the loudspeaker system can be used to alter and improve the acoustic characteristics. Several examples of the utilization of shape optimization within the

area of acoustics exist. Especially, the optimization of horn loudspeakers has been studied [1, 2, 3]. Also, shape, material and topology optimization have been applied to conventional loudspeaker design [4, 5, 6]. Additionally, vibro-acoustic parameter and level-set based shape optimization have also been applied improve the performance of hearing instruments [7, 8].

In the following, the implementation of a full vibro-acoustic model of a quarter symmetric loudspeaker system is presented. To simplify the modelling of the loudspeaker unit, the model includes a partially lumped element modelling (LPM) approach of the loudspeaker magnet, basket and spider. Typically, the loudspeaker unit in a speakerphone is not free of exterior objects in front of the loudspeaker, i.e., often a speaker grill, fabric, or other obstructions are affecting the loudspeaker unit. Here, the presented model will also include an acoustic lens that is placed in front of the loudspeaker unit. The lens is used to control the sound field, but also protect the loudspeaker unit. The underlying numerical modelling approach is mainly based on a structural and acoustic Finite Element Method (FEM) description with an acoustic-acoustic coupling between the FEM and the Boundary Elemement Method (BEM) to fulfill the exterior radiation conditions. Hereafter, the geometry is parameterized based on a cylindrical Free Form Deformation (FFD) approach. Finally, the FFD approach is used to optimize the acoustic lens and cabinet shape.

2 LOUDSPEAKER GEOMETRY, MATERIAL AND BOUNDARY CONDITIONS

To reduce the computational burden, the model of the loudspeaker is based on a quarter symmetric description. The structural part of the loudspeaker system is shown in Figure 1a. In the figure, the gray domain represents the cabinet and the lens geometry, the black domain is the loudspeaker surround, the blue domain is the loudspeaker diaphragm, and the green domain is the dustcap. Moreover, the dark red surfaces in Figure 1a are the surfaces where symmetry boundary conditions are applied. To simplify the modeling of the loudspeaker unit the remaining parts (voice-coil, basket, magnet and spider) are simply modeled through a lumped model. The lumped model creates two forces, a surface force acting on the cabinet through the reaction force from the basket and an edge force from the voice-coil applied to the edge connecting the diaphragm and the dustcap. Figure 1b shows the location of the surface force (purple surface) and the edge force (red line). The development of the lumped model is further described in Section 5. The structural material parameters used to model the cabinet, surround, diaphragm and dustcap are given in Table 1. Also, the surface of the loudspeaker at $z = 0$ has a fixed displacement boundary condition.

Table 1. The material properties used to model the loudspeaker system

Parts	Young's modulus (GPa)	Density (kg/m^3)	Loss factor	Poisson's ratio
Cabinet and lens	2.34	1190	0.019	0.35
Surround	0.023	67	0.04	0.45
Diaphragm	10	10	0.04	0.42
Dustcap	2.62	1050	0.04	0.37

3 VIBRO-ACOUSTIC FEM AND BEM MODEL OF THE LOUDSPEAKER

The underlying model of the loudspeaker is based on a FEM description of both the mechanical parts of the loudspeaker, but also the interior and exterior acoustic domains are modelled with the FEM. However, to fullfill the Sommerfeld radiation condition the exterior acoustic FEM domain is coupled to the BEM. Applying classical Galerkin FEM assuming the solution to be time-harmonic, the matrix equations for the mechanical domains become

$$\left((1+i\eta)\mathbf{K}_s - \omega^2\mathbf{M}_s\right)\mathbf{u} = \mathbf{f}_s, \tag{1}$$

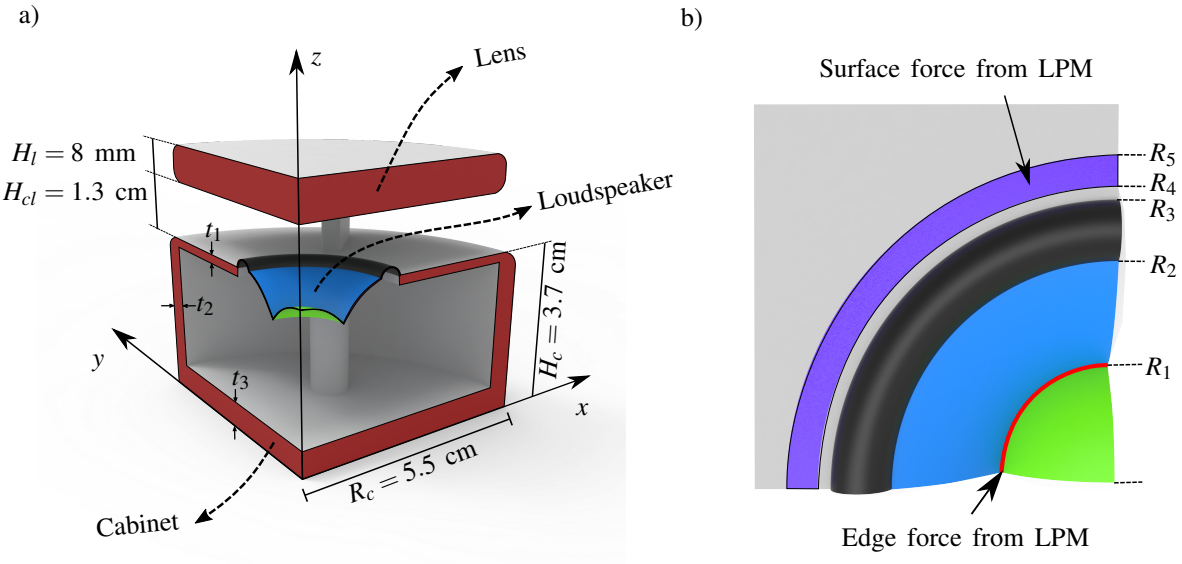


Figure 1. The structural part of the initial loudspeaker geometry. In the figure, a) is the entire structural part of the geometry and b) is a top view of the loudspeaker excluding the acoustic lens. Figure a .Figure b) also includes the location of the lumped element force conditions derived in Section 5. The size of the loudspeaker unit is given by the radii $R_1 = 9.5$ mm, $R_2 = 18$ mm, $R_3 = 22.9$ mm, $R_4 = 23.9$ mm and $R_4 = 26.4$ mm. Moreover, the thicknesses of the cabinet are given by $t_1 = 2$ mm, $t_2 = 5$ mm and $t_3 = 6$ mm.

where $\mathbf{K}_s$ and $\mathbf{M}_s$ are the mechanical stiffness and mass matrices, respectively. Moreover, the angular frequency is given by ω, $\mathbf{u}$ is the displacement vector, η is the stiffness proportional isotropic damping factor and $\mathbf{f}_s$ is the load vector. Similarly, the acoustic finite element domains can be described in matrix form as

$$\left(\mathbf{K}_f - \omega^2 \mathbf{M}_f\right)\mathbf{p} = \mathbf{S}\frac{\partial \mathbf{p}}{\partial n}, \tag{2}$$

where $\mathbf{K}_f$ is the acoustic stiffness matrix, $\mathbf{M}_f$ is the acoustic mass matrix, $\mathbf{p}$ is a vector with the acoustic pressure, $\mathbf{S}$ is the boundary mass matrix and $\frac{\partial \mathbf{p}}{\partial n}$ is a vector with the surface normal derivative of the acoustic pressure. The mechanical and acoustic coupling is performed using conformal mapping with the coupling matrix being

$$\mathbf{C}_{sf} = \int_{\Gamma_{sf}} \mathbf{N}_s^{\mathrm{T}} \mathbf{n} \mathbf{N}_f \mathrm{d}\Gamma_{sf}, \tag{3}$$

where $\mathbf{N}$ is the shape function matrix with the subscripts s and f representing either the structural or the fluid domains, respectively. Integration is carried out on the surface interface between the fluid and the structure,i.e. , Γ_{sf}. The model is extended to include exterior radiation conditions by an acoustic FEM-BEM coupling. Applying classical collocation BEM of the Helmholtz equation, the boundary element matrices can be written as

$$\mathbf{H}\mathbf{p} - \mathbf{G}\frac{\partial \mathbf{p}}{\partial n} = 0 \tag{4}$$

where $\mathbf{H}$ and $\mathbf{G}$ are the matrices arising from the double and single layer potentials, respectively. It should be noted that the BEM kernels are created from the assumption of quarter symmetry and an infinite baffle at $z = 0$. The acoustic FEM and BEM coupling is achieved by assuming continuity between $\mathbf{p}$ and $\frac{\partial \mathbf{p}}{\partial n}$. Hereby, it is possible to assemble a fully coupled system of equations for the vibro-acoustic behaviour as

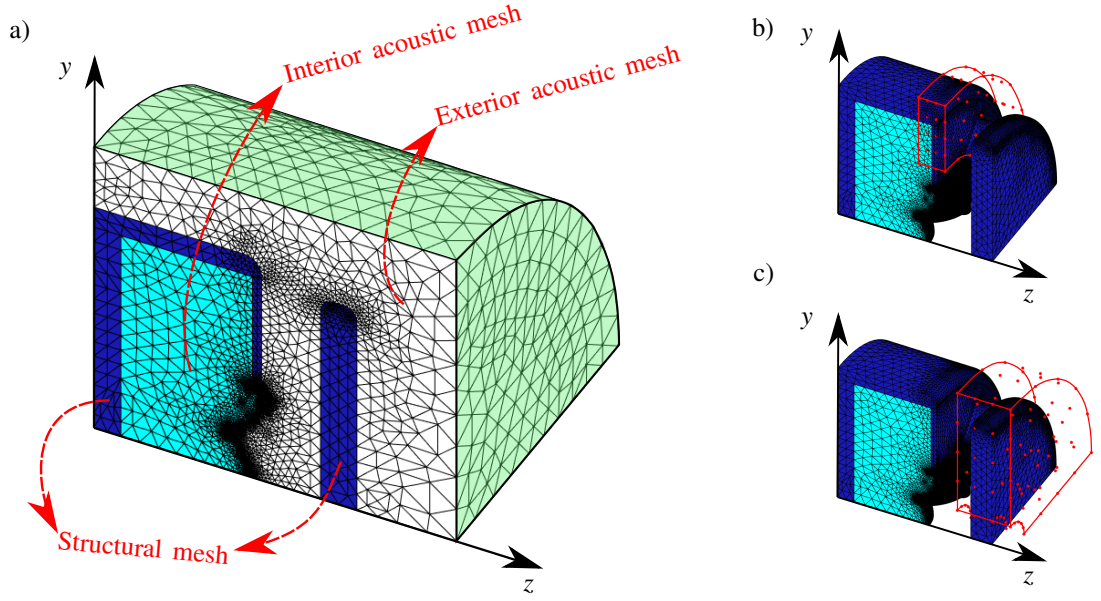


Figure 2. The computational mesh (a) and the FFD parametrization of the cabinet (b) and the lens (c). It should be noted that (b) and (c) exclude the exterior acoustic FEM mesh. However, this is done for visualization purposes, and the mesh is included and mapped to the FFD parametrization.

$$\mathbf{Q}_{sys}\mathbf{x} = \begin{bmatrix} \mathbf{A}_s & -\mathbf{C}_{sf} & \mathbf{0} \\ -\omega^2\rho_f\mathbf{C}_{sf}^{\mathrm{T}} & \mathbf{A}_f & -\mathbf{S}_b \\ \mathbf{0} & \mathbf{H} & -\mathbf{G} \end{bmatrix} \begin{bmatrix} \mathbf{u} \\ \mathbf{p} \\ \frac{\partial \mathbf{p}}{\partial n} \end{bmatrix} = \begin{bmatrix} \mathbf{f}_s \\ \mathbf{0} \\ \mathbf{0} \end{bmatrix} \tag{5}$$

where the stiffness and mass matrices from the structural and acoustic domains are condensed into the matrices A_s and A_f, respectively. Also, ρ_f is the density of air originating from utilizing Euler's relation and $\mathbf{S}_b$ is the boundary mass matrix evaluated at the FEM-BEM coupling surface. The finite element matrices are implemented within MATLAB and the assembly of the BEM matrices rely on a compiled C++/MEX implementation discussed in the Refs. [10, 11]. For the particular problem, the matrices are stored as sparse matrices and solved using the MUltifrontal Massively Parallel sparse direct Solver (MUMPS). It should be noted that this approach is only reasonable for problems where the BEM matrices are relatively small. The meshed geometry is shown in Figure 2a, where the dark blue, cyan and white domains are the structural, interior acoustic, and exterior acoustic finite element domains, respectively. The two light green surfaces correspond to the location of the acoustic-acoustic coupling between FEM and BEM. The complete mesh consists of 83135 quadratic tetrahedral elements.

4 PARAMETRIZATION USING FREE FORM DEFORMATION

The geometry is parameterized using FFD in cylindrical coordinates similar to the approach in Ref. [11] where Bernstein polynomials are used as basis functions. Here, two FFD regions are created; a region controlling the the shape of the lens (Figure 2c) and a region controlling the shape of the top of the loudspeaker cabinet (Figure 2b). For simplicity the control points in the FFD regions are only allowed to move in the z-direction. Also, to avoid unacceptable mesh deformations only control points inside the FFD region are free to move, i.e., the control points on the outer sides of the FFD region remain fixed. Moreover, the control points are only allowed to move ± 8 mm and ± 6 mm in the FFD regions respectively covering the lens and the cabinet. In total, the optimization problem consists of 72 design variables.

5 PARTIALLY LUMPED LOUDSPEAKER

To simplify the overall numerical model, some parts of the loudspeaker driver are modelled using LPM. In this case, the basket and the motor system of the driver are lumped to describe the forces acting on the loudspeaker diaphragm and the cabinet. From an impedance based derivation, the following two equations can be formulated

$$Z_{cone} v_{1,z} = F_{v_{1,z}} = F_0 - Z_T \left(v_{1,z} - v_{2,z}\right) - Z_{M_c} v_{1,z}, \tag{6}$$

$$Z_{box} v_{2,z} = F_{v_{2,z}} = Z_T \left(v_{1,z} - v_{2,z}\right) - F_0 - Z_{M_{m,ch}} v_{2,z}. \tag{7}$$

Here, $F_{v_{1,z}}$ is the total force applied to the edge connecting the diaphragm and the dust cap, and $F_{v_{2,z}}$ is the total force acting on a surface on top of the cabinet. Also, F_0 is the driving force, $Z_{M_{m,ch}}$, Z_{M_c} and Z_T are mechanical impedances, and Z_b is an electrical impedance. In Eqs. (6) and (7), the different forces and impedances are given by the lumped elements as

$$F_0 = \frac{Bl V_0}{Z_b}, \qquad Z_T = \frac{1}{i\omega C_c} + \frac{Bl^2}{Z_b}, \qquad Z_{M_c}, = i\omega M_c,$$

$$Z_{M_{m,ch}} = i\omega \left(M_m + M_{ch}\right), \qquad Z_b = \frac{\omega^2 L_2^2 R_2 + i\omega L_2 R_2^2}{\omega^2 L_2 R_2^2} + R_e + i\omega L_e.$$

In the above equations, $Bl = 2.558$ Wb/m is the force factor, $V_0 = \sqrt{8}$ V is the driving voltage, $R_e = 2.61$ Ω is the electrical voice coil resistance at DC, $L_e = 8.5 \cdot 10^{-5}$ H is the frequency independent part of the voice coil, $L_2 = 8.1 \cdot 10^{-5}$ H is the para-inductance of the voice coil, $R_2 = 0.67$ Ω is the electrical resistance due to eddy current losses, $M_m = 0.0434$ kg is the mass of the magnet, $M_{ch} = 3.47$ g is the mass of the loudspeaker chassis, and $C_c = 0.0025$ m/N is the compliance of the spider. The loudspeaker geometry and the location of the two forces are depicted in Figure 1b. In Eqs. (6) and (7), the velocities $v_{1,z}$ and $v_{2,z}$ represent the average velocity on the edge or surface, respectively. The average velocities are given from the shape functions as

$$v_{1,z} = i\omega \frac{\mathbf{N}_{s,z,1}}{L}\mathbf{u} \quad \text{and} \quad v_{2,z} = i\omega \frac{\mathbf{N}_{s,z,2}}{A}, \mathbf{u} \tag{8}$$

where L and A are the length and the area of the interface where the total force is applied, respectively. Also, the subscript z denotes that the shape functions only describe the z-component of the displacement. Substitution of the forces into the right-hand-side of the Eq. (5), yield

$$\mathbf{f}_{s,1} = \mathbf{N}_{s,z,1}^T \frac{F_0}{L} - i\omega Z_T \left(\mathbf{N}_{s,z,1}^T \frac{\mathbf{N}_{s,z,1}}{L^2} - \mathbf{N}_{s,z,2}^T \frac{\mathbf{N}_{s,z,2}}{A^2}\right)\mathbf{u} - i\omega Z_{M_c} \mathbf{N}_{s,z,1}^T \frac{\mathbf{N}_{s,z,1}}{L^2}\mathbf{u}, \tag{9}$$

$$\mathbf{f}_{s,2} = i\omega Z_T \left(\mathbf{N}_{s,z,1}^T \frac{\mathbf{N}_{s,z,1}}{L^2} - \mathbf{N}_{s,z,2}^T \frac{\mathbf{N}_{s,z,2}}{A^2}\right)\mathbf{u} - i\omega Z_{M_{m,ch}} \mathbf{N}_{s,z,2}^T \frac{\mathbf{N}_{s,z,2}}{A^2}\mathbf{u} - \mathbf{N}_{s,z,2}^T \frac{F_0}{A} \tag{10}$$

where

$$\mathbf{f}_s = \mathbf{f}_{s,1} + \mathbf{f}_{s,2}. \tag{11}$$

Rearranging, the system of equations for the structural part in Eq. (5) becomes

$$\left(\mathbf{A}_s + i\omega \left(\mathbf{D}_1 + \mathbf{D}_2\right)\right)\mathbf{u} = \mathbf{N}_{s,z,1}^T \frac{F_0}{L} - \mathbf{N}_{s,z,2}^T \frac{F_0}{A}, \tag{12}$$

where $\mathbf{D}_1$ and $\mathbf{D}_2$ contains the terms in Eqs. (9) and (10) which are multiplied with $\mathbf{u}$. A verification of the implementation is shown in Figure 3 where the SPL frequency response at the field point (0,0,1) m is computed and compared with a similar implementation in the simulation software COMSOL Multiphysics. The result shows a good agreement between the in-house implementation and the commercial simulation tool. It should be noted that the approach has been tested against a full vibro-acoustic model of the same loudspeaker driver showing reasonable agreement between the partially lumping approach and a full model, but with less computational effort. Nevertheless, the lumping approach might become less accurate at higher frequencies.

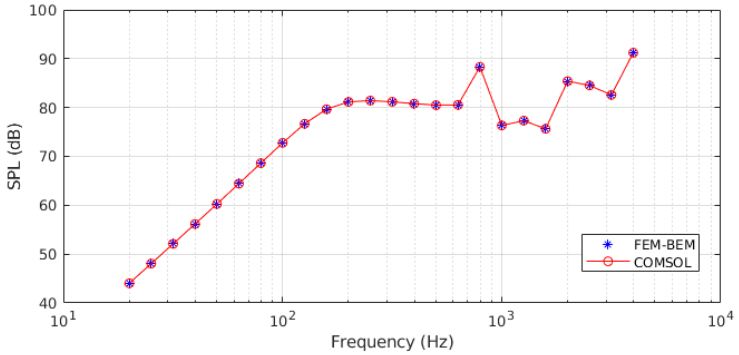


Figure 3. Comparison between the custom MATLAB C++/MEX FEM-BEM implementation and a similar implementation in the simulation tool COMSOL multiphysics. The SPL is evaluated at the field point (0,0,1) m.

6 OPTIMIZATION PROBLEMS

Two different cost functions are investigated. The first cost function is trying to direct the exterior acoustic energy to a specific direction, more specifically the pressure magnitude is maximized at the field point (0.82, 0, 0.57) m. The second cost function minimizes the difference between a target pressure and the pressure magnitude in the field point in an attempt to flatten the frequency response. A potential way to formulate this is by using the two cost functions given by

$$\phi_{k,1} = -|p_i|^2 \quad \text{and} \quad \phi_{k,2} = (T_p - |p_i|)^2 \tag{13}$$

where k indicates that the cost function is evaluated at the k-th frequency, p_i is the complex pressure at the field point, and $T_p = 0.3$ (corresponds to a SPL of 80.5 dB) is the target pressure magnitude. The design sensitivities are obtained following the semi-analytical adjoint approach in Ref. [11]. For multi-frequency optimization it is still an open research question how to formulate good performing cost functions and optimization approaches. However, unpublished research indicate that using a minimax formulation is a good candidate. Therefore, the cost functions are minimized using the minimax formulation in the MATLAB function *fminimax*. For both test cases the optimization is performed at 5 discrete frequencies logarithmically spaced between 1 kHz and 3 kHz.

7 OPTIMIZATION RESULTS

The results of the two shape optimization cases are shown in Figure 4. Figure 4a and 4b show the SPL frequency responses for the designs obtained using $\phi_{k,1}$ and $\phi_{k,2}$, respectively. The figures also includes the response of the initial design. As it is observed, it has been difficult for the optimization to drastically change the overall behaviour of the responses. This is to some extend attributed to the limited freedom given to control points in the FFD regions. Also, most of the optimization effort is put towards changing the response at 3 kHz. Inspecting the overlayed displacement magnitude at 3kHz seems to indicate that the optimizer uses a combined cabinet and loudspeaker driver resonance to increase the pressure output. At 3 kHz the top of the cabinet is vibrating but also a break-up resonance of the loudspeaker diaphragm can be observed. Even though optimizing with two different cost function definitions gives very similar results, it is observed that the location of the first cabinet resonance (around 800 Hz) can be manipulated as is evident when optimizing with $\phi_{k,1}$. Hence, it might be interesting to focus the optimization to this region.

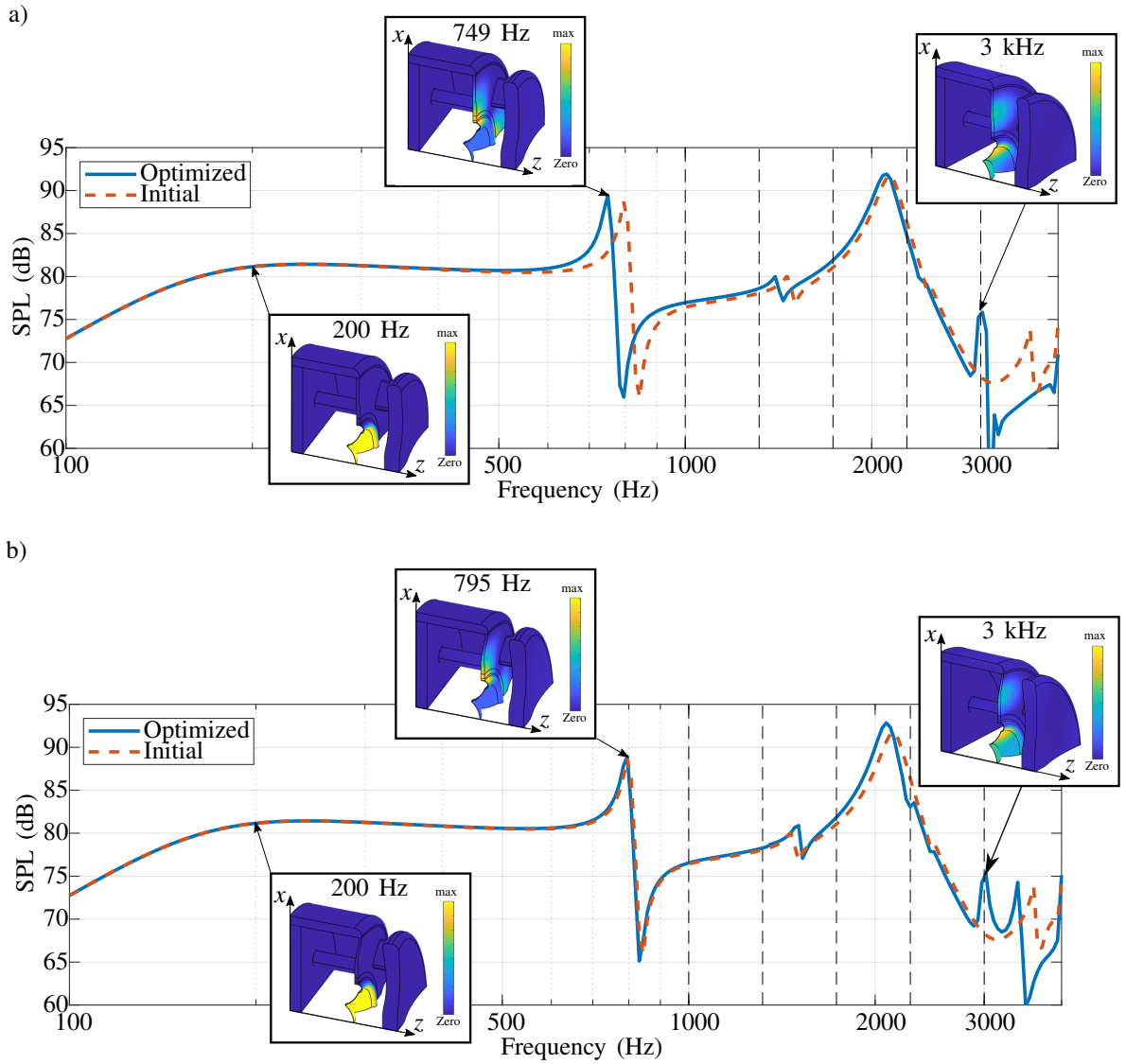


Figure 4. The SPL frequency response of optimized designs and the initial design. In the figure, a) and b) are the frequency responses of the designs optimized using $\phi_{k,1}$ and $\phi_{k,2}$, respectively. The overlaying plots are the magnitude of the z-component of the displacement and the vertical dashed black lines are the optimization frequencies.

8 DISCUSSION AND CONCLUSIONS

This work has presented implementation aspects of a three dimensional full vibro-acoustic shape optimization framework and its application to loudspeaker simulation and optimization. This includes the development of a partially lumping approach of the loudspeaker basket, magnet and spider that reduces the overall computational complexity of the loudspeaker model. Event though the optimization framework is working as intended, the results also showcase some of the many difficulties of broadband vibroacoustic optimization. One of the difficulties is the computational burden of 3D vibroacoustic optimization. For the given optimization problems, each of the optimization cases takes approximately 2 days to complete. Moreover, structural resonance phenomena are very local meaning that a much finer frequency resolution is required as compared

to what is presented here. Even with a fine frequency resolution it might be difficult to change the frequency response. Therefore, it will most likely be required to also play with different materials, damping and stiffening mechanisms, and starting guesses to limit the effect from structural resonances. Also, it has been decided to use a rather conservative range at which the control points in FFD region can move. Albeit increasing the range of the control points can result in more design freedom. However, it also brings the risk of distorting the elements too much. Hence, incorporating a more robust parametrization method such as level-set parametrzaiton perhaps in combination with a cut-element approach might be beneficial. Alternatively, nonlinear constraints can be incorporated that insures a sufficient element quality at all optimization iterations. Another approach is to use re-meshing that ensures sufficient element quality, which would be a technique well suited with FFD as the parameterization and the physics modeling is completely decoupled. Additionally, only two cost functions have been tested, a much larger range of cost functions should be tested in a comparative review, e.g. minimizing the displacement magnitude, directivity index etc.

REFERENCES

[1] Udawalpola R., Wadbro E., Berggren M. Optimization of a variable mouth acoustic horn. (2011) Int J Numer Methods Eng. 85(5) 591-606

[2] Udawalpola R., Berggren M. Optimization of an acoustic horn with respect to efficiency and directivity. (2008) Int J Numer Methods Eng. 73(11) 1571-1606

[3] Schmidt S., Wadbro E., Berggren M. Large-scale three-dimensional acoustic horn optimization. (2016) Siam Journal on Scientific Computing. 38(6) B917-B940.

[4] Bezzola A. Numerical optimization strategies for acoustic elements in loudspeaker design. (2018) Audio Engineering Society, 145th Audio Engineering Society International Convention.

[5] Christensen R. Shape and Topology Optimization of Loudspeaker Drivers. (2020) Proceedings from COMSOL Conference, Grenoble/Online.

[6] Nielsen D. G., Agerkvist F. T., Jensen J. S. Achieving a flat, wideband frequency response of a loudspeaker unit by numerical optimization with requirements on its directivity. (2021) Journal of the Acoustical Society of America. 150(2) 663-672

[7] Creixell Mediante E., Jensen J. S., Naets F., Brunskog J., Larsen M. Adaptive parametric model order reduction technique for optimization of vibro-acoustic models: Application to hearing aid design. (2018) Journal of Sound and Vibration. 424 208-223

[8] Dilgen S. B., Aage N., Jensen, J. S. Three dimensional vibroacoustic topology optimization of hearing instruments using cut elements. (2022) Journal of Sound and Vibration. 532 116984

[9] Sederberg T. Free-form Deformation of Solid Geometric Models. (1986) Computer Graphics. 20(4) 151-160

[10] Andersen P, Kook J, Cutanda Henríquez V, Aage N. Towards large-scale acoustic shape optimization for industrial applications using the boundary element method. Proceedings of 2020 International Congress on Noise Control Engineering, Inter-noise, Soul, South Korea, Online.

[11] Andersen P, Kook J, Cutanda Henríquez V, Aage N. 3D shape optimization of loudspeakers. Proceedings of 2021 International Congress on Noise Control Engineering, Inter-noise, Washington, United States of America, Online.

PROCEEDINGS of the
24th International Congress on Acoustics

October 24 to 28, 2022 in Gyeongju, Korea

ABS-0761

Directivity optimization of MEMS ultrasonic transducers by implementing acoustic horns

Tenia MEISEL[1]; Anton MELNIKOV[1]; Adrian ALEXANDER[1], Tim BRÄNDEL[1], Jorge M MONSALVE[1], Bert KAISER[1], Harald SCHENK[1,2]

[1] Fraunhofer IPMS, Dresden, Germany

[2] BTU Cottbus-Senftenberg, Cottbus, Germany

ABSTRACT

The applications of microscopic ultrasonic transducers are often limited due to their non-optimal directivity pattern. The aim of this work is to design passive structures to adapt the directivity pattern to an intended application, e.g. range finder. The horns were designed and optimized using a Finite-Element-Method (FEM) model and manufactured by a conventional 3d-printing technique. The experimental validation was done using a novel MEMS-based ultrasonic transducer based on lateral actuation developed by Fraunhofer IPMS. This transducer type generates sound waves by displacing air inside a 3x3 mm² silicon chip using microscopic sized beams instead of using a diaphragm. This article presents several horn structures that exhibit a pronounced main lobe, inter alia an exponential horn and a folded horn with reduced overall dimensions, both optimized for an operating frequency of 40 kHz. We have shown numerically and experimentally that directivity properties of the transducer were significantly improved considering peak pressure, reduction of the side lobes and main lobe width by simple horn geometries. The implementation of the designed horns will enable additional applications where a specific directivity pattern is required. Furthermore, the given results imply that the presented design strategies can be used to create various directivity patterns.

Keywords: acoustics, acoustic horn, directivity optimization, ultrasonic transducer, ultrasound

1. INTRODUCTION

Ultrasonic transducers have a wide range of applications in research and industry. They are used, among other things, for gesture recognition, collision warning, non-destructive material testing, and level measurements. Micromachined Ultrasonic Transducers (MUTs), which are fabricated with techniques developed for the microelectronics industry, benefit from a small size and have a better acoustic coupling with the surrounding air than the traditional bulk piezoelectric transducers.

Recently, a new sort of MUT has been developed at Fraunhofer IPMS, which is not based on the vertical ("out-of-plane") deflection of a membrane, but instead it induces a lateral ("in-plane") deflection an array of microbeams (1). A thourough description of this transducer can be found in (2). The core element of this transducer is a thin, rectangular beam placed in front of a fixed electrode that attracts the beam with an electrostatic force once a voltage difference is applied between them. This beam-stator arrangement was laid out in such a way that several beams can be placed next to each other in a single chip while ensuring their electrical connection. Figure 1 shows a layout of the in-plane electrostatic MUT that was analysed in this work.

In a previous study, we analysed the radiation pattern of this ultrasonic device, finding a high agreement of the experimental radiation pattern and that obtained by a COMSOL simulation with the boundary-element method (3). This simulation, which assumed the "subchips" in figure 1 as flat, square pistons led, to the conclusion that the radiation pattern of this ultrasonic device was heavily dependent on the immediate surroundings (i.e. the housing) of the chip, and not on the shape of its elementary beams. This is consistent with the fact that the length of the beams is less than λ/6, they count thus as point sources at the operation frequency. We observed, nonetheless, that at some of the

[1] jorge.mario.monsalve.guaracao@ipms.fraunhofer.de

frequencies of interest there were unwanted minima in the desired propagation direction, as well as undesired side lobes. Therefore, a further step in the design of this device is the enhancement of the directivity by means of passive structures (i.e. acoustic horns).

The aim of this work is to design an acoustic horn as a passive structure that maximizes acoustic pressure of the main lobe and at the same time reduces side lobes, which results in improved sound focusing. Additionally, the horn should not only meet the acoustic requirements, but also the physical ones. These include, above all, minimization of the installation space and simple production. The acoustic horns were designed using the COMSOL Multiphysics software and, in order to determine the accuracy the simulation, a verification experiment was conducted. Finally, this work will give an insight into the possibilities that arise when sound propagation can be manipulated in a desired manner.

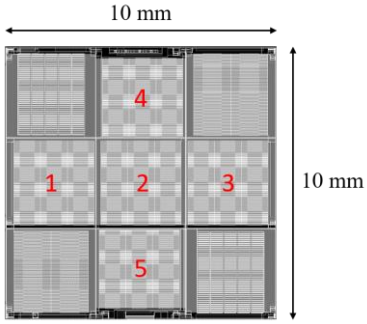


Figure 1 – Layout of the electrostatic in-plane MUT with five independent subchips with an area of 3x3 mm^2, each containing 258 microbeams connected in parallel.

2. METHODS

2.1 The FEM model

To simulate the propagation of the sound waves generated by the transducer and the influence of acoustic horns on its directivity pattern, a Finite-Element-Method (FEM) model was set up using the COMSOL Multiphysics software. Figure 2 shows the model, which was designed in a Cartesian coordinate system, with the point (0,0,0) representing the center of the transducer surface. It resembles the air domain above the transducer in positive z-direction. The implemented acoustic horns are adapted to the shape of the transducer. Within the defined domain of the model the Helmholtz equation in the frequency domain was solved (4, p. 202). Then the model used the Helmholtz-Kirchhoff integral to obtain the acoustic pressure in the exterior field outside of the defined domain (4, p. 214). The sound waves are assumed to be radiating with a frequency of 40 kHz from an infinite baffle toward an open half space.

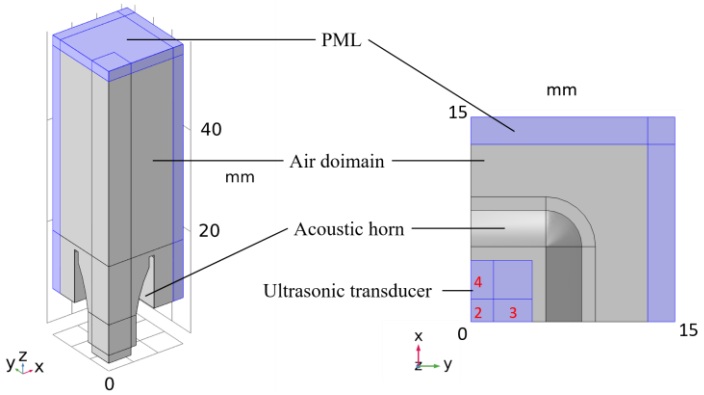


Figure 2 – FEM model of the transducer representing the air domain in positive z-direction.

The sound waves are generated by applying a normal velocity of 1 m/s at the outer transducer surface (Huygens principle, see 5, p. 27), which coincides with the x-y-plane at z = 0. Two different operating cases of the transducer units are used in the simulation: simultaneous operation of all units as a basis for optimization process, and individual operation of unit 2 for comparison purposes between simulation and experiment. The domain was discretized by $\lambda/10$ hexahedral elements with Lagrangian shape function of second order. To reduce the time of calculation a symmetry plane is

defined on the y-z-plane at $x = 0$ and on the x-z-plane at $y = 0$. A Cartesian perfectly matched layer (PML) is defined on the domains that confine the air space. It absorbs the outgoing sound waves in such a way that this artificial termination has no influence on the near field. The

2.2 Analytical design method – The Webster horn equation

Initial approach for a focusing horn design is the one-dimensional Webster horn equation (6, p. 135 and 7, p. 191)

$$\frac{\partial^2 p}{\partial z^2} + \frac{\mathrm{d}(\ln A)}{\mathrm{d}z}\frac{\partial p}{\partial z} = \frac{1}{c^2}\frac{\partial^2 p}{\partial t^2} \tag{1}$$

with acoustic pressure p, speed of sound c and cross section A. It describes the acoustic pressure as a function of the distance from the source for radially symmetrical horn shapes of infinite length and considers the cross section of the acoustic horn. With the approach for an exponential horn we obtain the partial solution for a diverging sound wave emerging from the horn

$$p(z) = p_0 e^{-\frac{az}{2}} e^{-ikz\sqrt{1-\frac{a^2}{4k^2}}} \tag{2}$$

where the parameter $a > 0$ describes the exponential increase of the horn. With constant distance from the radiator z and constant wave number k, equation 2 is now only dependent on the parameter a. Now, the question is for which a the acoustic pressure $p(a)$ becomes a maximum. After differentiation and numerical solving for $z = 100$ mm and k with an operating frequency of $f = 40$ kHz, we obtain

$$a = 1.036 \ \frac{1}{\mathrm{mm}} \tag{3}$$

Equation 3 then results in an exponential horn whose cross section is matched to the shape of the transducer and therefore is not radially symmetric.

2.3 Numerical designs method – The parametric sweep

Another design strategy is the numerical study about the influence of different design properties that define the shape of the horn. The number of parameters that are varied determines the degree of the numerical study. The parameters that currently describe the shape of the acoustic horn are the exponent a and the length of the horn l.

First, based on the initial design from section 2.2, a numerical study was conducted to investigate the influence of an additional tube attachment with length b on the directivity of the acoustic horn. For this purpose, a parameter variation was performed for a and l, respectively for the horn without and the horn with tube attachment. This parameter variation results in a $M \in |a| \times |l|$ matrix. From the results of the simulation, each entry of the matrix, i.e. each parameter combination describing the acoustic horn, can be assigned a value for different directivity metrics under investigation. From the resulting numerical plots of the metrics over the parameter matrices (5, p. 43), we can see the effect of the additional tube attachment on the directivity of the transducer. In addition, we can select the parameter combination that achieves the desired results: a maximization of acoustic pressure of the main lobe and a minimization of acoustic pressure of the first order side lobes.

Next, a parameter variation of higher degree, including the additional tube attachment b as a parameter, was applied. To obtain the parameter combination, which results in a horn that results in the desired directivity of the transducer, a parametric sweep as a build in COMSOL function, is applied. For each parameter, an individual range is specified (i.e. see section 3.4 Parametric sweep horn) in which each parameter is varied in equidistant intervals. To find the most ideal parameter combination in the solution space an evaluation function is applied. It calculates and sorts the directivity metrics for each parameter combination. The resulting vectors assign the value of their index to each parameter combination, so that the combination with the smallest sum represents the optimal solution (see 5, p. 53).

2.4 The folded horn method

Since the Webster horn equation from section 2.2 assumes an infinite long horn, its solution implies that in reality the acoustic pressure increases for longer horns. In order to achieve a further increase of acoustic pressure without enlarging the overall dimensions of the horn, a second opposite exponential horn is introduced into the existing horn (6, p. 424). This inner horn reflects the sound waves inside the horn back to the transducer surface and this way increases the acoustic pressure.

Thus, the sound waves do not have to propagate through a longer exponential horn but the acoustic pressure is increased already in the structure itself. The intended horn design is presented in figure 3.

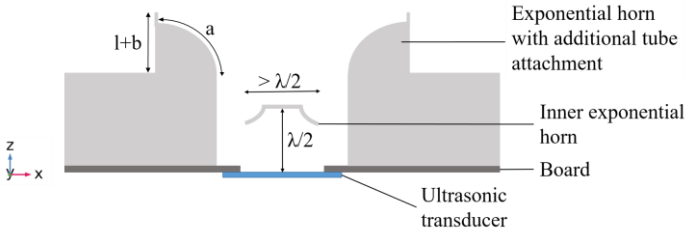


Figure 3 – Basic principle of the folded horn design. The inner horn is positions inside the outer horn with total length $l+b$, l length of the horn and b length of the tube attachment.

To allow the resonances to occur that lead to an increase in acoustic pressure, a multiple of the half wavelength above the transducer surface is chosen for the location of the inner exponential horn. The aperture of the inner horn is chosen bigger than half wavelength, in order to allow an interaction in such a way that reflection and not only diffraction effects occurs between the sound waves generated by the transducer and the inner acoustic horn.

2.5 Experimental Setup

The resulting horns are manufactured using a conventional 3d-printing technique and then attached to the board with the transducer. The measurement signal is generated by an audio analyzer, and is then amplified by a *Krohn-Hite 7602M* amplifier and provided with a constant offset. The sound waves are generated by unit 2 of the transducer only, which is operated at a bias voltage of 30 V and an amplitude voltage of 5 V. The acoustic field is measured with a *Microtech Gefell MM310* free-field microphone, which is amplified by *Microtech Gefell MV310* microphone amplifier. The microphone is positioned oppositely to the transducer with the horn. Then, at a constant distance z, the transducer is rotated by an angle of $\Phi = 360°$ azimuth while the microphone is rotated by an angle $\theta = 59°$ altitude, with the Linear Stage *M-403.8/6DG* and the Precision Rotation Stage *M-060.DG* respectively.

2.6 Directivity metrics

For comparison purposes, different metrics are obtained from the directivity patterns of simulation and experiment. The absolute acoustic pressure p_{ml}, the beam width of the main lobe θ_b and the degree of the first order side lobes p_{ml}/p_{sl}. The absolute acoustic pressure quantifies the acoustic pressure of the main lobe determined at $\Phi = \theta = 0°$, and $z = 100$ mm. The beam width of the main lobe is determined for 6 dB level down from $\Phi = \theta = 0°$. The degree of the first order side lobes is defined by the quotient of the absolute acoustic pressure of the main lobe p_{ml} and the absolute acoustic pressure of the first order side lobe p_{sl}.

3. RESULTS

3.1 No horn

The directivity patterns of normalized acoustic pressure on azimuth Φ at $\theta = 0°$ and $z = 100$ mm shown in figure 4 show a general agreement of simulation and experiment.

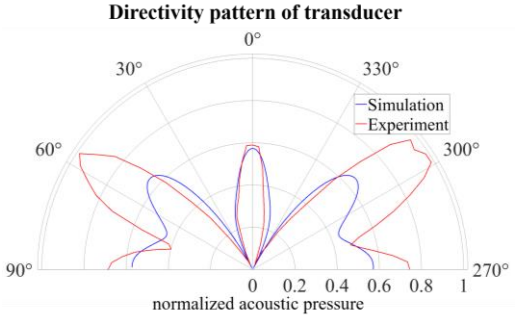


Figure 4 Directivity patterns of the transducer without acoustic horn for FEM simulation and experiment standardized to mean value.

The main lobes align well while the directivity patterns differ in their side lobes. The plot emphasizes the potential for improvement: For both plots, the main lobe shows a lower acoustic pressure than the side lobes that radiate at ±55° from the main lobe. The aim is therefore to minimize or even eliminate the side lobes and to maximize the acoustic pressure of the main lobe.

3.2 Webster horn

To investigate the correlation between the acoustic pressure at $\Phi = \theta = 0°$ and $z = 100$ mm and exponent a, the exponent is varied at constant horn length of 4 mm. The graph for the absolute acoustic pressure p_{ml} dependent on exponent a presented in figure 5a shows a local maximum at the exponent obtained from Webster's horn equation (eq. 3). Figure 5b shows the frequency at which the directivity pattern shows the highest acoustic pressure at $\Phi = \theta = 0°$, and $z = 100$ mm. This frequency is located around 40 kHz and therefore confirms that the Webster horn designed according to section 2.2 is optimized for the operating frequency of the transducer.

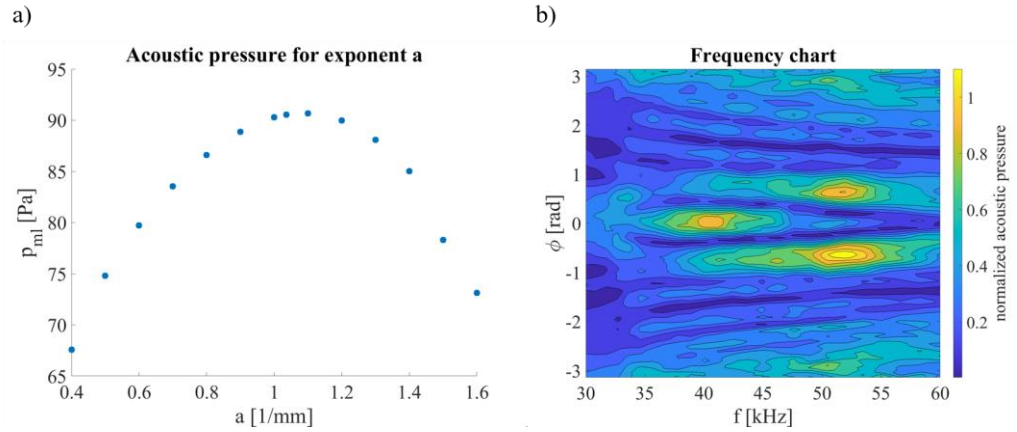


Figure 5 – a) Acoustic pressure p_{ml} over exponent a showing a local maximum around $a = 1.036$.

b) Frequency chart (polar diagrams for all measured frequencies) showing the optimal operating frequency at 40 kHz.

For individual operation unit 2, the directivity patterns of simulation and experiment are presented in figure 6a. The beam widths show a deviation of only 5 % with 36.1° and 34.4°, for simulation and experiment respectively. The main lobes match well, while the side lobes with ratio $p_{sl}/p_{ml} = 0.62$ are more pronounced in reality than they are assumed in the simulation. Compared to the transducer without an acoustic horn, this still means a reduction to almost one third of the previous value of $p_{sl}/p_{ml} = 1.68$ (see figure 6b). Additionally, the acoustic pressure of the main lobe was more than tripled.

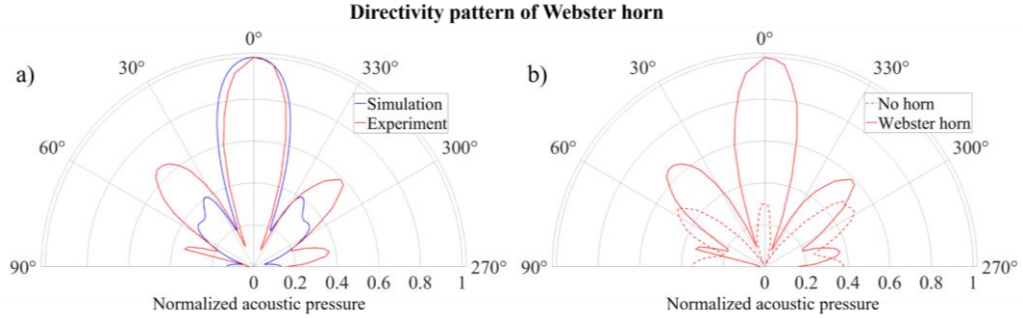


Figure 6 – a) FEM and experimental directivity patterns standardized to mean value in comparison.

b) Experimental directivity patterns of transducer and Webster horn standardized to maximum value of Webster horn in comparison.

While this is an improvement compared to the directivity pattern of the transducer without an acoustic horn, it still means that undesired side lobes continue to occur.

3.3 Folded horn

To further reduce side lobes, an additional structure in shape of a tube attachment with the length of $b = 1$ mm is implemented in the horn. A numerical study according to section 2.3 is conducted and

the resulting numerical plots in figure 7 show the influence of the tube attachment on the side lobes. It increases the acoustic pressure of the main lobe (see 5, p. 43) and, at the same time, reduces the side lobes. It is now possible to determine the parameter combination for which the directivity pattern fulfills the intended conditions. In this case, a horn with the parameters a = 0.6 1/mm and l = 2.5 mm

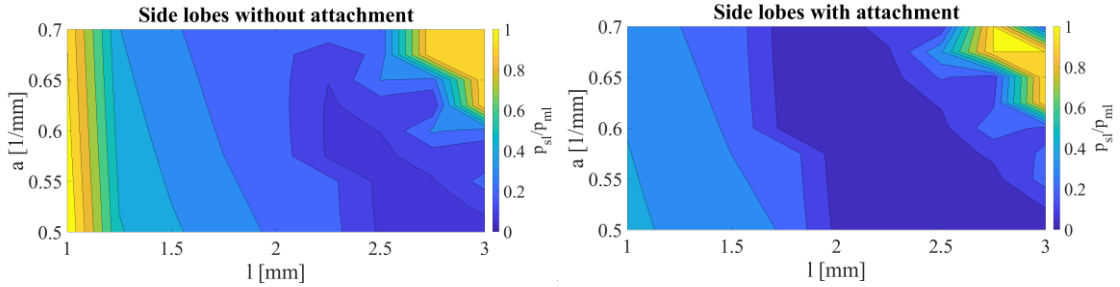


Figure 7 – Numerical plots for the degree of the first order side lobes p_{sl}/p_{ml} for the variation of a and l without and with additional tube attachment.

is selected. The directivity patterns of simulation and experiment presented in figure 8a show a very good match. The comparison of the Webster horn and the horn with the additional tube attachment shows an increase by 31 % of the acoustic pressure of the main lobe and a decrease by 48 % of the ratio p_{sl}/p_{ml} , resulting in p_{sl}/p_{ml} = 0.33 (figure 8b).

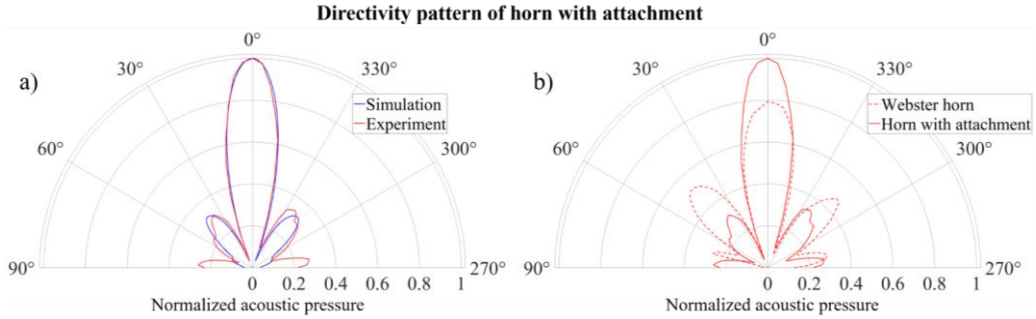


Figure 8 – a) FEM and experimental directivity patterns standardized to mean value in comparison. b) Experimental directivity patterns of Webster horn and horn with tube attachment standardized to maximum value of Horn with tube attachment in comparison.

Another numerical study is conducted for design parameter of the inner exponential horn. The directivity patterns of the resulting folded horn with a = 0.5 1/mm and l = 2 mm show a good match of the main lobes (figure 9a). However, the side lobes do not match, with the asymmetry of the side lobes in the experiment being particularly prominent. Figure 9b shows that this design method does not result in an increase of sound pressure for individual operation of unit 2. Nevertheless, simulation and experiment both show that the sound pressure is decreased by 50 % compared to the acoustic pressure of the horn with tube attachment.

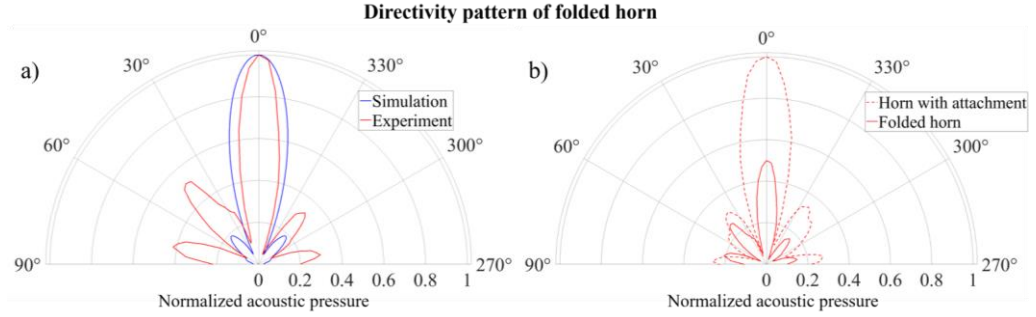


Figure 9 – a) FEM and experimental directivity patterns standardized to mean value in comparison. b) Experimental directivity patterns of horn with tube attachment and folded horn standardized to maximum value of horn with tube attachment in comparison.

3.4 Parametric sweep horn

The total length of the previously presented horns ranged from three to four millimeters. We now allow bigger overall dimensions but limit the total length $l+b$ to 12 mm. For the parametric sweep of higher degree, including b as a parameter, the parameter ranges shown in Table 1 are specified.

Table 1 – Specified ranges for the parametric sweep

Parameter	Lower Boundary	Scale	Upper Boundary	Description
$P_1 = a$	0.14 1/mm	0.0025 1/mm	0.2 1/mm	Exponent
$P_2 = l$	6 mm	0.25 mm	10 mm	Length of the horn
$P_3 = b$	0	0.25 mm	2 mm	Length of tube attachment

Again, as shown in figure 10a, the directivity patterns of simulation and experiment show very good match. The beam width and the ratio p_{sl}/p_{ml} both only show a deviation of 3.2% from the measured value. The implementation of the parametric sweep horn nearly quintuples the acoustic pressure of the main lobe, while the side lobes that now occur at an angle of $\pm 28°$ are reduced by 80 %. The beam width remains unchanged compared to the transducer without an acoustic horn (figure 10b).

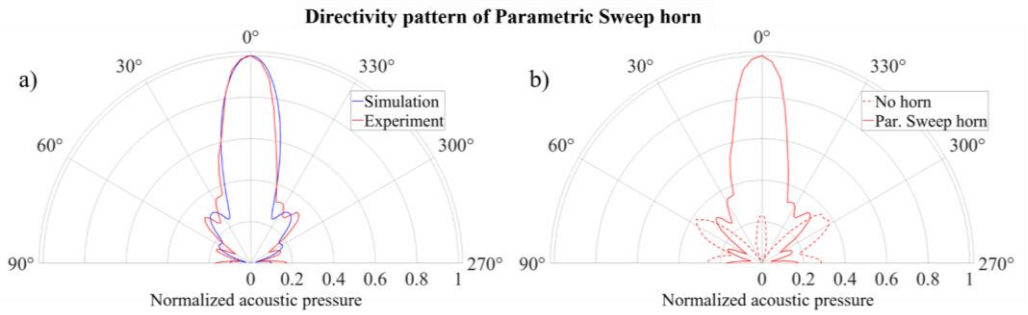


Figure 10 – a) FEM and experimental directivity patterns standardized to mean value in comparison. b) Experimental directivity patterns of transducer without acoustic horn and parametric sweep horn standardized to maximum value of parametric sweep horn in comparison.

4. DISCUSSION

The previously determined directivity patterns show a good agreement between simulation and experiment for all presented acoustic horns. Especially the accuracy of the simulation results of the main lobe was proven. In the cases where the side lobes do not show good match, they are larger in the experiment than they are assumed in the simulation. This is mainly due to the assumption of an infinite half space and an infinite baffle in contrast to the real geometry of the board. Apart from the Webster horn, the ratios of the measured sound pressures between the individual horns relative to the transducer without an acoustic horn show a deviation of 6% – 15%. Table 2 shows the resulting experimentally measured values of the directivity metrics.

Table 2 – Experimentally measured values of directivity metrics for all presented acoustic horns

horn design	p_{ml} [Pa]	θ_b [°]	p_{sl}/p_{ml}	$l + b$ [mm]
no horn (transducer)	47.4	30.2	1.68	-
Webster horn	153	34.4	0.62	4
tube attachment horn	199	27.8	0.33	4
double horn	99.6	24.2	0.42	4
parametric sweep horn	229	30.4	0.33	11

In sections 3.1 to 3.4, the directivity of the transducer was improved successively starting with the initial directivity of the transducer without an acoustic horn until the parametric sweep horn in section

3.4. The directivity pattern with individual operation of unit 2 of the transducer showed the optimization potential especially in the maximization of the main lobe and the minimization of the side lobes. The Webster horn as the initial approach increased acoustic pressure of the main lobe, but the limitations of this analytical approach lead to a reoccurrence of side lobes. The parameter optimization of the exponential horn according to the Webster horn equation refers to the maximization of the acoustic pressure on the z-axis of radially symmetrical horn shapes. Therefore, no conclusions can be drawn about the occurrence or the degree of the side lobes.

The tube attachment was then able to reduce the reoccurrence of side lobes while increasing the acoustic pressure of the main lobe (8). The presented folded exponential horn did not show the desired increase of the acoustic pressure. The main reason for this is that the fine structures of the folded horn could not be manufactured in a sufficient quality, which also leads to the asymmetry of the side lobes. With the condition of higher resolution manufacturing and simultaneous operation of all units, the FEM simulation shows the highest increase of acoustic pressure for the folded horn, in that case making it a promising prospect for a focusing horn design with reduced overall dimension.

Compared to the transducer without an acoustic horn the parameteric sweep horn shows the biggest increase in acoustic pressure of all the acoustic horns presented, in both simulation and experiment. With a total length of 11 mm, it takes up the most installation space among all the horns presented. Now, the question is why the final design of the acoustic horn differs from the analytical method. As mentioned earlier, Webster's horn equation is restricted to radially symmetrical horn shapes. Whereas, the parametric sweep horn uses impedance matching and constructive interference to maximize the acoustic pressure of the main lobe. If you consider constructive interference of a sound wave propagating through a single slit with $d \sim \lambda$, $\tan(\alpha) = \frac{\lambda}{d} = 27.7°$ gives the angle at which the side lobes of the first order occur for the parametric sweep horn. Ultimately, the decision, which design feature and directivity metrics to prioritize, depends on the type of operation of the transducer and the intended application of the horn.

5. CONCLUSIONS

By designing an acoustic horn using a FEM model, the directivity pattern of the MEMS-based ultrasonic transducer could be significantly improved. The influence of different horn parameters (including an additional tube attachment) on the directivity pattern was shown numerically and experimentally. Ultimately, various approaches to modeling acoustic horns were investigated, the application of which result in improved sound focusing. The designed horns in this article thus refer to a minimization of the beam width and the acoustic pressure of the side lobes, and to a maximization of the acoustic pressure of the main lobe.

Application offered by the implementation of focusing acoustic horns include improved distance and level measurements, where a wide directivity pattern leads to disturbing reflections from surrounding objects.

Since the generation of the intended directivity pattern by the presented acoustic horns has succeeded, this indicates that with further approaches or with the expansion of the presented approaches, different directivity patterns can be addressed. Since the sound is always received as it is emitted, the generation of sound propagation with a spherical characteristic could be of interest. It is also possible to optimize the shape of an acoustic horn that influences the directivity pattern in a wide range of acoustic medium parameters (e.g. the speed of sound). Furthermore, the results indicate that the ideal horn shape depends on the combination of simultaneously operated transducer units. The potential of this work lies not only in the fact that the acoustic horns show the intended directivity pattern, but also that they were manufactured using a conventional 3d-printing technique, which makes them inexpensive and easy to manufacture.

REFERENCES

1. Monsalve J.M., Melnikov A., Stolz M., Mrosk A., Jongmanns M., Wall F., Langa S., Marica-Bercu I., Brändel T., Kircher M., Schenk H.A.G., Kaiser B., Schenk H. Proof of Concept of an Air-Coupled Electrostatic Ultrasonic Transducer Based on Lateral Motion. Sensors and Actuators A: Physical; 2022.
2. Monsalve J.M., Kircher M., Wall F., Krenkel M., Kaiser B., Langa S., Schenk H. First Time of nanoscopic electrostatic drives pushing for ultrasonic transmission for gesture recognition. IEEE International Ultrasonics Symposium (IUS); 2020. DOI: https://doi.org/10.1109/IUS46767.2020.9251316
3. Melnikov A., Marica-Bercu I., Monsalve J. M., Jongmanns M., Kaiser B. Strahlcharakteristik eines

elektrostatischen, membranlosen MEMS-Ultraschallwandlers für Umgebungserfassung, MikroSystemTechnik Kongress 2021; 2021.
4. COMSOL. The Acoustics Module User's Guide.
5. Meisel T. Optimierung der Richtcharakteristik von MEMS-Ultraschallwandlern durch passive Strukturen. Bachelor Thesis. BTU Cottbus-Senftenberg, Fraunhofer IPMS. Cottbus, Dresden; 2022.
6. Lerch R., Sessler G., Wolf D. Technische Akustik. Springer Berlin Heidelberg; 2009.
7. Ginsberg J. H. Acoustics-A Textbook for Engineers and Physicists. Cham: Springer International Publishing; 2018.
8. De Boer B. Acoustic tubes with maximal and minimal resonance frequencies. The Journal of the Acoustical Society of America; 2008. DOI: 10.1121/1.2935231

ICA 2022
24th INTERNATIONAL CONGRESS ON ACOUSTICS
October 24(Mon) - 28(Fri), 2022 Gyeongju, Korea

PROCEEDINGS of the
24th International Congress on Acoustics

October 24 to 28, 2022 in Gyeongju, Korea

ABS-0768

Efficient placement of damping layers on an aircraft fuselage for cabin noise reduction

Sebastian ROTHE[(1)], Christopher BLECH[(2)], Steffen HOFFMANN[(3)], Sabine C. LANGER[(4)]

[(1)]TU Braunschweig, Institute for Acoustics, Germany, sebastian.rothe@tu-braunschweig.de

[(2)]TU Braunschweig, Institute for Acoustics, Germany, c.blech@tu-braunschweig.de

[(3)]TU Braunschweig, Institute for Acoustics, Germany, steffen.hoffmann@tu-braunschweig.de

[(4)]TU Braunschweig, Institute for Acoustics, Germany, s.langer@tu-braunschweig.de

ABSTRACT

A consideration of sound reduction measures in early design phases is expected to have a decisive advantage compared to design changes in later phases. The combination of numerically solved vibroacoustic models and robust identification criteria for the placement of measures enables one-shot design proposals with respect to acoustic objective functions. The sound pressure level within a passenger aircraft cabin is exemplarily considered within this contribution while a vibroacoustic finite element model of a fuselage section delivers the objective function. The sound pressure levels in the cabin are reduced by the application of damping layers on the outer skin of an aluminium airframe, whereby the distribution of such passive damping measures should be well-considered for cost, weight and efficiency reasons. In order to efficiently identify a distribution, a comparison of three approaches for the placement is shown: Sophisticated one-shot design criteria such as the deformation work and the mean squared velocity in skin fields and an intuitive engineering approach. Based on the results, recommendations for the efficient placement of damping layers in early design phases are delivered and potential extensions of the approaches are discussed.

Keywords: damping layer, placement, aircraft, acoustic-oriented design

1 INTRODUCTION

Vibrations in plate-like structures are often the cause of noise generated by technical products. Especially in automobiles and aeroplanes, passengers are surrounded by thin-walled structures. Exciting dynamic forces of the structures are unavoidable. It is therefore important to design and integrate acoustic measures already during the design and development phase that reduce or prevent the generation of noise.

One frequently used acoustic measure are damping layers, which can be designed as unconstrained or constrained layer damping. In order to use them efficiently, the placement and distribution should always be adapted to the vibroacoustic problem. An approach to meet this challenge is investigated in this paper.

Especially for noise prediction of large systems like aircraft cabins, which require a complex model with many degrees of freedom to predict the acoustic response with good accuracy, innovative and efficient approaches are needed. Complex optimisation loops to identify suitable areas and the design of the measure are to expensive and time-consuming. Therefore, the use of identification criteria, which can provide one-shot designs after one calculation, can support the early design process. On an realistic example the use of an acoustic identification criterion is demonstrated in this work. Criteria based on physical system quantities are used to identify a well suited distribution of damping layers on an aircraft outer skin. The aim is to reduce the sound pressure in the cabin for a defined critical frequency range in which, for example, a strong excitation of the engines is expected. A finite element model of a realistic aircraft segment serves as the basis.

2 PROBLEM STATEMENT

As motivated above, a complex vibroacoustic system is studied in order to derive one-shot design proposals for the placement of damping measures by use of acoustic identification criteria. The problem of sound transmitted within an aircraft fuselage segment is chosen as exemplary demonstrator. The model, shown in Figure 1, is solved in frequency domain by the finite element method (ABAQUS 2018) and directly delivers the sound pressure inside the passenger cabin. As excitation, a single point source is placed near the outer skin (2 m distance). The aircraft fuselage model comprises four fully coupled structural and acoustic domains:

- **Airframe** | Shell formulation (8-node quadrilaterals) for 3 mm aluminium modelled by a linear elastic isotropic material with structural damping. For simplicity, linear elastic properties of aluminium are considered within this paper. Future aircraft are mainly expected to be made of carbon-fibre reinforced plastic (CFRP), which allows the direct integration of damping layers. In Figure 1, 78 skin fields within the airframe are highlighted as design space for the proposed damping measure.

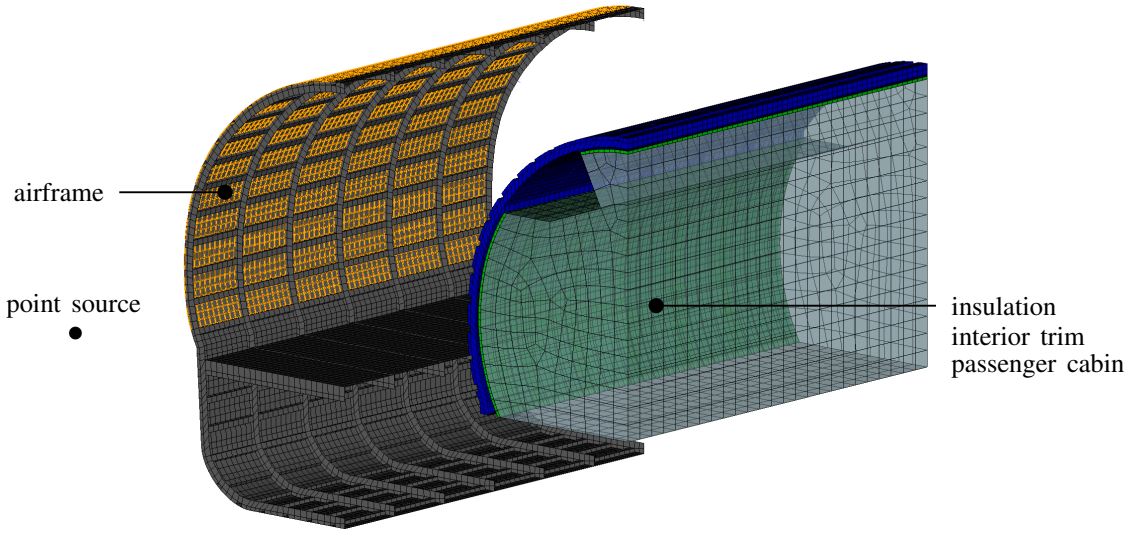


Figure 1. Finite element model of an aircraft fuselage segment with highlighted (orange) design space (78 skin fields).

- **Insulation** | Frequency-dependent complex-valued 3D Helmholtz domain for aircraft-grade glass wool
- **Interior trim panels** | Sandwich made of glass-fibre reinforced plastic (GFRP) top layers modelled by shells (8-node quadrilaterals, linear elastic orthotropic material with structural damping) and of a honeycomb core modelled by a 3D continuum (20-node hexahedrons, linear elastic orthotropic material with structural damping)
- **Passenger cabin** | 3D Helmholtz domain (20-node hexahedrons) with frequency-dependent complex-valued bulk modulus in order to consider homogenised damping

Details on the airframe material parameters are given in Table 1, while information on the three remaining mechanical domains can be found in [2].

Concerning the mesh size, non-conforming meshes are applied in the introduced domains fulfilling at least 10 nodes per wave length at the highest frequency of interest (580 Hz), respectively. As critical frequency range, 250 to 400 Hz is chosen exemplary as jet engine excitations and low transmission loss characteristics can be expected within this range (compare [2]).

Table 1. Considered material parameters (aluminium) for airframe

parameter	symbol	value
Young's modulus	E	$7 \cdot 10^{10}\,\mathrm{N/m^2}$
density	ρ	$2700\,\mathrm{kg/m^3}$
Poisson's ratio	ν	0.34
loss factor	η	0.02

The objective function is defined as the mean squared sound pressure in the cabin. For this purpose, a nodeset of 90 nodes is selected at head height in the area of one seat row. The nodeset is highlighted in red for different views on the fuselage segment in Figure 2.

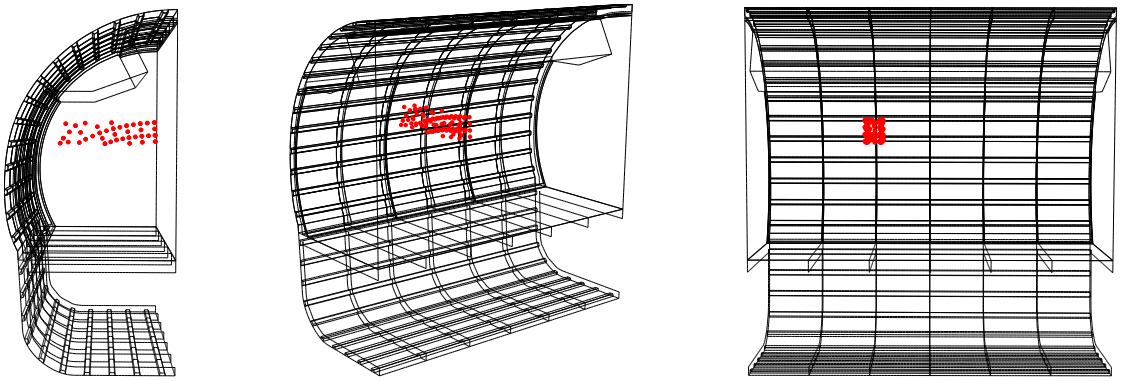


Figure 2. Defined nodeset for the calculation of the mean squared sound pressure from different views of the fuselage segment; from left to right: front view, iso view, side view.

In order to reduce the objective function — the mean squared sound pressure (MSP) in the critical frequency range — nine of the 78 skin fields (see Figure 1) are specifically damped. This corresponds to about 12% of the defined design area. Two acoustic identification criteria are used to identify suitable fields. First, the deformation work in the skin fields is used. The deformation work W_r is derived from the volume integral of the stresses σ and strains ε (Equation (1)).

$$W_\mathrm{r} = \int_V \sigma \varepsilon \, \mathrm{d}V \tag{1}$$

According to ROTHE [1], this quantity is suitable to specifically place damping layers on structures. To do so, the deformation work is calculated for each finite element in the centroid and averaged for the respective skin fields. Since these are frequency-dependent quantities, the next step is to sum over the critical frequency range. This results in an assessment quantity according to which the area with the highest deformation work is the most suitable for placing damping. More details about this procedure can be found in [1] and [4]. It should be mentioned that the approach proposed in the publications are shown to efficiently reduce structure-borne sound. The use of this approach for the reduction of an objective function in the fluid (MSP) is a new step. The same applies to the excitation of the structure via a point source.

Since the surface velocities are significantly responsible for the sound radiation, the previously described procedure is also carried out with the mean squared velocity (MSV) in the skin fields. It serves as another identification quantity, which results in the second identification criterion investigated in this study. Also in this case, the areas with the highest value (max.) are defined as the most suitable.

An intuitive engineering approach is used as the third alternative to be compared. For this purpose, the skin fields are selected intuitively according to engineering common sense. In addition, the variant in which all skin

fields are damped is also investigated in order to illustrate the maximum possible reduction.

As a passive acoustic measure, a highly damping polymer as an intermediate layer in the skin fields is assumed. This could be realised, for example, by combining an aluminium base and top layer with KRAIBONDAMP as an intermediate layer. Since the frequency-dependent behaviour of the storage and loss modulus is unknown, this is determined by vibroacoustic measurement in order to take a realistic loss factor into account. The measurement of the sandwich structures made of 3.0 mm aluminium and KRAIBONDAMP ($\eta_{\text{Comp}} \approx 0.2$) results in a thousandfold increase of the loss factor of the basic structure ($\eta_{\text{Al}} \approx 0.0002$) for several samples in the interesting frequency range around 0.5 kHz. The procedure for determining the material parameters of the composite and the inverse determination of the material properties of the intermediate layer is described in [3].

To model the damped skin fields, only the loss factor (structural damping) is increased in these areas and assumed to be constant over frequency ($\eta_{\text{damp}} = 0.2$). This has the advantage that only the position of the damping is rated and no additional influences due to the frequency-dependent damping modelling. The rest of the structure is modelled with a loss factor of $\eta = 0.02$. This is deliberately chosen to be higher than for pure aluminium, in order to take into account additional damping of joints. The difference in loss factors between damped areas (η_{damp}) and the basic structure (η) is therefore a factor of 10.

3 RESULTS

This section summarise the results of the investigations. The reference configuration and the fully damped variant (full damped) are shown in Figure 1. The resulting three variants using the identification criteria as well as the intuitive approach are shown in Figure 3. For the intuitive variant (intuitive damped), the 9 skin fields that are as close as possible to the sound source are damped (see Figure 3, left). The skin fields of the approaches with identification criteria according to maximum MSV (MSV (max.) damped) and maximum deformation work (DW (max.) damped) in the critical frequency range from 250 to 400 Hz are shown comparatively. The damped skin fields are highlighted in orange. In total, the same area is damped for all three variants.

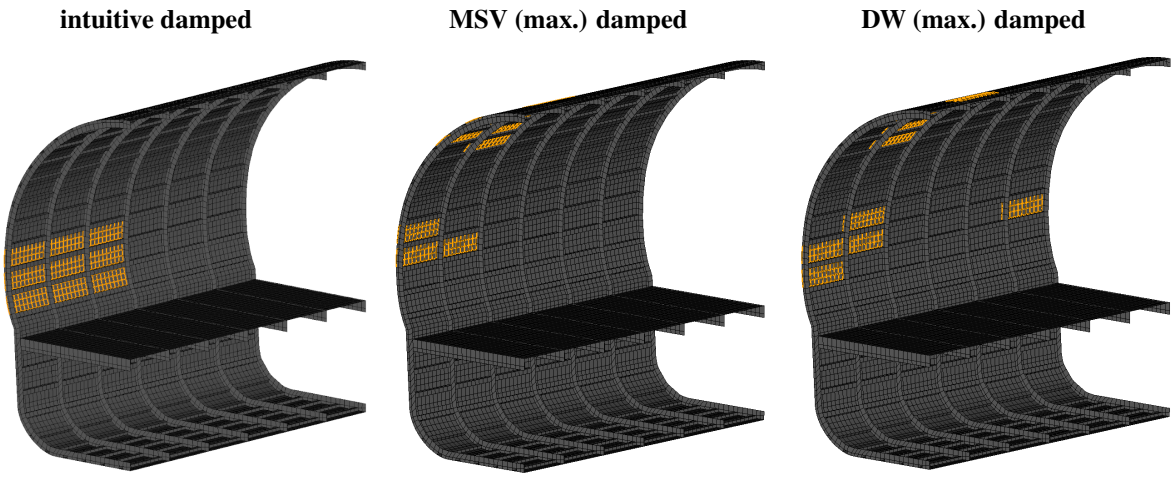


Figure 3. Design variants with highlighted damped skin fields; from left to right: Intuitive engineering solution near the sound source, maximum mean squared velocity, maximum deformation work.

In Figure 4, the resulting mean squared pressure is plotted in third octave band for the three proposed design variants. In addition, a full damping treatment of the entire design space is studied, which yields a total level reduction of 9.6 dB within the selected frequency range. By applying both the intuitive engineering approach and the two identification criteria (mean squared velocity, deformation work), a lower reduction is yielded as only 12% of the area is treated. For the intuitive approach, a reduction of 4.8 dB results, while the criteria yield a better improvement of 5.5 dB in the cabin. The difference is small but expected to increase for more complex

models. For instance, an aircraft fuselage with varying skin field thickness, distributed stochastic loads and full length hardly allow a simple intuitive engineering solution for a damping measure design.

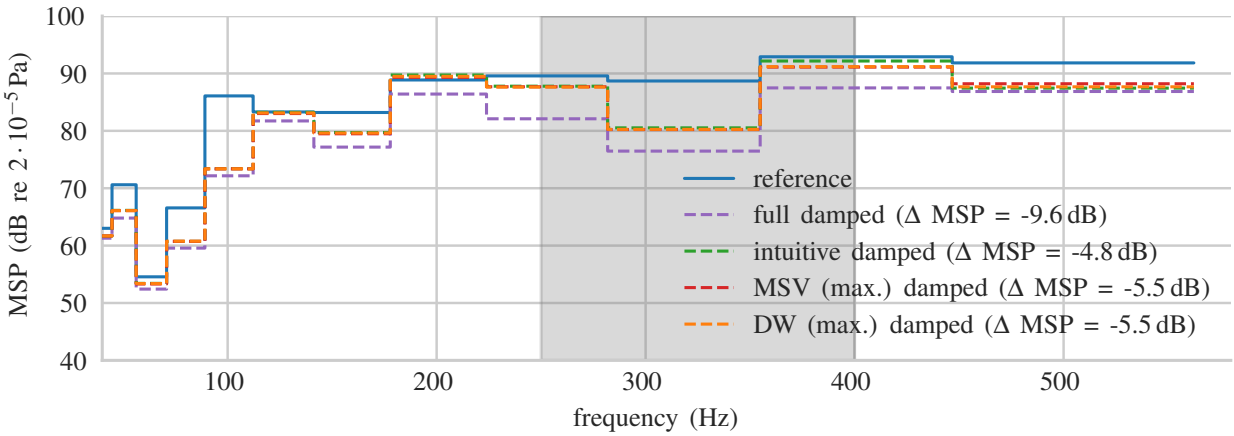


Figure 4. Mean squared pressure over frequency (third octave band) at selected seat row (ear height volume) for different design variants; critical frequency range highlighted in grey.

To illustrate the detailed frequency response of the sound pressure, it is shown in Figure 5 as a comparison of the reference configuration and the variant with 9 damped skin fields according to the deformation work. This shows that some peaks can be highly reduced. How far this reduction also brings a psychoacoustic advantage needs to be investigated with psychoacoustic metrics and cannot be assessed from this.

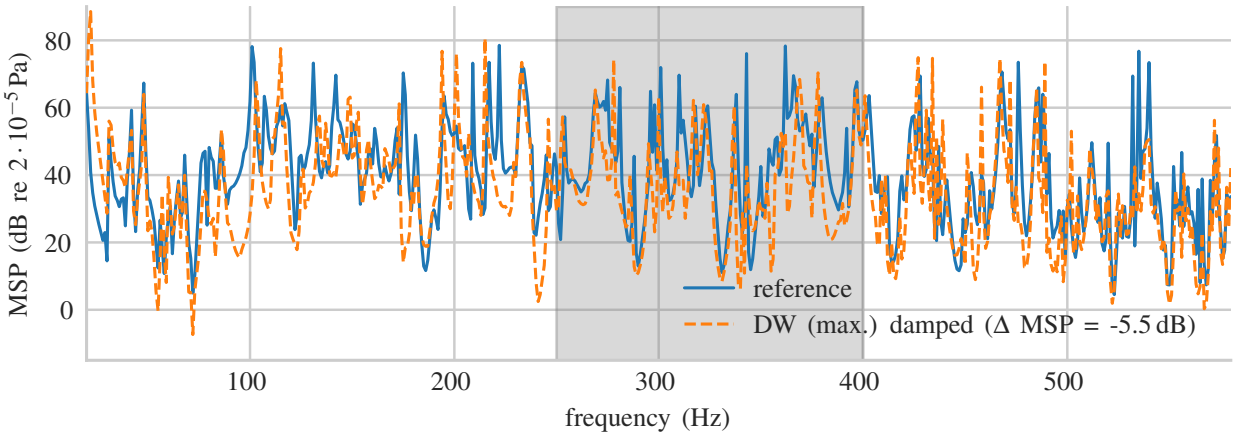


Figure 5. Mean squared pressure over frequency at selected seat row (ear height volume) for three design variants; critical frequency range highlighted in grey.

4 SUMMARY AND CONCLUSION

The investigations in this paper focus on the efficient placement of damping layers on an airframe to reduce cabin noise. A realistic finite element model of an aircraft fuselage segment is used for this purpose. The aim is to reduce the average sound pressure at a row of seats (ear height) by targeted damping of certain skin fields of the outer skin. For the efficient identification of suitable skin fields, two identification criteria and an intuitive engineering approach are used in comparison.

The results show that a targeted distribution of damping in relation to a critical frequency range is advantageous. In comparison to the intuitively dampened variant, an additional reduction in the mean squared sound pressure level of approx. 1 dB can be achieved with the same damped area. Both identification criteria provide a design proposal that results in a similar reduction — they also deliver a similar distribution pattern.

It should be noted that the identification criteria used in this paper are originally designed to reduce structure-borne sound within a structure (see [1]). In order to be able to apply them validly to objective functions that affect airborne sound, many more investigations are required. The investigations in this paper are only intended to show the basic methodology. Nevertheless, the results already show that suitable areas for damping placement can be identified very efficiently with the help of identification criteria.

In future investigations, the restriction to individual skin fields could be resolved in order to achieve a free design or distribution of the damping. This would possibly increase the efficiency of the applied damping measure. Additional expansion options also exist in the modeling of the outer skin. CFRP is of particular interest as a material for future aircraft designs. Here, damping material such as KRABONDAMP can be integrated directly into the CFRP layers, as in [5]. In addition, a closer look at the frequency-dependent material behaviour (stiffness, damping) is recommended and should be considered for further investigations.

REFERENCES

[1] Rothe S.: Design and placement of passive acoustic measures in early design phases. Schriften des Instituts für Akustik, Braunschweig, Shaker, 2022, 2.

[2] Blech C.: Wave-resolving aircraft cabin noise prediction. Schriften des Instituts für Akustik, Braunschweig, Shaker, 2022, 1.

[3] Hoffmann S., Rothe S., Langer S. C.: Vorgehen zur Charakterisierung und Modellierung von Mehrschichtbelägen. Conference proceedings of DAGA, Stuttgart, 2022.

[4] Rothe S., Hoffmann S., Langer S. C.: Efficient placement of damping patches based on an identification criterion. Proceedings of ISMA, 2022.

[5] Fasana, A., Ferraris A., Airale A. G., Polato D. B., Carello M.: Experimental characterisation of damped CFRP materials with an application to a lightweight car door. Shock and Vibration, 2017.

ICA 2022
24th INTERNATIONAL CONGRESS ON ACOUSTICS
October 24(Mon) - 28(Fri), 2022 Gyeongju, Korea

PROCEEDINGS of the
24th International Congress on Acoustics

October 24 to 28, 2022 in Gyeongju, Korea

ABS-0810

Energy-based non-negative surface contributing approximated for the volume of an inward radiating sphere

Caglar GURBUZ[(1)], Steffen MARBURG[(2)]

[(1)]Chair of Vibroacoustics of Vehicles and Machines, Germany, caglar.guerbuez@tum.de

[(2)]Chair of Vibroacoustics of Vehicles and Machines, Germany, steffen.marburg@tum.de

ABSTRACT

Investigating vibrating surfaces is a continuing concern within the analysis of acoustic cavities. One valuable tool to determine vibrating surfaces is the contribution analysis. However, a contribution analysis for an entire cavity is usually accompanied with the cumbersome evaluation of the related volume integral. In order to bypass that, this study aims to embed the approximative evaluation of the cavity in a contribution analysis. Therefore, the boundary element method is deployed for solving the three-dimensional Helmholtz equation. Moreover, the sound energy is used as the objective function, since the sound energy is sensitive to the sound pressure as well as the particle velocity. To validate the proposed method, the example of an inward radiating sphere is investigated. Initial results already show that cavity volumes can be analyzed within an energy-based contribution analysis. In this way, the proposed method designates an efficient technique to evaluate contributing surfaces inside an acoustic cavity.

Keywords: Sound energy, Contribution analysis, Boundary element method

1 INTRODUCTION

Panel or surface contributions are a central concern in the design of vehicle cabins, particularly, in terms of customer comfort. For this reason, various finite element software, e.g. COMSOL, LS-DYNA, or MSC Nastran, adopted this method in their repertoire. In these packages, the sound pressure is considered as the objective function. For interior acoustics, however, the sound energy density is suggested, since it is sensitive to the sound pressure and to the particle velocity [1, 2, 3]. In this way, contributing surfaces can be also recovered in regions with low sound pressure. In analogy to the non-negative intensity [4], the energy surface contributions are also non-negative. since they are formulated in a quadratic expression. By this means, acoustic short circuits due to alternating signs are circumvented. Another similarity is that the energy-based contributions are also implemented in a boundary element formulation. While the concept of energy densities has been already implemented in a contribution analysis scheme, it has been yet limited to the evaluation at a single field point [5]. This contribution aims to expand the energy-based contributions to the evaluation of an entire volume. Therefore, the cumbersome volume integral is bypassed by evaluating the energy at a grid with multiple field points. In this study, the proposed method is validated for an inward radiating sphere. Initial results emphasize that contributing surfaces regarding an entire volume can be retrieved by evaluating multiple field points, which are regularly distributed within the acoustic domain.

2 METHODS

By assuming the harmonic time dependence $e^{-i\omega t}$, the three-dimensional acoustic problem in the frequency domain is governed by the Helmholtz equation

$$\Delta p(\vec{x}) + k^2 p(\vec{x}) = 0 \qquad \boldsymbol{x} \in \Omega \subset \mathbb{R}^3, \tag{1}$$

with $p(\vec{\boldsymbol{x}})$ denoting the sound pressure in Ω and $k = \omega/c$ the wavenumber, which is composed by the angular frequency ω and the speed of sound c. The Helmholtz equation fulfills the Neumann boundary condition (BC)

$$v_f(\vec{\boldsymbol{x}}) = \frac{1}{\mathrm{i}\omega\rho}\frac{\partial p(\vec{\boldsymbol{x}})}{\partial n(\vec{\boldsymbol{x}})} \qquad \boldsymbol{x} \in \Gamma \subset \mathbb{R}^2 \tag{2}$$

and the Robin BC

$$v_f(\vec{\boldsymbol{x}}) - v_s(\vec{\boldsymbol{x}}) = Y(\vec{\boldsymbol{x}})p(\vec{\boldsymbol{x}}) \qquad \boldsymbol{x} \in \Gamma \subset \mathbb{R}^2. \tag{3}$$

with $v(\vec{\boldsymbol{x}})$ denoting the particle velocity. The subscripts s and f denote the structural and the fluid particle velocity.

The sound pressure at internal field points can be obtained by

$$p_i(\vec{\boldsymbol{y}}_i) = \mathrm{i}\omega\rho\int_\Gamma G(\vec{\boldsymbol{x}},\vec{\boldsymbol{y}}_i)v_s(\vec{\boldsymbol{x}})\mathrm{d}\Gamma(\vec{\boldsymbol{x}}) \quad - \int_\Gamma\left[\frac{\partial G(\vec{\boldsymbol{x}},\vec{\boldsymbol{y}}_i)}{\partial n(\vec{\boldsymbol{x}})} - \mathrm{i}\omega\rho\, G(\vec{\boldsymbol{x}},\vec{\boldsymbol{y}}_i)Y(\vec{\boldsymbol{x}})\right]p(\vec{\boldsymbol{x}})\mathrm{d}\Gamma(\vec{\boldsymbol{x}}) \qquad \vec{\boldsymbol{y}}_i \in \Omega, \tag{4}$$

with $\vec{\boldsymbol{y}}_i$ denoting the position of the field point. The field point has the subscript $i = 1,2,...N$, where N is the number of field points. Similarly, the particle velocity at internal field points can be computed by the normal derivative of Eq.(4)

$$\vec{\boldsymbol{v}}_i(\vec{\boldsymbol{y}}_i) = \int_\Gamma \vec{\nabla} G(\vec{\boldsymbol{x}},\vec{\boldsymbol{y}}_i)v_s(\vec{\boldsymbol{x}})\mathrm{d}\Gamma(\vec{\boldsymbol{x}}) \quad - \left[\int_\Gamma \vec{\nabla}\frac{1}{\mathrm{i}\omega\rho}\frac{\partial G(\vec{\boldsymbol{x}},\vec{\boldsymbol{y}}_i)}{\partial n(\vec{\boldsymbol{x}})} - \vec{\nabla} G(\vec{\boldsymbol{x}},\vec{\boldsymbol{y}}_i)Y(\vec{\boldsymbol{x}})\right]p(\vec{\boldsymbol{x}})\mathrm{d}\Gamma(\vec{\boldsymbol{x}}) \qquad \vec{\boldsymbol{y}}_i \in \Omega. \tag{5}$$

The sound pressure and the particle velocity at internal field points can be alternatively expressed in matrix form

$$p_i(\vec{\boldsymbol{y}}_i) = \boldsymbol{b}_i^T(\vec{\boldsymbol{y}}_i)\boldsymbol{v}_s \qquad \vec{\boldsymbol{y}}_i \in \Omega \tag{6}$$

$$\vec{\boldsymbol{v}}_i(\vec{\boldsymbol{y}}_i) = \tilde{\boldsymbol{b}}_i^T(\vec{\boldsymbol{y}}_i)\boldsymbol{v}_s \qquad \vec{\boldsymbol{y}}_i \in \Omega, \tag{7}$$

where $\boldsymbol{b}_i(\vec{\boldsymbol{y}}_i)$ and $\tilde{\boldsymbol{b}}_i(\vec{\boldsymbol{y}}_i)$ denote the influence coefficient vectors with respect to the sound pressure and the particle velocity at the internal field points. The total sound energy in the acoustic field can be obtained by

$$E_t = E_p + E_k = \frac{1}{2\rho c^2}\int_\Omega p(\vec{\boldsymbol{x}})^2\,\mathrm{d}\Omega + \frac{\rho}{4}\int_\Omega \vec{\boldsymbol{v}}_f(\vec{\boldsymbol{x}})\cdot\vec{\boldsymbol{v}}_f(\vec{\boldsymbol{x}})^*\,\mathrm{d}\Omega. \tag{8}$$

Within the scope of this work, the volume integral is approximated by evaluating the energy density at numerous field points, $\int_\Omega e\,\mathrm{d}\Omega \approx V\cdot\sum_{i=1}^N e_i$. The surface contributions with respect to the sound energy can be then obtained by

$$\begin{aligned} E_t = E_p + E_k &= \frac{1}{2\rho c^2}\sum_{i=1}^N(\boldsymbol{b}_i^T\boldsymbol{v}_s)^*(\boldsymbol{b}_i^T\boldsymbol{v}_s) + \frac{\rho}{4}\sum_{i=1}^N(\tilde{\boldsymbol{b}}_i^T\boldsymbol{v}_s)^*(\tilde{\boldsymbol{b}}_i^T\boldsymbol{v}_s) \\ &= \boldsymbol{v}_s^H\boldsymbol{A}_p\boldsymbol{v}_s + \boldsymbol{v}_s^H\boldsymbol{A}_k\boldsymbol{v}_s = \boldsymbol{v}_s^H\boldsymbol{A}_t\boldsymbol{v}_s \end{aligned} \tag{9}$$

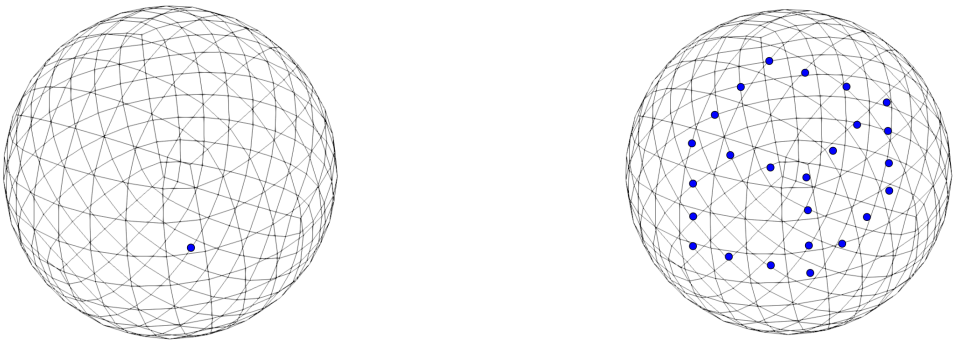
with $\boldsymbol{A}_p$, $\boldsymbol{A}_k$, and $\boldsymbol{A}_t$ denoting the coupling matrix regarding the potential energy, the kinetic energy, and the total energy. Finally, the energy-based surface contributions can be expressed by

$$E = \boldsymbol{v}_s^H\boldsymbol{A}\boldsymbol{v}_s = \boldsymbol{v}_s^H\sqrt{\boldsymbol{A}}^H\sqrt{\boldsymbol{A}}\boldsymbol{v}_s = \sum_{j=1}^{N_n}\alpha_j^*\alpha_j = \sum_{j=1}^{N_n}\mu_j, \tag{10}$$

with μ_j denoting the contribution from the node with the identity j. For further details on the derivation of the surface contributions, the interested reader is referred to [5].

3 NUMERICAL EXAMPLE

The sphere is of radius 1 m and is discretized by 384 boundary elements with constant, discontinuous interpolation functions. We assume full-reflecting boundaries, $Y = 0$, and excite all elements with the real-valued structural particle velocity, $v_s = 1.0\,\mathrm{m/s}$. The relevant frequency is $f = 100\,\mathrm{Hz}$ and we assume air as the acoustic medium ($\rho = 1.21\,\mathrm{kg/m^3}$, $c = 343\,\mathrm{m/s}$). Regarding the field point grids, we consider a single field point and a grid with 32 field points, which are regularly distributed. The mesh of the sphere and the related field point grids are depicted in Fig. 1.

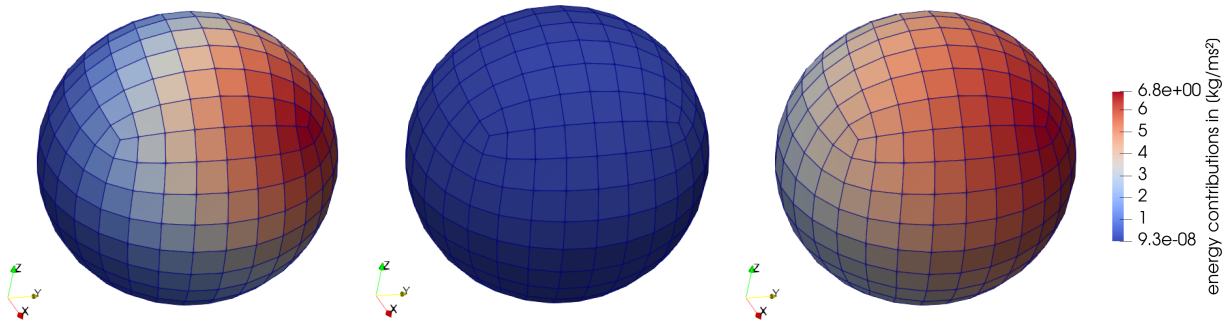


(a) Single field point

(b) Multiple field points

Figure 1. Sphere mesh and the field point grids: The first grid consists of only a single field point (a), the second grid contains 32 regularly distributed field points (b). The contribution analysis is performed 100 Hz. For the sake of overview, not all 32 evaluation points are depicted.

The single field point analysis indicates that surfaces contributing to the potential energy density can be identified at one side of the sphere, see Fig. 2a. Regarding the kinetic energy contributions, all surfaces appear inactive (Fig. 2b). As a result, the total energy surface contributions are very similar to those regarding the potential energy (Fig. 2c). The multi-point analysis, on the other hand, reveals high contributions from each



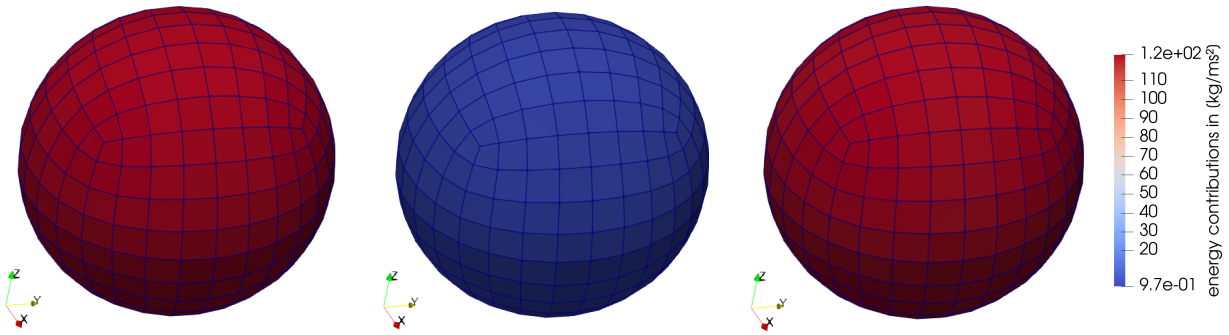
(a) Potential

(b) Kinetic

(c) Total

Figure 2. Surface contributions regarding the potential (a), kinetic (b), and total (c) energy at 100 Hz. The contributions are evaluated for a single field point.

surface to the potential energy, see Fig. 3a. Almost no contributions can be observed regarding the kinetic energy contributions (Fig. 3b). The total energy contributions, in turn, also indicates that all surfaces contribute to the total energy (Fig. 3c). By comparing the single field point analysis with the multi-point analysis, one can observe that the ratio between the potential energy and the kinetic energy are nearly the same. Moreover, it becomes apparent that contributing surfaces spread from one side of the sphere to the entire area. This result



(a) Potential (b) Kinetic (c) Total

Figure 3. Surface contributions regarding the potential (a), kinetic (b), and total (c) energy at 100 Hz. The contributions are evaluated for a grid with 32 regularly distributed field points.

already indicates that the surface contributions regarding the entire sphere volume can be obtained by evaluating the energy contributions at a grid with multiple field points. In this way, the contribution analysis with regard to multiple field points provides an efficient method to evaluate entire volumes.

4 CONCLUSIONS

In this work, a formulation was introduced for the evaluation of the surface contributions regarding an entire volume. For this purpose, the cumbersome computation of the volume integral was bypassed by the evaluation of the energy density at multiple field points, which were regularly distributed within the acoustic field. By using the energy density as an objective function, surface contributions can be also detected in regions with sound pressure. Furthermore, the energy-based contributions are non-negative by definition. In this way, acoustic short circuits can be effectively circumvented. The proposed method was implemented in a boundary element formulation and demonstrated for an academic example, the inward radiating sphere. The findings already indicate that the evaluation of a volume can be efficiently approximated by evaluating a grid with multiple field points. Future work will concentrate on the transfer to industrial application. In this context, a very interesting field of application, which also motivated this research, is the vehicle interior noise problem.

ACKNOWLEDGEMENTS

This research benefited from a grant from the German Research Foundation (DFG) under award 418936727.

REFERENCES

[1] Sommerfeldt S, Nashif PJ. An adaptive filtered-x algorithm for energy-based active control. J Acoust Soc Am. 1994;96:300-306.

[2] Cazzolato B, Hansen S, Colin H. Active control of sound transmission using structural error sensing. J Acoust Soc Am. 1998;104:2878-2889.

[3] Cazzolato B, Hansen S, Colin H. Errors arising from three-dimensional energy density sensing in one-dimensional sound fields. J Sound Vib. 2000;236:375-400.

[4] Marburg S, Lösche E, Peters H, Kessissoglou N. Surface contributions to radiated sound power. J Acoust Soc Am. 2013;133:3700-3705.

[5] Gurbuz C, Schmid JD, Luegmair M, Marburg S. Energy density-based non-negative surface contributions in interior acoustics. J Sound Vib. 2022;527:116824.

ICA 2022
24th INTERNATIONAL CONGRESS ON ACOUSTICS
October 24(Mon) - 28(Fri), 2022 Gyeongju, Korea

PROCEEDINGS of the
24th International Congress on Acoustics

October 24 to 28, 2022 in Gyeongju, Korea

ABS-0839

A reduced order model including viscothermal losses

Mikkel PALTORP SCHMITT[(1)]; Vicente CUTANDA HENRÍQUEZ[(2)]; Niels AAGE[(3)]; Peter RISBY ANDERSEN[(4)]

[(1)]Department of Electrical & Photonics Engineering, Technical University of Denmark, Denmark, mpasc@dtu.dk

[(2)]Centre for Acoustic-Mechanical Microsystems, Department of Electrical & Photonics Engineering, Technical University of Denmark, Denmark, vcuhe@elektro.dtu.dk

[(3)]Centre for Acoustic-Mechanical Microsystems, Department of Civil & Mechanical Engineering, Technical University of Denmark, Denmark, naage@mek.dtu.dk

[(4)]Audio Research, GN Audio A/S & Jabra, Denmark, prandersen@jabra.com

ABSTRACT

The Boundary Element Method (BEM) is a well-known numerical method for solving time harmonic acoustical problems. While the BEM has attractive features e.g. automatically satisfying the free field conditions, the frequency dependence of the Greens function makes is inconvenient for broadband simulations due to excessive computational costs. This problem becomes worse yet when viscous and thermal effects are included in the BE computations. Recently it has been suggested that a series expansion of the Greens function as well as its directional derivatives together with model order reduction techniques can relieve some of the computational demands. This paper applies similar ideas in the setting of the so-called boundary layer impedance boundary conditions used to approximate viscous and thermal effects. The final computational model can be used to efficiently perform broadband simulations including viscothermal losses of devices on the centimeter scale, thereby paving the path towards e.g. broadband shape optimization of small acoustical devices such as transducers, metamaterials and hearing aids.

Keywords: Boundary Element Method, Viscothermal Effects, Reduced Order Model

1 INTRODUCTION

The Boundary Element Method (BEM) is a well-known simulation technique where the underlying (partial) differential equation is solved through the discretization of a boundary integral. It is a popular choice for problems concerning semi-infinite and infinite domains, as the solution computed from the BEM automatically fulfills the so-called free-field conditions. As a result the method is widespread within the fields of electromagnetics and acoustics as these commonly deal with such domains. As opposed to the Finite Element Method (FEM) the discretization of the BEM result in frequency-depended and dense linear systems. The latter problem can be alleviated by utilizing compression techniques such as the Fast Multipole Method[1] (FMM) and $\mathscr{H}$-matrices[2]. While some details of the two approaches differ they are both based on the same ideas of so-called near and far field splits of the underlying integral operators. While these approaches solves the memory issue of the BEM they still require a reevaluation of the underlying boundary integrals for every frequency of interest. As a result the BEM is cumbersome to apply when one is interested in a wide range of frequencies. Several solutions to this problem has been proposed during the years, all with different pros and cons. These techniques are almost exclusively based on interpolations of either the discrete or continuous form of the boundary integral [3, 4, 5]. In this text the interpolation scheme chosen is that of a Taylor series expansion of the (derivatives of the) Green's function. This approach transforms the time-consuming boundary integral discretization into a sum of matrices. For small orders of Taylor expansions this reduces the assembly significantly, however the total memory used to store the derivatives matrices

makes this approach close to unusable in many cases. This memory increase can be diminished by following the approach taken in Panagiotopoulos et al. [6]. Here a projection matrix is created from the collection of Krylov vectors from specified frequencies. The full system is then projected resulting in a reduced number of DOFs. This approach works under the assumption the solution is spanned by said Krylov vectors, which is true for problems for which a Krylov based iterative solver converges quickly.

The main result presented in this paper is an extension of the model proposed in Panagiotopoulos et al. [6]. This extension makes it possible for the model to also handle the so-called Boundary Layer Impedance (BLI) boundary conditions [7]. The text is structured as follows: In section 2 we describe how the discrete BEM system representing the BLI boundary condition can be formulated as a Taylor series of frequency-decoupled matrices. Next, in section 3 the model order reduction procedure is explained. Finally, in section 4 the proposed model is numerically evaluated using a simple test case.

2 BOUNDARY ELEMENT METHOD WITH BLI BOUNDARY CONDITION

In this section a rudimental description of the BEM, the Boundary Layer Impedance (BLI) boundary condition and the Series Expansion Boundary Element Method (SEBEM) is given.

2.1 The Boundary Element method

The BEM for time-harmonic acoustical problems is based on the discretization of the Kirchoff-Helmholtz representation formula for the scalar Helmholtz equation. The representation formula has the following form

$$c(\mathbf{x})p(\mathbf{x}) = \int_\Gamma G(\mathbf{x},\mathbf{y})\frac{\partial p(\mathbf{y})}{\partial \mathbf{n}_\mathbf{y}}\ \mathrm{d}S_\mathbf{y} - \int_\Gamma \frac{\partial G(\mathbf{x},\mathbf{y})}{\partial \mathbf{n}_\mathbf{y}} p(\mathbf{y})\ \mathrm{d}S_\mathbf{y}, \quad \mathbf{x}\in\Omega, \tag{1}$$

where Ω is the domain with boundary Γ, $c(\mathbf{x})$ is the free coefficient depending only on the geometry at point $\mathbf{x}$ and $(\partial_n G)$ G is the (normal derivative of the) Green's function for the scalar Helmholtz equation, with the form

$$G(\mathbf{x},\mathbf{y}) = \frac{\exp\left(-\mathrm{i}k\|\mathbf{x}-\mathbf{y}\|_2\right)}{4\pi\|\mathbf{x}-\mathbf{y}\|_2}, \qquad \frac{\partial G(\mathbf{x},\mathbf{y})}{\partial \mathbf{n}_\mathbf{y}} = \frac{\exp\left(-\mathrm{i}k\|\mathbf{x}-\mathbf{y}\|_2\right)\left(1+\mathrm{i}k\|\mathbf{x}-\mathbf{y}\|_2\right)(\mathbf{x}-\mathbf{y})^\top \mathbf{n}_\mathbf{y}}{4\pi\|\mathbf{x}-\mathbf{y}\|_2^3}, \tag{2}$$

where $k = \frac{\omega}{c}$ is called the wavenumber. Due to the nonlinear coupling between the frequency-depended wavenumber and the variable of integration inside the exponential, the frequency can not be decoupled from the integration in (1). As a result the integral needs to be recomputed for every frequency of interest, making the use of BEM for large frequency sweeps inconvenient. In subsection 2.3 we describe how these can be decoupled through a Taylor series expansion.

2.2 The Boundary Layer Impedance

The Boundary Layer Impedance (BLI) boundary condition, described in Berggren et al. [7], is an impedance like boundary condition in the way that it linearly relates the pressure and its normal derivative. However, in addition to this relation there is also the addition of the tangential Laplacian

$$\frac{\partial p}{\partial \mathbf{n}} = \left[(\gamma-1)\frac{\mathrm{i}k^2}{k_h} - \frac{\mathrm{i}\Delta_\mathrm{T}}{k_v}\right] p, \tag{3}$$

where k_h and k_v are respectively the thermal and viscous wavenumbers and γ is the ratio of specific heats. The two additional wavenumbers are computed using the frequency and the physical properties of the fluid such as the thermal conductivity, specific heat capacity under constant pressure and the shear and bulk viscosity coefficients [8].

In the following the boundary of the domain is split into two parts. The first will be applied a Neumann boundary condition while the second will be applied the BLI boundary condition (Figure 1).

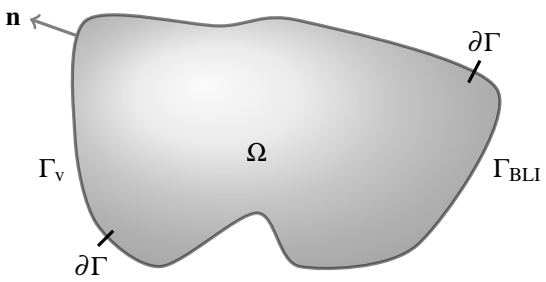


Figure 1. Domain of an interior problem. The boundary is split into two parts: One with a Neumann boundary condition (Γ_v) and one with the BLI boundary condition (Γ_BLI).

Using the boundary splitting and inserting (3) into the representation formula we attain the following

$$c(\mathbf{x})p(\mathbf{x}) = \int_{\Gamma_\mathrm{v}} G(\mathbf{x},\mathbf{y})\frac{\partial p(\mathbf{y})}{\partial \mathbf{n}_\mathbf{y}}\ \mathrm{d}S_\mathbf{y} + \int_{\Gamma_\mathrm{BLI}} G(\mathbf{x},\mathbf{y})\left[\frac{(\gamma-1)\mathrm{i}k^2}{k_h} - \frac{\mathrm{i}\Delta_\mathrm{T}}{k_v}\right] p(\mathbf{y})\ \mathrm{d}S_\mathbf{y} - \int_{\Gamma} \frac{\partial G(\mathbf{x},\mathbf{y})}{\partial \mathbf{n}_\mathbf{y}} p(\mathbf{y})\ \mathrm{d}S_\mathbf{y}. \tag{4}$$

Due to the polynomial representation of the pressure on each element the tangential Laplacian restricts the elements to be at least second order. To relax this restriction we apply integration by parts on the term including the tangential Laplacian. Setting the additional term equal to 0, similar to what is described in Berggren et al. [7], while rearranging a few terms we end up with the following equation of interest

$$\begin{aligned}\int_{\Gamma_\mathrm{v}} G(\mathbf{x},\mathbf{y})\frac{\partial p(\mathbf{y})}{\partial \mathbf{n}_\mathbf{y}}\ \mathrm{d}S_\mathbf{y} = c(\mathbf{x})p(\mathbf{x}) + \int_{\Gamma} \frac{\partial G(\mathbf{x},\mathbf{y})}{\partial \mathbf{n}_\mathbf{y}} p(\mathbf{y})\ \mathrm{d}S_\mathbf{y} \\ - \frac{(\gamma-1)\mathrm{i}k^2}{k_h}\int_{\Gamma_\mathrm{BLI}} G(\mathbf{x},\mathbf{y})p(\mathbf{y})\ \mathrm{d}S_\mathbf{y} - \frac{\mathrm{i}}{k_v}\int_{\Gamma_\mathrm{BLI}} \nabla_\mathrm{T} G(\mathbf{x},\mathbf{y})\cdot\nabla_\mathrm{T} p(\mathbf{y})\ \mathrm{d}S_\mathbf{y}.\end{aligned} \tag{5}$$

In the above only the tangential gradient of the pressure is needed, meaning that elements need only be of at least linear order. Finally, applying the element discretization on (5) the following linear system of equations is computed

$$\left(\mathrm{diag}(\mathbf{c}) + \mathbf{F}(k) - \frac{(\gamma-1)\mathrm{i}k^2}{k_h}\mathbf{H}(k) - \frac{\mathrm{i}}{k_v}\mathbf{T}(k)\right)\mathbf{p} = \mathbf{b}(k). \tag{6}$$

2.3 Series Expansion BEM

As mentioned previously a drawback of the BEM is the frequency-depended integrals. In order to resolve this issue all relevant kernels in (5) is expanded in terms of their respective Taylor series. This approach is sometimes referred to as the Series Expansion BEM (SEBEM), although other series representations of the kernels could have been utilized. The simplest of the Taylor series expansions is that of the Green's function

$$G(\mathbf{x},\mathbf{y}) = \frac{\exp\left(-\mathrm{i}k\|\mathbf{x}-\mathbf{y}\|_2\right)}{4\pi\|\mathbf{x}-\mathbf{y}\|_2} = \frac{1}{4\pi}\sum_{i=0}^{\infty}\frac{(k-k_0)^m}{m!}\frac{(-\mathrm{i}\|\mathbf{x}-\mathbf{y}\|_2)^m}{\|\mathbf{x}-\mathbf{y}\|_2}\exp\left(-\mathrm{i}k_0\|\mathbf{x}-\mathbf{y}\|_2\right), \tag{7}$$

where k_0 is the expansion wavenumber. Applying the analogous on the remaining kernels in (5) we have that the discrete form of (6) can be approximated as

$$\left(\mathrm{diag}(\mathbf{c}) + \sum_{m=0}^{M-1}\frac{(k-k_0)^m}{m!}\left[\mathbf{F}_m - \frac{(\gamma-1)\mathrm{i}k^2}{k_h}\mathbf{H}_m - \frac{\mathrm{i}}{k_v}\mathbf{T}_m\right]\right)\mathbf{p} = \sum_{m=0}^{M-1}\frac{(k-k_0)^m}{m!}\mathbf{b}_m. \tag{8}$$

Note that we already here have truncated the series the Taylor series to be order M (degree $M-1$). As a result the above should strictly speaking be an approximation. While the Series Expansion Boundary Element Method (SEBEM) reduces the assembly time by reducing the integral discretization to matrix additions, the

resulting model have a large memory footprint, stemming from the need to store intermediate matrices. A first fix could be to Taylor expand the full expression in (5) instead of the kernels separately. This would result in only needing to store one derivative matrix (for the total derivative) instead of the 3 required in (8) (one for each integral). However, the implementation of this approach would be significantly more complicated while most likely being less accurate.

3 BOUNDARY ELEMENT METHOD WITH MODEL ORDER REDUCTION

In order to reduce the large memory footprint of the SEBEM a Model Order Reduction (MOR) approach can be utilized. There exist several possible MOR techniques that can be applied with the one used here following that of Panagiotopoulos et al. [6]. In short this approach works under the assumption that the true solution can be well approximated by a lower-dimensional subspace, meaning that the total size of linear system can be reduced by projection onto this subspace.

3.1 Krylov projection

In general a projection based MOR utilizes the assumption that the solution as well as the right-hand side of the linear system of equations can be well-approximated by a lower-dimensional subspace. As such the following are assumed to be good approximations

$$\mathbf{p} \approx \mathbf{U}_\ell \mathbf{p}_\ell, \quad \mathbf{b}_m \approx \mathbf{U}_\ell \mathbf{b}_{\ell m}, \qquad \mathbf{U}_\ell \in \mathbb{C}^{N\times \ell}, \tag{9}$$

where the columns of $\mathbf{U}_\ell$ forms a basis for the lower-dimensional subspace. The Krylov projection technique is based on setting these columns equal to the first ℓ Krylov vectors of the system matrix (subsection 3.2). In order to reduce the system further, one can introduce a projection of the rows. If the projection of the rows is equal to the Hermitian transpose of the column projection, then the approach is called Galerkin. This is the approach taken here. As a result (8) can be approximated as

$$\mathbf{U}_\ell^{\mathsf{H}} \left(\operatorname{diag}(\mathbf{c}) + \sum_{m=0}^{M-1} \frac{(k-k_0)^m}{m!} \left[\mathbf{F}_m - \frac{(\gamma-1)\mathrm{i}k^2}{k_h}\mathbf{H}_m - \frac{\mathrm{i}}{k_v}\mathbf{T}_m \right] \right) \mathbf{U}_\ell \mathbf{p}_\ell = \mathbf{U}_\ell^{\mathsf{H}} \sum_{m=0}^{M-1} \frac{(k-k_0)^m}{m!} \mathbf{U}_\ell \mathbf{b}_{\ell m}. \tag{10}$$

Moving $\mathbf{U}_\ell$ and $\mathbf{U}_\ell^{\mathsf{H}}$ inside the parentheses and using that $\mathbf{U}_\ell$ is unitary, the above can be written as

$$\left(\mathbf{C}_\ell + \sum_{m=0}^{M-1} \frac{(k-k_0)^m}{m!} \left[\mathbf{F}_{\ell m} - \frac{(\gamma-1)\mathrm{i}k^2}{k_h}\mathbf{H}_{\ell m} - \frac{\mathrm{i}}{k_v}\mathbf{T}_{\ell m} \right] \right) \mathbf{p}_\ell = \sum_{m=0}^{M-1} \frac{(k-k_0)^m}{m!} \mathbf{b}_{\ell m}, \tag{11}$$

where all matrices are in $\mathbb{C}^{\ell\times\ell}$ and vectors in $\mathbb{C}^{\ell}$. Given that $\ell \ll N$ the above is a very efficient way of storing the information. In many practical cases one find that storing the full reduced SEBEM requires less memory than storing just a single of the original $N \times N$ matrices.

3.2 Creating a projection matrix

Computing a projection matrix $\mathbf{U}_\ell$ using just the information available at a single frequency does not result in a good approximation on the full frequency range (Figure 3). To resolve this issue information from multiple frequencies is utilized. The collection of frequencies for which this information is extracted will be referred to as *primary frequencies* (denoted by f_i). The total number of primary frequencies is denoted by L. At each primary frequency the full BEM system $(\mathbf{A}_{f_i}, \mathbf{b}_{f_i})$ is computed and the first q Krylov vectors computed using the Arnoldi Algorithm (Algorithm 1).

Algorithm 1 Arnoldi Algorithm

Assemble $\mathbf{A}_{f_i}$, $\mathbf{b}_{f_i}$
$\mathbf{k}_1 \leftarrow \mathbf{b}_{f_i} / \|\mathbf{b}_{f_i}\|_2$
$\mathbf{K}_{f_i} \leftarrow \begin{bmatrix} \mathbf{k}_1 \end{bmatrix}$
for $j = 2 : q$ **do**
  $\mathbf{k}_j \leftarrow \mathbf{A}_{f_i} \mathbf{k}_{j-1} - \sum_{l=1}^{j-1} \left(\mathbf{k}_l^{\mathsf{H}} \mathbf{A}_{f_i} \mathbf{k}_{j-1} \right) \mathbf{k}_l$
  $\mathbf{k}_j \leftarrow \mathbf{k}_j / \|\mathbf{k}_j\|_2$
  $\mathbf{K}_{f_i} \leftarrow \begin{bmatrix} \mathbf{K}_{f_i} & \mathbf{k}_j \end{bmatrix}$
end for

The idea is that by collecting all $\ell = qL$ Krylov vectors will result in a projection matrix that covers the full frequency range of interest. However, doing this without any additional computation will result in a projection matrix that is not necessarily unitary, which was a requirement in order to arrive at (11). In order to arrive at a unitary projection matrix the Singular Value Decomposition (SVD) is applied to the collection of the Krylov subspaces

$$\mathbf{U}_\ell \Sigma_\ell \mathbf{V}_\ell^{\mathsf{H}} = \operatorname{svd}\left(\begin{bmatrix} \mathbf{K}_{f_1} & \mathbf{K}_{f_2} & \dots & \mathbf{K}_{f_L} \end{bmatrix} \right), \tag{12}$$

where $\mathbf{U}_\ell$ is the final projection matrix.

4 NUMERICAL EVALUATION

In this section the accuracy of the Reduced Order Series Expansion Boundary Element Method (ROSEBEM) for the BLI boundary conditions is numerically evaluated. All simulation were performed using the Julia programming language [9, 10] on computational resources provided by the DTU Computing Center [11]. The core of the code was inspired by the OpenBEM software written in MATLAB [12, 13].

4.1 Simulation setups

In this section we numerically study a small tube of length 10 cm and radius 1 cm (Figure 2). The used mesh contained 1916 quadratic elements resulting in a total of 3834 DOFs. The frequency of interest is $[20\,\text{Hz},\ 10\,\text{kHz}]$, meaning that the mesh with $h_{\max} \approx 0.033\,\text{cm}$ had at minimum 10 elements per wavelength, satisfying the standard rule-of-thumb of [14]. The object is excited by applying a Neumann boundary condition at one of the tube ends (Figure 2) while the remaining part of the boundary were applied the BLI boundary condition. In order to evaluate the response the acoustic pressure were evaluated at a point on the opposite side of the Neumann condition.

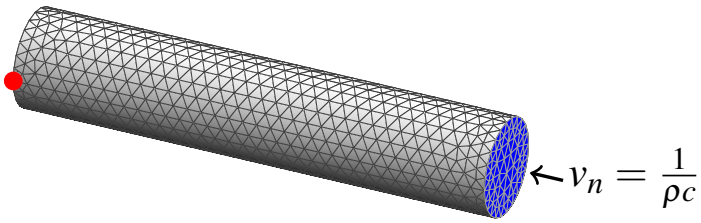


Figure 2. Cylinder with length 10 cm and radius 1 cm. The mesh has 1916 quadratic elements resulting in 3834 DOFs. The pressure is evaluated at the point shown in red, located at $\mathbf{x} = (0\,\text{cm},\ -1\,\text{cm},\ 0\,\text{cm})$.

Two different ROSEBEM with expansion frequency $f_0 = 5\,\text{kHz}$ where evaluated. The first used only the information available at the expansion frequency when creating the projection matrix whereas the second used two additional primary frequencies, meaning that $f_i \in \{1.5\,\text{kHz},\ 5\,\text{kHz},\ 8.5\,\text{kHz}\}$. In both cases the total size of the projection space was 450, resulting in a total reduction of DOFs of approximately 88%.

4.2 Frequency response

The acoustic response is evaluated at increments of 1 Hz in the interval [20 Hz, 10 kHz] resulting in a total of 9981 evaluations. Around the expansion frequency the two ROSEBEM setups are indistinguishable from the full BEM computations (Figure 3). However, at the two ends of the frequency range of interest the setup that only uses the information from the expansion frequency drifts away from the true solution (Figure 3). The pointwise relative error is significantly lower over the full domain when using three primary frequencies as compared to only one (Figure 3), albeit both setups experience large relative errors close to resonances.

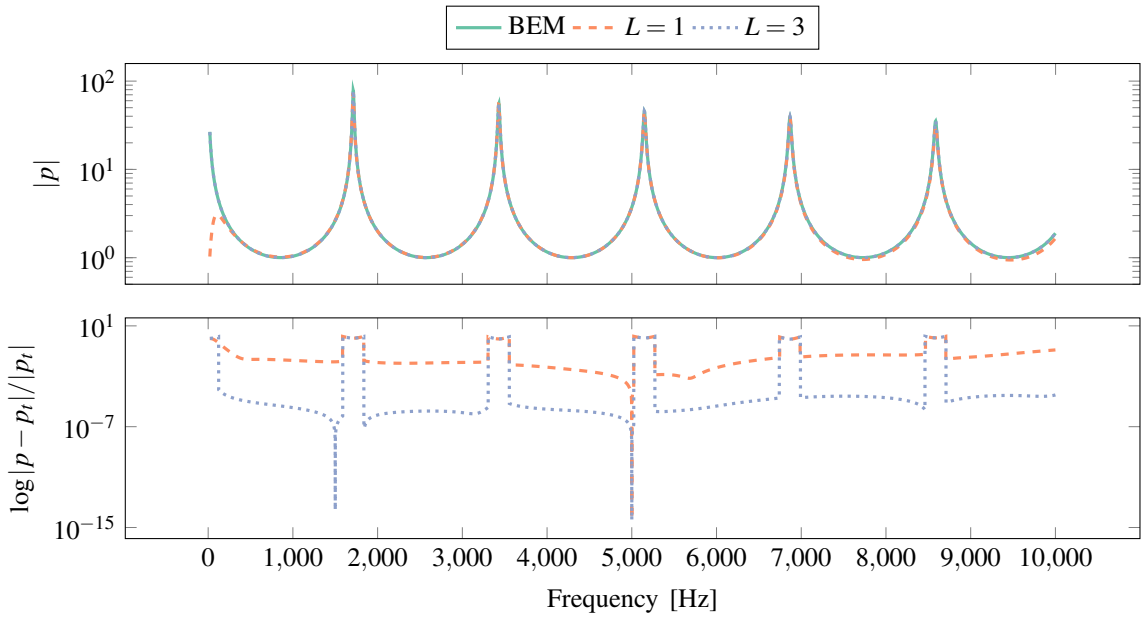


Figure 3. Top: Absolute value of the pressure at point $\mathbf{x}$ as a function of frequency. Bottom: Relative error of the ROSEBEM setups compared to the full BEM solution.

Comparing the computational efforts of the model can easily lead to skewed results as the efficiency greatly depend on the problem at hand. One of the more prominent of these dependencies is the number of frequencies evaluated. The more frequencies evaluated the better the ROSEBEM will perform compared to the full model. It is therefore better to think in terms of the computational and memory scaling of the various components that goes into the ROSEBEM. A good summary of these can be found in Table 1 in Panagiotopoulos et al. [6]. A general rule-of-thumb is that the ROSEBEM should only be utilized if the number of frequencies evaluated is larger than the order of the Taylor expansion.

For our specific setup there were almost 10,000 frequencies evaluated resulting in the ROSEBEM being around 106 times faster than the full solution (Table 1). In practical terms this meant that the total computational time went from close to 5 days to a little over an hour. Comparing the total memory, it was seen that the ROSEBEM used 370.789 MB which is 1.65 times more than the full BEM. Either decreasing or increasing the size of the projection matrix could change these results. However, had the ROM not been applied the SEBEM it would have used close to 27 GB of memory which highlights why the ROM is a crucial part of making the model applicable on regular machines.

Table 1. Computation efforts: Full BEM vs. ROSEBEM.

	Full BEM	ROSEBEM
Computational Time	6.914 min	65 min
Memory Consumption	224.297 MB	370.789 MB

5 CONCLUSIONS

In this short work we extended a Model Order Reduction (MOR) technique for the Series Expansion Boundary Element Method (SEBEM) to handle the Boundary Layer Impedance (BLI) boundary condition. Similar to the previous work the series expansion was based on the Taylor expansion of all relevant kernels and the reduced order model based on the Galerkin projection. Lastly the model was numerically verified and analyzed using a cylinder as a test case. It was found that information from a single frequency was not enough to create a suitable projection basis.

REFERENCES

[1] Liu Yijun. *Fast multipole boundary element method: Theory and applications in engineering*, volume 9780521116596. Cambridge University Press, 2009. ISBN 9780511605345, 0521116597, 9780521116596. doi: 10.1017/CBO9780511605345.

[2] Wolfgang Hackbusch. *Hierarchical Matrices: Algorithms and Analysis*. Springer, 2015. ISBN 3662473232, 3662473240, 9783662473238, 9783662473245.

[3] Suhaib Koji Baydoun, Matthias Voigt, and Steffen Marburg. Low-rank iteration schemes for the multi-frequency solution of acoustic boundary element equations. *Journal of Theoretical and Computational Acoustics*, 29(3), 2021. doi: 10.1142/S2591728521500043.

[4] SM Kirkup and DJ Henwood. Methods for speeding up the boundary element solution of acoustic radiation problems. *Journal of Vibration and Acoustics-transactions of the Asme*, 114(3):374–380, 1992. doi: 10.1115/1.2930272.

[5] Dionysios Panagiotopoulos, Elke Deckers, and Wim Desmet. A two-step reduction method for acoustic BEM systems. In *Forum Acusticum*, pages 2291–2298, Lyon, France, December 2020. doi: 10.48465/fa.2020.0712. URL https://hal.archives-ouvertes.fr/hal-03235474.

[6] Dionysios Panagiotopoulos, Elke Deckers, and Wim Desmet. Krylov subspaces recycling based model order reduction for acoustic bem systems and an error estimator. *Computer Methods in Applied Mechanics and Engineering*, 359, 2020. doi: 10.1016/j.cma.2019.112755.

[7] Martin Berggren, Anders Bernland, and Daniel Noreland. Acoustic boundary layers as boundary conditions. *Journal of Computational Physics*, 371:633–650, 2018. doi: 10.1016/j.jcp.2018.06.005.

[8] Vicente Cutanda Henriquez. *Numerical Transducer Modeling*. PhD thesis, Technical University of Denmark, 2002.

[9] Jeffrey Werner Bezanson, Alan Edelman., Massachusetts Institute of Technology. Dept. of Electrical Engineering, and Massachusetts Institute of Technology. Dept. of Electrical Engineering. Julia : an efficient dynamic language for technical computing - efficient dynamic language for technical computing. 2012.

[10] Jeff Bezanson, Alan Edelman, Stefan Karpinski, and Viral B Shah. Julia: A fresh approach to numerical computing. *SIAM review*, 59(1):65–98, 2017. URL 10.1137/141000671.

[11] DTU Computing Center. DTU Computing Center resources, 2021. URL https://doi.org/10.48714/DTU.HPC.0001.

[12] Vicente Cutanda Henríquez and Peter Møller Juhl. Openbem - an open source boundary element method software in acoustics. *Proceedings of Internoise 2010*, 7:5796–5805, 2010.

[13] MATLAB. *version 9.10.0 (R2021a)*. The MathWorks Inc., Natick, Massachusetts, 2021.

[14] Steffen Marburg. Six boundary elements per wavelength: Is that enough? *Journal of Computational Acoustics*, 10(1):25–51, 2002. doi: 10.1142/S0218396X02001401.

ICA 2022
24th INTERNATIONAL CONGRESS ON ACOUSTICS
October 24(Mon) - 28(Fri), 2022 Gyeongju, Korea

PROCEEDINGS of the
24th International Congress on Acoustics

October 24 to 28, 2022 in Gyeongju, Korea

ABS-0862

Acoustic design through similitude and sensitivity analysis

Christian ADAMS[1]

[(1)]Technical University of Darmstadt, Mechanical Engineering Department, System Reliability, Adaptive Structures, and Machine Acoustics SAM, Germany, christian.adams@sam.tu-darmstadt.de

ABSTRACT

Every physical equation must be dimensionally homogeneous. This statement seems self-evident. In fact, it is the starting point of similitude theory. In fluid mechanics and thermodynamics similitude methods were already developed in the 19th and 20th centuries to carry out model tests on scaled models and to predict the behaviour of the original. In vibroacoustics model tests based on similitude theory have not yet been able to establish themselves. On the other hand, model tests are well suited to validate vibroacoustic properties of mechanical engineering systems in early design phases. This paper describes a method that combines similitude theory with sensitivity analysis. This simplifies the derivation of scaling laws in early phases of product design processes since the method requires only input parameters and output parameters such as geometrical dimensions or material properties and, respectively, modal quantities or acoustic transfer functions. Two case studies, a vibrating car undercarriage structure and gear box housings, demonstrate how model tests can contribute to the acoustic design of these structures. Besides numerical simulations experimental validations will be discussed for the gear box housings as well.

Keywords: Acoustic Design, Similitude, Sensitivity analysis

1 INTRODUCTION

Similitude theory is founded on dimensional homogeneity [1]. Every physical relation on a model scale $\mathfrak{f}^{(\mathrm{m})}$ can be related to that of the original scale (prototype) $\mathfrak{f}^{(\mathrm{p})}$ by a scaling factor

$$\phi = \frac{\mathfrak{f}^{(\mathrm{m})}}{\mathfrak{f}^{(\mathrm{p})}}. \tag{1}$$

The scaling factors can be determined from dimensional analysis [1] or from equations of motion [2]. In vibroacoustics, a generalised modal approach can also be utilised [3, 4]. These approaches exactly replicate the prototype behaviour from that of a scaled model if model and prototype are completely similar. In practice, the similitude is often distorted, e.g. geometrical dimensions are scaled with different factors. The similitude methods can still replicate the prototype behaviour, but the accuracy reduces more and more the more the similitude is distorted [5].

This paper demonstrates in two case studies how similitude analysis can be used in early phases of product design to deepen the understanding of the vibration behaviour of structures. It is the combination with sensitivity analysis that enables similitude analyses in early phases of acoustic design. The first case study will show how sensitivity analysis is used to derive the scaling laws of a generic car undercarriage (generic means that it is simplified in its geometry) from numerical simulations. A parameter study will reveal the limits of applicability of scaling laws. The second case study is a gear box housing in different sizes. Natural frequencies are replicated for gear box housings in various sizes. Numerical analyses contribute to the derivation of scaling laws. The sensitivities are used to master geometrical distortion, and the proposed scaling law is validated in experiments.

2 METHOD

The method has been developed in [5, 6, 7] and is summarised in Figure 1. A power law is posed as scaling approach, which is motivated from Buckingham's Π-theorem of similitude theory [1]. Rewriting the power law in terms of scaling factors of input parameters and output parameters, which is motivated from sensitivity analysis, leads to a scaling law for each output parameter of interest Y_k depending on the input parameters to be scaled X_j.

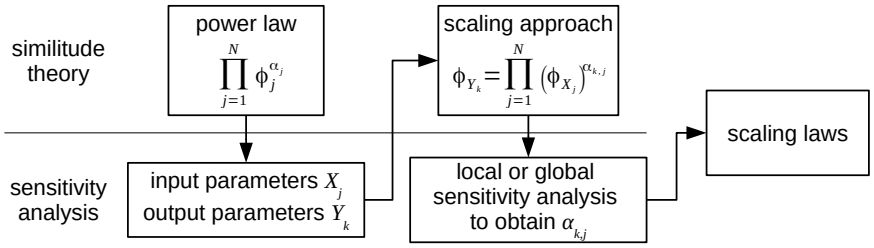


Figure 1. Flow chart of the method to derive scaling laws from similitude theory and sensitivity analysis

The exponents $\alpha_{k,j}$ are calculated from sensitivity analysis, where local or global sampling techniques can be used [5, 6]. It is a feature of the method that input parameters X_j are weighed by their influence on the output parameters Y_k, e.g. a certain input parameter is directly removed from the scaling law if the output parameter is insensitive (corresponding α equals zero) to that input parameter. Details on the method can be found in [5, 6].

3 CASE STUDY 1

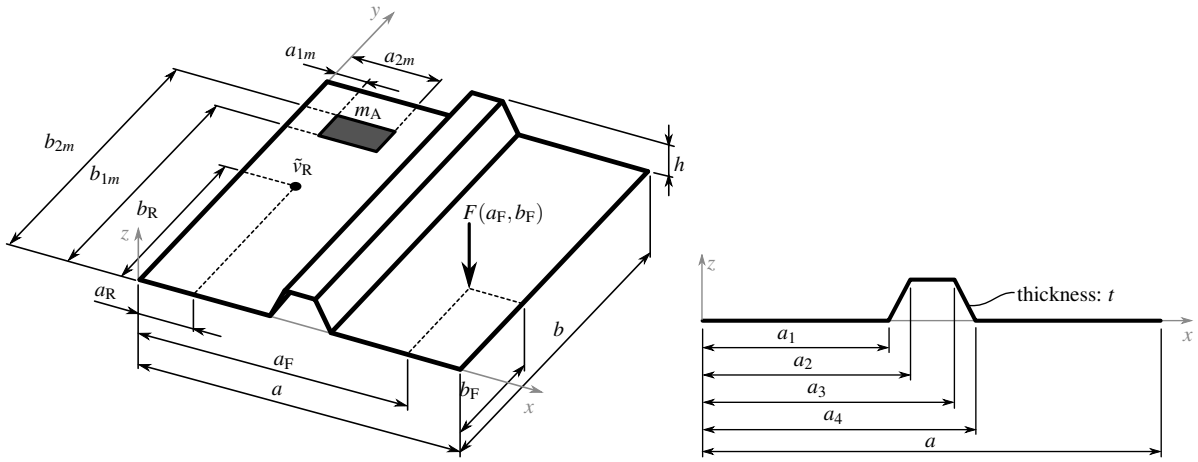
The first case study derives scaling laws for a generic car undercarriage. First, the model is briefly described. Second, scaling laws are derived for the generic car undercarriage. Third, a parameter study shows how the limits of applicability of scaling laws can be determined if the structure is distorted in thickness.

3.1 Model

The generic car undercarriage is illustrated in Figure 2 and its geometrical dimensions are listed in Table 1. We assume a carbon fibre reinforced composite material with $E_x = 1.39 \cdot 10^{11}$ N m^{-2}, $E_y = 1.06 \cdot 10^{10}$ N m^{-2} and $G_{xy} = 5.14 \cdot 10^{9}$ N m^{-2} being Young's modulus in x- and y-direction and shear modulus, respectively. Poisson's ratio, mass density and loss factor are $\mu = 0.28$, $\rho = 1524$ kg m^{-3} and 0.005, respectively. A finite element (FE) model is set up, see [5], with free boundary conditions at the edges. In this paper, only the free vibrations are taken into account, i.e. the excitation force $F(a_F, b_F) = 0$. Double eigenvalues are avoided by detuning one side of the structure with an additional mass m_A that equals 10% of the mass of the generic car undercarriage.

Table 1. Geometrical dimensions of the prototype generic car undercarriage in mm [5]

symbol	value	symbol	value	symbol	value	symbol	value
a	1350	a_1	546	a_{1m}	170	b_F	500
b	1470	a_2	610	a_{2m}	440	b_R	830
h	130	a_3	740	a_R	235	b_{1m}	1080
t	4	a_4	804	a_F	1175	b_{2m}	1250



(a) 3-D view (b) profile view

Figure 2. Prototype of the generic car undercarriage [5]

3.2 Scaling laws

Scaling laws are derived from a local sensitivity analysis of the structure. A central difference scheme is used to approximate the local sensitivities. Geometrical dimensions and material properties are the input parameters of the local sensitivity analysis and the first 20 natural frequencies are the output parameters. Complete similitude requires that the geometrical dimensions are scaled by the same factor. However, in order to investigate the effect of geometrical distortion, all length dimensions are scaled by the common factor ϕ_l, whereas the thickness is scaled with the factor ϕ_t. Material properties are assumed to remain in complete similitude to retain the modal base of the prototype in the model, i.e. Young's moduli and shear modulus are scaled by ϕ_E, mass density by ϕ_ρ and Poisson's ratio is assumed constant ($\phi_\mu \approx 1$). The scaling law for the natural frequencies f_n can then be determined from local sensitivity analysis [5]

$$\frac{f_n^{(\mathrm{m})}}{f_n^{(\mathrm{p})}} = \phi_{f_n} = \phi_l^{-2}\phi_t^{1}\phi_E^{0.5}\phi_\rho^{-0.5}. \tag{2}$$

3.3 Parameter study

The geometrical distortion, i.e. $\phi_l \neq \phi_t$, is investigated in two different manners. First, only the thickness is scaled by the factors $\phi_t = \{1.5,\ 2.0, \ldots,\ 7.0\}$, whereas all length dimensions are retained, i.e. $\phi_l = 1$. Second, the thickness remains constant, but all length dimensions are scaled down by the factors $\phi_l = \{0.9,\ 0.8, \ldots,\ 0.1\}$. It is assumed that the material for prototype and all models is the same, i.e. $\phi_E = \phi_\rho = 1$. Figure 3 shows the maximum error in percent of the first 20 natural frequencies replicated from Equation (2) compared to those obtained from FE calculations [5].

The maximum error more and more increases if the geometry is more and more distorted, which corresponds to an increase of ϕ_t or a decrease of ϕ_l. This behaviour can be expected since complete similitude conditions are more and more violated. However, the amount of error remains below 10% if ϕ_t is altered and if ϕ_l is altered between 0.2 and 1.0. Such small error appears acceptable, particular in early phases of product design, so that the scaling laws can replicate the prototype natural frequencies from those of scaled models with acceptable accuracy. In conclusion, complete similitude conditions can still be considered valid, although the geometry is actually distorted. This finding is in line with [8], where scaling laws for vibrating thin shells are derived.

4 CASE STUDY 2

The second case study uses scaling laws to replicate natural frequencies of gear box housings with various sizes (size range). First, the numerical model is briefly described. Second, scaling laws are derived, where the

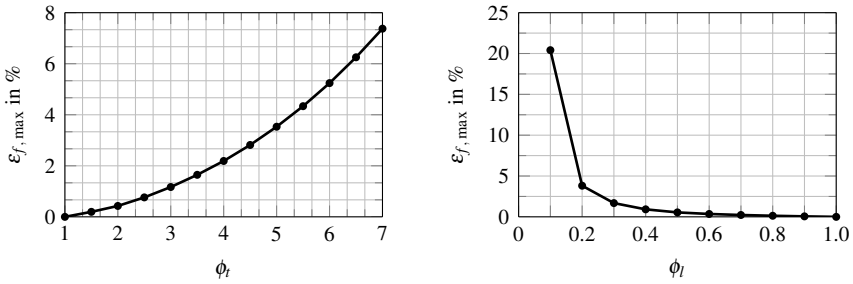


Figure 3. Maximum error of the first 20 replicated natural frequencies, left: distortion of the thickness, right: scale down of all length dimensions [5]

sensitivity is used to master geometrical distortions. Third, experimental results demonstrate that the method applies in practice sufficiently well.

4.1 Model

Three FE models are built as depicted in Figure 4. The material considered is cast iron ($E = 10^{11}\,\mathrm{N\,m^{-2}}$, $\rho = 7200\,\mathrm{kg\,m^{-3}}$, $\mu = 0.26$) and the boundary conditions are free suspensions. The models comprise the main geometrical features of the gear box housings used in the experiments only, but the geometrical dimensions are in distorted similitude. Due to the distorted geometrical similitude the models are referred to as *avatar* according to [3]. Details on the geometrical setup and the FE models can be found in [5]. Figure 5 illustrates the first 20 natural frequencies, which are calculated from the FE models.

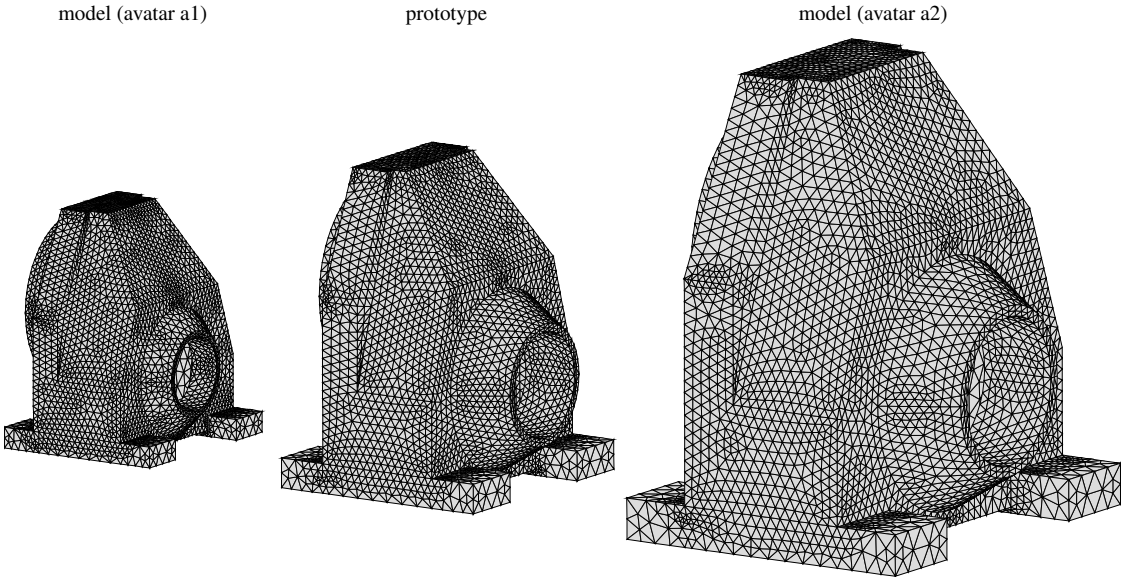


Figure 4. FE models of the three gear box housings [5]

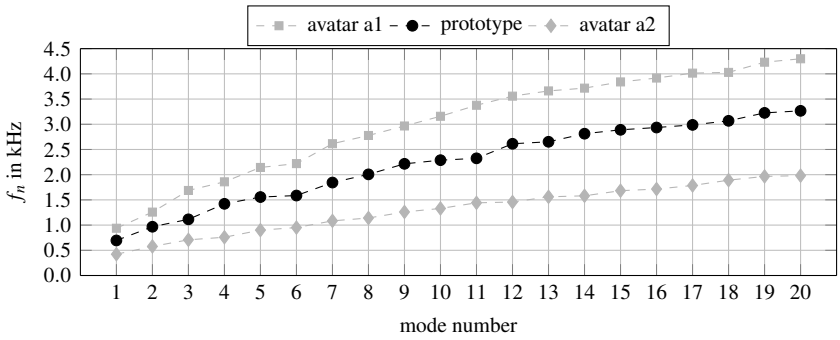


Figure 5. First 20 natural frequencies of the gear box housings [5]

4.2 Scaling laws

The scaling laws are obtained from a local sensitivity analysis of the gear box housings, where each geometrical design parameter is altered separately according to [5]. This leads to the scaling law

$$\frac{f_n^{(\mathrm{m})}}{f_n^{(\mathrm{p})}} = \phi_{f_n} = \overline{\phi}_l^{-1}. \tag{3}$$

The natural frequencies of the models are replicated from those of the prototype by empirically defining a suitable scaling factor $\overline{\phi}_l$ in Equation (3). A first scaling factor can be determined from the mean of all distorted geometrical design parameter, which yields

$$\overline{\phi}_l^{(\mathrm{a1})} = 0.90 \quad \text{and} \quad \overline{\phi}_l^{(\mathrm{a2})} = 1.48 \tag{4}$$

for avatar a1 and avatar a2, respectively [5]. A second scaling factor can be determined from the most sensitive distorted geometrical design parameters, which yields

$$\overline{\phi}_l^{(\mathrm{a1})} = 0.80 \quad \text{and} \quad \overline{\phi}_l^{(\mathrm{a2})} = 1.59 \tag{5}$$

for avatar a1 and avatar a2, respectively [5]. Figure 6 shows the replicated natural frequencies versus those from the FE calculation (cf. Figure 5). The accuracy of the replicated natural frequencies increases if only the most sensitive geometrical design parameters are considered. This can be seen from the fact that the points in Figure 6 are closer to the main diagonal if the scaling factors from Equation (5) are used [5]. Only those geometrical dimensions influence the scaling behaviour of a given natural frequency that exhibit significant vibrations of the corresponding mode shape in the vicinity of these geometrical dimensions. In conclusion, acoustic design can benefit from the sensitivity twofold: (1) Sensitivity analysis can be used to determine the scaling law, i.e. Equation (3). (2) Sensitivity analysis supports engineers to determine a suitable scaling factor in case of distorted geometrical similitude.

4.3 Experimental validation

Finally, the scaling law from Equation (3) is validated through experimental modal analyses. The scaling factors are empirically derived as

$$\overline{\phi}_l^{(\mathrm{a1})} = 0.72 \quad \text{and} \quad \overline{\phi}_l^{(\mathrm{a2})} = 1.56. \tag{6}$$

They are different to those from the numerical calculation since the geometry has been simplified in the FE models [5]. Figure 7 illustrates the three gear boxes on the test stand, where free boundary conditions are realised through air springs. Figure 8 shows the scaled natural frequencies versus those from experimental modal analysis. The numbers indicate the mode numbers since not all prototype modes could be identified in the experimental modal analyses of the models. Although some replicated natural frequencies deviate from the

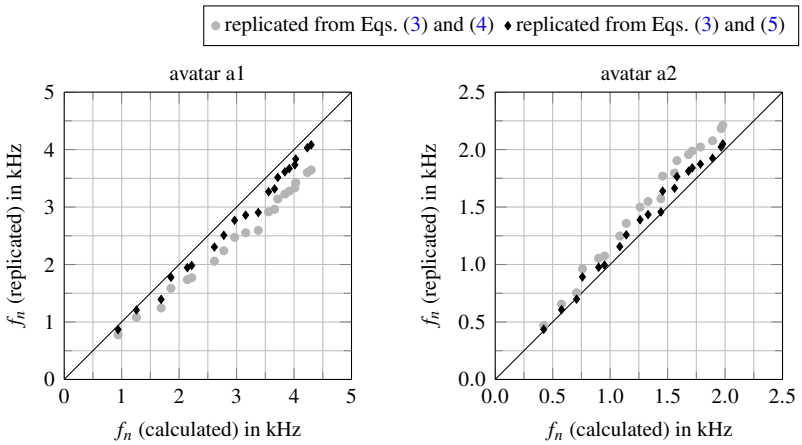


Figure 6. Scaled natural frequencies of the avatars a1 and a2 replicated from those of the prototype [5]

measured ones, the scaling law accurately replicates the natural frequencies of the models from those of the prototype. Thus, the scaling law can be experimentally validated. It should be noted that the modal base of the prototype can only be partially retained in the models due to distorted similitude. This can be seen as a reason for deviations in the scaled natural frequencies [5]. From the viewpoint of acoustic design, this is an important step since the validated method allows to design complex structures with virtual design tools (such as FE models) and to transfer the vibration behaviour to scaled models of a prototype.

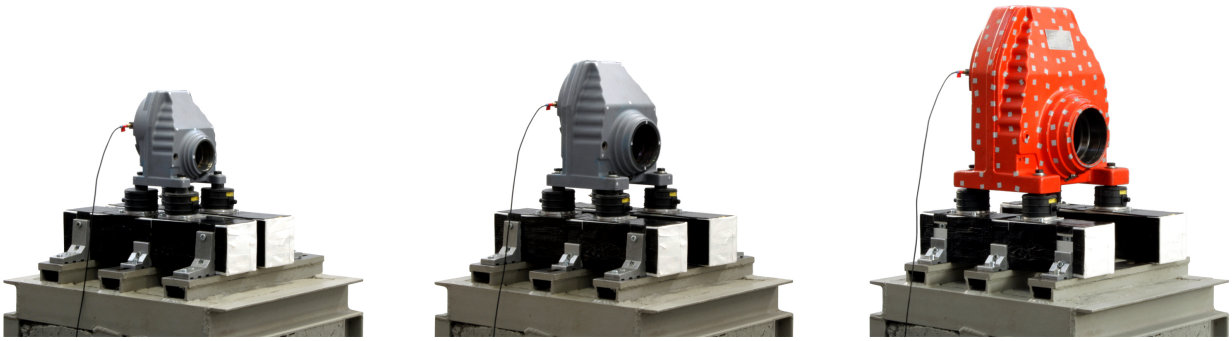


Figure 7. Test stand for experimental modal analysis of gear box housings from left to right: avatar a1, prototype, avatar a2 [5]

5 CONCLUSIONS

This paper demonstrates how similitude analysis can contribute to acoustic design in early design phases by combining similitude theory with sensitivity analysis. Two case studies show the applicability of the method developed in [5, 6, 7]. The combined method allows for deriving scaling laws directly from a sensitivity analysis. This makes the method suitable for early design phases, where numerical models are used and sensitivity analyses can easily be carried out. Furthermore, the sensitivity information can be used to master distorted geometrical similitude. It allows to prioritise geometrical parameters that are relevant for scaling so that relevant geometrical parameters can be selected for the calculation of a scaling factor. Numerical and experimental analyses show that the method applies to structures in complete and distorted similitude. It enables to design structures in a early phase of a product design process and to transfer the vibration behaviour on scaled models of a prototype. This can help to deepen physical understanding of the vibration behaviour of complex structures

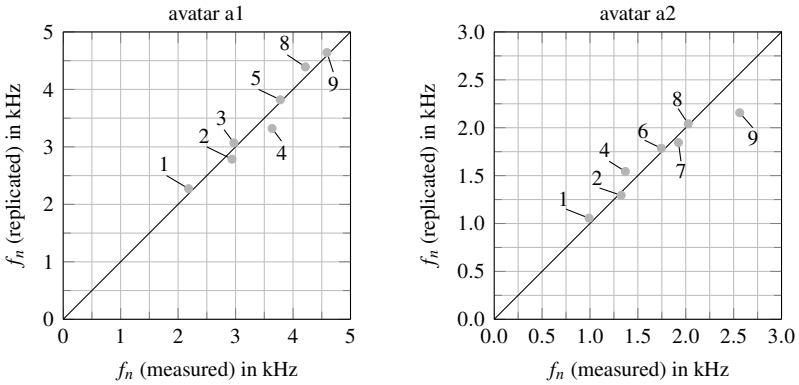


Figure 8. Scaled natural frequencies of avatar a1 and avatar a2 (numbers refer to mode numbers) [5]

so that an acoustic design can be implemented. Nevertheless, the accuracy of the similitude method reduces the more the similitude is distorted [5]. Future research will further improve the similitude method by incorporating the new concept of space scaling. A first study in [9] shows that the method is promising to overcome current limitations of similitude methods based on Buckingham's Π-theorem. But more research is required to develop the method towards distorted similitude in vibroacoustics. Particularly, the distortion of geometry and distortion due to damping will be in the focus.

REFERENCES

[1] Langhaar, H.L.: Dimensional Analysis and Theory of Models. John Wiley & Sons, New York, 1951.

[2] Kline, S.J.: Similitude and Approximation Theory. Springer, Berlin, 1986.

[3] De Rosa, S., Franco, F., Meruane, V.: Similitudes for the structural response of flexural plates. Proceedings of the Institution of Mechanical Engineers, Part C: Journal of Mechanical Engineering Science 230(2):174–188, 2016

[4] Casaburo, A.; Petrone, G.; Franco, F.; De Rosa, S. A review of similitude methods for structural engineering. Applied Mechanics Reviews, 71(3), 2019, 030802-1–030802-32.

[5] Adams, C.: Similitudes and sensitivities as contributions to scaling laws in machine acoustics. Dissertation, Technische Universität Darmstadt, Darmstadt, 2019

[6] Adams, C., Bös, J., Slomski, E.M., Melz, T.: Scaling laws obtained from a sensitivity analysis and applied to thin vibrating structures. Mechanical Systems and Signal Processing 110(2018):590–610, 2018

[7] Adams, C., Bös, J., Melz, T.: Performance of similitude methods for structural vibration analyses of rectangular plates. Mechanical Systems and Signal Processing 162:108074, 2022

[8] Soedel, W.: Similitude approximations for vibrating thin shells. The Journal of the Acoustical Society of America, 49(5):1535–1541, 1971.

[9] Davey, K., Sadeghi, H., Adams, C., Darvizeh, R.: Anisotropic scaling for thin-walled vibrating structures. Journal of Sound and Vibration, 2022, https://doi.org/10.1016/j.jsv.2022.117182, accepted for publication

PROCEEDINGS of the
24th International Congress on Acoustics

October 24 to 28, 2022, in Gyeongju, Korea

Extended abstract

ABS-0264

Observation of underwater noise during the operation of wind turbine in the Korea Southwest offshore wind farm

Young Geul YOON[1]; Dong-Gyun HAN[2]; Dae Hyeok LEE[3]; Jee Woong CHOI[4]

[1,3,4] Department of Marine Science and Convergence Engineering, Hanyang University ERICA, Korea

[2] Division of Ocean Sciences, Korea Polar Research Institute, Korea

[4] Department of Military Information Engineering, Hanyang University ERICA, Korea

ABSTRACT

As the number of offshore wind power plants continues to increase worldwide, there is concern that underwater noise generated by offshore wind farms may have a negative impact on the marine ecosystem. Although there have been many efforts to measure and predict the impact pile driving noise that occurs during the construction of offshore wind power plants, the measurement and characteristic analysis of underwater noise during operation has hardly been carried out. In this study, the underwater noise generated during the operation of a wind turbine in the *Korea southwest offshore wind farm* was measured for 10 days using a moored acoustic recorder. Underwater noise caused by turbine operation was characterized by several tonal components of which the frequencies changed with the rotor speed of the turbine at frequencies below 200 Hz. In addition, a strong tonal component was observed at a frequency of 198 Hz when the rotor speed reached the rated speed.

Keywords: Offshore wind turbine, Underwater noise, Operational noise

1. INTRODUCTION

An increase in offshore wind farm can lead to an increase in underwater noise levels and has the potential to have short- and long-term negative impacts on the marine environment (1,2,3). Until recently, the underwater noise caused by the operation of wind turbines was treated as insignificant because the noise level was relatively low compared to pile driving noise. However, the continued increase in the number and size of offshore wind turbines can lead to significant increases in operational noise levels (4). In this study, in order to understand the potential impact on the marine environment, the operational noise of wind turbine according to changes in wind speed and operating conditions was measured and analyzed.

2. MEASUREMENTS

Underwater operational noise measurements of wind turbine were made in February and March 2021 at the *Southwest offshore wind farm*, which was located in shallow water off the southwest coast of Korea. A self-recording hydrophone (SM3M/standard, Wildlife Acoustics, Inc., USA) was moored approximately 75m away from the wind turbine to measure the underwater noise from operating offshore wind turbine. Turbine operation information including wind speed and rotor speed during underwater noise measurement was provided by Korea Offshore Wind Power Co., Ltd.

3. RESULT

Operational noise was mainly generated at the low frequencies below several hundred Hz, and strong tonal components were observed at frequencies below 200 Hz. As wind speed increased, the

[1] ygyoon@hanyang.ac.kr
[2] edh0921@naver.com
[3] dghan@kopri.re.kr
[4] choijw@hanyang.ac.kr

tonal frequency below 100 Hz tended to increase with rotor speed from the lowest rotor speed of 6.4 rpm to the rated speed of 10.7 rpm. The rated speed was reached when the wind speed was ~8.1 m/s. However, after the rotor speed reached the rated speed, the tonal frequency did not increase even if the wind speed was further increased, and a very strong tonal component with a frequency of ~200 Hz was observed. As shown in Fig. 1(a), the periodicity in the spectrum observed at frequencies below 50 Hz seems to be flow noise caused by tidal changes.

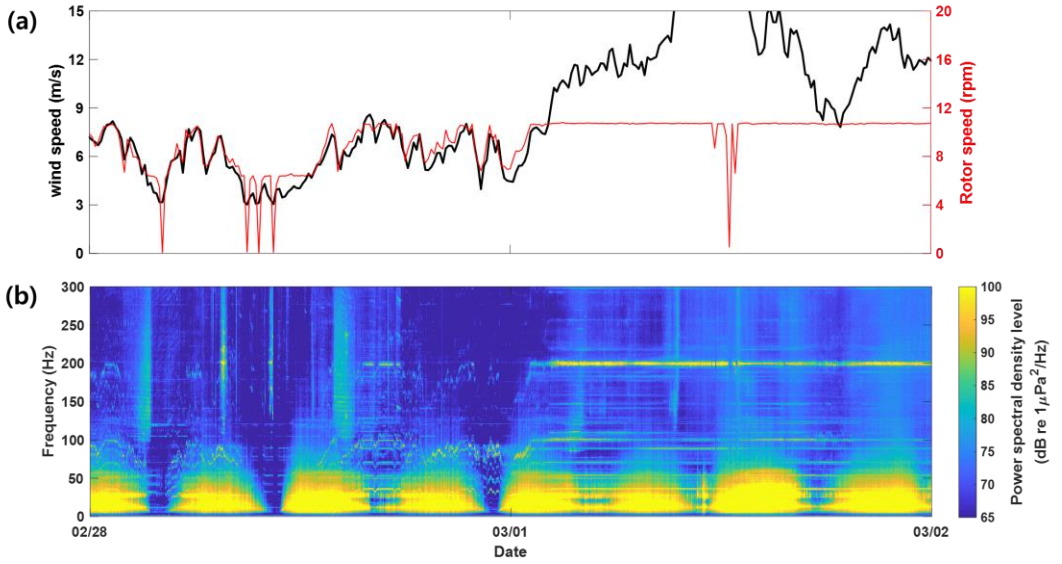


Figure 1 – Examples of (a) the time series data for wind speed and rotor speed measured SCADA system and (b) spectrogram of operational noise measured about 75 m from wind turbine.

4. CONCLUSIONS

In the *Southwest offshore wind farm*, which was located in shallow water off the southwest coast of Korea, the underwater noise radiated into the water during operation of a jacket-type wind turbine was measured. It was confirmed that the spectral properties of the operational noise depend on the rotational speed of the rotor due to the change in wind speed. The tonal frequency of the operational noise is estimated to be due to the gear mesh frequencies of the gearbox and their harmonics (4,5).

ACKNOWLEDGEMENTS

This work was supported by Korea Institute of Energy Technology Evaluation and Planning(KETEP) grant funded by the Korea Government (MOTIE) (20203030020080, Environmental Impact Analysis on the Offshore Wind Farm and Database System Development).

REFERENCES

1. Yang CM, Liu ZW, Lu LG, Yang GB, Huang LF, Jiang Y. Observation and comparison of tower vibration and underwater noise from offshore operational wind turbines in the East China Sea Bridge of Shanghai. J Acoust Soc Am. 2018;144(6):EL522.
2. Popper AN, Hice-Dunton L, Jenkins E, Higgs DM, Krebs J, Mooney A, Rice A, Roberts L, Thomsen F, Vigness-Raposa K, Zeddies D, Williams KA. Offshore wind energy development: Research priorities for sound and vibration effects on fishes and aquatic invertebrates. J Acoust Soc Am. 2022;151(1):205-215.
3. Han DG. Choi JW. Measurements and Spatial Distribution Simulation of Impact Pile Driving Underwater Noise Generated During the Construction of Offshore Wind Power Plant Off the Southwest Coast of Korea. Frontiers in Marine Science, 2022;8:654991.
4. Tougaard J, Hermannsen L, Madsen PT. How loud is the underwater noise from operating offshore wind turbines?. J Acoust Soc Am. 2020;148(5):2885-2893.
5. Pangerc T, Theobald PD, Wang LS, Robinson SP, Lepper PA. Measurement and characterisation of radiated underwater sound from a 3.6 MW monopile wind turbine. J Acoust Soc Am. 2016;140(4):2913-2922.

ICA 2022
24th INTERNATIONAL CONGRESS ON ACOUSTICS
October 24(Mon) - 28(Fri), 2022 Gyeongju, Korea

PROCEEDINGS of the
24th International Congress on Acoustics

October 24 to 28, 2022 in Gyeongju, Korea

ABS-0285

Influence of the pile geometry on the underwater noise during offshore pile driving.

Elin KLAGES, Stephan LIPPERT, Otto VON ESTORFF

Hamburg University of Technology (TUHH), Institute of Modelling and Computation, Germany, mub@tuhh.de

ABSTRACT
Offshore wind energy is evolving worldwide. Very often, impact-driven monopiles are used as foundations for offshore wind turbines. However, driving piles into the seabed causes very high underwater sound pressure levels, which might endanger animals living in the sea. Therefore, several prediction methods for the occurring underwater sound pressure levels from pile driving have been developed in the past years. Furthermore, different noise mitigation systems exist to decrease the noise emission into the water. Additional knowledge of the sound source, i.e., the driven pile, would simplify predictions and help the development of impact hammers or piles emitting less noise. The present paper applies findings from the theory of axisymmetric vibrations of cylindrical shells as well as their sound radiation to the field of offshore pile driving.

Keywords: Offshore pile driving, underwater noise, finite element method, shell theory, sound radiation

1 INTRODUCTION

Offshore wind energy is on the rise in many countries. In 2022, the German government decided to almost quadruple the nowadays installed capacity of offshore wind energy [1, 2]. Similar goals have been set by other countries. Although offshore wind energy is a renewable energy source, placing an offshore wind park in the sea also affects negatively its environment. One aspect is the sound emission during construction using monopiles, which are a very common foundation for offshore wind turbines. To drive a pile into the sea bed, an impact hammer is used. Due to the hammer impact on the pile head, waves are excited and travel along the pile. The vibrations of the pile excite sound waves in the surrounding air, water and sea bed. The resulting underwater sound pressure might be very high, possible dangerous for mammals and fishes [3]. Therefore many countries have imposed limits for resulting underwater sound pressure levels. Throughout this paper, the sound exposure level (SEL) is used as an exemplary limit [4]

$$\mathrm{SEL} = 10 \log_{10} \left(\frac{1}{t_0} \frac{\int_{t_1}^{t_2} p^2(t)\,\mathrm{d}t}{p_0^2} \right). \tag{1}$$

Often, noise mitigation systems to hinder sound propagation underwater, e.g. bubble curtains, are used to ensure these limits. Additionally, state of the art hammers cause a longer, smoother impact than hammers from a decade ago. However, the capacity, and therefore also the size as well as the mass of the installed offshore wind turbines increase and the pile dimensions increase as well. Unfortunately, larger piles cause higher sound pressure levels [5].

The present paper aims for explaining possible reasons why larger piles cause higher sound pressure levels, even if the same ram energy is used. Here, the effect of the pile diameter on the propagation of waves in the pile and the radiation into the water is taken into account.

To simplify the analysis, neither the conical top of the pile nor the influence of the wall thickness is considered. The pile is assumed to be a hollow cylinder of constant wall thickness of 100 mm and a diameter range from 1 m to 12 m.

A shell model for the vibration of the pile and and a radiation model for infinitely long cylinders are applied to realistic diameters and a frequency range up to 100 Hz. The results are compared with results from a numerical model and consequences for the reduction of pile driving noise are discussed.

2 MODELS

In the following, the three models applied here are presented. The first two are analytical models, namely a shell model to infer properties of the vibrations of the pile and a radiation model to estimate how much of the energy of the pile converts to sound energy in the water. The third one is a numerical model, a finite-element (FE) model, which is capable of taking a more realistic scenario into account, especially the finite length of the pile and the sea bed.

2.1 Shell model

A shell is a curved structure where one dimension is small compared to the other two. Different models exist for cylindrical shells. For the present paper, a by Means modified version of the Donnell model of a thin shell is used [6], [7]. The Donnell model is based on the bending theory. Means modified the model with respect to three aspects: the model was extended for the dynamic case; the model was further simplified for a very thin shell, i.e. all higher order terms were omitted, and the model was extended to include fluid loading, i.e. water outside of the shell. The model is represented by the equations

$$u_{\tau\tau} - \left[u_{x'x'} + \frac{1-\nu}{2} u_{y'y'} + \frac{1+\nu}{2} v_{x'y'} + \nu w_{x'} \right] = 0, \tag{2}$$

$$v_{\tau\tau} - \left[v_{y'y'} + \frac{1-\nu}{2} v_{x'x'} + \frac{1+\nu}{2} u_{x'y'} + w_{y'} \right] = 0, \tag{3}$$

$$w_{\tau\tau} + [\nu u_x + v_y + w] + \varepsilon \nabla^4 w = i\Omega Z' w. \tag{4}$$

Here, x is the axial and y the circumferential direction, i.e. $y = R\phi$ where R is the radius of the middle surface, i.e. $R = r_i + (r_e - r_i)/2$ if r_e is the outer radius and r_i the inner radius. The angle is denoted ϕ, x', y' stand for $x/R, y/R$ respectively. The displacements u, v and w of the middle surface refer to the directions x, y and the radial direction r. The dimensionless frequency is Ω defined as ω/ω_r with the ring frequency

$$\omega_r = \sqrt{\frac{E}{((1-\nu^2)\rho R^2)}}, \tag{5}$$

the Young's modulus E and the density ρ. The symbol τ refers to the dimensionless time $\omega_r t$. The poisson ratio is denoted ν and ε stands for $h^2/(12R^2)$, where h refers to the wall thickness. The fluid loading outside of the pile is included via the resulting force in radial direction, i.e. $i\Omega Z' w$, where i is the imaginary unit and Z' equal to $Z_{\text{rad}}/(\rho h \omega_r)$, where Z_{rad} is the radiation impedance. The radiation impedance may be approximated by that of a flat plate, in this case

$$Z' \approx \frac{\rho_f R}{\rho h \sqrt{\left(\frac{\omega_r^2 R^2}{c^2} - \frac{1}{1-\nu^2} \right)}}, \tag{6}$$

where ρ_f is the density and c the sound velocity of the fluid.

To solve these equations, planar waves, inside the cylinder cross section, of constant frequencies are assumed,

$$\begin{pmatrix} u \\ v \\ w \end{pmatrix} = \begin{pmatrix} A \\ B \\ C \end{pmatrix} e^{i(\alpha x' + \beta y' + \Omega \tau)}, \tag{7}$$

where, the dimensionless wave numbers are introduced, $\alpha = k_x R$ and $\alpha = k_y R$. Based on the two equations above, a system of algebraic equations and the corresponding dispersion equation (i.e. characteristic polynomial) can be derived. The here relevant case is for $\beta = 0$, i.e. waves propagating in direction of x. Finding the roots for this equation yields to possible waves travelling along the pile. For these waves, the ratio of C to A, as defined in Eq. (7), can be obtained, which is the reason why this model is used here. For quasi-longitudinal waves, an exemplary ratio of C to A with respect to the dimensionless frequency is shown in Figure 1s.

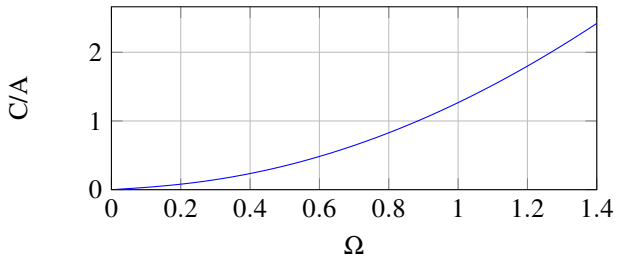


Figure 1. Amplitude of radial to axial displacement of quasi-longitudinal waves propagating in x-direction of the cylinder shell with respect to the dimensionless frequency based on [7]. The wall thickness to radius ratio is 0.01. The material parameters are: E=210 N/m^2, ρ=7850 kg/m^3,ν=0.3, ρ_f=1000, c=1500 m/s.

2.2 Radiation

The sound radiation of a cylinder can be estimated using Hankel functions to solve the linear wave equation in cylindrical coordinates as shown for example in Möser, 2010. The here relevant case in for axisymmetric waves propagating in x-direction. Here it is irrelevant if the cylinder is hollow or full.

Based on the sound pressure field, the radiation efficiency $10\log_{10}(\sigma)$ can be determined [8]. The ratio σ is defined as

$$\sigma = \frac{P}{\rho_f c S \,\mathrm{mean}\left\{v_{\mathrm{rms}}^2\right\}}, \tag{8}$$

where P is the radiated power, S the surface of the radiating body and $\mathrm{mean}\left\{v_{\mathrm{rms}}^2\right\}$ the spatial mean of the square of the root mean square particle velocity [8]. For a cylinder of infinite length, the radiation efficiency depends on the radial wave number in the surrounding medium k_r and the outer radius of the pile r_e [8], as shown in Figure 2.

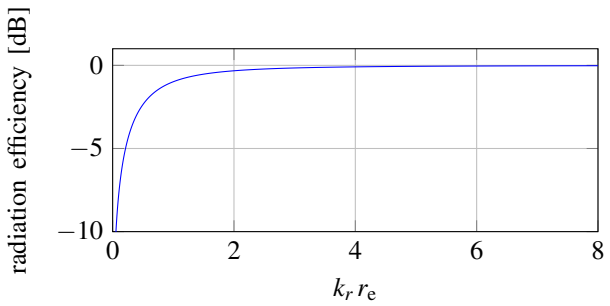


Figure 2. Radiation efficiency for an infinitely long cylinder for axisymmetric waves propagating in the direction of x [8].

2.3 Numerical model

A finite element model in the time domain is used to simulate the wave propagation due to the ram impulse in the pile, water and sea bed. The velocity at the pile head is defined as boundary condition to model the ram

impulse. The output of interest is the acoustic pressure, here in 10 m distance to the pile, from which the mean SEL can be calculated and the deformation velocity at the pile in z and r-direction, here exemplary at 30 m below the pile head. The pile is axisymmetric. The same can be assumed for the sea bed without affecting the analysis in the present paper, therefore a discretization of half the cross section is sufficient. The model was implemented within the program Abaqus.

The pile and sea bed are modelled as linear elastic. The latter is modelled with horizontal, parallel layers, where each layer is described using the following material parameters: the Young's modulus, the density, the poisson number, and rayleigh damping parameters. Here, the values obtained for wind park Bard Offshore I [9] were used. Rayleigh damping is also defined in the embedded part in the pile to model effects of damping of the sea bed which cannot be modelled by the linear elastic model of the sea bed. The linear wave equation is the governing equation for the water. The interface of water and pile, and water and sea bed are tied. The radius of the water and sea bed is 20 m. To avoid reflections at the border of the numerical model, which do not represent borders in reality, a matching impedance condition in water and infinite elements in the soil are used. The boundary condition at the water surface is $p = 0$.

Bilinear elements are used for the pile and soil. The size of the elements in the soil is approximately 20 cm x 20 cm. The height of the elements in the pile is as well 20 cm, but four elements per wall thickness are used. For the water, linear acoustic elements, approximately 20 cm x 20 cm, are employed. The total simulation time is $t = 0.15\,s$.

The model is largely based on the models developed during the project BORA [10], which were extensively validated [9].

3 ANALYSIS OF THE PILE AS SOUND SOURCE

In the following three subsections, the general theory introduced above, is applied to the exemplary pile dimensions ($d = 1, 2, \ldots, 12$ m, $h = 100$ mm) and frequency range (up to 100 Hz) used in the present paper.

3.1 Application of the shell model

The condition $h/R < 0.1$ for a thin shell is for a pile not necessarily true. For the chosen exemplary dimensions, this conditions are not fulfilled for the outer diameter of $d = 1$ m and 2 m. However, the condition $h/\lambda \ll 1$ is fulfilled for all considered frequencies. The most important difference might be that fluid loading is taken into account only outside the cylinder, not inside, since fluid loading has a significant effect on the vibrations of the pile. Also important to note is, that due to the assumption of the infinitely large shell, the effects of reflections at the ends are not taken into account.

Keeping these limitations in mind, the curve shown in Figure 1 can be applied for a specific pile diameter, using

$$f = \frac{1}{2\pi}\,\Omega\,\omega_r = \frac{1}{2\pi}\,\Omega\,\sqrt{\frac{E}{(1-\nu^2)\,\rho\,R^2}}. \tag{9}$$

The results for three exemplary pile diameters are shown in Figure 3, adapted to the here exemplary considered frequency range. These curves show that the ratio of the radial and axial component of the deformation increases significantly with frequency and diameter.

3.2 Radiation

Using $k_x = \sqrt{k_0^2 - k_r^2}$ [8] and the corresponding approximate sound velocities for water and steel, $c_w = 1500$m/s and $c_s = 6000$ m/s, one can determine the radiation efficiency for axisymmetric waves propagating in x-direction of the cylinder. The results are shown in Figure 4 for the pile diameters $d = 1, 6, 12$ m. The curves support the hypothesis that more energy is radiated as acoustic energy into the surrounding water the higher the frequencies are. Also, because of the decreasing ratio of wave length to pile diameter, the radiation efficiency increases significantly with larger pile diameters.

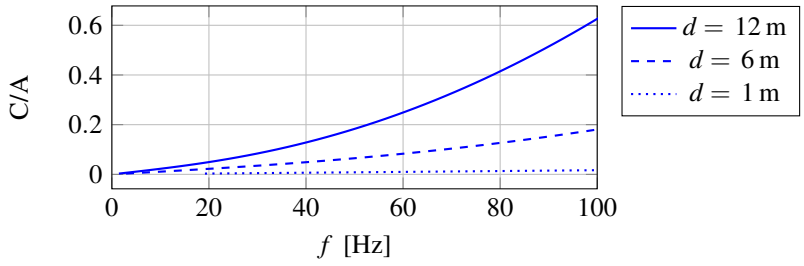


Figure 3. Amplitude of radial to axial displacement of quasi-longitudinal waves propagating along the axis of the cylinder for three exemplary diameters.

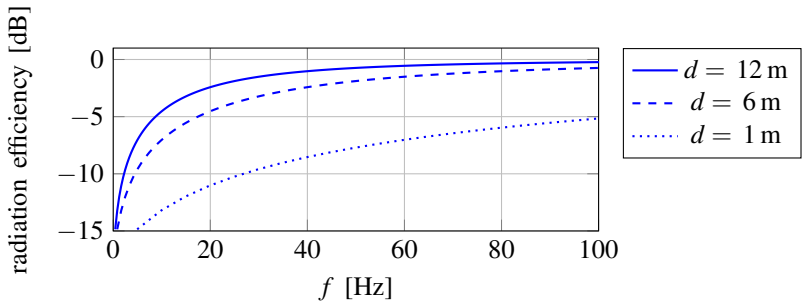


Figure 4. Radiation efficiency for an infinitely long cylinder,[8], made of steel and adapted for radiation into water for three exemplary diameters.

3.3 Numerical results

An artificial impulse was used for the ram impulse, i.e. the velocity at the pile head. The artificial impulse and its frequency spectrum are shown in Figure 5.

The numerical model allows to determine the axial and radial displacement as well as the sound pressure level. The mean ratio of the radial to axial velocity for each pile diameter is shown in Figure 6. For each pile diameter, exactly the same pile head velocity, as given in Figure 5, was used. Therefore, the results show that although the frequencies did not change, the ratio depends strongly on the pile diameter.

4 DISCUSSION

The SEL increases with an increasing pile diameter, even though the frequency spectrum does not change, as shown in Figure 6. This means, that a larger portion of the energy of the ram impulse is radiated as acoustical

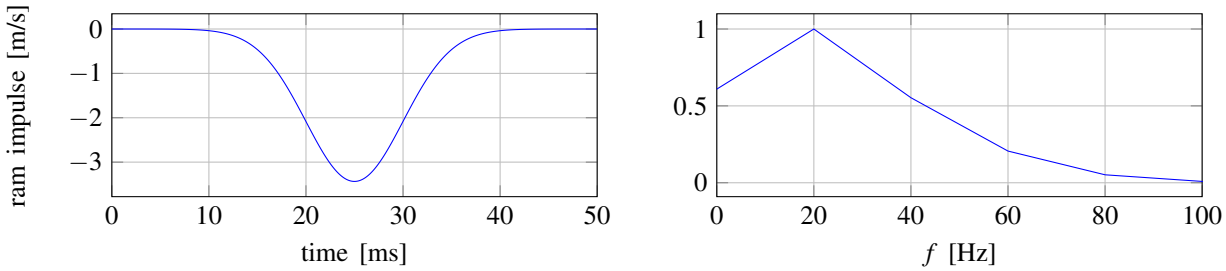


Figure 5. Artificial impulse which is set as the boundary condition at the pile head and the corresponding frequency spectrum.

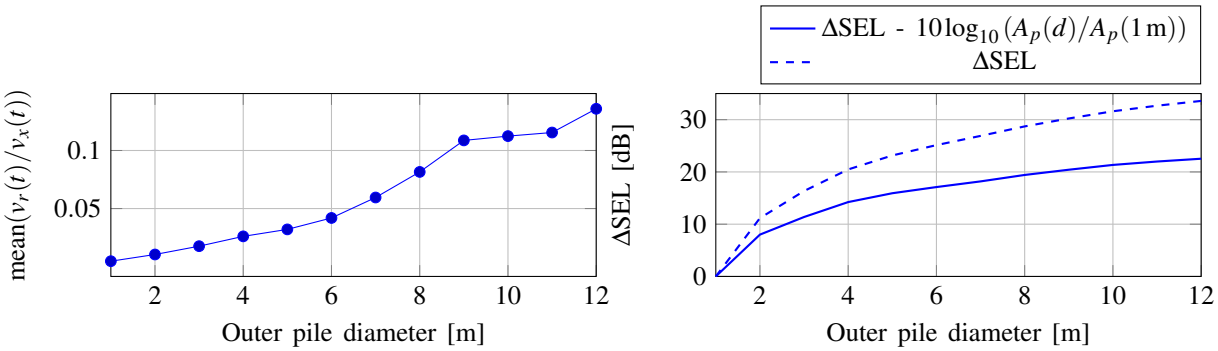


Figure 6. Numerical results: Mean ratio of radial to axial velocity at 30 m below the pile head. (left) ΔSEL at 15 m distance to the pile center for different radii but the same ram impulse. (right)

energy into the water. One reason might be the increasing relative radial amplitude. Based on the shell model, the ratio increases with increasing pile diameter, as shown in Figure 3. The results of the FE-simulations, for the ratio of the axial and radial velocity v_r/v_x, show a similar trend. The mean ratio increases with increasing pile diameter, as shown in Figure 6. Another possible reason is the increase in radiation efficiency with increasing pile diameters. Based on the theory for an infinitely long cylinder surrounded by water, the radiation efficiency increases, as shown in Figure 4.

The finite length of the pile, i.e. reflections at the ends, the influence of the embedded part of the pile and the water inside the pile are only considered in the FE-model. Despite of this, the results shown in Figure 6 match rather well with the expected qualitative behaviour based on the shell and radiation model.

To decrease noise during pile driving, based on the shown results, a smaller pile diameter and a ram impulse in the lower frequency spectrum appear to be beneficial. The former seems to be impractical, pile diameters for offshore wind turbines have been rising. The latter, in the form of a prolongation of the ram impulse to decrease noise, has been applied in state of the art hammers. The slower energy transmission due to a longer impulse itself is unlikely to be the reason for the decrease in the SEL, as long as the sound radiation still falls into the time period defined in Eq. (1). More likely are the reasons described here, namely a decreasing radial deformation and a decreasing radiation efficiency for lower frequencies.

Therefore, the approach might be to move the frequency spectrum of the impulse towards lower frequencies to reverse the effect of the larger pile diameter. However, two aspects cause difficulties here. First, a longer impulse, using the same ram energy, causes lower forces which leads to a conflict with the drivability. Second, although less energy in the lower frequency domain might be converted to acoustic energy, damping in the water, sea bed and also due to noise mitigation systems, e.g. a bubble curtain, might be less effective for lower frequencies.

5 CONCLUSIONS

Already known was that larger pile diameters tend to increase and that longer, smoother ram impulses tend to decrease sound pressure levels. The present paper provides a compelling explanation for both of these observations. The results from the shell model indicate that the radial component of the vibration of the pile increases with higher frequencies. The radiation model indicates that the same is true for the radiation of sound waves into the water. Depending on the pile diameter, the same frequency might be rather high or low, e.g. $f = 40\,\mathrm{Hz}$ is a rather low frequency for a diameter equal to 1 m but a rather high frequency for a diameter equal to 12 m.

Based on these results it seems beneficial to prolong the impulse, if the pile diameter increases, to maintain the ram energy in the frequency range where less energy is converted to acoustic energy in the water. However, additional analysis is required. Most importantly the SEL at 750 m distance in combination with secondary noise mitigation should be taken into account, because for lower frequencies, damping in the water and sea bed might be lower as well, which could reverse, at least partly, the noise reduction due to the longer impulse.

REFERENCES

[1] Koalitionsvertrag zwischen SPD, Bündnis 90/Die Grünen und FDP, 2021

[2] Status des Offshore-Windenergieausbaus in Deutschland - Jahr 2021, Deutsche WindGuard GmbH, 2022

[3] Thomsen, F.; Lüdemann, K,; Kafemann, R.; Piper, W., Effects of offshore wind farm noise on marine mammals and fish, biola, Hamburg, Germany on behalf of COWRIE Ltd, 2006

[4] Juretzek, C; Schmidt, B; Boethling, M., Turning scientific knowledge into regulation: effective measures for noise mitigation of pile driving. Journal of Marine Science and Engineering, 2021

[5] Koschinski, S.; Lüdemann, K., Noise mitigation for the construction of increasingly large offshore wind turbines, Bundesamt für Naturschutz (BfN), 2020

[6] Donnell LH, Stability of thin-walled tubes under torsion. NACA Rep. No. 479, 1935

[7] Means S.L., Wave phenomena of fluid loaded cylindrical shells. The Pennsylvania State University, 1994

[8] Möser M., Körperschall, Springer, 2010

[9] von Pein, J.; Lippert, S.; von Estorff, O., Validation of a finite element modelling approach for mitigated and unmitigated pile driving noise prognosis. The Journal of the Acoustical Society of America, 2021

[10] Heitmann, K.; Mallapur, S.; Lippert, T.; Ruhnau, M., Lippert, S.; von Estorff, O., Numerical determination of equivalent damping parameters for a finite element model to predict the underwater noise due to offshore pile driving. Proceedings of Euronoise 2015, Maastricht, Netherlands, 2015

ICA 2022
24th INTERNATIONAL CONGRESS ON ACOUSTICS
October 24(Mon) - 28(Fri), 2022 Gyeongju, Korea

PROCEEDINGS of the
24th International Congress on Acoustics

October 24 to 28, 2022 in Gyeongju, Korea

Extended abstract

ABS-0591

Numerical simulation of pile-driving induced-noise propagation into the ocean: effects of sedimentary basins and interaction of two distant pile driving operations

Paul Cristini[(1)], Louise Pacaut[(1)] and Nathalie Favretto-Cristini[(1)]

[(1)]Aix-Marseille Univ, CNRS, Centrale Marseille, LMA, Marseille, France

ABSTRACT

Pile driving is a major source of the noise generated by human activities in the ocean. The complex wavefield which is generated by this activity depends not only on the water column characteristics but also on the structure of the sediment layers beneath. In general, this structure is considered horizontally stratified with a gradient of mechanical properties. In this presentation, we propose to investigate a sediment configuration with a heterogeneous structure including two sedimentary basins. For this purpose, we performed several numerical simulations using a 2D time-domain spectral element method which allows for accurate handling of the characteristics of the complex marine environment (complex bathymetry and elastic sediments). We emphasize the presence of interface waves of the Stoneley-Scholte type. Additionally, we propose a method to generate 3D interaction maps of two distant pile driving operations using only one 2D simulation. Our results show the importance of taking into account the phase of the signals to correctly evaluate the interferences between the two operations.

Keywords: Pile driving, Wave propagation, Interface waves, Numerical modeling

1 INTRODUCTION

Pile driving is a major source of anthropogenic noise in the ocean. Many studies have been conducted on this topic, see for example the review article by A. Tsouvalas [1] and the references cited in this paper. Accurately predicting the noise levels generated in the water column by this type of source is fundamental for a reliable assessment of its potential hazards. In order to improve the understanding of the distribution of the ocean noise level generated by a pile-driving operation, this work aims to study the influence of a complex geological environment on the observed signals. Usually, a nearly horizontally stratified environment with a velocity gradient is considered, but this configuration may not reflect some situations where the sedimentary layer structure comes from a more complex geology. For example, sedimentary basins are known to strongly modify the acoustic wave field in the water column [3].

In this work, we chose to consider an ocean floor with two sedimentary basins and study how their presence can affect the propagation of acoustic waves in the water layer.

In a first step, a 2D model is built and used to perform numerical simulations in the time domain of acoustic and seismic wave propagation. Then, in a second step, the results of these numerical simulations are analyzed and some conclusions are drawn.

2 CONFIGURATION

We first design a 2D model of the structure of the ocean bottom with two sedimentary basins (se Figure 1) lying on a rock basement. The length of the model is 13 km. The first sedimentary basin is 10m deep with en extension of 3 km while the second sedimentary basin is 3m deep with a 2 km extension. In the vicinity of the pile, the sediment layer thickness is 2m. The water depth increases steadily with distance starting at 15m and ending at 50m. At the end of the model, far from the source, the layer structure is range independent.

In order to perform the numerical simulations, the entire domain is meshed with quadrilateral elements using the Gmsh Software[4].

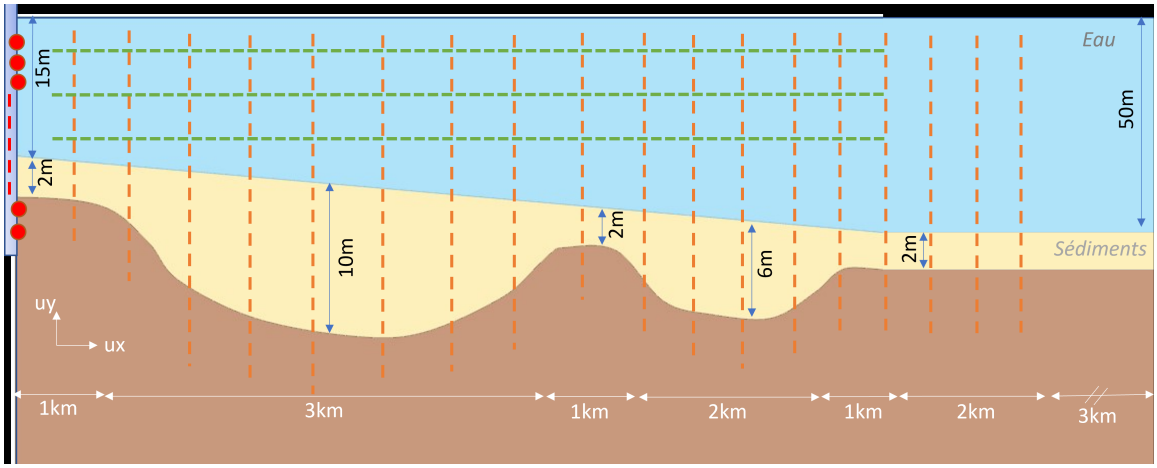


Figure 1. Bathymetry.

The numerical simulations are performed using the open-source software SPECFEM2D[1]. SPECFEM2D implements the spectral-element method. It is based upon a high-order piecewise polynomial approximation of the weak formulation of the wave equation. It combines the accuracy of the pseudospectral method with the flexibility of the finite-element method. In this method, the wavefield is represented in terms of high-degree Lagrange interpolants, and integrals are computed based upon Gauss–Lobatto–Legendre quadrature. This combination leads to a perfectly diagonal mass matrix, which in turn leads to a fully explicit time scheme that lends itself very well to numerical simulations on parallel computers. It is particularly well suited to handling complex geometries and interface conditions. As a consequence, the accurate simulation of surface wave propagation is straightforward without any additional cost. This is a very important feature in our configuration since the influence of interface waves (Stoneley-Scholte, Leaky Rayleigh, etc.) is known to be important. The numerical simulations are performed using the cylindrical coordinate system.

The source model of pile driving is taken from reference [2]. The source signal is a Ricker wavelet with a central frequency of 85 Hz. This means that the maximum frequency which is considered in the numerical simulations is 212.5 Hz.

The bottom of the ocean is considered as an elastic medium with the following physical characteristics:

- Water: ρ = 1000 kg/m^3, c_p = 1450 m/s
- Sediment: ρ = 2200 kg/m^3, c_p = 1750 m/s, c_s = 600 m/s
- Basement: ρ = 2700 kg/m^3, c_p = 3550 m/s, c_s = 2200 m/s

where ρ, c_p and c_s are respectively the density, the velocity of longitunal waves and the velocity of shear waves.

3 NUMERICAL RESULTS

In this section, we present the numerical results obtained with the configuration presented in section 2. First, we show the results of the evaluation of the Sound Exposure Level (SEL) at a depth of 14m. This parameter is given by the following relation:

$$SEL = 10\log\left(\int_0^T p^2(t)dt/p_0^2\right)$$

Then, we present the spectra of several signals recorded along the path from the source and finally the evaluation the interaction of two pile driving operations is presented. Finally, the interaction between two distant pile driving operations is studied.

[1]https://github.com/geodynamics/specfem2d

3.1 Sound exposure levels

The amplitude of the source is adjusted to give an SEL value of 190 dB at a distance of 100 m from the source.

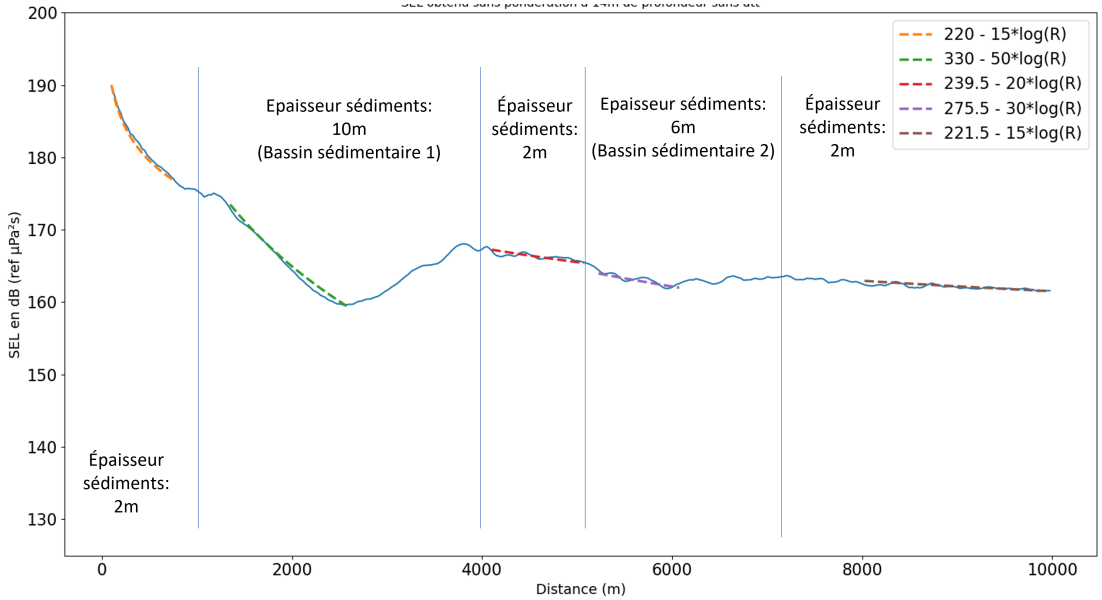
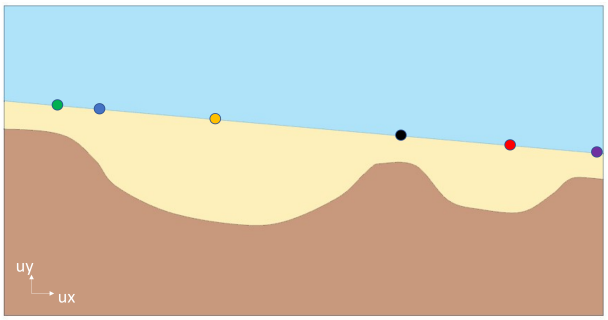


Figure 2. Variation of the SEL values with the distance to the source for receivers situated at a depth of 14m

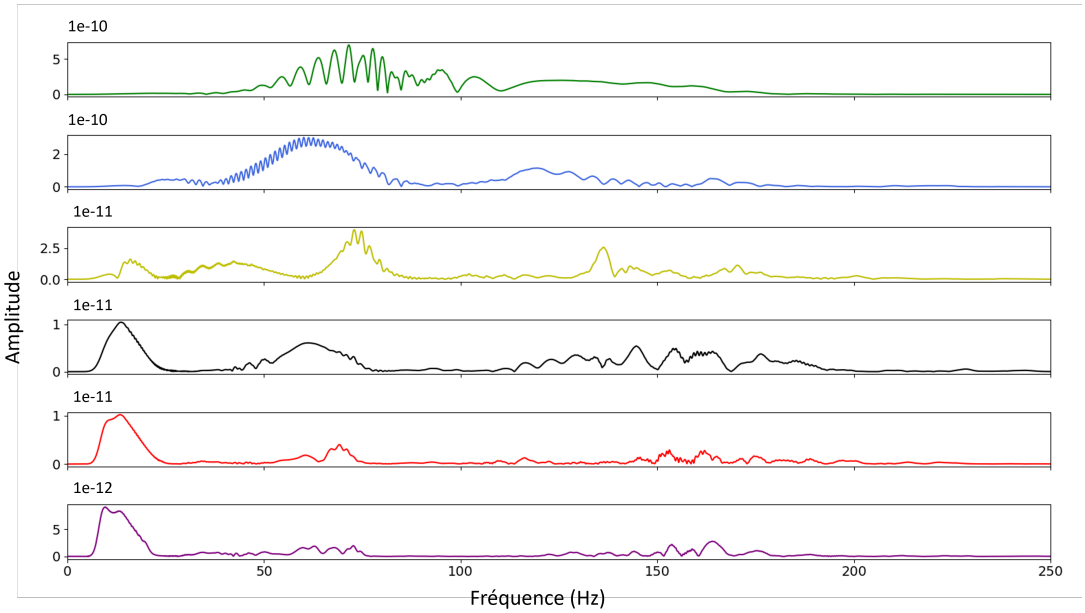
A strong decrease followed by a strong increase in SEL values can be observed in the first sedimentary basin. The increase reaches a value of 10 dB at the end of the first sedimentary basin. The effect of the second sedimentary basin is much smaller with a slight increase in SEL values. Nevertheless, it is clear that a site effect occurs, radically changing the behavior of the sound pressure decay. A complex geometry of the sedimentary structure can strongly affect the distribution of acoustic energy in the water column.

3.2 Spectrum evolution

In addition, it is also interesting to analyze how the spectral content of the signals evolves with the distance to the source. Indeed, it is known that site effects are characterized by a shift towards low fequencies of the spectra of the signals and also by a lengthening of the signal duration [5]. In this extended abstract, we will only tackle the frequency aspect of the site effect.



(a) Receiver positions



(b) Spectra

Figure 3. Spectra evolution of the horizontal component of the displacement. The color of the points indicated in subfigure a) corresponds to the color of the plots in subfigure b)

Figure 3 depicts the evolution of the spectral content of signals recorded at several receivers situated on the interface between water and sediments (see Figure 3a for the receiver positions). The shift towards low frequencies starts to be seen in the middle of the first sedimentary basin. At the end of the first sedimentary basin, it is very clear and this shift remains afterward. The frequency interval where the acoustic energy is the strongest shifts from the interval [30Hz-70Hz] to [10-15Hz]. It confirms the presence of a site effect due to the presence of a sedimentary basin.

This site effect may be due to the conversion of interface waves that may exist in this configuration. Depending on the frequency, the sedimentary basin may or may not affect wave propagation depending on its relative size to the wavelength of the interface wave and thus an energy transfer between the existing interface waves may be generated. In this configuration, we can have a Stoneley-Scholte wave at the water-sediment interface, a Stoneley-Scholte wave at the water-basement interface, and, a leaky Rayleigh wave at the water-basement interface. With the increase of the depth of the first sedimentary basin, we make the hypothesis that the high -requency part of the leaky Rayleigh wave at the water-basement interface may be converted into a Stoneley-Scholte wave at the water-sediment interface while the low-frequency part remains unchanged. This, of course, needs to be confirmed by a more in-depth analysis.

3.3 Interaction of two distant pile driving sources

As a preliminary step to the study of the interaction of two distant pile driving operations in 3D, we propose to generate pseudo 3D SEL maps from a single 2D simulation in cylindrical coordinates. For this purpose, we consider a common area corresponding to the planar part of the 2D simulation where we evaluate the interaction between the signals emitted by the two distant sources. We first store the signals received by 80 receivers located, in what we defined as the common area, between 8 km and 10 km at a given depth. Then, we construct the 3D map by adding these signals as shown in Figure 4. The resulting non-uniform 3D spatial sampling is made uniform using "Neareast Neighbor" interpolation.

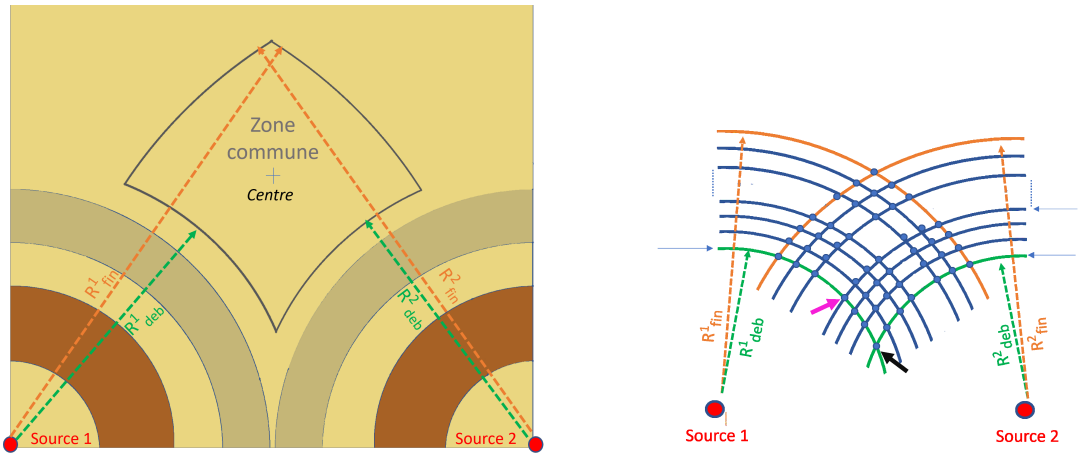


Figure 4. Schematic of the construction of a 3D map from one 2D simulation

The SEL maps are built in two ways to show the importance of taking into account the phase of the signals when there is an interaction. If p_1 and p_2 are respectively the sound pressure generated by Source 1 and Source 2, then the SELs can be evaluated using the following relation if we take into account the interaction between the two signals:

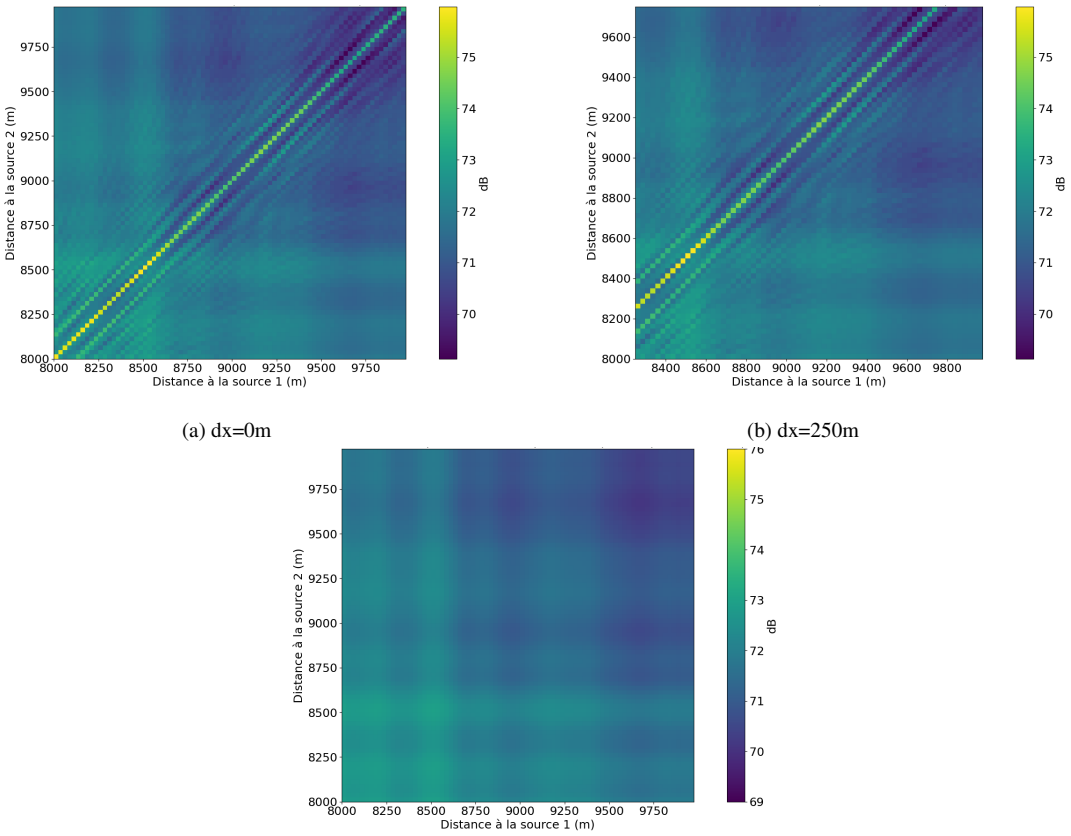
$$SEL = 10\log\left(\frac{\int_0^T (p_1(t)+p_2(t))^2\,dt}{p_0^2}\right)$$

Alternatively, if we do not take into account the interaction, the SELs are evaluated using:

$$SEL = 10\log\left(\frac{\int_0^T p_1^2(t)dt + \int_0^T p_2^2(t)dt}{p_0^2}\right)$$

The generated pseudo-3D maps are shown in Figure 5. Figure 5a represents the SELs for two sources which are at the same distance to the center of the common area. Stronger SELs are observed along and near the diagonal of the image corresponding to the places where constructive interferences between the two emitted signals occur. Figure 5b represents the SELs for two sources whose distance to the center of the common area is different. One of the sources is moved back by a distance of 250m. This results in a shift of the line where constructive interferences occur.

If the SELs are evaluated without taking into account the interaction between the signals the SEL map is very different (see Figure 5c). The SELS are uniforms.



(a) dx=0m

(b) dx=250m

(c) without interaction (dx=0m)

Figure 5. 3D SEL maps at a depth of 14m in the common area

4 CONCLUSION

In this expanded abstract, we investigated the structure of the acoustic wavefield generated by pile driving in the presence of a complex sediment structure. It was shown that the presence of sedimentary basins can strongly affect the distribution of acoustic energy on the water column both in terms of amplitude and. frequency content. In addition, we generated pseudo 3D SEL maps of the interaction of two distant pile driving operations using a single 2D simulation in cylindrical coordinates. These maps highlighted the importance of taking into account the interference of the two emitted signals.

ACKNOWLEDGEMENTS

This work was granted access to the HPC/AI resources of CINES under the allocation A0110410305 made by GENCI and of the Aix-Marseille Supercomputing Mesocenter under allocations h025.

REFERENCES

[1] A. Tsouvalas, Underwater Noise Emission Due to Offshore Pile Installation: A Review, Energies 2020, 13, 3037.

[2] P. G Reinhall and P. H Dahl. Underwater mach wave radiation from impact pile driving : Theory and observation. The Journal of the Acoustical Society of America, 130(3) :1209– 1216, 2011.

[3] N. Favretto-Cristini et al. Assessment of risks induced by counter-mining unexploded large-charge his-

torical ordnance in a shallow water environment: Part 2. Modeling of seismo-acoustic wave propagation. IEEE J Ocean Eng. 2022; 47(2): 374-398.

[4] C. Geuzaine and J.-F. Remacle. Gmsh: a three-dimensional finite element mesh generator with built-in pre- and post-processing facilities. International Journal for Numerical Methods in Engineering 79(11), pp. 1309-1331, 2009.

[5] P.-Y. Bard and M. Bouchon. The two-dimensional resonance of sediment-filled valleys. Bulletin of the Seismological Society of America, 75(2) :519–541, 1985.

ICA 2022
24th INTERNATIONAL CONGRESS ON ACOUSTICS
October 24(Mon) - 28(Fri), 2022 Gyeongju, Korea

PROCEEDINGS of the
24th International Congress on Acoustics

October 24 to 28, 2022 in Gyeongju, Korea

ABS-0777

Scaling offshore pile driving noise: Estimating the relevant sound pressure levels

Jonas VON PEIN[(1)], Tristan LIPPERT[(2)], Stephan LIPPERT[(1)], Otto VON ESTORFF[(1)]

[(1)]Hamburg University of Technology, Institute of Modelling and Computation, Denickestrasse 17, 21073 Hamburg, Germany, jonas.pein@tuhh.de

[(2)]AQUSTIX GbR, Katharinenstrasse 4, 20457 Hamburg, Germany

ABSTRACT

Underwater noise due to construction activities can reach sound pressure levels that are potentially harmful to the marine fauna. Percussive pile driving is the state-of-the-art installation technique for the foundations of offshore wind farms. The installation process leads to very high noise emissions. To protect the environment, limits have to be fulfilled for offshore pile driving noise in many countries. The assessment of the occurring sound pressure levels can be either done by numerical models or by simplified scaling methods. The scaling methods are especially useful at early stages of the planning phase, since a lot of input data that is necessary for the numerical models may not be available at that point. Within this contribution, the scalability of the relevant sound pressure levels such as the sound exposure level (SEL) and the peak sound pressure level ($\mathrm{SPL_{peak}}$) is shown with and without the application of a big bubble curtain (BBC).

Keywords: pile driving noise, underwater noise, scaling laws

1 INTRODUCTION

The most common foundation types for offshore wind farms are based on piles. The standard installation procedure is percussive pile driving. Every single strike on the pile head leads to the emission of underwater noise with comparably high sound pressure levels, when not properly mitigated. These noise emissions are potentially harmful to the marine environment [1]. Therefore, many countries have defined limits for the emitted sound pressure levels [2, 3].

Two important metrics for emitted pile driving noise are the sound exposure level (SEL) and the peak sound pressure level ($\mathrm{SPL_{peak}}$). The SEL is defined with the sound exposure E_p and the reference value $E_{p0} = 1\,\mu\mathrm{Pa^2\,s}$ by

$$\mathrm{SEL} = 10\log_{10}\left(\frac{E_p}{E_{p0}}\right) \qquad [\mathrm{dB\ re\ 1\mu Pa^2 s}]\,. \tag{1}$$

The sound exposure can be computed with the pressure time series $p(t)$ by $E_p = \int_{t_1}^{t_2} p^2(t)\,\mathrm{dt}$. The times t_1 and t_2 mark the beginning and the end of the sound event [4]. The $\mathrm{SPL_{peak}}$ is defined by the maximal amplitude of $p(t)$ and $p_0 = 1\,\mu\mathrm{Pa}$ with

$$\mathrm{SPL_{peak}} = 20\log_{10}\left(\frac{\max(|p(t)|)}{p_0}\right) \qquad [\mathrm{dB\ re\ 1\mu Pa}]\,. \tag{2}$$

The prediction of these sound pressure levels can be done by empirical or numerical models, c.f. Lippert *et al.* [5, 6] or Tsouvalas [7].

Both approaches, however, have the disadvantage of being only available to a few number of experts and institutions. Therefore, simple to apply scaling laws for the SEL have been developed by von Pein *et al.* for

unmitigated [8] as well as mitigated [9] pile driving noise. The contribution at hand is going to show the extension and application of such scaling laws for the estimation of the SPL_{peak}.

The paper is organized as follows: Within Section 2 the used modelling approach, which is based on the combination of a close range finite element method (FEM) model and a Parabolic Equation (PE) model, is briefly described. The scaling laws for the SEL as derived by von Pein *et al.* [8, 9] are provided in Section 3. Despite these already published dependencies for the SEL, scaling laws derived for the estimation of the SPL_{peak} are given. The application of the scaling laws for the sound pressure levels for unmitigated and mitigated pile driving scenarios is shown in Section 4. Therein, the scaled and measured results of six different sites are compared. A conclusion and an outlook on further research is given within Section 5.

2 MODELLING APPROACH

The modelling approach is described in more detail in von Pein *et al.* [9]. For reasons of completeness it is also summarized in the following:

The derivation of the scaling laws for unmitigated scenarios is done by applying a pile driving noise model based on the FEM [10].

The derivation of scaling laws for mitigated scenarios is done by a hybrid modelling approach. The close-range model is based on the FEM and the far-range model on the PE technique [11].

Within the FEM model the pile, soil, and water are discretized with a high level of detail. The pile head excitation is usually derived within a pre-calculation considering the original geometries of the hammer components. Within the acoustical model the derived pile head excitation is applied as a boundary condition at the pile head. At the lateral and lower end of the domain non-reflecting boundary conditions are applied. For a detailed description and validation of this modelling approach, see [10].

The far-range model is based on the split-step Padé approximation of the outgoing wave equation. A description of the hybrid modelling approach as well as a detailed validation is provided in von Pein *et al.* [12].

Noise mitigation systems are included into the PE model by multiplying the pressure field in the frequency domain by a frequency dependent transmission coefficient at its dedicated position. The depth and frequency dependent transmission coefficient of the BBC is derived with an approach suggested by Huisman *et al.* [13]. It is based on the differences of the impedance of the air water mixture and water as well as a first approximate of the bubble resonances. The bubble rise speed, the width of the BBC at the sea surface as well as the air supply are three parameters that need to be defined for the BBC model. Furthermore, the distance of the BBC to the pile is necessary for the computation.

3 SCALING LAWS FOR PILE DRIVING NOISE

The considered scaling laws for unmitigated pile driving noise are based on the dependencies derived and validated in von Pein *et al.* [8, 9]. However, only scaling laws for the SEL are presented therein. The corresponding dependencies of the SPL_{peak} are derived with the same data sets and compared to the dependencies on the SEL in the following.

Within von Pein *et al.* [8] it is shown that the found dependencies can be added up to derive an estimate of the SEL in the following way:

$$SEL_i = SEL_0 + \Delta SEL_E + \Delta SEL_d + \Delta SEL_{m_r} + \Delta SEL_h \,, \tag{3}$$

where SEL_0 is the measured or computed value of the reference site, ΔSEL_E is the difference caused by different strike energies, ΔSEL_E is the difference related to the pile diameters, ΔSEL_{m_r} is the difference induced due to different ram weights, and ΔSEL_h corresponds to the difference influenced by different water depths. The same approach is also valid for the scaling of the SPL_{peak}.

In the following, the dependency of the SEL and the SPL_{peak} for unmitigated as well as mitigated scenarios is scaled by

$$\Delta_E = 10 \log_{10} \left(E_i / E_0 \right) . \tag{4}$$

3.1 Scaling of unmitigated scenarios

The influence of the pile diameter d for unmitigated pile driving on the sound pressure levels is scaled by

$$\Delta_d = k_d \log_{10}\left(d_i/d_0\right) . \tag{5}$$

The factors $k_{d,\mathrm{SEL}} = 16.7$ and $k_{d,\mathrm{SPL_{peak}}} = 12.7$ have been derived with a best-fit approximation. Therefore, the $\mathrm{SPL_{peak}}$ increases slightly less than the SEL with increasing pile diameter, leading to a small difference between $\mathrm{SPL_{peak}}$ and SEL for bigger piles. The influence of the ram weight m_r was found to be scalable by

$$\Delta_{m_r} = -k_{m_r} \log_{10}\left(m_{r,i}/m_{r,0}\right) \tag{6}$$

with $k_{m_r,\mathrm{SEL}} = 10$ and $k_{m_r,\mathrm{SPL_{peak}}} = 11.5$. This result indicates that a greater ram weight leads to a higher reduction of the $\mathrm{SPL_{peak}}$ compared to the SEL.

The influence of the water depth on the SEL and $\mathrm{SPL_{peak}}$ can be approximated with the damping term of the damped cylindrical spreading model [14] and is defined with the reflection coefficient between water and soil R, in dependence on the water depth h, the propagation angle φ, and the distance r_i by

$$\Delta_h = \left(\frac{10\log_{10}(|R_i|^2)}{2\cot(\varphi)h_i} - \frac{10\log_{10}(|R_0|^2)}{2\cot(\varphi)h_0}\right) r_i . \tag{7}$$

The propagation angle φ is approximately 17° as shown by Reinhall and Dahl [15] and the reflection coefficient can be computed with the acoustical parameters of soil and water.

3.2 Scaling of mitigated scenarios

As described in von Pein *et al.* [9] the scaling laws with the consideration of a BBC have been derived with a best-fit approximation of the mean of 50 runs of the detailed numerical model with different soil and BBC properties. The multiple runs have been conducted in order to take the influence of uncertain soil and BBC properties into account.

The scaling of the influence of the diameter with the application of a BBC slightly differs compared to the trends derived for unmitigated pile driving. The influence of the diameter can be scaled by

$$\Delta_{d,\,\mathrm{BBC}} = k_{d,\,\mathrm{BBC}} \log_{10}\left(d_i/d_0\right) \tag{8}$$

with the corresponding parameters of $k_{d,\mathrm{SEL,BBC}} = 18.3$ and $k_{d,\mathrm{SPL_{peak},BBC}} = 15.3$. This trend is slightly higher than the relation considered for unmitigated pile driving. The presence of a BBC leads to a shift of the propagating frequency spectra to lower frequencies as the BBC has a greater insertion loss at higher frequencies. The change in pile diameter directly leads to a higher radiation efficiency at low frequencies. The interaction of these effects lead to the differences in the dependencies.

The best-fit of the mean of the ram weight influence is resulting in a scaling of

$$\Delta_{m_{r,\,\mathrm{BBC}}} = -k_{m_{r,\,\mathrm{BBC}}} \log_{10}\left(m_{r,i}/m_{r,0}\right) \tag{9}$$

with $k_{m_{r,\,\mathrm{SEL,BBC}}} = 9.2$ and a similar result of $k_{m_{r,\,\mathrm{SPL_{peak},BBC}}} = 9.6$. Therefore, the $\mathrm{SPL_{peak}}$ decreases a little more than the SEL with increasing ram weight. This difference is slightly smaller compared to the unmitigated scenarios.

The greatest difference between the unmitigated and mitigated scaling laws can be found in the water depth dependency. For the unmitigated scenarios the water depth effect is mainly induced by the differences in propagation loss which can be computed with the damped cylindrical spreading model. This effect is still present in the cases of the application of a BBC. However, it is combined with the water depth dependent insertion loss behavior of the BBC. An important influence on the insertion loss of the BBC is the water depth dependent bubble size. It effects the volume fraction of air within the air-water mixture and the resonance effects. The best-fit approximation of the results evaluated at 750 m leads to parameters of $k_{h_{w,\,\mathrm{SEL,BBC}}} = 16.2$ and $k_{h_{w,\,\mathrm{SPL_{peak},BBC}}} = 16.5$ to be used in

$$\Delta_{h_{w,\,\mathrm{BBC}}} = k_{h_{w,\,\mathrm{BBC}}} \log_{10}\left(h_{w,i}/15\,\mathrm{m}\right) . \tag{10}$$

3.3 Summary

All in all, the main difference between the scaling of the SEL and the SPL_{peak} can be identified in the dependence on the ram weight as well as on the pile diameter. This is the case for the dependencies found for mitigated as well as unmitigated scenarios. The SPL_{peak} is directly linked to the peak of the first stress wave within the pile. Both of these parameters have a direct influence on the stress within the pile and therefore show a different dependency for the SPL_{peak} compared to the dependencies of the SEL.

The greatest difference between the mitigated and unmitigated scaling laws are identified with respect to the water depth scaling.

4 APPLICATION OF THE SCALING LAWS

The applications of the scaling laws are conducted with the following measurement data sets: The data of the wind farms Sandbank (SB), Veja Mate (VM), Trianel (TR), and Deutsche Bucht (DB) are all taken from the data base MarineEARS [16]. Furthermore, data of Borkum West 2 (BW2) [17] and Global Tech I (GTI) [18] are used. The according data sets are listed in Table 1. They all have been derived with the application of a BBC. Furthermore, for all of these sites also measured data of an unmitigated scenario is available.

Table 1. Measurement data derived with the application of a BBC.

name	piles	SEL_{05} [dB]	SPL_{peak} [dB]	range [m]	strike energy [kJ]	pile diameter [m]	water depth [m]	ram weight [t]	hammer type
SB	3	162 - 163	182 - 185	663 - 757	1013 - 1522	6.8	26.8 - 29.6	175	MHU 3500S
VM	1	171	193	803	1893	7.8	39	200	Hydrohammer S-4000
TR	1	163	181	749	1457	8	28.3	150	Hydrohammer S-3000
DB	1	168	187	749	2150	8	39.3	200	Hydrohammer S-4000
BW2	2	160 - 163	187 - 188	750	1200	2.44	30	60	Hydrohammer S-1200
GTI	2	163 - 164	186 - 187	600 - 700	583	2.48	40	66	MHU 1200S

A common way of estimating the SEL and SPL_{peak} for mitigated scenarios is to derive an estimate for the unmitigated scenario and subtracting a noise mitigation specific insertion loss. The presented scaling laws allow to directly estimate the SEL and SPL_{peak} for mitigated as well as for unmitigated scenarios. To demonstrate this, the six sites of Table 1 are taken and five of the six sites are scaled to the considered site. The average is displayed together with the minimum and maximum value in Figure 1. These results are plotted right next to the actual measured sound pressure levels. The sound pressure levels of the unmitigated scenario are derived with 20 of 21 sites as shown by von Pein *et al.* [8] with the scaling laws provided within Section 3. This data set is now extended with the SPL_{peak}.

The comparison of the estimated sound pressure levels of the mitigated and unmitigated scenarios in Figure 1 allows new insights into the measured data:

The size of the errorbars indicating the lowest and highest estimate is in a similar range for the unmitigated and mitigated SEL. However, for the SPL_{peak} it is much greater for the mitigated scenarios. Since usually only the highest occurring SPL_{peak} is reported, the SPL_{peak} is much more likely to be influenced by dynamic effects related to the BBC performance as well as statistical outliers.

The estimations of the BBC results of SB show a very good agreement with the measurements and also indicate that the measurements were at the lower end of the considered data sets. At the same time the comparison of estimated and measured SEL and SPL_{peak} for the unmitigated scenario shows that these are the highest measured values in the data base. This new perspective allows a better classification of the actual BBC performance.

For VM the unmitigated SEL and SPL_{peak} estimation matches the measured result very well. The comparison of the measured and estimated SEL and SPL_{peak} with a BBC shows that the BBC performance is at the higher end of the range compared to the other sites.

The comparison of the TR results shows that for the unmitigated and the mitigated scenario the measured SEL and SPL_{peak} are at the lower end of the scaled range. However, the cause of this comparably low noise

site remains unclear. Furthermore, the measured mitigated SPL_{peak} is the lowest in the data base and the reason for the comparably great range of the errorbar.

The estimated results of DB, BW2, and GTI are also in good agreement with the derived estimation range.

The comparisons demonstrate that the approach of directly scaling the SEL and SPL_{peak} for scenarios with a BBC can provide new insights into the actual BBC performance and are another way of estimating the sound pressure levels with the application of a BBC.

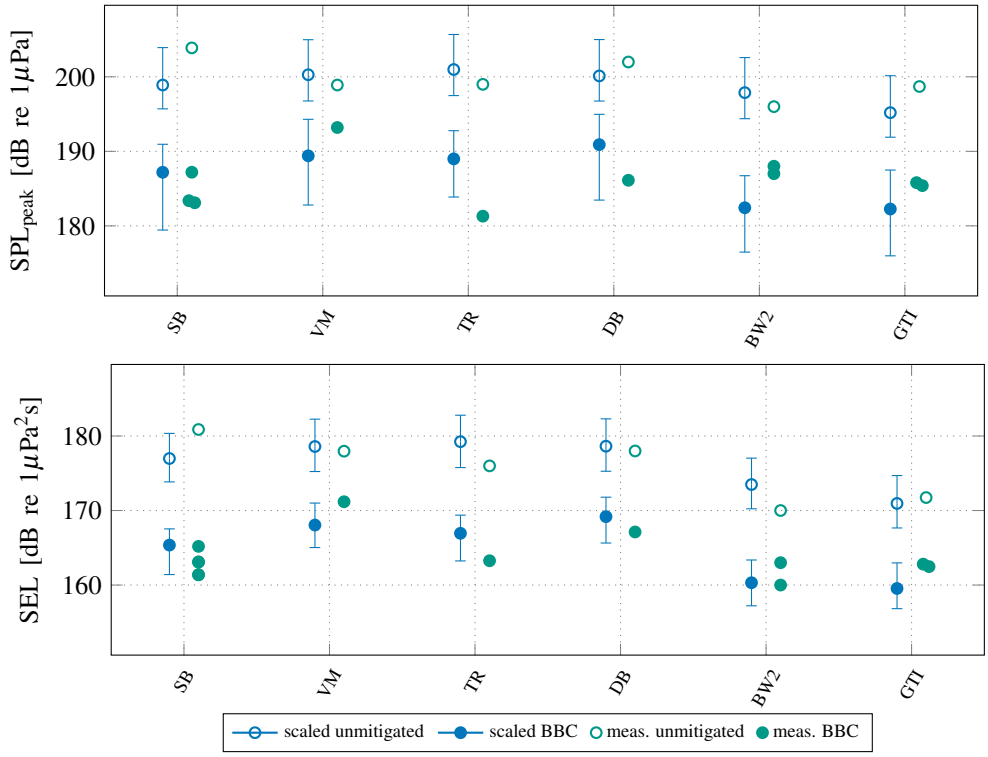


Figure 1. Comparison of the scaled and measured SEL and SPL_{peak} of six different sites with and without the application of a BBC.

5 CONCLUSIONS AND OUTLOOK

This contribution presents the possibility of scaling the SEL and the SPL_{peak} from one site to another. This is done by taking the influence of the strike energy, pile diameter, ram weight, and water depth into account. The scaling laws and their application are shown for unmitigated as well as for mitigated scenarios using a BBC.

With a decent data base of measurements the derived scaling laws are a useful tool for the estimation of the SEL and SPL_{peak}. Furthermore, they can be employed to get a good insight and benchmark of a BBC performance.

The next steps in the development of scaling laws for offshore pile driving noise are the adaptation to scenarios with a noise mitigation system in the direct vicinity of the pile, a double big bubble curtain, and their combination. Furthermore, the investigation of the according influences of the four parameters on the emitted frequency spectra will be conducted.

REFERENCES

[1] Tougaard, J.; Beedholm, K.; Madsen, P. T. Thresholds for noise induced hearing loss in harbor porpoises and phocid seals. J. Acoust. Soc. Am., 151(6), 2022, 4252-4263.

[2] National Marine Fisheries Service. 2018 revision to: Technical guidance for assessing the effects of anthropogenic sound on marine mammal hearing (version 2.0). National Oceanic and Atmospheric Administration, Washington DC, 167, 2018.

[3] Juretzek, C.; Schmidt, B.; Boethling, M. Turning Scientific Knowledge into Regulation: Effective Measures for Noise Mitigation of Pile Driving. Journal of Marine Science and Engineering, 9(8), 2021.

[4] International Organization for Standardization. DIN ISO18406:2018-08 - Underwater acoustics - Measurement of radiated underwater sound from percussive pile driving. 2018.

[5] Lippert, S.; Nijhof, M.; Lippert, T.; Wilkes, D.; Gavrilov, A.; Heitmann, K.; Ruhnau, M.; von Estorff, O.; Schäfke, A.; Schäfer, I.; Ehrlich, J.; MacGillivray, A.; Park, J.; Seong, W.; Ainslie, M.A.; de Jong, C.; Wood, M.; Wang, L.; Theobald, P. COMPILE — A generic benchmark case for predictions of marine pile-driving noise. IEEE J. Ocean. Eng., 41(4), 2016, 1061–1071.

[6] Lippert, S.; von Estorff, O.; Nijhof, M.; Lippert, T. COMPILE II — A benchmark of pile driving noise models against offshore measurements. In proceedings of Inter-Noise 2018 Chicago, 2018.

[7] Tsouvalas, A. Underwater noise emission due to offshore pile installation: A review. Energies, 13(12), 2020.

[8] von Pein, J.; Lippert, T.; Lippert, S.; von Estorff, O. Scaling Laws for Unmitigated Pile Driving: Dependence of Underwater Noise on Strike Energy, Pile Diameter, Ram Weight, and Water Depth. Journal of Applied Acoustics, 2022, (in print).

[9] von Pein, J.; Lippert, T.; Lippert, S.; von Estorff, O. Scaling offshore pile driving noise: A case study for scenarios with and without noise mitigation. Proceedings of Meetings on Acoustics, International Conference on Underwater Acoustics, Southampton, 2022, (in print).

[10] von Pein, J.; Lippert, S.; von Estorff, O. Validation of a finite element modelling approach for mitigated and unmitigated pile driving noise prognosis. J. Acoust. Soc. Am., 149(3), 2021, 1737-1748.

[11] von Pein, J.; Klages, E.; Lippert, S.; von Estorff, O. A hybrid model for the 3D computation of pile driving noise. In proceedings of OCEANS 2019, Marseille, France, 2019.

[12] von Pein, J.; Lippert, S.; von Estorff, O. Validation of a 3D pile driving noise model with noise mitigation measures. In proceedings of 6th Underwater Acoustics Conference and Exhibition, Crete, Greece, 44, 2021.

[13] Huisman, M.; Lederwasch, L.; Smidt Lützen, R. Bubble curtain modelling: analytical prediction of underwater piling noise mitigation. In proceedings of Inter-Noise 2021.

[14] Lippert, T.; Ainslie, M.A.; von Estorff, O. Pile driving acoustics made simple: Damped cylindrical spreading model. J. Acoust. Soc. Am., 143(1), 2018, 310-317.

[15] Reinhall, P.; Dahl, P. Underwater Mach wave radiation from impact pile driving: Theory and observation. J. Acoust. Soc. Am., 130(3), 2011, 1209-1216.

[16] MarinEARS – Marine Explorer and Registry of Sound; specialist information system for underwater noise and national noise-register for the notification of impulsive noise events in the German EEZ of the North- and Baltic Sea to the EU according to the MSFD, 2021.

[17] Diederichs, A.; Pehlke, H.; Nehls, G.; Bellmann, M.; Gerke, P.; Oldeland, J.; Grunau, C.; Witte, S.; Rose, A. Entwicklung und Erprobung des Großen Blasenschleiers zur Minderung der Hydroschallemissionen bei Offshore-Rammarbeiten (Development and testing of the Big Bubble Curtain to reduce hydro-acoustic emissions during offshore pile driving). 2014.

[18] Bellmann, M.; Gündert, S.; Remmers, P. Offshore Messkampagne 2 (OMK2) für das Projekt BORA im Offshore-Windpark Global Tech I (Offshore measurement campaign 2 (OMK2) for the BORA project at the wind farm Global Tech I). 2015.

PROCEEDINGS of the
24th International Congress on Acoustics

October 24 to 28, 2022, in Gyeongju, Korea

Extended abstract

ABS-0888

Numerical investigation of acoustic radiation efficiency of a wedge-shaped structure surrounded by air bubble layers

Sung-Ju PARK[1]; Cheolsoo PARK[2]; Kookhyun KIM[3]; Jaehyuk LEE[4]; Keunhwa LEE[5]; Cheolwon LEE[6]

[1] Tongmyong University, Korea

[2] Korea Research Institute of Ships & Ocean Engineering, Korea

[3] Tongmyong University, Korea

[4] Daewoo Shipbuilding & Marine Engineering CO., LTD., Korea

[5] Sejong University, Korea

[6] AL, Korea

ABSTRACT

Underwater noise pollution can affect marine life. This study explores the effect of acoustic radiation efficiency with a fluid-loaded structure based on the numerical investigation. The effect of the bubble layer is considered using the semi-numerical method. For validation of the proposed procedure, the acoustic-structure interaction analyses using the commercial finite element program COMSOL Multiphysics were performed for fluid-loaded plates with an air bubble layer. The semi-numerical method results show good agreement with the numerical one for 'plate-bubble-fluid' model in terms of sound power level from all the frequency domains. Subsequently, the proposed method was used to investigate the acoustic radiation efficiency of a wedge-shaped structure surrounded by air bubble layers. The numerical result provides the principal mechanism of underwater noise reduction depending on the characteristic of the bubble layer on the thin structure.

Keywords: Acoustic radiation efficiency, Air bubble layer, Equivalent bubble layer method, Acoustic-structure interaction

1. INTRODUCTION

The underwater noise is produced by a combination of mechanical and hydrodynamic noise. The air-bubble curtain is applied to reduce the sound radiated from the noise source such as the propeller, engine, offshore exploration, underwater structure, etc. The interaction of the air bubble and radiated sound has been studied for application to the engineering design. Würsig et al.(1) measured sound intensities near pile-driving in 6-8 m depth sea with the installation of a bubble curtain and presented that the sound reduction by the bubble curtain was evident. Park et al.(2) suggested the analysis solution for examining the insertion loss of fluid-loaded plate with bubble layers depending on the characteristic of bubble population, void fraction, and the thickness of the bubble layer. Lee et al.(3) studied elastic shell model surrounded by the bubble layer with various bubble distribution condition.

In this study, we proposed a semi-numerical method procedure and carried out the finite element analysis to investigate the acoustic radiation efficiency of structures surrounded by air-bubble. The behavior of the air-bubble layer was considered using the effective medium theory proposed by Commander and Properetti (4). The proposed procedure was validated through simulation of acoustic-structure interaction for the fluid-loaded plates. The effect of air bubbles to the structure was investigated in terms of acoustic radiation efficiency.

[1] parksj0314@tu.ac.kr
[2] parkcs@kriso.re.kr
[3] kimk@tu.ac.kr
[4] leehel7@naver.com
[5] nasalkh2@sejong.ac.kr
[6] lcw7376@gmail.com

2. THEORYTICAL BACKGROUND

2.1 Finite element method for acoustic-structure interaction

The behavior of an acoustic region in the frequency domain uses the inhomogeneous Helmholtz equation as:

$$\nabla \cdot \left(-\frac{1}{\rho}(\nabla p_t - \mathbf{q}_\mathrm{d}) \right) - \frac{k^2 p_t}{\rho} = Q_m \tag{1}$$

The p_t is the total pressure which is the sum of the background pressure field p_b and the scattered field p_s. The wave number k denotes the ratio of the angular frequency ω to the sound speed c. The sound pressure wave is propagating with density ρ at the sound speed. The terms Q_m and $\mathbf{q}_\mathrm{d}$ are the monopole and dipole domain sources, respectively. In equation 1, the sound pressure can be expressed in pressure varies with time as $p_t = p(\mathbf{x}, \omega) = p(\mathbf{x})e^{i\omega t}$.

The acoustic-structure coupling includes the fluid load on the structure and the structural acceleration caused by the fluid. The exterior boundaries expressed as:

$$-\mathbf{n} \cdot \left(-\frac{1}{\rho}(\nabla \mathrm{p_t} - \mathbf{q_d}) \right) = -\mathbf{n} \cdot \mathbf{u_{tt}} \tag{2}$$

$$\mathbf{F_A} = p_t \mathbf{n} \tag{3}$$

where $\mathbf{u_{tt}}$ is the structural acceleration, $\mathbf{n}$ is the normal vector to the surface. $\mathbf{F_A}$ is the force per unit area experienced by the structure. The internal boundary condition follows as:

$$-\mathbf{n} \cdot \left(-\frac{1}{\rho_c}(\nabla \mathrm{p_t} - \mathbf{q_d}) \right)_{up} = -\mathbf{n} \cdot \mathbf{u_{tt}} \tag{4}$$

$$-\mathbf{n} \cdot \left(-\frac{1}{\rho_c}(\nabla \mathrm{p_t} - \mathbf{q_d}) \right)_{down} = -\mathbf{n} \cdot \mathbf{u_{tt}} \tag{5}$$

$$\mathbf{F_A} = \left(p_{t,down} - p_{t,up} \right) \mathbf{n} \tag{6}$$

The up and down subscripts mean the two sides of the interior boundary.

2.2 Acoustic insertion loss by a bubble layer

As shown in Commander and Prosperetti (4), the equivalent wave number k_m of bubbly fluid give the following relation for pressure wave with a time dependence proportional to:

$$k_m^2 = \frac{\omega^2}{c^2} + 4\pi \int_0^\infty \frac{a f(a)}{\omega_0^2 - \omega^2 + 2i\delta\omega} da \tag{7}$$

The $f(a)$ is the function of the bubble distribution, the δ is a damping coefficient of bubble, ω_0 is the resonant frequency of bubble. The damping coefficient of the mixed medium of bubble and water is expressed by an imaginary part of equivalent wave number:

$$\alpha = Imag(k_m) \text{ [nepers/m]} \tag{8}$$

When the propagated to h [m], the attenuation α_e is correspond $8.686\,\alpha h$ [dB], approximately. The insertion loss was determined by the comparing the input sound pressure p_{in} and output sound pressure p_{out}, which is the transmission by the bubble layer:

$$IL = -20 \log_{10} \left| \frac{p_{out}}{p_{in}} \right| \tag{9}$$

To permit a simplification of the bubble layer in finite element analysis, this approximation can be assumed that the insertion loss is equivalent to attenuation as shown in Park et al. (2020).

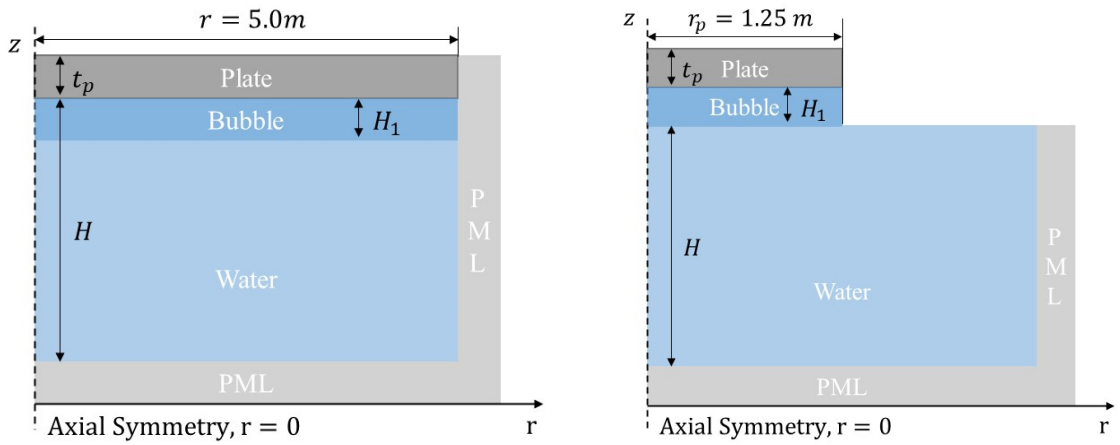
3. VALIDATION OF NUMERICAL METHODS

This paper carried out the acoustic structure interaction analysis for fluid-loaded finite and infinite plate models without a bubble layer. The sound pressure level was obtained from simulation, the

results considered a bubble layer was calculated under the assumption that insertion loss is equal to attenuation, i.e., the output sound pressure, which is after passed through the bubble layer, was calculated from the difference of the insertion loss and input sound pressure. This method was defined as semi-numerical simulation. To validate the proposed method, the simi-numerical simulation was compared with a fluid-loaded plate model with a bubble layer. The infinite plate model refers to Park et al. (2). The parameters for numerical simulation are presented in Table 1 and the model is illustrated in figure 1. Where the H_1=0.0 m only consists of "plate-water-PML" (without bubble layers).

Table 1 – parameters for fluid-loaded plate with bubble layer simulation

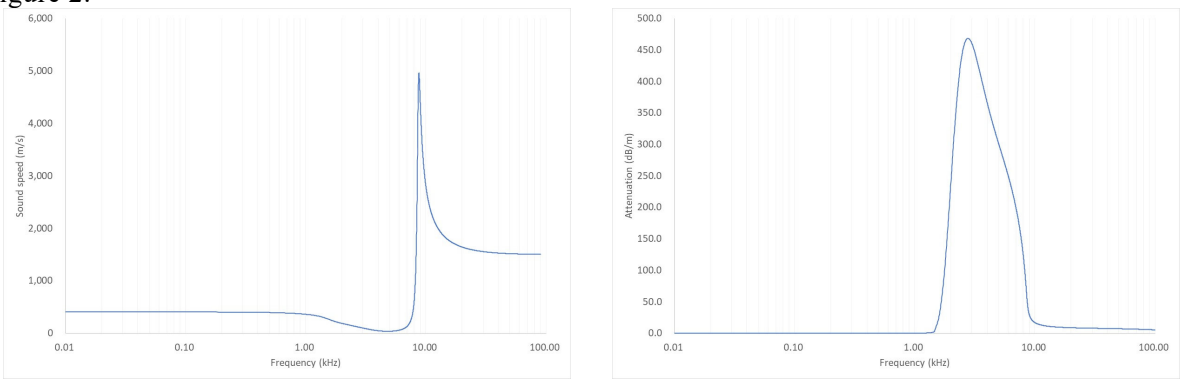
Medium	Parameter	Value
Plate	Thickness (t_p)	0.015 m
	Young's modulus (E)	$19.5 \times 10^{10}\mathrm{N/m^2}$
	Poisson's ratio (ν)	0.3
	Density (ρ_p)	$7{,}800\ \mathrm{kg/m^3}$
	Compressional sound of speed (c_p)	5801.2 m/s
	Structural loss factor (ζ)	0.005
Water	Depth (H)	3.0 m
	Density (ρ_w)	$1{,}000\ \mathrm{kg/m^3}$
	Sound of speed (c_w)	1,500 m/s
bubble	Bubble radius (a)	0.5 mm ~ 2.5 mm
	Specific heat ratio (γ)	1.4
	Layer thickness (H_1)	0.0 m, 0.1 m
	Wave Speed (c_b)	c_w/f
	Density (ρ_b)	$999\ \mathrm{kg/m^3}$



(a) Infinite plate model (b) Finite plate model

Figure 1 – The illustration of fluid-loaded plate with bubble layer.

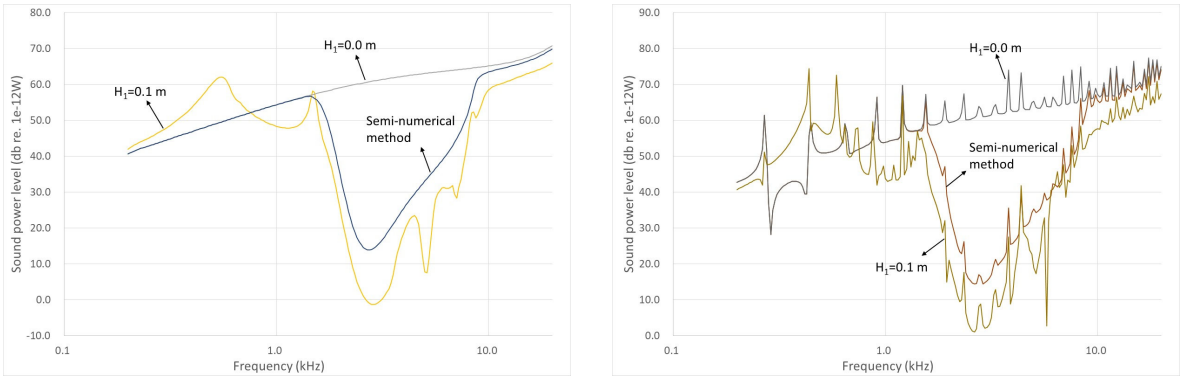
The 2D axisymmetric model was used for numerical simulation. The perfectly matched layer (PML) was added to the absorbing boundary for mimicking the open infinite domain. The pressure acoustic model of the bubble layer was defined as the speed of sound and attenuation coefficient as shown in figure 2.



(a) Sound speed (b) Attenuation

Figure 2 – The pressure acoustic model parameters for bubble layer

The point load was applied at the center of the top surface of the plate. The convergence study was performed to determine the element size for finite element analysis, the one bending wave of the plate was discretized with eight elements. As shown in figure 3, the sound power level was presented in comparison to $H_1 = 0.1$ m (plate-bubble-water), $H_1 = 0.0$ m (plate-water), and semi-numerical method results from 200 Hz - 20kHz. The presented procedure shows good agreement with the mode solution, approximately.



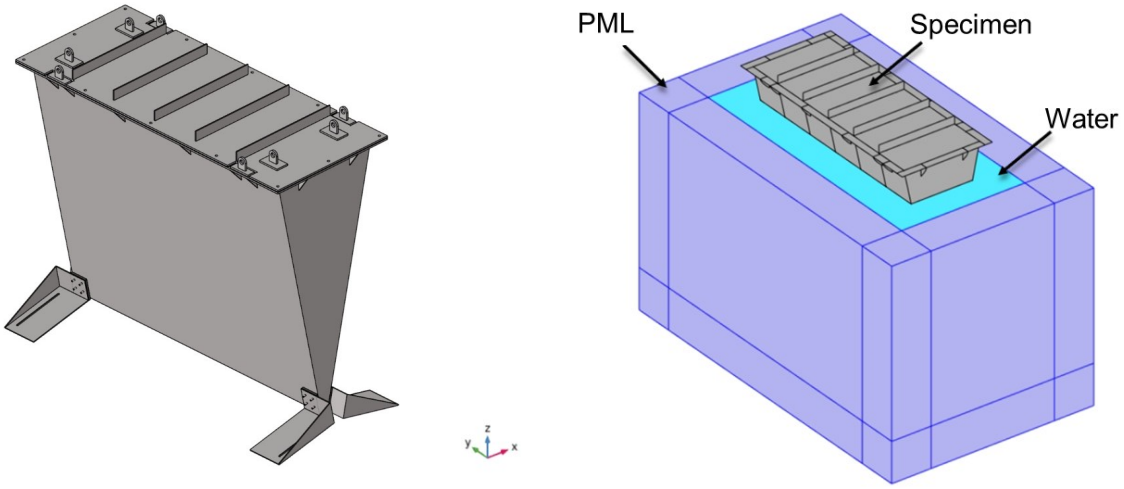
(c) Infinite plate model (d) Finite plate model

Figure 3 – The comparison of the sound power level between numerical and semi-numerical simulation

4. APPLICATION TO THE WEDGE-SHAPED STRUCTURE SURROUNDED BY AIR BUBBLE LAYERS

4.1 Model

The geometry and finite element model of the wedge-shaped structure were illustrated in figure 4. For structure, the material density, Young's modulus, and Poisson's ratio were 7,085 kg/m^3, 200e9 Pa, and 0.3, respectively. The density and speed of sound in water were 1,025 kg/m^3 and 1,500 m/s. The unity load was applied to the inner stiffener in the structure.



(a) Geometry (b) Finite elelemt model

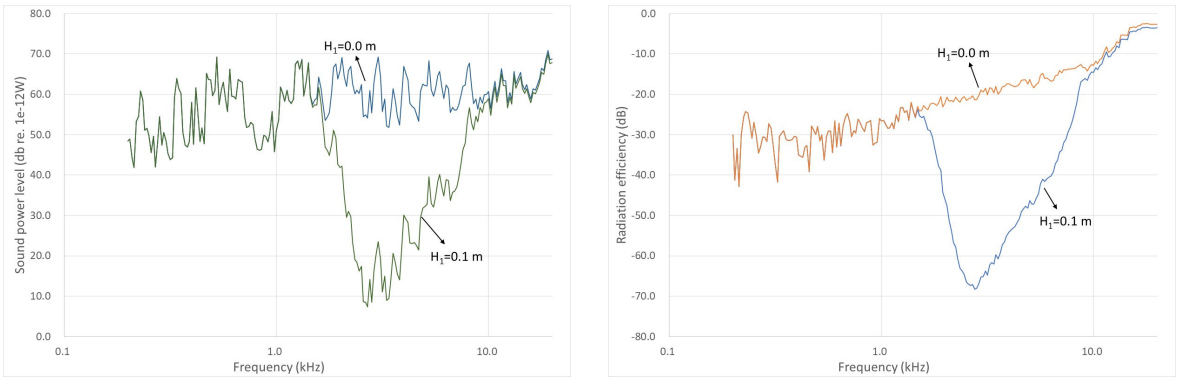
Figure 4 – The geometry and finite element model of wedge structure

4.2 Acoustic radiation efficiency

The radiation efficiency is defined as:

$$\sigma = \frac{W}{\rho c S \langle \bar{v}^2 \rangle}$$

where W is the sound power emitted by the vibrating structure, $\bar{v}^2$ is the mean square velocity in the entire area of the surface S. Figure 5 shows the sound power level and acoustic radiation of the water-loaded structure ($H_1 = 0.0$ m) and structure considered the effect of air-bubble ($H_1 = 0.1$ m). the characteristic of bubble layer refers to Table 1.



(a) Sound power level (b) Radiation efficiency

Figure 5 – The comparison of sound power level and radiation efficiency between water-loaded structure and structure surrounded air-bubble layer

5. RESULTS

The semi-numerical method of acoustic radiation efficiency for the structure surrounded by an air bubble layer is proposed based on finite element analysis and analytical method (2). The method is compared with the finite element analysis results through a fluid-loaded infinite and finite plate cases and then applied to the wedge structure surrounded by the air bubble layer. The results show the behavior of the noise reduction caused by the air-bubble layer in fluid-loaded structure in the water.

ACKNOWLEDGEMENTS

This work was supported by the Ministry of Trade, Industry and Energy (No. 20008585) and Korea Research Institute of Ships and Ocean engineering (2021B027), to which deep gratitude is expressed.

REFERENCES

1. Würsig B, Greene CR, Jefferson TA. Development of an air bubble curtain to reduce underwater noise of percussive piling. Mar Environ Res. 2000 Feb;49(1):79–93.
2. Park C, Jeong SW, Kim G Do, Moon I, Yim G. Acoustic insertion loss by a bubble layer for the application to air bubble curtain and air masker. J Acoust Soc Korea. 2020;39(4):227–36.
3. Lee K, Lee C, Park C. Insertion loss by bubble layer surrounding a spherical elastic shell submerged in water. J Acoust Soc Korea. 2022;41(2):147–83.
4. Commander KW, Prosperetti A. Linear pressure waves in bubbly liquids: Comparison between theory and experiments. J Acoust Soc Am. 1989 Feb;85(2):732–46.

vv

PROCEEDINGS of the
24th International Congress on Acoustics

October 24 to 28, 2022 in Gyeongju, Korea

ABS-0120

Comparison of linear and logarithmic sampling for a sensitivity analysis of a NVH vehicle body simulation

Sophie CRAM[1,2]; Marinus LUEGMAIR[1]; Johannes D. SCHMID[2]; Steffen MARBURG[2]

[1] BMW Group, Germany

[2] Technical University of Munich, Germany

ABSTRACT

In vibroacoustics, uncertainties are important for vehicle body simulations in an early development stage. A deterministic finite element model is typically evaluated several times with stochastic input parameters to gain stochastic results of the mobility of the vehicle body. It is our aim to reduce the number of stochastic parameters in this noise vibration harshness simulation for a vehicle body, i.e. on the one hand side to save simulation costs of the expensive car body model with many million degrees of freedom and on the other hand side to reduce the effort for parameter uncertainty quantifications. For this reduction, we conduct a sensitivity analysis with the generalized polynomial chaos expansion to get the Sobol' indices for which we need to sample the stochastic input parameters. Furthermore, it is our aim to focus on the most sensitive and therefore most relevant parameters of the noise vibration harshness simulation. The kind of sampling – linear or logarithmic – of widespread parameters influences the mean and standard deviation of the mobility curve. The resulting differences are shown and discussed.

Keywords: Vibroacoustics, Stochastic, Finite element car model, Parameter reduction

1. INTRODUCTION

Uncertainties significantly affect the vibroacoustics of a vehicle body as shown with differently conducted acoustic measurements:

Measurements are compared with an uncertainty-filled structural-acoustic car model by Durand et al. (1).

In 1993, Kompella et al. (2) evaluated the two transfer pathways of 57 pickup trucks and 99 cars, which were structure-borne and airborne, respectively. Each set of vehicles has the exact same configuration. The deviations in the frequency response functions range from 5 to 10 dB.

Hills et al. (3) conduct a larger investigation of measured vehicle acoustic data: They examine data from fleets of 316, 403, and 411 automobiles and display the resulting noise distributions.

In addition to these measurements, there are contributions which deal with uncertainties in simulations to cover the measured variations:

The NVH simulation of a vehicle is the main topic of Luegmair's and Schmid's (4) description of this process in terms of uncertainty. Uncertainty in the simulation's input parameters stems from differences in the manufacture, use, life cycle, and features that the client has chosen for his car.

The generalized polynomial chaos (gPC) expansion is added to this NVH finite element (FE) simulation procedure by Schmid et al. (5) . According to (6), we develop a two-step sensitivity analysis which reduces the uncertain parameters as well as the computation time based on the simulation method with gPC expansion.

The gPC expansion, the simulation process and the two-step sensitivity analysis will be covered later on in this contribution.

The considerable variance of the results, as shown in (7), necessitates the inclusion of unknown parameters in these simulations: To identify the types of distributions, we quantify the dynamic stiffness and damping of a car door seal and use the Pearson chart to assess the results.

According to (8), statistical factors are taken into consideration with a margin of safety in traditional design based on the manufacturing, ambient circumstances, and design procedures. This

[1] Sophie.Cram@bmw.de

margin causes the system to be designed in a way that exceeds its intended function. Because of this, a stochastic analysis is performed to investigate the impact on the vehicle shaking response (8).

Furthermore, we find comparisons of logarithmic and linear transformations (9), averaging (10) and sampling (11) in the literature. The latter compare phase approximations in the frequency domain which are logarithmic and linear.

The following queries are addressed in this contribution: How does a logarithmic or linear sampling of widespread uncertain parameters influence the admittance curves? How does the linear sampling affect the reduction of the uncertain parameters regarding the two-step sensitivity analysis as presented in (6)?

2. METHODS

In this section, a brief description of the sensitivity analysis is presented along with a short introduction to the gPC expansion. Then, we show the computation of the sensitivities using the Sobol' indices relying on the gPC expansion. To further aid in the comprehension of the two-step sensitivity analysis, the superelement method is also shortly introduced.

2.1 Sensitivity Analysis

We work with a sensitivity analysis in this article to show the dependencies between the input and output of a model (12). Especially, we focus on a so-called variance-based sensitivity analysis – a global analysis – that is dependent on the output variance. This variance is made up of ratios which are linked to sets of inputs or individuals (13). The first order sensitivity index, often known as the Sobol' index S_i, defines the averaged partial decrease for a model of k factors $f(x) = (x_1, x_2, \dots, x_k) \in \mathbb{R}^k$ in the unconditional variance $Var(y)$ of the output y for a set x_i and is stated as (14)

$$S_i = \frac{Var_{x_i}[E_{x\sim i}(y|x_i)]}{Var(y)}. \tag{1}$$

$E_{x\sim i}$ represents the inner mean across all factors except x_i (14).

2.2 Polynomial Chaos Expansion

The polynomial chaos expansion which can be used to calculate the Sobol' index analytically (15) is suggested for cases requiring intense computational power (13). Based on Wiener (16), the polynomial chaos expansion – a spectral based method – is enhanced by Cameron and Martin (17), Xiu and Karniadakis (18) and Ghanem and Spanos (19) to the generalized polynomial chaos (gPC) expansion. This method depicts the uncertainty in a system which is stochastic with infinite series expansion. A random variable $X(\boldsymbol{\xi})$ is presented in the spectral representation as

$$X(\boldsymbol{\xi}) = \sum_{i=0}^{\infty} x_i \Psi_i(\boldsymbol{\xi}), \;\; x_i \in \mathbb{R} \tag{2}$$

given a stochastic subspace where the basis polynomials $\Psi_i(\boldsymbol{\xi})$ are orthogonal with respect to each other. x_i are the deterministic coefficients. We recommend (5, 6) to find detailed information on the gPC expansion and its implementation with a deterministic FE model.

2.3 Computation of the Sobol' Indices with the Generalized Polynomial Chaos Expansion

Following the use of the gPC expansion, it just requires a minimal amount of additional work to calculate the so-called polynomial chaos based Sobol' indices, which Sudret (15, 20) published. The first order sensitivity index is defined as

$$S_i = \frac{\sum_{\alpha\in\mathfrak{J}_i} y_\alpha^2 \langle \Psi_\alpha^2(\xi_i)\rangle}{\sum_{j=1}^{N} y_j^2 \left\langle \Psi_j^2(\xi)\right\rangle} \tag{3}$$

and describes the impact of the i^{th} input variable ξ_i (21). According to Eq. (1), the numerator is

the variance of the terms which have the single parameter ξ_i included and it is divided by the output's overall variance. The terms in the expansion that only use the single variable ξ_i are extracted using the set of indices $\mathfrak{I}_\mathbf{i}$ (21).

2.4 Superelement

The linkage of substructures for dynamic analyses was first introduced by Craig and Bampton in 1968 (22). We use the method of superelements in Nastran as the study's FE solver which reduces the computation time by modal reduction. For interested readers, more information is provided in the Superelements User's Guide (23).

3. State-Of-The-Art NVH FE Simulation

Figure 1 depicts the FE NVH model that we study which has around 2.6 million elements, 18.4 million degrees of freedom and 3.1 million nodes.

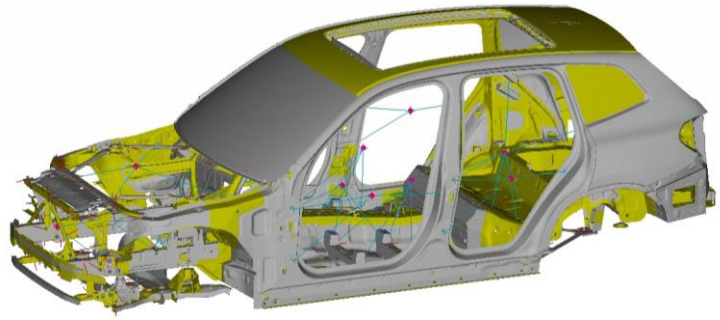


Figure 1 – FE NVH model in its entirety, including the physical part (body in white) and the additional vehicle components indicated by pink dots.

We divide this model in two parts: the body in white which we call the physical part and the additional vehicle components which are represented by cuboids with physical properties to reduce the simulation time.

This FE model is excited by four forces at the rear axle attachment points. Since the goal of the NVH simulation is to forecast NVH behavior prior to the vehicle's construction, it is noteworthy that uncertain parameters are inserted in the process. Therefore, a deterministic simulation is enabled due to the sampling of the distributions of the unknown parameters. To obtain a statistical outcome of the admittance, we iteratively run the deterministic simulation. More detailed information regarding the state-of-the-art NVH FE model and simulation process can be found in (6).

4. Parameter reduction regarding the sampling approach for a two-step sensitivity analysis

In this section, we describe the uncertain parameters and their sampling and the two-step sensitivity analysis which both were introduced in (6). Then, we compare the results of the parameter reduction.

4.1 Uncertain parameters and their sampling

First of all, we introduce the uncertain parameters with their ranges and numbers which we explain in (6) in detail: For the body in white, we chose the Young's moduli and the thicknesses of the shells and for the additional vehicle components the translational and rotational stiffnesses, the positions of the center of gravity of the cuboids, their moments of inertia, their products of inertia and their masses.

In sum, we have got 1,300 uncertain parameters which we vary for the sensitivity analysis. In the previous work (6), we sample the translational and rotational stiffnesses logarithmically because the value range varies in a wide range. Logarithmic sampling means that we sample linear on a logarithmic scale and therefore receive equal numbers of samples between 100 and 1,000, 1,000 and 10,000, and 10,000 to 100,000. With a linear sampling approach, we sample on a linear scale and therefore get equal numbers of samples as in the logarithmic example between 100 and 33,400, 33,400 and 66,700, and 66,700 and 100,000. The 1,300 uncertain parameters, their ranges, numbers and the sampling are presented in Table 1.

Table 1 – Uncertain parameters with their ranges, numbers and sampling.

Parameter	Range	Number	Sampling
Young's modulus	210 GPa ±6 % (197.4 to 222.6 GPa)	25	linear
Thickness	±5 %	606	linear
Translational stiffness	100 to 100,000 N/mm	246	logarithmic or linear
Rotational stiffness	100 to 100,000 Nmm/rad	246	logarithmic or linear
Position of the center of gravity	±50 mm	63	linear
Moments of inertia	±5 %	63	linear
Products of inertia	±5 % or neglected if equal 0	63 / 30	linear
Mass	±10 %	21	linear

In this contribution, we provide the results for linear sampling which we compare to the logarithmic results.

4.2 Comparison of the parameter reduction with the two-step sensitivity analysis

To answer the question if the two-step sensitivity analysis also achieves a high reduction for the linear sampling of the stiffnesses, we proceed this analysis again with the linear sampling which is described in detail in (6).

In the first step of the analysis, we start with all parameters of the additional vehicle components (669 parameters). This set of parameters has got the advantage that we are allowed to use a super-element of the physical part and receive an around 25 times faster computation times. We set a limit of 1 % and filter the Sobol' indices of each parameter if it is greater than this limit. Next, we compare the admittances of all 669 parameters with the reduced set of 135 uncertain parameters in Figure 2.

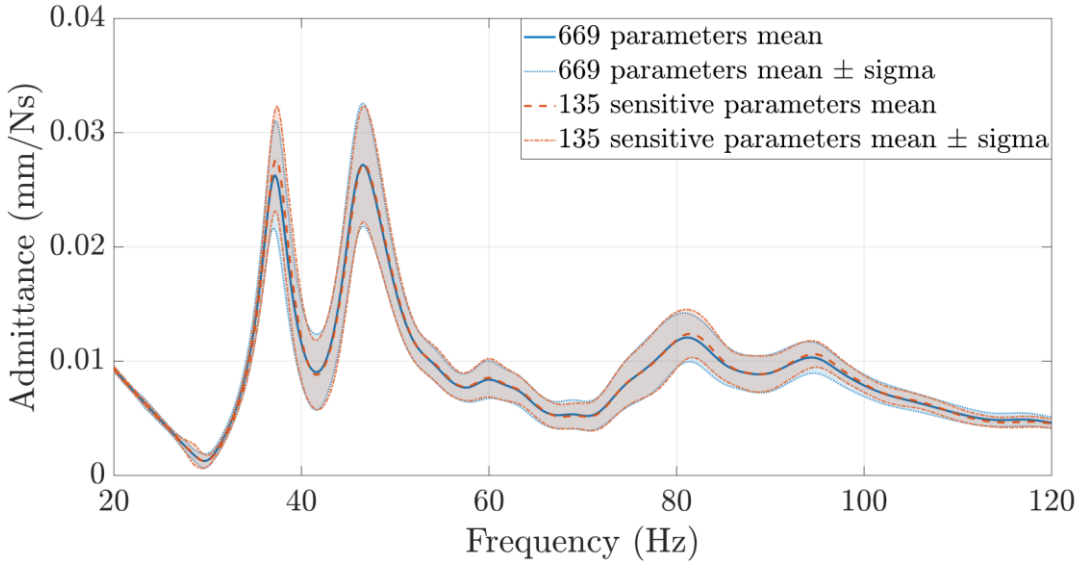


Figure 2 – First step of the sensitivity analysis with linear sampling: Comparison of the admittances of 669 uncertain parameters and the 135 sensitive parameters over the frequency.

The error of the mean is 1.9 % and 12.9 % of the standard deviation. Compared to the logarithmic sampling with 177 sensitive parameters, cf. (6), the mean value is 5.9 % smaller (logarithmic case: 7.8 %) and the standard deviation is 1.6 % higher (logarithmic case: 11.3 %). Because of these very small errors and the good fitting, we continue with the second step: We add all parameters of the body

in white – 631 ones – to the 135 sensitive parameters of the step before. We cannot use the superelement any more due to the parameter set of the physical part. In Figure 3, these results were compared with the 106 sensitive parameters which we get if we set the limit of the Sobol' indices again to 1 %.

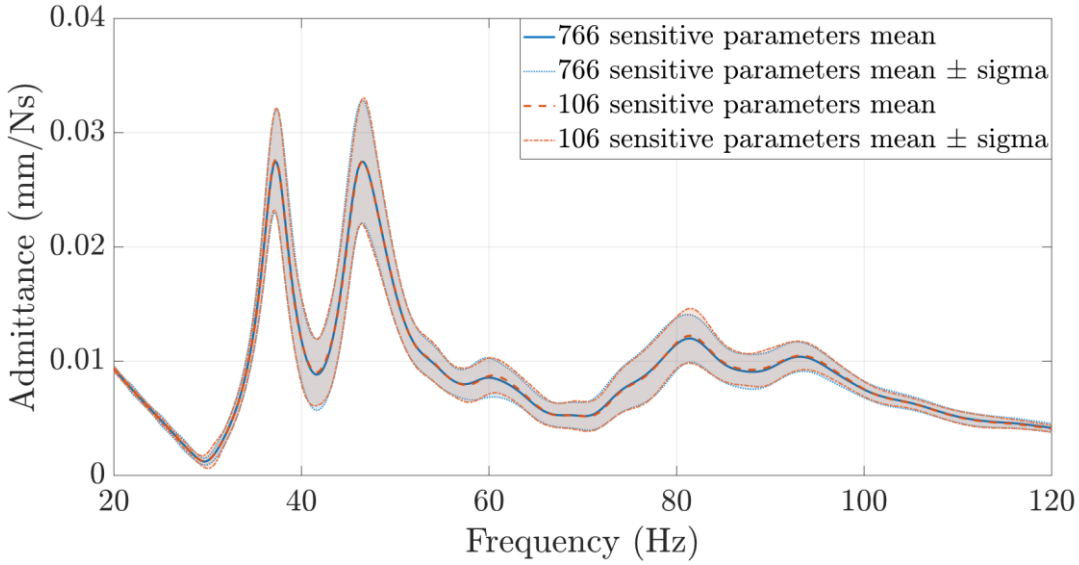


Figure 3 – Second step of the sensitivity analysis with linear sampling: Comparison of the admittances of 766 uncertain parameters and the 106 sensitive parameters over the frequency.

Again, the error of the mean is very small – only 1 % – as well as of the standard deviation – 10.4 %. In the end, we receive a parameter reduction of 91.9 %. In the logarithmic case, cf. (6), we receive an error of the mean of 3.5 % which is 2.5 % higher than in the linear case and an error of the standard deviation of 9.3 % which is 1.1 % smaller than the linear case by a parameter reduction of 92.2 %. We validate this result with a comparison of the results from the 106 sensitive parameters of the two-step sensitive analysis with the results from all 1,300 uncertain parameters in Figure 4.

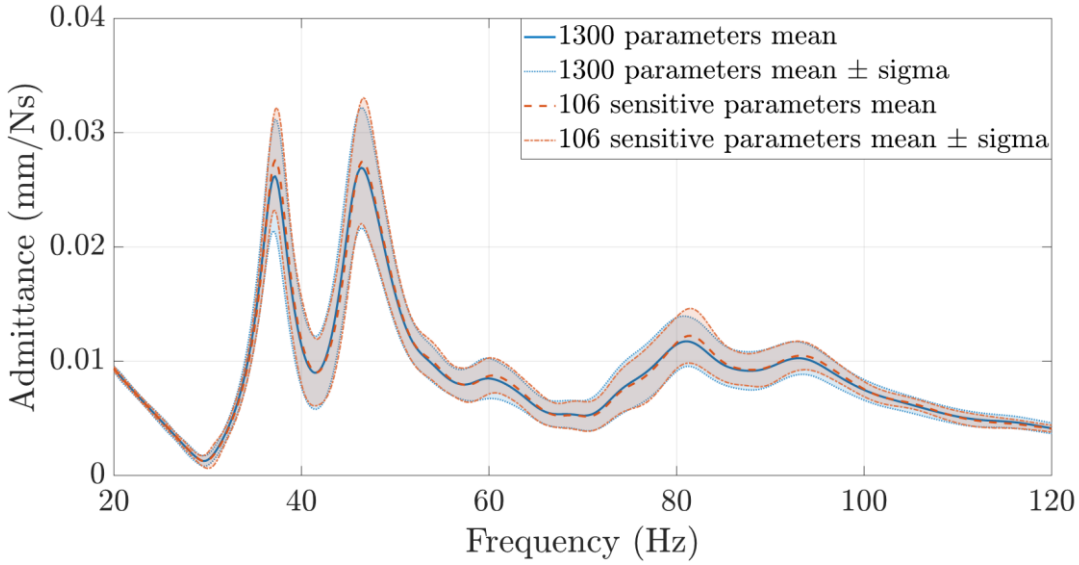


Figure 4 – Validation step of the sensitivity analysis with linear sampling: Comparison of the admittances of 1,300 uncertain parameters and the 106 sensitive parameters over the frequency.

The error of the mean is 2.2 % and of the standard deviation 15 %. The mean error is 6.8 % smaller

than in the logarithmic case (9 %) and the error of the standard deviation is only 0.5 % higher than in the logarithmic case (14.5 %), cf. (6).

4.3 Results

In Table 2, we sum up the linear and logarithmic sampling results: The total reduction of the uncertain parameters and the errors of the mean and the standard deviation for the first and second step of the two-step sensitivity analysis as well as for the validation.

Table 2 – Overview of the parameter reduction and the errors of the mean and of the standard deviation for the first step, second step and the validation.

	Linear sampling	**Logarithmic sampling**
Total reduction of parameters	91.9 %	92.2 %
	First step	
Error of the mean	1.9 %	7.8 %
Error of the standard deviation	12.9 %	11.3 %
	Second step	
Error of the mean	1 %	3.5 %
Error of the standard deviation	10.4 %	9.3 %
	Validation	
Error of the mean	2.2 %	9 %
Error of the standard deviation	15 %	14.5 %

We see that the mean error of the linear sampling is for each comparison between 2.5 % and 6.8 % smaller and the error of the standard deviation of the linear sampling is for each comparison between 0.5 % and 1.6 % higher.

Furthermore, we compare the influence of the logarithmic and linear sampling of the translational and rotational stiffnesses on the admittance curve over the frequency for the mean value and the standard deviation in Figure 5 for the first step of the sensitivity analysis with the parameters of the additional vehicle components.

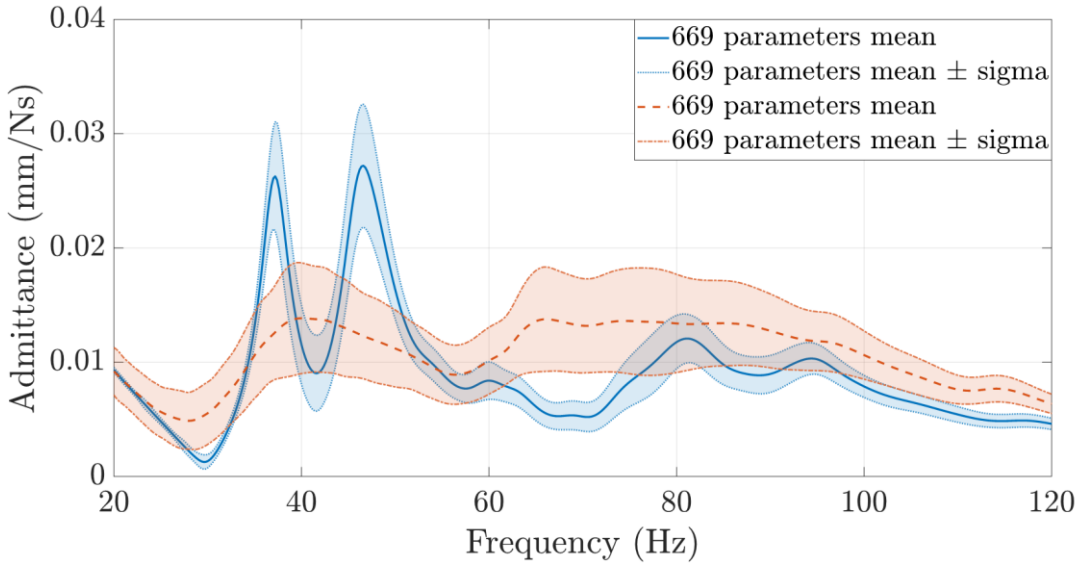


Figure 5 – Comparison of the admittance for logarithmic (red) and linear (blue) sampling of the stiffnesses over the frequency.

As we compare the curves of the admittance in Figure 5, we see extreme differences: The standard deviation of the linear sampling is smaller and the peaks of the linear case have got higher values compared to the logarithmic sampling. Due to the linear sampling, we got less values of small stiffnesses so that the samples are stiffer than in the logarithmic case.

Overall, we state that the sampling of the stiffnesses has got a huge influence on the admittance curve which must be taken into consideration if the result curves are further investigated. In addition, the linear sampling produces smaller errors but both sampling approaches show a very good reduction of the uncertain parameters (91.9 % and 92.2 %).

5. CONCLUSIONS

In this article, we gave a short introduction about the used methods as the sensitivity analysis, the gPC expansion and the computation of the first order Sobol' indices with the gPC expansion as well as the definition of a superelement. Next, we introduced the NVH FE process with its model that split up in two parts. These two parts were the basis for the two-step sensitivity analysis with in sum 1,300 uncertain parameters. These uncertain parameters were the Young's moduli, the thicknesses of the shells, the translational and rotational stiffnesses, the positions of the center of gravity of the cuboids, their moments of inertia, their products of inertia and their masses. Furthermore, we conducted the two-step sensitivity analysis with a linear sampling. In the results, we compared the admittance curves of the linear and logarithmic sampling of the translational and rotational stiffnesses and noted extreme differences. Over all comparisons, the mean error was smaller for the linear sampling and the error of the standard deviation was smaller for the logarithmic sampling. The parameter reduction was for both cases satisfying.

Henceforward, we use for these as unimportant classified parameters deterministic values and save a lot of computation time. Future research will focus on determining distributions of the unknown parameters and investigating the sensitive FE NVH model parameters. It would therefore be reasonable to examine the sensitivities using the new distributions and contrast them with this contribution, which made use of uniform distributions.

ACKNOWLEDGEMENTS

The contribution of Marinus Luegmair and Johannes D. Schmid is part of the joint project newAIDE under the consortium leadership of BMW AG with the partners Altair Engineering GmbH, divis intelligent solutions GmbH, MSC Software GmbH, Technical University of Munich, TWT GmbH. The project is supported by the Federal Ministry for Economic Affairs and Climate Action (BMWK) on the basis of a decision by the German Bundestag.

The authors thank Rafaella Dantas for adding a graphical user interface to the code.

REFERENCES

1. Durand J-F, Soize C, Gagliardini L. Structural-acoustic modeling of automotive vehicles in presence of uncertainties and experimental identification and validation. J Acoust Soc Am 2008; 124(3):1513–25.
2. Kompella MS, Bernhard RJ. Measurement of the Statistical Variation of Structural-Acoustic Characteristics of Automotive Vehicles. In: SAE Technical Paper Series. 400 Commonwealth Drive, Warrendale, PA, United States: SAE International; 1993 (SAE Technical Paper Series).
3. Hills E, Mace BR, Ferguson NS. Acoustic response variability in automotive vehicles. Journal of Sound and Vibration 2008:1–19.
4. Luegmair M, Schmid JD. Challenges in Vibroacoustic Vehicle Body Simulation Including Uncertainties. In: SAE Technical Paper Series. SAE International; 2020 (SAE Technical Paper Series).
5. Schmid JD, Luegmair M, Sepahvand K, Marburg S. Uncertainty Quantification in Vibroacoustic Analysis of a Vehicle Body Using Generalized Polynomial Chaos Expansion. In: SAE Technical Paper Series. SAE International; 2020 (SAE Technical Paper Series).
6. Cram S, Luegmair M, Schmid JD, Marburg S. Sensitivity Analysis of NVH Simulations with Stochastic Input Parameters for a Car Body. In: SAE Technical Paper Series. SAE International400 Commonwealth Drive, Warrendale, PA, United States; 2022 (SAE Technical Paper Series).
7. Cram S, Luegmair M, Di Nunno D, Marburg S. Uncertainty quantification of vehicle door parameters with Pearson charts in context of vibroacoustics. "Advances in Acoustics, Noise and Vibration – 2021", Proceedings of the 27th International Congress on Sound and Vibration, ICSV 2021 2021.
8. Avutapalli B, Vallurupalli S, Keshtkar H. Stochastic Analysis of a Body-on-Frame Vehicle to Achieve

Reliable and Robust Shake Performance. In: SAE Technical Paper Series. 400 Commonwealth Drive, Warrendale, PA, United States: SAE International; 2003 (SAE Technical Paper Series).
9. Kobayashi M, McAleer M. Tests of Linear and Logarithmic Transformations for Integrated Processes. Journal of the American Statistical Association 1999; 94(447):860–8.
10. Cox H. Linear versus Logarithmic Averaging. J Acoust Soc Am 1966; 39(4):688–90.
11. Buzan L, Rusu C, Bilcu RC, Kuosmanen P. Phase approximation in linear and logarithmic frequency domain. In: First International Symposium on Control, Communications and Signal Processing, 2004. IEEE; 2004. p. 709–12.
12. Iooss B, Saltelli A. Introduction To Sensitivity Analysis. In: Ghanem R, Higdon D, Owhadi H, editors. Handbook of uncertainty quantification. Cham: Springer; 2017 (Springer reference).
13. Razavi S, Jakeman A, Saltelli A, Prieur C, Iooss B, Borgonovo E et al. The Future of Sensitivity Analysis: An essential discipline for systems modeling and policy support. Environmental Modelling & Software 2021; 137:104954.
14. Puy A, Lo Piano S, Saltelli A. Is VARS more intuitive and efficient than Sobol' indices? Environmental Modelling & Software 2021; 137:104960.
15. Sudret B. Global sensitivity analysis using polynomial chaos expansions. Reliability Engineering & System Safety 2008; 93(7):964–79.
16. Wiener N. The Homogeneous Chaos. American Journal of Mathematics 1938; 60(4):897.
17. Cameron RH, Martin WT. The Orthogonal Development of Non-Linear Functionals in Series of Fourier-Hermite Functionals. The Annals of Mathematics 1947; 48(2):385.
18. Xiu D, Karniadakis GE. The Wiener-Askey Polynomial Chaos for Stochastic Differential Equations. SIAM J. Sci. Comput. 2002; 24(2):619–44.
19. Ghanem R, Spanos PD. Polynomial Chaos in Stochastic Finite Elements. J. Appl. Mech. 1990; 57(1):197–202.
20. Sudret B. Global sensitivity analysis using polynomial chaos expansion: In P. Spanos and G. Deodatis (Eds.), Proc. 5th Int. Conf. on Comp. Stoch. Mech (CSM5), Rhodos, Greece.; 2006.
21. Garcia-Cabrejo O, Valocchi A. Global Sensitivity Analysis for multivariate output using Polynomial Chaos Expansion. Reliability Engineering & System Safety 2014; 126:25–36.
22. Craig RR, Bampton MCC. Coupling of substructures for dynamic analyses. AIAA Journal 1968; 6(7):1313–9.
23. MSC Software Corporation. MSC Nastran 2017.1 Superelements User's Guide; 2017.

ICA 2022
24th INTERNATIONAL CONGRESS ON ACOUSTICS
October 24(Mon) - 28(Fri), 2022 Gyeongju, Korea

PROCEEDINGS of the
24th International Congress on Acoustics

October 24 to 28, 2022 in Gyeongju, Korea

ABS-0235

Model-based machine learning in acoustics applications from a Bayesian perspective

Ning Xiang[(1)] and Ziqi Chen[(1)] Jiahua Zhang[(1)] Mélanie Nolan[(1)]

[(1)]Graduate Program in Architectural Acoustics, Rensselaer Polytechnic Institute, Troy, New York USA, xiangn@rpi.edu

ABSTRACT

Recent acoustics investigations increasingly employ machine learning methods to analyze experimental data. Using well-understood models or hypotheses, acoustics analyses often embody two levels of inference: model selection and parameter estimation based on the chosen model. Model-based Bayesian analysis provides solutions of both inference levels centered around Bayes' theorem within a unified framework. The data-driven machine learning method represents a learning process from data in order to update our knowledge. This is exactly consistent with the core of Bayesian probability theory, which represents how our prior knowledge is updated in presence of the data. This paper discusses the model-based machine learning methods in a way of thinking like a Bayesian. In particular, it emphasizes that the well-understood models are considered as a part of the prior knowledge which are readily incorporated in the learning process. This paper highlights data-driven machine learning methods from a Bayesian perspective based on recent acoustics investigations, such as acoustic array signal processing, normal incident impedance tube measurements, chamber-based absorption measurements and wavenumber spectral analysis in enclosed spaces. Numerical challenges and promising solutions for two-levels of Bayesian learning are also discussed.

Keywords: machine learning, Bayesian inference, data-driven algorithms, model-based analysis

1 INTRODUCTION

Machine Learning (ML) refers to the process by which computers or algorithms are able to make predictions based on data and learn from data, possibly adjust some pertinent properties without being specifically programmed to do so. In recent machine learning literature, sometimes it is also referred to as data-driven machine learning. This paper sheds some light on the data-driven machine learning from Bayesian perspective, primarily based on Bayesian probability theory. One of core issues within Bayesian paradigms is that the probability is interpreted as degree/strength of implication or confirmation. In details, degree of implication can quantitatively encode state of knowledge or state of information in probabilities [1]. While Bayesian probability theory, centered around Bayes' theorem represents how our prior knowledge is updated in the presence of data, computers or algorithms equipped with the machine learning capability are able to learn from data and make predictions based on data. This exactly represents the Bayesian viewpoint, that we empower the computers and the specific algorithms to update the prior knowledge when involving (experimental) data based on Bayesian probability theory, that also includes all valid rules of statistics for relating and manipulating probabilities. Therefore we view this fundamental scientific exploration, to learn from real-world by conducting experiments in acquiring data, as *Bayesian learning*.

This paper highlights data-driven machine learning methods from a Bayesian perspective based on recent acoustics applications, discusses the two-levels of Bayesian inference to carry out the data-driven machine learning, exploiting well established and/or well understood models, specifically *model-based Bayesian learning from experimental data*. In the following we formulate two levels of Bayesian inference within a unified learning framework. Then we discuss a number of recent investigations using either the first level of inference, Bayesian parameter estimation or the second level, Bayesian model selection.

2 A UNIFIED INFERENTIAL FRAMEWORK OF BAYESIAN ANALYSIS

This paper focuses on a specific class of Bayesian learning, namely model-based inference. Many acoustical applications have in common the existence of well established, or at least well understood models for predicting the processes under investigation. In order to learn the process, acousticians conduct experimental measurements to obtain a set of experimental data. The prediction models can be physical or phenomenological, they can also be analytical or numerical. This Section discusses the two levels of model-based Bayesian learning, namely model selection and parameter estimation. The model selection represents higher (second) level of inference, while the parameter estimation is the lower (first) level one. Many machine learning approaches, such as optimizations are within the first level of learning. However, if one engages a wrong model or a redundant model for any sort of optimizations, the estimations/optimizations become also wrong or redundant, no matter how well the model-based optimization will be. The following Section applies a top-down approach in formulating the two levels of probabilistic inference.

2.1 Bayesian model selection

In some applications the investigators are challenged to consider a handful number of models $\mathbf{M}$, they are competing to each other to predict the data $\mathbf{D}$. Among them the investigators want to learn from the data which model among the considered set of models is preferred. This situation can be formulated as background information I as

> 'the models specified by index $n = 1,2,3,\ldots$ may all describe the data reasonably well.'

Taking this background information, the model selection applies the Bayesian theorem to evaluate the probability of M_n among a set of models $\mathbf{M} = \{M_1,\ldots,M_n,\ldots,M_N\}$ for $n = 1,2,\ldots,N$ given the data $\mathbf{D}$, [1]

$$p(\mathbf{M}|\mathbf{D},I) = \frac{p(\mathbf{D}|\mathbf{M},I)\,p(\mathbf{M}|I)}{p(\mathbf{D}|I)}. \tag{1}$$

The Bayesian theorem in Eq. (1) as applied to this set of models $\mathbf{M}$ represents how the investigator's prior knowledge $p(\mathbf{M}|I)$ about the models, given the background information I as stated above, is updated in presence of the data as represented by $p(\mathbf{D}|\mathbf{M},I)$. It is termed *marginal likelihood* within the context of Bayesian model selection, while $p(\mathbf{M}|I)$ is the prior probability of the models, often referred to *prior* in short. Quantity $p(\mathbf{D}|I)$ in the denominator is a normalization constant. Upon the presence of the data, this learning process updates the prior via the data based on the model incorporated in $p(\mathbf{D}|\mathbf{M},I)$, which leads to $p(\mathbf{M}|\mathbf{D},I)$. It becomes the *posterior* (probability) of the models given the data and the above stated background information I. The background information in this specific model learning includes a number (N) of the competing models with model index n .

At the model selection level, which is a higher level of inference, detailed model parameters Θ are deferred into the background. Among the posteriors of the limited number of models M_N, the Bayesian model selection evaluates *Bayes' factor*, a posterior ratio [1],

$$B_{ij} = \frac{p(M_i|\mathbf{D},I)}{p(M_j|\mathbf{D},I)} = \frac{p(\mathbf{D}|M_i,I)}{p(\mathbf{D}|M_j,I)}\,\frac{p(M_i|I)}{p(M_j|I)}. \tag{2}$$

The Bayes' factor B_{ij} indicates how much the model M_i is preferred over model M_j given the data $\mathbf{D}$, while the second ratio on the right-hand side of Eq. (2) represents the investigator's prior preference of model M_i over model M_j before involving the data, termed *prior ratio*. If the investigator has no prior preference to any models among the model set, the prior ratios being 1 for all model pairs exactly encode this state of preference. This represents that the model selection only relies on the first ratio on the right-hand side. It is termed *Bayesian evidence* ratio (evidence ratio in short).

When implementing the model selection in the machine learning, a logarithm of Bayes' factors is often calculated

$$\zeta_{ij} = 10\log_{10}(B_{ij}) = (\zeta_i - \zeta_j) + [10\log_{10}(\Pi_i) - 10\log_{10}(\Pi_j)],\ [\text{db}], \tag{3}$$

with $\mathbf{Z}_i = p(M_i|\mathbf{D},I)$, $\zeta_i = 10\log_{10}(\mathbf{Z}_i)$, and $\Pi_i = p(M_i|I)$ to simplify the notations . When encoding 'no preference' to any model, the second term of Eq. (3) would become zero, so as to rely solely on the evidence ratio. The logarithmic Bayes' ratio is expressed in unit 'decibans', [1] or 'db' in short. In some large-scale applications, instead of directly estimating the evidence, the inverse Bayesian information criteria (IBIC) or inverse Deviance information criteria (IDIC) will allow for more computationally feasible approximation of the evidence [1], rather computationally prohibitive. The Bayesian model selection quantitatively implements Occam's razor '*when two models predict the data equally well, the simpler one is preferred*' [1].

2.2 Bayesian parameter estimation

After a specific model is selected from the pre-selected model set through Bayes' factor discussed above, the parameter estimation pursues further learning of the model parameters Θ given model M_N from the data $\mathbf{D}$. The first (lower) level of inference, the parameter estimation, engages once again the Bayesian theorem to evaluate the probability of the parameters Θ

$$p(\Theta|\mathbf{D},M_N,I) = \frac{p(\mathbf{D}|\Theta,M_N,I)\,p(\Theta|M_N,I)}{p(\mathbf{D}|M_N,I)}. \tag{4}$$

Within this parameter estimation level, the background information I becomes more specific, including that

> 'A specific model noted as M_N has been selected given the data $\mathbf{D}$. This model specified now by value N encapsulates model parameters Θ. The model then will predict the data well if the parameters are well estimated.'

Beyond the background information along with the well established model, no further information is available at this point.

2.3 Unified learning framework

The denominator $p(\mathbf{D}|M_N,I)$ in Eq. (4) is a normalization constant to ensure that the posterior probability of the parameters is integrated to unity over the entire parameter space. Integration of both sides of Eq. (4) results in

$$\mathbf{Z}_N = p(\mathbf{D}|M_N,I) = \int_\Theta p(\mathbf{D}|\Theta,M_N,I)\,p(\Theta|M_N,I)\,\mathrm{d}\Theta. \tag{5}$$

Although the denominator is of less importance at the level of the Bayesian parameter estimation, it exactly equals the marginal likelihood in Eqs. (1,2). Applying short-hand notations $\Pi(\Theta) = p(\Theta|M_N,I)$ and $\mathscr{L}(\Theta) = p(\mathbf{D}|\Theta,M_N,I)$, Equation (4) is simplified to

$$\overbrace{p(\Theta|\mathbf{D},M,I)}^{\text{posterior}} \times \overbrace{\mathbf{Z}}^{\text{evidence}} = \overbrace{\mathscr{L}(\Theta)}^{\text{likelihood}} \times \overbrace{\Pi(\Theta)}^{\text{prior}}, \tag{6}$$

where the subscript of model is dropped from now on for simplicity and Bayesian evidence $\mathbf{Z} = p(\mathbf{D}|M_N,I)$ is determined using Eq. (5). Yet readers should still bear in mind that the model has been selected from now on.

Equation (6) indicates that both levels of inference (model selection and parameter estimation) can be pursued within one unified framework. Furthermore, Eq. (6) also explicitly expresses the relationship among the four quantities of Bayes' theorem; the likelihood and the prior are two probabilistic inputs to the Bayesian analysis while the posterior and the evidence are two outputs. More specifically, the likelihood also represents one of priors which is the quantity to incorporate the data and the prediction model into the learning process. On one hand, the model is part of prior knowledge. Some models are often established based on generations of learning and education in many applications. On the other hand, the likelihood offers a mechanism for the process to be driven by the data. In order to proceed, two priors (the prior and the likelihood) need to be assigned. The prior probabilities encode what the investigator knows *a priori*. At the start of the learning process, not much is known (otherwise there is no need to learn), therefore, the assignment based on Bayesian probabilistic theory follows the principle of the maximum entropy [1].

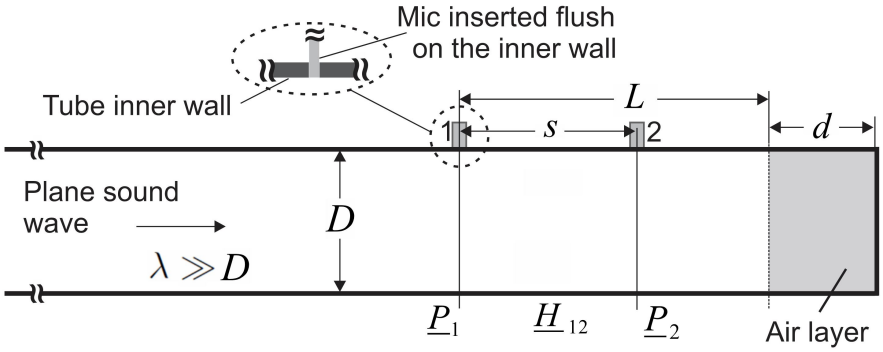


Figure 1. Two-microphone method in an impedance tube for normal incidence reflection/absorption coefficient measurement [2]. D is diameter of the tube, λ is the acoustic wavelength used for the measurements

Furthermore, the evidence represents the key output quantity for the Bayesian model selection [**?**], it quantitatively implements Occam's razor. In many applications, the Bayes' factor in Eqs. (2,3) needs to be evaluated among the pre-selected model set, this evaluation predominantly relies on the Bayesian evidence of each individual model [1]. The posterior represents the key output for estimating the corresponding model parameters given the specified model.

3 APPLICATION EXAMPLES

Acoustics has increasingly seen model-based Bayesian inference applications, some apply the first level of inference (for example in Sec. 3.1 and Sec. 3.2), while some others the both levels of inference (for example in Sec. 3.3 and Sec. 3.4). This paper uses the most recent examples to demonstrate a wide variety of data-driven machine learning applications.

3.1 Dissipation and sound speed estimation in impedance tubes

The recent work [2] can also be classified as a typical data-driven machine learning application, where the experimental data are obtained by experimentally measuring the transfer functions between two microphone positions inside the tube. Figure 1 schematically illustrates the tube measurement set up. The measurement data at two microphone positions (labeled 1, and 2) are processed to yield the reflection coefficient of a 'material' under test [3]

$$\underline{R}_{\mathrm{D}} = \frac{\underline{H}_{12} - \mathrm{e}^{-\underline{\gamma} s}}{\mathrm{e}^{\underline{\gamma} s} - \underline{H}_{12}} \mathrm{e}^{2\underline{\gamma} L}, \quad \text{with} \quad \underline{\gamma} = \frac{\alpha_\zeta \, c + \mathrm{j}\omega}{c}, \tag{7}$$

where $\underline{H}_{12} = \underline{P}_2 / \underline{P}_1$ is the transfer function between the pressure spectrum at microphone position '2' and that of position '1'. $\underline{\gamma}$ represents the complex-valued propagation coefficient, α_ζ is the damping coefficient, ω is the angular frequency and c is the sound speed.

These data obtained using Eq. (7) drive the machine learning algorithm to accurately estimate the tube wall dissipation, the sound speed, and optionally the microphone positions. In order to facilitate the model-based learning, Chen et al.[3] established a prediction model for a hypothesized air layer in front of a rigid termination of the impedance tube

$$\underline{R}_{\mathrm{M}} = \mathrm{e}^{-2\underline{\gamma} d}. \tag{8}$$

In this data-driven machine learning application, the prediction model encapsulates model parameters $\Theta = [c, \zeta]$ in form of the surface reflection coefficient $\underline{R}_{\mathrm{M}}$ of the air layer in Eq. (8) with a Bayesian parameter estimation approach, an application for the first level of inference in this study. In the context of Bayesian parameter estimation as expressed in Eq. (4), the reflection coefficient $\underline{R}_{\mathrm{M}}$ represents the given model M_N, while the reflection coefficient of Eq. (7) is the data $\mathbf{D}$ in Eq. (4). Detailed formulations of Bayesian learning and its implementation are beyond the scope of the current paper, see a recent publication [3] for more details.

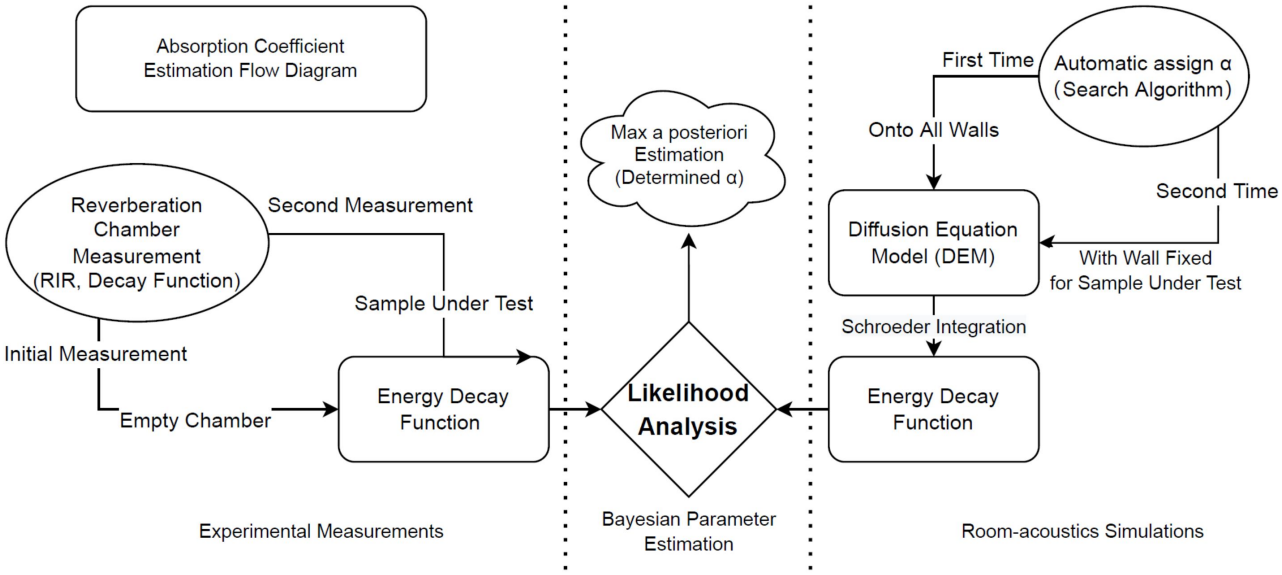


Figure 2. Flow diagram of data-driven machine learning for model-based Bayesian absorption coefficient estimation. [4].

3.2 Chamber-based absorption coefficient measurement

Chamber-based measurements of random incidence absorption coefficients have recently emerged on a debatable stage. Some challenging issues have been debated for possible solutions. The standardized measurement technique overlooks the non-diffused sound field in the room acoustics. That may result in decreased accuracy and even conflicting results. Zhang *et al.* [4] apply a diffusion equation model to room-acoustic simulations of standardized reverberation chambers (see Fig. 2). They numerically solve the room-acoustic finite difference simulations in time domain (Fig. 2 right). This machine learning example engages a numerical model of a simulated reverberant chamber, while the data-driven machine learning relies on experimentally measured sound energy decays in the standardized reverberant chamber with/without the absorber of standardized size (Fig. 2 left).

In case of the empty chamber measurement, the experimentally measured energy decay function drives the learning algorithm. The learning process iteratively adjusts the absorption coefficient throughout the interior surfaces of the simulated chamber of the same geometry/dimensions at the same source/receiver locations until the maximum *a posteriori* absorption coefficient is reached. Then the machine learning algorithm switches its focus on the absorber measurement. The energy decay data experimentally measured in the chamber drive again the algorithm during the second adjustment of absorption coefficient only on the absorber under test in the simulated chamber, while keeping all the other interior surfaces fixed at the previously obtained estimate.

This machine learning task represents an estimation of one-parameter value, yet it runs twice in a sequential manner based on the diffusion equation model which is solved numerically using the finite difference approach. The Bayesian learning (Fig. 2 middle) is accomplished with a high computational efficiency since the diffusion equation-based modeling relies on a highly sparse meshing condition of the domain which is dictated by the mean-free path length rather wavelengths. This method essentially conducts a machine learning driven by the experimentally measured data in the reverberation chamber. Interpreted in a Bayesian view, the process learns from the experimental data, iteratively updates an initial vague knowledge of sound absorption coefficient to arrive at sharply accurate estimates. More details can be obtained from a paper in this proceedings [4].

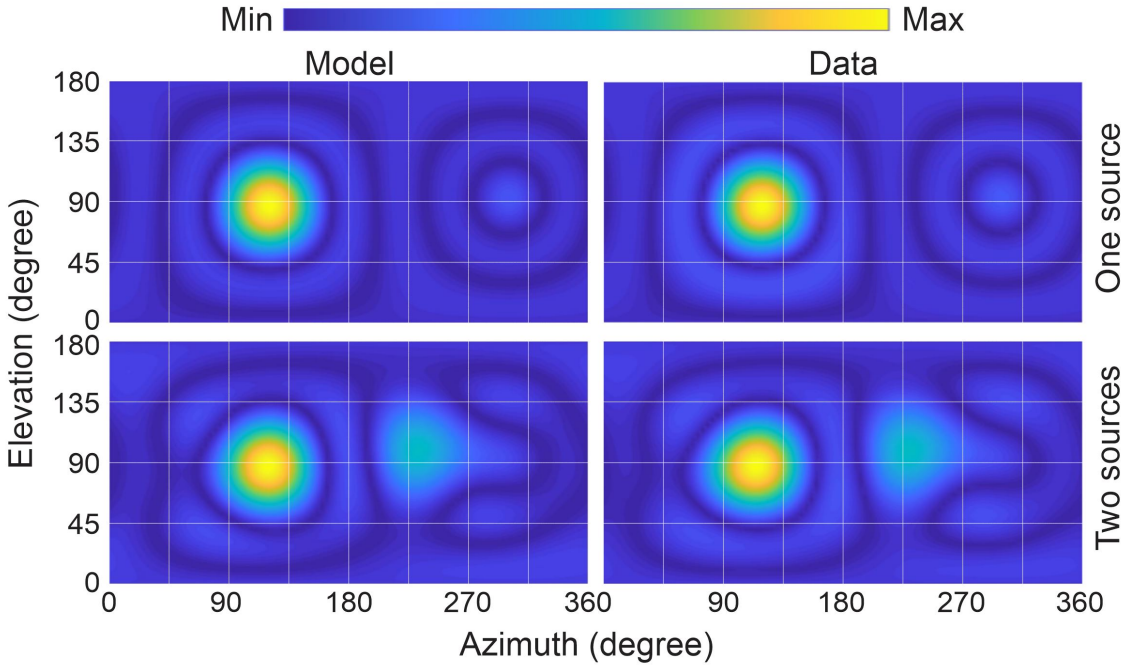


Figure 3. Comparison between experimentally measured data maps with those predicted by the beamforming model. In one source scenario, the sound source finds itself at 5 cm distance from the origin of the sphere, while for two source scenario, the second source finds itself at 5.5 cm distance [5].

3.3 Source enumeration and localization using a spherical microphone array

This application intends to localize potentially multiple co-existing sound sources in near-field around a spherical microphone array. Spherical microphone data are processed to analyse incoming sound fields. Sound pressure signals $P_{\text{mic}}(k,a,\theta_i)$ of M microphones flush-mounted on the rigid spherical surface of radius a are Fourier transformed by [5]

$$D(\theta) = \sum_{n=0}^{N} \sum_{m=-n}^{n} Y_n^m(\theta) P_{nm}^2, \quad \text{with} \quad P_{nm} = \frac{4\pi}{M} \sum_{i=1}^{M} P_{\text{mic}}(k,a,\theta_i) [Y_n^m(\theta_i)]^*, \tag{9}$$

where θ, θ_i represent (beamforming) looking directions, the microphone positions on the spherical array, respectively. $Y_n^m(\cdot)$ represents spherical harmonics and P_{nm} the transformed microphone signals in spherical harmonics domain. $k = \omega/\mathrm{c}$ is the propagation coefficient with ω and c being the angular frequency and sound speed, respectively. In this data-driven processing $D(\theta)$ is in two-dimensional matrix form, denoted as $\mathbf{D}$ when using Eq. (6) for the two-levels of Bayesian learning. Figure 3 illustrates so achieved beamforming data for one or two co-existing sound sources.

For the model-based Bayesian inference, the prediction models need to incorporate an unknown number of sound sources along with localization parameters including source distances $\mathbf{r}_\mathrm{s}$ and directions of arrivals $\theta_\mathrm{s} = [\vartheta_\mathrm{s}, \phi_\mathrm{s}]$ over a potential looking angles $\theta = [\vartheta, \phi]$ of interest,

$$M_S(\Theta) = \sum_{s=1}^{S} A_s g^2(\Theta), \quad \text{with} \quad g(\theta_\mathrm{s}, \mathbf{r}_\mathrm{s}) = \sum_{n=0}^{N} \sum_{m=-n}^{n} B_n^\mathrm{s}(k, \mathbf{r}_\mathrm{s}) [Y_n^m(\theta_\mathrm{s})]^* Y_n^m(\theta), \tag{10}$$

where $\Theta = [\vartheta_S, \phi_S, \mathbf{r}_S]$ collectively includes all the localization parameters for potentially S number of sound sources, the near-field modal strength,

$$B_n^\mathrm{s}(k, \mathbf{r}_\mathrm{s}) = \mathrm{j}k \left[j_n(ka) - \frac{j_n'(ka)}{h_n'(ka)} h_n(ka) \right] h_n(k\mathbf{r}_\mathrm{s}), \tag{11}$$

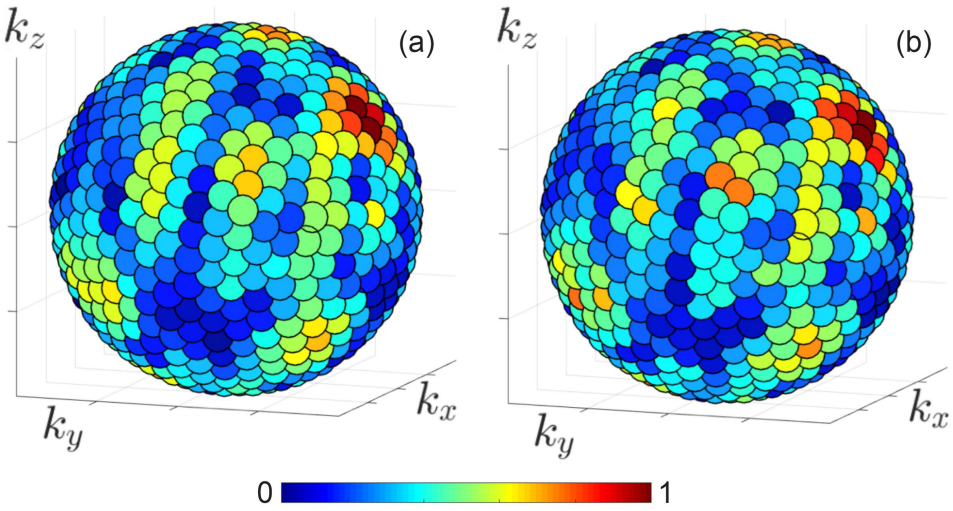


Figure 4. Wavenumber spectral analysis based on a set of sound pressures experimentally measured in an undamped room. Bayesian learning leads to 634 plane waves for this set of data. (a) Regularized learning [7]. (b) Bayesian learning [6],

where $j_n()$, $h_n()$ and $j_n'()$, $h_n'()$ are spherical Bessel, Hankel functions and their derivatives, respectively. Figure 3 also illustrates the predicted data using the model $M_2(\Theta)$ of Eq. (10).

3.4 Wavenumber spectral analysis in reverberant spaces

This application intends to quantify the degree of isotropy of sound fields in reverberation chambers [6]. For this purpose, a wavenumber spectrum is analysed based on decomosition of plane waves. Experimental data $\mathbf{D}$ are acquired via a robot-arm driving a microphone for measuring sound pressures at Q positions in the sound field. Based on the plane wave expansion, the sound pressures at these measuring positions can be predicted as a large number (L) of plane waves [6]

$$\mathbf{M}(\mathbf{r}_q) = \left[\mathrm{e}^{-\mathrm{j}\mathbf{k}_l\cdot\mathbf{r}_q}\right]\left[\tilde{P}(\mathbf{k}_l)\right], \quad \text{with,} \quad 1 \le l \le L, \quad 1 \le q \le Q, \tag{12}$$

where the plane wave propagation $\mathrm{e}^{-\mathrm{j}\mathbf{k}_l\cdot\mathbf{r}_m}$ on the right-hand side is expressed as a matrix of dimension $Q \times L$ and the plane wave pressure amplitude $\tilde{P}$ is expressed as column vector of $L \times 1$ elements. The left-hand side contains a column vector of $Q \times 1$ elements. $\mathbf{M}$ in Eq. (12) represents the prediction models $\mathbf{M} = [M_1, M_2, \ldots]$, when two-levels of inference are involved using Eq. (6). The task is to infer complex-valued amplitudes of the plane waves from experimental measurements $\mathbf{D}$ with an array of microphones or a robot-arm holding a microphone. Nolan *et al.* [6] apply the data-driven Bayesian learning using the two levels of inference to estimate the complex-valued amplitudes in the plane-wave expansion. The unified framework learns the plane wave parameters from the data. Figure 4 illustrates comparison of machine learning results between the regularized learning in Fig. 4 (a) and the Bayesian inferential learning in Fig. 4 (b).

The applications discussed in Sec. 3.3 and 3.4 represent the data-driven two-levels of Bayesian learning examples, since the higher level of inference, the model selection needs to be involved. In Sec. 3.3, the model selection has to be first applied to a number of models $M_S(\mathbf{x})$ for $S = 1, 2, \ldots$ for the data to drive the estimation of how many sound sources are present before the localization parameters of the right number of sound sources are inferred, through the lower level of inference. In Sec. 3.4, the number (L) of plane waves has to be estimated. Without the higher level of inference, any algorithms at the lower level, including some efficient optimizations, may lead to wrongly, at least redundantly 'optimized' parameters. In accomplishing the two levels of inference Eq. (6) plays a central role, explicitly indicates that the two levels of machine learning can be carried out within the unified Bayesian framework.

4 SUMMARY

This paper reviews recent applications of Bayesian learning in acoustics investigations. A wide variety of machine learning algorithms can be put in context of Bayesian learning, particularly when well established, well understood models for the prediction of the data are incorporated in the analysis. They are model-based machine learning methods, intended to learn from data, then update the initial hypotheses (prior knowledge) to improve the learning outcomes, whether it be the prediction models to be selected or the parameters to be estimated. Such approaches represent the data-driven learning processes which are consistent with the core of Bayesian probabilistic theory, learning from the data in order to update our prior knowledge.

ACKNOWLEDGEMENTS

The authors are grateful to Mr. S. Weikel and Mr. T. Metzger for their contributions to the sound source localization using a spherical microphone array.

References

[1] Xiang N, Model-based Bayesian analysis in acoustics – A tutorial, J. Acoust. Soc. Am. 2020;148:1101-20.

[2] Chen Z, Xiang N, Bayesian inference for sound speed and dissipation estimations in impedance tubes, 24th Intl. Con. Acoust. (this proceedings), Gyeongju, Korea, Aug. 2022

[3] Chen Z, Xiang N, Fackler CJ, Bayesian estimations of dissipation, sound speed, and microphone positions in impedance tubes, J. Acoust. Soc. Am. Express Lett.;2(8):083601-6 (DOI: 10.1121/10.0012993), 2022.

[4] Zhang J, Nolan M, Xiang N, Navarro JM, Diffusion equation-based modelling of reverberation chambers for sound absorption measurements, 24th Intl. Con. Acoust. (this proceedings), Gyeongju, Korea, Aug. 2022.

[5] Xiang N, Metzger T, Near-field localization of sound sources using a spherical microphone array, 24th Intl. Con. Acoust. (this proceedings), Gyeongju, Korea, Aug. 2022.

[6] Nolan M, Xiang N, Bayesian wavenumber spectrum inference for sound field analysis in reverberant spaces, 24th Intl. Con. Acoust. (this proceedings), Gyeongju, Korea, Aug. 2022.

[7] Nolan M, Berzborn M, Fernandez-Grande E, Isotropy in decaying reverberant sound fields, J. Acoust. Soc. Am.2020;148(2):1077-88,

[8] Xiang N, Fackler CJ, Hou Y, Schmitt A, Bayesian design of broadband multilayered microperforated panel absorbers, J. Acoust. Soc. Am.2022;151:3091-3103.

ICA 2022
24th INTERNATIONAL CONGRESS ON ACOUSTICS
October 24(Mon) - 28(Fri), 2022 Gyeongju, Korea

PROCEEDINGS of the
24th International Congress on Acoustics

October 24 to 28, 2022 in Gyeongju, Korea

ABS-0731

Multi-fidelity modeling using Gaussian Processes for the Helmholtz Equation

Caglar GURBUZ[(1)], Martin ESER[(2)], Johannes SCHAFFNER, Steffen MARBURG[(3)]

[(1)]Chair of Vibroacoustics of Vehicles and Machines, Germany, caglar.guerbuez@tum.de

[(2)]Chair of Vibroacoustics of Vehicles and Machines, Germany, martin.eser@tum.de

[(3)]Chair of Vibroacoustics of Vehicles and Machines, Germany, steffen.marburg@tum.de

ABSTRACT

In engineering practice, accurate physical experiments as well as large-scale numerical simulations are often accompanied with high resource and time expenses. Therefore, the data generation process can only be performed for a limited number of sample size which leads to insufficient model results. The idea of multi-fidelity modeling is to holistically evaluate data from different sources with varying complexity and costs. For instance, high-fidelity models expose highly accurate results at high costs, whereas low-fidelity models are rather inaccurate but fast to evaluate. In general, physical experiments and large-scale numerical simulations belong to the group of high-fidelity models, while analytical solutions as well as numerical simulations at small scale can be considered as low-fidelity models. For an ideally positive correlation between the low-fidelity and the high-fidelity models, multi-fidelity models allow to obtain additional data at lower costs. The aim of this contribution is to present a multi-fidelity model applied on a sound propagation problem in interior acoustics. Regarding the high-fidelity model, a boundary element model with a finer mesh is considered, whereas a model with a coarser mesh is adopted as the low-fidelity model. The multi-fidelity model is realized as a vector-valued Gaussian process.

Keywords: Multi-fidelity modeling, Gaussian Processes, Helmholtz equation, Boundary element method

1 INTRODUCTION

To assess the behavior of an acoustic system, engineers and specialists are usually faced with the challenge to choose an appropriate model for the problem at hand. Ideally, the model should efficient to evaluate and highly accurate. However, in practice, this is rarely the case. Models, which are usually fast to evaluate, lack of accuracy, whereas models with a high prediction capability are expensive in terms of computational costs or time expenses. Multi-fidelity models seek to combine the advantages of both worlds meaning the efficiency of a so-called low-fidelity model and the accuracy of a so-called high-fidelity model. In this context, low-fidelity models can be analytical solutions or numerical models at small scale. On the other hand, large-scale numerical models as well as cumbersome physical experiments are considered as high-fidelity models. For this purpose, Gaussian Processes (GPs) are deployed to melt the characteristics of the low- and the high-fidelity model. GPs designate a regression method combining the observed data with a user-defined kernel function. By this means, they provide an intuitive and at the same time data-driven approach. In addition to this, GPs also account for the quantification of uncertainties, which can arise due to manufacturing tolerances or model assumptions. To evaluate the frequency response of an acoustic system with the boundary element method (BEM), numerous evaluations at various frequencies are usually required. For highly accurate results, however, time and resource expenses are enormously high. This contribution aims at the development of a multi-fidelity model for accurate predictions with a reduced the number evaluations. Therefore, GPs are adopted allowing for an additional quantification of uncertainties. The multi-fidelity model is applied on a vehicle interior noise problem, for which a model with two different numbers of degrees of freedom is investigated. The model with a large number of DOFs is considered as the high-fidelity model, whereas the model with a low number

of DOFs is considered as the low-fidelity model. Initial results already demonstrate the effectiveness of the proposed method, as the multi-fidelity model allows for accurate predictions with a drastically reduced number of forward simulations.

2 METHODS

In this section, the fundamentals GPs and multi-fidelity GPs are briefly introduced. The interested reader is referred to for further details on GPs [2]. A thorough presentation of the theory of multi-fidelity models is detailed in [1].

2.1 Gaussian Processes

A Gaussian Process (GP) is defined to be a collection of random variables which are jointly Gaussian distributed and indexed by an infinite index set

$$f(x) \sim \mathscr{GP}\left(m(x), k(x,x')\right), \tag{1}$$

where f is the GP with the mean function m and the covariance function k. These functions expect the input variables x and x', which are both from the input space X. In practice, Gaussian Processes can be interpreted as infinite dimensional joint normal distributions, which are reduced to a finite dimensional joint normal distribution in a numerical implementation:

$$\mathbf{f} \sim \mathscr{N}\left(\begin{bmatrix} m_1(x_1) \\ m_2(x_2) \\ \vdots \\ m_N(x_N) \end{bmatrix}, \begin{bmatrix} k_{11}(\mathbf{x},\mathbf{x}') & k_{12}(\mathbf{x},\mathbf{x}') & \cdots & k_{1N}(\mathbf{x},\mathbf{x}') \\ k_{21}(\mathbf{x},\mathbf{x}') & k_{22}(\mathbf{x},\mathbf{x}') & \cdots & k_{2N}(\mathbf{x},\mathbf{x}') \\ \vdots & \vdots & \ddots & \vdots \\ k_{N1}(\mathbf{x},\mathbf{x}') & k_{N2}(\mathbf{x},\mathbf{x}') & \cdots & k_{NN}(\mathbf{x},\mathbf{x}') \end{bmatrix}\right), \tag{2}$$

where $\mathbf{x}$ is a vector that collects N inputs. The vector $\mathbf{f}$ collects the random variables f_i with $i = 1,...,N$ with the mean values m_i and the elements of the covariance matrix k_{ij}.

The entries of the covariance matrix are defined by the covariance function or kernel $k(x,x')$, which describes how the random variables f_i are correlated. In this contribution, the focus is on the squared exponential kernel:

$$k(x,x') = \sigma_f^2 \exp\left(-\frac{1}{2l^2}(x-x')^T(x-x')\right). \tag{3}$$

This kernel implements the expectation that the closer together two inputs are in the input space, the more the maps should correlate [2]. The width of the kernel and the distance in the input space is defined by the characteristic length l. The amplitude of the kernel is given as σ_f^2. These variables are called the hyperparameters of the kernel. Note that the kernel does not depend on the output of any measured data. In this way, prior beliefs on the unknown function can be expressed without introducing any measured data. The prior distribution of the measured outputs (training points) $\mathbf{f}$ can be then written as

$$\mathbf{f} \sim \mathscr{N}\left(\mathbf{0}, k(\mathbf{x},\mathbf{x}')\right). \tag{4}$$

In this initial study, the mean is set to be zero. This prior can be extended to express the joint distribution of $\mathbf{f}$ and the predicted outputs $\mathbf{f}_*$, where the training inputs are collected in an array $\mathbf{x}$ and the test inputs in $\mathbf{x}_*$. These data arrays can be then used to express the joint distribution of $\mathbf{f}$ and $\mathbf{f}_*$:

$$\begin{bmatrix} \mathbf{f} \\ \mathbf{f}_* \end{bmatrix} \sim \mathscr{N}\left(\begin{bmatrix} \mathbf{0} \\ \mathbf{0} \end{bmatrix}, \begin{bmatrix} k(\mathbf{x},\mathbf{x}) & k(\mathbf{x},\mathbf{x}_*) \\ k(\mathbf{x}_*,\mathbf{x}) & k(\mathbf{x}_*,\mathbf{x}_*) \end{bmatrix}\right). \tag{5}$$

By conditioning the GP on the observed data, the posterior probability distribution can be defined as

$$p(\mathbf{f}_*|\mathbf{x}_*,\mathbf{x},\mathbf{f}) = \mathscr{N}(k(\mathbf{x}_*,\mathbf{x})^T k(\mathbf{x},\mathbf{x})^{-1}\mathbf{f}, k(\mathbf{x}_*,\mathbf{x}_*) - k(\mathbf{x}_*,\mathbf{x})^T k(\mathbf{x},\mathbf{x})^{-1} k(\mathbf{x},\mathbf{x}_*)). \tag{6}$$

Typically, the training data is not noiseless. In this case, the observations are expressed by $y = f(x) + \varepsilon$, where $\varepsilon \sim \mathcal{N}(\mathbf{0}, \sigma_n^2 \mathbf{I})$. The joint distribution of $\mathbf{y}$ and $\mathbf{f}_*$ is then

$$\begin{bmatrix} \mathbf{y} \\ \mathbf{f}_* \end{bmatrix} \sim \mathcal{N}\left(\begin{bmatrix} \mathbf{0} \\ \mathbf{0} \end{bmatrix}, \begin{bmatrix} k(\mathbf{x},\mathbf{x}) + \sigma_n^2 \mathbf{I} & k(\mathbf{x},\mathbf{x}_*) \\ k(\mathbf{x}_*,\mathbf{x}) & k(\mathbf{x}_*,\mathbf{x}_*) \end{bmatrix} \right), \tag{7}$$

and the posterior becomes:

$$p(f_*|\mathbf{x}_*,\mathbf{x},\mathbf{y}) = \mathcal{N}(k(\mathbf{x}_*,\mathbf{x})^T (k(\mathbf{x},\mathbf{x}) + \sigma_n^2 \mathbf{I})^{-1} \mathbf{y}, k(\mathbf{x}_*,\mathbf{x}_*) - k(\mathbf{x}_*,\mathbf{x})^T (k(\mathbf{x},\mathbf{x}) + \sigma_n^2 \mathbf{I})^{-1} k(\mathbf{x},\mathbf{x}_*)). \tag{8}$$

To find the optimal hyperparameters that define the kernel, the negative log marginal likelihood function:

$$\log p(\mathbf{y}|\mathbf{x}) = -\frac{1}{2}\mathbf{y}^T (\mathbf{K} + \sigma_n^2 \mathbf{I}))\mathbf{y} - \frac{1}{2}\log|\mathbf{K} + \sigma_n^2 \mathbf{I}| - \frac{n}{2}\log 2\pi \tag{9}$$

is minimized. The negative log marginal likelihood indicates how likely the training data is for the given hyperparameters. This optimization process determines the training process of the GP [2].

2.2 Multi-fidelity using Gaussian Processes

The multi-fidelity scheme in this contribution is closely related to the model in [3]. In this multi-fidelity model, two different fidelity levels are in general related with

$$f_h(x) = \rho f_l(x) + \delta(x), \tag{10}$$

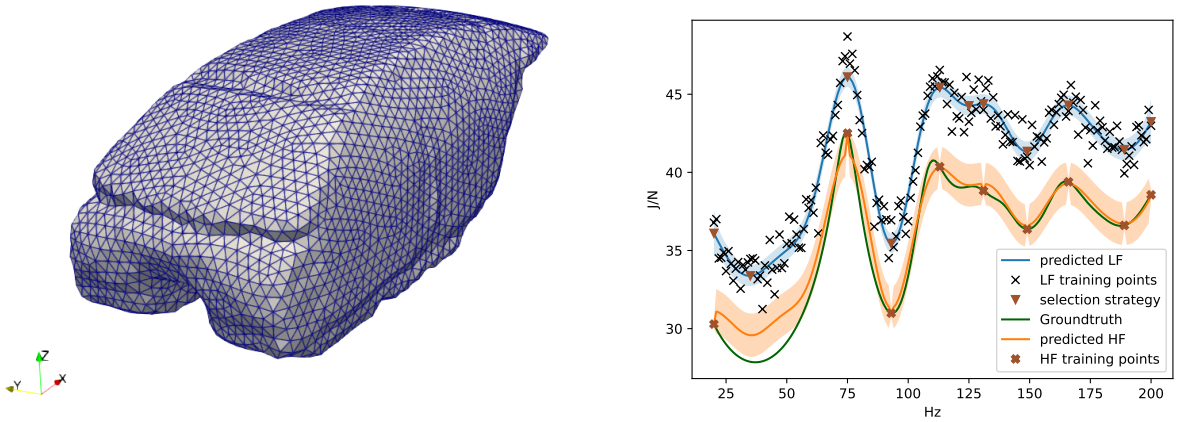
such that the searched for high fidelity function consists in part of the low fidelity solution. How large that part is, is denoted by ρ. If ρ would be zero, the correlation between low- and high-fidelity data would be zero. With this assumption the prior Gaussian Process for the combined low and high fidelity function can be expressed as:

$$\begin{bmatrix} f_l \\ f_h \end{bmatrix} \sim \mathcal{N}\left(\begin{bmatrix} \mathbf{0} \\ \mathbf{0} \end{bmatrix}, \begin{bmatrix} k_l(\mathbf{x}_l) & \rho k_l(\mathbf{x}_l,\mathbf{x}_h) \\ \rho k_l(\mathbf{x}_h,\mathbf{x}_l) & \rho^2 k_l(\mathbf{x}_h) + k_\delta(\mathbf{x}_h) \end{bmatrix} \right) \tag{11}$$

For the sake of brevity, the detailed presentation of the formulation and its adaptation to noisy data is omitted here.

3 NUMERICAL EXAMPLE

The problem at hand is closely related to the numerical example in [4, 5], where the acoustic behavior of a vehicle cabin was investigated. Therefore, the three-dimensional Helmholtz equation for interior problems is solved with the boundary element method. The cabin mesh is depicted in Fig. 1a. This mesh has 24036 DOFs and is considered as the high-fidelity model. The same model with a coarse resolution of 4420 DOFs is considered as the low-fidelity model. The multi-fidelity GP for the energy density at the driver's position is shown in Fig. 1b. In this study, we choose 8 high-fidelity points and 181 low-fidelity points. It becomes apparent that the low-fidelity model exposes higher energy density levels than the high-fidelity model. Interestingly, one can observe a good agreement between the multi-fidelity GP approximation and the ground truth result, which is the evaluation of the high-fidelity model at each frequency. This initial result already shows that multi-fidelity GPs can be used as an approximation for the high-fidelity model. In comparison with the reference solution, the proposed method requires only 8 forward simulations, whereas 181 simulations were required for the reference solution. In this way, the proposed method provides an efficient technique to approximate the behavior of an acoustic system. In addition to this, uncertainties within the system are inherently quantified.



(a) Cabin mesh

(b) 181 LF and 9 HF data points

Figure 1. The cabin mesh with 24036 DOFs (a) and the multi-fidelity model for 181 low-fidelity (black crosses) and 9 high-fidelity data points (red crosses). The approximation of the multi-fidelity model (orange) is compared to the reference solution (blue). The uncertainty area refers to the 95% confidence interval (light orange).

4 CONCLUSIONS

In this contribution, a method was introduced for the approximation of tedious data generation processes such as industrial numerical simulations. Therefore, we implemented a multi-fidelity model combining the prediction capabilities of a high-fidelity and a low-fidelity model. This model is based on Gaussian Processes, which provide an intuitive and at the same time data-driven technique. Due to their probabilistic nature, the quantification of uncertainties is inherent to Gaussian Processes. The proposed method was investigated for a boundary element method setup, where a cabin mesh with two different degrees of refinement was examined. The initial findings already show that the acoustic behavior of the cabin can be efficiently approximated by using multi-fidelity GPs. Future work will focus on further industrial applications and on the influence of noisy observations.

ACKNOWLEDGEMENTS

This research was funded by the German Research Foundation (DFG) under award 418936727.

REFERENCES

[1] Kennedy, MC.; O'Hagan, A. Predicting the output from a complex computer code when fast approximations are available. Biometrika 87.1, 2000. p. 1-13.

[2] Williams, CKI.; Rasmussen CE. Gaussian Processes for machine learning, MIT press, Cambridge (MA), vol.2, 2006.

[3] Guo, M.; Manzoni, A.; Amendt, M.; Conti, P.; Hesthaven, JS. Multi-fidelity regression using artificial neural networks: efficient approximation of parameter-dependent output quantities. Comput Methods Appl Mech Eng. 389:114378, 2022.

[4] Gurbuz, C.; Eser, M.; Schmid, JD.; Marburg, S.; Luegmair, M. Gaussian Processes for Transfer Path Analysis Applied on Vehicle Body Vibration Problems. SAE Technical Paper. 2022

[5] Gurbuz, C.; Schmid, JD.; Luegmair, M.; Marburg, S. Energy density-based non-negative surface contributions in interior acoustics. J Sound Vib. 527:116824. 2022.

ICA 2022
24th INTERNATIONAL CONGRESS ON ACOUSTICS
October 24(Mon) - 28(Fri), 2022 Gyeongju, Korea

PROCEEDINGS of the
24th International Congress on Acoustics

October 24 to 28, 2022 in Gyeongju, Korea

ABS-0926

Deterministic and statistical reconstruction of rough surfaces from acoustic scattering

Jacques CUENCA[(1)], Timo LÄHIVAARA[(2)], Giulio DOLCETTI[(3,4)], Mansour ALKMIM[(1,6)], Laurent DE RYCK[(1)], Michael-David JOHNSON[(5)], Anton KRYNKIN[(5)]

[(1)]Siemens Industry Software NV, Leuven, Belgium, jacques.cuenca@siemens.com

[(2)]Department of Applied Physics, University of Eastern Finland, Kuopio, Finland

[(3)]Department of Civil, Environmental and Mechanical Engineering, University of Trento, Trento, Italy

[(4)]Department of Civil and Structural Engineering, the University of Sheffield, Sheffield, United Kingdom

[(5)]Department of Mechanical Engineering, the University of Sheffield, Sheffield, United Kingdom

[(6)]Department of Mechanical Engineering, KU Leuven, Leuven, Belgium

ABSTRACT

This work proposes a model inversion framework for the reconstruction of the elevation profile of a rough surface from acoustic scattering. The latter is measured at a microphone array while the surface is insonified with a broadband source. The forward model makes use of the Kirchhoff approximation, which provides reasonable accuracy at high frequencies or in the far field, while enabling an efficient exploration of the design space. A particular challenge in the inversion is the detailed reconstruction of an arbitrary surface of relatively large size from a limited set of microphones, leading to an under-determined problem. An initial estimate of the surface roughness profile is obtained in a deterministic manner by solving the inverse problem using a gradient-based optimiser. The inverse problem is then formulated in a statistical sense and solved using Bayesian inference. The sequential use of deterministic and statistical inversion yields a feasible solution and an uncertainty envelope. The procedure is demonstrated for a surface with a one-dimensional roughness profile.

Keywords: Inverse scattering, surface reconstruction, optimisation, Bayesian inference

1 MOTIVATION

Non-contact reconstruction of the elevation profile of rough surfaces is of crucial interest in applications such as sea floor mapping, river and sea surface monitoring [1]. Recent work demonstrates the use of a sound source and a linear array of microphones for the reconstruction of static rigid rough surfaces using inverse scattering. The techniques used therein include the linearisation of the propagation problem allowing for its inversion in matrix form [1] as well as the use of a random forest algorithm [2] or numerical optimisation [3]. While the current techniques allow for robust and efficient reconstructions, the efforts have thus far focused on obtaining deterministic point estimates.

The present work proposes a methodology for reconstructing the elevation profile of a rough surface, together with an uncertainty estimate. In order to do so, the inverse scattering problem is formulated in a statistical sense using a Bayesian framework, allowing to sample the desired posterior distribution using a Markov chain Monte Carlo method. In practice, the number of unknown elevation points on the surface is larger than the available number of microphones, thus yielding an under-determined problem. An assumption of surface smoothness is introduced, which mitigates the ill-posedness of the problem without restricting the scope of the method. In addition, a deterministic estimate is used as an initial guess for the statistical inversion procedure. This brief report summarises the methodology and provides an experimental application example.

2 MODEL

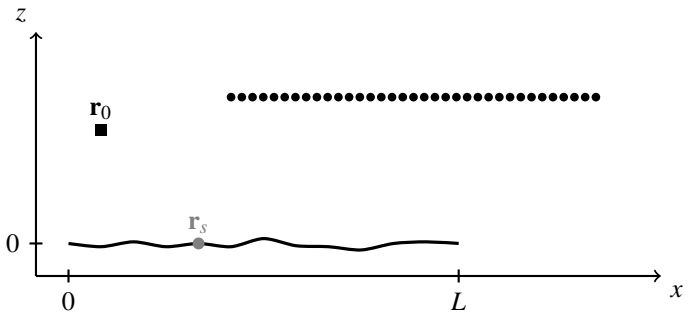


Figure 1. Scattering problem. ⁓ Rough surface; ■ source; • microphones; ● a point on the surface.

The purpose of the work is to obtain an estimate of the elevation profile ζ of a rough surface from scattered sound. Fig. 1 illustrates the experimental setup used, consisting of a sound source and an array of microphones above the surface of interest. The present study is restricted to surfaces whose roughness varies along one dimension, namely $\zeta = \zeta(x)$. The acoustic field is modelled using an integral formulation and approximated by means of a stationary phase expansion [4]. Furthermore, by using a directive loudspeaker oriented towards the centre of the surface, the direct field can be ignored at the microphones. The acoustic pressure at a microphone position $\mathbf{r}$ is then obtained as

$$p(\mathbf{r}) \simeq e^{i\pi/4}\sqrt{\frac{2\pi}{k}}\int_{x_s=0}^{x_s=L} A(\mathbf{r}_s)\sqrt{\frac{|\mathbf{r}_s-\mathbf{r}_0||\mathbf{r}-\mathbf{r}_s|}{|\mathbf{r}_s-\mathbf{r}_0|+|\mathbf{r}-\mathbf{r}_s|}}G(\mathbf{r},\mathbf{r}_s)G(\mathbf{r}_s,\mathbf{r}_0) \left(\left(ik-\frac{1}{|\mathbf{r}-\mathbf{r}_s|}\right)\cos(|\mathbf{r}-\mathbf{r}_s|,\mathbf{n}_s)-\left(ik-\frac{1}{|\mathbf{r}_s-\mathbf{r}_0|}\right)\cos(|\mathbf{r}_s-\mathbf{r}_0|,\mathbf{n}_s)\right)dx_s, \quad (1)$$

where k is the wavenumber in air, A is the directivity of the source, G is the Green function in free field, $\mathbf{r}_0$ is the source position, $\mathbf{r}_s = (x_s, \zeta)$ is a point along the surface, and $\mathbf{n}_s$ is the outgoing normal to the surface at $\mathbf{r}_s$. In practice, the surface is discretised along x, yielding a finite number of unknown elevation points, gathered in the vector

$$\mathbf{z} = \begin{bmatrix}\zeta_1 & \cdots & \zeta_s & \cdots & \zeta_N\end{bmatrix}^{\mathrm{T}}. \quad (2)$$

The surface is assumed to be smooth, and the smoothness is modelled as a parameter $\beta \in [0,1]$, implemented as a low-pass Butterworth filter [5] and considered as an additional unknown in the problem. The introduction of a smoothness parameter renders the surface elevation points interdependent and thus has a regularising effect. It is worth noting that the limiting case $\beta = 0$ corresponds to uncorrelated elevation points and therefore the introduction of the extra unknown does not restrict the generality of the problem.

3 INVERSE METHOD

The acoustic pressure is acquired at the microphones across a discrete range of frequencies. By gathering all the measured data in a vector $\mathbf{p}$, an observation model can be proposed, as

$$\mathbf{p}^{(\mathrm{meas})} = \mathbf{p}(\mathbf{z}) + \mathbf{e}, \quad (3)$$

where $\mathbf{e}$ is the modelling and measurement error that separates the model from the ground truth. This error is here assumed Gaussian, with a diagonal covariance matrix $\Gamma_\varepsilon = \sigma_\varepsilon^2\mathbf{I}$, with σ_ε the error standard deviation.

The first strategy for solving the inverse problem of estimating $\mathbf{z}$ from the measured pressure data $\mathbf{p}^{(\mathrm{meas})}$ is to minimise the error $\mathbf{e}$ in a least-squares sense. In the present work this is done by means of a numerical optimiser using the globally convergent method of moving asymptotes [6].

The second strategy consists in formulating the inverse problem in a statistical sense using a Bayesian framework. Here, the standard deviation of the error σ_ε can be estimated as well by considering it as a random variable itself. Using Bayes' formula [7], the posterior probability of the unknowns $\mathbf{z}$, β and σ_ε can be expressed as

$$P(\mathbf{z}, \sigma_\varepsilon, \beta | \mathbf{p}^{(\text{meas})}) \propto P(\mathbf{p}^{(\text{meas})} | \mathbf{z}, \sigma_\varepsilon, \beta) P(\mathbf{z}, \sigma_\varepsilon, \beta), \tag{4}$$

where $P(\mathbf{p}^{(\text{meas})} | \mathbf{z}, \sigma_\varepsilon, \beta)$ is the likelihood of the measurement given the unknowns, and $P(\mathbf{z}, \sigma_\varepsilon, \beta)$ is the prior knowledge on the unknowns. Owing to the properties of the error, the likelihood is Gaussian. Furthermore, uniform priors are assumed for all unknowns in the present study. In order to reduce the computational burden of the statistical sampling procedure, the solution obtained by deterministic inversion is used as a starting point. The statistical inversion procedure is carried out using an adaptive Metropolis scheme [8], from which the maximum a posteriori (MAP) estimate as well as 95% credible intervals are extracted.

4 RESULTS

The proposed method is here applied to a medium density fibreboard surface of length $L = 60\,\text{cm}$, milled with a controlled roughness profile. The setup consisted of a directive Visaton G 25 FFL dome tweeter as the source and 34 linearly spaced 1/4" G.R.A.S. microphones. The experimental data for the present inversion consists of 21 frequency lines between 16 kHz and 21 kHz. The surface is discretised into $N = 150$ points, yielding a total of 151 and 152 unknowns for the deterministic and statistical procedures, respectively. The sampling procedure consists of 100000 usable samples, with a further 20000 discarded as burn-in. Figure 2 shows the elevation profile of the surface as well as the deterministic and statistical estimates. Figure 3 depicts the probability distributions of the additional unknowns, namely the standard deviation of the error, σ_ε, and the surface smoothness, β.

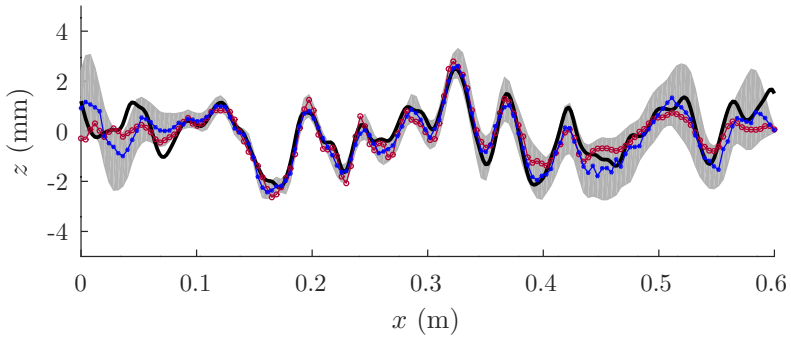


Figure 2. Estimated surface elevation profile. — True profile; deterministic estimate; MAP estimate; 95% credible intervals.

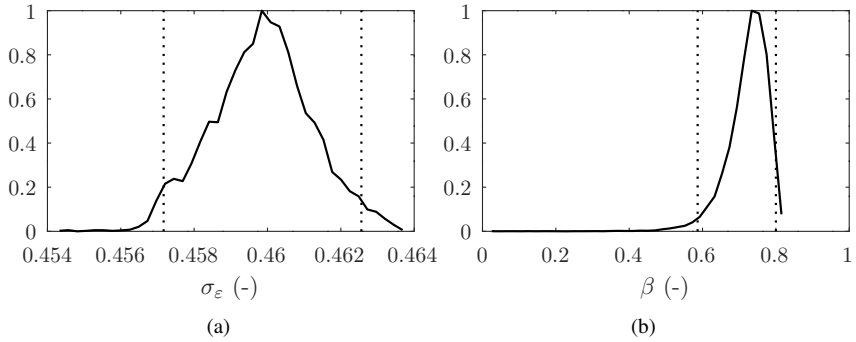


Figure 3. Probability distribution of the additional unknowns (a) σ_ε and (b) β.

5 DISCUSSION

It can be observed that the elevation profile of the surface of interest is accurately retrieved. Overall, the 95% credible interval is 1.69 mm and the 75% credible interval is 1.01 mm. It is worth noting that the precision of the reconstruction is higher in the central region of the specimen. This is due to the finite aperture of the microphone array as well as to the directivity of the source. A further notable outcome is the existence of a single maximum in the probability distributions of the additional unknowns. The results here presented show that the proposed methodology stands as a viable technique for the estimation of surface roughness. In particular, the statistical inversion procedure can be used in conjunction with robust deterministic tools as a means to gain an insight on the estimation uncertainty.

REFERENCES

[1] G. Dolcetti, M. Alkmim, J. Cuenca, L. De Ryck, and A. Krynkin, "Robust reconstruction of scattering surfaces using a linear microphone array," *Journal of Sound and Vibration*, vol. 494, p. 115902, 2021.

[2] M.-D. Johnson, A. Krynkin, G. Dolcetti, M. Alkmim, J. Cuenca, and L. De Ryck, "Surface shape reconstruction from phaseless scattered acoustic data using a random forest algorithm," *Journal of the Acoustical Society of America*, vol. 152, no. 2, pp. 1045–1057, 2022.

[3] Y. Li, J. Cuenca, L. De Ryck, M. Alkmim, O. Atak, W. Desmet, G. Dolcetti, and A. Krynkin, "Robust reconstruction of scattering surfaces using a linear microphone array," *Submitted to Journal of Sound and Vibration*, 2022.

[4] C. M. Bender and S. A. Orszag, *Advanced mathematical methods for scientists and engineers I: Asymptotic methods and perturbation theory*. Springer Science & Business Media, 2013.

[5] A. V. Oppenheim and R. W. Schafer, *Discrete-time signal processing*. Pearson, 3rd ed., 2010.

[6] K. Svanberg, "A class of globally convergent optimization methods based on conservative convex separable approximations," *SIAM Journal on Optimization*, vol. 12, no. 2, p. 555, 2002.

[7] J. Kaipio and E. Somersalo, *Statistical and Computational Inverse Problems*. Springer-Verlag, 2005.

[8] H. Haario, E. Saksman, and J. Tamminen, "An adaptive Metropolis algorithm," *Bernoulli*, vol. 7, pp. 223–242, 2001.

ICA 2022
24th INTERNATIONAL CONGRESS ON ACOUSTICS
October 24(Mon) - 28(Fri), 2022 Gyeongju, Korea

PROCEEDINGS of the
24th International Congress on Acoustics

October 24 to 28, 2022 in Gyeongju, Korea

ABS-0932

Physics-informed deep learning in computational elastodynamics

Johannes D. SCHMID*, Philipp BAUERSCHMIDT, Caglar GURBUZ and Steffen MARBURG [(1)]

[(1)] Technical University of Munich, Chair of Vibroacoustics of Vehicles and Machines, Germany

ABSTRACT

Conventional numerical methods in computational elastodynamics are primarily based on discretization like the finite element method. However, it is challenging to incorporate observed data into the model, resulting in a recurring loop of updating the input parameters until the model fits measured data. Purely data-driven methods, on the other hand, may fit observations well, but predictions outside the labeled training data are often physically inconsistent. Physics-informed neural networks (PINNs) combine the advantages of both approaches and in this contribution, PINNs are used to solve the equations of elastodynamics in a data-driven manner. It is the idea to incorporate the residual of the governing partial differential equation into the loss function of a neural network. The training process of the neural network minimizes the residual of the differential equation and the discrepancy of the boundary conditions by only considering training data on the boundary. The applicability of PINNs is shown on an elastodynamic benchmark model and its performance is compared to an ordinary neural network and a finite element reference solution. The additional physical prior knowledge allows for good generalization of the displacement field inside the domain and provides a robust machine learning method even in the small training data regime.

Keywords: Machine learning, data-driven methods, elastodynamics, structural dynamics

1 INTRODUCTION

The numerical methods in computational elastodynamics and vibroacoustics are dominated from purely physics-based models, which mainly rely on discretization like the finite element method (FEM) [1]. Those methods are well established, but it is the drawback that the computational costs considerably increase with finer discretization, which makes tasks with a high number of model evaluations, e.g. uncertainty quantification, optimization and inverse problems very hard to solve [2, 3]. Furthermore, with deterministic physics-based methods it is very challenging to incorporate measured and potentially noisy data into the models. This makes it very hard to identify model parameters based on observed data and it results in an ever recurring loop of updating the input parameters until the simulation model fits experimental data. In contrast, a constantly increasing amount of data is being collected from simulation and experiment and the computational power of the hardware continuously increases, which strengthens the need for data-driven methods.

In the past decades, machine learning (ML) methods and especially the methods based on artificial neural networks, called deep learning (DL), have shown great potential in the fields of computer vision, speech and image recognition and natural language processing. Though, purely data-driven methods may fit observations from the training data well, they often suffer from poor generalization, meaning that they fail in making predictions outside the labeled training data. Specifically in the field of computational physics, the main drawback of purely data-driven methods is that the predictions may be physically inconsistent and the model parameters are not physically interpretable. Raissi et al. [4] introduced physics-informed neural networks (PINNs), which combine the advantages from both, physics-based methods and data-driven methods. The main idea is to incorporate physics information in the form of a differential equation into the loss function of an artificial neural network. This is done by incorporating the residual of the governing partial differential equation (PDE) into

*johannes.d.schmid@tum.de

the loss function of a neural network. By training the neural network, the loss function is minimized, which means that the PDE residual will be minimized simultaneously. This way, the PINN learns a solution, which implicitly satisfied the PDE and the boundary conditions. Karniadakis et al. [5] give a good review over the method and practical applications in the fields of fluid flow and thermodynamics. PINNs have been applied in different field of computational physics including fluid dynamics [6, 7], acoustics [8], heat transfer [9] and photonics [10]. In elastodynamics, PINNs have been used to solve selected forward problems, including Kirchhoff plate bending [11], elastic plate and bar problems [12, 13], hyperelasticity and plasticity [14] and continuum micromechanics [15]. Furthermore, PINNs have been applied to the solution of inverse problems for parameter identification [16] and fault detection [17].
In this contribution, PINNs are used to solve the three-dimensional elastodynamics equation in the frequency domain applied on the so called Cook's Membrane, a benchmark model in solid mechanics [18]. The displacement field within the structure is solved using PINNs by only considering the PDE and training data on the boundary of the domain. By incorporating the additional physics prior information, PINNs are able to generalize better compared to purely supervised neural networks, even it only a limited number of training data on the boundary is available.

2 ELASTODYNAMICS MODEL

The model chosen in this investigations is a benchmark model in solid mechanics, called Cook's Membrane [19]. The special geometry and load configuration results in a combined bending and shear load [18]. The geometry of the Cook's membrane is shown in Fig. 1. It consists of a three-dimensional trapezoid cantilever, where the left side of the structure (in blue) is clamped and the right side (in red) is loaded with a harmonic shear load of $u_z = 0.001\,\mathrm{m}$ at a frequency of $f = 2180\,\mathrm{Hz}$ in vertical direction. All other boundaries are considered to be traction free.

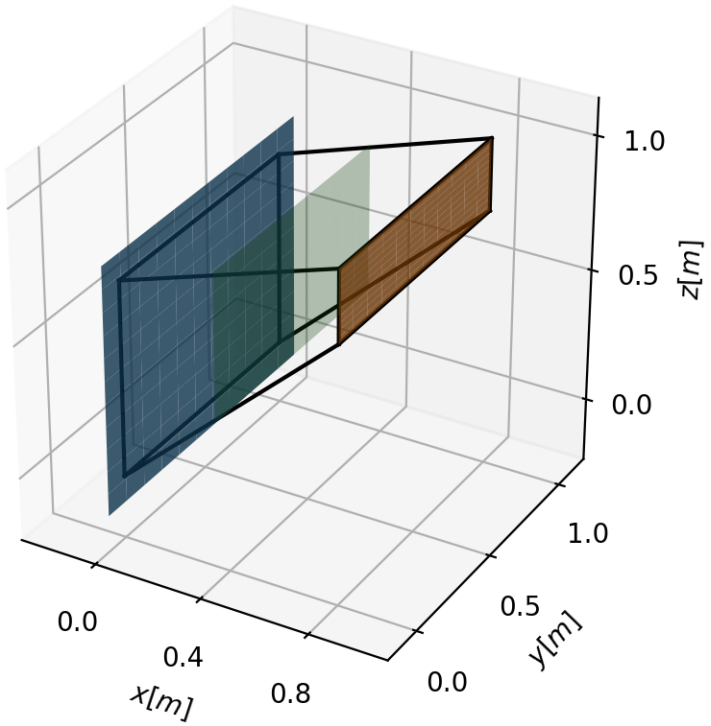


Figure 1. Cook's Membrane benchmark model in elastodynamics with clamped boundary condition on the left (in blue) and harmonic vertical shear load on the right (in red). The green surface (CS1) represents a cross-section at $x = 0.34\,\mathrm{m}$.

The equations to be solved are the elastodynamics equations in three dimensions, known as the Navier-Lamé equations, in the frequency domain. The boundary conditions (BCs) are Dirichlet conditions on the boundary Γ. The boundary value problem can consequently be formulated, as

$$\begin{aligned} \omega^2 \rho\, \mathbf{u} + \mu\, \Delta \mathbf{u} + (\lambda + \mu) \nabla(\nabla \cdot \mathbf{u}) = \mathbf{0} \quad & \text{in } \Omega \\ \mathbf{u} = \bar{\mathbf{u}} \quad & \text{on } \Gamma, \end{aligned} \tag{1}$$

with the displacement vector field $\mathbf{u}$, the angular frequency $\omega = 2\pi f$, the Lamé parameters μ and λ and the material density ρ. The structure is considered to be made out of steel with the material properties $\rho = 7850\,\mathrm{kg\,m^{-3}}$, $\lambda = 10.2 \times 10^{10}\,\mathrm{N\,m^{-2}}$ and $\mu = 8 \times 10^{10}\,\mathrm{N\,m^{-2}}$. It should be noted that the traction free Neumann BCs are transformed into a Dirichlet problem, by computing the displacement field via FEM and using the solution as training data for the PINN. The FEM reference solution is computed using COMSOL Multiphysics.

3 PHYSICS-INFORMED NEURAL NETWORKS

PINNs are typically built upon a feed-forward neural network, also known as multilayer perceptron and the only difference is the loss function to be minimized during the training process. The loss function of a PINN contains at least one term, which incorporates physics information about the system. The standard way of including the physical knowledge is to add the residual of the PDE and the mean square error (MSE) of the boundary conditions to the loss function. The structure of a PINN is schematically illustrated in Fig. 2, starting with the spatial input parameters of a multilayer perceptron on the left-hand side. On the right, the elastodynamics equation indicates the physics information, formulated as a residual, which is evaluated by computing the relevant spatial derivatives. The advantage of having a neural network model is that the gradients can be computed easily using backpropagation and automatic differentiation. The residuals of both, the PDE and the boundary conditions are combined into the loss function, which is minimized during training. The PDE residual $\mathscr{R}$ is evaluated at a certain number of collocation points $\mathbf{x}_{cp}$, which are randomly sampled within the computational domain Ω.

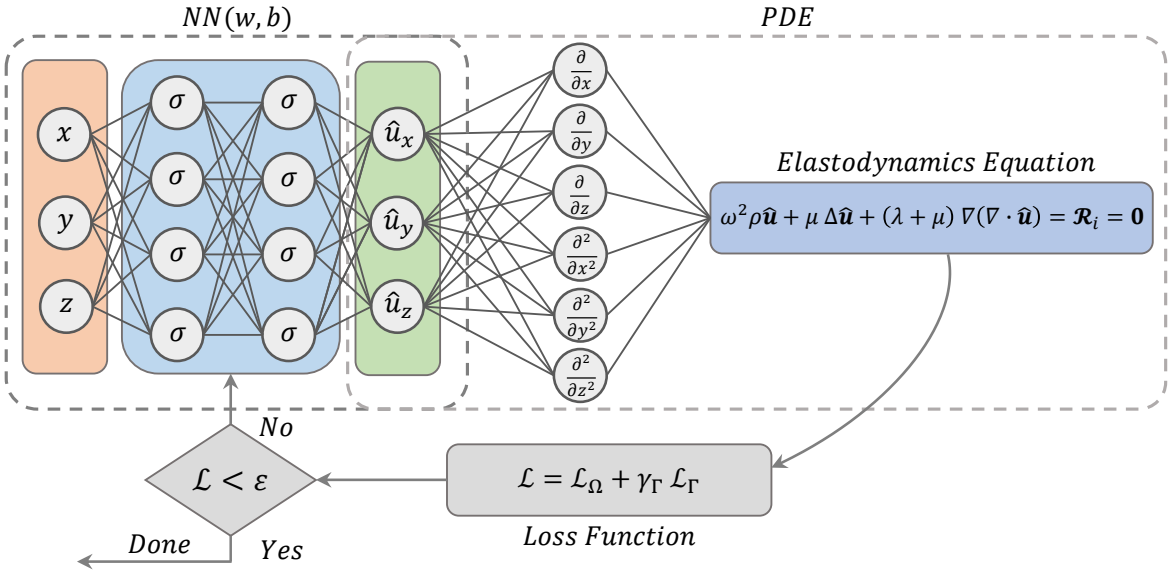


Figure 2. Schematic illustration of a PINN with a multilayer perceptron (left) and the physics information in the form of the elastodynamics equations (right). The residuals of both, the PDE and the boundary conditions are incorporated into the loss function, which is minimized during training.

The PDE loss can be written as the MSE residual over all collocation points, as

$$\mathscr{L}_\Omega = \frac{1}{N_{cp}} \sum_{i=1}^{N_{cp}} \| \rho \omega^2 \hat{\mathbf{u}}(\mathbf{x}_{cp,i}) + \mu \Delta \hat{\mathbf{u}}(\mathbf{x}_{cp,i})) + (\lambda + \mu) \nabla (\nabla \cdot \hat{\mathbf{u}}(\mathbf{x}_{cp,i})) \|^2, \tag{2}$$

where $\hat{\mathbf{u}}$ stands for the PINN approximation of the displacement vector $\mathbf{u}$. As the PDE has an infinite number of solutions, but we are only interested in the unique solution that satisfies the boundary value problem, we have to also include the BCs into the loss function. The Dirichlet BC loss is written as the MSE between the networks predictions $\hat{\mathbf{u}}$ and the prescribed Dirichlet displacements $\bar{\mathbf{u}}$ at the boundary and results in

$$\mathscr{L}_\Gamma = \frac{1}{N_{bc}} \sum_{i=1}^{N_{bc}} \| \hat{\mathbf{u}}(\mathbf{x}_{bc,i}) - \bar{\mathbf{u}}_i \|^2. \tag{3}$$

Both loss terms are combined to the total PINN loss function, as

$$\mathscr{L} = \mathscr{L}_\Omega + \lambda_\Gamma \mathscr{L}_\Gamma, \tag{4}$$

where λ_Γ represents a scaling factor for adjusting the proportion of the BC loss term compared to the PDE loss. Our investigations have shown that it is very important for the convergence towards the correct solution that both loss terms are well balanced and within the same order of magnitude. During training, the weights and biases $\boldsymbol{\theta}$ of the neural network are adjusted in the way that the loss function $\mathscr{L}$ is minimized. This is done using gradient based optimization algorithms and the minimization problem of training the network can finally be expressed as

$$\hat{\boldsymbol{\theta}} = \arg\min_{\boldsymbol{\theta}} \mathscr{L}(\mathscr{D}, \boldsymbol{\theta}), \tag{5}$$

where $\hat{\boldsymbol{\theta}}$ is the converged set of neural network parameters and $\mathscr{D}$ is the set of training data.

4 NETWORK ARCHITECTURE

PINNs are used to predict the displacement field in Ω by only utilizing deformation data on 1000 uniformly distributed training data points $\mathbf{x}_{bc}$ on the boundary. The PDE residual is evaluated at 10,000 randomly sampled collocation points $\mathbf{x}_{cp}$ within the computational domain Ω. The neural network consists of an input layer with three neurons, representing the spatial coordinates x, y and z. The output layer has three neurons, associated to the displacement field in the three spatial dimensions $\hat{u}_x$, $\hat{u}_y$ and $\hat{u}_z$. The neural network is schematically illustrated on the left-hand side of Fig. 2. The neural network is built using PyTorch [20] and the optimal network architecture was found by performing a hyperparameter optimization using Ray Tune [21]. A grid search method was used and the search space as well as the optimal choice of hyperparameters are summarized in Tab. 1.

Table 1. Search space for the grid search hyperparameter optimization and optimized hyperparameters.

Hyperparameter	Grid search space	Optimized parameter
Number of layers	{8, 12, 16}	12
Neurons per layer	{10, 15, 20}	20
Learning rate	{0.1, 0.01, 0.004, 0.001}	0.004
Learning rate decay	{0.3, 0.5}	0.5
Epochs for decay	{200, 800}	800
Batch size	{(50, 500), (200, 2000)}	(50, 500)

The activation functions are chosen to be hyperbolic tangents and all models are trained using the Adam optimization algorithm for a total number of 9000 epochs. During training, the learning rate is reduced by the

factor *learning rate decay* every time, the number of *epochs for decay* in Tab. 1 is reached. The batch size listed in Tab. 1 contains two values with the first one representing the batch size for the boundary conditions and the second one the batch size for the collocation points.

5 RESULTS

The displacement field of the Cook's membrane is computed by solving the Navier-Lamé equations using PINNs. Fig. 3 shows the displacement field on the cross section CS1 at $x = 0.34\,\mathrm{m}$, which is marked in green in Fig. 1. The PINN prediction is compared to the FEM reference solution and a deviation plot indicates the absolute prediction error.

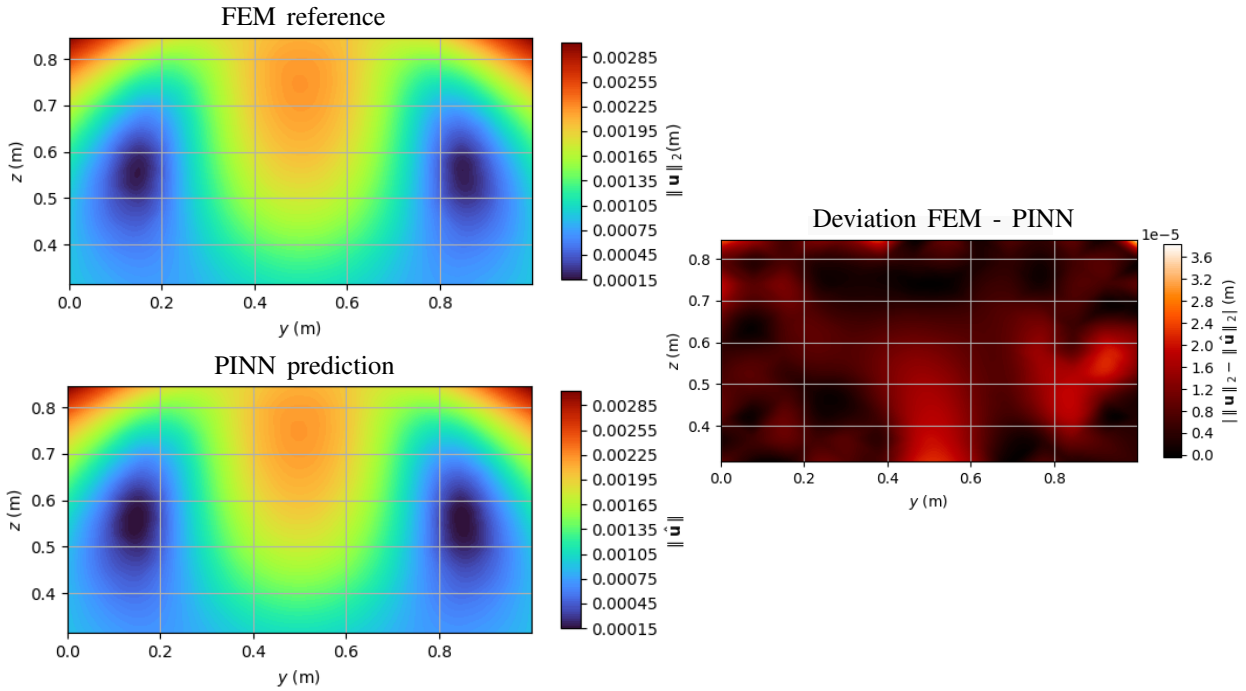


Figure 3. Magnitude of the displacement field vector $\mathbf{u}$ at the cross section CS1 of the Cook's membrane. The FEM reference solution (top) is compared to the PINN prediction (bottom) and the deviation plot (right) shows the spatial absolute error.

The PINN method is able to predict the displacement magnitude with an mean absolute error of $7.78 \times 10^{-6}\,\mathrm{m}$ within the computational domain. This corresponds to an average percentage error of 1.4 %, which is considered to be a very accurate approximation. For comparison, also an ordinary neural network with the exact same network architecture and hyperparameters was trained on the boundary displacement data. This corresponds to a purely supervised training of the boundary displacements $\mathbf{x}_{bc}$, without any physics information. The loss function in this case only consists of a single MSE term, as the physical loss $\mathscr{L}_\Omega$ is neglected. It turns out that the mean absolute error of the supervised neural network compared to the FEM solution is 27 %, which is about an order of magnitude worse than the PINN and considered to be insufficient in this case. This proves that a purely supervised neural network fails in capturing the elastodynamic field and that the physics information within PINNs is essential for a correct and physically consistent prediction of the displacement field in this elastodynamics problem. The computational times for training the PINN in the offline step takes about 3 h, compared to one FEM solution of 3 s. However, once the PINN is trained once, one forward pass will only take about 0.001 s.

6 CONCLUSIONS AND OUTLOOK

The method of physics-informed neural networks (PINNs) have been used to solve the Navier-Lamé equations of elastodynamics in the frequency domain on the three-dimensional benchmark case of the Cook's membrane. A Dirichlet boundary value problem was considered with displacement training data on the boundary of the structure. The studies show that PINNs are able to solve the PDE with a very high accuracy of less than one percent in comparison to a FEM reference solution. Even if only training data on the boundary were used, the PINN is able to generalize the displacement solution inside the domain very well. The comparison to a neural network with purely supervised training shows that the physics information highly improves the prediction not only in terms of accuracy but also in terms of physical interpretability.

As an outlook, PINNs show a high potential for data-driven but yet physics-informed surrogate modeling. As the forward evaluation of a pre-trained PINN is very efficient, it could be highly advantageous for applications with many model evaluations, e.g. optimization, uncertainty quantification or the sampling-based solution of inverse problems. In conclusion, the authors would like to emphasize that PINNs may not replace traditional solvers, but instead they offer a promising approach to seamlessly integrate simulated and experimental data within one consistent framework.

ACKNOWLEDGEMENTS

This contribution is part of the joint project *newAIDE* under the consortium leadership of BMW AG with the partners Altair Engineering GmbH, divis intelligent solutions GmbH, MSC Software GmbH and TWT GmbH. The project is supported by the Federal Ministry for Economic Affairs and Climate Action (BMWK) on the basis of a decision by the German Bundestag.

References

[1] MARBURG, S. *Computational Acoustics of Noise Propagation in Fluids - Finite and Boundary Element Methods*. Berlin, Heidelberg: Springer Berlin / Heidelberg, 2008.

[2] LUEGMAIR, M. and SCHMID, J. D. "Challenges in Vibroacoustic Vehicle Body Simulation Including Uncertainties". In: *SAE Technical Paper Series*. SAE Technical Paper Series. SAE International, 2020.

[3] SCHMID, J. D., LUEGMAIR, M., SEPAHVAND, K., and MARBURG, S. "Uncertainty Quantification in Vibroacoustic Analysis of a Vehicle Body Using Generalized Polynomial Chaos Expansion". In: *SAE Technical Paper Series*. SAE Technical Paper Series. SAE International, 2020.

[4] RAISSI, M., PERDIKARIS, P., and KARNIADAKIS, G. E. "Physics-informed neural networks: A deep learning framework for solving forward and inverse problems involving nonlinear partial differential equations". In: *Journal of Computational Physics* 378 (2019), pp. 686–707.

[5] KARNIADAKIS, G. E., KEVREKIDIS, I. G., LU, L., PERDIKARIS, P., WANG, S., and YANG, L. "Physics-informed machine learning". In: *Nature Reviews Physics* 3.6 (2021), pp. 422–440.

[6] RAO, C., SUN, H., and LIU, Y. "Physics-informed deep learning for incompressible laminar flows". In: *Theoretical and Applied Mechanics Letters* 10.3 (2020), pp. 207–212.

[7] JAGTAP, A. D., KHARAZMI, E., and KARNIADAKIS, G. E. "Conservative physics-informed neural networks on discrete domains for conservation laws: Applications to forward and inverse problems". In: *Computer Methods in Applied Mechanics and Engineering* 365 (2020), p. 113028.

[8] BORREL-JENSEN, N., ENGSIG-KARUP, A. P., and JEONG, C.-H. "Physics-informed neural networks for one-dimensional sound field predictions with parameterized sources and impedance boundaries". In: *JASA Express Letters* 1.12 (2021), p. 122402.

[9] SHENGZE CAI, ZHICHENG WANG, SIFAN WANG, PARIS PERDIKARIS, and GEORGE EM KARNIADAKIS. "Physics-informed neural networks for heat transfer problems". In: *Journal of Heat Transfer* 143.6 (2021).

[10] LIM, J. and PSALTIS, D. "MaxwellNet: Physics-driven deep neural network training based on Maxwell's equations". In: *APL Photonics* 7.1 (2022), p. 011301.

[11] GUO, H., ZHUANG, X., and RABCZUK, T. "A Deep Collocation Method for the Bending Analysis of Kirchhoff Plate". In: *Computers, Materials & Continua* 59.2 (2019), pp. 433–456.

[12] MOHAMMAD VAHAB, EHSAN HAGHIGHAT, MARYAM KHALEGHI, and NASSER KHALILI. "A Physics-Informed Neural Network Approach to Solution and Identification of Biharmonic Equations of Elasticity". In: *Journal of Engineering Mechanics* 148.2 (2022), p. 04021154.

[13] CHENGPING RAO, HAO SUN, and YANG LIU. "Physics-Informed Deep Learning for Computational Elastodynamics without Labeled Data". In: *Journal of Engineering Mechanics* 147.8 (2021), p. 04021043.

[14] ABUEIDDA, D. W., LU, Q., and KORIC, S. "Meshless physics–informed deep learning method for three–dimensional solid mechanics". In: *International Journal for Numerical Methods in Engineering* 122.23 (2021), pp. 7182–7201.

[15] HENKES, A., WESSELS, H., and MAHNKEN, R. "Physics informed neural networks for continuum micromechanics". In: *Computer Methods in Applied Mechanics and Engineering* 393 (2022), p. 114790.

[16] HAGHIGHAT, E., RAISSI, M., MOURE, A., GOMEZ, H., and JUANES, R. "A physics-informed deep learning framework for inversion and surrogate modeling in solid mechanics". In: *Computer Methods in Applied Mechanics and Engineering* 379 (2021), p. 113741.

[17] ZHANG, E., DAO, M., KARNIADAKIS, G. E., and SURESH, S. "Analyses of internal structures and defects in materials using physics-informed neural networks". In: *Science advances* 8.7 (2022), eabk0644.

[18] SCHRÖDER, J., WICK, T., REESE, S., WRIGGERS, P., MÜLLER, R., KOLLMANNSBERGER, S., KÄSTNER, M., SCHWARZ, A., IGELBÜSCHER, M., VIEBAHN, N., BAYAT, H. R., WULFINGHOFF, S., MANG, K., RANK, E., BOG, T., D'ANGELLA, D., ELHADDAD, M., HENNIG, P., DÜSTER, A., GARHUOM, W., HUBRICH, S., WALLOTH, M., WOLLNER, W., KUHN, C., and HEISTER, T. "A Selection of Benchmark Problems in Solid Mechanics and Applied Mathematics". In: *Archives of Computational Methods in Engineering* 28.2 (2021), pp. 713–751.

[19] ROBERT DAVIS COOK. "Improved Two-Dimensional Finite Element". In: *Journal of the Structural Division* 100 (1974), pp. 1851–1863.

[20] PASZKE, A., GROSS, S., MASSA, F., LERER, A., BRADBURY, J., CHANAN, G., KILLEEN, T., LIN, Z., GIMELSHEIN, N., ANTIGA, L., DESMAISON, A., KOPF, A., YANG, E., DEVITO, Z., RAISON, M., TEJANI, A., CHILAMKURTHY, S., STEINER, B., FANG, L., BAI, J., and CHINTALA, S. "PyTorch: An Imperative Style, High-Performance Deep Learning Library". In: *Advances in Neural Information Processing Systems 32*. Curran Associates, Inc, 2019, pp. 8024–8035.

[21] LIAW, R., LIANG, E., NISHIHARA, R., MORITZ, P., GONZALEZ, J. E., and STOICA, I. "Tune: A Research Platform for Distributed Model Selection and Training". In: *arXiv preprint arXiv:1807.05118* (2018).

ICA 2022
24th INTERNATIONAL CONGRESS ON ACOUSTICS
October 24(Mon) - 28(Fri), 2022 Gyeongju, Korea

PROCEEDINGS of the
24th International Congress on Acoustics

October 24 to 28, 2022 in Gyeongju, Korea

ABS-0948

Design of Acoustic Metamaterials Using Conditional Wasserstein Generative Adversarial Networks

Feruza A. Amirkulova[(1)], Peter Lai[(2)], Diego Soto[(3)]

[(1)]Mechanical Engineering Department, San José State University, San José, 95192, USA, feruza.amirkulova@sjsu.edu

[(2)]Mechanical Engineering Department, San José State University, San José, 95192, USA, peter.lai@sjsu.edu

[(3)]Mechanical Engineering Department, San José State University, San José, 95192, USA, diego.sotolopez@sjsu.edu

ABSTRACT

In this talk, we present a method for the reduction of the total scattering cross section (TSCS) for a planar configuration of cylinders through multi-scattering, generative modeling and deep learning. We first summarize and illustrate existing approaches in the inverse design of metamaterials then discuss current algorithmic limitations and open challenges to preview possible future developments in metamaterial design. We then show a novel method [1, 2] to design broadband acoustic metamaterial configurations using deep learning and generative modeling targeting low TSCS responses. We combine a conditional Wasserstein Generative Adversarial Network (cWGAN) with a standard convolutional neural networks (CNN) to generate metacluster configurations with a specified TSCS. The proposed cWGAN model is enhanced by adding to it a coordinate convolution layer [3]. Particularly placed scattering elements can achieve minimal TSCS producing a broadband cloaking effect at discrete sets of wavenumbers. The method is demonstrated giving examples for planar uniform configurations of rigid cylinders.

Keywords: Acoustic Metamaterials, Deep Learning, Generative Modeling, Wasserstein Generative Adversarial Networks, Convolutional Neural Networks

1 INTRODUCTION

Metamaterials [4–7] are engineered materials with unique properties not found in nature such as negative refraction, negative mass density, and negative Poisson's ratio, producing exotic effects such as cloaking, superfocusing, beam forming, wave steering, and absorption. Even though the traditional optimization techniques such as gradient based optimization, shape optimization, topology optimization and stochastic algorithms, and computational methods in direct metamaterial design have shown great achievements, such approaches are inefficient in inverse design of complex structures. To the contrary, the potential that machine learning offers for the discovery of new materials, devices and functionalities, is drawing increasing attention from a growing community of researchers worldwide [8–15]. The generative networks such as generative adversarial networks (GAN) [16–18] and variational autoencoder (VAE) [19] have had a huge success since they were introduced in 2014. Generative modeling have been applied in inverse design of material microstructure [20, 21] and metamaterials [22–31], and in solving inverse scattering problems [32, 33]. The generative networks have ability to generate better optimized complex devices and structures [34–37] enabling an automated design process of metamaterials and metadevices.

In this talk, we will present a novel data-driven method [1, 2] based on generative networks to inversely design broadband acoustic metamaterials. To illustrate the approach, specifically, we will design acoustic cloaks consisting of uniform planar configurations of cylindrical structure by means of multiple scattering theory [38] implementing cWGAN model that targets low TSCS responses. We will present the model performance of proposed cWGAN model for two- and four-scatterer configurations.

2 METHOD

2.1 Problem formulation

We consider acoustic multiple scattering by an arbitrary planar configuration of M cylindrical scatterers in the context of the acoustic time harmonic wave equation [39, 40]. For simplicity of implementation, we consider rigid cylinders of constant radii $a = 1$m situated in water within the circular region of radius $R_{out} = 15$m as shown in Figure 1. As a measure of scattering we consider the total scattering cross section (TSCS), denoted by σ that can be written in terms of the forward scattering amplitude via optical theorem [1, 12, 39]: $\sigma = -2\mathrm{Re}\, f(0)$. where $f(0) = f(\theta = 0)$ is the forward scattering amplitude. Here, the far-field amplitude form function, $f(\theta) = f(\theta, \mathbf{r}_1, \ldots, \mathbf{r}_M)$, $\theta = \arg(\mathbf{x})$, is defined by the scattered pressure p_{sc} in the far-field, [39, 40] where $\mathbf{r}_1, \ldots, \mathbf{r}_M$ are the position vectors and M is the total number of cylinders.

2.2 Data collection

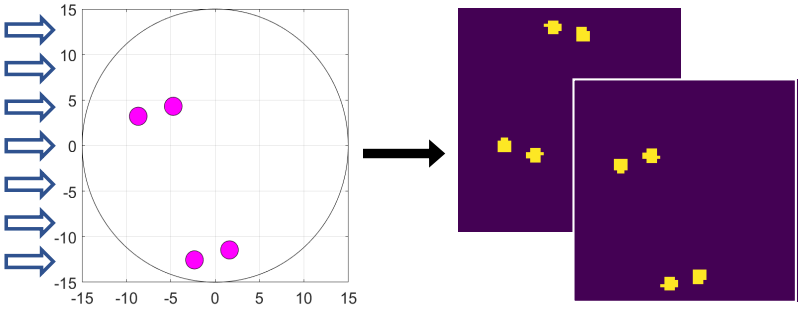


Figure 1. Physical scatterer configuration (left) and the corresponding scaled pixel images (right) that are scaled to 64x64 pixel resolution size with scattering elements (yellow) and exterior fluid medium (dark magenta).

We evaluate the TSCS, σ, in MATLAB using our multiple scattering solver [40, 41] for each configuration at discrete values of normalized wavenumber $k_i a \in [0.35, 0.45]$, $i = 1, \ldots, 11$ with an interval of 0.01, and reserve them as labels for the semi-supervised learning process. To implement cWGAN and CNN models we generate two types of datasets, one with random configurations of scatterers and one with optimal configurations obtained in MATLAB using *MultiStart* from Global optimization toolbox with *fmincon* nonlinear programming solver. We generate data-sets consisting of $60,000$ samples for random two-scatterer and four-scatterer uniform configurations separately and compute their corresponding TSCS values. We also generate two datasets of optimal configurations of $M = 2$ and $M = 4$ cylinders that produce near zero values of $\sigma(ka)$ at 11 values of ka. Each optimal dataset consist of 105 samples. For two-scatterer configurations and 105 data samples, only 7 unique optimal TSCS solutions are observed. It is difficult to optimize the TSCS at low frequencies in general, and, especially using only the interaction between two rigid scatterers. However, considering four-scatterer configurations, given the larger variety of four-scatterer configurations, the optimal dataset in not limited to only a few unique solutions.

In this work, we design planar metamaterial structures. Therefore, we use the scatterer coordinates to generate a planar configuration image and convert it into a 64x64 pixel resolution image array. Figure 1 illustrates the physical scatterer configuration (left) and the corresponding scaled pixel images (right). The incident normal plane wave is propagating in the positive x direction indicated by blue arrows in Figure 1 in the physical configuration image. The image is scaled to 64x64 pixel resolution size with scattering elements denoted by yellow color and dark magenta color stands for exterior fluid medium. Each scatterer in the physical space is altered from its cylindrical shape to fit within the discrete pixel space. To further improve training and increase the number of samples in the dataset, both the original image and the flipped Y-axis image shown in Figure 1 can be used as they give the same TSCS but this useful information has not been used in cWGAN model training and will be considered elsewhere.

2.3 Training with generative adversarial networks

In this work, we build and train cWGAN model to propose images on planar configuration of scatterers given expected TSCS value. We enhance the cWGAN architecture and its performance by adding to it a coordinate convolution (CoordConv) layer [3]. As illustrated Figure 2, the proposed cWGAN model comprises of a CoordConv implemented generator and critic, and the externally trained regressor that has CNN architecture [29]. A Gaussian distributed noise vector of size 256 is concatenated with the desired TSCS label and is fed into the generator. The generator produces a fake image and passes it to both the critic and the regressor. The critic computes the Wasserstein distance between the real image and the generated image and determines weather the image is real or fake. The regressor predicts the TSCS value from the generated image and the MSE between predicted and desired TSCS is evaluated. Both Wasserstein loss and MSE loss is backpropagated through the network to train the generator. The full description of the proposed cWGAN model including the loss functions and network architecture for each component of cWGAN, and the details of its training process and hyper-parameters found are provided in [1].

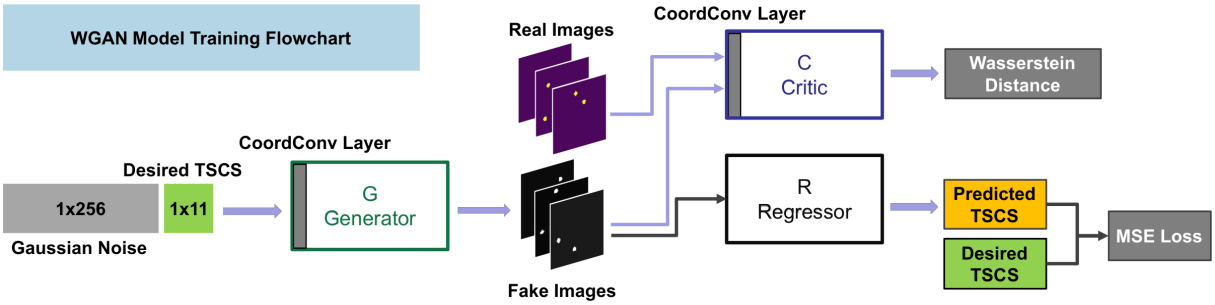


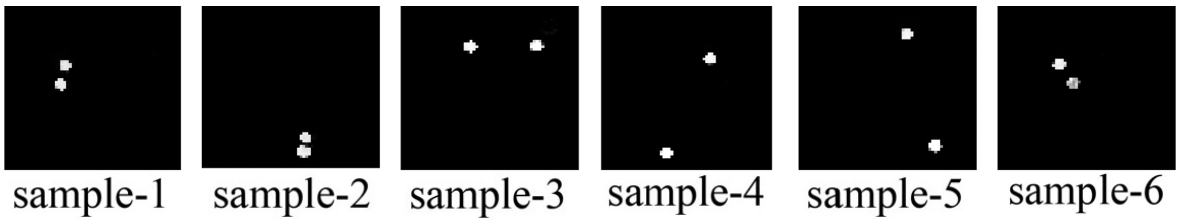
Figure 2. Schematic of cWGAN model [1] which comprises of a CoordConv implemented generator and critic, as well as the externally trained regressor.

3 NUMERICAL RESULTS

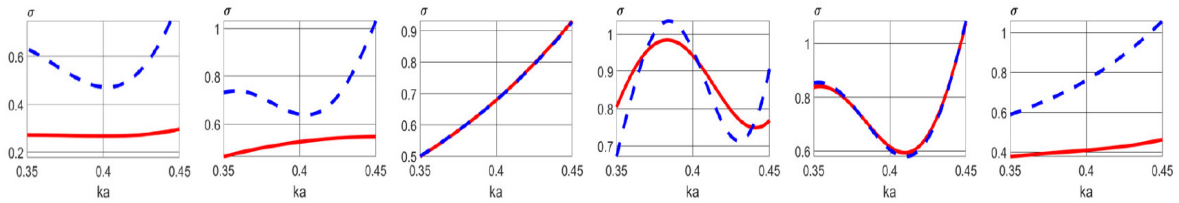
3.1 The optimal results generated by cWGAN model

We train the cWGAN model using datasets described in Section 2.2 and after training the cWGAN, we investigate the performance of the model for two- and four-scatterer configurations by generating an image and verifying the values of σ, TSCS function within and outside the optimized range of wavenumbers. Once generative networks are properly trained, they can achieve the optimal performance beyond the parameter given in the training dataset. The presented cWGAN model can produce optimal configurations that bring about near zero TSCS values. The cWGAN model, previously trained on random configurations of 2-scatterer or 4-scatterer configurations, is tested with the optimal configuration dataset. The *fmincon* minimized σ labels are concatenated to a noise vector and passed to the generator to produce new images. The generator repeatedly generates scatterer configurations and images with a regressor predicted σ MAE of 0.07 and 0.15, for two-scatterer and four-scatterer configurations respectively are collected. Out of 7 unique optimal TSCS solutions for two-scatterer configurations, the cWGAN model produced design for six of them.

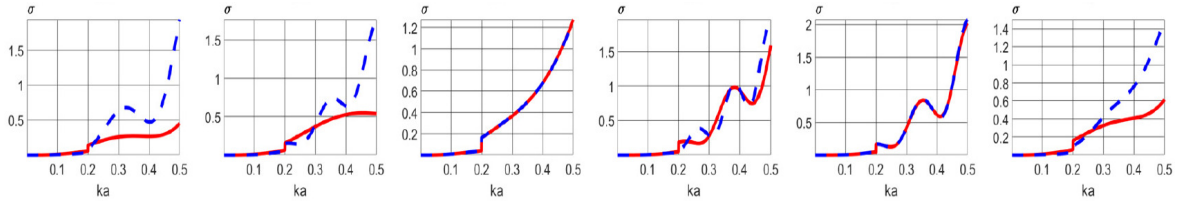
Figure 3 illustrates the generated two-scatterer configuration images of six samples and the variation of their corresponding TSCS values with wavenumbers, where the red continuous curved lines correspond to TSCS values produced by generated configurations and the blue dashed lines depict results for real configurations. Note that cWGAN model is only trained for wavenumbers $ka \in [0.35, 0.45]$. Figures 3b illustrate the variation of TSCS with wavenumber ka in optimized range: $ka \in [0.35, 0.45]$ and 3c show the results for TSCS versus ka for extended wavenumber range $ka \in [0, 0.50]$. Most samples show a strong correlation between the evaluated TSCS, σ, from generated configurations and real configurations. The MAE for all generated images of samples 1 through sample 6 in Figure 3 across the specified wavenumber range is 0.0266 and the average error across the samples is -0.0173. The negative average error shows that the majority of generated images have values of



(a) Generated configurations of $M = 2$ scatterers



(b) The variation of σ with wavenumber ka within the optimized wavenumber range



(c) The variation of σ with wavenumber ka beyond the optimized wavenumber range

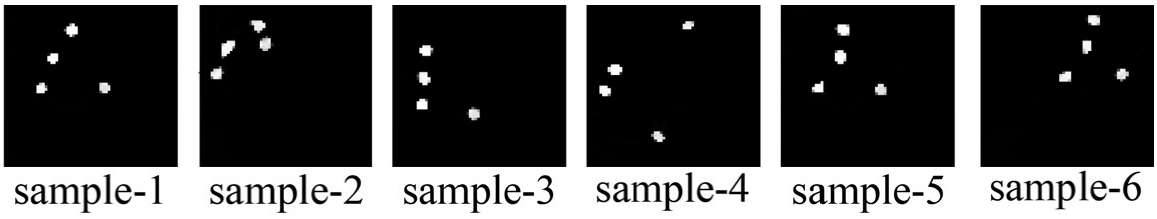
Figure 3. Sample cWGAN generated images for $M = 2$ optimized two-scatterer configurations (a), resulting TSCS comparison for the optimized wavenumber range: $ka \in [0.35, 0.45]$ (b) and for extended wavenumber range $ka \in [0, 0.50]$ (c). In Figures 3b and 3c, the red continuous curved lines correspond to TSCS produced by generated configurations and the blue dashed lines represent results for real configurations.

TSCS, σ, that is lower than the expected σ.

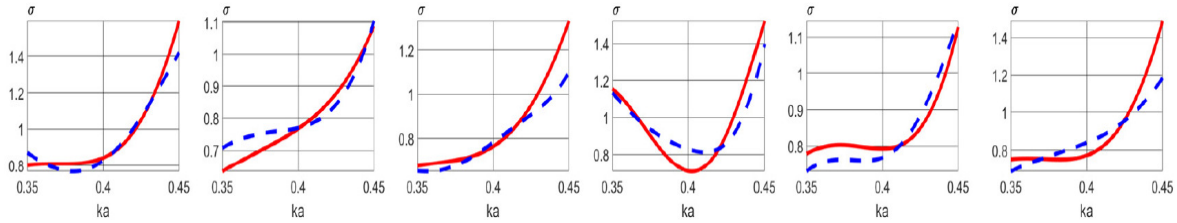
Figure 4 presents the generated four-scatterer images and their corresponding TSCS graphs versus wavenumbers, correspondingly for six samples. Here, the red continuous and blue dashed lines correspond to TSCS produced by generated and real configurations respectively. Although the average MAE for all tested samples is 0.1561, we examined some of the best performing generated configurations. The average MAE for the six samples shown in Figure 4 is 0.0494 with a standard deviation of 0.0173. The TSCS comparison in the extended range show that the model is capable of archiving good performance even outside the the range at which the device was optimized as shown for several presented samples. In addition, as can be seen from Figures 3 and 4, when viewing within the optimized range, few samples show even lower evaluated TSCS than the expected result. Figures 3 and 4 demonstrate that for two- and four-scatterer configurations cWGAN can produce images with responses similar, or better, than the expected σ within and outside the optimized range.

4 CONCLUSIONS

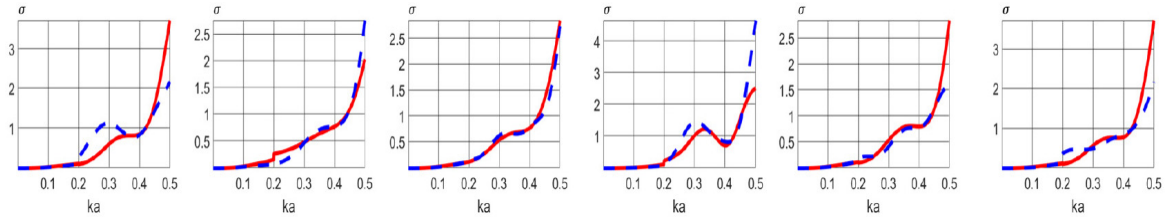
A novel data-driven method using deep learning and generative modeling instead of traditional optimization algorithms is introduced to design broadband acoustic metamaterial configurations targeting near zero TSCS. By implementing the conditional functionality to the standard WGAN [17, 42] architecture, the model is able to learn the relation between scatterer configurations and the corresponding TSCS. Applying the CoordConv layer to the generator and critic noticeably improved the quality and accuracy of generated designs. We use the random configuration dataset to train the cWGAN to produce TSCS optimized designs. Resulting images



(a) Generated configurations of $M = 4$ scatterers



(b) The variation of σ with wavenumber ka within the optimized wavenumber range



(c) The variation of σ with wavenumber ka beyond the optimized wavenumber range

Figure 4. Sample cWGAN generated images for $M = 4$ optimized four-scatterer configurations (a), resulting TSCS comparison for the optimized wavenumber range $ka \in [0.35, 0.45]$ (b) and for extended wavenumber range $ka \in [0, 0.50]$ (c). In Figure 4b and 4c, the red continuous and blue dashed lines represent the TSCS values produced by generated and real configurations correspondingly.

and evaluated TSCS show the model's capability to produce comparable or, sometimes, even better performing metacluster designs in regards to minimal TSCS. This work is a necessary step toward more complex acoustic applications with metaclusters, materials, and devices. The presented cWGAN model is generalizable can be applied in design of various metamaterial structures including pentamode metamaterials [43,44], to manipulate and control the propagation and scattering of various types of waves including flexural, elastodynamic, ultrasound, optical and electromagnetic waves.

Further work will improve the capability of cWGAN model to automatically generate configurations with a much larger number of scatterers to allow for model scaling and to be compatible with more complex acoustic applications such as cloaking, superfocusing, and wave steering effects. To increase the degrees of freedom and the number of material properties stored in each scatterer visually, tunable color channels may be introduced where different hues of color will correspond to a normalized material property value.

REFERENCES

[1] Peter Lai, Feruza Amirkulova, and Peter Gerstoft. Conditional Wasserstein generative adversarial networks applied to acoustic metamaterial design. *The Journal of the Acoustical Society of America*, 150(6):4362–4374, dec 2021.

[2] Peter Lai and Feruza Amirkulova. Acoustic metamaterial design using conditional Wasserstein generative adversarial networks. *The Journal of the Acoustical Society of America*, 151(4):A253–A253, apr 2022.

[3] Rosanne Liu, Joel Lehman, Piero Molino, Felipe Petroski Such, Eric Frank, Alex Sergeev, and Jason Yosinski. An intriguing failing of convolutional neural networks and the coordconv solution. *arXiv:1807.03247v2 [cs.CV]*, 2018.

[4] Constantin. R. Simovski. Material parameters of metamaterials (a Review). *Optics and Spectroscopy*, 107(5):726–753, nov 2009.

[5] Pierre A. Deymier, editor. *Acoustic metamaterials and phononic crystals*. Springer-Verlag, 2013.

[6] Steven A. Cummer. *Acoustic metamaterials.*, chapter Transformation acoustics, pages 197 – 218. Springer Series in Materials Science, 2013.

[7] Michael R. Haberman and Matthew D. Guild. Acoustic metamaterials. *Phys. Today*, 69(6):42–48, jun 2016.

[8] Jan-Hendrik Bastek, Siddhant Kumar, Bastian Telgen, Raphaël N. Glaesener, and Dennis M. Kochmann. Inverting the structure–property map of truss metamaterials by deep learning. *Proceedings of the National Academy of Sciences*, 119(1), dec 2021.

[9] Le Liu, Long-Xiang Xie, Weichun Huang, Xiu Juan Zhang, Ming-Hui Lu, and Yan-Feng Chen. Broadband acoustic absorbing metamaterial via deep learning approach. *Applied Physics Letters*, 120(25):251701, jun 2022.

[10] Anthony P. Garland, Benjamin C. White, Scott C. Jensen, and Brad L. Boyce. Pragmatic generative optimization of novel structural lattice metamaterials with machine learning. *Materials & Design*, 203:109632, may 2021.

[11] Zhi Chen, Alexander Ogren, Chiara Daraio, L. Catherine Brinson, and Cynthia Rudin. How to see hidden patterns in metamaterials with interpretable machine learning. r arXiv:2111.05949v1, 2021.

[12] Tristan Shah, Linwei Zhuo, Peter Lai, Amaris De La Rosa-Moreno, Feruza Amirkulova, and Peter Gerstoft. Reinforcement learning applied to metamaterial design. *The Journal of the Acoustical Society of America*, 150(1), July 2021.

[13] Ying-Tao Luo, Peng-Qi Li, Dong-Ting Li, Yu-Gui Peng, Zhi-Guo Geng, Shu-Huan Xie, Yong Li, Andrea Alù, Jie Zhu, and Xue-Feng Zhu. Probability-density-based deep learning paradigm for the fuzzy design of functional metastructures. *Research*, 2020:1–11, sep 2020.

[14] Rih-Teng Wu, Ting-Wei Liu, Mohammad R. Jahanshahi, and Fabio Semperlotti. Design of one-dimensional acoustic metamaterials using machine learning and cell concatenation. *Structural and Multidisciplinary Optimization*, 63(5):2399–2423, feb 2021.

[15] Chao Qian and Hongsheng Chen. A perspective on the next generation of invisibility cloaks—intelligent cloaks. *Applied Physics Letters*, 118(18):180501, may 2021.

[16] Ian J. Goodfellow, Jean Pouget-Abadie, Mehdi Mirza, Bing Xu, David Warde-Farley, Sherjil Ozair, Aaron Courville, and Yoshua Bengio. Generative adversarial nets. In *Advances in Neural Information Processing Systems 27 (NIPS 2014)*, 2014.

[17] Martin Arjovsky, Soumith Chintala, and Léon Bottou. Wasserstein Generative Adversarial Networks. In *Proceedings of the 34th International Conference on Machine Learning*, 2017.

[18] Yoann Boget. Adversarial regression. Generative adversarial networks for non-linear regression: Theory and assessment. Master's thesis, University of Neuchâtel, 2019.

[19] M. Kingma, D. Welling. Auto-encoding variational bayes. *arXiv:1312.6114v10*, 2014.

[20] Liwei Wang, Yu-Chin Chan, Faez Ahmed, Zhao Liu, Ping Zhu, and Wei Chen. Deep generative modeling for mechanistic-based learning and design of metamaterial systems. *Computer Methods in Applied Mechanics and Engineering*, 372:113377, Dec 2020.

[21] Ren Kai Tan, Nevin L. Zhang, and Wenjing Ye. A deep learning–based method for the design of microstructural materials. *Structural and Multidisciplinary Optimization*, 61(4):1417–1438, nov 2019.

[22] Yunwei Mao, Qi He, and Xuanhe Zhao. Designing complex architectured materials with generative adversarial networks. *Science Advances*, 6(17), apr 2020.

[23] Hongjia Zhang, Yang Wang, Honggang Zhao, Keyu Lu, Dianlong Yu, and Jihong Wen. Accelerated topological design of metaporous materials of broadband sound absorption performance by generative adversarial networks. *Materials & Design*, 207:109855, sep 2021.

[24] Thang Tran, Feruza Amirkulova, and Ehsan Khatami. Acoustic cloak design via machine learning. *arXiv:2111.01230*, 2021.

[25] Feruza Amirkulova, Thang Tran, and Ehsan Khatami. Generative deep learning model for broadband acoustic metamaterial design. *The Journal of the Acoustical Society of America*, 150(4):A209–A209, oct 2021.

[26] Linwei Zhuo and Feruza Amirkulova. Design of acoustic cloak using generative modeling and gradient-based optimization. *INTER-NOISE and NOISE-CON Congress and Conference Proceedings*, 263(3):3511–3522 https://doi.org/10.3397/IN–2021–2431, aug 2021.

[27] Caglar Gurbuz, Felix Kronowetter, Christoph Dietz, Martin Eser, Jonas Schmid, and Steffen Marburg. Generative adversarial networks for the design of acoustic metamaterials. *The Journal of the Acoustical Society of America*, 149(2):1162–1174, feb 2021.

[28] Waqas W. Ahmed, Mohamed Farhat, Xiangliang Zhang, and Ying Wu. Deterministic and probabilistic deep learning models for inverse design of broadband acoustic cloak. *Physical Review Research*, 3(1), feb 2021.

[29] Thang Tran, Ehsan Khatami, and Feruza Amirkulova. Total multiple scattering cross section evaluation using convolutional neural networks for forward and inverse designs of acoustic metamaterials. *The Journal of the Acoustical Society of America*, 149(4):A129–A129, apr 2021.

[30] Thang Tran, Feruza A. Amirkulova, and Ehsan Khatami. For consideration of publication in the 30th anniversary special issue of JTCA, "BROADBAND ACOUSTIC METAMATERIAL DESIGN VIA MACHINE LEARNING". *Journal of Theoretical and Computational Acoustics*, aug 2022.

[31] Feruza Amirkulova, Linwei Zhou, Anam Abbas, Peter Lai, Cheng Qiu, and Tristan A. Shah. Acoustic metamaterial design framework using deep learning and generative modeling. *The Journal of the Acoustical Society of America*, 151(4):A253–A253, apr 2022.

[32] W. W. Ahmed, M. Farhat, P. Y. Chen, X. Zhang, and Y. Wu. A generative deep learning approach for shape recognition of arbitrary objects from phaseless acoustic scattering data. July 2022.

[33] Rih-Teng Wu, Mehdi Jokar, Mohammad R. Jahanshahi, and Fabio Semperlotti. A physics-constrained deep learning based approach for acoustic inverse scattering problems. *Mechanical Systems and Signal Processing*, 164:108190, feb 2022.

[34] Daniel C. Elton, Zois Boukouvalas, Mark D. Fuge, and Peter W. Chung. Deep learning for molecular design—a review of the state of the art. *Molecular Systems Design & Engineering*, 4(4):828–849, 2019.

[35] Sunae So, Trevon Badloe, Jaebum Noh, Junsuk Rho, and Jorge Bravo-Abad. Deep learning enabled inverse design in nanophotonics. *Nanophotonics*, 9(5):1041–1057, feb 2020.

[36] Zihan Wang, Weikang Xian, M. Ridha Baccouche, Horst Lanzerath, Ying Li, and Hongyi Xu. Design of phononic bandgap metamaterials based on gaussian mixture beta variational autoencoder and iterative model updating. *Journal of Mechanical Design*, 144(4), feb 2022.

[37] Yabin Jin, Liangshu He, Zhihui Wen, Bohayra Mortazavi, Hongwei Guo, Daniel Torrent, Bahram Djafari-Rouhani, Timon Rabczuk, Xiaoying Zhuang, and Yan Li. Intelligent on-demand design of phononic metamaterials. *Nanophotonics*, 11(3):439–460, jan 2022.

[38] P. A. Martin. *Multiple Scattering: Interaction of Time-harmonic Waves with N Obstacles*. Cambridge University Press, New York, 2006.

[39] Feruza A. Amirkulova and Andrew N. Norris. The gradient of total multiple scattering cross-section and its application to acoustic cloaking. *Journal of Theoretical and Computational Acoustics*, page 1950016, mar 2020.

[40] Feruza A. Amirkulova. *Acoustic and Elastic Multiple Scattering and Radiation from Cylindrical Structures*. PhD thesis, Rutgers University, Piscataway, NJ, USA, 2014.

[41] Feruza A. Amirkulova and Andrew N. Norris. Acoustic multiple scattering using recursive algorithms. *Journal of Computational Physics*, 299:787–803, oct 2015.

[42] Ishaan Gulrajani, Faruk Ahmed, Martin Arjovsky, Vincent Dumoulin, and Aaron Courville. Improved training of Wasserstein GANs. *arXiv:1704.00028 [cs.LG]*, 2017.

[43] Cheng Qiu, Anam Abbas, and Feruza Amirkulova. Pentamode metamaterial design via generative modeling and deep learning. *The Journal of the Acoustical Society of America*, 151(4):A255–A255, apr 2022.

[44] Anam Abbas, Cheng Qiu, and Feruza Amirkulova. Deep learning assisted pentamode metamaterial design. In *Proceedings of the 24th International Congress on Acoustics*, 2022.

ICA 2022
24th INTERNATIONAL CONGRESS ON ACOUSTICS
October 24(Mon) - 28(Fri), 2022 Gyeongju, Korea

PROCEEDINGS of the
24th International Congress on Acoustics

October 24 to 28, 2022 in Gyeongju, Korea

ABS-0961

The 2D-global optimization networks (2D-GLOnets) model for acoustic metamaterial design

Wei-Ching Wang[(1)], Feruza Amirkulova[(2)]

[(1)]San Jose State University, USA, wei-ching.wang@sjsu.edu

[(2)]San Jose State University, USA, feruza.amirkulova@sjsu.edu

ABSTRACT

This study aims to contribute to the development of innovative data-driven approaches for metamaterial design using global optimization, deep learning, and generative modeling. The 2D-Global Optimization Networks (2D-GLOnets) technique is implemented to design acoustic metamaterials. The 2D-GLOnets optimize the probability of providing globally optimized meta-devices in the design space. A reparametrization technique is developed and is applied to constrain the scatterers into a feasible region. The gradients of the loss (objective) function with respect to the weights are calculated from backpropagation, and they update the weights of the generator. The physics-based gradients are calculated analytically from a multiple scattering solver [1] and used in backpropagation. The 2D-GLOnets generate a batch of metamaterials in each iteration and calculate the loss (objective) function over the entire training. The 2D-GLOnets gradually use the information provided to the model. The method is employed for sound localization and acoustic lens design. In a broadband acoustic lens design, the 2D-GLOnets maximize the absolute pressure at the focal point at discrete wavenumber values. The method is illustrated with examples of planar configurations of cylindrical scatterers producing sound localization and focusing effects.

Keywords: Global Optimization, Machine Learning, Generative Modeling, Acoustic Metamaterials

1 Introduction

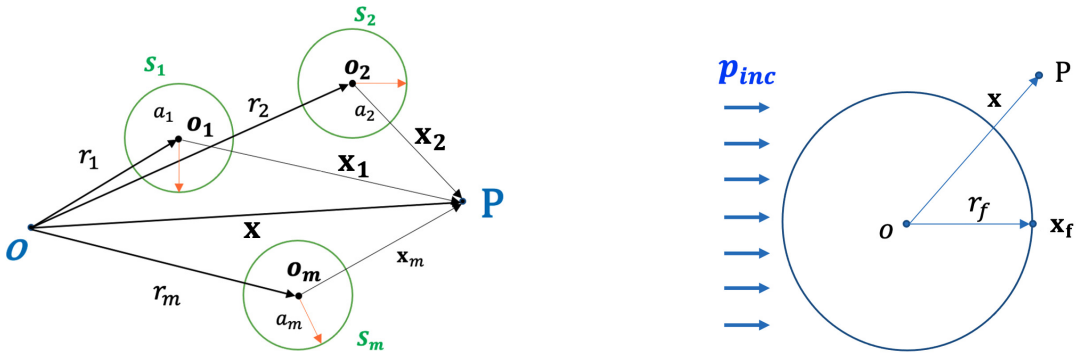
Metamaterials [2]are artificially engineered materials capable of controlling and directing wave energy flow, allowing sound, electromagnetic, and mechanical wave manipulations beyond typical materials. There are several ways in which these effects can be manifested, including super-focusing, cloaking, negative refraction, and negative mass density. These special properties of metamaterials are useful for applications, such as biomedical imaging [3], health monitoring of structure [4], etc. In recent years, the research on nanophotonic devices and acoustic metamaterials using deep learning (DL) and generative modeling has produced remarkable results [5–9]. In generative modeling, data patterns can be found without supervision. The models have the ability to generate data on their own based on the original training dataset for the model [10]. Inverse design can benefit from generative models since they can learn a real distribution [10]. Nowadays, automated design synthesis can revolutionize engineering design with generative modeling [10]. Hence, generative modeling can be applied to solve various inverse design problems when generating expensive data [11]. Examples of generative models include Generative Adversarial Networks (GAN) [12], GLOnets [13, 14], and Variational Autoencoders (VAE) [15]. Data-driven generative models can assist inverse materials design with high-efficiency computations and material databases. GANs have been employed in inverse design of organic molecules [11], photonic devices [16] and acoustic metamaterials [9, 17]. VAE, a deep

generative model, reduces dimensions and extracts features [11]. A supervised VAE (SVAE) and a conditional VAE (CVAE) [18, 19] were implemented for the total scattering cross section suppression.

Fan et al. [13] presented an alternative global optimization approach introducing a generative model 1D-GLOnets applicable to gradient-based optimization. The 1D-GLOnets [13] take into account a population of optimal devices simultaneously and optimize the deflection efficiency in relation to wavelength and outgoing angle. Chen et al. [16] developed reparameterization for 1D-GLOnets to impose geometric constraints on devices. Zhuo and Amirkulova [14] generalized the 1D-GLOnets of Fan et al. [13,16] by extending the model from a one-dimensional to a two-dimensional representation and developed a 2D-Global Optimization Networks (2D-GLOnets) introducing the reparametrization scheme to design the acoustic cloak. In comparison to conventional optimization solvers such as *fmincon*, the results obtained by these researchers were thrilling as the 2D-GLOnets model [14] outperformed traditional optimization algorithms *fmincon*, and inspired us to employ the idea for acoustic lens design. We will use DL and generative methods and employ 2D-GLOnets to design acoustic lenses. The optimization of the parameters of the generator's network architecture is performed with gradient information provided to the 2D-GLOnets model.

2 Methodologies

1 Problem Formulation



(a) An arbitrary configuration of scatterers; **(b)** A near-field view of the focal point $\mathbf{x}_f$;

Figure 1: Figure 1a illustrates an arbitrary configuration consisting of M rigid cylinders S_m with radius a_m, $m = \overline{1,M}$, and position vector $\mathbf{r}_m$; the $\mathbf{x}$ vector indicates the position of arbitrary point P with respect to origin O. Figure 1b depicts a near-field view of the lens; the incident plane wave of unit amplitude is denoted by p_{inc}; the focal point is denoted $\mathbf{x}_f$ vector, which has a magnitude of r_f.

Acoustic multiple scattering is considered, employing multiple scattering theory in the context of the 2D acoustic wave equation by assuming time harmonic dependence $e^{-i\omega t}$ but omitting in the following. The governing equation for acoustic pressure $p(\mathbf{x})$, $\mathbf{x} \in \mathscr{R}^2$, is the Helmholtz equation:

$$\nabla^2 p + k^2 p = 0, \tag{2.1}$$

where $k = \omega/c$ is the wavenumber, c is the acoustic speed, and ω is the frequency.
The total acoustic pressure field $p(\mathbf{x})$ is defined as: $p = p_{inc} + p_{sc}$, the sum of incident p_{inc} and scattered p_{sc} pressure fields. The absolute value of total pressure is defined as: $|p| = (pp^*)^{1/2}$ where the asterisk $*$ denotes the complex conjugate. The incident field comprises a planar wave that interacts with a configuration of M cylindrical scatterers as shown in Figure 1a. For simplicity, rigid cylinders are utilized.
We aim to maximize the amplitude of acoustic pressure at the focal point by rearranging scatterers' positions as indicated by the vectors $\{\mathbf{r}_m\}$ in Figure 1a. Figure 1b depicts the schematics of lens region and the location of the

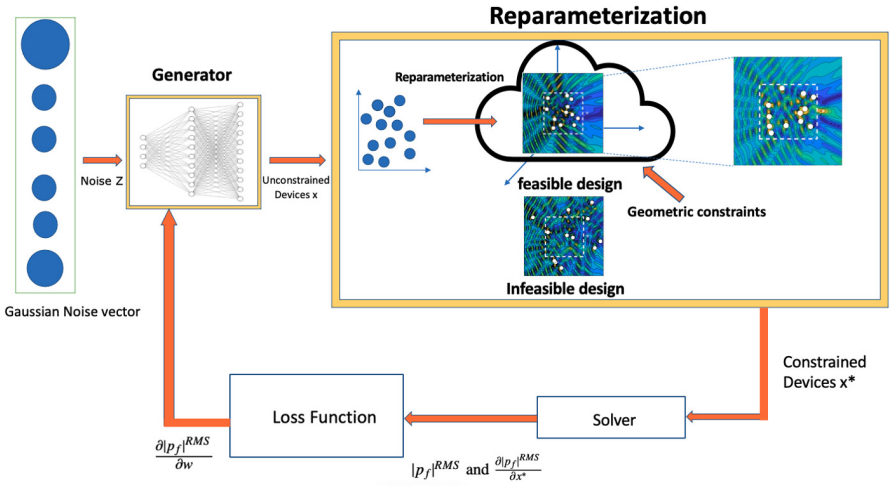


Figure 2: The 2D-GLOnets architecture includes a Gaussian noise vector, generator, reparametrization, loss function, and a multiple scattering solver evaluating the RMS of pressure amplitude $|p_f|^{RMS}$ at the focal point and its gradient.

focal point $\mathbf{x}_f$ which is fixed and predefined. The total acoustic pressure at the focal point $p_f(\{\mathbf{r}_m\}) = p(\mathbf{x}_f)$ is defined [20] for a given set of the position vectors $\{\mathbf{r}_m\}$ and given by Equation 1.4 in Appendix A.

2 2D-GLOnets Architecture

Figure 2 illustrates a machine learning framework for the 2D-GLOnets, which could be used for inverse design. The Gaussian noise of size 1 by 128 is used as an input. The generator, a device to generate unconstrained configurations of the scatterers, has an architecture of the FCNN of 8 layers. The input is aggregated in the generator with a size of 1 by 128, i.e., $U \times M = 128$, where U is the batch size, and M is the number of the scatterers. From the 1st to 7th layers, the *LeakyReLU* is used as an activation function. The *tanh* activation function is used in the last layer.

3 Loss Function

Our goal for the acoustic lens design is to maximize the RMS of absolute pressure amplitude $|p_f^{(rms)}|$ at the focal point. Adapting conceptions from Zhuo and Amirkulova [14] and Chen et al. [16], we formulated the loss function to train the acoustic lens model as follows:

$$L = -\frac{1}{\gamma}\sum_{\gamma=1}^{\Gamma}(1/\sigma)exp\frac{|p_f^{(rms)}(x^{\gamma})|}{\sigma}\mathbf{n}^{(\gamma)}\cdot\mathbf{q}_{\mathbf{j}}^{\mathbf{RMS}}, \tag{2.2}$$

where γ is the number of unconstrained devices in a batch, σ is tunable hyperparameter, $|p_f(\{\mathbf{r}_m\})|$ the total absolute pressure field at the focal point is given in vector form by Equation 1.4, the gradients $\mathbf{q}_j^{RMS}$ are computed analytically given by Equation 1.7 in the vector form, and $\mathbf{n}^{(\gamma)}$ are gradients of the unconstrained device with respect to the constrained device in the vector form. It is necessary to tune the hyperparameters until the loss function approaches a range of minor fluctuations because of the nonlinearity of the optimization problem considered. During training, the loss function may follow the trend of pressure amplitude. The loss function calculates the gradients $\frac{\partial |p_f|^{RMS}}{\partial w}$ and updates the weights w through backpropagation.

3 Results

Zhuo and Amirkulova [14, 20]'s concepts were adapted, and we used the capabilities of the 2D-GLOnets and gradient information to automate acoustic lens design. The 2D-GLOnets are implemented using PyTorch Python libraries calling MATLAB engine from Python libraries. The water density $\rho_0 = 1000kg/m^3$ and the speed of sound in water $c_0 = 1480m/s$ are considered for rigid cylinders submerged underwater. The wavenumbers considered are $ka \in [0.35, 0.45]$ and $ka \in [1.35, 1.45]$. Numerical results for the design of acoustic lenses are presented using the 2D-GLOnets model for $N_k = 11$ discretized values with an increment of 0.1. A comparison between the results of the 2D-GLOnets and that of *fmincon* with the *MultiStart* solver will be analyzed.

1 Numerical Results for 2D-GLOnets at Lower Values of Wavenumbers ka $\in [0.35, 0.45]$

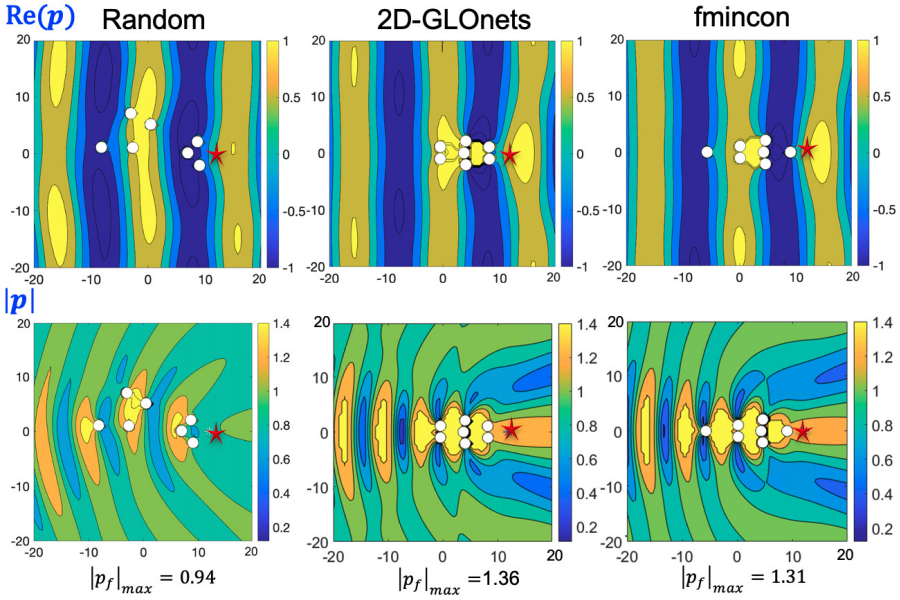
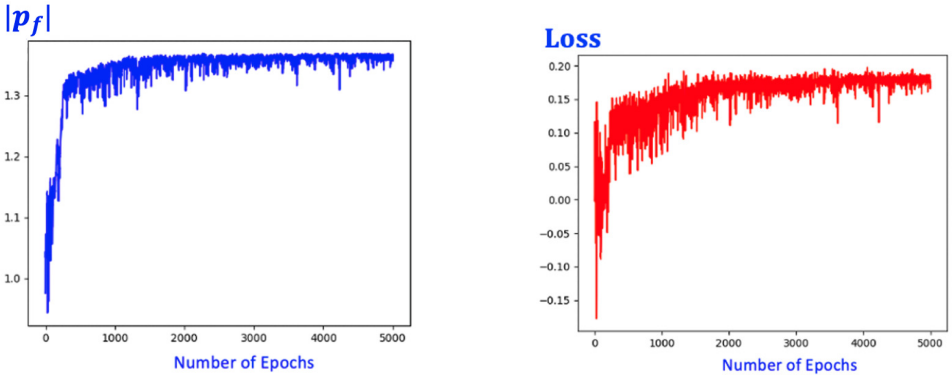


Figure 3: Comparison of pressure fields between arbitrary random configuration (left column), 2D-GLOnets (middle column), and *fmincon* (right column). The variation of real part of total pressure, $Re(p)$, (top figures) and absolute pressure amplitude, $|p|$, (bottom figures) at plane wave incidence on configurations of $M = 7$ cylinders at $ka = 0.40$.

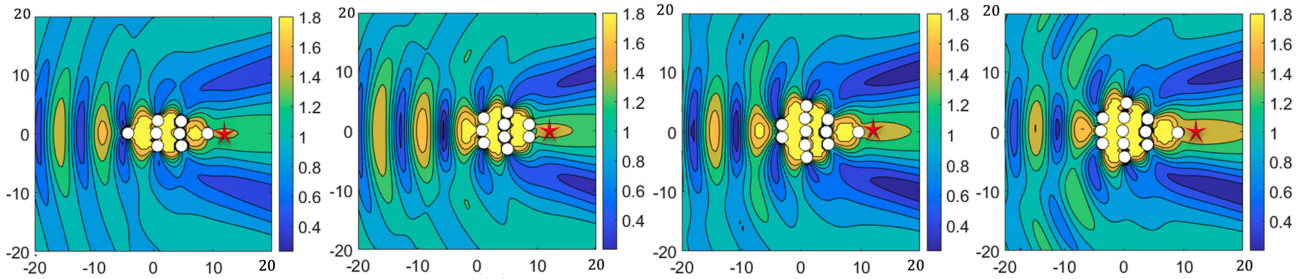
The 2D plots of total pressure fields are shown in Figure 3 for configurations of $M = 7$ rigid cylinder at $ka = 0.40$. The upper and bottom figures indicate the real part of the total acoustic pressure field, $Re(p)$, and the total absolute acoustic pressure field $|p|$, correspondingly. The left, middle, and right figures display the random configuration, 2D-GLOnets optimized configuration, and *fmincon* optimized configuration, respectively. The $Re(p)$ illustrates the interaction of the plane waves with the configuration during wave propagation in the fluid. The absolute pressure amplitude $|p|$ exhibits the magnitude of pressure amplitude. The color spectrum bar from blue to yellow on the right side of each figure shows the magnitude of the absolute pressure values. An asterisk denotes the focal point $(12, 0)$ at which the waves propagate in a left-to-right direction with normal incidence get focused. Figure 3 shows the outperformance of the 2D-GLOnets compared to *fmincon* at $ka = 0.40$. The focusing effects are distinct for the 2D-GLOnets. The 2D-GLOnets and *fmincon* display symmetrical scatterer patterns oriented along the x-axis. We plot the variance of the absolute pressure amplitude in Figure 4a and the loss in Figure 4b with number of epochs at $ka \in [0.35, 0.45]$ for configuration of $M = 7$ scatterers optimized by 2D-GLOnets given in Figure 3. In Figure 4a, the absolute pressure amplitude $|p_f|$ shows a converging trend with a decreasing variance as the number



(a) absolute pressure amplitude; **(b)** loss function;

Figure 4: The variation of absolute pressure amplitude $|p_f|$ and loss function versus the number of epochs using the 2D-GLOnets for $M = 7$ at $ka \in [0.35, 0.45]$

of epochs increases. The 2D-GLOnets have an optimized absolute pressure amplitude of $|p_f| \approx 1.36$, which is greater than $|p_f| = 1.32$ by *fmincon*. From Figure 4b, we can see fluctuations in the loss function. Because of the loss function formulation, it is satisfactory as long as it converges to a range of numbers. Figure 5 shows



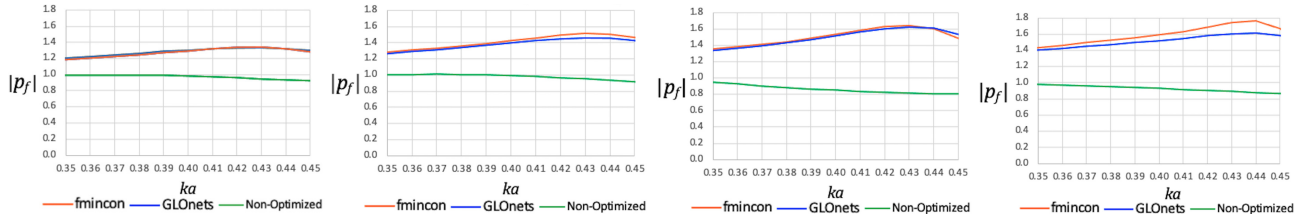
(a) $M = 8$, $|p|_{max} = 1.38$; **(b)** $M = 9$, $|p|_{max} = 1.46$; **(c)** $M = 11$, $|p|_{max} = 1.51$; **(d)** $M = 12$, $|p|_{max} = 1.52$;

Figure 5: 2D-GLOnets optimized results for the absolute pressure field $|p|$ with $M = 8, 9, 11$, and 12 at $ka = 0.40$.

the absolute pressure amplitude with a varying number of cylinders. The absolute pressure amplitudes at the focal point $|p_f|$ for $M = 8, 9, 11$, and 12 scatterers were plotted. In these four examples, the 2D-GLOnets perform better than *fmincon*, showing the focusing effects. The 2D-GLOnets and *fmincon* results show a symmetry pattern about the x-axis. Figure 6 illustrates the absolute pressure amplitude at the focal point is optimized at $ka \in [0.35, 0.45]$ for the optimized configurations of $M = 6, 8, 10$, and 12 cylinders at plane wave incidence. Here, the comparison of 2D-GLOnets results with *fmincon* results is conducted, and the results for non-optimized random configuration are given in green color as a reference. A non-optimized configuration's absolute pressure amplitude appears much lower than that of a 2D-GLOnets configuration and that of *fmincon* at $ka \in [0.35, 0.45]$. The 2D-GLOnets results are comparable with *fmincon* results at $ka \in [0.35, 0.45]$, which is the optimized frequency range. A similar performance is achieved by 2D-GLOnets and *fmincon* for $M = 6$ and $M = 10$. Compared with *fmincon*, the 2D-GLOnets perform slightly worse for $M = 8$ and $M = 12$.

2 Numerical Results for 2D-GLOnets at Higher Values of Wavenumbers ka $\in [1.35, 1.45]$

Figure 7 shows a comparison between a random configuration on the left column and optimized configurations consisting of the 2D-GLOnets results on the middle column and *fmincon* results on the right column at high wavenumbers $ka \in [1.35, 1.45]$. $Re(p)$ is the real part of total pressure, and $|p|$ is the absolute pressure amplitude. A



(a) $M = 6$; **(b)** $M = 8$; **(c)** $M = 10$; **(d)** $M = 12$;

Figure 6: The dependency of absolute pressure amplitude on $ka \in [0.35, 0.45]$ for fixed numbers of scatterers: $M = 6, 8, 10, 12$.

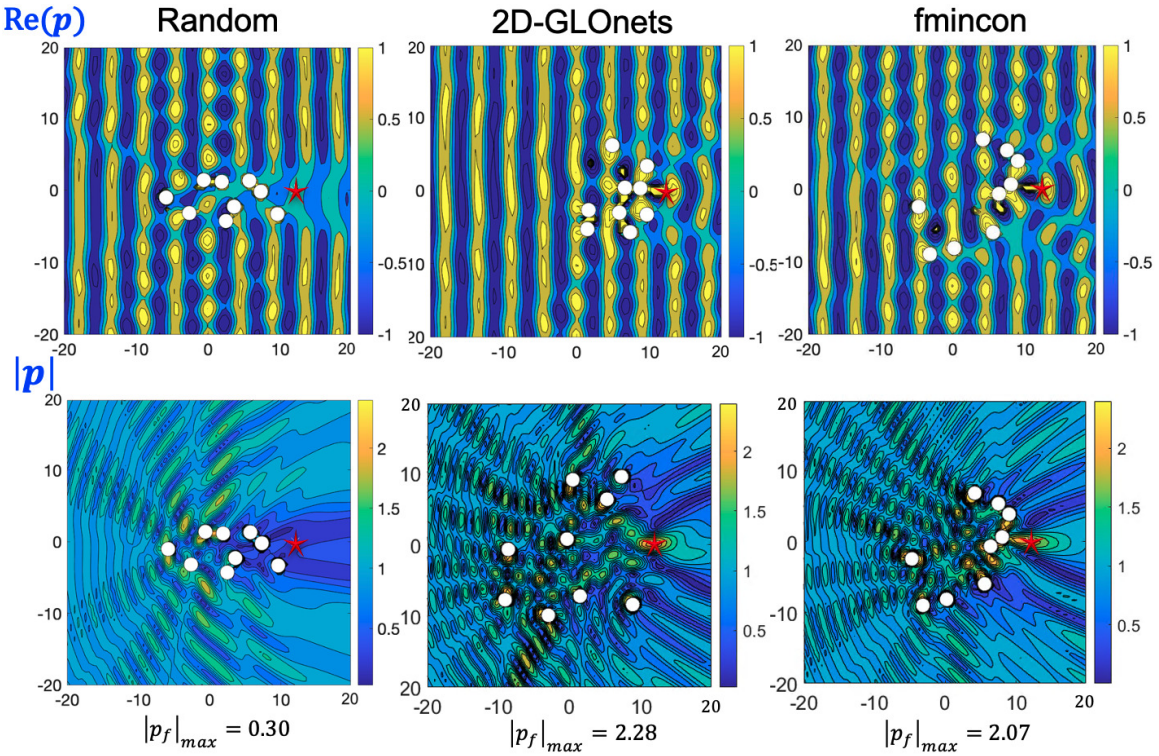
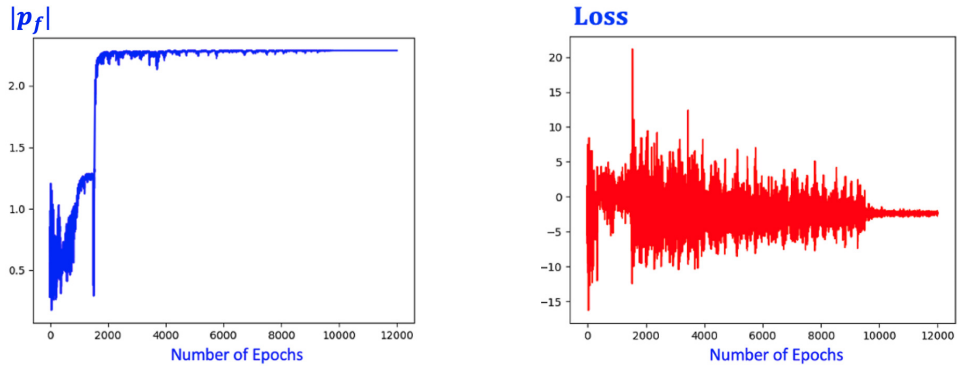


Figure 7: Comparison of pressure fields between random configuration, 2D-GLOnets, *fmincon* at $ka = 1.40$. At normal plane wave incidence, the real part of total pressure $Re(p)$ is shown on the top figures, and absolute pressure amplitude $|p|$ is shown on the bottom figures for configurations $M = 9$ rigid cylinders $ka = 1.40$. The left, middle, and right columns show an arbitrary random configuration, a 2D-GLOnets configuration, and a *fmincon* configuration, respectively.

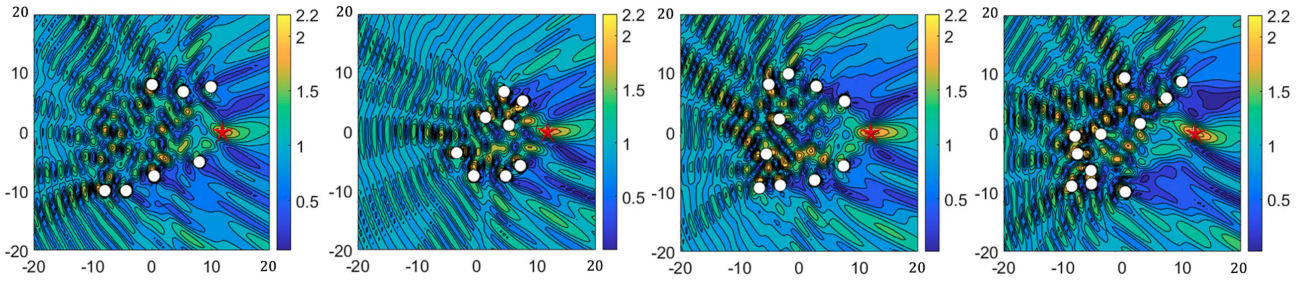
more scattered configuration is achieved as a result of optimizing the cylinders. This particular instance shows that the 2D-GLOnets produces $|p|_{max} = 2.28$ that outperforms the *fmincon* solver producing $|p|_{max} = 2.07$. In contrast to the random configuration, the 2D-GLOnets model produces distinct focusing effects at the focal point as identified with an asterisk in Figure 7.



(a) absolute pressure amplitude; **(b)** loss function;

Figure 8: The variation of absolute pressure amplitude $|p_f|$ and loss function with the number of epochs using 2D-GLOnets for $M = 9$ at $ka \in [1.35, 1.45]$.

The training curve for $|p_f|$ the loss function versus the epoch numbers are given correspondingly in Figure 8a and in Figure 8b. We used a batch size U of 15. A fluctuating amplitude of the absolute pressure is observed at the focal point at the beginning of the training. Due to the 2D-GLOnets being able to exit local minima and reach global maxima, it is ascertained that there is a sudden drop and rise in absolute pressure. Successful convergence of the loss function is achieved after the oscillations. Around the 9500th epoch of the training, the absolute total pressure amplitude and loss function show significant reductions in noise.
Figure 9 displays the 2D-GLOnets results for absolute total pressure amplitude $|p|$ for $M = 7, 8, 10$, and 11 at a selected wavenumber $ka = 1.40$. The normal incident wave has an absolute pressure of $|p_{inc}| = 1.0$. These examples demonstrate that 2D-GLOnets optimized configurations outperform *fmincon* configurations. The asterisk indicates the focal point where focusing effects of the optimized configurations are observed. The sound localization and focusing effects at high frequencies are clearly visible in the absolute total pressure field.



(a) $M = 7$, $|p|_{max} = 2.02$; **(b)** $M = 8$, $|p|_{max} = 2.04$; **(c)** $M = 10$, $|p|_{max} = 2.16$; **(d)** $M = 11$, $|p|_{max} = 2.18$;

Figure 9: The absolute value of the total acoustic pressure field $|p|$ for the optimized configurations of $M = 7, 8, 10$, and 11 optimized by 2D-GLOnets at $ka = 1.40$.

Figure 10 depicts examples of the absolute value of the total acoustic pressure fields $|p|$ that are outside the optimized wavenumber range, i.e., $ka \in [1.35, 1.45]$. For $ka = 1.45$, 1.5, and 1.6, which are outside the optimal wavenumber range, the number of scatterers $M = 8$ (top row) and $M = 10$ (bottom row) are considered. The middle column figures show that lens devices still produce a focusing effect at wavenumber at $ka = 1.5$, which is outside the range where the device was optimized. As the wavenumber ka increases, the focusing effects diminish.

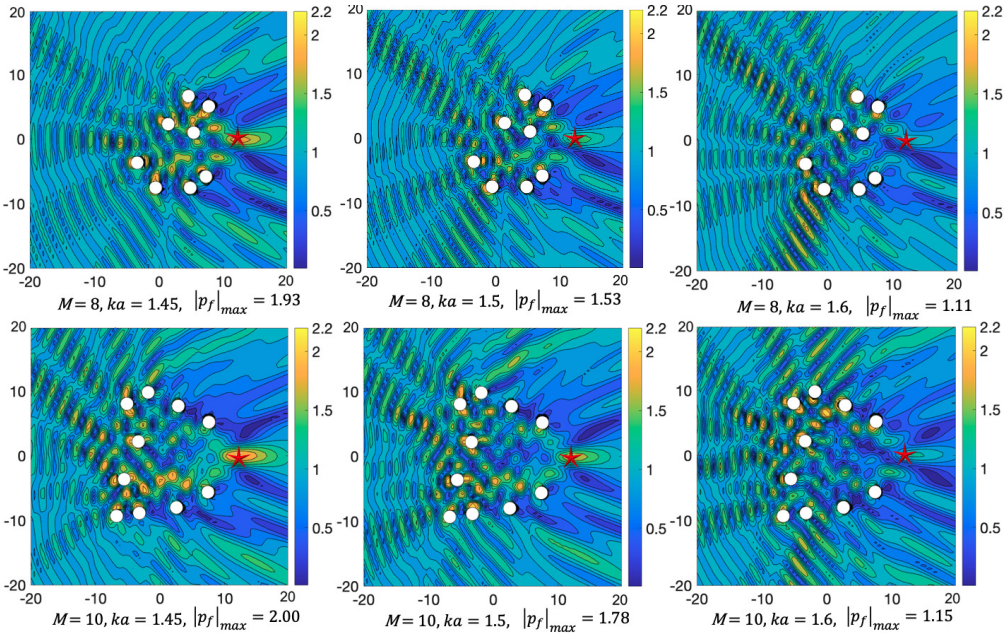


Figure 10: The absolute total acoustic pressure $|p|$ for $M = 8$ is shown on the top row and $M = 10$ is depicted on the bottom row; the results at $ka = 1.45$ give on the left, $ka = 1.5$ shown on the middle, and at $ka = 1.6$ depicted on the right columns. Here, the wavenumbers ka outside the optimized range $ka \in [1.35, 1.45]$ are investigated.

4 Conclusion and Future Work

The acoustic lenses have been successfully designed using the 2D-GLOnets. Focusing effects can be achieved at two ranges of frequencies, i.e. at low ($ka \in [0.35, 0.45]$) and high ($ka \in [1.35, 1.45]$) values of wavenumbers. There is a successful convergence of the absolute pressure amplitude. Model performance is validated by state-of-the-art gradient-based optimization algorithms of the *fmincon* solver. The problem becomes more challenging when there are more scatterers, as the reparametrization consumes much memory in GPUs. There is a possibility that 2D-GLOnets may produce better results than current state-of-the-art optimization algorithms with a more powerful computational resource.

Future work includes exploring a variety of non-uniform configurations considered with different material properties, scatterers' radii, shell structures, etc. We will consider optimizing the 2D-GLOnets by alternating the radii and positions of the scatterers in non-uniform configurations. We can employ high-performance computing to speed up the computing time. By doing this, the optimized configurations can accommodate more scatterers. The reparametrization scheme will not be needed if radii variance is considered by removing the scatterer adjustment and enabling practical designs with a larger number of scatterers in the low-frequency and high-frequency ranges.

A APPENDIX

1 Position Dependent Acoustic Pressure at the Focal Point

The incident wave is the normal plane wave of unit amplitude, and the incident pressure at fixed focal point P_f is: $p_{inc}(\mathbf{x}_f) = e^{ik\mathbf{e}_\psi \cdot \mathbf{x}_f}$. The scattered field in the neighborhood of cylinder S_m is given by [20]:

$$p_{sc}(\mathbf{x}) = \sum_{m=1}^{M} \sum_{n=-\infty}^{\infty} B_n^{(m)} V_n^+(\mathbf{x}_m), \tag{1.3}$$

where $\mathbf{x}_m$ is a position vector of point P with respect to the cylinder center at O_m: $\mathbf{x}_m = \mathbf{x} - \mathbf{r}_m$, and the function $V_n^{\pm}(\mathbf{x})$ is defined as: $V_n^{\pm}(\mathbf{x}) = H_n^{(1)}(k|\mathbf{x}|)e^{\pm in \arg \mathbf{x}}$, where $H_n^{(1)}$ is the Hankel function of the first kind of order n. The total pressure at the fixed focal point P_f [20] is:

$$p_f = e^{ik\mathbf{e}_\psi \cdot \mathbf{x}_f} + \sum_{m=1}^{M} \sum_{n=-\infty}^{\infty} B_n^{(m)} V_n^+(\mathbf{x}_f - \mathbf{r}_m) = e^{ik\mathbf{e}_\psi \cdot \mathbf{x}_f} + \mathbf{v}^T \mathbf{b}, \tag{1.4}$$

where we introduced vectors $\mathbf{b}, \mathbf{v} \in \mathscr{C}^{M \times (2N+1)}$. The elements of the dual vector $\mathbf{v} = \{V_n^{(j)}\} = \{V_n(\mathbf{r}_j)\}$ were defined into the form [20]: $V_n^{(m)} = V_n^+(\mathbf{r}_{fm})$, where $\mathbf{r}_{fm} = \mathbf{x}_f - \mathbf{r}_m$ is the position of focal point with respect to local coordinate at O_m and $\mathbf{r}_m$ is the position of scatterer with respect to origin at O. The components of the scattering coefficient vector $\mathbf{b} = \{B_n^{(j)}\}$, $j \in (1, M)$, $n \in (-N, N)$, are $B_n^{(j)} = \{B_n(\mathbf{r}_j)\}$, and written in column vector form [20]: $\mathbf{b} = \left(\mathbf{b}^{(1)}\mathbf{b}^{(2)} \ldots \mathbf{b}^{(M)}\right)^T$, $\mathbf{b}^{(j)} = \left(B_{-N}^{(j)} B_{-N+1}^{(j)} \ldots B_N^{(j)}\right)^T$ where T means transpose, to execute this, we let N be the truncation value of the infinite sum in Equation 1.4. We select the value as: $N = 2ka$.

2 Absolute Pressure Amplitude Function and its Gradients for Acoustic Lens

Broadband optimization was performed using root mean square (RMS) of absolute pressure at the focal point $|p_f|$ evaluated over some range of normalized wavenumbers $k_i a\,(i = 1, 2, ..., N_k)$, i.e., $|p_f(\{\mathbf{r}_m\})|^{RMS}$ [20]:

$$|p_f(\{\mathbf{r}_m\})|^{RMS} = \left(\frac{1}{N_k}\left[|p_f(k_1 a, \{\mathbf{r}_m\})|^2 + |p_f(k_2 a, \{\mathbf{r}_m\})|^2 + ... + |p_f(k_{N_k} a, \{\mathbf{r}_m\})|^2\right]\right)^{1/2}, \tag{1.5}$$

where each of absolute pressure amplitude $|p_f(\{k_i a, \mathbf{r}_m\})|$ can be computed for each $k_i a$ value ($i = \overline{1, N_k}$) using Equation 1.4 in Appendix A. In our simulation, we consider $N_k = 11$, i.e. is 11 discrete values of normalized wavenumbers ka where a is the cylinder radius. The vector $\mathbf{q}_j$ defined as gradient of the absolute value of total pressure field $|p_f(\{\mathbf{r}_m\})|$ with respect to positions $\mathbf{r}_j$ and is evaluated in [20] as:

$$\mathbf{q}_j = \frac{\partial |p_f|}{\partial \mathbf{r}_j} = \frac{1}{2|p_f|}\left(p_f^* \mathbf{p}_j + p_f \mathbf{p}_j^*\right), \tag{1.6}$$

where $*$ indicates the complex conjugate and $\mathbf{p}_j = \frac{\partial p_f}{\partial \mathbf{r}_j}$. The broadband gradient vectors are defined as:

$$\mathbf{q}_j^{RMS} = \frac{\partial |p_f(\{\mathbf{r}_m\})|^{RMS}}{\partial \mathbf{r}_j} = \frac{1}{|p_f|^{RMS}} \frac{1}{N_k}\Big(|p_f(k_1 a)|\mathbf{q}_j(k_1 a) + ... + |p_f(k_{N_k} a)|\mathbf{q}_j(k_{N_k} a)\Big), \quad j = 1, 2, \ldots M. \tag{1.7}$$

REFERENCES

[1] Feruza A. Amirkulova and Andrew N. Norris. Acoustic multiple scattering using recursive algorithms. *Journal of Computational Physics*, 299:787–803, oct 2015.

[2] J. B. Pendry, D. Schurig, and D. R. Smith. Controlling electromagnetic fields. *Science*, 312(5781):1780–1782, 2006.

[3] A. Spadoni and C. Daraio. Generation and control of sound bullets with a nonlinear acoustic lens. *Proceedings of the National Academy of Sciences*, 107(16):7230–7234, Apr 2010.

[4] Fabio Semperlotti and Hongfei Zhu. Metamaterial based acoustic lens for structural health monitoring. *United States Patent Application Publication*, 2015.

[5] Tian Zhang, Jia Wang, Qi Liu, Jinzan Zhou, Jian Dai, Xu Han, Yue Zhou, and Kun Xu. Efficient spectrum prediction and inverse design for plasmonic waveguide systems based on artificial neural networks. *Photonics Research*, 7(3):368, mar 2019.

[6] Mohammad H. Tahersima, Keisuke Kojima, Toshiaki Koike-Akino, Devesh Jha, Bingnan Wang, Chungwei Lin, and Kieran Parsons. Deep neural network inverse design of integrated photonic power splitters. *Scientific Reports*, 9(1):1368, feb 2019.

[7] Tristan Shah, Linwei Zhuo, Peter Lai, Amaris De La Rosa-Moreno, Feruza Amirkulova, and Peter Gerstoft. Reinforcement learning applied to metamaterial design. *Journal of the Acoustical Society of America*, 150(1), July 2021 https://doi.org/10.1121/10.0005545.

[8] Linwei Zhuo. Acoustic cloak design generative modeling and reinforcement learning. Master's thesis, San Jose State University, USA, 2022.

[9] Peter Lai, Feruza Amirkulova, and Peter Gerstoft. Conditional Wasserstein generative adversarial networks applied to acoustic metamaterial design. *Journal of the Acoustical Society of America*, 2021.

[10] Lyle Regenwetter, Amin Heyrani Nobari, and Faez Ahmed. Deep generative models in engineering design: A review. *ASME*, 144:1–15, 10 2021.

[11] Litao Chen, Wentao Zhang, Zhiwei Nie, Shunning Li, and Feng Pan. Generative models for inverse design of inorganic solid materials. *Journal of Materials Informatics*, 07 2021.

[12] Ian J. Goodfellow, Jean Pouget-Abadie, Mehdi Mirza, Bing Xu, David Warde-Farley, Sherjil Ozair, Aaron Courville, and Yoshua Bengio. Generative adversarial nets. In *Advances in Neural Information Processing Systems 27 (NIPS 2014)*, 2014.

[13] Jiaqi Jiang and Jonathan A. Fan. Global optimization of dielectric metasurfaces using a physics-driven neural network. *Nano Letters*, 19(8):5366–5372, jul 2019.

[14] Linwei Zhuo and Feruza Amirkulova. Design of acoustic cloak using generative modeling and gradient-based optimization. *INTER-NOISE and NOISE-CON Congress and Conference Proceedings*, 263(3):3511–3522 https://doi.org/10.3397/IN–2021–2431, aug 2021.

[15] M. Kingma, D. Welling. Auto-encoding variational bayes. *arXiv:1312.6114v10*, 2014.

[16] Mingkun Chen, Jiaqi Jiang, and Jonathan Fan. Design space reparameterization enforces hard geometric constraints in inverse-designed nanophotonic devices. *ACS Photonics*, 15, 11 2020.

[17] Caglar Gurbuz, Felix Kronowetter, Christoph Dietz, Martin Eser, Jonas Schmid, and Steffen Marburg. Generative adversarial networks for the design of acoustic metamaterials. *Journal of the Acoustical Society of America*, 149(2):1162–1174, feb 2021.

[18] Thang Tran, Feruza Amirkulova, and Ehsan Khatami. Acoustic cloak design via machine learning. *Journal of Theoretical and Computational Acoustics*, (accepted), 07 2022.

[19] Thang Tran, Ehsan Khatami, and Feruza Amirkulova. Total multiple scattering cross section evaluation using convolutional neural networks for forward and inverse designs of acoustic metamaterials. *Journal of the Acoustical Society of America*, 149, 06 2021.

[20] F. A Amirkulova, S. Gerges, and A. N. Norris. Sound localization through multi-scattering and gradient-based optimization. *MDPI Mathematics*, 2021.

ICA 2022
24th INTERNATIONAL CONGRESS ON ACOUSTICS
October 24(Mon) - 28(Fri), 2022 Gyeongju, Korea

PROCEEDINGS of the
24th International Congress on Acoustics

October 24 to 28, 2022 in Gyeongju, Korea

ABS-0965

Deep learning assisted PM metamaterial design

Anam Abbas[(1)], Cheng Qiu[(2)], Feruza Amirkulova[(3)]

[(1)]Mechanical Engineering Department, San José State University, San José, 95192, USA, anam.abbas@sjsu.edu

[(2)]Mechanical Engineering Department, San José State University, San José, 95192, USA, cheng.qiu@sjsu.edu

[(3)]Mechanical Engineering Department, San José State University, San José, 95192, USA, feruza.amirkulova@sjsu.edu

ABSTRACT

In this work, we present deep learning-assisted models for design of tetrahedral PM unit cells to construct a 3D lattice structure that is highly anisotropic and mimics the acoustic properties of water. We optimize unit cell design via forward techniques by altering the design parameter and building datasets to train deep learning models. We implement conditional Wasserstein generative adversarial networks (cWGAN) and convolutional neural networks (CNN) models utilizing TensorFlow Python libraries with Keras API. The purpose of establishing the deep learning framework is to create more data on the parameters of unit cells such that we can select the cells whose mechanical properties fit our design goal.

Keywords: Pentamode Metamaterials, Deep Learning, Generative Modeling, Wasserstein Generative Adversarial Networks, Convolutional Neural Networks

1 INTRODUCTION

1.1 The development of pentamode (PM) metamaterials

The theoretical model of pentamode (PM) metamaterial first introduced by Milton and Cherkaev in 1995, is a model of a three-dimensional lattice of a solid structure formed with tetrahedral PM unit cells [1]. This PM structure has a high bulk modulus and low shear modulus. Kadic et al. [2] used the finite connection to replace the strictly point-like tips and found the ratio of bulk modulus to shear modulus of the 3D structure can realistically be made as large as about 1000. The feasibility of PM metamaterials acoustic cloaks was theoretically conceived by Milton et al. [3] and further improved by Norris [4].

1.2 Applying deep learning and generative adversarial networks (GAN) to metamaterial design

Deep learning [5, 6] is a subset of machine learning widely applied to the design of metamaterials. Wang et al. [7] invented a framework that has a variational autoencoder and a regressor for property prediction. The regressor plays a unique role to predict the labels for generated images in the deeper learning network. Shah et al. [8] introduced a semi-analytical method of suppressing acoustic scattering in which a reinforcement learning agent is used to control the parameters of cylindrical scatterers in water. Wiest et al. [9] studied how to improve the feasibility of using additive manufacturing technology for acoustic metamaterials and metasurfaces by multiple methods, including finite element method and appropriate metamodel for Monte Carlo simulations. Zaghloul et al. [10] built anisotropic radio-frequency metamaterial unit cells for metasurface arrays by employing deep convolutional GAN. Marburg et al. [11] invented a new method that uses conditional GAN to build a framework to generate unit cells for sound insulation purposes. Lai et al. [12] presented a method of developing the conditional Wasserstein GAN model to reduce the total scattering cross-section to near zero for a planar configuration of cylinders.

2 METHOD

The aim of this work is to design tetrahedral PM cells to construct a 3D lattice structure. The lattice structure is expected to have a high bulk modulus, low shear modulus, and acoustic properties similar to water.

2.1 PM model and data collection

The PM model studied by Matthew Kelsten et al. [13, 14] from Rutgers University is used as a reference for our design. In Figure 1, the unit cell is a face-centered cubic diamond-shaped lattice structure made up of cone linkages. The unit cells are modeled in COMSOL Multiphysics Commercial software using finite element analysis and Floquet-Bloch periodicity boundary conditions. The dimension and mechanical properties of the unit cells including the height, radius and connection angle of the cone, the density, impedance, bulk modulus and shear modulus, cutoff frequencies of upper and lower boundary of bandgap, are recorded in the excel file and split by the ratio of 6:1 into a training and testing set, and then loaded to the training networks as a CSV file.

Dimension of Unit Cell		Mechanical Properties	
Height(cm)	3.80	Density (g/m^3)	1.07
Ratio of two cones' radius	1.30	Ratio of bulk modulus vs. shear modulus	34.77
Ratio of height vs radius	1.30	Impedance (MPa·s/m)	3.43
Connection angle (degree)	135.00	Upper boundary cutoff frequency of bandgap(kHz)	126.65
Bottom radius vs. tip radius of the cone	4.00	Lower boundary cutoff frequency of bandgap(kHz)	78.90

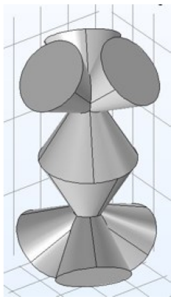


Figure 1. An example of the cell parameters and appearance. The dimensions of the cell in the left table are used to build the cell shown in the right image. The mechanical properties are obtained in COMSOL simulation and SOLIDWORKS.

2.2 Training with generative adversarial networks

In the inverse design process, we adapt ideas from Lai et al.'s conditional WGAN model [12] to fit our design. The flow for our network is shown in Figure 2. The generator is provided with random input vectors with real labels as a guide for image generation. The generated images and real images are provided to the critic. The critic learns to distinguish the images and generates a linear score between -1 and 1 which is fed back to the generator. The generator then learns to generate images such that the score decreases with each epoch, this makes the generator produce images that are more realistic. The fake images are fed to the auxiliary regressor, CNN model which is trained to predict the labels given the parameters of PM unit cell depicted in Figure 1. To assist the critic and generator to identify images, a CoordConv layer is added prior to the networks' convolutional layers. As the training loop executes, the GAN model loss is minimized as the generator and the critic losses converge and approach zero.

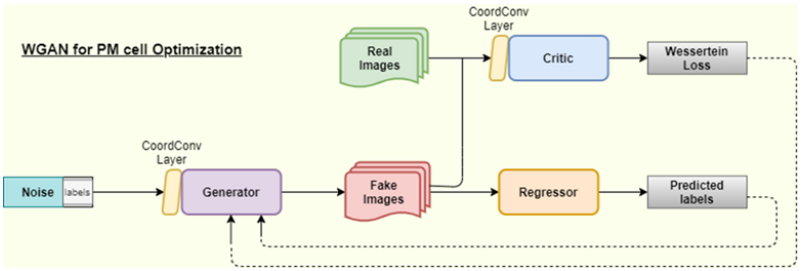


Figure 2. Conditional Wasserstein GAN (cWGAN) framework [12, 15].

3 RESULT

3.1 The result of cWGAN and CNN model

From the generated output, we carefully choose several sets of the unit cell (Table 1) whose mechanical properties fit the set requirements: impedance and density are closed to water. We find the ratio of bulk modulus vs. shear modulus is 35-45, and the gap between the cutoff frequency is about 40 kHz.

Dimension of Unit Cell				Mechanical Properties				
Height(cm)	Ratio of Two Cones' Radius	Ratio of Height vs Radius	Connection Angle (Degree)	Density (g/m^3)	Ratio of Bulk Modulus vs. Shear Modulus	Impedance (MPa·s/m)	Upper Boundary Cutoff Frequency of Bandgap(KHz)	Lower Boundary Cutoff Frequency of Bandgap(KHz)
3.800	1.300	1.405	135.863	1.020	44.106	1.452	117.484	76.676
4.212	1.300	1.347	135.868	1.053	40.538	1.509	110.706	70.041
4.410	1.348	1.350	135.813	1.050	41.412	1.516	104.289	65.126
3.911	1.300	1.300	135.954	1.087	37.827	1.523	123.311	77.337

Table 1. Properties of the generated unit cell. The left four columns show the dimension of the cell which determines the cell's mechanical properties shown in the five right columns. The impedance and the density are very close to the water.

3.2 The result of optimized cell and lattice design

We choose one of the optimized cells for PM lattice construction. The optimized unit cell is constructed and assembled into a lattice structure in SOLIDWORKS before importing to COMSOL. The full-wave simulation is conducted on the optimized PM lattice. The background pressure field of amplitude 1Pa is propagated from the left water body to the right. The amplitude of the reflected wave in the left water body is much smaller than the amplitude of the transmitted wave in the right water body at 22.5kHz as shown in Figure 3.

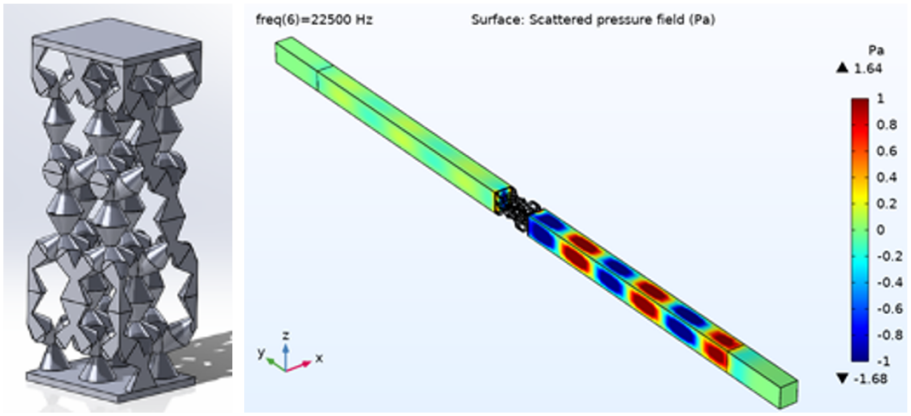


Figure 3. The left image is the lattice constructed by the optimized cells which are built by the generated parameters from the networks. The right image shows the scattered pressure field at 22.5 kHz during the full-wave simulation.

4 CONCLUSIONS

PM cell with high bulk modulus and low shear is designed with tetrahedral cones. The lattice built with PM cell is density matched with water initially. It is later matched with the acoustic impedance of water by inverse design using cWGAN. The cWGAN and CNN provide images of the cells along with the design parameters. The trained network is able to generate reasonably accurate designs for impedance matching. We utilize COMSOL Multiphysics, which proved to be an effective tool for conducting FEA analysis of the structures, performing

the acoustic study and full wave simulation. The result of full-wave transmission in COMSOL shows that the titanium lattice structure can transmit waves through it with minimum backward scattering waves.

REFERENCES

[1] Milton G. W. and Cherkaev A. V. Which Elasticity Tensors are Realizable? *Journal of Engineering Materials and Technology*, 117(4):483–493, 10 1995.

[2] Kadic M., Bückmann T., Stenger N., Thiel M., and Wegener M. On the practicability of pentamode mechanical metamaterials. *Applied Physics Letters*, 100(19):191901, 2012.

[3] Milton G., Briane M., and Willis J. On cloaking for elasticity and physical equations with a transformation invariant form. *New Journal of Physics*, 8(10):248–248, oct 2006.

[4] Norris A. Acoustic cloaking theory. *Proceedings of the Royal Society A: Mathematical, Physical and Engineering Sciences*, 464(2097):2411–2434, 2008.

[5] F. Chollet. *Deep Learning with Python*. Shelter Island, NY : Manning Publications Co.,, 2018.

[6] J. Brownlee. *Deep Learning With Python: Develop Deep Learning Models on Theano and TensorFlow Using Keras*. Machine Learning Mastery, 2016.

[7] Wang L.W., Chan Y. C., Ahmed F., Liu Z., Zhu P., and Chen W. Deep generative modeling for mechanistic-based learning and design of metamaterial systems. *Computer Methods in Applied Mechanics and Engineering*, 372:113377, 2020.

[8] Shah T., Zhuo L. W., Lai P., De La Rosa-Moreno A., Amirkulova F., and Gerstoft P. Reinforcement learning applied to metamaterial design. *The Journal of the Acoustical Society of America*, 150(1):321–338, 2021.

[9] Wiest T., Seepersad C., and Haberman M. Robust design of an asymmetrically absorbing willis acoustic metasurface subject to manufacturing-induced dimensional variations. *The Journal of the Acoustical Society of America*, 151(1):216–231, 2022.

[10] Hodge J. A., Mishra K. V., and Zaghloul A. I. Rf metasurface array design using deep convolutional generative adversarial networks. *presented at the 2019 IEEE International Symposium on Phased Array System & Technology, Waltham MA, USA*, pages 1–6, Oct.2019.

[11] Gurbuz C., Kronowetter F., Dietz C., Eser M., Schmid J., and Marburg S. Generative adversarial networks for the design of acoustic metamaterials. *The Journal of the Acoustical Society of America*, 149(2):1162–1174, 2021.

[12] Lai P., Amirkulova F., and Gerstoft P. Conditional wasserstein generative adversarial networks applied to acoustic metamaterial design. *The Journal of the Acoustical Society of America*, 150(6):4362–4374, 2021.

[13] Cushing C.W., Kelsten M.J., Su X.S., Wilson P.S., Haberman M.R., and Norris A.N. Design and characterization of a three-dimensional anisotropic additively manufactured pentamode material. *The Journal of the Acoustical Society of America*, 151(1):168–179, 2022.

[14] Kelsten M. Controlling wave propagation with acoustic and elastic metamaterials. *PhD Dissertation, Rutgers University*, Oct. 2021.

[15] Abbas A. Pentamode metamaterial design via full wave simulation and deep learning. *MSME Project Report, San Jose State University*, May 2021.

PROCEEDINGS of the
24th International Congress on Acoustics

October 24 to 28, 2022, in Gyeongju, Korea

Extended abstract

ABS-0036

Viscosity-Induced Nonreciprocity in Fluid-Solid Phononic Crystals With Broken Space Inversion Symmetry

Arkadii KROKHIN[1]; Hyeonu HEO[1]; Yuqi JIN[1]; Yurii ZUBOV[1]; Dmitrii SHYMKIV[1]; Tae-Youl CHOI[1]; Ezekiel WALKER[2]; Arup NEOGI[3]

[1] University of North Texas, USA

[2] Echonovus Inc., USA

[3] University of Electronic Science and Technology of China, China

ABSTRACT

Nonreciprocal propagation of sound becomes possible if the time reversal symmetry (*T* symmetry) of elastic medium is broken. Recent methods of *T* symmetry breaking are based on scattering actuated by nonlinear electric circuits, spinning of fluid, or nontrivial topological bands in acoustic spectrum. Here we report nonreciprocity in sound propagation in a phononic crystal (PhC) with broken *PT* symmetry. *T* symmetry is naturally broken in any fluid due to viscosity, however it is currently not recognized as a source of nonreciprocity. We show that dissipation leads not only to irreversibility but also to nonreciprocity if space inversion symmetry (*P* symmetry) is also broken. We study nonreciprocal propagation of sound through a PhC of asymmetric metal rods imbedded in water. Experiment is supported by numerical solution of the Navier-Stokes equation. It is shown that the viscous dissipation in a PhC with broken *P*-symmetry is nonreciprocal. Nonreciprocal contribution is separated from asymmetry by considering the limit of inviscid fluid.

Keywords: Boundary layer, Viscous dissipation, Acoustic diode

1. INTRODUCTION

In an ideal (inviscid) fluid sound transmission is reciprocal, i.e., acoustic pressure from the source emitting at point $\mathbf{r}_A$ and measured at point $\mathbf{r}_B$ is invariant with respect to switching of the positions of emitter and receiver,

$$p_A(\mathbf{r}_B) = p_B(\mathbf{r}_A). \tag{1}$$

As it was shown by Rayleigh [1], this property is due to potential flow of ideal fluid, where $\nabla \times \mathbf{v} = 0$, while the fluid velocity $\mathbf{v}$ in general case does not possess the reciprocal symmetry (1). The luck of this symmetry is attributed to asymmetry in scattering, caused by broken inversion symmetry (*P* symmetry) in the distribution of scatterers in space. As a result, the sound intensity $I(\mathbf{r}) = p(\mathbf{r})v(\mathbf{r})$ is also asymmetric, $I_A(\mathbf{r}_B) \neq I_B(\mathbf{r}_A)$, as well as the transmission coefficient obtained by integration of intensity over some area. The asymmetry of the transmission coefficient has been used for the design of sound rectification devices [2-4]. While they provide almost unidirectional propagation of sound, they are reciprocal by nature [5] since they do not break time-reversibility, if dissipative losses are neglected. Viscosity is a natural factor that makes fluid dynamics irreversible and nonreciprocal. However, for a long time it was considered that viscosity does not violate reciprocity in transmission of acoustic signals. Even very recent reviews claim that since Eq. (1) remains valid for a viscous fluid, viscous damping breaks reversibility but not reciprocity [6,7]. Here we demonstrate that broken *P* symmetry, that leads to asymmetry in transmission in an ideal fluid, serves as a source of *nonreciprocal dissipation* in a viscous fluid, thus adding truly nonreciprocal contribution to the transmission.

[1] arkady@unt.edu

2. NONRECIPROCAL TRANSMISSION TROUGH PHONONIC CRYSTAL WITH ASYMMETRIC SCATTERERS

The power dissipated within some volume V due to viscous attenuation of sound wave depends on all spatial derivatives of the velocity vector $\mathbf{v}$

$$\dot{Q} = -\int \left[\frac{\eta}{2}\left(\frac{\partial v_i}{\partial x_k} + \frac{\partial v_k}{\partial x_i}\right)^2 + \xi(\nabla \cdot \mathbf{v})^2\right] dV. \quad (2)$$

Here η and ξ are the viscosity coefficients. In a system of scatterers with broken P symmetry the distribution of velocities in space is different for the opposite directions of propagation of sound. This leads to different levels of dissipated power, i.e., transmission is not reciprocal. In an inviscid fluid the transmission contains the asymmetric part which should be subtracted in order to get truly nonreciprocal transmission caused by nonreciprocal dissipation. In presence of solid scatterers dissipation occurs mainly within a narrow boundary layer $\delta = \sqrt{2\eta/\omega\rho}$ formed around each scatterer. Here the level of turbulency reaches its maximum since the value of $\nabla \times \mathbf{v}$ exceeds much that value in the bulk. This means that dissipative losses in the bulk can be neglected, and attenuation of sound occurs due to viscous losses in the layer δ [8].

For experimental demonstration of nonreciprocal transmission [9], a phononic crystal of aluminum rods in water environment was used, see Fig. 1. The period of the phononic crystal lattice is 5.5 mm,

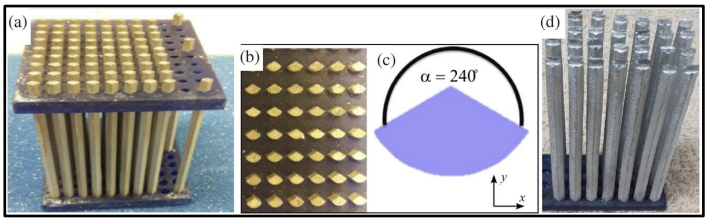


Fig. 1. (a) View of the sample with anodized rods. (b) The P symmetry is broken along the vertical axis. (c) Square unit cell. The angle α is a measure of broken P symmetry. (d) Sample with 4×7 rows of unanodized aluminum rods [9].

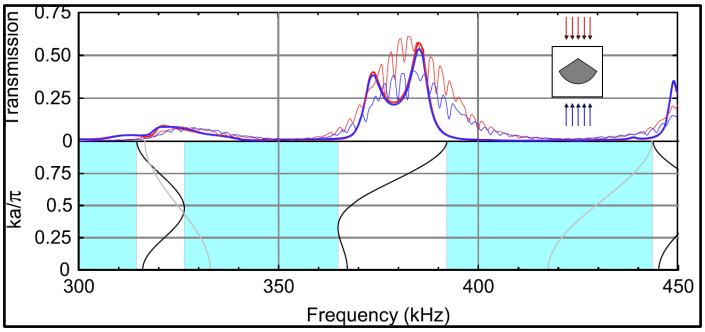


Fig. 2. Lower panel: Band structure for sound propagating along the direction of broken P symmetry. Gaps between the even zones (black) are shaded. The odd zones (grey) are def at normal incidence. Upper panel: Thin (thin) red and blue lines are experimental (numerical) spectra for forward and backward propagation. Insert: orientation of the unit cell with respect to the incoming wave [9].

and the radius of the 120° circle sector is 2.2 mm. Two V301 1`` Panametrics 0.5 MHz immersion transducers in a bistatic setup were arranged to measure forward and backward transmission. First, the transmission was measured along the symmetric direction. Due to the inverse symmetry, the transmission does not exhibit any regular feature of nonreciprocity. The sound waves experience anisotropic scattering at each rod, but they follow the same "path" propagating forward and backward.

Unlike this, the transmission spectra for propagation along the line of broken P symmetry exhibit regular features of nonreciprocity. In Fig. 2, experimental (thin lines) and numerical results (thick lines) for the transmission in two opposite directions are plotted together. Theoretical and experimental results are in reasonable agreement. All the gaps and passing bands of the band structure in Fig. 2 are seen in the measured transmission spectra. The experimental curve exhibits fast oscillations which originate from weak irregular fluctuations of the transmitted energy in Fig. 3. While there is a general agreement between the theory and experiment, it is clearly seen that the measured nonreciprocity exceeds the numerically simulated one. We attribute this difference to microscopic roughness of the aluminum rods. The rods were anodized to increase their resistance against oxidation in water. It is known that the surface of an anodized sample may have roughness of the size order from a few to dozens of microns. At this scale, the surface of the rods is not flat. At the frequencies $\omega \sim 10^6\ s^{-1}$ the thickness of the viscous boundary layer δ is estimated to be ideally about a few microns. Roughness not only changes fluid dynamics within the boundary layer but it also increases the effective area where the energy dissipates. Thus, surface roughness increases the dissipation of sound energy that leads to stronger nonreciprocity. In the experiment with unanodized rods possessing

more rough surfaces the level of nonreciprocity reached 30 dB [9]. Random roughness also can be considered as a stochastic element of the system that breaks the *P* symmetry at the microscopic level. At the same time, the micron-size roughness does not contribute much to scattering, because the wavelength of sound in water is about 4-5 mm. A phononic crystal where each cylinder has half of its surface flat and the other half is rough is an example of a system with weakly broken *P* symmetry and weak asymmetry in transmission [10].

Controlled roughness was introduced to the cylindrical rods using sandblasting and sandpaper of varying grain sizes where the average roughness σ = 140 μm [10]. Stainless steel rods of diameter *D* = 6.35mm were cut from quarter-inch stock and arranged in a square lattice with period *a* = 10.3 mm. Each rod was masked using a mould and a razor blade to uniformly cover half of the rod with tape. The tape acted as a resist when the rods were sandblasted to create lower levels of surface roughness. For increased roughness, a grit of sandpaper was chosen for testing with the thickness of the sandpaper measured as a tenth of a millimetre. The sandpaper covering precisely half of the cylindrical surface was cut using a laser cutter. After the sandpaper strips were cut to size, they were glued to the rods using cyanoacrylate adhesive to have the best bond between the sandpaper and the steel rod.

For frequencies within the interval 400–600 kHz, the wavelength λ changes from 3.7 to 2.5 mm. For any frequency from this region, the inequality $\sigma, \delta \ll \lambda$ is satisfied, that guarantees weak random scattering at the rough side of each cylinder. In Fig. 3a the transmission spectra measured along the

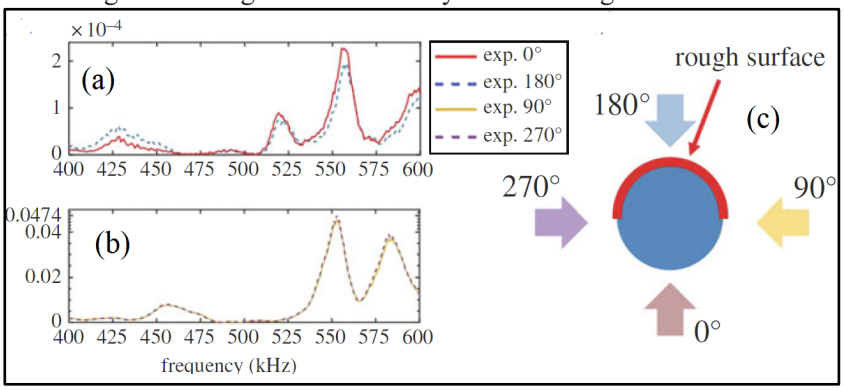


Fig. 3. Experimental spectra for phononic crystal with roughness σ = 140 μm . (a) Transmission along the direction with broken *P* symmetry. Nonreciprocity is clearly seen. (b) The transmission is reciprocal along the *P* symmetric direction. (c) The directions of the incident wave are shown with respect to the orientation of asymmetric cylindrical scatterer.

direction of broken *P* symmetry exhibit nonreciprocity [10]. Since the asymmetry in transmission is minimal for the cylindrical scatterers, the difference in transmission is mostly due to nonreciprocity in viscous absorption. For the *P* symmetric direction the transmission spectra are identical, see Fig. 3b.

To separate exactly the asymmetric and nonreciprocal contributions, numerical simulations were performed for a hard cylindrical scatterer of the same diameter *D* = 6.35 mm as was used in the experiment. One half of the cylinder was flat, and the other is covered by regular roughness with either σ=10 μm or σ=100 μm, see Fig. 4a. Sound emitter and receiver were placed at the symmetrical points *A* and *B*. To verify the reciprocal relation (1) the following parameter

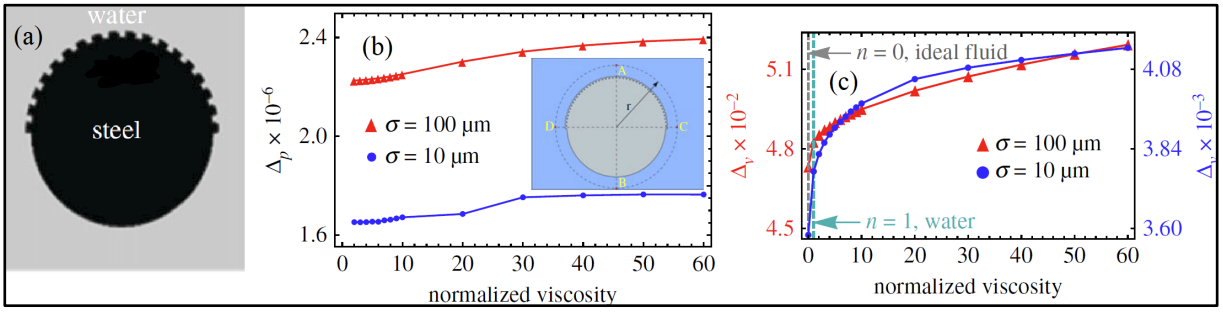


Fig. 4. Numerically simulated nonreciprocity for a single scatterer. (a) Cylindrical hard scatterer with roughness. (b) Non-reciprocity for pressure versus normalized viscosity η/ηwater calculated for the source and receiver placed at the symmetrical points *A* and *B* situated 5mm away from the center. (c) Non-reciprocity for velocity **v** versus normalized viscosity η/η_{water} calculated for the source and receiver placed at the symmetrical points *A* and *B* situated 5 mm away from the center. The left (right) vertical axis is for roughness with σ = 100μm (σ = 10μm).

$$\Delta_p = 2\frac{p_A(\mathbf{r}_B) - p_B(\mathbf{r}_A)}{p_A(\mathbf{r}_B) + p_B(\mathbf{r}_A)} \qquad (3)$$

was plotted as a function of normalized viscosity η/η_{water} in Fig. 4b. Similar parameter, Δ_v, was

calculated for the modulus of velocity v of water oscillations and it was plotted in Fig. 4c. The numerical values for Δ_p presented in Fig. 4b are very small and they do not grow with viscosity. This result suggests that pressure is a reciprocal quantity even in a viscous fluid. The graphs in Fig. 4c clearly demonstrate that the non-reciprocity in v, which exists even in ideal fluid $\eta = 0$, grows fast with η. The difference $v(\eta) - v(\eta = 0)$ is the contribution of the vorticity mode with $\nabla \times \mathbf{v} \neq 0$ of velocity to non-reciprocity. Two curves for σ = 10 and 100μm demonstrate the same monotonic behavior. Both curves exhibit square-root dependence at $\eta \to 0$, which is due to $\delta \sim \sqrt{\eta}$. The values of non-reciprocity obtained for σ = 10μm (right vertical axis in Fig. 4c) are approximately 10 times less than the values obtained for σ = 100μm (left vertical axis), i.e., $\Delta_v \sim \sigma$. This linear scaling of velocity corresponds to quadratic scaling of dissipation in Eq. (2), where $\dot{Q}$ is a quadratic functional of $\mathbf{v}$.

3. CONCLUSIONS

Nonreciprocal acoustic transmission through a dissipative phononic crystal with asymmetric scatterers was demonstrated experimentally and numerically. The time-reversal symmetry is naturally broken by viscous losses. Nonreciprocal contribution to acoustic transmission appears due to asymmetry in the field of fluid velocities that leads to nonequal viscous dissipation for the opposite directions of sound propagation. The asymmetry in distribution of velocities appears even in ideal (inviscid) fluid. Presence of viscosity leads to formation of the viscous boundary layers near each scatterer, where vortex component of velocity gives truly nonreciprocal contribution to attenuation of sound. This natural mechanism of nonreciprocity opens a possibility for engineering of acoustic nonreciprocal devises, like acoustic diode, which operate without external sources of energy.

ACKNOWLEDGEMENTS

This work was supported by the National Science Foundation under EFRI grant no. 1741677.

REFERENCES

1. Rayleigh JWS. The theory of sound. 2nd ed. New York, USA: Macmillan;1896.
2. Liang B, Guo XS, Tu J, Zhang D, Cheng JC. An acoustic rectifier. Nat. Mater. 2010; 9: 989–992.
3. Li X-F, Ni X, Feng L, Lu M-H, He C, Chen Y-F. Tunable unidirectional sound propagation through a sonic-crystal-based acoustic diode. Phys. Rev. Lett. 2011; 106: 084301.
4. Zhu J, Zhu X, Yin X, Wang Y, Zhang X. Unidirectional extraordinary sound transmission with mode-selective resonant materials. Phys. Rev. Appl. 2020; 13: 041001.
5. Maznev AA, Every AG, Wright OB. Reciprocity in reflection and transmission: what is a 'phonon diode'? Wave Motion. 2013; 50: 776.
6. Nassar H, Yousefzadeh B, Fleury R, Ruzzene M, Alú A, Daraio Ch., Norris AN, Huang G, Haberman MR. Nonreciprocity in acoustic and elastic materials. Nat. Rev. Mater. 2020; 5: 667–685.
7. Rasmussen C, Quan L, Alù A. Acoustic nonreciprocity. J. Appl. Phys. 2021; 129: 210903.
8. IbariasM, Zubov Yu., Arriaga J, Krokhin AA. Phononic crystal as a homogeneous viscous metamaterial. Phys. Rev. Res. 2020; 2: 022053.
9. Walker E, Neogi A, Bozhko A, Zubov Yu., Arriaga J, Heo H, Ju J, Krokhin AA. Nonreciprocal linear transmission of sound in a viscous environment with broken P symmetry. Phys. Rev. Lett. 2018; 120: 204501.
10. Heo H, Walker E, Zubov Y, Shymkiv D, Wages D, Krokhin A, Choi T-Y, Neogi A. Non-reciprocal acoustics in a viscous environment. Proc. R. Soc. A. 2020; 476: 20200657.

PROCEEDINGS of the
24th International Congress on Acoustics
October 24 to 28, 2022, in Gyeongju, Korea

Extended abstract

ABS-0051

Hybrid analytic model between the transfer-matrix method and the modal decomposition to design Acoustic Metamaterials: Application to degenerate resonators

Vicente ROMERO-GARCÍA[1,*], Jean-Philippe GROBY[2], Noé JIMÉNEZ[3], Aurelien MERKEL[4], Vincent TOURNAT[2], Georgios THEOCHARIS[2], Olivier RICHOUX[2] and Vincent PAGNEUX[2]

[1]Instituto Universitario de Matemática Pura y Aplicada, Departamento de Matemática Aplicada, Universitat Politècnica de València, Camino de Vera s/n, 46022, València, Spain

[2]Laboratoire d'Acoustique de l'Université du Mans (LAUM), LAUM UMR CNRS 6613, Institut d'Acoustique—Graduate School (IA-GS), CNRS, Le Mans Université, France

[3]Instituto de Instrumentación para Imagen Molecular, Consejo Superior de Investigaciones Científicas, Universitat Politècnica de València, Camino de vera s/n, València 46022, Spain, Spain

[4]Institut Jean Lamour, University of Lorraine, 2 allée André Guinier, 54011 Nancy, France, France

ABSTRACT

Plane waves are usually assumed to design acoustic metamaterials. This assumption is most of the times satisfying, but prevents from accounting for the possible evanescent coupling between the elements of the acoustic metamaterial. In this talk, we present a hybrid analytical model between the transfer-matrix method inside the structured material and the modal decomposition in the surrounding domains. We apply this method to the analysis of the scattering properties of a mirror-symmetric absorber made of several slits loaded by Helmholtz resonators. The transfer-matrix model is used to describe the propagation within each slit, while the modal decomposition is used to described the acoustic field in the surrounding domains. Modal decomposition assumes Bloch waves; thus, it accounts for the possible evanescent coupling between the slits. The domains are matched through the continuity conditions between the exterior media and each slit. This method is coupled to an optimization procedure to design single frequency perfect mirror symmetric absorbers. The results are numerically and experimentally validated showing good agreement with the proposed hybrid model.

Keywords: Sound, Insulation, Transmission

1. INTRODUCTION

Metamaterials made of Helmholtz resonators (HRs) have been exploited during the last year to control acoustic waves [1-4]. Different applications have been developed to attenuate [5], to control the directivity [6, 7] or to absorb acoustic waves [8-11]. In most of the cases the resulting structures are periodic to simplify its modeling. Usually, the transfer matrix method is used to analytically describe the behavior of these systems, i.e., assuming propagation of plane waves and neglecting the higher orders. Moreover, the periodicity implies the existence of Bloch waves that can also produce possible evanescent coupling between the building blocks of the metamaterials. Sometimes, and in some regions of frequencies these Bloch waves can be neglected, but in general and in reality, they produce couplings that make the modeling by the transfer matrix method wrong.

In this work we show an anytically a hybrid model combining transfer matrix and modal decomposition methods used to model a metascreen consisting of a periodic array of slits loaded by different HRs. The transfer matrix model [12] is used to describe the propagation within each slit while the modal decomposition is used to obtain the propagation in the exterior domain considering the Bloch waves accounting for the possible evanescent coupling between the slits. The two domains are coupled through the continuity conditions between the exterior medium and each slit. A full-wave numerical simulation is used to validate the analytical model. A design of a metascreen made of mirror-symmetric resonant building blocks possessing degenerate resonances is used to show the dramatic effect of the evanescent coupling on the acoustic perfect absorption. The metascreen is experimentally tested in a square cross-sectional impedance tube showing very good agreement with the analytical and numerical predictions.

2. THE SETUP

The schematic view of the metascreen design that we analyze in this work, shown in Fig. 1(a), is a combination of slits loaded by one and two resonators [11]. The HRs are made by combining two different elements playing the role of the neck and the cavity. Due to the symmetry of the system, the scattering is reciprocal and symmetric. The metascreen is radiated by a plane wave from the top to the bottom in the medium $\Theta^{(0+)}$. Viscothermal losses are accounted for by using the Stinson's equivalent expressions for the complex and frequency dependent of the density and wavenumber in the slits, necks and cavities of the structure [13].

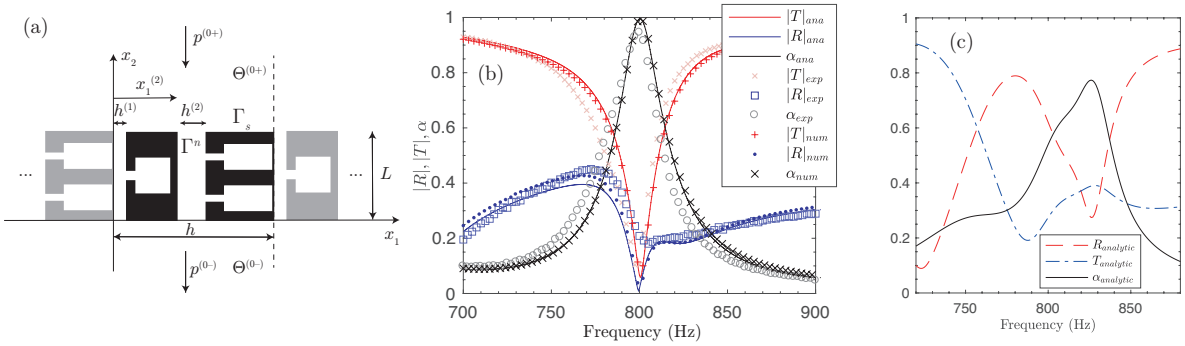


Figure 1. (a) Schematic view of the analyzed metascreen made of two slits loaded by Helmholtz resonators. (b) Analytical, numerical and experimental scattering coefficients of the metascreen. (c) Scattering coefficients considering only the plane wave approximation, i.e., the transfer matrix method.

3. THEORETICAL MODELING

The acoustic field in the exterior domains ($\Theta^{(0+)}$ and $\Theta^{(0-)}$ as defined in Fig. 1(a)), when the system is excited by a plane wave $\vec{\mathrm{k}}=(\mathrm{k}_1,\mathrm{k}_2)$ can be written as

$$p^{0+}=\sum_q\left[e^{-\imath k_{2q}^0(x_2-L)}\delta_q+R_q e^{\imath k_{2q}^0(x_2-L)}\right]e^{\imath k_{1q}^0 x_1} \quad \text{in} \quad \Theta^{0+}$$

$$p^{(0-)}=\sum_q T_q e^{\imath k_{1q}^0 x_1-\imath k_{2q}^0 x_2} \quad in \quad \Theta^{0-},$$

where the subindex q indicates the order of the Bloch wave, with $k_{1q}^0=2q\pi/2d_0+k_1^i$ and $k_{2q}^0=\sqrt{\left(\left|\overrightarrow{k^0}\right|\right)^2-\left(k_{1q}^0\right)^2}$, with $Re\left(k_{2q}^0\right)\geq 0$, R_q and T_q are the reflection and transmission coefficients of the q-th Bloch wave, δ_q is the Kronecker's delta and L is the thickness of the acoustic metascreen.

Wave propagation in each slit is modeled by the transfer matrix method (TMM), in which the HRs are considered as 1D point scatterers. Matrices describing the propagation in the slit, to the side branch resonators and to the section mismatch are assembled giving the total transfer matrix. The TMM assumes the plane-wave propagation in each element, which is valid in the low frequency regime. The radiation corrections are included in the impedances of the resonators to mimic the effect of the higher order modes. Therefore, the wave propagation through the slit *n* can be modeled as

$$\begin{bmatrix} p^{(n)} \\ v_2^{(n)} \end{bmatrix}_{x_2=L} = \begin{bmatrix} T_{11}^{(n)} & T_{12}^{(n)} \\ T_{21}^{(n)} & T_{22}^{(n)} \end{bmatrix} \begin{bmatrix} p^{(n)} \\ v_2^{(n)} \end{bmatrix}_{x_2=0},$$

where the final transfer matrix is given by the product of the transfer matrices of the *N* elements in the *n*-th slit.

Once the acoustic fields inside each domain of the problem are defined, the continuity boundary conditions must be applied. These conditions read as

$$p^{(0+)} = p^n \ on \ \Gamma^n \ at \ x_2 = L,$$
$$p^{(0-)} = p^n \ on \ \Gamma^n \ at \ x_2 = 0,$$
$$v_2^{(0+)} = v_2^n \ on \ \Gamma^n \ at \ x_2 = L,$$
$$v_2^{(0+)} = 0 \ on \ \Gamma_s \ at \ x_2 = L,$$
$$v_2^{(0-)} = v_2^n \ on \ \Gamma^n \ at \ x_2 = 0,$$
$$v_2^{(0-)} = 0 \ on \ \Gamma_s \ at \ x_2 = 0,$$

where Γ_s represents the rigid interfaces on the two faces of the metascreen, and Γ^n is the interface between the *n*-th slit and the surrounding media $\Theta^{(0^+)}$ and $\Theta^{(0^-)}$. These conditions lead to a system of equations after projection on the adequate orthogonal modes. The system is solved for the scattering coefficients of the system.

In order to validate this model, we have used a finite element method (FEM) simulation. A plane wave impinges the system and the complete geometry is considered using the radiation conditions that simulate the Sommerfeld conditions at the limits of the numerical domain.

4. RESULTS

The model is used to calculate the absorption coefficient of the designed metascreen. Figure 1(b) shows the scattering coefficients of the full transmission problem. The agreement between the model, the numerical simulations and the experimental results is very good. Note here that the presence of the Bloch waves is crucial in this kind of systems: if only plane waves had been accounted for in the system, the model would not have reproduced the whole wave process because the evanescent coupling would have been neglected as shown in Fig. 1(c). When the Bloch waves are considered, a perfect absorption peak is observed at 800 Hz as analytically, numerically and experimentally observed. It is worth noting here that perfect absorption is very sensible to the geometry of the resonators, and this would explain the slight discrepancies between the analytical or numerical predictions and the experimental results.

5. CONCLUSIONS

The resonant scattering produced by the metascreen is analytically studied by a hybrid model mixing the transfer matrix method and the modal decomposition accounting for the Bloch waves in order to consider the possible coupling between the slits. Note that this coupling is particularly important for the present topology. If no higher order Bloch waves had been accounted for, i.e., if only the plane wave had been accounted for outside the metascreen, the analytical model would not have been in agreement with neither the full-wave numerical simulation nor the experimental results. The structure is experimentally tested in a square impedance tube showing good agreement with the analytical and numerical predictions. The Physics behind this work will motivate the development of broadband and perfect absorption for ventilation problems using cascade processes similar to the case of the rainbow trapping for the unidirectional absorption.

ACKNOWLEDGEMENTS

The authors gratefully acknowledge the ANR-RGC METARoom (ANR-18-CE08-0021) project. This publication is part of the R&D&I Project/Grant No. PID2020-112759GB-I00 funded by MCIN/AEI/10.13039/501100011033/.

REFERENCES

1. A. Merkel, G. Theocharis, O. Richoux, V. Romero-García, and V. Pagneux, “Control of acoustic absorption in one-dimensional scattering by resonant scatterers,” Appl. Phys. Lett. 107, 244102 (2015), https://doi.org/10.1063/1.4938121.
2. J.-P. Groby, W. Huang, A. Lardeau, and Y. Aurégan, “The use of slow waves to design simple sound

absorbing materials," J. Appl. Phys. 117, 124903 (2015), https://doi.org/10.1063/1.4915115.
3. J.-P. Groby, R. Pommier, and Y. Aurégan, "Use of slow sound to design perfect and broadband passive sound ab- sorbing materials," J. Acoust. Soc. Am. 139, 1660–1671 (2016), https://doi.org/10.1121/1.4945101.
4. P. Wei, C. Croënne, S. Tak Chu, and J. Li, "Symmetrical and anti-symmetrical coherent perfect absorption for acoustic waves," Appl. Phys. Lett. 104, 121902 (2014), https://doi.org/10.1063/1.4869462.
5. G. Theocharis, O. Richoux, V. Romero-García, A. Merkel, and V. Tournat, "Limits of slow sound and transparency in lossy locally resonant periodic structures," New J. Phys. 16, 093017 (2014).
6. N. Jiménez, T.J. Cox, V. Romero-García, J.-P. Groby, Metadiffusers: Deep-subwavelength sound diffusers, Scientific reports 7 (1), 1-12, (2017).
7. E. Ballestero, N. Jiménez, J.-P. Groby, H. Aygun, S. Dance, V. Romero-García, Metadiffusers for quasi-perfect and broadband sound diffusion, Applied Physics Letters 119 (4), 044101, (2021)
8. N. Jiménez, W. Huang, V. Romero-García, V. Pag- neux, and J.-P. Groby, "Ultra-thin metamaterial for perfect and quasi-omnidirectional sound absorption," Appl. Phys. Lett. 109, 121902 (2016), https://doi.org/10.1063/1.4962328.
9. N. Jiménez, V. Romero-García, V. Pagneux, and J.-P. Groby, "Rainbow-trapping absorbers: Broadband, perfect and asymmetric sound absorption by subwavelength panels for transmission problems," Sci. Rep. 7, 13595 (2017).
10. M. Yang, C. Meng, C. Fu, Y. Li, Z. Yang, and P. Sheng, "Subwavelength total acoustic absorption with degenerate resonators," Appl. Phys. Lett. 107, 104104 (2015), https://doi.org/10.1063/1.4930944.
11. V. Romero-García, N. Jiménez, J.-P. Groby, A. Merkel, V. Tournat, G. Theocharis, O. Richoux, V. Pagneux, Perfect absorption in mirror-symmetric acoustic metascreens, Physical Review Applied 14 (5), 054055, (2020)
12. Jiménez N., Groby JP., Romero-García V. (2021) The Transfer Matrix Method in Acoustics. In: Jiménez N., Umnova O., Groby JP. (eds) Acoustic Waves in Periodic Structures, Metamaterials, and Porous Media. Topics in Applied Physics, vol 143, pp. 103-164. Springer, Cham. https://doi.org/10.1007/978-3-030-84300-7_4
13. M. R. Stinson, "The propagation of plane sound waves in narrow and wide circular tubes, and generalization to uniform tubes of arbitrary cross-sectional shape," J. Acoust. Soc. Am. 89, 550–558 (1991), https://doi.org/10.1121/1.400379.

PROCEEDINGS of the
24th International Congress on Acoustics

October 24 to 28, 2022, in Gyeongju, Korea

Extended abstract

ABS-0053

Shannon entropy applied to acoustics: Characterization of avoided crossings in acoustic superlattices

José SÁNCHEZ-DEHESA[1] and J. Ricardo ARIAS-GONZALEZ[2]

[1]Department of Electronic Engineering, Wave Phenomena Group, Universitat Politècnica de València, Spain

[2]Department of Applied Physics, Centro de Tecnologías Físicas, Universitat Politècnica de València, Spain

ABSTRACT

Shannon's information entropy is here employed as a characterization tool in acoustics. The displacement field u(r) is used to define the probability distribution function P(r), which is further embedded in the well-known formula of Shannon entropy, $S_u(r)$. We show that $S_u(r)$ describes fairly well the delocalization of the acoustic modes appearing in the Zener-like effect characterized in ultrasonic superlattices [see Phys. Rev. Lett., 98, 134301 (2007)]. We analyze the case of a multilayer made of coupled water cavities separated by metamaterial slabs. The results demonstrate that the acoustic's Shannon entropy maximizes at the critical gradient where the two eigenmodes anticross, indicating maximum spreading of both modes. Our proposal can be considered as an alternative to the inverse participation ratio, which is usually employed to characterize localization effects.

Keywords: Shannon entropy, Zener-like effect, acoustic superlattices.

1. INTRODUCTION

Shannon's informational entropy [1] has been applied in the study of novel and counterintuitive ways of processing and transmitting information in the quantum realm. More recently, the application of Shannon's formula to different physical phenomena in crystallography [2] and atomic physics [3] opened new avenues of interpretation.

This work introduces Shannon entropy in specific situations in the acoustic realm where the localization of acoustic eigenmodes plays a relevant role. To characterize the spatial spreading of eigenmodes there are several indicators like the inverse participation ratio [4]. However, since the Shannon entropy is a more global concept, we explore here its application as a new characterization tool in acoustics.

The proposed formula for the Shannon entropy in acoustics is based on the displacement fields of the corresponding eigenmodes and it is applied to characterize the delocalization effect taking place in the Zener-like effect discovered in acoustic superlattices [5, 6].

2. SHANNON ENTROPY IN ACOUSTICS

The formula for the Shannon entropy in atomic physics, S_ϱ, employs the probability density distribution of a given electronic state $\varrho(\vec{r}) = |\Psi(\vec{r})|^2$ to define $S_\varrho = -\int \varrho(\vec{r})\, ln\varrho(\vec{r}) d\vec{r}$. To introduce the corresponding formula in acoustics, we exploit the analogy between bound or quasi-bound states in electronic superlattices with the localized or quasi-localized states in slabs made of cylindrical rods embedded in a fluid-like background [7]. The displacement field, $u(\vec{r})$, characterize the localization of the acoustic eigenstates, which will decay after some delay time. Therefore, the corresponding probability distribution function is:

[1] jsdehesa@upv.es
[2] ricardo.ariasgonzalez@upv.es

$$P(\vec{r}) = {|u(\vec{r})|^2}\Big/{\int |u(\vec{r})|^2 d\vec{r}}\ , \tag{1}$$

which is obtained by normalizing the square of the displacement field of the acoustic level under consideration. Therefore, the Shannon entropy is

$$S_u = -\int \mathcal{P}(\vec{r}) ln \mathcal{P}(\vec{r}) d\vec{r} \tag{2}$$

This quantity should be considered as a measure of the uncertainty of the localization of sound. Notice that this quantity increases with the spreading of the displacement field of the acoustic eigenstate and, consequently, increases with increasing uncertainty. Since we are in the approach of linear acoustics, the Shannon entropy in (1) can be also obtained by using alternative expressions for the probability $\mathcal{P}(\vec{r})$ in (1), involving the particle velocity or the acoustic pressure.

3. CHARACTERIZATION OF AVOIDED CROSSING IN ACOUSTIC SUPERLATTICES

Avoided crossing between two electronic states has been characterized, for example, in atomic physics when the levels are submitted to strong parallel magnetic and electric fields [3]. In acoustics, the phenomenon of avoided crossing between two acoustics eigenmodes has been described in the acoustic analog of the Zener effect, where one component of an acoustic superlattice consists of a gradient of thicknesses [5-6]. In what follows, it is shown how the expressions (1)-(2) defining the Shannon entropy in acoustics describe fairly well the localization effects taking place around the critical gradient where the avoided crossing appears.

Let us consider the case of a finite acoustic superlattice consisting of m coupled water cavities W_m separated by m+1 slabs A made of a two-dimensional periodic distribution of rigid rods embedded in the water background [6,8. In the homogenization limit, slabs A can be tailored with the following dynamical mass density and sound speed: $\rho_A = 5\rho_W$ and $c_A = 0.78c_W$, where ρ_A and c_W are, respectively, the density and sound speed in the water; i.e., ρ_W=1 g/cm^3 and c_W=1480 m/s. The results for the case of a perfect superlattice (with m=8 and d_W=2d_A) are represented in Figure 1(a), where the transmission spectrum (right panel) shows two clear minibands MB1 and MB2. The left panel represents the $\log|u(z)|^2$ and shows that modes in MB1 are strongly localized in the water cavities while the localization of modes in MB2 is not clearly defied. In order to observe the avoided crossing, we follow the procedure described in [5] and introduce a gradient in the thicknesses of water cavities, $\Delta(1/d_{W\ell})$, which is defined as

$$\Delta(1/d_W) = [(1/d_{W\ell}) - (1/d_{W\ell-1}] / (1/d_{W1}), \tag{3}$$

where d_{W1} = 0.08 cm is the thickness of the first (ℓ = 1) cavity.

Figure 1(b) shows the results corresponding to the critical gradient (10.04%) where the Zener-tunneling (ZT) like effect takes place. The transmission profile shows a double peak defined by ZT in Fig. 1(b).

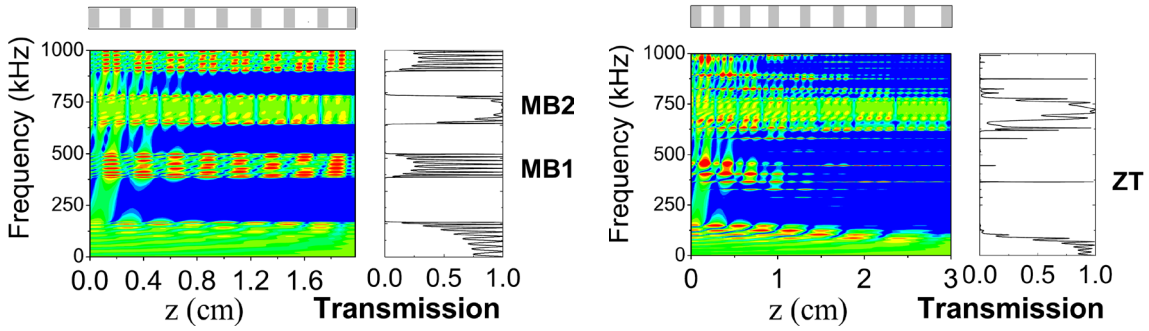


Figure 1: (a) Transfer matrix calculation for the square of the displacement field amplitude of the sound in the acoustic superlattice schematically deployed on top. White (grayed) stripes represent

the water (metamaterial) slabs. (b) The results correspond to the case in which the water layers have a critical gradient of thicknesses and the Zener tunneling (ZT) appears.

The double peak indicating the avoided crossing is better described in Fig. 2, where the shape of the ZT peak is represented for several values of the gradient (in %). The minimum separation between levels corresponds to the critical gradient.

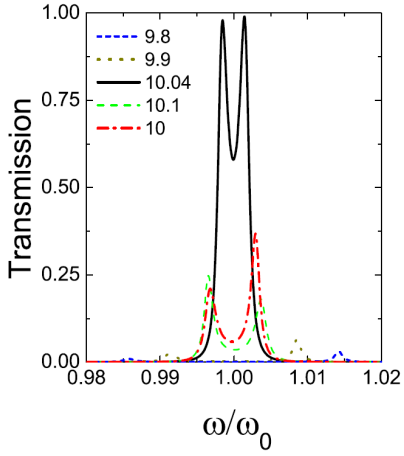


Figure 2. Transmission spectrum of an acoustic multilayer made of eight layers of water surrounded by nine layers of metamaterial slabs. The transmission is plotted for several values of the gradient (in %) of thicknesses applied to the water cavities. All the metamaterial slabs have the same thickness d_A. The frequencies are in reduced units, where ω_0 is the central frequency at each gradient.

The frequency and Shannon entropy on the pair of levels involved in the avoided crossing are represented in Fig. 3(a) and 3(b), respectively. In Fig. 3(a), it is observed how the lower level u_1 (blue line) and the upper-level u_2 (red line) anticross at the critical gradient of 10.04%. On the other hand, in Fig. 3(b), it is observed how the Shannon entropy takes maximum values for both levels at the critical gradient, indicating the maximum delocalization of both levels.

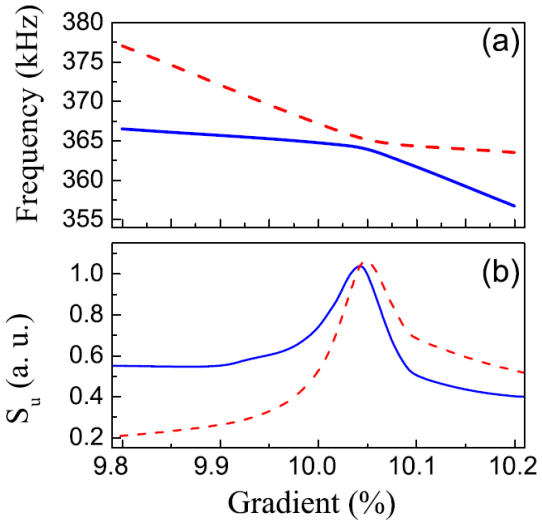


Figure 3: (a) Frequency of the two interacting modes calculated as a function of the gradient of the water cavities defining the acoustic superlattice. (b) The corresponding Shannon entropy calculated with the expressions (1)-(2).

In order to support the claim of maximum delocalization described by the values of the Shannon entropy at the critical gradient, Fig. 4 depicts the amplitude of the acoustic modes for three values of the gradient. Notice how the spreading of the modes is dependent on the gradient defining the thicknesses of the water layers. Particularly, at the critical gradient, where a "bonding-antibonding" combination of the respective "wavefunction" takes place, the spreading of both levels is maximum. Therefore, the Shannon entropy can be considered a useful characterization tool to describe the anti-crossing of levels appearing in acoustic structures. A maximum value of the Shannon entropy indicates the maximum spreading of the acoustic levels and, therefore, the exact location of the avoided-

crossing effect [9].

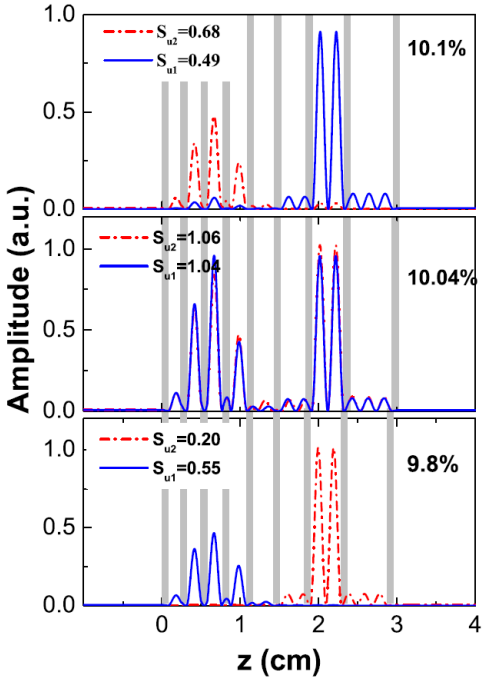


Figure 4: Amplitude of the acoustic modes u_1 (blue lines) and u_2 (red lines) involved in the Zener-like acoustic phenomenon. The amplitude is depicted for three values of the gradient defining the thicknesses, $d_{W\ell}$, of the water cavities. The vertical grayed stripes define the metamaterial slabs enclosing the water cavities. At the critical gradient of 10.04% (central panel), both modes show the maximum spreading across the acoustic structure.

ACKNOWLEDGEMENTS

Both authors acknowledge Helios Sanchis-Alepuz for his contribution to this work. JS-D acknowledges the financial support by the RDI grant PID2020-112759GB-2I100 funded by MCIN/AEI/10.13039/501100011033. The work of JRA-G has been supported by the grant with Ref. PID2019-107391RB-I00.

REFERENCES

1. Shannon CE. A mathematical theory of communications Bell Syst. Tech. J. 1948; 27: 379-656.
2. Menendez-Velazquez A, Gracía-Granda SB, Stearns SD. Adaptive Signal Processing. Englewood Cliffs, New Jersey, USA: Prentice-Hall; 1985.
3. Gonzalez-Férez R, Dehesa JS. Shannon-entropy as an indicator of atomic avoided crossing in strong parallel magnetic and electric fields. Phys. Rev. Lett., 2003; 91: 113001.
4. Thouless DJ. Electrons in disordered systems and the theory of localization. Phys. Rep 1974; 13: 93-142.
5. Sánchez-Dehesa J, Sanchis-Alepuz H, Kosevich YA, Torrent D. Acoustic analog of electronic Bloch oscillations and Zener tunneling, J. Acoust. Soc. Am. 2006; 120(1):3283-3283.
6. Sanchis-Alepuz H, Kosevich YA, Sánchez-Dehesa J. Acoustic Analogue of Electronic Bloch Oscillations and Resonant Zener Tunneling in Ultrasonic Superlattices. Phys. Rev. Lett. 2007; 98: 134301.
7. Sanchis L, Håkansson, Cervera F, Sánchez-Dehesa J. Acoustic interferometers based on two-dimensional arrays of rigid cylinders in air. Phys. Rev. B. 2003; 67: 035422.
8. He Z, Peng S, Cai F, Ke M, Liu Z. Acoustic Bloch oscillations in a two-dimensional phononic crystal, Phys. Rev. E. 2007; 76: 056605
9. Sánchez-Dehesa J, Arias-Gonzalez JR. Characterization of avoided crossings in acoustic superlattices: The Shannon entropy in acoustics. Frontiers in Physics 2022; 10: 971171.

PROCEEDINGS of the
24th International Congress on Acoustics

October 24 to 28, 2022, in Gyeongju, Korea

Extended abstract

ABS-0212

Deep learning models for acoustic scattering problems

Waqas W. Ahmed[1]; Mohamed Farhat[1]; Pai-Yen Chen[2]; Xiangliang Zhang[1,3]; Ying Wu[1]

[1] King Abdullah University of Science and Technology (KAUST), Thuwal, 23955-6900, Saudi Arabia

[2] University of Illinois at Chicago, Chicago, IL60607, United States of America

[3] University of Notre Dame, Notre Dame, IN 46556, United States of America

ABSTRACT

We develop deep learning (DL) models based on discriminative and generative networks to solve the forward and inverse acoustic scattering problems and show how these models streamlines the inverse design process by eliminating the degenerate solution space. Specifically, we present DL frameworks for designing broadband acoustic cloaks and arbitrarily-shape acoustic object recognition for underwater applications.

Keywords: Inverse scattering, Deep Learning, Acoustic Cloaks, Shape recognition

1. INTRODUCTION

Wave physics models based on analytical and numerical schemes often rely on hit and trial modeling of physical variables or physics-informed optimization for 'on demand' scattering properties. In general, those methods are computationally expensive, and become prohibitively slow especially when devices become more complex such that the degrees of freedom significantly increase in the design space. As a result, intelligent models that can capture the underlying correlation between various physical quantities and streamline the inverse design process are desirable. Recently, data driven approaches were on the main stream of research due to their ability to solve a wide range of physical problems with unprecedented speed and accuracy[1,2]. Despite of this progress, there have been limited efforts to using deep learning techniques to learn input-output mappings with diverse designs and inverse design insights. In this work, novel deep learning models are developed for the design of broadband acoustic cloak and arbitrary object recognition in water. As a surrogate physical model, discriminative neural networks are designed for forward process of one-to-one mapping. However, generative neural networks based on variational inference and adversarial learning are designed for the inverse process of one-to-many mapping, where the fundamental issue of nonuniqueness is addressed by learning the latent distribution of data structures.

2. Results

2.1 Broadband Acoustic Cloaks

Acoustic cloaks, making an object invisible for sound waves, are usually build from artificially structured acoustic metamaterials. The realization of metamaterial-based cloak faces multiple challenges, such as stringent requirements on the material parameters and narrow operating bandwidth. To address these issues, we propose a design of acoustic cloak with a four-layer core-shell configuration driven by machine learning as shown in Fig. 1(a). The performance of the system is quantified by the ratio of total scattering cross-section (TSCS) spectra for the cloaked object and the bare object, computed using transfer matrix method (TMM). The design space (D) consists of eight design parameters, including material and geometrical parameters, and response space (R) is discretized TSCS spectrum in the frequency range $0 \leq k_0 a \leq \pi$. To achieve broadband invisiblity, we first train a forward neural network (FNN) to learn the mapping between the design and response space using training data. Once trained, the pretrained FNN is cascaded behind the inverse neural (INN) network forming a probabilistic encoder-decoder-like structure to capture the underlying physics

[1] ying.wu@kaust.edu.sa

to generate a variety of design parameters for one desired spectral response. In additions, it helps to identify the sensitivity of design parameters through statistical learning and uncovers that material parameters (bulk moduli) are less sensitive than geometrical paramters (shell thickness) on the cloaking behavior [3].

2.2 Acoustic Object Shape Recognition

Shape recognition, which relies on inverse scattering, has a wide range of applications, such as sonar detection, remote sensing, underwater imaging, and nondestructive testing. For underwater objects, however, accurate shape recognition is extremely challenging because of high nonlinearity, large background index contrast, and one-to-many mapping in the solution space. Here, we consider a 2D arbitrarily shaped steel scatterer submerged in water and propose the idea of a latent space to learn the nonlinear mapping between acoustic objects and its far-field scattering patterns once illuminated [see Fig. 1(b)]. The non-unique solution space is eliminated by training the probalistic networks with multi-frequency phaseless far-field amplitudes. The scatterer is discretized as a pixel-based binary image, with zeros and ones representing water and steel, respectively. A commercial software based on finite-element, COMSOL Multiphysics, is used to simulate the far-field patterns of random geometries at five different frequencies across the full angular range. The proposed deep-learning model employs an adversarial autoencoder as a training method for Generator, which generates geometric patterns from the latent distribution of arbitrary-shaped objects. The inverse neural network (INN) predicts the 2D object with the matrix of 64 × 64 for given the multifrequency far-field patterns. The method can be used to determine the shape of arbitrary objects using multifrequency far-field data in half-angular space, which allows it to be applied to detecting submarines, fish species, and other underwater activity [4].

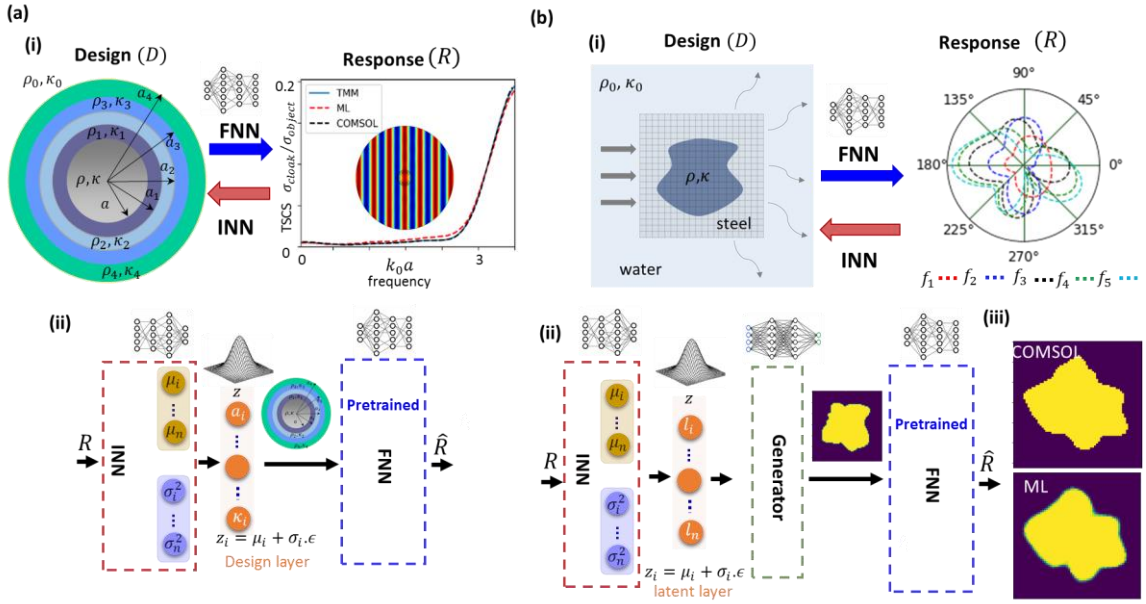


Fig. 1. Deep learning frameworks for inverse acoustic scattering predictions (a) broadband cloak design (b) arbitrary-shape objection detection.

To conclude, we present generative models for learning latent distributions of discrete data structures (for acoustic cloaks) and image data structures (for acoustic object recognition). With a wide variety of design parameters, deep learning models demonstrate excellent performance over test data, making them highly appealing for feasible acoustic devices. It opens up new opportunities for solving complex inverse scattering problems since no complex analytical calculations are required.

ACKNOWLEDGEMENTS

The work described in here is supported by King Abdullah University of Science and Technology (KAUST) Artificial Intelligence Initiative Fund and KAUST Baseline Research Fund No. BAS/1/1626-01-01.

REFERENCES

1. Jiang J, Chen M, Fan JA. Deep neural networks for the evaluation and design of photonic devices. 2021; Nat Rev Mater 6, 679–700.
2. Bianco MJ, Gerstoft P, Traer J, Ozanich E, Roch MA, Gannot S, Deledalle CA. Machine learning in acoustics: Theory and applications. 2019: J Acoust Soc Am *146*(5); 3590-3628.
3. Ahmed WW, Farhat M, Zhang X, and Wu Y. Deterministic and probabilistic deep learning models for inverse design of broadband acoustic cloak. 2021; Phys Rev Research, *3*(1): 013142.
4. Ahmed WW, Farhat M, Chen P.-Y, Zhang X, Wu Y. A Generative deep learning approach for shape recognition of arbitrary objects from phaseless acoustic scattering data 2022; arXiv preprint arXiv:2207.05433

PROCEEDINGS of the
24th International Congress on Acoustics

October 24 to 28, 2022, in Gyeongju, Korea

Extended abstract

ABS-0241

Decay Coefficient of Sound in Phononic Crystals with Viscous Background

Jesús ARRIAGA[1]; Martín IBARIAS[2]; Arkadii KROKHIN[3]

[1] Institute of Physics, Benemérita Universidad Autónoma de Puebla, México

[2] Institute of Physics, Benemérita Universidad Autónoma de Puebla, México

[3] Department of Physics, University of North Texas, USA

ABSTRACT

Using the analytical results in phonon crystals, we calculate the decay coefficient of sound waves propagating at low-frequencies in a 2D phononic crystal with viscous background. The analytical result is valid for structures with arbitrary Bravais lattices and arbitrary cross sections of the cylinders. It is demonstrated that the effective viscosity of phononic crystal may exceed by 2-4 orders of magnitude the viscosity of the background fluid. Moreover, the decay coefficient exhibits dependence on the direction of propagation, i.e., a homogenized phononic crystal behaves like anisotropic viscous fluid. Strong dependence on the filling fraction of solid scatterers gives the possibility of tuning the effective viscosity of phononic structure that may be used for evaluation of the efficiency of phononic devices.

Keywords: Phononic Crystals, Homogenization

1. INTRODUCTION

The pressure in a plane sound wave propagating in a viscous homogeneous fluid decays exponentially with distance according to, $p(x) \sim e^{-\gamma_0 x}$, The decay coefficient γ_0 grows quadratically with frequency ω, and depends on fluid density ρ, two viscosity coefficients η and ξ, and speed of sound c [1]. The decay length of sound ($1/\gamma_0$) in water at frequency of 50 kHz is about15 km, meaning that in water, dissipative losses can be ignored. However, dissipative losses is strongly increased if sound wave meets a solid object on its way. Oscillating fluid sticks to solid boundaries, forming a narrow viscous layer of thickness δ, where velocity gradients greatly exceed the gradients in a free fluid, leading to much higher viscous losses. In a phononic crystal, the volume occupied by the viscous boundary layers formed around solid scatterers usually constitutes a small part of the volume of the whole sample. It, however, strongly reduces acoustic transmission. For example, if sound propagates through a 2D periodic lattice of cylindrical rods embedded in water, the decay length is reduced by two orders of magnitude. Here, we use the recent develop analytical approach, for exact calculation of the attenuation coefficient in a two-dimensional (2D) phononic crystal in the low-frequency limit [2], to tune the decay coefficient for different 2D Bravais lattices and different cross sections of the scatterers.

2. DISSIPATION OF ACOUSTIC ENERGY

Propagating sound waves generate vibrations of pressure $p(r,t)=p(r)\exp(-i\omega t)$ and velocity $v(r,t)=v(r)\exp(-i\omega t)$. Within the boundary layer δ, velocity in a viscous fluid decays exponentially from its value in the bulk to zero at the interface of a motionless hard scatterer. The acoustic power (per unit length of a cylinder) dissipated around a hard scatterer is given by the following contour integral [1]:

[1] arriaga@ifuap.buap.mx
[2] mibarias@ifuap.buap.mx
[3] Arkadii.Krokhin@unt.edu

$$\dot{Q} = \frac{1}{2\sqrt{2}} \sqrt{\rho\omega\eta} \oint_{l_0} |\mathbf{v}(\mathbf{r})|^2 \, dl \qquad (1)$$

The integration runs over contour l_0, which is the circumference of the scatterer. This equation is used for the calculation of the dissipated power within a unit cell of 2D phononic crystal, and is valid if the interface can be considered as flat within the lengths ~δ, i.e., $\delta << L_0$ where L_0 is the length of the contour l_0 that separates fluid from solid. This inequality, together with the condition of homogenization, $ka_0 << 1$, defines the frequency interval where the proposed theory is valid. The decay coefficient for a wave propagating in a homogeneous dissipative medium is given by the ratio,

$$\gamma_{ph} = \frac{\dot{Q}}{2c_{eff} E_c} \qquad (2)$$

The explicit for of the factors of eq. (3) appears in Ref. [3]. These factors take into account the microstructure of the phononic crystal and the details of the formation of the boundary layer.

2.1 Decay coefficient of an anisotropic lattice

We apply the previous results for a phononic crystal for three different lattices of solid cylinders in viscous water background for different scatterers but the same filling fraction, f = 30%. The decay coefficient given by Eq. (2) is plotted in a polar diagram in Fig. 1, showing the angular dependence of the decay coefficient. The three curves appearing are ellipses with semiaxes representing maximum and minimum attenuation of sound along the corresponding directions. The plots in Fig. (1) demonstrate that viscous losses strongly depend on the shape of the scatterers. The main factors that define viscous attenuation are the narrow channels between the neighboring scatterers, the number of corners per unit length and their sharpness. Combination of these factors leads to a complicated anisotropic pattern of viscous losses which is impossible to analyze using only qualitative or phenomenological approach.

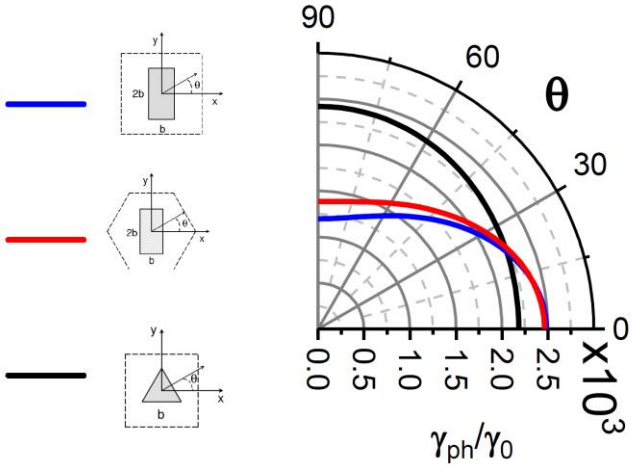


Figure 1. Normalized decay coefficient of sound for anisotropic unit cells as function of angle θ. Figures inset: square lattice with rectangular rods oriented by its longer side along y-direction, hexagonal lattice with rectangular rods, and square lattice with equilateral triangular rods.

ACKNOWLEDGEMENTS

This work was partially supported by CONACyT (México) through Grant No. A1-S-23120.

[1]. [2] [3] M. Ibarias, Yu. Zubov, J. Arriaga, and A. A. Krokhin, Phys. Rev. Res., 2, pp. 022053(R), 2020.

REFERENCES

1. L. D. Landau and E. M. Lifshitz, Fluid Mechanics, 2nd ed. Elsevier, Oxford, 1984.
2. A. A. Krokhin, J. Arriaga, and L. N. Gumen, Speed of Sound in Periodic Elastic Composites, Phys. Rev. Lett. 2003; 91:264302.
3. M. Ibarias, Yu. Zukov, J. Arriaga, and A. A. Krokhin, Phononic Crystal as a homogeneous viscous metamaterial, Phys. Rev. Res. 2020; 2:022053.

PROCEEDINGS of the
24th International Congress on Acoustics
October 24 to 28, 2022 in Gyeongju, Korea

ABS-0402

Design and experiment of metaliner for sound insulation in a duct with flow

Tae Seok Oh[1]; Wonju JEON[1]

[1] Department of Mechanical Engineering, Korea Advanced Institute of Science and Technology, Republic of Korea

ABSTRACT

We propose a metaliner that insulates duct noise while allowing fluid passage with little flow resistance. A unit cell of a metaliner consists of two different subwavelength Helmholtz resonators, and the unit cells are alternately arranged along the direction of sound propagation underneath the duct. To predict sound insulation of the metaliner in a duct with grazing flow, we establish an effective impedance model of the metaliner, considering the effect of flow. We design metaliners with target frequencies of 500Hz or 1000Hz that achieve high transmission loss for various flow speeds. The experimental results show that designed metaliners exhibit transmission loss above 45 dB/m within $\pm 5\%$ of target frequencies for different flow speeds of 0, 17, and 34 m/s.

Keywords: Metaliner, Sound insulation, Flow

1. INTRODUCTION

Noise attenuation in ducts is important in a variety of industrial applications, such as air intake of cooling towers or vehicle ventilation systems. Acoustic treatments, such as conventional acoustic louvers or mufflers, have been widely used to reduce duct noise (1-2), but they have poor sound attenuation in the low-frequency range and worsen the functionality of the products or facilities by blocking the air passage due to a low air-flow area. Recently, acoustic metamaterials have been developed to solve the problem of low-frequency sound insulation while allowing fluid passage (3-6). However, the previous studies focused on improving the sound insulation of the acoustic metamaterials for a stationary medium, so they could not guarantee sound insulation in a duct with a flow.

In this study, we propose a metaliner that can insulate duct noise in the presence of grazing flow. First, we establish a theoretical model for the effective impedance of the metaliner that accounts for the effects of flow, based on the recent study (7). The transmission loss of the metaliner in a duct with a flow is predicted by numerical simulation. Then, we design metaliners that exhibit transmission loss per unit length above 45 dB/m within $\pm$ 5% of the target frequencies of 500 and 1000 Hz for different flow speeds of 0, 17, and 34 m/s. The sound insulation for different flow speeds is experimentally validated.

2. RESULTS AND DISCUSSIONS

Figure 1 describes the geometry of the metaliner. Two different Helmholtz resonators of subwavelength scale are arranged alternately along the direction of sound propagation under the rectangular duct with an edge length of 51 mm. The metaliner is cuboid with dimensions of 406 mm × 51 mm × 30 mm.

wonju.jeon@kaist.ac.kr

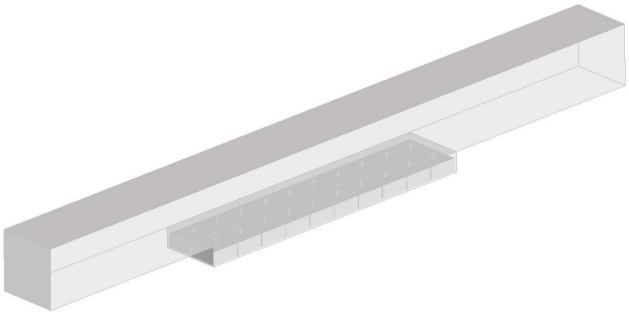


Figure 1 – Geometry of a metaliner installed under a rectangular duct

Figure 2 shows the transmission loss spectra of designed metaliners with target frequencies of 500 Hz and 1000 Hz for different average flow speeds of 0, 17, and 34 m/s. The experimental results show good agreement with the numerical results. Experiments confirm that the metaliners maintain transmission loss per unit length above 45 dB/m in the target frequency range (475–525 Hz or 950–1050 Hz) for average flow speeds of 0, 17, and 34 m/s. In addition, the sound insulation was realized not only at target flow speeds (0, 17, 34 m/s) but also at flow speeds between 0–34 m/s, as detailed in reference (8).

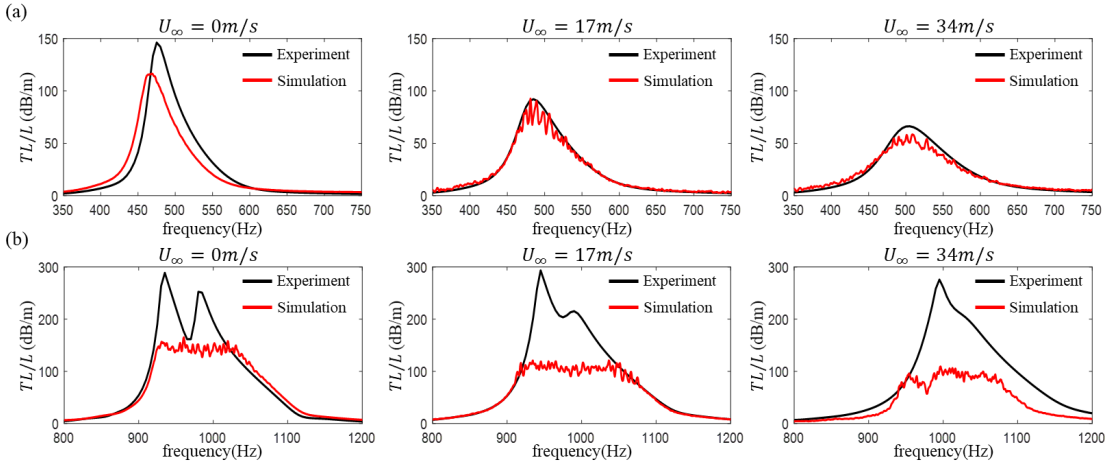


Figure 2 – Transmission loss per unit length according to the flow speeds of 0, 17, and 34 m/s for the metaliner with target frequencies of (a) 500 Hz and (b) 1000 Hz

REFERENCES

1. A. Craggs, A finite method for modelling dissipative mufflers with a locally reactive lining, J. Sound Vib., 54 (1977) 285-296.
2. E. B. Viveiros, B. M. Gibbs, S. N. Y. Gerges, Measurement of sound insulation of acoustic louvers by an impulse method, Appl. Acoust., 63 (2002) 1301-1313.
3. H. -L. Zhang, Y. -F. Zhu, B. Liang, J. Yang, J. Yang, and J. -C. Cheng, Sound insulation in a hollow pipe with subwavelength thickness, Sci. Rep., 7 (2016) 44106.
4. X. Yu, Z. Lu, L. Cheng, and F. Cui, On the sound insulation of acoustic metasurface using a sub-structuring approach, J. Sound Vib., 401 (2017) 190-203.
5. R. Ghaffarivardavagh, J. Nikolajczyk, S. Anderson, and X. Zhang, Ultra-open acoustic metamaterial silencer based on Fano-like interference, Phys. Rev. B, 99 (2019) 024302.
6. J. W. Jung, J. E. Kim, and J. W. Lee, Acoustic metamaterial panel for both fluid passage and broadband soundproofing in the audible frequency range, Appl. Phys. Lett., 112 (2018) 041903.
7. H. Ryoo and W. Jeon, Dual-frequency sound-absorbing metasurface based on visco-thermal effects with frequency dependence, J. Appl. Phys., 123 (2018) 115110.
8. T. S. Oh and W. Jeon, Acoustic metaliners for sound insulation in a duct with little flow resistance, Appl. Phys. Lett., 120 (2022) 044103.

ICA 2022
24th INTERNATIONAL CONGRESS ON ACOUSTICS
October 24(Mon) - 28(Fri), 2022 Gyeongju, Korea

PROCEEDINGS of the
24th International Congress on Acoustics

October 24 to 28, 2022 in Gyeongju, Korea

ABS-0448

Manipulation of scattered sound fields with spatiotemporally modulated acoustic metasurfaces

Janghoon KANG[(1)], Michael R. HABERMAN[(1)]

[(1)]Walker Department of Mechanical Engineering, The University of Texas at Austin; Austin, Texas, USA;
jh3010.kang@utexas.edu, haberman@utexas.edu

ABSTRACT

Spatiotemporal modulation of material properties has been used in unbounded electromagnetic and acoustic domains to provide enhanced control of propagating waves via nonreciprocity. This idea was recently expanded to consider the vibration of finite-length Euler beams with spatiotemporally modulated material properties by introducing a modal expansion technique that includes modulation harmonics to show that losses are required to observe nonreciprocal vibrational motion [Goldsberry et al., *Phys. Rev.,* B 102, 2020]. Using a similar same modal expansion method, we have shown that spatiotemporally modulated surface admittance at the boundary of an acoustic domain improves sound diffuser performance by altering the direction of scattered diffraction modes via the introduction of modulation harmonics for all diffracted orders [Kang et al., *J. Acoust. Soc. Amer.,* 150(4), A108, (2021)]. This work employs the same generalized semi-analytical model to investigate the effects of the modulation function on the acoustic field scattered from spatiotemporally modulated surfaces. We consider parameters such as the modulation frequency and amplitude as well as functional forms, e.g. superposition of sinusoids. Results are presented in terms of the angular dependence of the scattered field and we discuss how the scattered sound field may be manipulated for either improved diffusion or directional dependence solely based on choice of modulation function.

Keywords: Spatiotemporal modulation, Nonreciprocity, Acoustic Metasurface

1 INTRODUCTION

The principle of reciprocity for acoustic and elastic waves restricts the transmission between to points in an arbitrary domain to be symmetric when the source and receiver positions are interchanged (1, 2). One consequence of the Onsager-Casimir principle from thermodynamics is that transmission between any two points in an acoustic domain will be reciprocal when the system is linear and time-invariant and obeys time-reversal symmetry at scales that are much smaller than propagating wavelengths (1, 2). Based on this principle and later macroscopic extensions, recent studies on the creation of systems that enable nonreciprocal wave transport have focused on violating the assumptions such as a linearity and a time-invariance. One mechanism to generate nonreciprocal wave motion is to break time-invariance through the spatiotemporal modulation of material properties (2). Inspired by early work that imposed spatiotemporal modulation in the form of a pump wave in a medium (3), recent research has studied the case of spatiotemporal modulation of material properties, such as a density or a stiffness, in the form of a traveling wave acoustic and elastic wave propagation (4, 5, 6, 7, 8, 9, 10). In metasurfaces, the modulation has also been shown to have a potential for a nonreciprocal transmission and reflection (10, 11) as well as Doppler-like frequency shifting (12, 13) and total power combining (14). In this work, we focus on the temporal and spatial harmonics caused by the modulation of an input admittance of a periodic reflective surface and its effects on scattered sound field. We show that the scattered sound energy can be redirected into a range of directions due to the fact that surface impedance modulation introduce frequency harmonics into the reflected field. As such, we observe changes in the backscattered directivity that differs from the diffraction orders that are proportional to the spatial periodicity of the surface. The result presented here is a

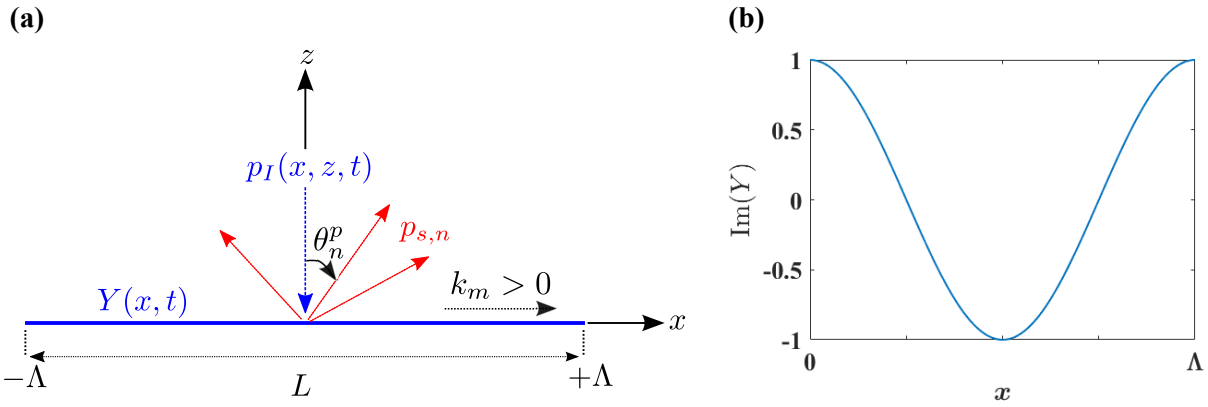


Figure 1. (a) The geometry of a flat surface with the incident sound pressure, $p_{\mathrm{I}}(x,z,t)$, and the scattered sound $p_{\mathrm{s,n}}(x,z,t)$ of n^{th} diffracted order and p^{th} modulation harmonic propagating into the direction of θ_n^p with respect to the surface normal. The modulation function of a surface is represented as $Y(x,t) = Y_0(x) + jY_{\mathrm{m}}\cos(\omega_{\mathrm{m}}t - k_{\mathrm{m}}x)$ and the direction of modulation depends on the sign of k_{m}. For modulation propagating in the positive x-direction, $k_{\mathrm{m}} > 0$. (b) The modulation function for one spatial period and the case of $Y_0 = 0$ and $Y_{\mathrm{m}} = 1$ at $t = 0$.

generalization of recent work by our group (15) which showed that spatiotemporal modulation of the surface admittance of a sound diffuser can drastically improve the diffusion performance of a conventional sound diffuser such as Schroeder diffuser (16) through the introduction of harmonics in both the frequency and wavenumber of the backscattered field (15). That work showed that the far field scattering pattern depends on the direction of the direction of spatiotemporal modulation, which indicates the possibility of generating highly nonreciprocal reflective acoustic metasurfaces (AMS) by tuning the spatiotemporal modulation of the input acoustic admittance. Here we extend the a semi-analytical approach introduced to analyzing nonreciprocal vibration in Euler Beams (7) to analyze the sound field scattered from a spatiotemporally modulated reflective AMS with spatial periodicity. We assume that the surface admittance is modulated in the form of a travelling wave with the modulation frequency ω_m and the amplitude Y_m. We then perform parametric studies of the modulation to identify pairs of modulation parameters that maximize the degree of the nonreciprocity in the reflection from the surface by calculating a nonreciprocity metric based on the difference in the angle-dependent backscattered sound pressures depending on the direction of modulation. We show that the far field scattering response calculated with the semi-analytical model is nonreciprocal and that the degree of nonreciprocity can be varied with moderate changes in the modulation function. The predictions from the semi-analytical model are then validated using a time-domain finite element method (FEM) where we observe similar results as obtained using the semi-analytical model. The results demonstrate that, by using the proper selection of spatiotemporal modulation of surface admittance, one may tune the sound field scattered from a flat surface to achieve nonreciprocal or diffuse directivity in the reflected field.

2 SEMI-ANALYTICAL MODEL

Previous work by the authors has resulted in a semi-analytical model to calculate the acoustic field scattered from a sound diffuser whose input impedance is modulated spatiotemporally (15). Here we use the same approach to calculate the reflected field at each point on a flat surface that has spatiotemporally modulated input admittance, as indicated in Fig. 1(a). The far-field, angle-dependent backscattered field is then determined using the approach outlined below. Given a normalized acoustic surface admittance, $Y = \rho_0 c_0 / Z$, where Z is the surface input impedance, and the produce of the background fluid density, ρ_0, and sound speed, c_0, yields its characteristic acoustic impedance, the flat surface is assumed to be modulated in the form of a travelling wave represented in Fig, 1(b) in the form $Y(x,t) = Y_0(x) + jY_{\mathrm{m}}\cos(\omega_{\mathrm{m}}t - k_{\mathrm{m}}x)$. Here $Y_0(x)$ is the uniform surface

admittance of the unmodulated sound diffuser, $k_\mathrm{m} = 2\pi/\Lambda$ is the modulation wavelength, ω_m is the modulation frequency, and Λ is the spatial period of the modulation. To represent the temporal modulation, the terms of both the incident and scattered sound pressure at the interface of the flat AMS and the background fluid are expressed as a function of space and time using the following expansions on the modulation frequency and wavenumber,

$$p(x,z,t) = p_\mathrm{I}(x,z,t) + p_\mathrm{s}(x,z,t) = a_\mathrm{I} e^{j(\omega_0 t - k_\mathrm{x} x + k_\mathrm{z} z)} + \sum_{n=-\infty}^{\infty} a_\mathrm{n}(t) e^{-j(\beta_\mathrm{n} x + \gamma_\mathrm{n} z)}. \tag{1}$$

In Eq. 1, ω_0 represents the frequency of the incident wave, $k_\mathrm{x} = k\sin\theta_\mathrm{I}$ and $k_\mathrm{z} = k\cos\theta_\mathrm{I}$ represent the projection of the incident wavenumber on the x- and z-directions, θ_I is the angle of incidence, β_n and γ_n are the wave numbers of the n^th diffracted order in the x- and z-direction, respectively. Further, the classical grating equation requires that $\beta_n = k_x + 2n\pi/\Lambda$. Considering that the modulation function can be expressed as an expansion of harmonic terms, the modal amplitude $a_\mathrm{n}(t)$ can also be represented with a Fourier expansion of the harmonics of the modulation frequency as

$$a_\mathrm{n}(t) = \sum_{p=-\infty}^{\infty} \hat{a}_\mathrm{n}^p e^{j(\omega_0 + p\omega_\mathrm{m})t}, \tag{2}$$

where $\hat{a}_\mathrm{n}^p$ is the scattering amplitude of n^th diffracted order and p^th modulation harmonic. The wavenumber associated with the scattering amplitude, $\hat{a}_\mathrm{n}^p$, in the z-direction can be expressed as $\left(\gamma_\mathrm{n}^\mathrm{p}\right)^2 = \left(\omega_\mathrm{p}/c_0\right)^2 - \beta_n^2$, where $\omega_p = \omega_0 + p\omega_\mathrm{m}$ and ω_0 is the incident frequency. This shows that the number of propagating modes, i.e. the modes where $\gamma_\mathrm{n}^\mathrm{p}$ is real, is a function of the diffracted order and the modulation harmonic. Therefore, the propagating diffraction modes can be shifted into multiple directions and then related to backscattering angles associated with the propagating diffraction modes and the harmonics.

$$\theta_n^p = \sin^{-1}\left(\frac{\beta_n}{\omega_p/c_0}\right) = \sin^{-1}\left(\frac{\sin\theta_\mathrm{I} + \frac{\lambda_0}{\Lambda}n}{1 + p\frac{\omega_\mathrm{m}}{\omega_0}}\right), \tag{3}$$

Conservation of momentum must be established at the interface between the AMS and the background fluid in order to determine the backscattered field. For this configuration, we can use the linearized momentum equation and the definition of input impedance to relate the normal component of input impedance of a flat surface, and the total acoustic pressure and normal component of the velocity, $u_\mathrm{z}(x,t)$, at $z = 0$ as

$$\rho_0 \frac{\partial u_z}{\partial t}\Big|_{z=0} = -\frac{\partial p}{\partial z}\Big|_{z=0}, \qquad u_\mathrm{z}(x,t)|_{z=0} = -\frac{p(x,t)}{Z(x,t)}\Big|_{z=0} \tag{4}$$

Equations 1, 2, and 4, are then used to determine the scattering amplitude, $\hat{a}_\mathrm{n}^p$, from a large matrix equation for the $(2N+1)(2P+1)$ solutions with the truncated terms of the diffracted orders and the modulation harmonics as $n \in [-N, N]$ and $p \in [-P, P]$ (15). The scattering amplitudes are then used to calculate the scattered sound pressure from the flat surface with spatiotemporally modulated input impedance with the summation

$$p_\mathrm{s}(x, z=0, t) = \sum_{p=-P}^{P}\left(\sum_{n=-N}^{N} \hat{a}_\mathrm{n}^p e^{-j\beta_\mathrm{n} x}\right) e^{j\omega_p t} = \sum_{p=-P}^{P} \hat{a}^p(x) e^{j\omega_p t}. \tag{5}$$

We next employ the Fraunhofer approximation to determine the backscattered directivity for each harmonic in the far-field by using the spatial Fourier transform of $\hat{a}^p(x)$. Finally, by summing the far-field responses for all modulation harmonics, the far-field sound power due to contributions from all propagating modes can be determined for a single incident plane wave with prescribed frequency and direction. Given the symmetric geometry of a flat surface, the difference of the far-field responses associated with the direction of the modulation shows the degree of the nonreciprocity (7), which can be calculated using the metric

$$\Upsilon = \frac{\sum_{i=1}^{m}\left(10^{L_i^+/10} - 10^{L_i^-/10}\right)^2}{\sum_{i=1}^{m}\left(10^{L_i^+/10}\right)^2 + \sum_{i=1}^{m}\left(10^{L_i^-/10}\right)^2}, \tag{6}$$

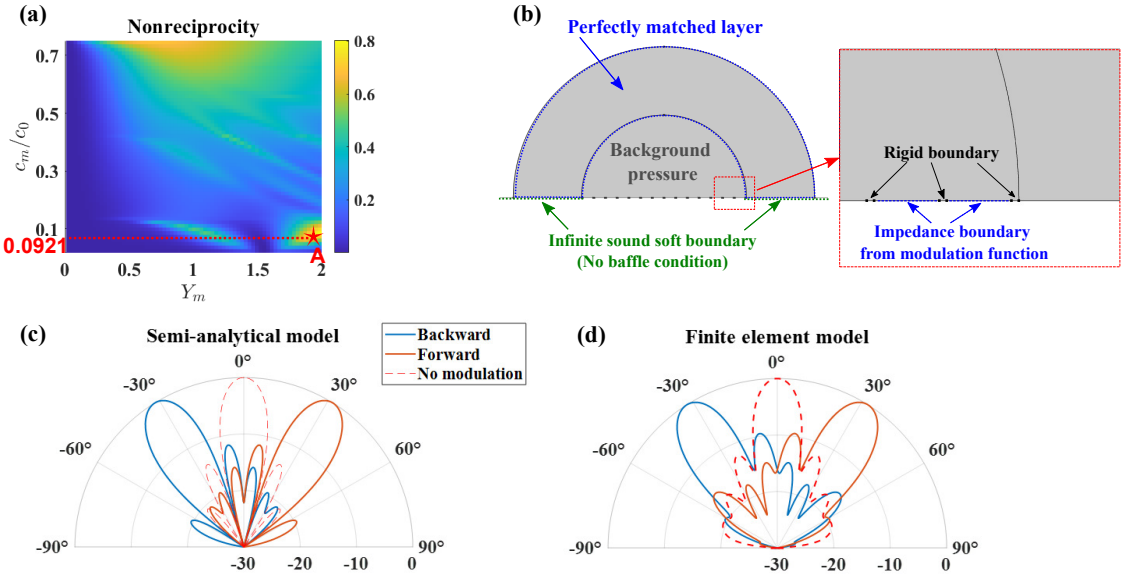


Figure 2. (a) Degree of nonreciprocity with respect to the modulation speed, which is a function of the modulation frequency, and the modulation amplitude. The case marked as "A" is selected for the demonstration of a nonreciprocal sound field. (b) The finite element model in Comsol including the impedance boundary condition and the infinite sound soft boundary. The far-field response for case A is shown in (c) when using the semi-analytical model, and in (d) using a time-domain finite element model.

where $L_i^{\pm}$ is the sound pressure level for two opposite modulation directions, forward(+) and backward(-), and m is the index of the positions in the polar angle, which we have assumed to be equally spaced for $\theta \in [-90^\circ\ 90^\circ]$.

3 PARAMETRIC STUDY

The semi-analytical model and the modulation function for the surface admittance of a flat surface in Fig. 1 can be used to perform a parametric study on the two modulation parameters: the modulation frequency ω_m and the modulation magnitude, Y_m. We note that the spatial wavenumber of the modulation is fixed with the predetermined length of one period, Λ, which we fix as $L/2$. The plot of the result from a parametric study in Fig. 2(a) shows that some modulation parameter pairs generate a high degree of nonreciprocity, while others do not. We further investigated the case of $c_\mathrm{m}/c_0 = 0.092$ and $Y_\mathrm{m} = 1.97$ which is labeled with "A" in Fig. 2(a). The far-field scattered directivity response for this case determined using the semi-analytical model as described above is provided in Fig. 2(c), which shows that the response changes significantly depending on the direction of spatial modulation. These results demonstrate that the symmetric (flat) geometry of the surface enables the use of spatiotemporal modulation and a specific set of modulation parameters to produce a high degree of nonreciprocal scattering. The plot of the magnitude of the scattering amplitudes provided in Fig. 3(a) shows that for the case considered here, the sound energy is concentrated in the direction of the mode of $n = 1$ and $p = 1$ and that when the direction of modulation reverses, sound is scattered primarily in the direction of the $n = -1$ and $p = -1$ mode, leading to strongly nonreciprocal scattering. The iso-frequency curves (i.e. slowness contours) and the dispersion diagram in Figs. 3(c) and (b), respectively, shows a convenient representation of how the spatiotemporal modulation leads the control of backscattered sound energy and mode selection for propagating or evanescent modes. Finally, we have compared the far-field response determined using the semi-analytical model with the results obtained using time-domain finite element modeling with the same geometry and the same modulation function as shown in Fig. 2(d). The finite element model was implemented in Comsol Multiphysics in Fig. 2(b). Modulated surface admittance was realized using an impedance boundary condition defined with

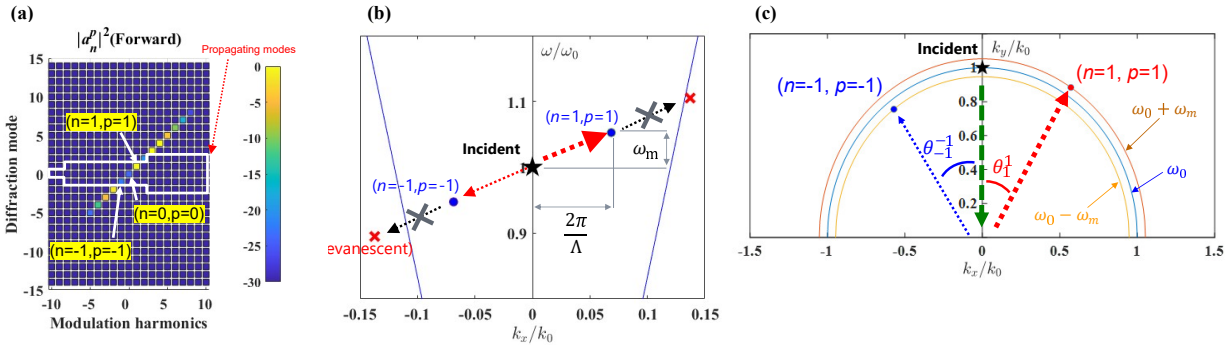


Figure 3. (a) Magnitudes of the scattering amplitudes as a function of the diffraction mode and the modulation harmonic. (b) The dispersion diagram represents the propagating modes and the evanescent modes depending on the wavenumber of the scattered sound in the x-direction and the shifted frequencies. Modes inside the "sonic lines" will propagate, while those outside them will be evanescent. (c) Propagating and scattered sound modes shown on a slowness surface (wavenumber space). The concentric half-circles represent iso-frequency contours in wavenumber-space for the incident and the frequency-modulated frequencies. The angles $\theta_{-1}^{-1} = -37.1^\circ$ and $\theta_1^1 = 32.9^\circ$ are determined from the location of scattered propagating modes with the diffracted order and modulation frequency pairs $(p,n) = (-1,-1)$ and $(p,n) = (1,1)$ on the iso-frequency contours.

the modulation function in Fig. 1. The far-field polar responses were then determined using "exterior field calculation" using the acoustic field at the boundary between the simulation domain and a perfectly matched layer (PML), which is used to approximate an infinite half-space above the reflecting plane. The "exterior field calculation" calculates the far-field using exact Kirchhoff-Helmholtz integral and a "sound-soft" (i.e. pressure release) boundary condition is employed within the PML. The responses predicted using FEM are in good agreement with those from the semi-analytical model, clearly showing a strong nonreciprocal scattering of the sound field depending on the modulation direction and validating the semi-analytical model. As a visual aid for the effects of the spatiotemporal modulation, the geometry in Fig. 2(b) was modified to simulate a more realistic geometry. Specifically, a finite surface with a length of two periods. From the transient numerical simulation with this revised geometry, we can show the non-reciprocal response by inspecting the scattered acoustic pressure by plotting the scattered acoustic pressure a single instant in time as in shown in Fig. 4. Those results clearly indicate the difference scattered field near the AMS depending on the direction of the modulation.

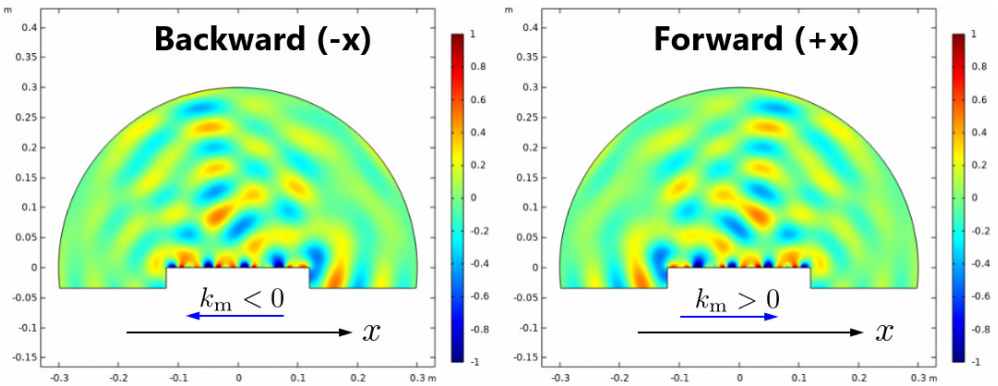


Figure 4. The scattered sound field for two different modulation directions obtained using a time-domain finite element simulation.

4 CONCLUSIONS

A semi-analytical model developed in previous work to model the performance of a spatiotemporally modulated sound diffuser was employed in this work to show that flat surfaces with spatiotemporal modulation of the input impedance can be used to generate nonreciprocal scattering behavior. This was explored by investigating the frequency and wavenumber shifting of the reflected field caused by the time and space modulation of the surface response. Continuity of momentum at the AMS-fluid interface imposes the scattering of energy into the directions of various diffraction modes at frequencies shifted from the incident wave by integer multiples of the modulation frequencies. We have shown that the diversification of propagating modes can be used to improve diffusion performance or to generate a nonreciprocal sound scattering depending on the selection of the appropriate modulation parameters. We have selected a representative nonreciprocal scattering case by performing a parametric study of the modulation parameters and evaluating the performance with a nonreciprocity metric. The far-field responses obtained from the semi-analytical model and finite element model clearly show that the scattered sound field becomes asymmetric under modulation and that the direction of asymmetric is controlled by the modulation direction.

ACKNOWLEDGEMENTS

J.K. acknowledges support from Samsung Electronics.

References

[1] Fleury R, Sounas D, Haberman MR, Alu A. Nonreciprocal acoustics. Acoustics Today. 2015;11(ARTICLE):14-21.

[2] Nassar H, Yousefzadeh B, Fleury R, Ruzzene M, Alù A, Daraio C, et al. Nonreciprocity in acoustic and elastic materials. Nature Reviews Materials. 2020;5(9):667-85.

[3] Cassedy ES, Oliner AA. Dispersion relations in time-space periodic media: Part I—Stable interactions. Proceedings of the IEEE. 1963;51(10):1342-59.

[4] Trainiti G, Ruzzene M. Non-reciprocal elastic wave propagation in spatiotemporal periodic structures. New Journal of Physics. 2016;18(8):083047.

[5] Nassar H, Chen H, Norris A, Haberman M, Huang G. Non-reciprocal wave propagation in modulated elastic metamaterials. Proceedings of the Royal Society A: Mathematical, Physical and Engineering Sciences. 2017;473(2202):20170188.

[6] Trainiti G, Xia Y, Marconi J, Cazzulani G, Erturk A, Ruzzene M. Time-periodic stiffness modulation in elastic metamaterials for selective wave filtering: Theory and experiment. Physical review letters. 2019;122(12):124301.

[7] Goldsberry BM, Wallen SP, Haberman MR. Nonreciprocal vibrations of finite elastic structures with spatiotemporally modulated material properties. Physical Review B. 2020;102(1):014312.

[8] Shen C, Zhu X, Li J, Cummer SA. Nonreciprocal acoustic transmission in space-time modulated coupled resonators. Physical Review B. 2019;100(5):054302.

[9] Li J, Shen C, Zhu X, Xie Y, Cummer SA. Nonreciprocal sound propagation in space-time modulated media. Physical Review B. 2019;99(14):144311.

[10] Zhu X, Li J, Shen C, Peng X, Song A, Li L, et al. Non-reciprocal acoustic transmission via space-time modulated membranes. Applied Physics Letters. 2020;116(3):034101.

[11] Adlakha R, Moghaddaszadeh M, Attarzadeh MA, Aref A, Nouh M. Frequency selective wave beaming in nonreciprocal acoustic phased arrays. Scientific reports. 2020;10(1):1-14.

[12] Shaltout A, Kildishev A, Shalaev V. Time-varying metasurfaces and Lorentz non-reciprocity. Optical Materials Express. 2015;5(11):2459-67.

[13] Shaltout AM, Shalaev VM, Brongersma ML. Spatiotemporal light control with active metasurfaces. Science. 2019;364(6441):eaat3100.

[14] Wang X, Asadchy VS, Fan S, Tretyakov SA. Space–Time Metasurfaces for Power Combining of Waves. ACS Photonics. 2021;8(10):3034-41.

[15] Kang J, Haberman MR. Sound diffusion with spatiotemporally modulated acoustic metasurfaces. arXiv preprint arXiv:220500089. 2022.

[16] Schroeder MR. Binaural dissimilarity and optimum ceilings for concert halls: More lateral sound diffusion. Journal of the Acoustical Society of America. 1979;65:958-63.

ICA 2022
24th INTERNATIONAL CONGRESS ON ACOUSTICS
October 24(Mon) - 28(Fri), 2022 Gyeongju, Korea

PROCEEDINGS of the
24th International Congress on Acoustics

October 24 to 28, 2022 in Gyeongju, Korea

ABS-0607

Extending the angle range of high absorption of metasurfaces by adding a multilayered medium

Diana Maria GARZA-AGUDELO[(1)]*, Vicente CUTANDA HENRIQUEZ[(1)], Cheol-Ho JEONG[(1)], Peter Risby ANDERSEN[(2)], Martin IBARIAS[(3)]

[(1)]Technical University of Denmark, Acoustic Technology, DTU Electrical and Photonics Engineering, Ørsteds Plads, Building 352, Kongens Lyngby 2800, Denmark, dmgag@dtu.dk

[(2)]GN Audio A/S & Jabra, Audio Research, Lautrupbjerg 7, Ballerup 2750, Denmark

[(3)]Universitat Politècnica de València, Department of Electronic Engineering, Camino de Vera s.n., Building 7F, ES-46022 Valencia, Spain

ABSTRACT

Surfaces consisting of periodic arrangements of resonators can be considered to be locally reacting, and thus have a limited range of angles for which they can achieve high absorption. In particular, achieving significant absorption in a wide angle range becomes more difficult in the region approaching grazing incidence. For some applications such as reflection control in disproportionate rooms, reflection control at large angles can be desirable. In this work, it is shown how the angle range of high absorption of periodic surfaces of resonators can be significantly extended by adding a multilayered media above them. Two cases are demonstrated, one that considers a single-frequency performance and another that considers the average performance over an octave band. The behavior of the surfaces is estimated analytically using the transfer matrix method and numerically using the finite element model.

Keywords: Oblique incidence absorption, Absorbing metasurface, Multilayered media

1 INTRODUCTION

Periodic surfaces of Helmholtz or quarter wavelength resonators have been shown to be effective absorbers at frequencies with wavelengths that are very large compared to their thickness [1, 2, 3, 4]. At the same time, the combination of resonators tuned to different frequencies allows to extend the frequency range of high absorption [3, 5, 6]. Thus, this type of metasurfaces represents promising solutions to control low frequency acoustic reflections. Nevertheless, their behavior is approximately locally reacting, and therefore the angle range for which they can achieve high absorption is limited [7, 8]. In particular, achieving significant absorption in a wide angle range becomes more difficult in the region approaching grazing incidence given the high variation of the radiation impedance as a function of the angle. For different applications, it is desirable to control waves impinging the surface from several directions. For instance, for sound level control inside rooms where there are several sound source positions and/or reflecting objects. Reflection control for large incidence angles is of special interest in disproportionate rooms [9].

In this work, a metasurface that consists on a parallel arrangement of 2D Helmholtz resonators topped by a multilayered medium is presented. Its key feature is that it allows to extend the angle range where high absorption is achieved compared to that of a surface that includes only the resonators. More explicitly, the multilayered medium is realized using an array of cylinders distributed following a hexagonal lattice.

*dmgag@dtu.dk

2 ANALYTIC MODEL FOR THE MULTILAYER ABSORBER

The type of absorbers proposed in this work are a combination in series of different media. An example of a unit cell of a surface of this kind, which includes $N_{\mathrm{HR}} = 3$ different resonators and $N_{\mathrm{l}} = 4$ layers of cylinders, is shown in Figure 1. From top to bottom, the elements of the series assembly are: layer N_{l}, N_{l}-1, ..., 1 of the cylinder arrangement, and the periodic surface of resonators. Using a transfer matrix model (TMM), the system is described by a global transfer matrix $\mathbf{T_G}$ as

$$\mathbf{T_G} = \mathbf{T_L}^{(N_{\mathrm{l}})}\mathbf{T_L}^{(N_{\mathrm{L}}-1)}...\mathbf{T_L}^{(1)}\mathbf{T_P}, \tag{1}$$

where the transfer matrix of each of the layers is of the form [10]

$$\mathbf{T_L}^{(l)} = \begin{bmatrix} \cos\left(\dfrac{\omega}{c_{\mathrm{eff}}^{(l)}}\cos\theta^{(l)}h\right) & \mathrm{i}\dfrac{c_{\mathrm{eff}}^{(l)}\rho_{\mathrm{eff}}^{(l)}}{\cos\theta^{(l)}}\sin\left(\dfrac{\omega}{c_{\mathrm{eff}}^{(l)}}\cos\theta^{(l)}h\right) \\ \mathrm{i}\dfrac{\cos\theta^{(l)}}{c_{\mathrm{eff}}^{(l)}\rho_{\mathrm{eff}}^{(l)}}\sin\left(\dfrac{\omega}{c_{\mathrm{eff}}^{(l)}}\cos\theta^{(l)}h\right) & \cos\left(\dfrac{\omega}{c_{\mathrm{eff}}^{(l)}}\cos\theta^{(l)}h\right) \end{bmatrix}, \tag{2}$$

ω, $c_{\mathrm{eff}}^{(l)}$, $\rho_{\mathrm{eff}}^{(l)}$, and $\theta^{(l)}$ are respectively the angular frequency, the complex effective speed of sound and density, and the propagation angle inside layer l. From Snell's law, the propagation angle inside the first layer can be found from the wavenumber in air $k_0 = \omega/c_0$, the incidence angle of the wave with respect to the surface normal θ_{i}, and the equality $k_0 \sin\theta_{\mathrm{i}} = k^{(1)}\sin\theta^{(1)}$, where $k^{(l)} = \omega/c_{\mathrm{eff}}^{(l)}$. For all subsequent layers, it can be found from the equality $k^{(l-1)}\sin\theta^{(l-1)} = k^{(l)}\sin\theta^{(l)}$.

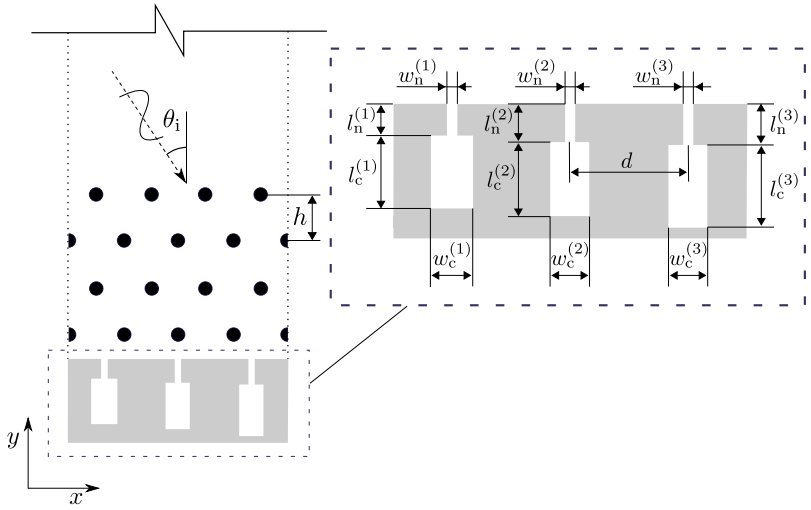


Figure 1. Unit cell of a metasurface consisting of a periodic arrangement of three parallel 2D Helmholtz resonators which are equidistantly placed, and a multilayer arrangement of cylinders following a hexagonal lattice distribution.

The complex effective wave propagation properties ($c_{\mathrm{eff}}^{(l)}$, and $\rho_{\mathrm{eff}}^{(l)}$) inside each row of cylinders are obtained from homogenized properties of the sonic crystal. More explicitly, from the speed of sound (c_{hom}), mass density (ρ_{hom}) and viscous attenuation coefficient of the sound wave (γ_{hom}), which are obtained from the models by Krokin et al. [11], Gumen et al. [12] and Ibarias et al. [13] respectively. They describe the crystal's low frequency behavior and are a function of the frequency, lattice parameter and filling fraction (ff). Then, the complex effective properties, which include viscous losses, for a fluid that is equivalent to a row of cylinders are be obtained as

$$c_{\text{eff}}(f) = \frac{\omega}{k_{\text{eff}}} = \frac{\omega}{\omega/c_{\text{hom}} - \mathrm{i}\gamma_{\text{hom}}(f)} \tag{3}$$

$$\rho_{\text{eff}}(f) = \rho_{\text{hom}} \left(\frac{c_{\text{hom}}}{c_{\text{eff}}(f)} \right)^2, \tag{4}$$

In turn, the transfer matrix of the parallel arrangement of equally spaced resonators, is defined as [14]

$$\mathbf{T_P} = \frac{-1}{ry_{21}^{(N_{\text{HR}})}} \begin{bmatrix} ry_{22}^{(N_{\text{HR}})} & -1 \\ ry_{22}^{(N_{\text{HR}})} \left(\sum_{n=1}^{N_{\text{HR}}} ry_{11}^{(n)} - \sum_{m=1}^{N_{\text{HR}}-1} r\frac{y_{12}^{(m)} y_{21}^{(m)}}{y_{22}^{(m)}} \right) - r^2 y_{12}^{(N_{\text{HR}})} y_{21}^{(N_{\text{HR}})} & \sum_{m=1}^{N_{\text{HR}}-1} r\frac{y_{12}^{(m)} y_{21}^{(m)}}{y_{22}^{(m)}} - \sum_{n=1}^{N_{\text{HR}}} ry_{11}^{(n)} \end{bmatrix} \tag{5}$$

where $r = 1/N_{\text{HR}}$ is the fraction of the unit cell length that is occupied by each different resonator, and $y_{ij}^{(i)}$ is the ij-th element of the admittance matrix of n-th resonator. This matrix is defined as

$$\mathbf{Y}^{(n)} = \frac{1}{t_{12}^{(n)}} \begin{bmatrix} t_{22}^{(n)} & t_{12}^{(n)} t_{21}^{(n)} - t_{22}^{(n)} t_{11}^{(n)} \\ 1 & -t_{11}^{(n)} \end{bmatrix}, \tag{6}$$

where the elements are related to the the transfer matrix of each resonator

$$\mathbf{T_{HR}} = \begin{bmatrix} t_{11} & t_{12} \\ t_{21} & t_{22} \end{bmatrix} = \begin{bmatrix} 1 & \mathrm{i}k_{\text{n}}\Delta l_{\text{n}}^{(\text{out})} Z_{\text{n}} \\ 0 & 1 \end{bmatrix} \begin{bmatrix} \cos(k_{\text{n}} l_{\text{n}}) & \mathrm{i}Z_{\text{n}} \sin(k_{\text{n}} l_{\text{n}}) \\ \mathrm{i}\dfrac{\sin(k_{\text{n}} l_{\text{n}})}{Z_{\text{n}}} & \cos(k_{\text{n}} l_{\text{n}}) \end{bmatrix} \begin{bmatrix} 1 & \mathrm{i}k_{\text{n}}\Delta l_{\text{n}}^{(\text{in})} Z_{\text{n}} \\ 0 & 1 \end{bmatrix} \begin{bmatrix} \cos(k_{\text{c}} l_{\text{c}}) & \mathrm{i}Z_{\text{c}} \sin(k_{\text{c}} l_{\text{c}}) \\ \mathrm{i}\dfrac{\sin(k_{\text{c}} l_{\text{c}})}{Z_{\text{c}}} & \cos(k_{\text{c}} l_{\text{c}}) \end{bmatrix}, \tag{7}$$

where the subscripts n and c indicate whether the quantities are related to the neck or cavity of the resonator, and k and Z are respectively the wavenumber and characteristic impedance of a homogeneous fluid layer that is equivalent to the neck and cavity sections of the resonator. The wavenumber and characteristic impedance inside the neck and cavity can be estimated using Stinson's expressions for sound propagation through narrow slits [15]. In turn, $\Delta l_{\text{n}}^{(\text{out})}$ and $\Delta l_{\text{n}}^{(\text{in})}$ are the inner and outer end corrections of the neck's length. They are estimated using Smits and Kostens expressions for surfaces with slit-like perforations assuming constant pressure over the slit [16].

Once the global matrix of the system $\mathbf{T_G}$ is obtained, the absorption coefficient follows as

$$\alpha(f, \theta_{\text{i}}) = 1 - \left| \frac{\dfrac{z_{\text{s}}}{z_{\text{r}}} - 1}{\dfrac{z_{\text{s}}}{z_{\text{r}}} + 1} \right|^2 = 1 - \left| \frac{\dfrac{\text{T}_{\text{G},11} \cos\theta_{\text{i}}}{\text{T}_{\text{G},21}\rho_0 c_0} - 1}{\dfrac{\text{T}_{\text{G},11} \cos\theta_{\text{i}}}{\text{T}_{\text{G},21}\rho_0 c_0} + 1} \right|^2, \tag{8}$$

where ρ_0 is the density of air, $z_{\text{s}} = \text{T}_{\text{G},11}/\text{T}_{\text{G},21}$ is the surface impedance, and $z_{\text{r}} = \rho_0 c_0 / \cos\theta_{\text{i}}$ is the radiation impedance of an infinite surface.

3 DESIGN BY OPTIMIZATION

We considered the design of surfaces with broad angular absorption at: (1) a single frequency of 250 Hz, and (2) over the octave band with center frequency at 250 Hz. For the first case, only one resonator was included in the unit cell, for the second case six resonators were included in the unit cell in order to cover the broader frequency range. The lattice parameter for the cylinder arrangements was kept at a constant value of 0.111 cm, and 10 layers of cylinders were included. The parameters defined as variables in the design were the four

dimensions of each of the resonators, as shown in Figure 1, and the filling fraction (ff) of each of the layers. Their final values were obtained by solving an optimization problem defined as

$$\min_{x} \qquad \Phi = \frac{1}{N_\theta}\sum_{j=1}^{N_\theta}\left(1-\bar{\alpha}(\theta_{\mathrm{i}}^{(j)},\mathbf{x})\right) \tag{9}$$
$$\text{subject to} \quad 0 \le x_k \le 1, \quad k = 1,...,4N_{\mathrm{HR}}+N_{\mathrm{l}},$$

where N_θ is the number of incidence angles included in the optimization, $\bar{\alpha}$ is the absorption coefficient value averaged over the frequencies of interest, and the design variables were interpolation variables related to the metasurfaces' parameters as

$$w_n^{(k)} = w_{n,\min} + x_k\left(w_{n,\max} - w_{n,\min}\right) \qquad \text{for } k = 1,...,N_{\mathrm{HR}}, \tag{10}$$
$$l_n^{(k-N_{\mathrm{HR}})} = l_{n,\min} + x_k\left(l_{n,\max} - l_{n,\min}\right) \qquad \text{for } k = N_{\mathrm{HR}}+1,...,2N_{\mathrm{HR}}, \tag{11}$$
$$w_c^{(k-2N_{\mathrm{HR}})} = w_{c,\min} + x_k\left(w_{c,\max} - w_{c,\min}\right) \qquad \text{for } k = 2N_{\mathrm{HR}}+1,...,3N_{\mathrm{HR}}, \tag{12}$$
$$l_c^{(k-3N_{\mathrm{HR}})} = l_{c,\min} + x_k\left(l_{c,\max} - l_{c,\min}\right) \qquad \text{for } k = 3N_{\mathrm{HR}}+1,...,4N_{\mathrm{HR}}, \tag{13}$$
$$ff^{(k-4N_{\mathrm{HR}})} = ff_{\min} + x_k\left(ff_{\max} - ff_{\min}\right) \qquad \text{for } k = 4N_{\mathrm{HR}}+1,...,4N_{\mathrm{HR}}+N_{\mathrm{l}}. \tag{14}$$

The minimum and maximum allowable values for the parameters can be found in Table 1.

Table 1. Box constraints for the parameters of the metasurfaces designed for broad angular absorption. The dimensions of the resonator's components are given in mm.

	w_n	l_n	w_c	l_c	ff
Min.	0.8	8	20	40	0
Max.	1.2	30	90	150	0.8

For the single frequency case the distance between resonators was set to 10 cm, and for the multifrequency case the distance between resonators was included as an additional design variable. Its allowable value was constrained to the range $[5,8]$ cm. The set of angles used to calculate the cost function included the range $0^\circ \le \theta_{\mathrm{i}} \le 60^\circ$ discretized in steps of 15°, and the range $61^\circ \le \theta_{\mathrm{i}} \le 89^\circ$ discretized in steps of 1°. An over-representation of the angles close to grazing incidence was used since it is the range where it is more challenging to maintain high absorption [8]. The solution to the problem was found using the sequential quadratic programming algorithm available in the *fmincon* function of MATLAB® [17]. The gradient estimation was done using forward finite difference with a step size of 1.49×10^{-8}, and the problem was solved using 10 initial random guesses for the single-frequency problem, and 5 different initial random guesses for the multi-frequency problem.

4 RESULTS

The optimized values of the metasurface's parameters for the two cases considered can be seen in Table 2. The performance of the absorber designed for single-frequency excitation can be seen in Figure 2. Figure 2a shows the absorption coefficient at 250 Hz as a function of the incidence angle. For reference, the angle-dependent performance of an optimized surface consisting only of a periodic arrangement of resonators, without the added cylinder structure, is overlayed. It can be seen that there is a significant improvement on the performance, especially for the incidence angles close to the normal. The range for which the absorption coefficient takes values equal or higher than 0.9 corresponds to $63^\circ \le \theta_{\mathrm{i}} \le 83$ for the metasurface with only resonators, and to $0^\circ \le \theta_{\mathrm{i}} \le 83$ for the metasurface that combines the resonators and the array of cylinders. Nevertheless, a drawback from this design, is that the cylinder structure increases the absorber's thickness. The optimized

surface has a total thickness of 17.3 cm, about $1/8$ times the wavelength at the design frequency (250 Hz), from which 9.7 cm corresponds to the multilayered media. This aspect can be a limitation for the use of this type of surfaces for applications were there are high space limitations.

Table 2. Optimized values for the parameters of the metasurfaces with broad angle range of high absorption. The dimensions of the resonators' components are given in mm.

Surface optimized for a single frequency															
i	$w_n^{(i)}$	$l_n^{(i)}$	$w_c^{(i)}$	$l_c^{(i)}$	d	$ff^{(1)}$	$ff^{(2)}$	$ff^{(3)}$	$ff^{(4)}$	$ff^{(5)}$	$ff^{(6)}$	$ff^{(7)}$	$ff^{(8)}$	$ff^{(9)}$	$ff^{(10)}$
1	0.8	30	20	46.8	100	0	0	0	0	0	0	0.8	0.8	0.8	0.8
Surface optimized for an octave band															
i	$w_n^{(i)}$	$l_n^{(i)}$	$w_c^{(i)}$	$l_c^{(i)}$	d	$ff^{(1)}$	$ff^{(2)}$	$ff^{(3)}$	$ff^{(4)}$	$ff^{(5)}$	$ff^{(6)}$	$ff^{(7)}$	$ff^{(8)}$	$ff^{(9)}$	$ff^{(10)}$
1	1.2	8.0	45.0	41.0	50	0	0	0	0	0	0	0	0.8	0.8	0.8
2	1.2	8.0	45.0	41.0											
3	0.8	17.0	36.8	40.0											
4	0.8	17.3	45.0	46.6											
5	0.8	9.4	45.0	120.6											
6	0.8	15.1	29.3	40.0											

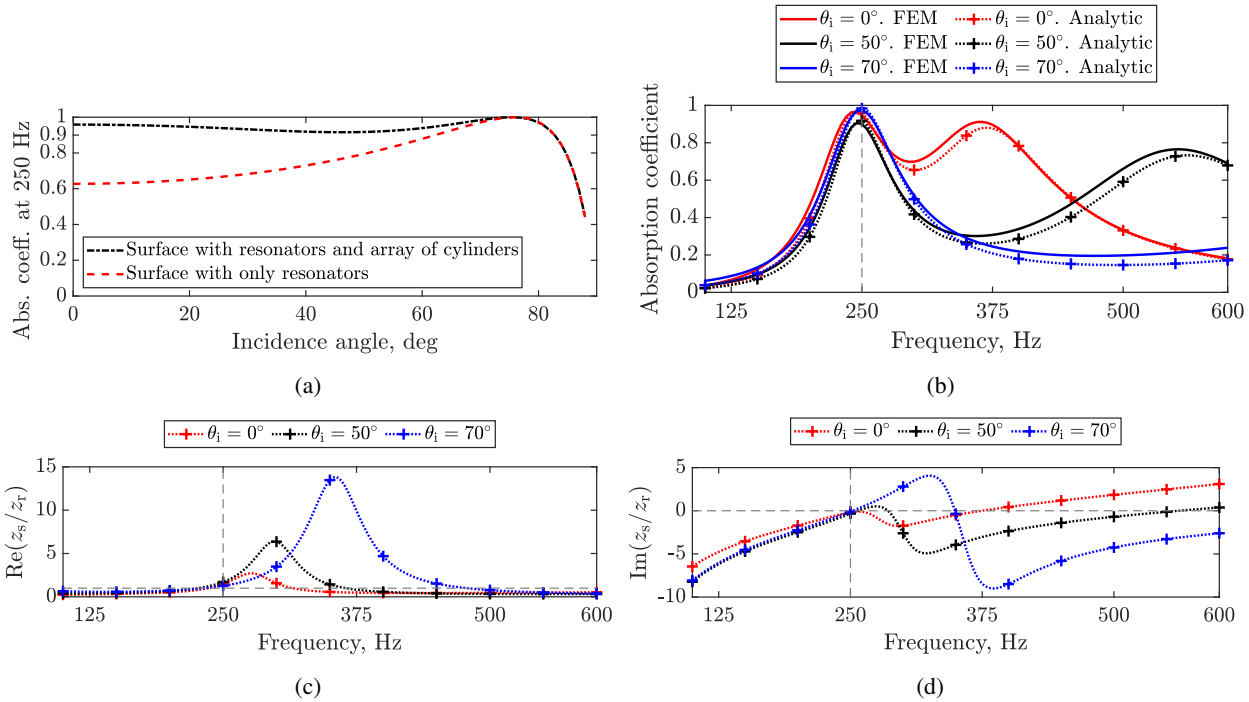
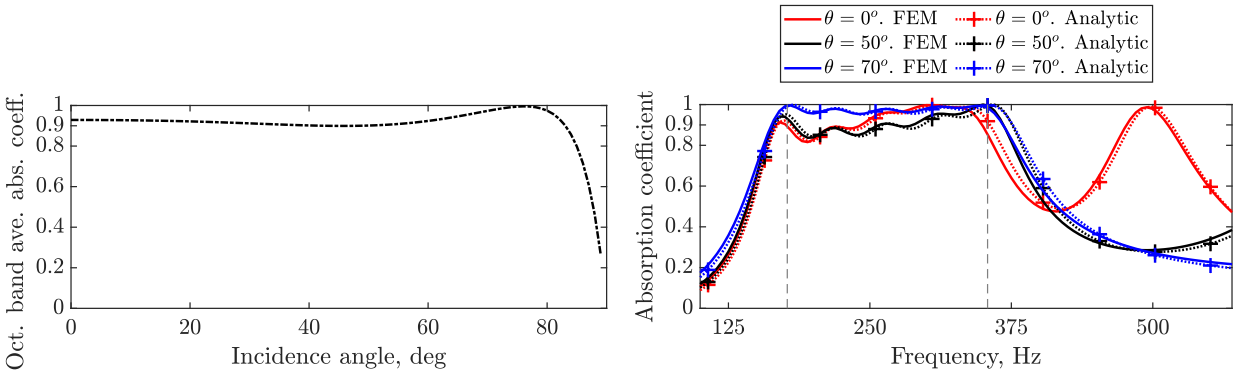


Figure 2. Performance of the optimized metasurface for single frequency excitation. **2a:** Angle dependent absorption coefficient for the 250 Hz frequency for the proposed absorber and an optimized surface including only resonators. **2b:** Frequency-dependent absorption coefficient for selected incidence angles. Analytic and numeric results are overlayed for verification. **2c:** Real part of the normalized surface impedance. **2d:** Imaginary part of the normalized surface impedance. The vertical dashed lines identify the frequency used for the optimization and the horizontal lines mark the condition to achieve an absorption coefficient of one according to Eq. 8.

Figure 2b shows the absorption coefficient as a function of frequency for selected incidence angles. Results from a finite element model (FEM) are also included. In the FEM model, a solution was found for the acoustic pressure for a unit cell of each of the optimized metasurfaces. Floquet periodicity boundary conditions where assigned at both sides of the unit cell, a perfectly match layer was placed at 2.4 m from the absorber to simulate an open field, and viscous and thermal losses happening at the boundaries of the cylinders and the resonators were included using the boundary layer impedance boundary condition [18, 19].

The combination of the resonators and the cylinder structure creates a multiresonant system that has a behavior that is not locally reacting, i.e. the surface impedance is not independent from the wave incidence direction anymore. This can be seen on Figures 2c and 2d, where the real and imaginary parts of the normalized surface impedance can be seen for the same three incidence angles used in Figure 2b. The normalization is done with respect to the radiation impedance. The multiple zero-crossings of the imaginary part of the surface impedance show the multiresonant nature of the system. Moreover, the frequency of the second zero-crossing of each of the curves changes with the incidence angle. This explains the shift in frequency that is observed for the second peak in the absorption coefficient curves in Figure 2b. This is because a better impedance matching between the outer field and the absorber is obtained when $\mathrm{Im}\,(z_\mathrm{s}/z_\mathrm{r}) = 0$, as can be seen from Eq. (8).

The performance of the metasurface designed for multifrequency absorption is shown in Figure 3. Its performance as a function of the incidence angle is similar to the one for the single frequency case. Namely, frequency averaged absorption coefficient values above 0.9 can be seen in the angle range between 0° and 83°. Thus showing that it is possible to use this type of surfaces also for multifrequency applications.



(a) (b)

Figure 3. Performance of the optimized metasurface for octave-band excitation. **3a:** Frequency averaged angle dependent absorption coefficient for the octave band with center frequency at 250 Hz. **3b:** Frequency-dependent performance for selected incidence angles. Analytic and numeric results are overlayed for verification. The vertical dashed lines indicate the limits of the octave band considered.

5 CONCLUSIONS

In this work, a type of metasurface has been proposed which is able to achieve high absorption coefficient values at a broad range of incidence angles for both single and multifrequency cases. These type of surfaces are realized as a combination of a periodic surface of resonators topped by a multilayer arrangement of cylinders. Results show that they can achieve a significantly broader angular performance than a surface that consists only on a parallel arrangement of resonators.

ACKNOWLEDGMENTS

The authors would like to thank José Sanchez-Dehesa for the useful discussions. This research was carried out within the Signature project, a collaboration between the Technical University of Denmark and the Korea

Advanced Institute of Science and Technology in the research of metamaterials for sound insulation, radiation, and absorption.

REFERENCES

[1] K. Donda et al. "Extreme low-frequency ultrathin acoustic absorbing metasurface". eng. In: *Applied Physics Letters* 115.17 (2019), p. 173506. ISSN: 10773118, 00036951. DOI: 10.1063/1.5122704.

[2] Y. Li and B. M. Assouar. "Acoustic metasurface-based perfect absorber with deep subwavelength thickness". eng. In: *Applied Physics Letters* 108.6 (2016), p. 063502. ISSN: 10773118, 00036951. DOI: 10.1063/1.4941338.

[3] M. Yang et al. "Optimal sound-absorbing structures". In: *Mater. Horiz.* 4 (4 2017), pp. 673–680. DOI: 10.1039/C7MH00129K. URL: http://dx.doi.org/10.1039/C7MH00129K.

[4] S. Degraeve and J. Oclee-brown. "metamaterial absorber for loudspeaker enclosures". In: *Journal of the Audio Angineering Society* (May 2020).

[5] N. Jiménez et al. "Rainbow-trapping absorbers: Broadband, perfect and asymmetric sound absorption by subwavelength panels for transmission problems". eng. In: *Scientific Reports* 7.1 (2017), pp. 13595, 13595. ISSN: 20452322. DOI: 10.1038/s41598-017-13706-4.

[6] J. Ji et al. "Low-Frequency Broadband Acoustic Metasurface Absorbing Panels". eng. In: *Frontiers in Mechanical Engineering* 6 (2020), pp. 1–13. ISSN: 2297-3079. DOI: 10.3389/fmech.2020.586249.

[7] N. Jiménez et al. "Iridescent perfect absorption in critically-coupled acoustic metamaterials using the transfer matrix method". eng. In: *Applied Sciences (switzerland)* 7.6 (2017), p. 618. ISSN: 20763417. DOI: 10.3390/app7060618.

[8] D. M. Garza-Agudelo et al. "Characterization and optimization of the angle dependent acoustic absorption of 2D infinite periodic surfaces of Helmholtz resonators". In: *Journal of Theoretical and Computational Acoustics* (2022). Accepted/In press. DOI: 10.1142/S2591728522500104.

[9] M. Hodgson and A. Wareing. "Comparisons of predicted steady-state levels in rooms with extended- and local-reaction bounding surfaces". eng. In: *Journal of Sound and Vibration* 309.1-2 (2008), pp. 167–177. ISSN: 10958568, 0022460x. DOI: 10.1016/j.jsv.2007.06.069.

[10] J. F. Allard and N. Atalla. *Propagation of Sound in Porous Media: Modelling Sound Absorbing Materials*. eng. John Wiley and Sons, 2009, pp. 1–358. ISBN: 0470747331, 9780470746615, 9780470747339, 1282349538, 0470746610, 047074734x, 9786612349539. DOI: 10.1002/9780470747339.

[11] A. A. Krokhin, J. Arriaga, and L. N. Gumen. "Speed of sound in periodic elastic composites". eng. In: *Physical Review Letters* 91.26 (2003), pp. 264302/1–4. ISSN: 00319007, 10797114. DOI: 10.1103/PhysRevLett.91.264302.

[12] L. N. Gumen, J. Arriaga, and A. A. Krokhin. "Metafluid with anisotropic dynamic mass". eng. In: *Low Temperature Physics* 37.11 (2012), pp. 975–978. ISSN: 10906517, 1063777x. DOI: 10.1063/1.3672821.

[13] M. Ibarias et al. "Phononic crystal as a homogeneous viscous metamaterial". eng. In: *Physical Review Research* 2.2 (2020), p. 022053. ISSN: 26431564. DOI: 10.1103/PhysRevResearch.2.022053.

[14] K. Verdière et al. "Transfer matrix method applied to the parallel assembly of sound absorbing materials". eng. In: *Journal of the Acoustical Society of America* 134.6 (2013), pp. 4648–4658. ISSN: 15208524, 00014966, 01630962. DOI: 10.1121/1.4824839.

[15] M. R. Stinson. "The propagation of plane sound waves in narrow and wide circular tubes, and generalization to uniform tubes of arbitrary cross-sectional shape". eng. In: *Journal of the Acoustical Society of America* 89.2 (1991), pp. 550–8. ISSN: 00014966, 15208524. DOI: 10.1121/1.400379.

[16] J. M. A. Smits and C. W. Kosten. "Sound absorption by slit resonators". In: *Acustica* 1 (1951), pp. 114–122.

[17] MATLAB® V. 9.9.0.1592791 (R2020b) Update 5. The MathWorks Inc, Natick, Massachusetts.

[18] M. Nijhof. “Viscothermal wave propagation”. English. PhD thesis. Netherlands: University of Twente, Dec. 2010. ISBN: 9789036531191. DOI: 10.3990/1.9789036531191.

[19] M. Berggren, A. Bernland, and D. Noreland. “Acoustic boundary layers as boundary conditions”. eng. In: *Journal of Computational Physics* 371 (2018), pp. 633–650. ISSN: 10902716, 00219991. DOI: 10.1016/j.jcp.2018.06.005.

ICA 2022
24th INTERNATIONAL CONGRESS ON ACOUSTICS
October 24(Mon) - 28(Fri), 2022 Gyeongju, Korea

PROCEEDINGS of the
24th International Congress on Acoustics

October 24 to 28, 2022 in Gyeongju, Korea

ABS-0763

Interaction of acoustic meta-atoms as additional degrees of freedom for metamaterial tuning

Felix Kronowetter[(1)], Steffen Marburg[(2)]

[(1)]Chair of Vibro-Acoustics of Vehicles and Machines, Department of Engineering Physics and Computation, Technical University of Munich, TUM School of Engineering and Design,Germany, felix.kronowetter@tum.de

[(2)]Chair of Vibro-Acoustics of Vehicles and Machines, Department of Engineering Physics and Computation, Technical University of Munich, TUM School of Engineering and Design, Germany, steffen.marburg@tum.de

ABSTRACT

Acoustic metamaterials have a widespread range of application, e.g. acoustic cloaking and acoustic lenses, and usually consist of an arrangement of meta-atoms. These meta-atoms are often based on the principle of local resonances. Herein, we theoretically study the case of two meta-atoms in an unbounded two-dimensional fluid domain in order to analyze their mutual interaction. Furthermore, we vary distance, orientation and detuning while observing the eigenfrequencies of two interacting modes. Certain configurations of the varying parameters mentioned before lead to regions of modal degeneracy, hence to maxima in the transmission loss if excited by a plane wave. Thus, we make use of this phenomenon in order to improve the wave attenuation properties of the meta-atoms..

Keywords: Acoustic metamaterial, Metamaterial tuning, Sound insulation

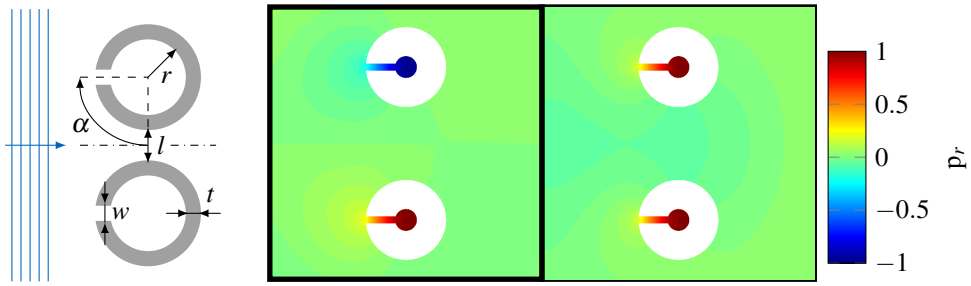
1 INTRODUCTION

Methods to increase sound attenuation are usually determined by increasing mass (low frequencies) or by increasing stiffness (high frequencies). A new type of materials called acoustic metamaterials are able to break the mass rule and hence are subject of numerous scientific studies. They commonly consist of an arrangement of mostly periodic meta-atoms that lead to non-natural material properties beneficial for noise control applications [1–4]. Non-natural material properties are, for example, a negative effective mass density [5, 6], negative bulk modulus [7] or negative refractive index [8]. Meta-atoms work like local resonators interacting with the incoming sound waves. Furthermore, since meta-atoms are sub-wavelength structures and arranged close to each other, pressure coupling between the individual meta-atoms occurs [9]. Pressure coupling affects each individual meta-atom, can be used as tuning parameter and hence lead to enhanced sound transmission [10]. Coupling effects have been used for tuning electro-magnetic metamaterials [11, 12]. Another analogy comes from the study of organ pipes, where coupling is a well known effect [13–16]. There are various studies about coupling of acoustic resonators in waveguides [9, 17–19]. Coupling as tuning parameter of local resonators within a unit cell are investigated in recent years [20–22]. Furthermore, coupling is applied to tune acoustic lenses [10] and metagratings [23].

We investigate the interaction of two C-shaped meta-atoms in a two-dimensional domain of infinite extend. The eigenfrequencies of the system are studied for parameters like distance, orientation, detuning and radiation losses. We analyze underlying effect and use the coupled mode theory to get a better understanding of the coupling mechanisms. We demonstrate how the sound attenuation of meta-atoms can be improved and tuned. The aim is to show how the interaction of meta-atoms affects the performance of the metamaterial in terms of sound attenuation.

2 RESULTS

Figure 1(a) shows the basic geometry and dimensions of the pair of resonators, which are simplified as two-dimensional C-shapes [24, 25]. The influence of the two ends for real C-shaped cylinders of finite height is hence neglected. Furthermore, the system is considered lossless. Thermo-viscous boundary layer losses are significant for structures with narrow geometry features. However, the chosen aperture width is large compared to the expected boundary layer thickness. The C-shapes have an inner radius $r = 18.77\,\mathrm{mm}$, an aperture width $w = 4\,\mathrm{mm}$, and a thickness $t = 2\,\mathrm{mm}$. This configuration leads to the complex individual resonant frequency $\bar{\omega} = 1000 + 53i\,\mathrm{Hz}$, with $\bar{\omega} = \omega/2\pi$. The length l denotes the shortest distance between the two C-shapes. Initially, both apertures face the incident plane wave. The resonator pair is surrounded by a large circular air domain, which is in turn surrounded by a perfectly matched layer. All studies in this section are conducted as finite element simulations in *COMSOL Multiphysics* [26], first and foremost in form of modal analyses, then by the transmission response for harmonic excitation by a plane wave. The symmetric and antisymmetric modes are depicted in Figure 1(b).



(a) Geometry. (b) Antisymmetric (left) and symmetric (right) mode.

Figure 1. Resonator pair geometry and dimensions, specified by inner radius r, aperture width w, wall thickness t, and inter-resonator distance l are shown in Figure 1(a). Figure 1(b) displays the antisymmetric mode (mode 1) and symmetric mode (mode 2), where p_r denotes the real part of the total pressure normalized to its maximum value.

2.1 Inter-resonator distance

The first parameter to be studied is the distance l between two resonators. It is varied from zero to twice the resonant wavelength. The real part of the complex eigenfrequencies $\bar{\omega} = f + \mathrm{i}\gamma$ is the resonant frequency f, the imaginary part γ characterizes the radiation loss. Figs. 2(a) and 2(b) show the eigenfrequencies of the cavity resonant modes (modes with high quality factors) $\bar{\omega}$ as a function of the inter-resonator distance l.

Both real and imaginary parts in the coupled system oscillate around the complex resonant frequency of the individual resonators. The oscillation period matches the resonant wavelength $\lambda = 343\,\mathrm{mm}$, similar to the Fabry-Pérot interference observed by Hein et al. [27] for duct-cavity systems. We obtain crossing points of the two modes at periodic distances of $\Delta l = \lambda/2$ and observe that the crossing points of real and imaginary parts are shifted against each other by about a quarter wavelength. Furthermore, the mode with the smaller imaginary part dominates the decay process.

To explain the degeneracy of coupled modes for small detuning we use the coupled mode theory (CMT). Assuming that a_1, a_2 are the modal amplitudes with the time dependence $\exp(\mathrm{i}\omega_i t)$ of two weakly uncoupled resonators, the dynamics of the system are given by Haus et al. [28]:

$$\frac{\mathrm{d}}{\mathrm{d}t}\begin{pmatrix} a_1 \\ a_2 \end{pmatrix} = \begin{bmatrix} \mathrm{i}\omega_1 & \mathrm{i}\kappa \\ \mathrm{i}\kappa & \mathrm{i}\omega_2 \end{bmatrix}\begin{pmatrix} a_1 \\ a_2 \end{pmatrix}. \tag{1}$$

The coupling coefficient is denoted κ. For a better understanding of the underlying effects causing synchro-

nization and coupling, we derive a surrogate model representing κ:

$$\kappa = c_\kappa \left[\left[\cos\left(\frac{\pi}{c_p}(l-l_0)\right)\left(1+\frac{1}{l}\right)\right] \mathrm{i} + \left[\sin\left(\frac{\pi}{c_p}(l-l_0)\right)\left(1+\frac{l_0}{l}\right)\right]\right]. \tag{2}$$

The period constant is defined by $c_p = \bar{\lambda}/2 - 2(r+t)/p_c$, with p_c being an adjustable coefficient implying scattering effects.

Analogously, the distance of the first crossing is formulated as $l_0 = \frac{\bar{\lambda}}{4} - 2\frac{r+t}{c_c}$, whereat c_c is an adjustable crossing coefficient.

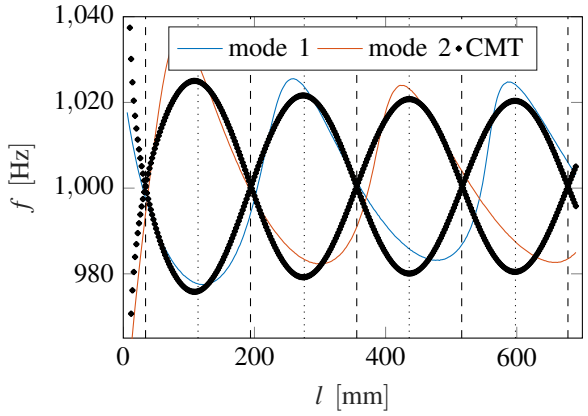
To obtain the coupling coefficient, both complex resonant frequencies are put into relation via their corresponding quality factors $c_\kappa = Q_1/Q_2$. Figure 3 shows the cavity resonant frequencies as well as the results of the CMT dependent on the inter-resonator distance l. We here consider three cases. In case 1, the two resonators are identical. In Figs. 2(a) and 2(b) we can see, that the results of the CMT match the simulated data quite accurately. The modal crossings are replicated by the analytical model. Furthermore, the period is sustained and so is the decay of the amplitude. Same can be observed regarding the imaginary part. In the second case, we introduce a detuning of $\Delta = 5\,\%$ in resonator two. The two modes no longer cross in the real part but do so in the imaginary part. Hence, the state of degenerate modes is not realizable (except for the first crossing). The detuning leads to poorer sound attenuation properties compared to the case of identical resonators. The analytical model again replicates the modal anti-crossings in the real part as well as the increased periodicity of the imaginary part. We merely note, that the antisymmetric fluctuations in the imaginary part of Figure 2(d) show an enhanced deviation from the simulated data compared to Figure 2(b). In the third case, we increase the size of the aperture to increase the coupling, hence to counteract the anti-crossings. By increasing the radiation loss, we manage to restore the modal crossings and hence obtain degenerate modes again. Thus, increased radiation loss stabilizes the system against detuning. As we can extract from Figure 2(e), the analytical model also represents this case. Minor inaccuracies can be identified in the imaginary part in Figure 2(f). This is due to increasing inaccuracy of the model coming along with increased inter-resonator distance l.

A crucial parameter to understand the fundamental coupling effects is the complex coupling coefficient κ. In Figure 3 the behavior of κ is displayed for the second and third case mentioned in Figure 2.

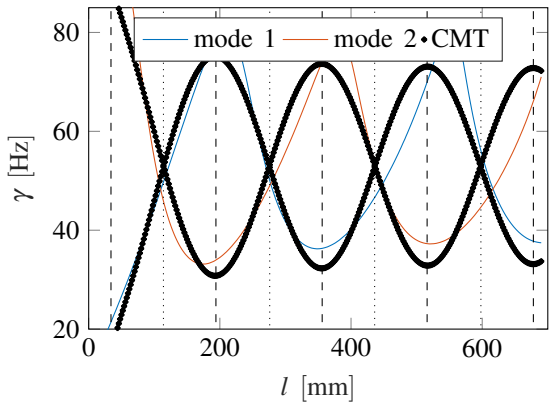
The absolute value of the coupling coefficient decays with increased inter-resonator distance l. Fischer et al. [13] show, that the coupling strength is supposed to be a function of the distance between the pipes, with a sound attenuation of $1/r^2$ in the near field and $1/r$ in the far field matching our results. Additionally, the zeros of the real and imaginary parts occur periodically. The former concur with the maximum frequency mismatch of mode 1 and mode 2 and the latter with the modal (anti-)crossings, represented by the dotted and dashed lines in Figs. 2(c) and 2(e). A noteworthy finding taken from Figs. 2 and 3 is the imaginary part of the coupling coefficient turning zero at modal (anti)crossings and thus we fulfill the criterion that the real part of two modes become degenerate for a purely imaginary coupling. The analytical model also predicts the reciprocal behavior of $\Re(\kappa)$ turning zero, where the real parts of mode 1 and mode 2 show a maximum deviation and the imaginary parts cross. These results correlate with the findings by Haus et al. [28]. Since we increase the aperture width in Figure 2(e), κ also increases and hence, the modal crossings of the real part are restored. Furthermore, the model also replicates the decreased periodicity of modal crossings in the imaginary part and the additional degeneracies of the imaginary parts disappear.

2.2 Relative orientation

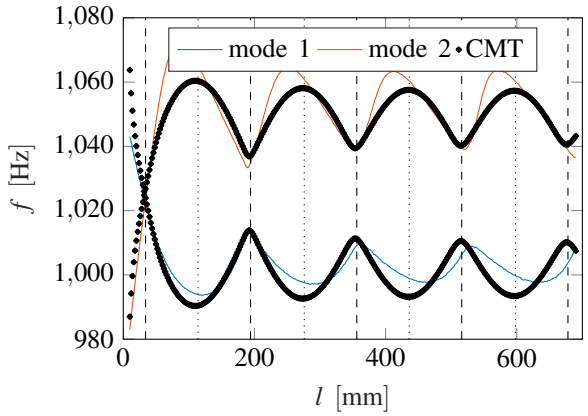
We now examine the relative orientation of the C-shapes' apertures. Powell et al. [12] show that it is relevant in electromagnetic metamaterials. Additionally, Powell et al. [11] and Hesmer et al. [29] suggest that the relative orientation plays a major role for the coupling of split ring resonators, hence it may also be of importance for the acoustic meta-atoms. The apertures face each other for zero twist angle $\alpha = 0°$, the two C-shapes are rotated and reach the configuration in Figure 1(a) for $\alpha = 90°$. The apertures look away from each other for $\alpha = 180°$. Figure 4(a) displays the absolute difference between the cavity resonant frequencies $\Delta f = |\Re(\bar{\omega}_1 - \bar{\omega}_2)|$ in the parameter plane of inter-resonator distance l and twist angle α. The dark blue regions indicate the course of degenerate modes with $\Delta f = 0$. The modal crossings provide the locations of possible transmission minima, that



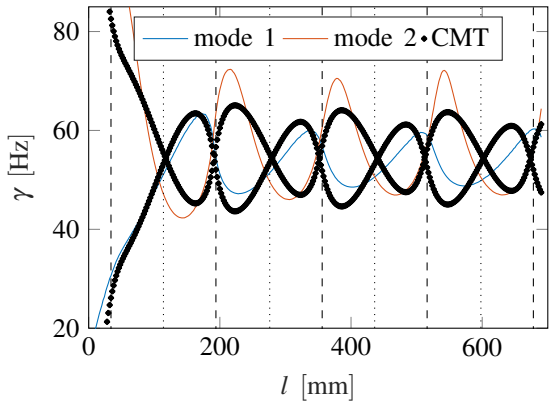
(a) real part.



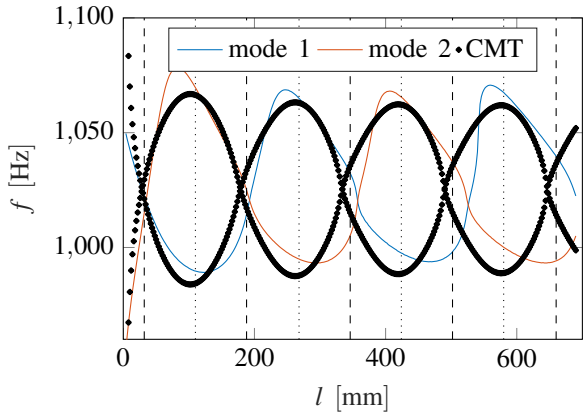
(b) imaginary part.



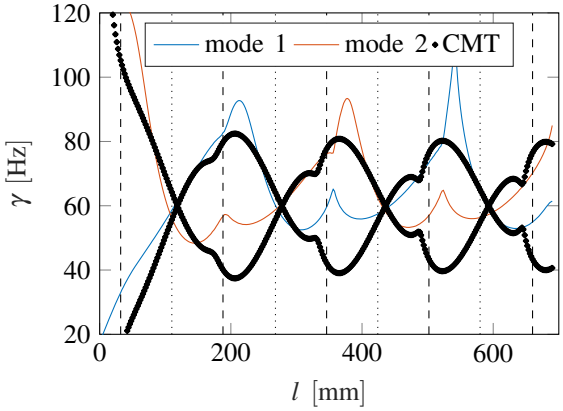
(c) real part, frequency detuning $\Delta = 5\,\%$.



(d) imaginary part, frequency detuning $\Delta = 5\,\%$.

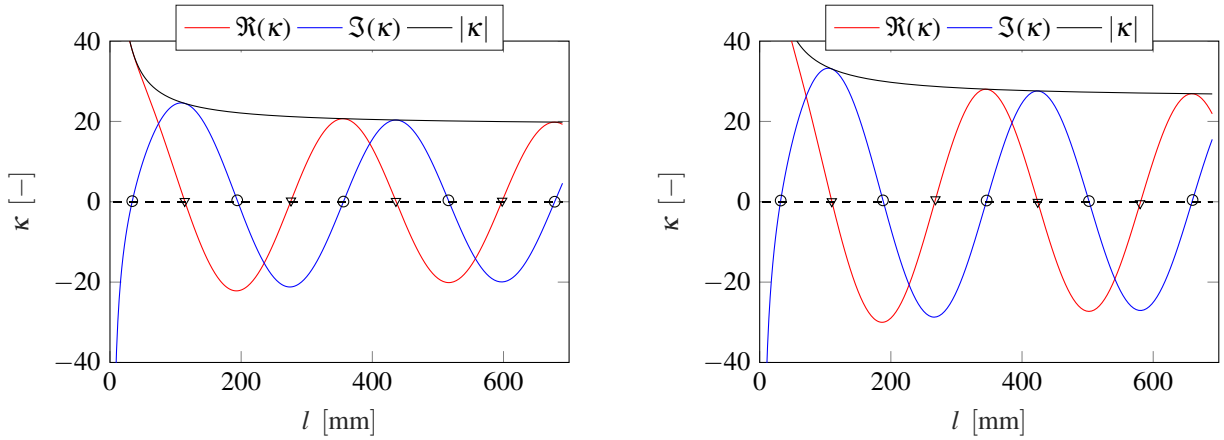


(e) real part, frequency detuning $\Delta = 5\,\%$, increased aperture width $w_A = 6\,\text{mm}$ (initially $w_A = 4\,\text{mm}$).



(f) imaginary part, frequency detuning $\Delta = 5\,\%$, increased aperture width $w_A = 6\,\text{mm}$ (initially $w_A = 4\,\text{mm}$).

Figure 2. Real and imaginary part of the cavity resonant frequencies $\bar{\omega}$ [Hz] as a function of the inter-resonator distance l [mm]. The dashed black lines indicate the zeros of $\Re(\kappa)$ and the dotted lines the zeros of $\Im(\kappa)$.



(a) 2nd case.

(b) 3rd case.

Figure 3. κ is displayed for the second and third case mentioned in Figure 2. The absolute value is plotted as black line, the real part as red line and the imaginary part as blue line.

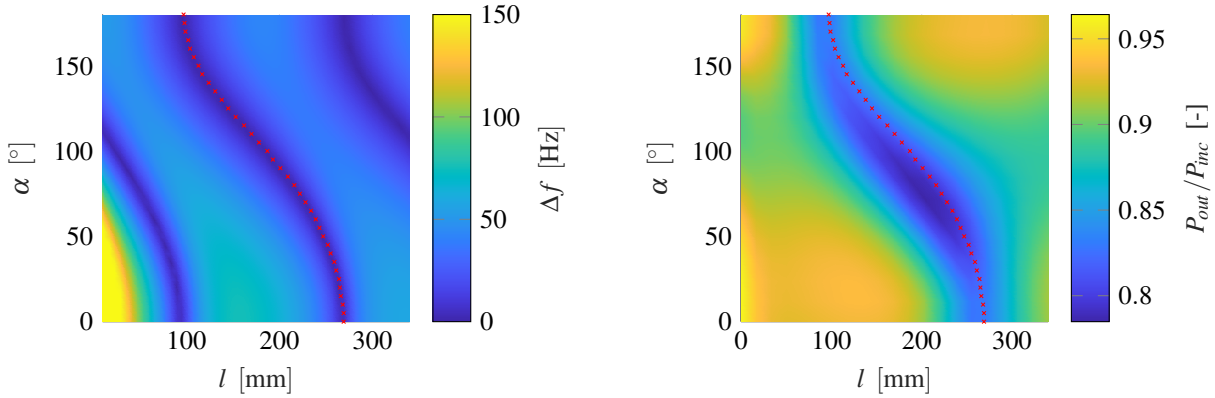
is attenuation maxima.

The normalized total transmitted sound power P_{out}/P_{inc} in the α-l-plane is presented in Figure 4(b). The incident wave with $f = 1000\,\mathrm{Hz}$ is matching the C-shapes' resonant frequency. As a result, transmission dips and modal crossings occur at the same distances and twist angles. For comparison, the crossings are indicated with red crosses in both plots in Figure 4. The transmission dips only occur where the symmetric mode dominates, because of the relative orientation of resonators and incident wave.

The dark blue regions with $\Delta f = 0$ in Figure 4(a) cover a certain range regarding the inter resonator distance. Furthermore, we can shift the point of degenerate modes to certain distances by adjusting the orientation of the C-shapes. Thus, the period of degenerate points is maintained. The transmission study shows that the attenuation maxima can be found at the points of modal degeneracy. This leads to the conclusion that distance and orientation are tuning parameters for metamaterials. Surprisingly, the attenuation maxima for this configuration is not found at $\alpha = 90°$ but at $\alpha = 72°$ and $l = 204\mathrm{mm}$. Similar results are observed by varying frequencies of the incoming wave.

3 CONCLUSIONS

Two cavity resonant modes of a pair of identical coupled Helmholtz resonators were found. With varying separation distance, the corresponding eigenfrequencies oscillate around the uncoupled resonant frequency. A period equal to the uncoupled resonant wavelength $\bar{\lambda}$ means that the two modes cross every $\bar{\lambda}/2$. One mode is symmetric, the other one is antisymmetric, implying in- and anti-phase oscillation of the two resonators, respectively. The identity of resonant frequencies at the modal crossings holds within a certain range of frequency detuning, the region of modal degeneracy. Consequently, certain separation distances might enable larger manufacturing tolerances than others. C-shapes with larger aperture width and a separation distance corresponding to a modal crossing could be used to mitigate the effect of fabrication inaccuracies. This allows for higher manufacturing tolerances in exchange for increased losses. Coupling induces the possibility of tuning via the resonators' relative arrangement, that is distance and orientation. Starting with facing apertures, the two resonators were twisted in opposite directions. Thereby, the modal synchronization points can be shifted to arbitrary distances, while the period is maintained. This means that the coupling strength depends on both relative orientation and distance. Accordingly, these two influence parameters offer additional degrees of freedom for tuning the metamaterial response with unchanged components. Additionally, a new surrogate model based on the CMT was derived that predicts the modal behavior of the system and, hence, replaces the time-consuming numerical analysis. In



(a) cavity resonant frequency difference.

(b) normalized total transmitted sound power.

Figure 4. **(a)** Difference between the real parts of the cavity resonant frequencies $\Delta f = |\Re(\bar{\omega}_1 - \bar{\omega}_2)|$ [Hz] of mode 1 and 2 in the plane of inter-resonator distance l [mm] and angle α [°]. The modal crossings are represented by the dark blue lines with zero frequency difference $\Delta f = 0$. The black line indicates a constant inter-aperture distance l_a starting at the second crossing point for $\alpha = 0°$. **(b)** Normalized total transmitted sound power P_{out}/P_{inc} [−] for a plane wave with $f = 1000\,\text{Hz}$ in the plane of inter-resonator distance l [mm] and angle α [°]. **(a, b)** For comparison, the second modal crossing is indicated by red crosses in both figures.

conclusion, one can state that the interaction between the resonators in a metamaterial structure significantly affects its characteristics. The better the understanding, the larger the benefits of including synchronization and coupling effects in the design of acoustic metamaterials.

References

[1] S. A. Cummer, J. Christensen, and A. Alù. "Controlling sound with acoustic metamaterials". In: *Nature Reviews Materials* 1.3 (2016), p. 16001. DOI: 10.1038/natrevmats.2016.1.

[2] P. A. Deymier. *Acoustic Metamaterials and Phononic Crystals*. Springer, 2013. DOI: 10.1007/978-3-642-31232-8.

[3] G. Ma and P. Sheng. "Acoustic metamaterials: From local resonances to broad horizons". In: *Science Advances* 2.2 (2016). DOI: 10.1126/sciadv.1501595.

[4] F. Zangeneh-Nejad and R. Fleury. "Active times for acoustic metamaterials". In: *Reviews in Physics* 4 (2019), p. 100031. DOI: 10.1016/j.revip.2019.100031.

[5] G. W. Milton and J. R. Willis. "On modifications of Newton's second law and linear continuum elastodynamics". In: *Proceedings of the Royal Society A: Mathematical, Physical and Engineering Sciences* 463.2079 (2007), pp. 855–880. DOI: 10.1098/rspa.2006.1795.

[6] S. Yao, X. Zhou, and G. Hu. "Experimental study on negative effective mass in a 1D mass–spring system". In: *New Journal of Physics* 10.4 (2008), p. 43020. DOI: 10.1088/1367-2630/10/4/043020.

[7] N. Fang et al. "Ultrasonic metamaterials with negative modulus". In: *Nature Materials* 5.6 (2006), pp. 452–456. DOI: 10.1038/nmat1644.

[8] J. B. Pendry. "Negative Refraction Makes a Perfect Lens". In: *Phys. Rev. Lett.* 85.18 (2000), pp. 3966–3969. DOI: 10.1103/PhysRevLett.85.3966.

[9] Y.-F. Wang and V. Laude. "Longitudinal Near-Field Coupling between Acoustic Resonators Grafted onto a Waveguide". In: *Crystals* 7 (Jan. 2017). DOI: 10.3390/cryst7110323.

[10] X. Yang et al. “Acoustic superlens using Helmholtz-resonator-based metamaterials”. In: *Applied Physics Letters* 107.19 (2015), p. 193505. DOI: 10.1063/1.4935589. eprint: https://doi.org/10.1063/1.4935589. URL: https://doi.org/10.1063/1.4935589.

[11] D. A. Powell et al. “Metamaterial tuning by manipulation of near-field interaction”. In: *Phys. Rev. B* 82.15 (2010), p. 155128. DOI: 10.1103/PhysRevB.82.155128.

[12] D. A. Powell, K. Hannam, I. V. Shadrivov, and Y. S. Kivshar. “Near-field interaction of twisted split-ring resonators”. In: *Phys. Rev. B* 83.23 (2011), p. 235420. DOI: 10.1103/PhysRevB.83.235420.

[13] J. L. Fischer, R. Bader, and M. Abel. “Aeroacoustical coupling and synchronization of organ pipes”. In: *The Journal of the Acoustical Society of America* 140.4 (2016), pp. 2344–2351. DOI: 10.1121/1.4964135.

[14] J. W. Strutt. *The Theory of Sound*. Vol. 1. Cambridge Library Collection - Physical Sciences. Cambridge University Press, 2011. DOI: 10.1017/CBO9781139058087.

[15] J. Sawicki, M. Abel, and E. Schöll. “Synchronization of organ pipes”. In: *European Physical Journal B* 91.2 (2018), pp. 1–9. DOI: 10.1140/epjb/e2017-80485-8.

[16] T. A. Johansson and M. Kleiner. “Theory and experiments on the coupling of two Helmholtz resonators”. In: *The Journal of the Acoustical Society of America* 110.3 (2001), pp. 1315–1328. DOI: 10.1121/1.1394741.

[17] I. Herrero-Durá et al. “Sound Absorption and Diffusion by 2D Arrays of Helmholtz Resonators”. In: *Applied Sciences* 10.5 (2020). ISSN: 2076-3417. DOI: 10.3390/app10051690. URL: https://www.mdpi.com/2076-3417/10/5/1690.

[18] R. Aljahdali and Y. Wu. “Coupled Resonators for Sound Trapping and Absorption”. In: *Scientific Reports* 8 (Sept. 2018). DOI: 10.1038/s41598-018-32135-5.

[19] Y. Zhou et al. “Acoustic Multiband Double Negativity from Coupled Single-Negative Resonators”. In: *Phys. Rev. Applied* 10 (4 Oct. 2018), p. 044006. DOI: 10.1103/PhysRevApplied.10.044006. URL: https://link.aps.org/doi/10.1103/PhysRevApplied.10.044006.

[20] T. Cavalieri et al. “Three-dimensional multiresonant lossy sonic crystal for broadband acoustic attenuation: Application to train noise reduction”. In: *Applied Acoustics* 146 (Mar. 2019), pp. 1–8. DOI: 10.1016/j.apacoust.2018.10.020.

[21] T. Lee and H. Iizuka. “Bragg scattering based acoustic topological transition controlled by local resonance”. In: *Physical Review B* 99 (Feb. 2019), p. 064305. DOI: 10.1103/PhysRevB.99.064305.

[22] M. Krasikova et al. “Noise reduction using structures based on coupled Helmholtz resonators”. In: *AIP Conference Proceedings* 2300.1 (2020), p. 020069. DOI: 10.1063/5.0032103.

[23] Y. Dong et al. “Broadband and wide-angle blazed acoustic gratings using multiple coupled Helmholtz resonators”. In: *Applied Physics Express* 10.9 (Sept. 2017), p. 097201. DOI: 10.7567/APEX.10.097201.

[24] D. P. Elford, L. Chalmers, F. V. Kusmartsev, and G. M. Swallowe. “Matryoshka locally resonant sonic crystal”. In: *The Journal of the Acoustical Society of America* 130.5 (2011), pp. 2746–2755. DOI: 10.1121/1.3643818.

[25] L. Chalmers, D. P. Elford, F. V. Kusmartsev, and G. M. Swallowe. “Acoustic band gap formation in two-dimensional locally resonant sonic crystals comprised of helmholtz resonators”. In: *International Journal of Modern Physics B* 23.20-21 (2009), pp. 4234–4243. DOI: 10.1142/S0217979209063390.

[26] COMSOL Inc. *COMSOL Multiphysics v5.6*. Stockholm, Sweden, 2021.

[27] S. Hein, W. Koch, and L. Nannen. “Trapped modes and Fano resonances in two-dimensional acoustical duct-cavity systems”. In: *Journal of Fluid Mechanics* 692 (2012), pp. 257–287. DOI: 10.1017/jfm.2011.509.

[28] H. A. Haus and W. Huang. “Coupled-mode theory”. In: *Proceedings of the IEEE* 79.10 (1991), pp. 1505–1518. DOI: 10.1109/5.104225.

[29] F. Hesmer et al. “Coupling mechanisms for split ring resonators: Theory and experiment”. In: *physica status solidi (b)* 244 (2007), pp. 1170–1175. DOI: 10.1002/pssb.200674501.

ICA 2022
24th INTERNATIONAL CONGRESS ON ACOUSTICS
October 24(Mon) - 28(Fri), 2022 Gyeongju, Korea

PROCEEDINGS of the
24th International Congress on Acoustics

October 24 to 28, 2022 in Gyeongju, Korea

ABS-0959

Broadband acoustic lens design using gradient-based optimization

Feruza Amirkulova[(1)], Samer Gerges[(2)], Andrew N. Norris[(3)]

[(1)]Mechanical Engineering Department, San José State University, San José, 95192, USA, feruza.amirkulova@sjsu.edu

[(2)]Mechanical Engineering Department, San José State University, San José, 95192, USA, samer.gerges@sjsu.edu

[(3)]Mechanical and Aerospace Engineering Department, Rutgers University, Piscataway, 08854, USA, norris@rutgers.edu

ABSTRACT

In this work, we present a gradient-based optimization (GBO) method [1, 2] for the design of a broadband acoustic lens. This design is based on an optimization process using the semi-analytical optimization approach by means of multiple scattering theory. The GBO algorithm maximizes the sound amplification at the focal point by evaluating pressure derivative with respect to the cylinder positions and then perturbatively optimizing the position of each cylinder in the lens. The results of the GBO of the uni- and multi-directional broadband acoustic lens designs are presented including performance measures for the frequency and the incidence angle dependency. Examples of sound localization and focusing effects produced by planar nonuniform and uniform configurations of cylindrical structures such as rigid or void cylinders as well as thin elastic shells are shown.

Keywords: Sound localization, Gradient-based optimization, Acoustic metamaterials

1 INTRODUCTION

The manipulation and control of sound stimulated the development of critical technologies such as acoustic cloaking [3], sound focusing [4], ultrasound imaging, wavefront manipulation [5], beam splitting [6], absorption [7], vibration attenuation [8], and sound diffusion [9]. Adapting ideas from optics, acoustic lenses are capable of focusing sound in like manner as optical lenses apt to focus light. The ability to focus sound facilitate enhancements in biomedical imaging [10], structural health monitoring, and enable radar reflection to make stealth aircraft visible on radar screens [11]. Sound super-focusing effect can be achieved using acoustic metamaterials with the acoustic anisotropy required by transformation acoustics [12–15]. Here, we consider more limited focusing for a single incidence and a range of incidence directions at a single frequency and band of frequencies by maximizing the absolute pressure amplitude at the focal point produced by a given configuration of scatterers, and develop uni- and multi-directional broadband acoustic lens designs. We specifically design the multi-directional broadband acoustic lens to localize the sound and to focus acoustic incident waves received from multiple directions onto a prearranged localization region or focal point. We achieve this with an appropriate arrangement of the target metastructures made of conventional simple isotropic materials that are available in nature and obtain useful and interesting effects.

Optimization methods [16, 17] such as stochastic algorithms [18–20], topology optimization [21–23], shape optimization [24], and gradient-based optimization (GBO) [24–26] have proven to be a powerful tool for designing metamaterials and metadevices. In this work, we present the implementation of a semi-direct method for broadband acoustic lens design using GBO strategy [1, 26, 27] by means of multiple scattering theory [28] which mimics the behavior and performance of acoustic Luneburg lens that adepts to focus the incoming plane sound wave at the focal point on the other side of the lens. Instead of using glass and mirrors, our acoustic lens designs consist of arbitrary planar configurations of cylindrical structures such as rigid or void cylinders as well as thin elastic shells embedded in water environment. We obtained an analytical formula for the gradients of the absolute pressure amplitude at the focal point with respect to positions of a set of cylinders in closed form rather than relying on finite difference schemes. This is of preeminent importance for efficient calculations in the optimization process. The closed analytical form of the gradients enhances modeling capability and

computational efficiency when combined with GBO algorithms and parallel computing via use of *fmincon* and *MultiStart* Global optimization solvers on MATLAB.

2 PROBLEM FORMULATION

Consider acoustic multiple scattering [28] by an arbitrary planar configuration of M cylindrical structures in the context of the 2D acoustic time harmonic wave equation. The total acoustic pressure $p(\mathbf{x})$ is defined as: $p = p_{inc} + p_{sc}$, where p_{inc} is the incident and p_{sc} is the scattered pressure fields which satisfy the Helmholtz equation [26, 28]. The incident wave p_{inc} is the plane wave of unit amplitude in the direction ψ. We denote the total acoustic pressure at the focal point $\mathbf{x}_f$ by $p_f \equiv p(\mathbf{x}_f)$ for a given set of scatterer positions $\{\mathbf{x}_m\}$, $m = 1, \ldots, M$. see Fig. 1. The evaluation of $p_f \equiv p(\mathbf{x}_f)$ using the forward and reciprocal formulations of inverse design of acoustic lens are provided in [1]. Our goal here is to rearrange the target cylinders to find an optimal set $\{\mathbf{x}_m\}$ that maximizes the absolute value $|p_f| = (p_f p_f^*)^{1/2}$ where $*$ denotes the complex conjugate.

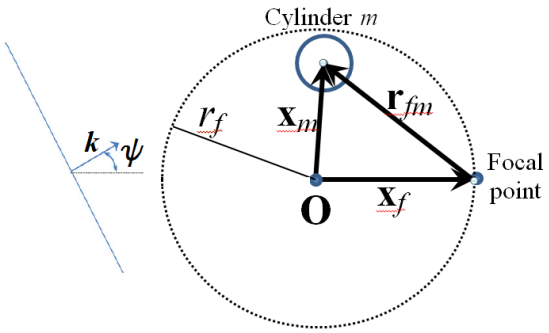


Figure 1. The schematic of an acoustic lens in the near field. The incident wave is a plane wave of unit amplitude in the direction $\boldsymbol{k}$ shown under the angle of incidence ψ. The cylinders are constrained to stay within the circular region of radius R_{out}, the artificial boundary, denoted by black dotted line.

2.1 Broadband multi-directional lens design

The broadband multi-directional acoustic lens model maximizes the root mean square (RMS) of a set of the absolute pressure at the focal point $|p_f|$ over a range of wavenumbers and angles of incidence, by iteratively rearranging the position of each cylinder starting from a random configuration. The procedure for a broadband multi-directional GBO strategy is as follows. We define the objective function as the RMS of a set of the absolute pressure amplitudes $|p_f|$ at the focal point over some range of normalized wavenumbers $k_i a\,(i = 1, 2, ..., N_k)$ and over a range of incident angles $\psi_l\,(l = 1, 2, ..., N_l)$:

$$|p_f(\{\mathbf{x}_m\})|^{RMS} = \left(\frac{1}{N_k}\frac{1}{N_\psi}\sum_{i=1}^{N_k}\sum_{l=1}^{N_\psi}|p_f(k_i a, \psi_l, \{\mathbf{x}_m\})|^2\right)^{1/2}. \tag{1}$$

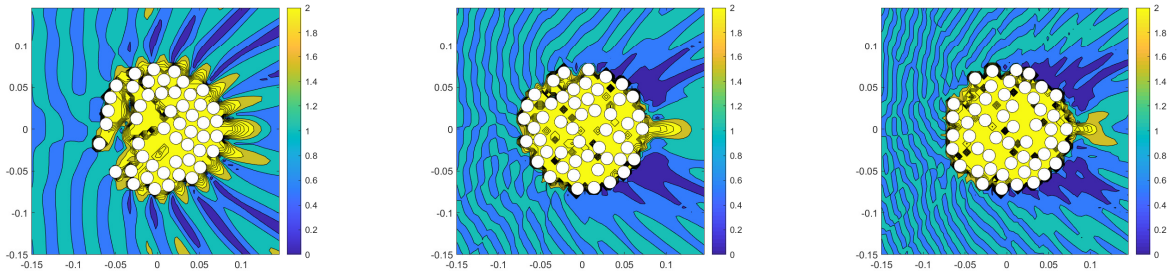
This objective function is non-convex and highly non-linear; it has many local maxima and global maximum at infinity. We solve the non-convex optimization problems with non-linear constraints. To avoid cylinder overlapping the distance between the centers of cylinders are constrained to be greater than minimal allowable distance that is chosen greater than the diameters of the cylinders. In addition, the cylinders are constrained to move inside a fixed circular region.

To enhance the GBO process, we define the broadband gradient vectors $\mathbf{q}_j^{RMS}$ with respect to positions $\mathbf{r}_j$ which can be found in terms of the individual single frequency gradients $\mathbf{q}_j(k_i a)$ as:

$$\mathbf{q}_j^{RMS} = \frac{\partial|p_f(\{\mathbf{x}_m\})|^{RMS}}{\partial \mathbf{x}_j} = \frac{1}{|p_f|^{RMS}}\frac{1}{N_k}\frac{1}{N_\psi}\sum_{i=1}^{N_k}\sum_{l=1}^{N_\psi}|p_f(k_i a, \psi_l, \{\mathbf{x}_m\})|\,\mathbf{q}_j(k_i a, \psi_l), \quad j = 1, 2, \ldots M, \tag{2}$$

where $|p_f|^{RMS}$ and $\mathbf{q}_j(k_i a)$ are defined at the normalized wavenumbers $k_i a\,(i = 1, 2, ..., N_k)$ and angles of incidence $\psi_l\,(l = 1, 2, ..., N_l)$, and the derivation of gradients $\mathbf{q}_j$ is provided in [1].

3 NUMERICAL RESULTS



(a) $ka = 0.75 : p_{rel} = 6.43$ (b) $ka = 1.5 : p_{rel} = 4.13$ (c) $ka = 2 : p_{rel} = 4.62$

Figure 2. The illustration of absolute total acoustic pressure field p (**a**) at normalized wavenumbers $ka = 0.75 : |p_f|_{rel} = \frac{|p_f|}{p_i(x_f)} = 6.43$, (**b**) $ka = 1.5$ with $p_{rel} = 4.13$, and (**c**) $ka = 2$ with $p_{rel} = 4.62$ for the optimized uniform configurations of $M = 50$ rigid cylinders. The focal point is located at $\mathbf{x}_f = (0.0865, 0)m$. For drawing purposes values higher than 2 are denoted by yellow color.

The numerical results of the GBO of the uni- and multi- directional acoustic lens designs are demonstrated. Computations are performed on MATLAB using *MultiStart* and *fmincon* solvers along with sequential quadratic programming (SQP) algorithms, while supplying the gradient of the pressure at the focal point and the gradient of the nonlinear geometrical constraints. Several configurations of randomly placed scatterers, via *MultiStart*, are initialized. *MultiStart* has efficient local solvers, and can search a wide variety of start points in parallel. Providing the analytical gradients of the pressure amplitude enhances the optimized solution accuracy, reduces run time, and enables parallel computing using *MultiStart*. The multiple scattering solver [1, 26] evaluates the absolute RMS pressure at the focal point as well as it gradients with respect to positions for each configuration, and *fmincon* combined with *MultiStart* solver continue to perturb the scatterer positions toward minimized gradients until the optimal configurations are found. We investigate the sound localization effect for a plane wave incident on a configuration of cylindrical scatterers considering various values of normalized wavenumber, ka and the total number of scatterers in acoustic lens, M.

3.1 Sound localization at single frequency and normal plane wave incidence

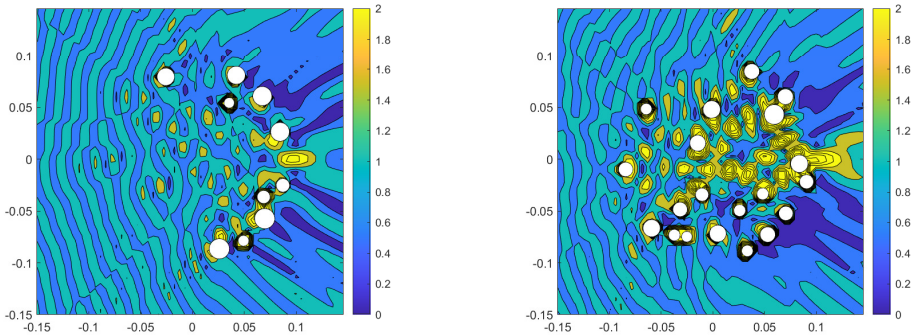
In this section, we present the numerical results for the unidirectional lens designs at single frequency and normal plane wave incidence on uniform and non-uniform configurations of rigid cylinders. 100 configurations of randomly placed scatterers, via *MultiStart*, are initialized.

3.1.1 Sound localization using uniform configuration of rigid cylinders

Here we present the localization effect for a plane wave incident on uniform configuration of 50 rigid cylinders at various discrete values of normalized wavenumber: $ka = 0.75, 1.5,$ and 2. The optimized lens configuration is a uniform configuration of identical rigid cylinders of radius $a = 0.0075$m located inside of circular region of radius $R_{out} = 0.0715$ m. The focus of the lens is located at $\mathbf{x}_f = (0.0865, 0)m$. Figure 2 illustrates the absolute total acoustic pressure $|p|$ computed at normal plane wave incidence for a uniform configuration of $M = 50$ rigid cylinders at fixed normalized wavenumbers $ka = 0.75, 1.5,$ and 2. We computed the absolute pressure $|p_f|_rel$ relative to the incident background pressure at the focal points specified as: $|p_f|_{rel} = \frac{|p_f|}{p_i(x_f)}$. The $|p_f|_{rel}$ values are given in Figure 2 for each optimized configuration at each $ka = 0.75, 1.5,$ and 2. As expected, the sound focusing and localization effects are enhanced with the increase of the wavenumber.

3.1.2 Sound localization using non-uniform configuration of rigid cylinders

Now we consider a normal plane wave incidence on non-uniform planar configurations of rigid cylinders of radii $a \in [a_{min}, a_{max}]$ where $a_{min} = 0.005$m and $a_{max} = 0.01$m. Figure 3 illustrates the absolute total acoustic pressure $|p|$ computed for the optimized nonuniform configurations of $M = 10, 20, 25$, and $M = 30$ and $ka_{max} = 2$ with $a_{max} = 0.01$m. The value of $|p_{rel}|$, the absolute pressure relative to incident background, are provided in Figure 3 for each optimized configuration. The focusing and localization effect becomes more noticeable and improves with the increase of the number of scatterers. At $ka_{max} = 2$, the highest amplitude is achieved producing $p_{rel} = 4.5769$ for $M = 30$ scatterer nonuniform configuration. These results are comparable to those shown previously in section 3.1.1 for the optimized uniform configuration with much larger number of identical rigid scatterers, i.e. $M = 50$.



(a) $M = 10 : p_{rel} = 2.7036$ (b) $M = 20 : p_{rel} = 3.7112$

(c) $M = 25 : p_{rel} = 4.1243$ (d) $M = 30 : p_{rel} = 4.5769$

Figure 3. The illustration of absolute total acoustic pressure field p at normalized wavenumbers $ka_{max} = 2$ for the optimized non-uniform configurations of $M = 10$ with $p_f|_{rel} =$ (**a**), $M = 20 : p_{rel} = 3.7112$ (**b**), $M = 25 : p_{rel} = 4.1243$(**c**), and $M = 30$ with $p_{rel} = 4.5769$ (**d**) rigid cylinders. The focal point is located at $\mathbf{x}_f = (0.102, 0)$m where radii of cylinders vary between $a_{min} = 0.005$m and $a_{max} = 0.01$m. For drawing purposes values higher than 2 are denoted by yellow color.

3.2 Broadband sound localization using uniform configuration of cylindrical scatterers

3.2.1 Sound localization implementing uni-directional lens

Here we study the focusing and localization frequency over the range of wavenumbers. Numerical results are presented for uniform cylindrical void configurations and uniform sets of thin elastic shells for various number of scatterers $M = 10, 20$ and 30 and ranges of wavenumbers: $ka \in [0.6, 1.0]$, $ka \in [1.0, 1.4]$, $ka \in [1.4, 1.8]$ and $ka \in [1.6, 1.8]$. 50 uniform configurations of randomly placed scatterers, via *MultiStart*, are initialized. Figure 4 illustrates the localization effect for a normal plane wave incident on uniform configurations of cylindrical voids at various discrete values of normalized wavenumber, $ka \in [0.6, 1]$ depicted at top row figures (a)-(c)

and $ka \in [1, 1.4]$ given at middle row figures (d)-(f), and $ka \in [1.6, 1.8]$ shown in bottom row figures (g)-(i) varying the total number of scatterers $M = 10, 20$ and 30. Figure 5 illustrates similar localization effects for uniform configurations of elastic thin cylindrical shells at various discrete values of normalized wavenumber, $ka \in [0.6, 1]$ depicted at top row figures (a)-(c) and $ka \in [1, 1.4]$ shown in bottom row figures (d)-(f) varying the total number of scatterers $M = 10, 20$ and 30. Figure 4 and 5 show 9 black dots the horizontal axis indicating considered discrete values of ka and results for unoptimized initial random configuration denoted by blue color curves that are included for a comparison. Generally, as the number of optimization wavenumbers raises and as the number of scatterers increases, the distribution of the focal absolute pressure becomes more uniform under the optimization process. Specifically, for $|p_f|^{RMS}$ computed at 9 values of ka shown by green curves, a more uniform broad focusing performance is achieved within the considered range of wavenumbers.

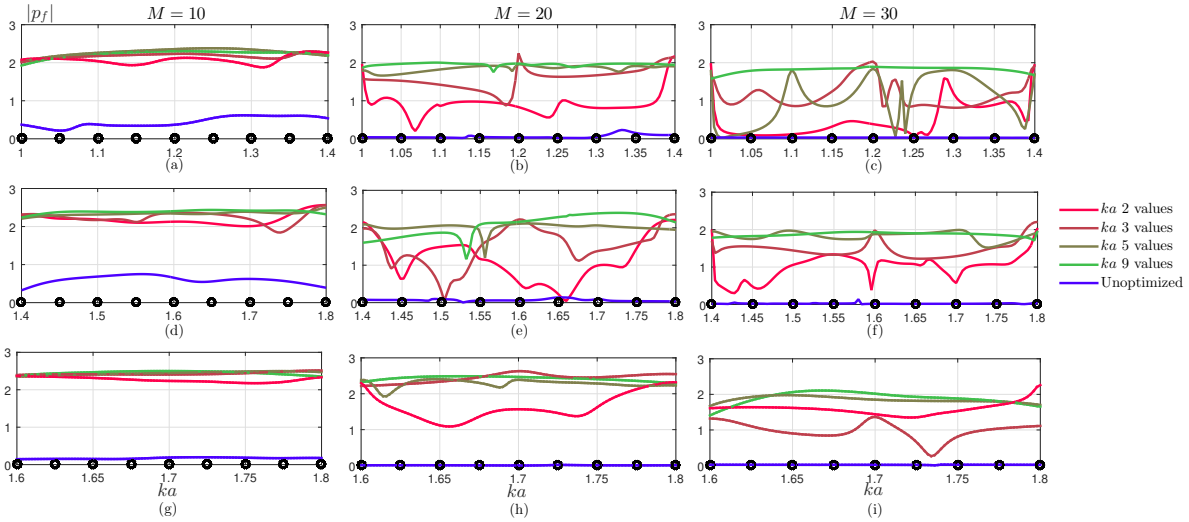


Figure 4. The absolute pressure at focal point, $|pf|$, optimized at 2, 3, 5, and 9 equally spaced values of wavenumber $ka \in [1.0, 1.4]$ depicted at the top row Figures 4(a)-(c), $ka \in [1.4, 1.8]$ shown at the middle row Figures 4(d)-(f), and $ka \in [1.6, 1.8]$ given at the bottom row Figures 4(g)-(i) for uniform configurations of $M = 10$ (**left column**), $M = 20$ (**middle column**) and $M = 30$ (**right column**) cylindrical voids. The focal point is $\mathbf{x}_f = (0.0865, 0)m$. The plots for unoptimized initial random uniform configuration are denoted by blue color curves and are included for a comparison.

3.2.2 Sound localization developing multi-directional lens

Now we present the numerical results illustrating the performance of multi- directional acoustic lens designs initializing 100 uniform configurations of randomly placed scatterers, via *MultiStart*. Figure 6 illustrates $|p_f|^{RMS}$, as a function of angle of incidence ψ and the normalized wavenumber ka performing concurrently a multi-frequency and multi-angle optimization of function $|p_f|^{RMS}$ at a broad range of the incidence angle $\psi \in [-\pi/4, \pi/4]$ and 3 values of wavenumber $ka \in [0.35, 0.55]$ for configurations of $M = 50$ rigid cylinders. The optimized configuration on left top corner of Figure 6 is the result of GBO for 3 values of wave number ka and 9 incidence angles. The results for unoptimized initial random uniform configuration is depicted by blue color curves.

4 CONCLUSIONS

We presented the GBO strategy which combines the multiple scattering theory with the principle of acoustic reciprocity and leads to an effective method to optimally position scatterers so as to produce acoustic focusing. The GBO technique uses semi-analytic expressions for the gradient of the focal pressure with respect to the po-

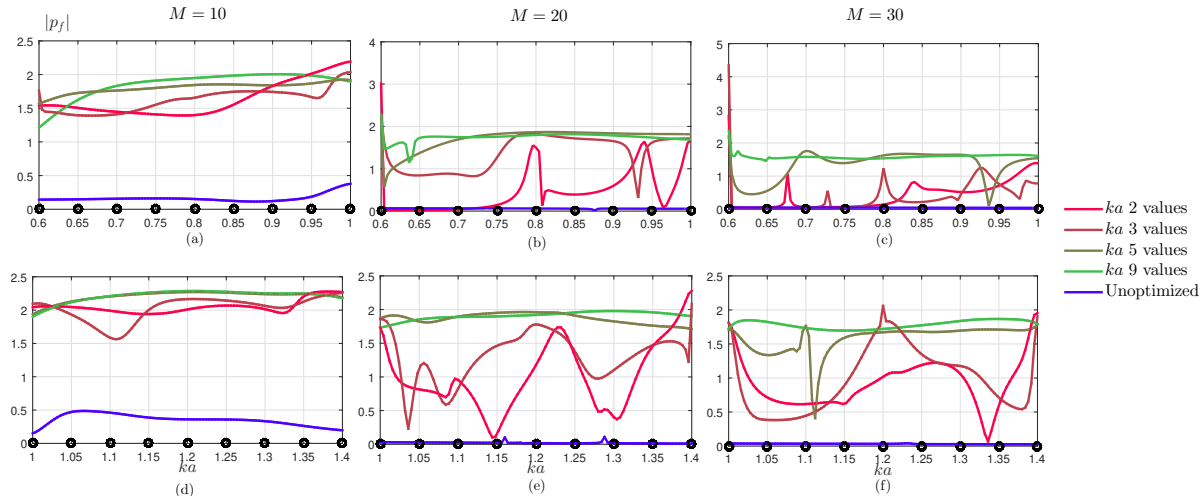


Figure 5. The absolute pressure at focal point, $|pf|$, optimized at 2, 3, 5, and 9 equally spaced values of wavenumber $ka \in [0.6, 1.0]$ depicted at the top row Figures 5(a)-(c), and $ka \in [1.0, 1.4]]$ illustrated at the bottom row Figures 5(d)-(f) for uniform configurations of $M = 10$ (**left column**), $M = 20$ (**middle column**) and $M = 30$ (**right column**) empty elastic cylindrical thin shells with material properties given in [2]. The focal point is $\mathbf{x}_f = (0.0865, 0)m$.

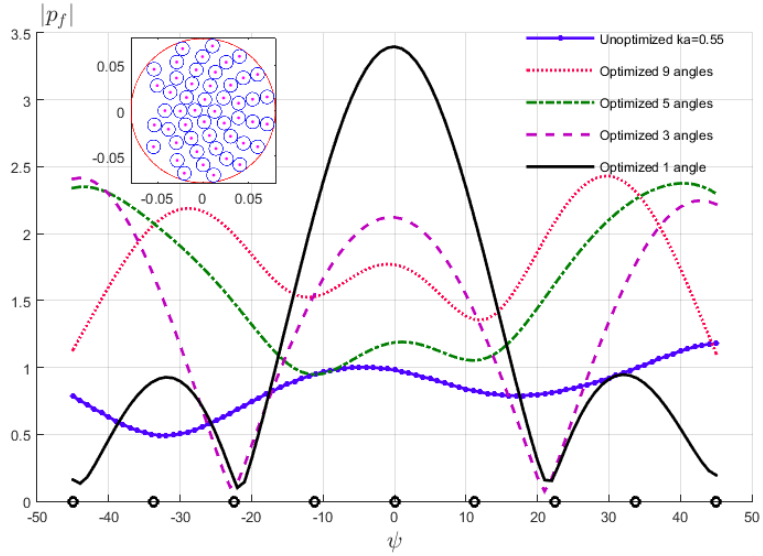


Figure 6. The absolute pressure at focal point, $|pf|$, optimized at 1, 3, 5, and 9 equally spaced values of angle of incidence ψ and three values of wavenumber $ka = 0.35, 0.45,$ and0.55 for the optimized uniform configurations of $M = 50$ rigid cylinders. The focal point is $\mathbf{x}_f = (0.0865, 0)m$. The results for unoptimized initial random uniform configuration are depicted by blue color curves. The performance of lens is shown at normalized wavenumber $ka = 0.55$.

sitions of each scatterer. The results presented for the uni- and multi-directional broadband acoustic lens designs display that a considerable sound pressure amplification can be achieved by optimal scatterer replacement using this analytical-numerical technique. Providing the gradient information, the GBO strategy can be integrated with deep reinforcement learning algorithms [29] and generative neural networks [30] which have potentials to search for the globally optimized devices over a broad range of parameters and can provide better solutions than ones produced by traditional optimization methods. Optimized lens models obtained by using non-uniform

configurations allowed for the reduction of compute time achieving a similar performance as produced by uniform configurations but employing lesser number of scatterers. The presented GBO assisted acoustic lens model can be further improved by considering the cylinder radii as an additional design parameter which will require deriving analytical formulas for the gradients of absolute pressure with respect to cylinder radii. This study is under the development and the preliminary results for an implementation of lens design via radii and position adjustments will be presented at the ICA2022 meeting.

ACKNOWLEDGEMENTS

FA acknowledges Small Grant Project grant support from San Jose State University.

References

[1] Feruza Amirkulova, Samer Gerges, and Andrew Norris. Sound localization through multi-scattering and gradient-based optimization. *Mathematics*, 9(22):2862, 10.3390/math9222862, nov 2021.

[2] Feruza Amirkulova, Linwei Zhou, Anam Abbas, Peter Lai, Cheng Qiu, and Tristan A. Shah. Acoustic metamaterial design framework using deep learning and generative modeling. *The Journal of the Acoustical Society of America*, 151(4):A253–A253, apr 2022.

[3] A. N. Norris. Faxen relations in solids - a generalized approach to particle motion in elasticity and viscoelasticity. *Journal of the Acoustical Society of America*, 123(1):99–108, 2008.

[4] A.-C. Hladky-Hennion, J. O. Vasseur, G. Haw, C. Croënne, L. Haumesser, and A. N. Norris. Negative refraction of acoustic waves using a foam-like metallic structure. *Appl. Phys. Lett.*, 102(14):144103, 2013.

[5] Hongchen Chu, Qi Li, Bingbing Liu, Jie Luo, Shulin Sun, Zhi Hong Hang, Lei Zhou, and Yun Lai. A hybrid invisibility cloak based on integration of transparent metasurfaces and zero-index materials. *Light: Science & Applications*, 7(1), aug 2018.

[6] Jierong Cheng, Sandeep Inampudi, and Hossein Mosallaei. Optimization-based dielectric metasurfaces for angle-selective multifunctional beam deflection. *Scientific Reports*, 7(1), sep 2017.

[7] Clément Lagarrigue and Damien Lecoq. Acoustic metamaterials for industrial applications. wiley online library. Wiley Online Library, aug 2019.

[8] Xinyue Wu, Yabin Jin, Abdelkrim Khelif, Xiaoying Zhuang, Timon Rabczuk, and Bahram Djafari-Rouhani. Topological surface wave metamaterials for robust vibration attenuation and energy harvesting. *Mechanics of Advanced Materials and Structures*, pages 1–9, jun 2021.

[9] Noé Jiménez, Jean-Philippe Groby, and Vicent Romero-García. Spiral sound-diffusing metasurfaces based on holographic vortices. *Scientific Reports*, 11(1), may 2021.

[10] A. Spadoni and C. Daraio. Generation and control of sound bullets with a nonlinear acoustic lens. *Proceedings of the National Academy of Sciences*, 107(16):7230–7234, Apr 2010.

[11] Dario Leone. How luneburg lens radar reflectors are used to make stealth aircraft visible on radar screens. https://theaviationgeekclub.com/these-devices-make-stealth-aircraft-visible-on-radar-screens/, June 2021.

[12] Steven A. Cummer. *Acoustic metamaterials.*, chapter Transformation acoustics, pages 197 – 218. Springer Series in Materials Science, 2013.

[13] Andrew N. Norris. Acoustic metafluids. *Journal of the Acoustical Society of America*, 125(2):839–849, 2009.

[14] Anne-Christine Hladky-Hennion, Charles Croenne, Jerome O. Vasseur, Lionel Haumesser, and Andrew N. Norris. Focusing capability of a phononic crystal based on a hollow metallic structure. *IEEE Transactions on Ultrasonics, Ferroelectrics, and Frequency Control*, 61(8):1314–1321, aug 2014.

[15] Xiaoshi Su, Andrew N Norris, Colby W Cushing, Michael R Haberman, and Preston S Wilson. Broadband focusing of underwater sound using a transparent pentamode lens. *Journal of the Acoustical Society of America*, 141(6):4408–4417, 2017.

[16] Sawyer D. Campbell, David Sell, Ronald P. Jenkins, Eric B. Whiting, Jonathan A. Fan, and Douglas H. Werner. Review of numerical optimization techniques for meta-device design [invited]. *Optical Materials Express*, 9(4):1842, mar 2019.

[17] K. Diest, editor. *Numerical Methods for Metamaterial Design*, volume 127 of *Topics in Applied Physics*. Springer, 2013.

[18] Andreas Håkansson, Francisco Cervera, and José Sánchez-Dehesa. Sound focusing by flat acoustic lenses without negative refraction. *Appl. Phys. Lett.*, 86:054102, 2005.

[19] Zhimiao Lu, Lorenzo Sanchis, Jihong Wen, Li Cai, Yafeng Bi, and José Sánchez-Dehesa. Acoustic cloak based on Bézier scatterers. *Scientific Reports*, 8(1), aug 2018.

[20] Javier Torre, Jonas Brunskog, Vicente Henriquez, and Jaesoon Jung. Hybrid analytical-numerical optimization design methodology of acoustic metamaterials for sound insulation. *The Journal of the Acoustical Society of America*, 149(6):4398–4409, jun 2021.

[21] Jacob Andkjær and Ole Sigmund. Topology optimized low-contrast all-dielectric optical cloak. *Applied Physics Letters*, 98(2):021112, jan 2011.

[22] J. Andkjær and O. Sigmund. Topology optimized acoustic and all-dielectric optical cloaks. In *Photonic Crystals: Moulding the flow of lightroceedings of Metamaterials 2011: The Fifth International Congress on Advanced Electromagnetic Materials in Microwave and Optics, October 10-13 2011.*, October 10-13 2011.

[23] J. Andkjær and O. Sigmund. Topology optimized cloak for airborne sound. *Journal of Vibration and Acoustics*, 135:041011, 2013.

[24] P. Andersen, V. Henriquez, L. Sanchis, and J. Sánchez-Dehesa. Design of multi-directional acoustic cloaks using two-dimensional shape optimization and the boundary element method. In *Proc. of ICA 2019 AND EAA EUROREGIO Deutsche Gesellschaft für Akustik e.V.*, pages 5600–5606. Department of Electrical Engineering, Acoustic Technology, Technical University of Denmark, 2019.

[25] Neel Shah and Feruza Amirkulova. Broadband optimization of volumetric sound metadiffusers. *The Journal of the Acoustical Society of America*, 149(4):A13–A13, apr 2021.

[26] Feruza A. Amirkulova and Andrew N. Norris. The gradient of total multiple scattering cross-section and its application to acoustic cloaking. *Journal of Theoretical and Computational Acoustics*, page 1950016, mar 2020.

[27] Feruza A. Amirkulova, Samer Gerges, and Andrew N. Norris. Broadband acoustic lens design by reciprocity and optimization. *JASA Express Letters*, 2(2):024005, feb 2022.

[28] P. A. Martin. *Multiple Scattering: Interaction of Time-harmonic Waves with N Obstacles*. Cambridge University Press, New York, 2006.

[29] Tristan Shah, Linwei Zhuo, Peter Lai, Amaris De La Rosa-Moreno, Feruza Amirkulova, and Peter Gerstoft. Reinforcement learning applied to metamaterial design. *The Journal of the Acoustical Society of America*, 150(1), July 2021.

[30] Linwei Zhuo and Feruza Amirkulova. Design of acoustic cloak using generative modeling and gradient-based optimization. *INTER-NOISE and NOISE-CON Congress and Conference Proceedings*, 263(3):3511–3522 https://doi.org/10.3397/IN–2021–2431, aug 2021.

ICA 2022
24th INTERNATIONAL CONGRESS ON ACOUSTICS
October 24(Mon) - 28(Fri), 2022 Gyeongju, Korea

PROCEEDINGS of the
24th International Congress on Acoustics

October 24 to 28, 2022 in Gyeongju, Korea

ABS-0054

Identification and assessment of flow-induced sound sources inside encapsulated flow domains - Investigating a clinically applied hydraulic prosthesis

Andreas WURZINGER[(1)], Bernhard MAYR-MITTERMÜLLER[(2)], Harald SIMA[(2)], Manfred KALTENBACHER[(1)], Stefan SCHODER[(1)]

[(1)]Graz University of Technology, IGTE, A-8010 Graz, Austria, andreas.wurzinger@tugraz.at
[(2)]Otto Bock Healthcare Products GmbH, A-1110 Wien, Austria

ABSTRACT
Noise emissions of hydraulic prostheses can have significant negative impacts on users and their environment. In this context, the sound production mechanisms inside the hydraulics of a clinically-applied knee prosthesis were investigated with the goal to identify tonal and broadband source regions and assess counter measures. Therefore, scale resolving incompressible and weakly compressible flow simulations are used to calculate acoustic sources based on common aero-acoustic formulations inside the encapsulated flow domain. These sources are visualized both in time and frequency domain to obtain qualitative information about their location and underlying source mechanisms. This analysis allows to distinguish between wall excitation based on turbulent incompressible flow phenomena on the one hand and compressible wave propagation effects on the other. Finally, validation experiments show a reduction of noise emissions obtained by adaptation of the flow guidance based on elimination of one source mechanism that is identified during the analysis.

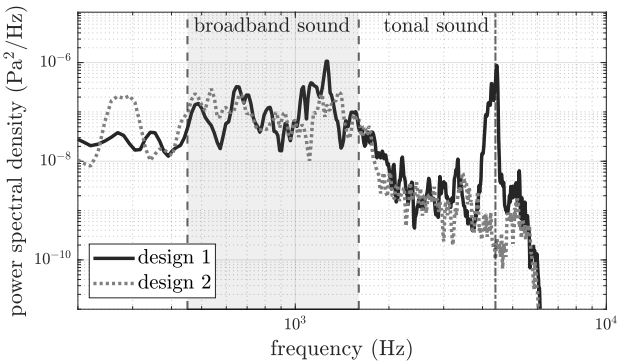
Keywords: Computational Acoustics

1 INTRODUCTION

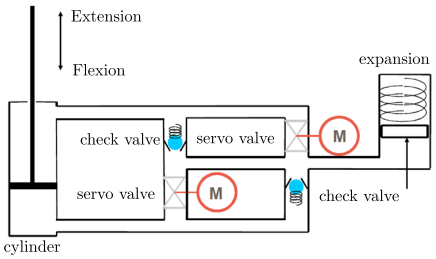
The human knee joint allows people a functional, self-healing, low-noise [11] and impact-tolerant [1] force transmission during walking. Unfortunately, accidents and maladies can lead to the fatal situations in which over-knee amputation of the leg is a medical necessity. In 2014 only, 57.637 amputations of the lower extremities were performed in Germany [3]. Technical aids like a leg-prosthesis can help in these difficult circumstances to significantly improve the life quality. Providers of medical equipment in the field of prosthetics as *Otto Bock Healthcare Products GmbH* are therefore interested in the development of prostheses that allow for safe, natural human walking. Therefore, the knee-prosthesis under investigation in this work is based on a mechatronic, controlled hydraulic damping system. Apart from mechanical and functional requirements sound emissions in several use-cases are of major interest, as the generated noise can be a stress factor for the user and also unpleasant for both user and the user's environment [4]. Figure 1a shows the sound power density spectrum emitted by the prosthesis under investigation (design 1) in a certain use-case. The sound emissions consist of broad-band noise between 500 Hz and 1.5 kHz as well as a tonal *whistling sound* at approximately 4.5 kHz. Especially, the tonal components of the emitted sound should be avoided, which most often requires minor changes to the overall design only (eg. design 2). To detect acoustic hot-spots as early as possible in the development process, a simulation workflow for identification and systematic analysis and prevention of acoustic source hot-spots is developed in the funded project *VirtualProsthesis*[1].

Figure 1b depicts the schematic of the hydraulic system applied in the prosthesis under investigation. The system is used to control the damping of the artificial knee joint and consists of a double-chamber piston,

[1]https://projekte.ffg.at/projekt/4163257



(a) Power spectrum of the sound emissions of the investigated prosthesis (design 1) and an improved design 2. Frequency ranges of interest for broadband noise and tonal noise are marked.



(b) Schematic of the hydraulic system. Separated flow guides for extension and flexion movement.

Figure 1. Microphone measurement of 2 design variants of the prosthesis and a schematic of the hydraulic system.

which is moved in extension direction, when no force is applied due to the static pressure. For each direction of piston movement, flexion and extension, the hydraulic fluid flows through separate servo and check valves. These servo valves can be controlled from fully closed to fully open to meet the target resistance for each gate phase.

2 METHODOLOGY

2.1 Flow simulation

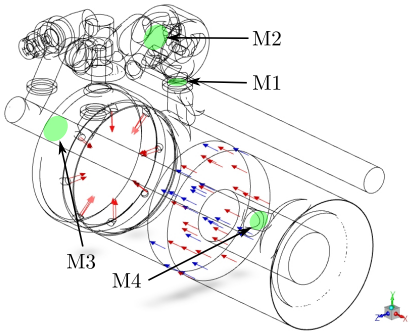
To reduce complexity and numerical effort of the problem, the hydraulic system is approximated by a simplified stationary system (see Fig. 2a) that models the flexion motion. This assumption is based on the phase relation and the tones observed by experimental investigation. Therefore, the piston is replaced by velocity inlet and mass flow outlet and the expansion chamber by constant pressure boundary conditions respectively.

The computational domain is discretized by a combination of hexahedral, polyhedral and wedge elements with edge sizes between $5 \cdot 10^{-5}$ and $4 \cdot 10^{-4}$ m. All walls are refined with 8 prism layers to achieve full resolution ($y^+ < 1$) of the boundary layer. The hydraulic fluid is modeled by either an incompressible or a weakly compressible fluid based on the Tait equation with nominal density $\rho = 860\,kg/m^3$, dynamic viscosity $\eta = 0.02752\,$Pa s, isothermal compression modulus $K = 1.5 \cdot 10^9\,$Pa, and adiabatic exponent $n = 7$. A scale resolving Stress-Blended Eddy simulation (SBES) [6], similar to hybrid approaches used eg. in [7], is used to efficiently resolve sufficient turbulent scales. It uses a k-ω-SST turbulence model and a Wall-Adapting Local Eddy-viscosity (WALE) sub-grid-scale model. The incompressible continuity equation is fulfilled by the direct coupling of the pressure correction equation. Spatial discretization is of order 2 and time integration is done by an implicit 2nd order scheme with a fixed time step of $\Delta t = 5 \cdot 10^{-6}\,$s. The described setup was computed with *Ansys Fluent* and performed on the Vienna Scientific Cluster Vienna Scientific Cluster[2] (VSC). The overall computational effort for simulating 8000 time steps was about 14500 CPU h and 24000 CPU h for the incompressible and weakly compressible setups respectively.

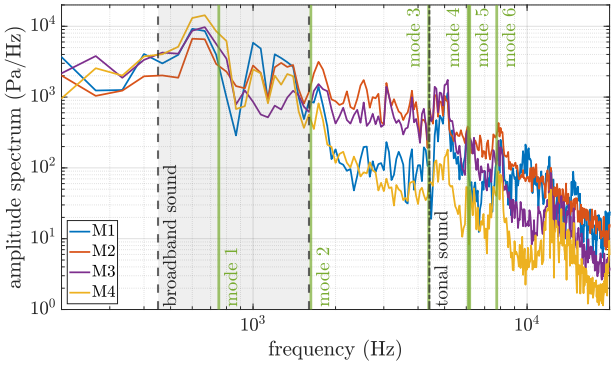
Figures 2b and 2c show the average of 5 point spectra (center and 4 points close to walls) of the static pressure at 4 monitoring cross-sections indicated in Fig. 2a for both the weakly compressible and the incompressible fluid model (as investigated in [12]). The spectra in monitor 2 and 3 show dominant broad band character due to turbulent pressure fluctuations while the spectra in monitor 1 and 4 differ significantly to the

[2] vsc.ac.at

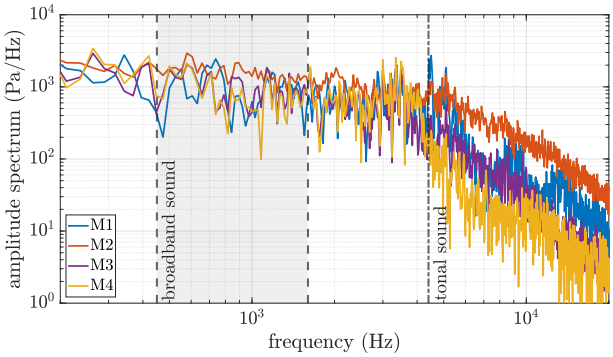
incompressible spectra that show broad band character mostly. Further investigation shows, that the spectra are significantly modulated by compressible modes. The frequencies of the amplitude peaks coincide roughly with those obtained solving the Helmholtz equation for a point source at monitor 2 with the finite element-based multi-physics solver *openCFS*[3], as done in [12].



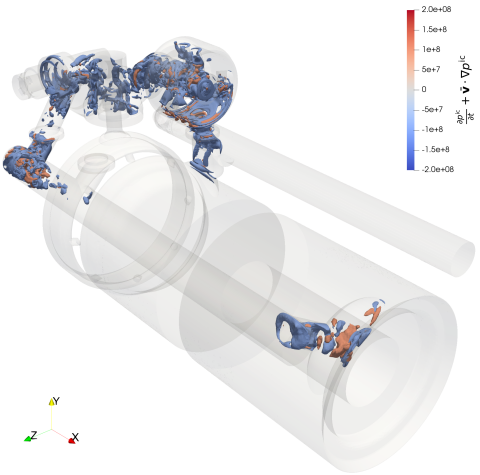
(a) Outline of the simplified flow domain. Inlet and outlet boundary conditions on the piston surfaces, and a pressure boundary condition towards the expansion chamber. Servo and check valves closed during extension neglected.



(b) Averaged spectra of the static pressure of 5 points in the monitoring cross-sections indicated in Fig. 2a. Compressible modes obtained from the frequency response function (FRF) of a point source located in M2 [12], Fig. 8 are indicated.



(c) Averaged spectra of the incompressible static pressure of 5 points in the monitoring cross-sections indicated in Fig. 2a (as depicted in [12], Fig. 5).



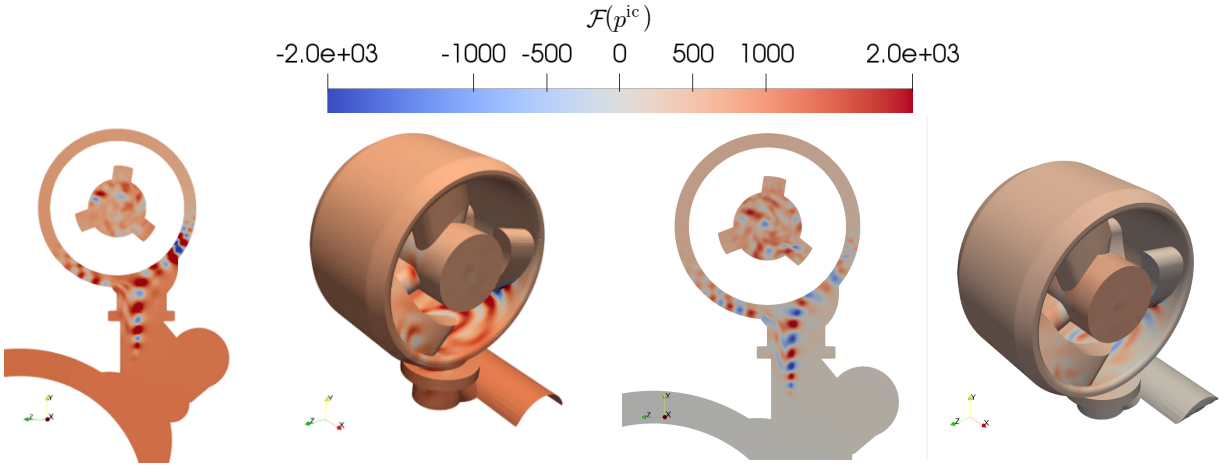
(d) Iso-contours at $\pm 10^8 \frac{\text{Pa}}{\text{s}}$ of the acoustic source term based on the PCWE formulation.

Figure 2. Computational Fluid Dynamics (CFD) simulation setup and resulting pressure spectra and acoustic sources based on incompressible CFD.

2.2 Acoustic sources

To obtain information about the acoustic source hot-spots, several formulations of hybrid aero-acoustic workflows [8] can be used to calculate an acoustic source term. Visualizing the source terms can help understand the source characteristics during a detailed cause-effect analysis [9]. In Fig. 2d iso-contours of the RHS source of the *Perturbed Convective Wave Equation* [2]

[3] opencfs.org



(a) Real part of the fieldFFT of the incompressible static pressure at $f = 4500\,\mathrm{Hz}$.

(b) Real part of the fieldFFT of the static pressure at $f = 4654\,\mathrm{Hz}$ based on the weakly compressible CFD.

Figure 3. Visualizations of the fieldFFT computed from incompressible and compressible flow pressure fields.

$$\frac{1}{c^2}\frac{\mathrm{D}^2\psi^a}{\mathrm{D}t^2} - \nabla\cdot\nabla\psi^a = -\frac{1}{\bar{\rho}c^2}\frac{\mathrm{D}p^{ic}}{\mathrm{D}t} \tag{1}$$

with $\frac{\mathrm{D}\bullet}{\mathrm{D}t} = \frac{\partial\bullet}{\partial t} + \bar{v}\cdot\nabla\bullet$ are depicted. Thereby, p^{ic} is the incompressible flow pressure, and $\bar{v}$ the mean flow velocity. Therein, the main regions of acoustic sources can be observed: At the inlet and outlet of the servo valve, at the check valve, and at 2 bends of the side channel in the vicinity of M3 and M4 according to Fig. 2a.

To get further insight in the structure of the acoustic sources, the flow pressure time data was transformed into the frequency domain by using a field fast Fourier transform (fieldFFT). Figure 3a shows the real part of the incompressible static pressure obtained by the fieldFFT in a plane at the inlet of the servo valve, for the frequency of the tonal component of the measurement $f = 4500\,\mathrm{Hz}$.

Most apparent, one can observe structures of pressure fluctuations, that convect with the flow velocity. This behavior indicates vortex generation by a mixing layer instability phenomenon, which explains the peaks in the amplitude spectrum of Fig. 2c at approximately 4500 Hz. However, further investigations have to be made to understand this mechanism, as it seems that the instability is triggered by compressible effects even though the analyzed data set stems from an incompressible CFD. Counterintuitively, such global pressure fluctuations can be observed in Fig. 3a. These can be related to artificial compressible phenomena introduced by numerical inaccuracy as the pressure correction equation

$$\nabla^2 p' = -\nabla\cdot\nabla\cdot\rho\left(v^{ic}\otimes v^{ic}\right) - \nabla^2 p_0 + \nabla\cdot\nabla\cdot\tau \tag{2}$$

with the viscous stress tensor τ, the pressure correction $p' = p^{ic} - p_0$, and the initial guess for the pressure p_0 allows for a pressure correction $|p'| > 0$. It is noted at this point that Eq. 2 is equivalent to a degenerated form of Lighthill's inhomogeneous wave equation [5] for the case if speed of sound tends towards infinity and consequently the wave operator turning into a Laplace operator. Consequently, these artificial compressible effects vanish with increased convergence of the CFD solver for the incompressible material model. Interestingly enough, this artificial compressibility yields similar results in triggering the mixing layer instability to the weakly compressible approach, as the Mach number doesn't exceed $\mathrm{Ma} < 0.02$. This leads to insignificant errors, introduced by the violation of the phase relation by neglecting wave traveling effects for low Mach number flows[10]. Figure 3b shows the real part of the Fourier transformed flow pressure from the weakly compressible CFD for the slightly higher frequency $f = 4654\,\mathrm{Hz}$. Again the vortices are visible, however the extensive pressure fluctuations change phase at the valve inlet and are of much lower magnitude at this frequency.

3 CONCLUSIONS

A simplified stationary model of the fluid dynamics during the flexion motion of a hydraulic knee prosthesis was established that has been solved both for the incompressible and the compressible pressure fields. Comparison to compressible modes obtained from FRFs shows the influence of compressibility on the flow pressure field. Furthermore visualization of both the pressure fields and acoustic source terms based on aero-acoustic formulations yield insight in the spatial distribution of flow-induced sound source hot-spots and source characteristics like flow instability triggered by coupled compressible effects, that cannot be predicted reliably by an incompressible flow simulation. Therefore, special care has to be taken for flows that are prone to become unstable like mixing layers, which will be the focus of further investigations.

ACKNOWLEDGEMENTS

This project has received funding from the Austrian Research Promotion Agency (FFG) under the Bridge project No. [71694]. The computational results presented have been achieved in part using the Vienna Scientific Cluster (VSC).

REFERENCES

[1] A. Hoshino and W. Wallace. Impact-absorbing properties of the human knee. The Journal of bone and joint surgery. British volume, (5), 1987.

[2] M. Kaltenbacher. Computational Acoustics. CISM International Centre for Mechanical Sciences. Springer International Publishing, 2017.

[3] K. Kröger, C. Berg, F. Santosa, N. Malyar, and H. Reinecke. Amputationen der unteren extremität in deutschland. Dtsch Arztebl Int, 2017.

[4] S. Kumar, H. M. Forster, P. Bailey, and T. D. Griffiths. Mapping unpleasantness of sounds to their auditory representation. The Journal of the Acoustical Society of America, (6), 2008.

[5] M. J. Lighthill. On sound generated aerodynamically I. General theory. Proceedings of the Royal Society of London, 1951.

[6] F. Menter. Stress-blended eddy simulation (SBES)—A new paradigm in hybrid RANS-LES modeling. In *Symposium on Hybrid RANS-LES methods*, 2016.

[7] S. Schoder, C. Junger, and M. Kaltenbacher. Computational aeroacoustics of the eaa benchmark case of an axial fan. Acta Acustica, (5), 2020.

[8] S. Schoder and M. Kaltenbacher. Hybrid aeroacoustic computations: state of art and new achievements. Journal of Theoretical and Computational Acoustics, (04), 2019.

[9] S. Schoder, P. Maurerlehner, A. Wurzinger, A. Hauser, S. Falk, S. Kniesburges, M. Döllinger, and M. Kaltenbacher. Aeroacoustic sound source characterization of the human voice production-perturbed convective wave equation. Applied Sciences, (6), 2021.

[10] S. J. Schoder. *Aeroacoustic analogies based on compressible flow data*. PhD thesis, Wien, 2018.

[11] L.-K. Shark, H. Chen, and J. Goodacre. Knee acoustic emission: a potential biomarker for quantitative assessment of joint ageing and degeneration. Medical engineering & physics, (5), 2011.

[12] A. Wurzinger, B. Mayr-Mittermüller, M. Kaltenbacher, and S. Schoder. Untersuchung strömungsakustischer quellen einer klinisch angewandten hydraulischen knieprothese. In *DAGA 2022-48. Jahrestagung für Akustik*, 2022.

ICA 2022
24th INTERNATIONAL CONGRESS ON ACOUSTICS
October 24(Mon) - 28(Fri), 2022 Gyeongju, Korea

PROCEEDINGS of the
24th International Congress on Acoustics

October 24 to 28, 2022 in Gyeongju, Korea

ABS-0071

Aeroacoustic formulations for coupling of confined flows with the flow-guiding structure

Paul MAURERLEHNER[(1)], Johannes TIEBER[(2)], Stefan SCHODER[(1)], Helfried STEINER[(2)], Günter BRENN[(2)], Florian TOTH[(3)], Manfred KALTENBACHER[(1)]

[(1)]Institute of Fundamentals and Theory in Electrical Engineering, Graz University of Technology, Austria, paul.maurerlehner@tugraz.at

[(2)]Institute of Fluid Mechanics and Heat Transfer, Graz University of Technology, Austria, helfried.steiner@tugraz.at

[(3)]Institute of Mechanics and Mechatronics, TU Wien, Austria, florian.toth@tuwien.ac.at

ABSTRACT

Two aeroacoustic formulations, namely Lighthill's wave equation and the Perturbed Convective Wave Equation (PCWE), are applied within the hybrid aeroacoustic approach to compute the propagation of flow-induced sound in a pipe flow. A low Mach number flow (Ma=0.06) through a diverging and remerging plastic branch pipe is investigated. An analysis of the source terms computed by Large-Eddy Simulation (LES) reveals that the primary acoustic sources occur at flow detachments downstream of the sharp edges of the branch. Spectral results of the wall pressure estimated by the PCWE show good agreement with measurements. In contrast, the spectral peaks due to acoustic resonances are overestimated by Lighthill's wave equation by at least an order of magnitude, while correctly reproducing the incompressible pressure field. Overall, the results indicate that the PCWE is better suited for the present flow configuration. By coupling the internal acoustic domain with the surrounding structural domain through appropriate interface conditions, the interaction of the fluid and the structure is simulated. The comparison with results of the non-coupled simulations and the measurement shows that Fluid-Structure Interaction (FSI) must be modeled for accurate results, because the damping of the structure mitigates the occurring acoustic resonances.

Keywords: Computational Aeroacoustics, Fluid-Structure Interaction, Finite-Element Method, Duct Acoustics

1 INTRODUCTION

The hybrid aeroacoustic approach is an efficient way to address the issue of the disparity of scales in Computational Aero-Acoustics (CAA) at low Mach number [1]. In literature, the application to various kinds of flow configurations, such as fans [2, 3], jets [4], other external flows [5, 6], and internal flows [7, 8, 9] can be found. Furthermore, the PCWE, in particular, has been applied to compute human voice production using a hybrid approach [10, 11].

When applying this two-step approach for the computation of flow-induced sound in ducts, the sound radiation of the flow-guiding structure can be additionally obtained by coupling the fluid and the solid domains via appropriate coupling conditions. Furthermore, a strong coupling of the internal fluid domain and the confining structural domain must be considered when FSI is involved, which typically appears for flexible structures. For the particular case of small deformations, where the fluid flow is not affected by the deformation, a coupling of the internal acoustics and the structure is sufficient. Consequently, the strong coupling can be realized in the acoustic propagation simulation within the hybrid aeroacoustic approach avoiding FSI in the relatively costly Computational Fluid Dynamics (CFD) simulation.

In this work, the hybrid (two-step) approach is applied to predict the sound generation and propagation of a confined low Mach number flow. A diverging and remerging pipe flow (simply called pipe branch in the following), obtained by combing two T-junctions, is investigated. Dedicated measurements were performed in a flow through a geometry manufactured in a single part using 3D printing. This plastic part is modeled in the simulations when FSI is considered. The first step of the simulation workflow consists of computing the aeroacoustic source terms by performing an incompressible LES based on the Finite-Volume (FV) method. For the subsequent Computational Acoustics (CA) simulation, two aeroacoustic formulations, namely Lighthill's wave equation and the PCWE, are applied. The governing equations are solved using the Finite-Element (FE) multiphysics solver openCFS [12]. Comparing the resulting Power Spectral Densitiy (PSD) of the wall pressure with measurements shows that the PCWE yields more accurate results than Lighthill's wave equation. The Lighthill source term involves spatial derivatives and, thus, strongly depends on the spatial discretization and the numerical approximation of the derivative. In contrast, the relevant source term of the PCWE consists of the substantial time derivative of the incompressible pressure. Considering FSI within the (coupled) PCWE-based CA simulation improves the agreement with the measurements by mitigating acoustic resonances by the damped structure, revealing the relevance of FSI in the investigated flow configuration.

2 AEROACOUSTIC FORMULATIONS

In the following, two aeroacoustic formulations are considered within the hybrid aeroacoustic workflow to solve for the propagation of flow-induced sound. The PCWE is based on a perturbation ansatz, which decomposes the flow quantities, namely the pressure p, the flow velocity $\boldsymbol{v}$, and the density ρ into a mean part ($\bar{p}$, $\bar{\boldsymbol{v}}$, $\bar{\rho}$) and fluctuating incompressible ($p^{\mathrm{ic}\prime}$, $\boldsymbol{v}^{\mathrm{ic}\prime}$), and acoustic components (p^{a}, $\boldsymbol{v}^{\mathrm{a}}$, ρ^{a}). For the pressure p and velocity $\boldsymbol{v}$, this splitting approach reads

$$p = \bar{p} + p' = \underbrace{\bar{p} + p^{\mathrm{ic}\prime}}_{p^{\mathrm{ic}}} + p^{\mathrm{a}} \text{ and} \tag{1}$$

$$\boldsymbol{v} = \bar{\boldsymbol{v}} + \boldsymbol{v}' = \underbrace{\bar{\boldsymbol{v}} + \boldsymbol{v}^{\mathrm{ic}\prime}}_{\boldsymbol{v}^{\mathrm{ic}}} + \boldsymbol{v}^{\mathrm{a}}. \tag{2}$$

Application of this perturbation approach to the compressible flow equations, yields the inhomogeneous wave equation

$$\frac{1}{c_0^2}\frac{D^2\psi^{\mathrm{a}}}{Dt^2} - \nabla\cdot\nabla\psi^{\mathrm{a}} = -\frac{1}{\rho_0 c^2}\frac{Dp^{\mathrm{ic}\prime}}{Dt} = Q^{\mathrm{ic}}_{\mathrm{PCWE}}, \tag{3}$$

which is solved for the scalar acoustic potential ψ^{a} with $\boldsymbol{v}^{\mathrm{a}} = -\nabla\psi^{\mathrm{a}}$, where $\boldsymbol{v}^{\mathrm{a}}$ denotes the irrotational particle velocity [13]. In (3), c_0 denotes the constant speed of sound and ρ_0 the density of the uniform medium. The substantial derivative $\frac{D}{Dt} = \frac{\partial}{\partial t} + \bar{\boldsymbol{v}}\cdot\nabla$ in the wave operator and in the source term considers the convection of acoustic waves. The acoustic pressure is obtained by the relation $p^{\mathrm{a}} = \rho_0\frac{D\psi^{\mathrm{a}}}{Dt}$. The source term $Q^{\mathrm{ic}}_{\mathrm{PCWE}}$ and the mean velocity $\bar{\boldsymbol{v}}$ in the wave operator are provided by the incompressible CFD simulation.

While the PCWE solves for a purely acoustic quantity, Lighthill's wave equation in the pressure formulation reading

$$\frac{1}{c_0^2}\frac{\partial^2}{\partial t^2}p' - \nabla\cdot\nabla p' = \nabla\cdot\nabla\cdot[\boldsymbol{T}] = Q_{\mathrm{LH}} \tag{4}$$

solves for the pressure fluctuation p'. The right hand side (RHS) of (4) defines the acoustic source term denoted as Q_{LH} consisting of the double divergence of the Lighthill stress tensor $[\boldsymbol{T}]$ containing non-linear convective fluxes, an excess term and a viscous stress term. For low Mach number flows, where the flow can be assumed as incompressible, the latter can be neglected, reducing the stress tensor to solely the non-linear velocity product

$$[\boldsymbol{T}]^{\mathrm{ic}} = \rho_0\boldsymbol{v}^{\mathrm{ic}}\otimes\boldsymbol{v}^{\mathrm{ic}} \tag{5}$$

and the Lighthill source term becomes

$$Q_{\mathrm{LH}}^{\mathrm{ic}} = \nabla \cdot \nabla \cdot [\boldsymbol{T}]^{\mathrm{ic}}. \tag{6}$$

The source term (6) is again obtained by an incompressible flow simulation.

For a strong coupling of acoustics and structural dynamics, dynamic (continuity of forces) and kinematic (continuity of normal velocity) coupling condition must be fulfilled at the coupling interface Γ_C [14]. For the PCWE, the dynamic coupling condition reads

$$p^{\mathrm{a}}\boldsymbol{n} = \rho_0 \frac{D\psi^{\mathrm{a}}}{Dt}\boldsymbol{n} = -[\boldsymbol{\sigma}_{\mathrm{mech}}]\cdot\boldsymbol{n}, \tag{7}$$

where $\boldsymbol{n}$ denotes the normal unit vector on Γ_C. Additionally, the kinematic coupling condition is enforced by

$$\nabla\psi^{\mathrm{a}}\cdot\boldsymbol{n} = -\frac{\partial \boldsymbol{u}_{\mathrm{mech}}}{\partial t}\cdot\boldsymbol{n}, \tag{8}$$

with u_{mech} being the mechanical displacement. For the non-coupled case, Γ_C is a rigid boundary, where $\boldsymbol{u}_{\mathrm{mech}} = 0$, reducing (8) to zero, which corresponds to a soundhard boundary condition.

3 WORKFLOW

The presented simulation workflow is based on the hybrid approach, which divides the task of sound computation into a CFD simulation and a Computational Acoustic (CA) simulation (propagation simulation), as displayed in Fig. 1. As a part of this concept, the computed source terms are interpolated onto the CA mesh

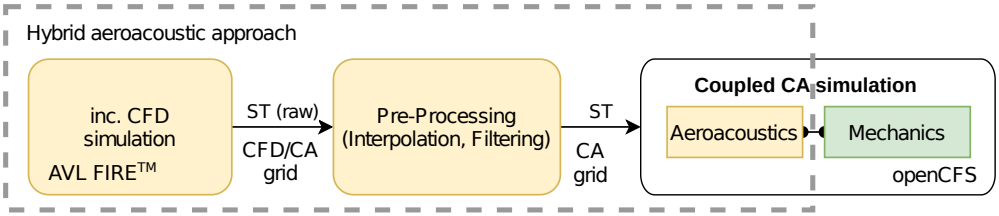
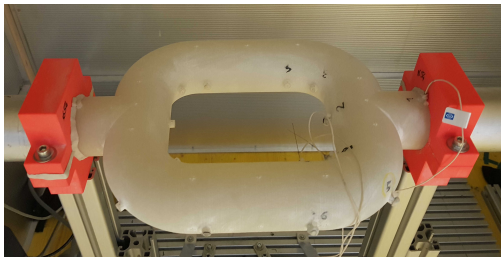


Figure 1. Simulation workflow for strong coupling of fluid and structure based on the hybrid aeroacoustic approach.

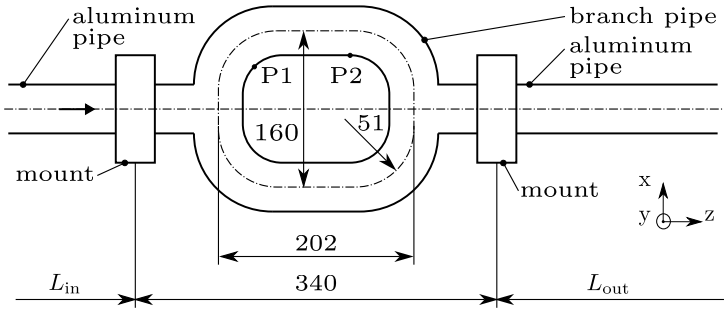
during the source data export in AVL FIRE™, where conservation of energy is enforced by considering the intersection of the CFD grid and the CA mesh [15]. Furthermore, mean values of the source term, which do not contribute to sound generation, are removed prior to the propagation simulation [16]. For the consideration of FSI, strong coupling of the fluid region and the structural mechanical region is considered in the propagation simulation. The structural mechanical domain is governed classically by the balance of momentum and a linear stress-strain relationship. The weak forms of the coupled partial differential equations governing the aeroacoustics and structural dynamics are solved using the FE-based solver openCFS.

4 APPLICATION

The presented workflow is applied to a fully developed turbulent airflow with bulk inflow velocity $U = 20.8\,\mathrm{m/s}$ (Ma=0.06), passing through a diverging and remerging branch pipe (see Fig. 2). The inner diameter is $D =$ 50mm, the wall thickness of the branch pipe is 2mm. For the CFD domain, the inlet and outlet section of a length of $L_{\mathrm{in}} = 4.2D$ and $L_{\mathrm{out}} = 10.3D$ is considered, respectively. In the validation experiment, the internal wall pressure is captured by pressure transducers (Kulite XCS-093) at selected positions P1 and P2 (see Fig. 2b). More information on the experimental setup can be found in [17].



(a) Picture of the experimental setup with inserted pressure transducers (Kulite).



(b) Geometry of the fluid and structural domain including sensor positions of the wall pressure probes P1 and P2 (all measures in mm).

Figure 2. Experimental setup and corresponding definition of the simulation domains. The inflow L_{in} and outflow length L_{out} define the fluid domain of the CFD and CA simulation.

The fluid density $\rho_0 = 1.176\,\mathrm{kg/m^3}$, the dynamic viscosity $\mu_0 = 18.3\,\mu\mathrm{Pa\,s}$, and the speed of sound $c_0 = 345.2\,\mathrm{m/s}$ are chosen as the material parameters required for the simulations. The plastic mounts at both ends of the pipe are considered in the simulation, where the bottom surface is assumed to be fixed according to the experimental setup. The material parameters (Young's modulus E, Poisson ratio ν, and density ρ) of the 3D printed branch and mounts are listed in Tab. 1. The mass-proportional damping coefficient α_R and stiffness-proportional damping coefficient β_R for Rayleigh damping of the structure are fitted for the damping ratio (of selected structural modes) obtained from experimental modal analysis in the range of 0 to 5 kHz.

Table 1. Structural mechanical material parameters (Young's modulus E, Poisson ratio ν, and density ρ).

Part	E (MPa)	ν	ρ (kg/m^3)	α_R	β_R
Branch pipe	2 000	0.43	900	777	1.387e-5
Mounts	2 200	0.40	840	777	1.387e-5

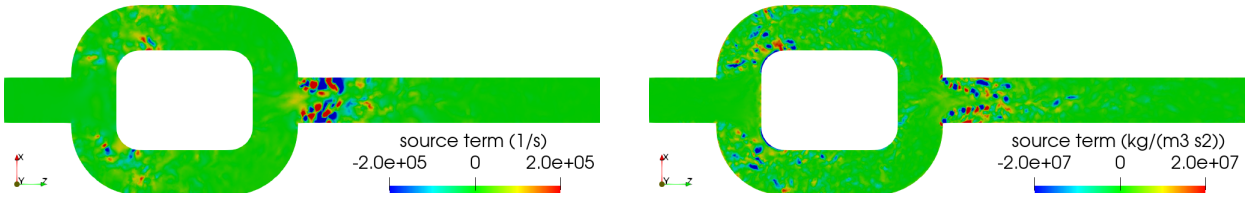
4.1 INCOMPRESSIBLE FLOW SIMULATION

The incompressible Navier-Stokes equations are solved using LES in AVL FIRE™ based on the FV method. At the inlet face, a turbulent fluctuating velocity distribution was prescribed, which was generated in a precursor LES, considering fully developed, axially periodic, turbulent flow through a $5D$ long pipe. At the outflow boundary, an averaged pressure boundary condition (BC) was used. The computational grid of the $25D$ long domain consisted of about 8.14 million FV cells. The time step was set to 10 µs, and the simulation time was 0.62 s where convergence was reached, while additional 0.2 s were simulated for the export of the source terms. More information about the simulation setup is provided in [18], where a LES of a similar flow configuration was carried out and validated. These predicted source terms were further interpolated onto the CA mesh for the subsequent propagation simulation and the mean value was removed in a filtering process.

Figure 3 shows the instantaneous source terms for both considered aeroacoustic formulations. Large source terms occur downstream of the sharp edges at the diverging and converging branches, respectively. The Lighthill source terms indicate the detachment of vortices at the sharp-edges, especially at the converging branch (Fig. 3b).

4.2 PROPAGATION SIMULATION

The propagation simulations are carried out by the multiphysics solver openCFS, applying the FE method [12]. A time step size of $\Delta t = 10\,\mu\mathrm{s}$ was chosen, and a zero initial condition was used. The simulation time was 0.2 s, corresponding to the export time of the CFD simulation. At the first 80 time steps, a temporal blending function

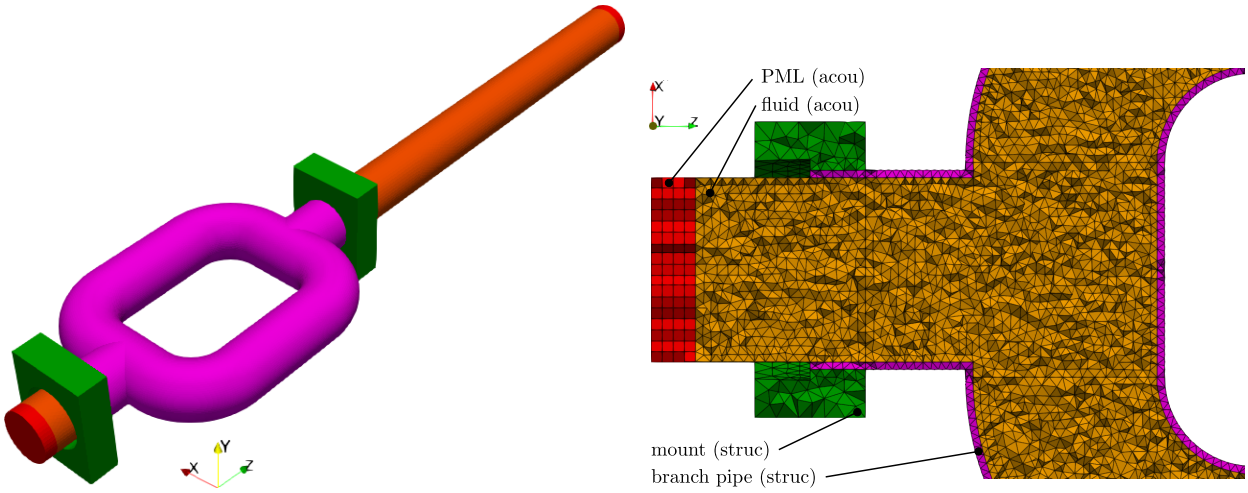


(a) PCWE source term $Q^{\text{ic}}_{\text{PCWE}}$.

(b) Lighthill source term $Q^{\text{ic}}_{\text{LH}}$.

Figure 3. Instantaneous contours of the source terms obtained by incompressible LES.

was used to smoothly activate the acoustic sources to avoid impulsive excitation. In Fig. 4a, the computational domains and in Fig. 4b a detail of the multiphysics mesh are displayed. The mesh consists of the internal



(a) Full setup with inlet left and outlet right.

(b) Clipped view of the mesh in horizontal plane at the inlet.

Figure 4. FE simulation setup for the coupled propagation simulation.

aeroacoustic domain (orange) including the aeroacoustic sources and the structural mechanical domains of the mounts (green) and the branch pipe (pink). Adjacent Perfectly Matched Layer (PML) regions (red) at the inlet and outlet avoid reflections at the open boundaries [19]. At the bottom surfaces of the mounts, all three degrees of freedom are locked for the coupled simulation. The total number of elements sums up to approximately 1.2 million. The maximum element size in the fluid domain is 3 mm (see Tab. 2), resolving acoustic waves up to $f_{\text{max}} = 11\,\text{kHz}$ by at least ten finite elements. Linear elements are used for the aeroacoustic domain, while quadratic FE basis functions are applied to the structural mechanical domain. More information about the multiphysics mesh is provided in Tab. 2.

Figure 5 shows the Power Spectral Densities (PSDs) of the wall pressure estimated by the incompressible LES and the PCWE-based propagation simulation at the positions P1 and P2 (see Fig. 2b). The pressure from the incompressible CFD simulation must be added to the pressure estimated by the PCWE according to (1) to be comparable with the wall pressure measurements. At P2, various peaks are visible in the measured spectrum, which is caused by the excitation of acoustic resonances, where the length of the centerline loop $L_{\text{lp}} = 0.63\,\text{m}$ of the branch pipe coincides with a multiple of the acoustic wavelength λ_i. This results in a resonance frequency $f_i = \frac{c_0\, i}{L_{\text{lp}}}$, where i denotes the order of the mode. In Figs. 6a and 6b, the real part of the Fourier transformed acoustic pressure predicted by the PCWE is depicted at frequencies $f_3 = 1667.2\,\text{Hz}$ and $f_8 = 4134.7\,\text{Hz}$, respectively. The contours clearly exhibit the acoustic resonances, where the latter is above

Table 2. Details of the multiphysics mesh for the coupled propagation simulation.

Region	domain	no. regions	no. elements	max el. size	el. order	el. type
Fluid	acoustic	1	1 002 171	3mm	1	tetrahedron
PML	acoustic	2	2 016	3mm	1	wedge
Branch pipe	struct. mech.	1	163 938	2mm	2	tetrahedron
Mount	struct. mech.	2	14 817	3mm	2	tetrahedron
Total		6	1 199 775	2-6mm		

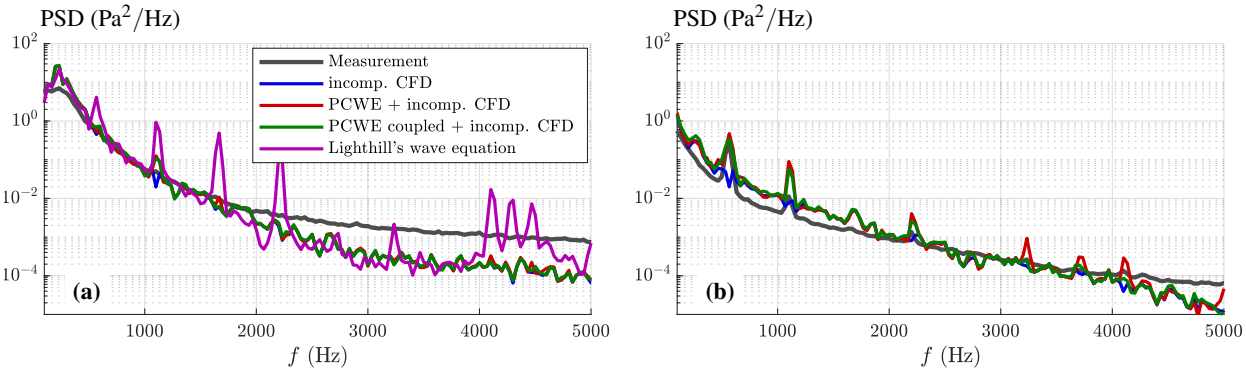


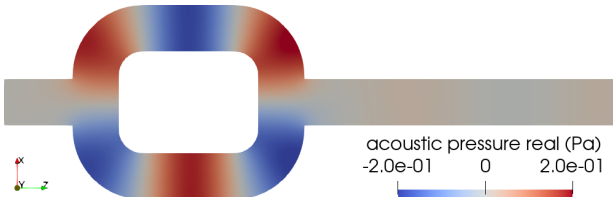
Figure 5. PSDs of the internal wall pressure at the two sensor positions (a) P1 and (b) P2.

the cut-off frequency for plane wave propagation $f_c = 4046\,\text{Hz}$. Due to the assumption of incompressible flow, the LES does not capture these acoustic modes. When adding the acoustic pressure predicted by the PCWE, the spectrum of the measurement is reproduced well (Fig. 5a). The peaks of the acoustic resonances are not visible in the PSD of P1 due to the local dominating superimposed turbulent pressure fluctuations. Overall, the pressure fluctuations are underestimated in P1, especially in the higher frequency range. For P1 (Fig. 5a), the result of Lighthill's wave equation is also shown (for better visibility, it is not shown for P2 in Fig. 5b.). The spectra resulting from Lighthill's wave equation partly overestimate the acoustic pressure, especially above the cut-off frequency. Comparing the contour of the pressure fluctuation p' at an instantaneous time step in Fig. 6d reveals that the pressure from the incompressible CFD (of the LES in Fig. 6c) is reproduced well.

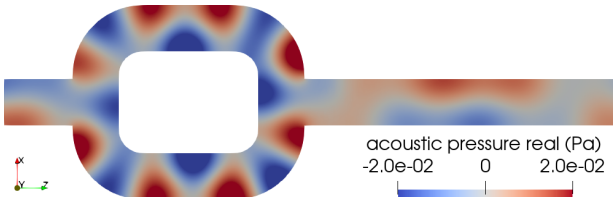
Additionally, strong coupling is considered for the PCWE-based propagation simulation (which yielded more accurate results) to evaluate the impact of FSI. The coupling does not have a significant impact on the PSD in P1 (Fig. 5a). In P2, the strong coupling results in reduced amplitudes at the higher acoustic resonances (above 3000 Hz), showing that these resonances are mitigated by the (Rayleigh) damped structure.

5 CONCLUSIONS

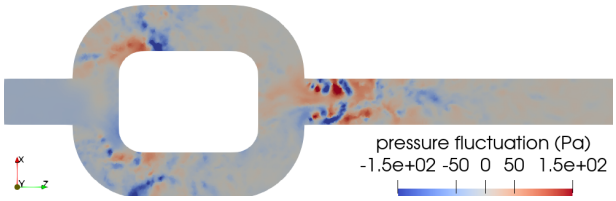
Two aeroacoustic formulations, namely the PCWE and Lighthill's wave equation, were applied to compute the flow-induced sound in a diverging and remerging branch pipe flow based on the hybrid aeroacoustic approach. Strong coupling of the acoustic and the structural mechanical domains allows for considering FSI within the FE framework of openCFS. Incompressible LES is used to compute the acoustic source terms of the low Mach number flow. Contours of the source terms showed that the dominating acoustic sources occur in the detached flow region downstream of the sharp edges of the branch. The result of the PCWE yielded good agreement with wall pressure measurements, while the propagation simulation based on Lighthill's wave equation overesti-



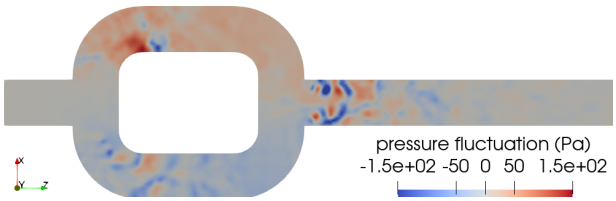
(a) CA (PCWE): Real part of the Fourier transformed acoustic pressure $\Re(p^{\mathrm{a}})$ at $f_3 = 1667.2\,\mathrm{Hz}$.



(b) CA (PCWE): Real part of the Fourier transformed acoustic pressure at $\Re(p^{\mathrm{a}})$ at $f_8 = 4134.7\,\mathrm{Hz}$.



(c) CFD: Instantaneous incompressible pressure $p^{\mathrm{ic}\prime}$.



(d) CA (Lighthill): Instantaneous pressure fluctuation p'.

Figure 6. Field visualizations of the non-coupled simulation results.

mates the amplitudes of the acoustic resonances at least by an order of magnitude, especially above the cut-off frequency. Consideration of strong coupling in the PCWE-based propagation simulation showed, that for accurate results, FSI must be considered to model the mitigation of the acoustic resonances in the higher frequency range.

ACKNOWLEDGEMENT

The support from the Austrian Research Promotion Agency (FFG) under no. 874784 and from AVL List GmbH Graz are gratefully acknowledged.

REFERENCES

[1] S. Schoder and M. Kaltenbacher, "Hybrid aeroacoustic computations: State of art and new achievements," *Journal of Theoretical and Computational Acoustics*, vol. 27, p. 1950020, 2019.

[2] M. Piellard and B. Coutty, "Application of a hybrid computational aeroacoustics method to an automotive blower," in *Vehicle Thermal Management Systems Conference and Exhibition (VTMS10)*, pp. 447–455, Woodhead Publishing, 2011.

[3] S. Schoder, C. Junger, and M. Kaltenbacher, "Computational aeroacoustics of the EAA benchmark case of an axial fan," *Acta Acustica*, vol. 4, p. 22, 2020.

[4] M. Tautz, K. Besserer, S. Becker, and M. Kaltenbacher, "Source formulations and boundary treatments for Lighthill's analogy applied to incompressible flows," *AIAA Journal*, vol. 56, pp. 2769–2781, 2018.

[5] M. Kaltenbacher, M. Escobar, S. Becker, and I. Ali, "Numerical simulation of flow-induced noise using LES/SAS and Lighthill's acoustic analogy," *International journal for numerical methods in fluids*, vol. 63, pp. 1103–1122, 2010.

[6] A. A. Oberai, F. Roknaldin, and T. J. Hughes, "Computational procedures for determining structural-acoustic response due to hydrodynamic sources," *Computer Methods in Applied Mechanics and Engineering*, vol. 190, pp. 345–361, 2000.

[7] S. De Reboul, N. Zerbib, and A. Heather, "Use openfoam coupled with finite and boundary element

formulations for computational aero-acoustics for ducted obstacles," in *INTER-NOISE and NOISE-CON Congress and Conference Proceedings*, pp. 4811–4826, Institute of Noise Control Engineering, 2019.

[8] M. Bayati and M. Tadjfar, "High Helmholtz sound prediction generated by confined flows and propagation within ducts," *International Journal of Acoustics and Vibration*, vol. 20, p. 47, 2015.

[9] E. Longatte, P. Lafon, and S. Candel, "Computation of noise generation by turbulence in internal flows," in *4th AIAA/CEAS Aeroacoustics Conference*, p. 2332, 1998.

[10] S. Schoder, M. Weitz, P. Maurerlehner, A. Hauser, S. Falk, S. Kniesburges, M. Döllinger, and M. Kaltenbacher, "Hybrid aeroacoustic approach for the efficient numerical simulation of human phonation," *The Journal of the Acoustical Society of America*, vol. 147, pp. 1179–1194, 2020.

[11] S. Schoder, P. Maurerlehner, A. Wurzinger, A. Hauser, S. Falk, S. Kniesburges, M. Döllinger, and M. Kaltenbacher, "Aeroacoustic sound source characterization of the human voice production-perturbed convective wave equation," *Applied Sciences*, vol. 11, p. 2614, 2021.

[12] Finite element multiphysics solver openCFS, "opencfs.org," 2021.

[13] M. Kaltenbacher, A. Hüppe, A. Reppenhagen, F. Zenger, and S. Becker, "Computational aeroacoustics for rotating systems with application to an axial fan," *AIAA Journal*, vol. 55, pp. 3831–3838, 2017.

[14] M. Kaltenbacher, *Numerical Simulation of Mechatronic Sensors and Actuators: Finite Elements for Computational Multiphysics*. Springer Berlin Heidelberg, 2015.

[15] S. Schoder, C. Junger, M. Weitz, and M. Kaltenbacher, "Conservative source term interpolation for hybrid aeroacoustic computations," in *25th AIAA/CEAS Aeroacoustics Conference*, 2019-2538, 2019.

[16] C. Bogey, C. Bailly, and D. Juvé, "Computation of flow noise using source terms in linearized Euler's equations," *AIAA Journal*, vol. 40, pp. 235–243, 2002.

[17] P. Maurerlehner, S. Schoder, S. Floss, J. Tieber, H. Steiner, G. Brenn, and M. Kaltenbacher, "Validation setup for the investigation of aeroacoustic and vibroacoustic sound emission of confined turbulent flows," in *INTER-NOISE and NOISE-CON Congress and Conference Proceedings*, pp. 519–525, Institute of Noise Control Engineering, 2021.

[18] J. Tieber, H. Steiner, P. Maurerlehner, S. Schoder, M. Kaltenbacher, and G. Brenn, "Aeroacoustic sources in turbulent flow through a 90° pipe bend predicted by large-eddy simulation," in *DAGA 2022-48. Jahrestagung für Akustik*, pp. 1230–1233, 2022.

[19] B. Kaltenbacher, M. Kaltenbacher, and I. Sim, "A modified and stable version of a perfectly matched layer technique for the 3-d second order wave equation in time domain with an application to aeroacoustics," *Journal of Computational Physics*, vol. 235, pp. 407–422, 2013.

ICA 2022
24th INTERNATIONAL CONGRESS ON ACOUSTICS
October 24(Mon) - 28(Fri), 2022 Gyeongju, Korea

PROCEEDINGS of the
24th International Congress on Acoustics

October 24 to 28, 2022 in Gyeongju, Korea

ABS-0075

A non-conforming and overlapping DG formulation for the acoustic conservation equations

Johannes HEINZ[(1)]; Manfred KALTENBACHER[(2)]

[(1)]TU Wien, Institute of Mechanics and Mechatronics, 1060 Vienna, Austria, Email: johannes.heinz@tuwien.ac.at

[(2)]TU Graz, Institute of Fundamentals and Theory in Electrical Engineering, 8010 Graz, Austria, Email: manfred.kaltenbacher@tugraz.at

ABSTRACT

High-order discontinuous Galerkin (DG) methods are ideally suited to solve the acoustic conservation equations in the time domain. To compute, e.g., the acoustic field originating from a ventilator, it is common to use two mesh regions. One of the regions rotates while the other one stays fixed. To solve this kind of problems, we need implementations that can deal with non-conformities at mesh interfaces. If elements do not precisely represent the geometry, i.e., by using non-uniform rational B-splines, it is not sufficient to utilize non-conforming interfaces alone. Within this work, we show that Nitsches' idea — which is commonly used at non-conforming interfaces — can be applied for overlapping elements straightforward. Instead of using complex element cut algorithms, we directly use element faces at non-conforming transitions as integration domains. To counteract aliasing, we use over-integration to generate a stable method.

Keywords: Discontinuous Galerkin, Non-matching methods, Moving meshes

1 INTRODUCTION

While nonconforming interfaces (NCIs) have the nice property of easy modular mesh generation, overlapping meshes enhance this property. This is because boundaries of mesh regions do not have to coincide anymore. This becomes especially relevant in simulations in which elements move relative to each other. Imagine the computation of the aeroacoustic sound field around a rotating fan. In this case the computational mesh typically consists of two regions, a rectangular outer region with a cylindrical hole and a cylinder as inner region. The outer region stays fixed, while the inner domain — containing the rotor blades — rotates, see e.g. [13, 23]. Solving this kind of problems using NCIs would require the surface of the cylinder to exactly coincide with the surface of the hole in the outer domain. This can only be achieved using isogeometric analysis, i.e. use non-uniform rational B-splines, see, e.g. [20]. Using overlaps between the region, it is possible to compute the emerging sound field without the use of isogeometric analysis.

To account for the rotating inner domain typically arbitrary Lagrangian–Eulerian (ALE) methods are used. The derivation of ALE methods for mass, momentum, and energy conservation equations is given in [5]. This approach has been succesfully applied to the acoustic conservation equations in [8] in a FEM setting.

Nitsche presented the idea to incorporate Dirichlet boundary conditions in the weak form in [19]. Nitsches' method lead to non-conforming discretizations using the same principle — see amongst others [14, 21, 10] — and naturally extends from non-conforming interfaces to overlapping meshes. Typically element cut algorithms are used to ensure integration in the same integration points on the non-conformingly connected or overlapping meshes, see e.g. [17, 13, 23, 22]. The implementation for those cut cell algorithms is a challenging endover. Element cut algorithms in the overlapping case are espescially complicated and thus it is desirable to avoid them. A different approach for NCIs is to consequently evaluate all quantities in the integration points dictated by the master element, see [10, 16]. This methodology is also referred to as point-to-point interpolation and has been compared to the mortar approach in [16]. To supress aliasing an over-integration at non-conforming cell

faces is necessary [16]. To the best of the authors knowledge this approach has not been applied to overlapping elements to this date.
Following the point-to-point interpolation method we proposed a non-conforming discontinuous Galerkin discretization for the acoustic conservation equations in [9]. If elements on a NCI do not contain hanging nodes, the method collapses to the standard DG discretization. With this work we extend mentioned methodology to rotating overlapping mesh regions and provide a test case which highlights that the method is well suited for the computation of aeroacoustic borne sound around a fan as described above.

2 GOVERNING EQUATIONS

The governing equations are the well known acoustic conservation equations and are stated in Eulerian description amongst others in [18, 12, 15]. To be able to consider moving meshes we have to transferre the equations into the arbitrary Lagrangian–Eulerian description. For the derivation of the equations we referre to [5]. On a time dependent domain $\Omega(t) \subset \mathbb{R}^d$ of dimension d and in a time interval $t \in [0,T]$ they read

$$\left.\frac{\partial \boldsymbol{u}}{\partial t}\right|_{\boldsymbol{\chi}} - \nabla \boldsymbol{u}\boldsymbol{u}^{\mathrm{g}} + \frac{1}{\rho}\nabla p = 0 \quad \text{on } \Omega(t) \tag{1}$$

$$\left.\frac{\partial p}{\partial t}\right|_{\boldsymbol{\chi}} - \boldsymbol{u}^{\mathrm{g}} \cdot \nabla p + \rho c^2 \nabla \cdot \boldsymbol{u} = c^2 F \quad \text{on } \Omega(t) \tag{2}$$

$$p = g_p \quad \text{on } \partial\Omega_p^{\mathrm{D}}(t), \tag{3}$$

$$\rho c \boldsymbol{u} \cdot \boldsymbol{n} = Y p \quad \text{on } \partial\Omega^{\mathrm{Y}}(t). \tag{4}$$

In the equations, the material parameters c and ρ are the speed of sound, and the density of the underlying material respectively. The acoustic pressure is denoted as p, the acoustic particle velocity is $\boldsymbol{u} = (u_1, ..., u_d)^T$, and the velocity of an ALE observer at position $\boldsymbol{\chi} = (\chi_1, ..., \chi_d)^T$ is $\boldsymbol{u}^g = (u_1^g, ..., u_d^g)^T$. We can apply pressure Dirichlet boundary conditions (BCs) Eq. (3), and admittance BCs Eq. (4) at the corresponding domain boundaries $\partial\Omega_p^{\mathrm{D}}(t)$, or $\partial\Omega^{\mathrm{Y}}(t)$. g_p is the acoustic pressure prescribed at Dirichlet boundaries. The first-order absorbing BC [6] is obtained with admittance $Y = 1$, while a reflecting boundary requires $Y = 0$.

3 NUMERICAL METHOD

3.1 Notation

The physical domain $\Omega(t)$ depends on time t if domain boundaries move $\partial\Omega(t)$. The computational domain $\Omega_h(t)$ represents the physical domain and also dependents on time if its boundaries $\partial\Omega_h$ do not move since the mesh might also move in its internal. The computational domain consists of N_{el} possibly overlapping rectangular/hexahedal finite elements. Each finite element has a volume of $\Omega_e(t)$ and is restricted by $\partial\Omega_e(t)$. The acoustic pressure und acoustic particle velocity are approximated as p_h and $\boldsymbol{u}_h$ by means of shape functions N_i^k of polynomial degree k which are constructed from Lagrange polynomials

$$\tilde{p}_h^e(\boldsymbol{\xi}) = \sum_{i=1}^{n_{N^{k_p}}} N_i^{k_p}(\boldsymbol{\xi}) p_i^e; \quad \tilde{\boldsymbol{u}}_h^e(\boldsymbol{\xi}) = \sum_{i=1}^{n_{N^{k_u}}} N_i^{k_u}(\boldsymbol{\xi}) \boldsymbol{u}_i^e. \tag{5}$$

In Eq. (5), n_N represents the number of shape functions used for a volume element. Throughout the work we use the same polynomial degree for pressure and velocity $k_u = k_p$. Corresponding broken polynomial spaces $\mathscr{V}_h$ for test and trial functions are those of [9]

$$\mathscr{V}_h^u = \left\{ \boldsymbol{u}_h \in \ [L_2(\Omega_h(t))]^d : \boldsymbol{u}_h(\boldsymbol{x})|_{\Omega^e(t)} = \tilde{\boldsymbol{u}}(\boldsymbol{\xi})|_{\tilde{\Omega}^e(t)} \in [\mathscr{P}_{k_u}(\tilde{\Omega}^e)]^d, \forall e \in [1, N_{\mathrm{el}}] \right\}, \tag{6}$$

$$\mathscr{V}_h^p = \left\{ p_h \in \ L_2(\Omega_h(t)) : p_h|_{\Omega^e(t)} = \tilde{p}_h|_{\tilde{\Omega}^e(t)} \in \mathscr{P}_{k_p}(\tilde{\Omega}^e), \forall e \in [1, N_{\mathrm{el}}] \right\}, \tag{7}$$

where $\mathscr{P}_k$ is the space of shape functions of polynomial degree k.

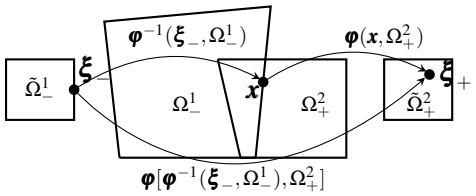


Figure 1. Picture adapted from [9]. The integration point $\boldsymbol{\xi}_-$ on the reference element $\tilde{\Omega}^1_-$ is associated to the edge of the master element Ω^1_- which is connected to the other mesh region via NCI or overlap. The mapping to the physical space followed by the mapping to the slave reference element $\tilde{\Omega}^2_+$ yields an integration point $\boldsymbol{\xi}_+$ which can be located inside the slave reference element.

The bidirectional mapping used in [9] now depends on time

$$\boldsymbol{\varphi}(t): \begin{cases} \Omega^e(t) \to \tilde{\Omega}^e \\ \boldsymbol{x}(t) \mapsto \boldsymbol{\xi} = \boldsymbol{\varphi}(\boldsymbol{x}(t), \Omega^e(t)) \end{cases} ; \quad \boldsymbol{\varphi}^{-1}(t): \begin{cases} \tilde{\Omega}^e \to \Omega^e(t) \\ \boldsymbol{\xi} \mapsto \boldsymbol{x}(t) = \boldsymbol{\varphi}^{-1}(\boldsymbol{\xi}, \Omega^e(t)) \end{cases} . \tag{8}$$

It transfers reference coordinates $\boldsymbol{\xi} = (\xi_1, ..., \xi_d)^T$ to the corresponding physical coordinates $\boldsymbol{x}(t) = (x_1(t), ..., x_d(t))^T$ and vice versa, see Fig. 1. As in [9] the implementations of the mapping is realized by means of a search algorithm. Since the mapping depends on time it is now required to search for the integration points each time step.

Interior informations of a specific element $\Omega^e(t)$ are denoted with $(\cdot)^-$; exterior informations are denoted with $(\cdot)^+$. The element under consideration $\Omega^e_-(t)$ is also called master element within the following. Exterior information appears on slave elements which are those connected to the master element Ω^e_+; this connection can be achieved via coinciding element boundaries or if an element overlaps an element boundary of the master element. Each facet of the master element has an outward pointing normal vector $\boldsymbol{n}^-(t)$. If element boundaries coincide $\boldsymbol{n}(t) = \boldsymbol{n}^-(t) = -\boldsymbol{n}^+(t)$ with the normal vector of the slave element $\boldsymbol{n}^+(t)$. If the slave element is an overlapping one we imagine the element boundary of the master element as an artificial truncation of the slave element and require the same identity. An arbitrary scalar or vectorial quantity b is always defined on the master element if no superscript occurs, i.e. $b = b^-$. We use the notation of Bassi *et al.* [3, 4] for the averaging operator $\{\{\cdot\}\}$, jump operator $[\cdot]$, and normal jump operator $[\![\cdot]\!]$; i.e. $\{\{b\}\} = {}^{(b^- + b^+)}/_2$, $[b] = b^- - b^+$, and $[\![b]\!] = b^- \otimes n^- + b^+ \otimes n^+$. Integrals are expressed in the usual compressed notation $(a,b)_{\Omega_e(t)} = \int_{\Omega_e(t)} a \cdot b \ \mathrm{d}\Omega(t)$ and $(a,b)_{\partial\Omega_e(t)} = \int_{\partial\Omega_e(t)} a \cdot b \ \mathrm{d}\Gamma(t)$. Here, $\cdot$ implys an inner product and a is a different arbitrary scalar or vectorial quantity. As in [10, 16, 9] faces of the master elements serve as integration domains directly, independent how master and slave elements are connected.

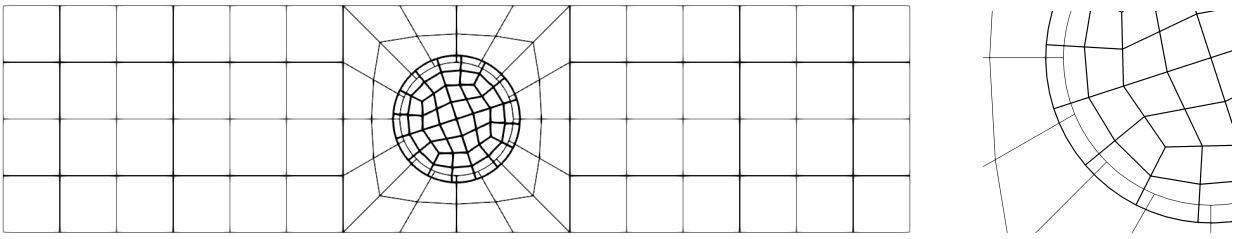
Standard Gaussian quadrature is used for numerical integration. Volume integrals are computed using $n_q = (k+1)^d$ quadrature points, where d is the spatial dimension. Integrals over element facets inside each mesh region use $n_q = (k+1)^{d-1}$ quadrature points. To suppress aliasing we use $n_q = (2k+1)^{d-1}$ quadrature points on element facets which are on a non-conforming or overlapping interface. We apply boundary conditions using the mirror principle, cf. [11]. Hence, outer information for acoustic pressure and acoustic particle velocity at domain boundaries read

$$p^+ = -p^- + 2g_p; \quad \boldsymbol{u}^+ = \boldsymbol{u}^- \qquad \text{on } \partial\Omega^{\mathrm{D}}_p(t), \tag{9}$$

$$p^+ = p^- \qquad \boldsymbol{u}^+ = \left(\frac{2Y}{\rho c} p^- - \boldsymbol{u}^- \cdot \boldsymbol{n}\right)\boldsymbol{n} \qquad \text{on } \partial\Omega^{\mathrm{Y}}(t). \tag{10}$$

3.2 SPATIAL DISCRETIZATION

The ALE observer is thought to move with the grid. We are evaluating the integration points at the deforemed elements instead of computing on a reference domain. This approach automatically fulfills the discrete geometric



(a) Computational domain at refinement ref = 1

(b) Overlap $\delta = \frac{0.03}{2^{\text{ref}}}$

Figure 2. The computational domain consists of two mesh regions. The outer (rectangular) one stays fixed, while the inner (circular) region rotates counter-clockwise with $\omega = 2\pi \ \frac{\text{rad}}{\text{s}}$.

conservation law [7]. For the spatial discretization we multiply the governing equations by the test functions $\boldsymbol{w}$ and q. Resulting system of equations is integrated by parts and numerical fluxes, denoted with superscript *, are introduced to arrive at the weak formulation. We are integrating the formulation by parts once more. This gives us surface integrals which have to vanish and is commonly referred to as the strong formulation cf. [11]. The resulting semi-discrete system of equations reads

$$\begin{aligned}\left(\boldsymbol{w}_h, \left.\frac{\partial \boldsymbol{u}_h}{\partial t}\right|_{\boldsymbol{\chi}}\right)_{\Omega^e(t)} &- (\boldsymbol{w}_h, \nabla \boldsymbol{u}_h \boldsymbol{u}_h^{\mathrm{g}})_{\Omega^e(t)} + \left(\frac{1}{\rho}\boldsymbol{w}_h, \nabla p_h\right)_{\Omega^e(t)} \\ &- \left(\boldsymbol{w}_h(\boldsymbol{u}_h^{\mathrm{g}}\cdot\boldsymbol{n}), \boldsymbol{u}_{h,c}^* - \boldsymbol{u}_h\right)_{\partial\Omega^e(t)} + \left(\frac{1}{\rho}\boldsymbol{w}_h\cdot\boldsymbol{n}, p_h^* - p_h\right)_{\partial\Omega^e(t)} = 0 \end{aligned} \qquad \forall \boldsymbol{w}_h \in \mathscr{V}_h^u, \quad (11)$$

$$\begin{aligned}\left(q_h, \left.\frac{\partial p_h}{\partial t}\right|_{\boldsymbol{\chi}}\right)\Omega^e(t) &- (q_h, \boldsymbol{u}_h^{\mathrm{g}}\cdot\nabla p)_{\Omega^e(t)} + \left(\rho c^2 q_h, \nabla\cdot\boldsymbol{u}_h\right)_{\Omega^e(t)} \\ &- \left(q_h\boldsymbol{u}_h^{\mathrm{g}}\cdot\boldsymbol{n}, p_{h,c}^* - p_h\right)_{\partial\Omega^e(t)} + \left(\rho c^2 q_h\cdot\boldsymbol{n}, \boldsymbol{u}_h^* - \boldsymbol{u}_h\right)_{\partial\Omega^e(t)} = \left(c^2 q_h, F\right)_{\Omega^e(t)} \end{aligned} \qquad \forall q_h \in \mathscr{V}_h^p. \quad (12)$$

As fluxes in the pressure gradient and velocity divergence term we use the Lax–Friedrichs fluxes

$$p_h^* = \{\{p_h\}\} + \frac{\tau}{2}[\![\boldsymbol{u}_h]\!]; \quad \boldsymbol{u}_h^* = \{\{\boldsymbol{u}_h\}\} + \frac{\gamma}{2}[\![p_h]\!], \quad (13)$$

with penalty parameters $\tau = \rho c$ and $\gamma = \frac{1}{\rho c}$, cf. [18, 12, 15, 24]. As fluxes for the convective terms, central fluxes are sufficient

$$p_{h,c}^* = \{\{p_h\}\}; \quad \boldsymbol{u}_{h,c}^* = \{\{\boldsymbol{u}_h\}\}. \quad (14)$$

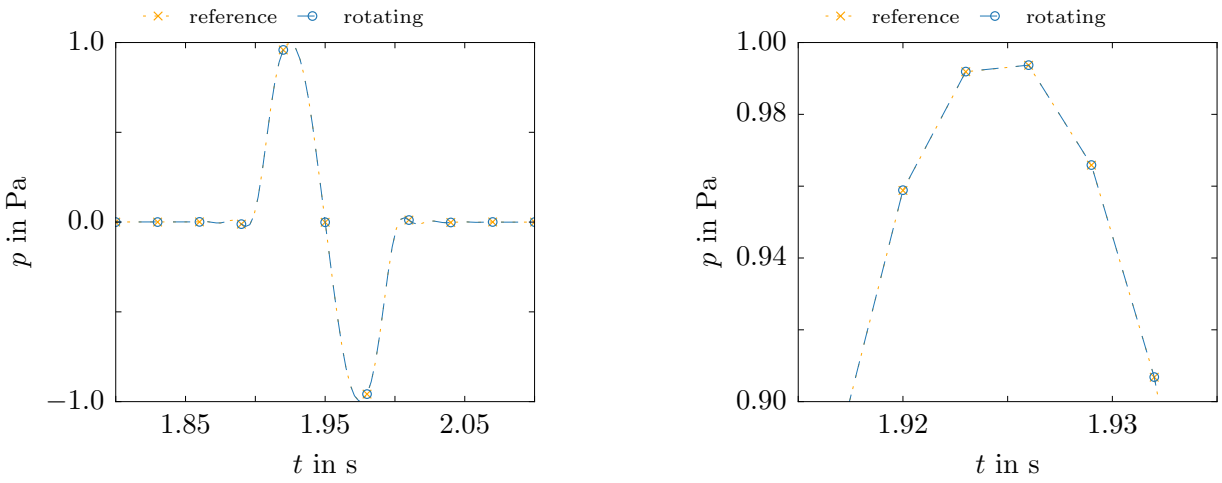
Overlapping and non-conforming element edges are treated by the consistent evaluation of integration points and over-integration as de-aliasing routine as described before or more precicely in [16].

4 NUMERICAL RESULTS

Our implementations build on the open source software project `EXADG` [2] which internally uses the software library `deal.II` [1]. Hereinafter, all spatial values are given in m.

4.1 PLANE WAVE IN DUCT

The density is $\rho = 1 \ \frac{\text{kg}}{\text{m}^3}$ and the speed of sound is $c = 1 \ \frac{\text{m}}{\text{s}}$. To verify the non-conforming rotating implementation we compare the results of a computation with and without a non-conforming rotating interface. For the rotational computation the setup is as follows: The computational domain is a channel $\Omega_{h,\text{outer}} = (-1,-0.25)\times(1,0.25)$ with a hole of radius $r = 0.125$, centered around $\boldsymbol{x}_\text{c} = (0,0)^T$. A circle is placed above the hole and rotates counter-clockwise with an angular velocity $\omega = 2\pi \ \frac{\text{rad}}{\text{s}}$. To steer the spatial resolution the



(a) Full pressure wave

(b) Detail view

Figure 3. Acoustic pressure p over time t at $\boldsymbol{x} = (0.9, 0.0)^T$.

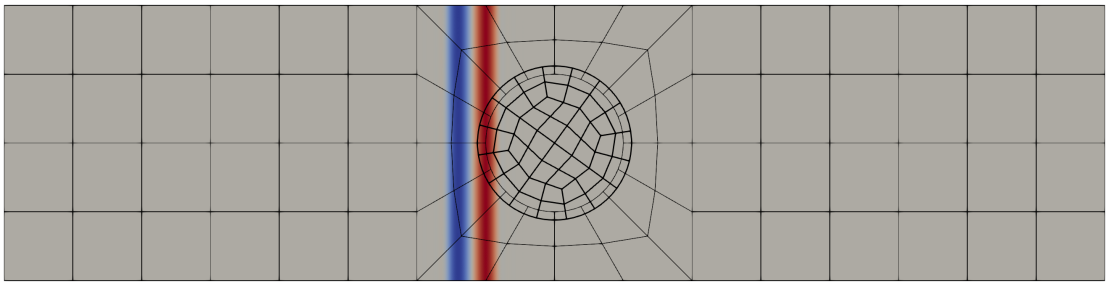
elements of the mesh can be refined by splitting. Given a certain spatial refinement ref, the element size h computes as $h = \frac{h_{\text{initial}}}{2^{\text{ref}}}$. Figure 2a shows the computational domain at $t = 1.5 \cdot 10^{-1}$ s with mesh refinement ref $= 1$. To ensure all integration points can be found at any time, the circle is of radius $r = 0.125 + \delta$. Here, δ describes the overlap between inner and outer domain and is defined as $\delta = \frac{0.03}{2^{\text{ref}}}$, cf. Figure 2b. For the conforming computation without any rotation we choose $\omega = 0$ and $\delta = 0$.
At the left side of the channel Γ_{left} we excite a single plane pressure wave by means of a pressure Dirichlet boundary condition

$$g_p = \begin{cases} \sin\left(\frac{2\pi}{0.1} t\right) & \text{if } t < 0.1 \text{ s} \\ 0 & \text{else} \end{cases} \quad \text{on } \Gamma_{\text{left}}. \tag{15}$$

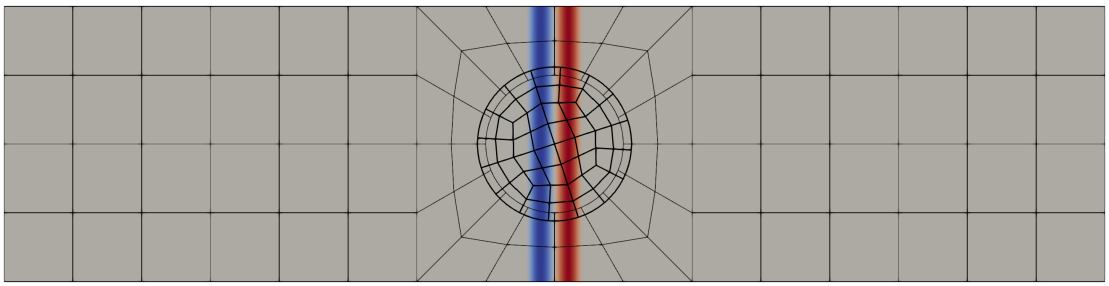
At the top and botton we apply reflecting boundary conditions and at the right side of the channel we apply a first-order absorbing boundary condition. All computations are performed with a polynomial degree of $k = 4$ and a spatial refinement of ref $= 4$. For temporal discretization we apply an explicit Euler scheme with a time step size of $\Delta t = 6 \cdot 10^{-7}$.
The pressure wave traversing the rotating domain is depicted in Fig. 4. For comprehensibly the grid in Fig 4 is obtained with ref $= 1$ while the result is obtained with ref $= 4$. The pressure results over time at $\boldsymbol{x} = (0.9, 0.0)^T$ can be found in Fig. 3. Especially in the detail view in Fig. 3b we can see that the results are in good agreement.

5 CONCLUSIONS

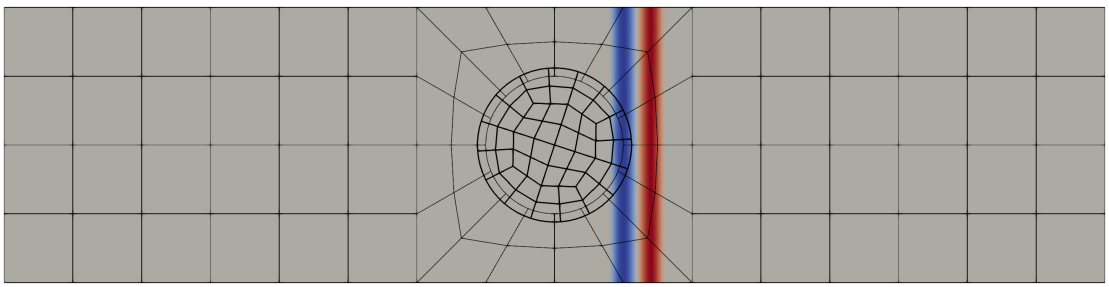
We used Nitsches' idea to generate a DG discretization for the acoustic conservation laws which can deal with overlapping elements and moving meshes. Instead of using element cut algorithms we evaluate quantities on slave elements in integration points dictated by the master element. To avoid aliasing the approach uses over-integration at domain regions [16]. A test case using this strategy and a test case without non-conformities and without any mesh movement yield the same results. This highlights that the method is well suited for aeroacoustic applications such as a rotating fan.



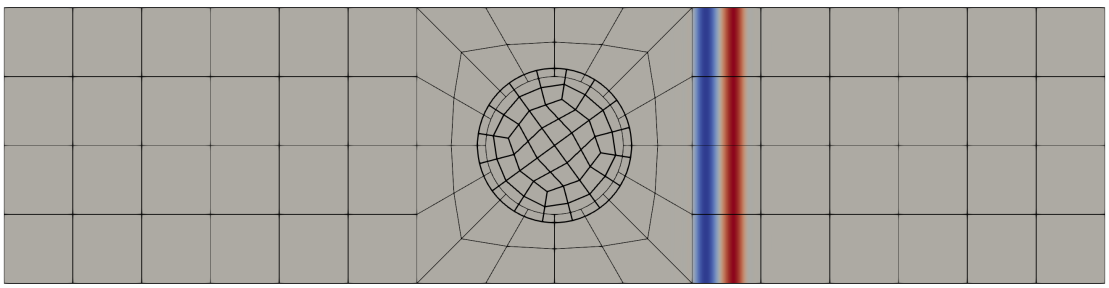
(a) $t = 0.9$ s



(b) $t = 1.05$ s



(c) $t = 1.2$ s



(d) $t = 1.35$ s

Figure 4. Pressure pulse traversing rotating domain. Note, that displayed result is achieved with ref $= 4$ but the mesh is the one of ref $= 1$ to keep the plots comprehensible.

ACKNOWLEDGEMENTS

This project has received funding from the European Union's Framework Programme for Research and Innovation Horizon 2020 (2014-2020) under the Marie Skłodowska–Curie Grant Agreement No. [812719].
The computational results presented have been achieved in part using the Vienna Scientific Cluster (VSC).

REFERENCES

[1] D. Arndt, W. Bangerth, M. Feder, M. Fehling, R. Gassmöller, T. Heister, L. Heltai, M. Kronbichler, M. Maier, P. Munch, J.-P. Pelteret, S. Sticko, B. Turcksin, and D. Wells. The `deal.II` library, version 9.4. Journal of Numerical Mathematics, 2022.

[2] D. Arndt, N. Fehn, G. Kanschat, K. Kormann, M. Kronbichler, P. Munch, W. A. Wall, and J. Witte. ExaDG: high-order discontinuous Galerkin for the exa-scale. In *Software for Exascale Computing - SPPEXA 2016-2019*. Springer International Publishing, 2020.

[3] F. Bassi, A. Crivellini, D. D. Pietro, and S. Rebay. An artificial compressibility flux for the discontinuous Galerkin solution of the incompressible Navier-Stokes equations. Journal of Computational Physics, (2), 2006.

[4] F. Bassi, A. Crivellini, D. A. D. Pietro, and S. Rebay. An implicit high-order discontinuous Galerkin method for steady and unsteady incompressible flows. Computers & Fluids, (10), 2007.

[5] J. Donea, A. Huerta, J.-P. Ponthot, and A. Rodríguez-Ferran. *Arbitrary Lagrangian-Eulerian methods*. In *Encyclopedia of Computational Mechanics*. American Cancer Society, 2004. Chapter 14.

[6] B. Engquist and A. Majda. Absorbing boundary conditions for the numerical simulation of waves. Mathematics of Computation, (139), 1977.

[7] C. Förster, W. A. Wall, and E. Ramm. On the geometric conservation law in transient flow calculations on deforming domains. International Journal for Numerical Methods in Fluids, (12), 2006.

[8] O. Guasch, M. Arnela, R. Codina, and H. Espinoza. A stabilized finite element method for the mixed wave equation in an ALE framework with application to diphthong production. Acta Acustica united with Acustica, (1), 2016.

[9] J. Heinz and M. Kaltenbacher. A nonconforming DG formulation for the acoustic conservation laws. In *Fortschritte der Akustik - DAGA 2022*. Deutsche Gesellschaft für Akustik e.V. (DEGA), 2022.

[10] V. Hermann, M. Käser, and C. E. Castro. Non-conforming hybrid meshes for efficient 2-D wave propagation using the discontinuous Galerkin method. Geophysical Journal International, (2), 2010.

[11] J. S. Hesthaven and T. Warburton. Nodal Discontinuous Galerkin Methods. Springer, New York, NY, 1, 2008.

[12] M. Hochbruck, T. Pažur, A. Schulz, E. Thawinan, and C. Wieners. Efficient time integration for discontinuous Galerkin approximations of linear wave equations. ZAMM - Journal of Applied Mathematics and Mechanics / Zeitschrift für Angewandte Mathematik und Mechanik, (3), 2014.

[13] A. Hüppe, J. Grabinger, M. Kaltenbacher, A. Reppenhagen, G. Dutzler, and W. Kühnel. A non-conforming finite element method for computational aeroacoustics in rotating systems. In *20th AIAA/CEAS Aeroacoustics Conference*. American Institute of Aeronautics and Astronautics, 2014.

[14] M. Kaltenbacher and S. Floss. Nonconforming finite elements based on nitsche-type mortaring for inhomogeneous wave equation. Journal of Theoretical and Computational Acoustics, (03), 2018.

[15] M. Kronbichler, S. Schoeder, C. Müller, and W. A. Wall. Comparison of implicit and explicit hybridizable discontinuous Galerkin methods for the acoustic wave equation. International Journal for Numerical Methods in Engineering, (9), 2016.

[16] E. Laughton, G. Tabor, and D. Moxey. A comparison of interpolation techniques for non-conformal high-order discontinuous Galerkin methods. Computer Methods in Applied Mechanics and Engineering, 2021.

[17] A. Massing, M. G. Larson, and A. Logg. Efficient implementation of finite element methods on nonmatching and overlapping meshes in three dimensions. SIAM Journal on Scientific Computing, (1), 2013.

[18] N. Nguyen, J. Peraire, and B. Cockburn. High-order implicit hybridizable discontinuous Galerkin methods for acoustics and elastodynamics. Journal of Computational Physics, (10), 2011.

[19] J. Nitsche. Über ein Variationsprinzip zur Lösung von Dirichlet-Problemen bei Verwendung von Teilräumen, die keinen Randbedingungen unterworfen sind. Abhandlungen aus dem Mathematischen Seminar der Universität Hamburg, (1), 1971.

[20] S. Pezzano and R. Duvigneau. A fully-conservative sliding grid algorithm for compressible flows using an isogeometric discontinuous Galerkin scheme. Computer Methods in Applied Mechanics and Engineering, 2022.

[21] K. Roppert, S. Schoder, F. Toth, and M. Kaltenbacher. Non-conforming Nitsche interfaces for edge elements in curl–curl-type problems. IEEE Transactions on Magnetics, (5), 2020.

[22] K. Roppert, S. Schoder, G. Wallinger, and M. Kaltenbacher. Sliding non-conforming interfaces for edge elements in eddy current problems. IEEE Transactions on Magnetics, (3), 2021.

[23] S. Schoder, C. Junger, and M. Kaltenbacher. Computational aeroacoustics of the EAA benchmark case of an axial fan. Acta Acustica, (5), 2020.

[24] H. Wang, I. Sihar, R. P. Muñoz, and M. Hornikx. Room acoustics modelling in the time-domain with the nodal discontinuous Galerkin method. The Journal of the Acoustical Society of America, (4), 2019.

ICA 2022
24th INTERNATIONAL CONGRESS ON ACOUSTICS
October 24(Mon) - 28(Fri), 2022 Gyeongju, Korea

PROCEEDINGS of the
24th International Congress on Acoustics

October 24 to 28, 2022 in Gyeongju, Korea

ABS-0136

Adjoint-based analyzes in acoustic time-domain simulations

Mathias LEMKE

Technische Universität Berlin, Germany, mathias.lemke@tnt.tu-berlin.de

ABSTRACT

This manuscript presents an adjoint-based approach for analyzing acoustic configurations in the time domain. The technique allows the optimization and the identification of sound sources considering effects like diffraction. As an example, the identification of rotating sound sources based on microphone array measurements is demonstrated. All parameters sought, including rotation speed, relative positions and amplitudes of the sources, are identified using a measurement time corresponding to one rotation of the sources. In addition, preliminary results concerning the consideration of boundary conditions within the approach are presented. It is shown that reflections and diffraction can support the identification of sound sources.

Keywords: time domain, adjoint approach, source identification

1 INTRODUCTION

Wave-based acoustic time-domain simulations enable the description of effects that are difficult to account for in geometric acoustics, for example, diffraction. In addition, they often offer higher accuracy compared to frequency-based methods. These advantages often justify the higher numerical effort compared to classic, geometric or frequency-based methods.

A large number of acoustical problems, such as the search for optimal driving functions or geometric arrangements of loudspeakers as well as the optimal design of walls using acoustic materials, can be described as high-dimensional optimization tasks in the time domain. An adjoint-based approach has proven suitable for these problems since the computation time is mainly independent of the number of parameters examined.

This contribution presents the application of the adjoint approach for identifying rotating sound sources using microphone array measurements. In addition, it is shown that reflecting boundary conditions do not only hinder the identification of sound sources but instead can help to provide extra information for the identification.

Sound source identification is a typical problem in acoustics. Various parameters of one or more sound sources are sought, including signal and position. Usually, microphone array measurement techniques are used, in particular the so-called beamforming. Depending on the acoustic setup considered, different algorithms are used, operating in the time or frequency domain. A recent overview of algorithms is given by [1]. An adjoint-based method for the identification of stationary and moving sound sources in the time domain is presented in [2] and [3] respectively.

2 FRAMEWORK

2.1 Adjoint in general

In general, adjoint equations arise from a scalar-valued objective function J, defined by the user. The function encodes the goal of the analysis, for example, the localization of sound sources. It is given by the scalar product between a weight vector g and a system state vector q

$$J = g \cdot q = g^{\mathrm{T}} q \qquad g, q \in \mathbb{R}^n. \tag{1}$$

The system state q is the solution of the system under consideration

$$Mq = s \qquad M \in \mathbb{R}^{n \times n}, s \in \mathbb{R}^n, \tag{2}$$

with M as the governing operator and s as (sound) sources on the right-hand side. To optimize J using the n entries of s, the governing equation must be solved $n+1$ times.

To reduce the computational effort the adjoint equation can be used instead

$$M^{\mathrm{T}} q^* = g \qquad q^* \in \mathbb{R}^n, \tag{3}$$

with the adjoint variable q^*. Using

$$J = g^{\mathrm{T}} q = \left(M^{\mathrm{T}} q^*\right)^{\mathrm{T}} q = q^{*\mathrm{T}} M q = q^{*\mathrm{T}} s = q^* \cdot s, \tag{4}$$

a formulation is found, which allows the objective J to be computed without solving equation (2) for various s. By solving the adjoint equation (3) once, the objective can be computed by a scalar product. Thus, the adjoint approach allows efficient computation of gradients for J as a function of s.

2.2 Adjoint Euler equations

In the following, the definition of the used variables is adjusted in the context of a Cartesian tensor notation. The scalar objective function J is defined in space and time with $\mathrm{d}\Omega = \mathrm{d}x_1 \mathrm{d}x_2 \mathrm{d}x_3 \mathrm{d}t$ throughout the computational domain:

$$J = \frac{1}{2} \int \left(q - q^{\mathrm{mic}}\right)^2 \mathrm{d}\Omega. \tag{5}$$

The field variable $q(x_j,t)$ contains the complete state $q = [\rho, u_j, p]$ of the system governed by the Euler equations.

$$\partial_t \begin{pmatrix} \rho \\ \rho u_j \\ \frac{p}{\gamma - 1} \end{pmatrix} + \partial_{x_i} \begin{pmatrix} \rho u_i \\ \rho u_i u_j + p\delta_{ij} \\ \frac{u_i p \gamma}{\gamma - 1} \end{pmatrix} - u_i \partial_{x_i} \begin{pmatrix} 0 \\ 0 \\ p \end{pmatrix} = \begin{pmatrix} 0 \\ 0 \\ s_p \end{pmatrix} \tag{6}$$

Therein, ρ denotes the density, u_j the velocity in the x_j direction, γ the isentropic exponent and p the pressure. The source terms $s(x_j,t) = [0,0,s_p]$ describe monopole sound sources that allow controlling the system state and the solution of the equations, respectively. For details on the formulation, in particular, the reformulation of the energy equation in terms of pressure, see [4].

For the identification of sound sources by means of microphone measurements, the objective function depends only on the pressure and the pressure fluctuation:

$$J = \frac{1}{2} \int \left(p - p^{\mathrm{mic}}\right)^2 \sigma \ \mathrm{d}\Omega, \tag{7}$$

where p^{mic} contains the microphone measurements. The additional weight $\sigma(x_i,t)$ defines where and when the target is evaluated, i.e. the microphone positions and sampling rate.

To simplify the derivation of the adjoint, the above system of partial differential equations is abbreviated by

$$\mathscr{E}(q,s) := E(q) - s = 0. \tag{8}$$

The overall goal is the acquisition of a solution of the Euler equations that reduces the objective functional (7) by adjusting s. Thus, an optimization of s corresponds to an identification of the sound sources sought.

In order to optimize s with the adjoint approach, the governing system (6) and the objective function (7) must be linearized. This leads to

$$\delta J = \int \underbrace{\left(q - q^{\mathrm{target}}\right) \sigma}_{=g} \delta q \mathrm{d}\Omega \tag{9}$$

and

$$E_{\mathrm{lin}}(q)\delta q - \delta s = 0, \tag{10}$$

with $\delta q(x_j,t) = [\delta\rho, \delta u_j, \delta p]$ and $\delta s(x_j,t) = [0,0,\delta s_p]$. The weight $g(x_j,t) = (q - q^{\text{target}})\sigma$ corresponds to the difference between the numerical solution of (8) and the measured target field.

$$\delta J = \int \underbrace{\left(p - p^{\text{target}}\right)\sigma}_{=g} \delta p \mathrm{d}\Omega \tag{11}$$

By combining the linearized system and the objective function in a Lagrangian manner

$$\begin{aligned} \delta J &= g^{\mathrm{T}}\delta q - q^{*\mathrm{T}} \underbrace{\left(E_{\text{lin}}(q)\delta q - \delta s\right)}_{=0} && (12)\\ &= q^{*\mathrm{T}}\delta s + \delta q^{\mathrm{T}}\left(g - E_{\text{lin}}^{\mathrm{T}}(q)q^*\right) && (13) \end{aligned}$$

results. Note that the spatial and temporal integrals are not shown for simplicity.

The adjoint equation sought results from the requirement

$$\mathscr{E}^*(q,q^*,g) := g - E_{\text{lin}}^{\mathrm{T}}(q)q^* = 0, \tag{14}$$

with $q^*(x_j,t) = [\rho^*, u_j^*, p^*]$ as adjoint state variable. See [5] for a detailed derivation of the adjoint Euler equations.

Finally, the change in the objective function is given by

$$\delta J = q^{*\mathrm{T}}\delta s. \tag{15}$$

The solution of the adjoint equation can again be interpreted as the gradient of J with respect to the source terms s

$$\nabla_s J = q^*. \tag{16}$$

The adjoint-based gradient is typically used iteratively: First, the Euler equations are solved forward in time. Then, the adjoint equations are calculated using the direct solution and g backward in time. Based on the adjoint solution, the gradient $\nabla_s J$ is determined and employed to update the source distribution s^l using a gradient approach:

$$s^{l+1} = s^l + \alpha\nabla_s J, \tag{17}$$

where α denotes a suitable step size and l denotes the iteration number. The gradient is calculated for the entire computational region and the entire simulation time.

For the determination of sound sources with a known position, the gradient is evaluated exclusively at these locations. The procedure is repeated with the current s^l until a suitable convergence criterion is reached. For acoustic problems, convergence is typically achieved within 20 loops or less.

The identification of a global optimum is not guaranteed since the method optimizes towards local extrema. The computational costs of the approach are independent of the number of sources and their arrangement. However, they depend on the size and the spatial and temporal resolution of the computational domain defined by the considered frequency range.

2.3 Moving sound sources

In particular, when $s^0 = 0$ holds, the first adjoint solution already contains information about the position of the sources. By summing the absolute adjoint sensitivity p^* point-wise over time

$$\bar{p}(x_j) = \sum_{t_n=0}^{t_{n=\text{end}}} |p^*(x_j,t)|, \tag{18}$$

the positions that have the highest impact on the objective function can be identified.

For tracking of moving sources, time moving averages of the sensitivities over $2N+1$ samples can be used

$$\bar{p}(x_j,t) = \sum_{n=-N}^{N} |p^*(x_j,t-\delta t_n)|, \tag{19}$$

as well as methods of image processing, such as shift or rotation and convolution filters.

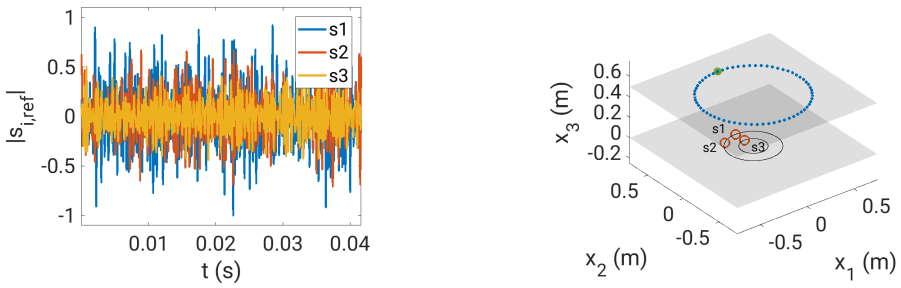


Figure 1. (Left) Signals of the three rotating sound sources s_i. The amplitude ratios compared to the first source s_1 correspond to -3 dB and -6 dB, respectively. (Right) Considered configuration to identify three rotating incoherent sound sources ○ based on 64 microphones circularly arranged in a plane ●.

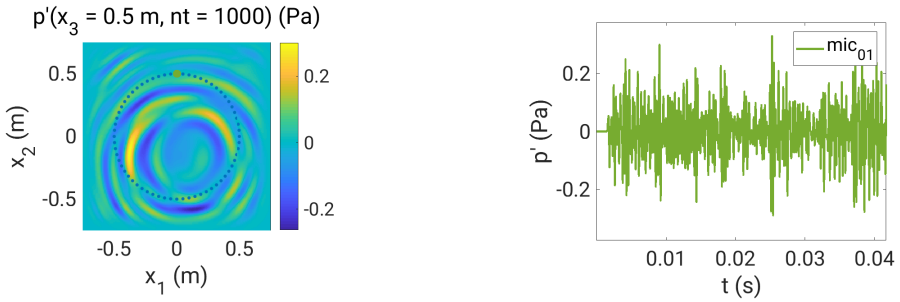


Figure 2. (Left) Reference sound field in the plane of the microphones ($x_3 = 0.5$ m, ●) for a selected time step. (Right) Reference measurement signal over the whole time of 2000 samples considered, measured at microphone position 1, highlighted by ● in the figure above.

3 EXAMPLE: THREE ROTATING SOURCES

As an example, a synthetic system similar to [6] is studied. Three incoherent sound sources ○ rotating at 1500 rpm in a quiet and anechoic environment are considered. The signals are bandlimited to 1250 - 4500 Hz with the following amplitude ratios: 1.00, 0.71 (-3 dB) and 0.50 (-6 dB), see Fig. 1 (left). For the measurement, 64 microphones ● are centered 0.5 m above the plane of rotation arranged in a circle with equal distances, see Figs. 1 (right) and 2 (left). For the analysis, 2000 samples at a sampling rate of 48 kHz are used, which corresponds to approximately one rotation of the sources. The goal is to identify the three sound sources, in particular their rotation speed, the position of the sound sources and their relative amplitudes based on the microphone data, exemplified for a microphone shown in Fig. 2 (right).

The adjoint solution $q^*(\mathbf{x},t)$ and $p^*(\mathbf{x},t)$, respectively, is calculated and used analogous to [2, 5, 7] for the identification of sound sources. Figure 3 (left) shows a selected time step.

A simple image processing method was used to evaluate the adjoint solution. The sensitivities $p^*(\mathbf{x},t)$ are rotated in the plane of the sources with different angles corresponding to different rotation speeds, see Fig. 3 (right). Integration of such rotated absolute sensitivities corresponding to equation (18) over time and subsequent determination of the maximum values results in the curve in Fig. 4 (left). Consistent with expectations, the maximum is reached at the reference rotation speed of 1500 rpm. The integrated absolute sensitivity for the same plane considering the previously determined rotation speed is shown in Fig. 4 (right). The positions of the sensitivity maxima correspond to the relative positions of the sound sources. The amplitude ratios of the sensitivities were found to be 1.00, 0.76 and 0.54, i.e. in good agreement with the reference values. To increase the accuracy, further iterative optimization is possible.

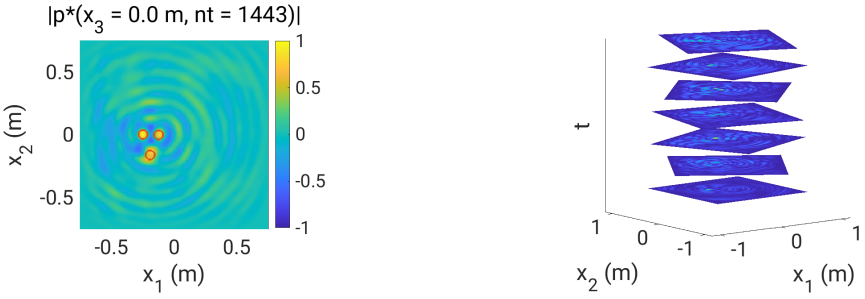


Figure 3. (Left) Normalized adjoint-based sensitivities p^* for a selected time step in the plane of the rotating sources. Current positions of the reference sources are marked by ○. (Right) Rotation of the adjoint-based sensitivities over time for subsequent integration, see text for details.

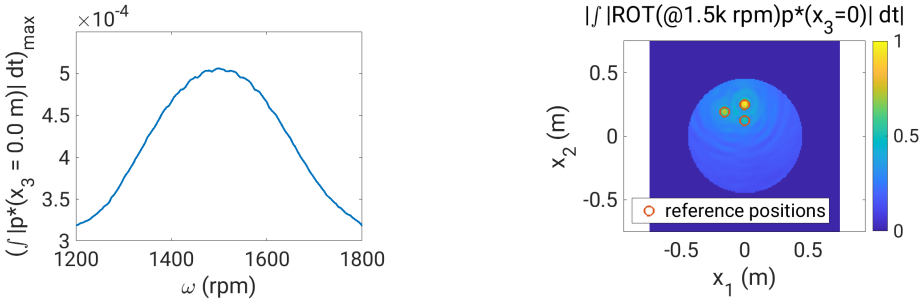


Figure 4. (Left) Maximum values after time integration of the absolute sensitivities to determine the rotation speed (reference: 1500 rpm). (Right) Normalized absolute adjoint-based sensitivities considering the previously identified rotation speed of 1500 rpm. Reference positions are marked by ○.

Thus, the rotational velocity was determined from 2000 samples (corresponding to 42 ms) of the synthetic microphone data without additional information. Furthermore, the low-frequency sources (relative to the dimensions of the microphone array) were spatially separated and the amplitude ratios were determined in good agreement with the reference.

4 CONSIDERATION OF BOUNDARY CONDITIONS

The localization of sound sources typically involves the presumption of an anechoic environment. The sound propagation between source and microphone is usually modeled by free-field Green's functions.

Many practical problems, however, involve impedance-impaired boundaries. To consider such boundary conditions tailored transfer functions can be used [8]. The functions are determined either analytically, numerically or experimentally. The first is restricted to simple conditions like a straight fully reflecting wall. The latter requires a high effort.

The presented adjoint-based approach allows a simple consideration of boundaries by including them in the governing and the corresponding adjoint equations. Here, the boundaries are modeled using a volume penalization approach, enabling the consideration of complex impedance conditions [3].

As a representative example, a simple synthetic system is studied. A single sound source ○ is considered, see Fig. 5. In detail, the source is defined by white noise, band-limited in the range from 750 to 4000 Hz. For measurement, 8 microphones • located at $x_1 = 0.75$ m are employed. For the analysis, 7500 samples are used at a sampling rate of 96 kHz, which corresponds to a measurement time of less than 0.1 s.

Three cases are examined in detail: (a) localization of the source in an anechoic environment, (b) source

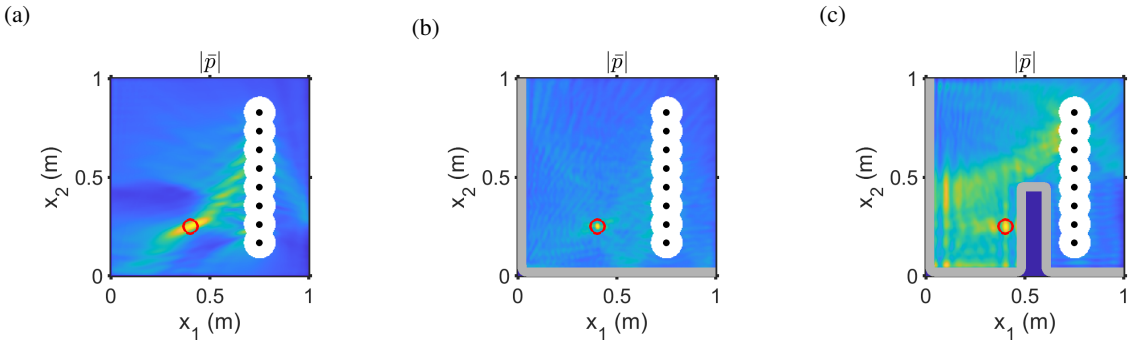


Figure 5. Normalized absolute adjoint-based sensitivities: (a) source in anechoic environment, (b) source in front of a rigid edge (c) source located behind a wedge. The reference position of the sound source is marked by ○. The position of the microphones by ●.

located in front of a rigid edge and (c) source located behind a wedge.

The objective is to identify the source position by means of the adjoint-based sensitivities (18). Corresponding results are shown in Fig. 5. In all three cases, the localization of the reference sound source is successful. In case (a), however, the uncertainty with regard to the depth position, which is typical for a planar microphone array, becomes apparent. The consideration of existing ridig walls in case (b) improves the result significantly. The reflections increase the information density or rather the observability [5] of the sound source.

By directly considering existing walls, configurations become accessible in which there is no line of sight between the sound source and the microphone array. In case (c), the source is covered by a rigid wedge, see Fig. 5. Nevertheless, the maximum of the absolute adjoint-based sensitivity is found at the reference position. Thus, the identification of the sound source employing microphone array measurement succeeds here only by accounting reflections and diffraction.

5 CONCLUSION

An adjoint-based method for identifying moving sound sources in the time domain was presented. The method was successfully validated using a synthetic example of three rotating incoherent sources.

The approach allows the determination of the parameters sought based on a few measurement samples. In perspective, the integration of complex boundary conditions into the approach [3], the consideration of base flows [9] as well as the identification of directional characteristics [10] are possible.

ACKNOWLEDGEMENTS

The author acknowledges financial support by the Deutsche Forschungsgemeinschaft (DFG) within the project LE 3888/2.

References

[1] R. Merino-Martinez, P. Sijtsma, M. Snellen, T. Ahlefeldt, J. Antoni, C. J. Bahr, D. Blacodon, D. Ernst, A. Finez, S. Funke, *et al.*, "A review of acoustic imaging methods using phased microphone arrays," *CEAS Aeronautical Journal*, vol. 10, no. 1, pp. 197–230, 2019.

[2] M. Lemke, C. Westphal, J. Reiss, and J. Sesterhenn, "Adjoint based data assimilation of sound sources," in *Fortschritte der Akustik: Tagungsband d. 41. DAGA, Nürnberg*, pp. 635–638, 2015.

[3] M. Lemke and J. Reiss, "Approximate acoustic boundary conditions in the time-domain using volume penalization." preprint arXiv:2203.04790, 2022.

[4] M. Lemke, J. Reiss, and J. Sesterhenn, "Adjoint based optimisation of reactive compressible flows," *Combustion and Flame*, vol. 161, no. 10, pp. 2552 – 2564, 2014.

[5] M. Lemke, *Adjoint based data assimilation in compressible flows with application to pressure determination from PIV data*. PhD thesis, Technische Universität Berlin, 2015.

[6] G. Herold, "Microphone array benchmark b11: Rotating point sources." `http://dx.doi.org/10.14279/depositonce-8460`, 2017.

[7] M. Lemke and L. Stein, "Adjoint-based identification of sound sources for sound reinforcement and source localization," in *Fundamentals of High Lift for Future Civil Aircraft: Contributions to the Final Symposium of the Collaborative Research Center 880, December 17-18, 2019, Braunschweig, Germany* (R. Radespiel and R. Semaan, eds.), pp. 263–278, Springer International Publishing, 2021.

[8] M. Lehmann, D. Ernst, M. Schneider, C. Spehr, and M. Lummer, "Beamforming for measurements under disturbed propagation conditions using numerically calculated green's functions," *Journal of Sound and Vibration*, vol. 520, p. 116638, 2022.

[9] L. Stein, F. Straube, J. Sesterhenn, S. Weinzierl, and M. Lemke, "Adjoint-based optimization of sound reinforcement including non-uniform flow," *The Journal of the Acoustical Society of America*, vol. 146, no. 3, pp. 1774–1785, 2019.

[10] L. Stein, F. Straube, S. Weinzierl, and M. Lemke, "Directional sound source modeling using the adjoint euler equations in a finite-difference time-domain approach," *The Journal of the Acoustical Society of America*, vol. 148, no. 5, pp. 3075–3085, 2020.

PROCEEDINGS of the
24th International Congress on Acoustics

October 24 to 28, 2022, in Gyeongju, Korea

Extended abstract

ABS-0508

Prediction of turbulent flow-induced noise in the cavity

Bon-Heon Ku[1]; Young-Woo Yi[1]; Dong-Sub Lee[2]; Chin-Suk Hong[3]; Hee-Chang Lim[1, a]

[1] *School of Mechanical Engineering, Pusan National University, Busandaehak-ro 63beon-gil 2, Geumjgeong-gu, Busan, Korea*

[2] *Agency for Defense Development, Korea*

[3] *School of Mechanical Engineering, Ulsan College, Bongsu-ro 101, Dong-gu, Ulsan, Korea*

ABSTRACT

As the contribution of sonar self-noise by flow has recently increased, a numerical prediction method for the noise, generated by the wall pressure fluctuations in the turbulent boundary layer is of interest. In this study, the prediction method of the flow induced noise of a cuboid cavity, simplified sonar model, were studied. The random vibroacoustics is adapted to reflect the temporal/spatial randomness of the wall pressure fluctuations. The structural excitation by the wall pressure fluctuation was modelled by the Corcos model and Smol'yakov-Tkachenko model. The acoustics-structural reciprocity technique was applied to effectively calculate the noise transfer functions, required for the random vibroacoustic model. This application technique leads to effectively calculate the noise transfer functions for many points, and to apply random vibroacoustics. In order to verify the acoustic-structural reciprocity technique, the noise transfer functions in the direct and reciprocal directions were compared and showed a good agreement. The effects of flow velocity on noise in the cuboid cavity were studied and showed that the noise level increases as the flow velocity increases. We developed a method for predicting noise by flow in structures for potential use for internal sound field estimation.

Keywords: wall pressure fluctuation, flow induced noise, random vibroacoustics, acoustics-structural reciprocity, noise transfer functions

1. Introduction

Although there have been many relevant studies during last several decades, the flow noise phenomenon caused by the wall fluctuating pressure under the turbulent boundary layer has been of the most great importance in various industrial fields such as watercrafts, aviation vehicles, and spacecrafts [1-3]. In addition, structural noises are mainly caused by those structural and acoustic noises in fluids. Recently, as the running speed of ship and aircraft objects has increased, a turbulent boundary layer is formed over the surface of the structure due to the fluid viscosity. As the operating speed increases, therefore, the thickness of the turbulent boundary layer becomes thinner, and the wall fluctuating pressure is generated close to the surface of the bodies, which would be due to the complex behavior of the eddy in the turbulent boundary layer. Finally, the wall pressure fluctuation within the turbulent boundary layer causes a random load to occur on the surface of the structure, causing vibration and flow noise inside the structure.

In this study, since last several decades there have been actively studied in the area of flow noise phenomena in relatively complex shapes in the mainly industrial sectors, but this study aims to find the details of flow noise in a simplified shape such as a cuboid cavity. The turbulent boundary layer has been thoroughly analyzed to understand the effect of turbulent flow on the wall pressure fluctuation close to the elastic plate under the turbulent boundary layer. The mathematical model proposed by Corcos[4] has been used for modelling the wall fluctuation pressure caused by the turbulent flow over the flat plate. The finite element method was applied for obtaining the transfer function of acoustic-structural noise, and the sound field level inside the cuboid cavity model was

[a] Corresponding author : hclim@pusan.ac.kr

estimated by the free-stream velocity.

2. Finite element modeling of wall pressure fluctuation

In this study, we used a finite element method suggested by Hong et al.[5] to implement turbulent boundary layer to a simple supported beam such as acting wall fluctuation pressure on the flat plate. In addition, depending on the free-stream velocity, the level of the internal sound pressure was also predicted by the calculation of the turbulent-induced fluctuating pressure and the appropriate noise transfer function.

2.1. Modeling of Wall pressure fluctuation

In this study, the Corcos model was used to model the wall pressure fluctuation, and it is mathematically expressed as follows.

$$S_{pq}(\xi,\eta,\omega) = S_{pp}(\omega)e^{-\alpha\left|\frac{\omega\xi}{U_c}\right|}e^{-\beta\left|\frac{\omega\eta}{U_c}\right|}e^{-i\left(\frac{\omega\xi}{U_c}\right)} \quad (1)$$

where the S_{pq} expresses the cross spectral density function of the wall pressure fluctuation, the S_{pp} is the auto spectral density function, and the symbol α, β are the longitudinal and lateral decay rates of the coherences direction, and U_c is the convection velocity necessarily required for obtaining the Corcos model numerically. Based on the extensive study, Eq.(1) can be expressed as a function of the similarity variables $\frac{\omega\xi}{U_c}$ and $\frac{\omega\eta}{U_c}$, respectively.

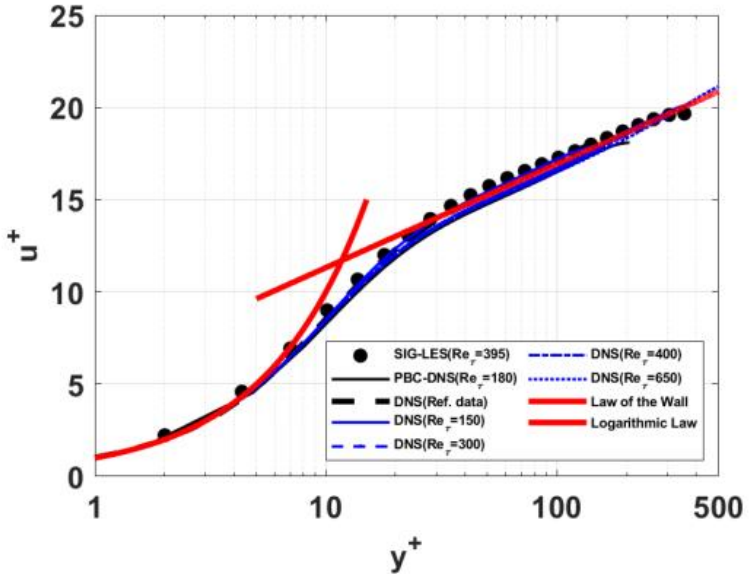


Fig.1. Mean streamwise velocity profiles through DNS numerical analysis

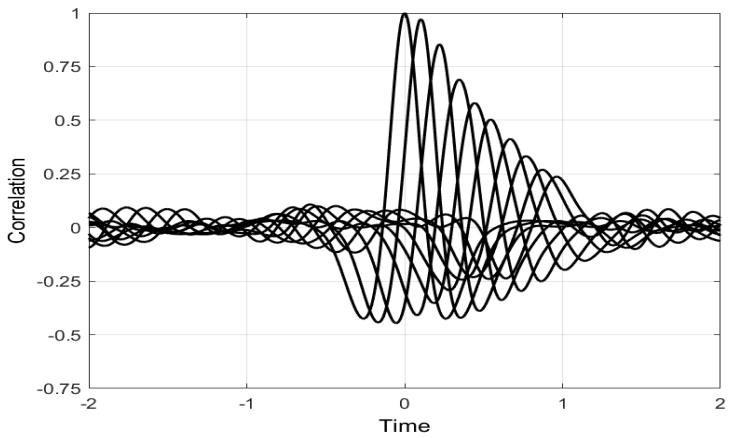


Fig. 2 Cross-correlation distribution of fluctuating pressure near the wall by using DNS calculation

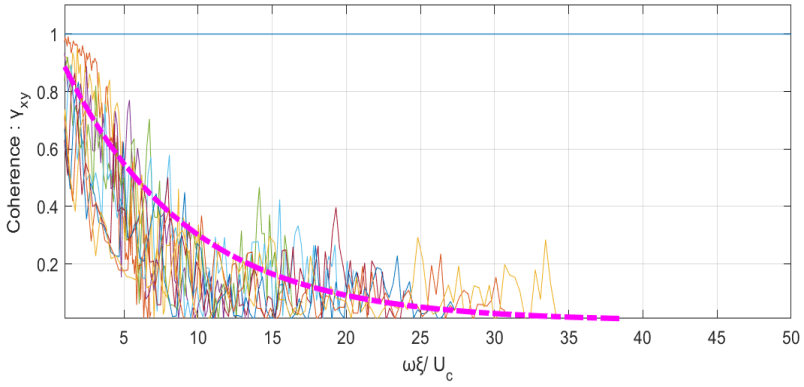


Fig.3 Coherence of fluctuating pressure near the wall by using DNS simulation

2.2. Modeling of flow induced noise

The characteristics of wall pressure fluctuation due to turbulent boundary layers appears in the form of random loads on thick elastic structures. Based on the random vibroacoustics theory, when an ergodic random load is applied to an elastic structure targeting a linear system or a deterministic system, the response appears to be a form of power spectral density or auto-correlation function and the RMS values such as the terms of displacement, velocity, acceleration, and a sound pressure. Finite element method was used to obtain the noise transfer function caused by a random force under the turbulent boundary layer. The structural response must be assessed by applying a unit force of $1N$ to all nodes modelled in the finite element structure. However, when a unit force is applied to all nodes, the calculation becomes costly.

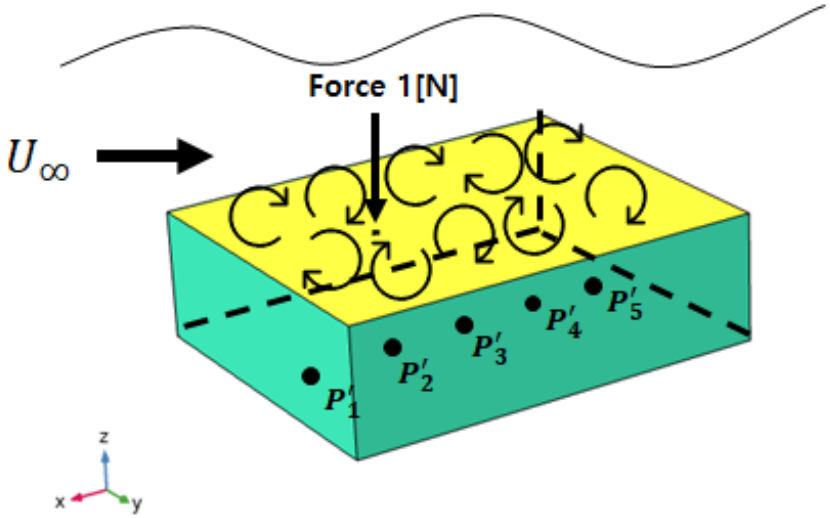


Fig. 4 FEM Cuboid cavity model

In order to overcome this problem, the acoustics-structural reciprocity technique[6] was used to verify and apply the calculated results.

The idea of acoustics-structural reciprocity is expressed as follows.

$$\frac{P}{F} = \frac{v_n}{Q} \quad (2)$$

where the symbols F, P are the force $[N]$ and the pressure $[N/m^2]$, and the others Q, v_n are a kind of sound source (monopole source) $[m^3/s]$ and the wall-normal velocity $[m/s]$ on the wall.

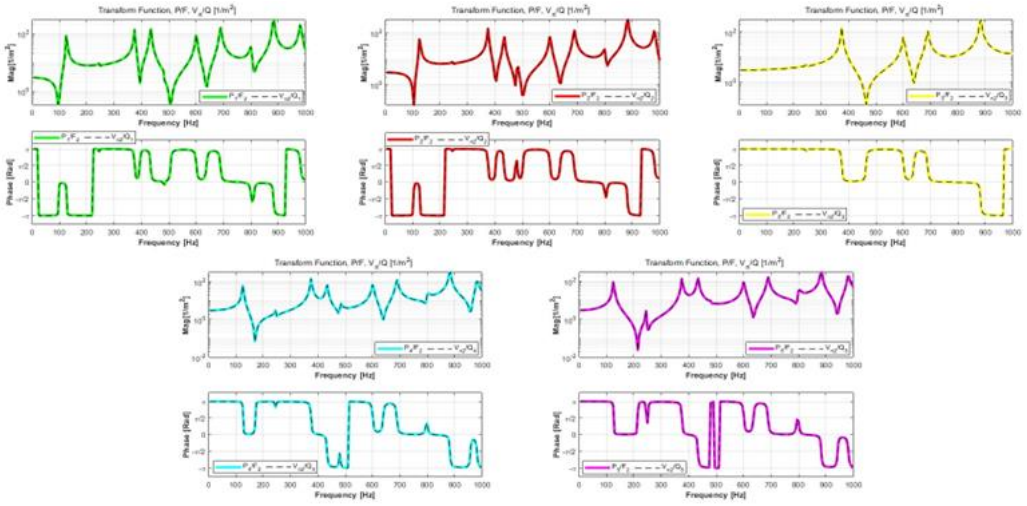


Fig. 5 Verify of the acoustic-structural reciprocity technique

This study performs the prediction of the internal sound field at any point inside the Cuboid cavity model in terms of the various free-stream velocity based on these verification methods.

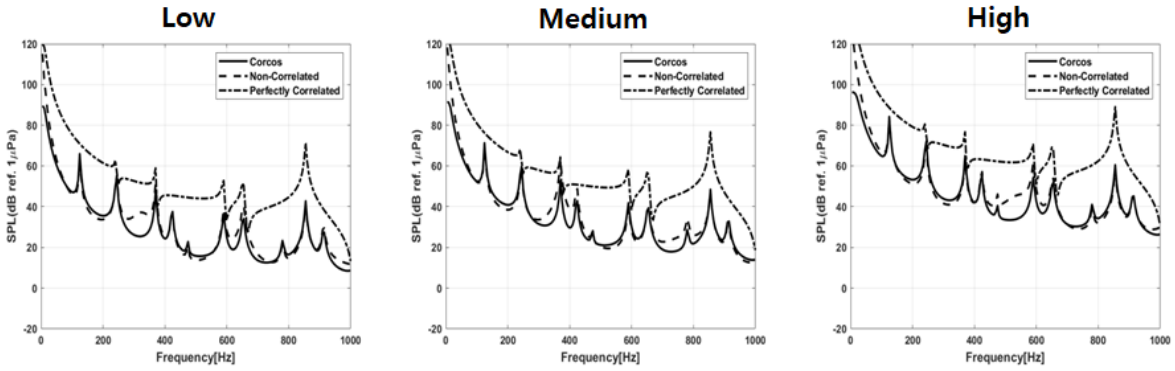


Fig.6 The effects of flow velocity on noise in the Cuboid cavity model

3. RESULTS

In this study, the wall pressure fluctuation was modeled by the calculation of the DNS simulation. As shown in Fig. 1, the characteristics of the turbulent boundary layer were precisely compared our current data with other existing data, and reference DNS data. It was found that the characteristics of the distribution of the turbulent boundary layer showed well the well-known typical turbulent boundary layer according to various Reynolds numbers(Re_τ) and analysis techniques. In Fig. 2, it is confirmed that the convection velocity (U_c) agrees well with almost 73% of the free-stream velocity(U_∞). In this study, the convection velocity (U_c) was assumed to be 70% of the free-stream velocity. As shown in Fig. 3, as the frequency increases, it tends to be exponentially decreased, and the turbulence coherence (α) along the streamwise direction is assumed to be 0.1.

As shown in Fig. 5, the noise transfer functions to which the acoustic-structure reciprocity is applied are expressed in $Mag[1/m^2]$ and $Phase[Rad]$, confirming that the results agree well. Fig. 6 predicted the sound level inside the cuboid cavity model according to various flow rates. This study conducted to predict the internal sound field of the cuboid cavity model in terms of various free-stream velocity by comparing three scaled models - the Corcos, the non-correlated, and perfectly-correlated models. When the frequency (f) is large, it was confirmed that the Corcos and non-correlated models have similar internal sound fields. On the other hand, regarding the perfectly-correlated model, it can be seen that the internal sound field tends to be relatively higher than that of the two models. In addition, as the free-stream velocity increased, it is confirmed that the internal sound field also increased.

4. CONCLUSIONS

In this study, using direct numerical analysis (DNS) and finite element method (FEM) techniques, we performed to predict the internal sound field of the cuboid cavity model by modeling the wall fluctuation pressure of the turbulent boundary layer and developing a noise transfer function calculation technique. The results can be summarized as follows.

1. The characteristics of wall pressure fluctuation has been modeled using the Corcos model by the results of DNS simulation.
2. The noise transfer function was also calculated and well applied by using the finite element method.
3. The internal sound field caused by the free-stream velocity was confirmed through various flow-induced force models.

ACKNOWLEDGEMENTS

The authors gratefully acknowledge the financial support provided by the Agency for Defense Development under the contract UD190002DD.

REFERENCES

1. Zhao, X., Lei, J., 2020. Improved Technique for Evaluation of Wall Pressure Fluctuations from Turbulent Boundary Layer. AIAA Journal 58, 3320–3331.
2. Magionesi, F., Di Mascio, A., 2016. Investigation and modelling of the turbulent wall pressure fluctuations on the bulbous bow of a ship. Journal of Fluids and Structures 67, 219–240.
3. Karthik, K., Jeyakumar, S., Sebastin, J.S., 2021. Numerical prediction of flow noise levels on towed sonar array. Proceedings of the Institution of Mechanical Engineers, Part M: Journal of Engineering for the Maritime Environment 235, 600–606.
4. Corcos, G. M., 1963, Resolution of Pressure in Turbulence, JASA, 35(2), 192-199
5. Hong. C. S., Shin K. K., and Kim, S. Y. A Modelling of Structural Excitation Forces Due to Wall Pressure Fluctuations in a Turbulent Boundary Layer. 2001;11(2):226-233.
6. Fahy, F.J., 2003. Some applications of the reciprocity principle in experimental vibroacoustics. Acoust. Phys. 49, 217–229.

PROCEEDINGS of the
24th International Congress on Acoustics

October 24 to 28, 2022, in Gyeongju, Korea

Extended abstract

ABS-0510

Modelling of spectral properties of wall pressure fluctuations beneath turbulent boundary layers

Young-Woo Yi[1]; Dong-Sub Lee[2]; Chin-Suk Hong[3]; Hee-Chang Lim[1, a]

[1] *School of Mechanical Engineering, Pusan National University, Busandaehak-ro 63beon-gil 2, Geumjgeong-gu, Busan, Korea*

[2] *Agency for Defense Development, Korea*

[3] *School of Mechanical Engineering, Ulsan College, Bongsu-ro 101, Dong-gu, Ulsan, Korea*

ABSTRACT

Large Eddy Simulation(LES) has been popularly and used in the last several decades to simulate turbulent boundary layer in the numerical domain. Synthetic Inflow Generation(SIG), which is based on exponential correlation function both in space and in time is also widely used for a fully developed turbulent boundary layer flow simulation. Recent results show that the flow characteristics of the results of LES-SIG are well matched with the results of Direct Numerical Simulation(DNS) and theoretical results. In this study, we compared the fluctuating pressure near the wall of LES-SIG with those of DNS results and suggested the proper model for the modeling the fluctuating pressure near the wall. As a results, the fluctuating pressure near the wall of LES-SIG are very close to those of DNS and new model related to the Smol'yakov-Tkachenko model are suggested.

Keywords: Large Eddy Simulation(LES), Synthetic Inflow Generation(SIG), Smol'yakov-Tkachenko model

1. INTRODUCTION

The noise generated by the turbulent boundary layer over various bluff bodies has been major issue for a wide range of engineering applications. Examples include the noise generated by propellers, rotors, wind turbines, fans, wings, and hydrofoils. Even having no disturbances in the oncoming flow, bluff bodies can generate noise due to an unsteady turbulent flow and wake. This so-called self-noise or leading edge noise would be a major contributor to the overall noise generated by an induced noise by bluff bodies [1-3]. Reducing self-noise is challenging and requires an efficient method for describing and understanding the sources of noise near the bluff bodies.

On the other hand, turbulent boundary layer over bluff bodies has also been taken great attention over a long period of time regarding the understanding of heat and mass transfer mechanisms [4]. In order to understand the source noise from the turbulent boundary layer, it is requisite to generate the turbulent flow over the bluff bodies as well as flat plates. There have been several techniques to generate turbulent flow in a calculation domain. The most straightforward approach to simulate a spatially developing turbulent boundary layer, which start the calculation far upstream with a laminar profile having some random disturbances and then allow a natural transition to generate realistic turbulence [5]. In order to reduce the cost of simulation for this transition process, most of spatially evolving simulations start with a synthetic inflow generator(SIG) having a short distance domain. This method generates inlet velocity conditions for the simulation from the correlation based on the length scales of the turbulent flow [6].

In this study, we analyze the fluctuating pressure as a sound source in turbulent boundary layer come from both direct numerical simulation using periodic boundary conditions (PBC-DNS) and large eddy simulation using synthetic inflow generator (SIG-LES) and find out the common characteristics of the fluctuating pressure in turbulent boundary layer regardless of the method of simulation and changing Reynolds number.

[a] Corresponding author : hclim@pusan.ac.kr

2. EVALUATION OF WALL TURBULENT BOUNDARY LAYER

We firstly aimed to generate the fluctuating pressure near the wall, allowing the turbulent boundary layer develop in the domain. Figure 1 shows the mean streamwise velocity profiles among different approaches and turbulent Reynolds number (Re_τ). The turbulent Reynolds number (Re_τ) was drawn by friction velocity (u_τ) at the flat plate and a half height of the channel (d). In the simulation, no-slip condition was used at the top and bottom flat plates and periodic condition at side the flow properties should not be diffused.

In SIG-LES, the size of the domain was $20\pi d \times 2d \times \pi d$ (here d is channel height), which stands for streamwise, vertical, and spanwise direction. The free-stream velocity (U_∞) was almost 20 and kinematic viscosity (ν) was 2.5e-2. The turbulent Reynolds number in this case (Re_τ=395) was same as DNS case [5]. In case of the PBC-DNS, the size of the domain was $12d \times 2d \times 6d$, which has the same domain height as the SIG-LES. The free-stream velocity (U_∞) was set to 1.14 and kinematic viscosity (ν) was 3.1e-4. Turbulent Reynolds number in this case (Re_τ=180) was nearly half of the SIG-LES case.

In order to evaluate the mean statistics of turbulent boundary layer, we compare the current results (i.e., SIG-LES and PBC-DNS) with reference DNS data [5] and the existing theory [7]. As can be seen in the figure, the mean streamwise velocity profile for all two cases of different approaches shows excellent agreement with the DNS data obtained within the wall distance range, i.e., the linear

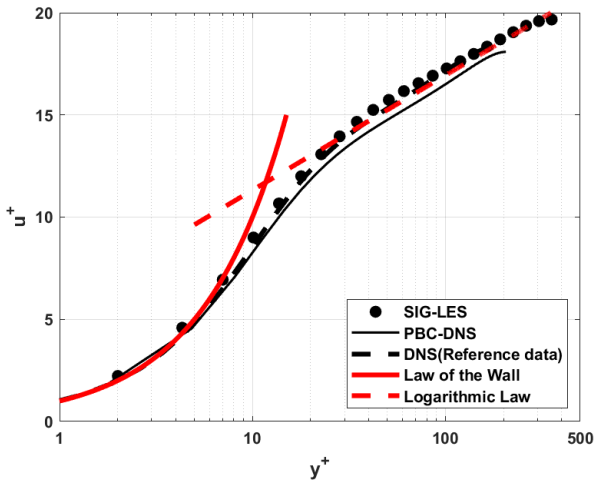


Fig. 1 Mean streamwise velocity profiles among SIG-LES(Re_τ=395), PBC-DNS(Re_τ=180), DNS [5], and theoretical results

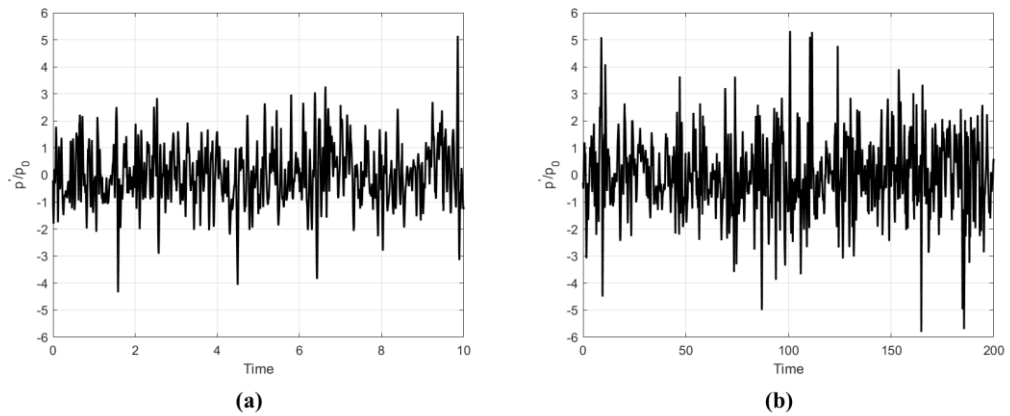


Fig. 2 Temporal variation of non-dimensional fluctuating pressure near the wall by using (a) SIG-LES, (b) PBC-DNS

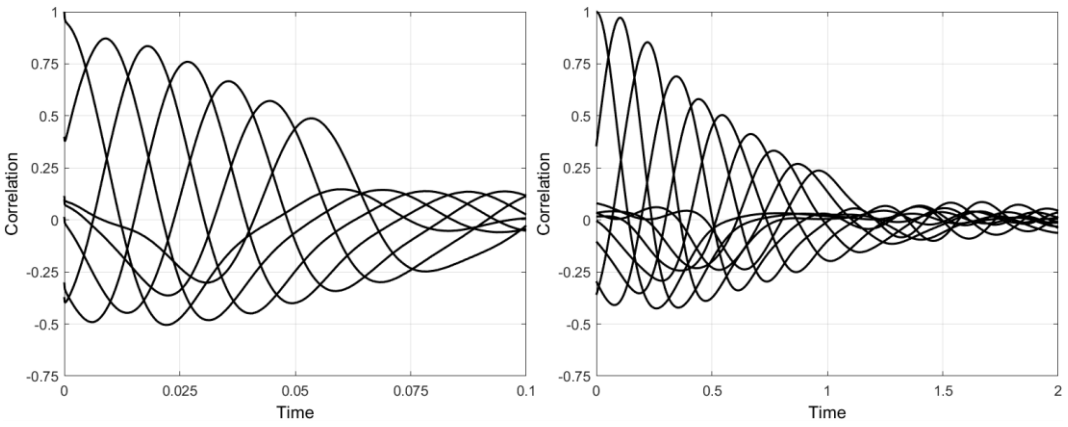


Fig. 3 Cross-correlation distribution of fluctuating pressure near the wall by using (a)SIG-LES, (b) PBC-DNS.

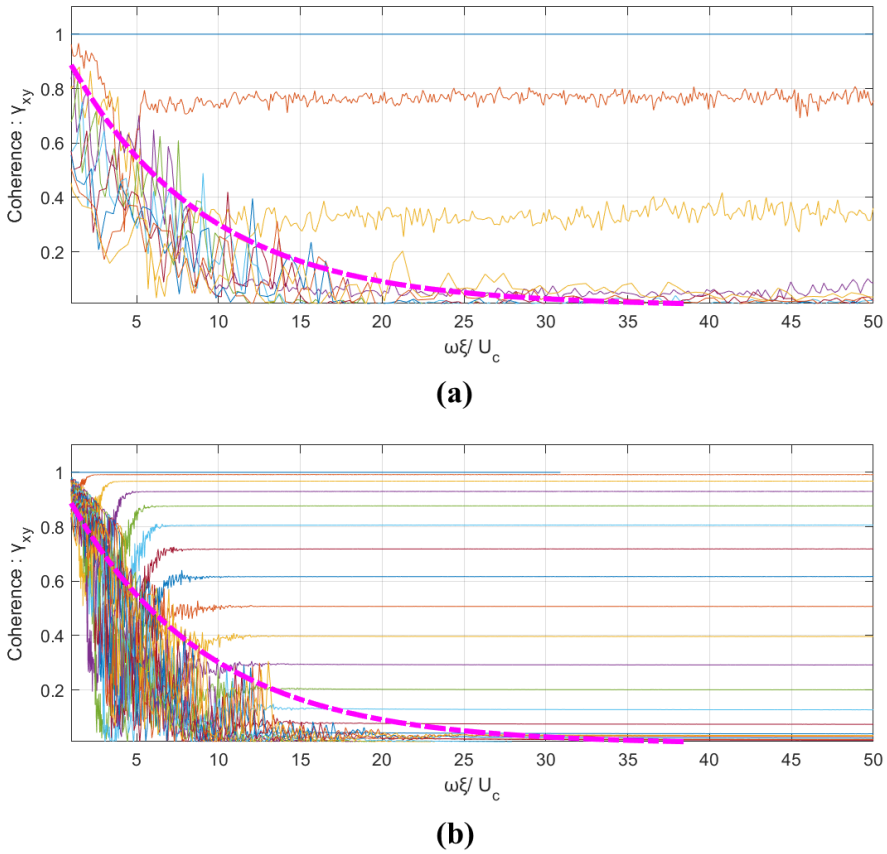


Fig. 4 Coherence of fluctuating pressure near the wall by using (a) SIG-LES, (b) PBC-DNS

viscous sublayer, buffer layer, and logarithmic region.

3. RESULTS

Figure 2 show the temporal variation of fluctuating pressure in turbulent boundary layer at the closest grid of the wall. The fluctuating pressure is non-dimensionalized by p_0 (=$(\phi_p(0)\times \Delta\omega)^{1/2}$), which was calculated by the auto spectrum of pressure at the frequency 0 ($\phi_p(0)$) and the gradient of angular frequency ($\Delta\omega$). As shown in the figure, the variation was mostly spanning in the range of -5 and 5 regardless of the simulation method. Even the simulation has been made in different Reynolds number over the range of 180 -395, the variation was limited in this range.

As shown in Fig.3, the cross-correlation of fluctuating pressure is a good indicator for analyzing and modelling the pressure spectrum near the wall. The convection velocity (U_C) can be computed by using the difference between two points having the duration time of first peak of cross-correlation profile. Based on this result, it turns out that the convection velocity of the turbulent boundary layer would be estimated by the 70% of the freestream velocity (U_∞).

Figure 4 shows the coherence distribution computed from fluctuating pressure close to the wall by using SIG-LES and PBC-DNS. The coherence describes the correlation among waves or noises at different points in space, either streamwise or spanwise direction [8]. In this study, the coherence of streamwise direction can be calcualated. As shown in Fig.4, the quantity is subject to exponential decay having the coefficient of α=0.06 for both cases.

4. CONCLUSIONS

This study has tackled one of properties in predicting sound and self-noise sources - fluctuating pressure in turbulent boundary layer by using direct numerical simulation and large eddy simulation and found the common characteristics of the fluctuating pressure in turbulent boundary layer. The work is summarized as follows.

1. The method of SIG-LES and PBC-DNS have found to be suitable for generating a turbulent boundary layer in the domain.
2. The variation of temporal fluctuating pressure fell in a certain range regardless of simulation method and changing Reynolds number.
3. It turns out that the characteristics of fluctuating pressure shows an interesting feature such as the ratio of convection velocity (U_C) to freestream velocity (U_∞) and the coherence (α) structure.

ACKNOWLEDGEMENTS

The authors gratefully acknowledge the financial support provided by the Agency for Defense Development under the contract UD190002DD.

REFERENCES

1. Kim, J. N. and Sung, H. J. Wall pressure fluctuations and flow-induced noise in a turbulent boundary layer over a bump. Journal of fluid dynamics. 2006;558(10):79-102.
2. Shin, K. K., Hong C. S. and Lee, H. G., A study of Flow Induced Noise for Multilayered Cylinder due to Turbulent Boundary Layer. 1996;6(5):671-677.
3. Hong. C. S., Shin K. K., and Kim, S. Y. A Modelling of Structural Excitation Forces Due to Wall Pressure Fluctuations in a Turbulent Boundary Layer. 2001;11(2):226-233.
4. Kovasznay, L. S. Turbulent Boundary Layer. Annual Review of Fluid Mechanics. 1970;2(1):95-112.
5. Moser, R. D. and Kim, J. Direct numerical simulation of turbulent channel flow up to Re_τ=590. Physics of fluids. 1999;11(4):943-945.
6. Xie, Z. T. and Castro, I. P. Efficient generation of inflow conditions for large eddy simulation of street-scale flows. turbulence and combustion. 2008;81(3):449-470.
7. Pope, S. B. Turbulent Flows. 1st revised ed . Cambridge, UK: Cambridge University Press & Assessment; 2000. p. 272-274.
8. Hecht, E. Optics. 3rd ed. New York, USA: Eddison Wesley Longman Inc. 1998. p. 554-574

ICA 2022
24th INTERNATIONAL CONGRESS ON ACOUSTICS
October 24(Mon) - 28(Fri), 2022 Gyeongju, Korea

PROCEEDINGS of the
24th International Congress on Acoustics

October 24 to 28, 2022 in Gyeongju, Korea

ABS-0744

Linearized perturbed compressible equation (LPCE) for low Mach number aeroacoustics: a review of theory and application

Young J. Moon[(1)], Jung-Hee Seo[(2)]

[(1)]Korea University, Korea, Rep. of, yjmoon@korea.ac.kr
[(2)]Johns Hopkins University, USA, jhseo@jhu.edu

ABSTRACT
The linearized perturbed compressible equation (LPCE) proposed for various low Mach number aeroacoustic problems is reviewed. In this method, the acoustic field is predicted by acquiring the noise source, DP/Dt, from the hydrodynamic flow field computed by large-eddy simulation. We present theoretical backgrounds of LES/LPCE hybrid approach and its application to turbulent edge-scattering noise.

Keywords: Linearized perturbed compressible equation (LPCE), Low Mach number, Aeroacoustics

1 INTRODUCTION

Many industrial flow applications such as automobiles, fans, and etc. operate at low Mach numbers, e.g. $M \leq 0.3$. Direct numerical simulation (DNS) of low Mach number aeroacoustics still remains a challenging problem because of scale disparities between the hydrodynamic vortical motions and the acoustic waves. In this regard, a hydrodynamic/acoustic splitting method is considered a good alternative for prediction of flow noise at low Mach numbers. Since a flow at low Mach number is obtained much faster by solving the incompressible Navier-Stokes equations, the hydrodynamic/acoustic splitting method is considered computationally more efficient than the direct numerical simulation as well as the other hybrid methods, based on the compressible Navier-Stokes equations (see Figure 1). Moreover, computational efficiency can be further enhanced, if grid systems for flow and acoustics are treated separately.

In previous hydrodynamic/acoustic splitting methods, a flow field is obtained by solving the incompressible Navier-Stokes equations, while the acoustic field is predicted by the perturbed Euler equations (PEE) which are derived by subtracting the incompressible Navier-Stokes equations from the compressible ones, neglecting the 'viscous terms'. It is, however, to be noted that the perturbed Euler equations are mixed-scales, non-linear equations, in which a coupling effect is allowed between the incompressible flow variables and the perturbed quantities. Through this coupling effect, a 'perturbed vorticity' is generated in the perturbed system, which is acoustically a non-radiating vortical component. Although role of perturbed vorticity on sound generation is negligible at low Mach numbers, this perturbed quantity can easily become unstable for various reasons and eventually becomes self-excited. As a result, inconsistent acoustic solutions may result from the perturbed Euler equations.

The perturbed compressible equations (PCE) proposed by Seo and Moon (1) remedy the false generation of perturbed vorticity by handling its generation and diffusion properly, especially when noise source is in the shear flow. In PCE, the perturbed Euler equations are modified by introducing the 'perturbed viscous stresses' in the momentum equations and the perturbed energy equation is formally derived from the compressible thermal energy equation. The PCE has been tested for various applications, including laminar dipole tone from a circular cylinder at $Re_D = 200$ and $M_\infty = 0.3$. For this problem, the PCE solution was shown to be accurate as the DNS solution. In parallel, computational efficiency and accuracy of the PCE in conjunction with the 'grid-splitting' technique has been investigated. It has been shown that perturbed vorticity could become unstable, if acoustic grid resolution is not properly used. This is because the length scale of the perturbed vorticity is not comparable

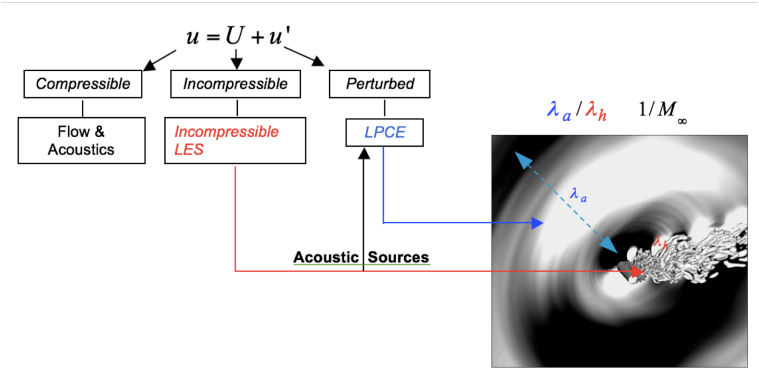


Figure 1. LES/LPCE hybrid method for prediction of turbulent flow noise at low Mach numbers

to that of acoustic waves but closer to the hydrodynamic vortical scale. Thereby, in some cases, grid-dependent acoustic solutions may result from the falsely resolved perturbed vorticity.

In order to resolve aforementioned matters, the linearized perturbed compressible equations (LPCE), a modified version of the original PCE, are proposed by Seo and Moon (2). In LPCE, generation of perturbed vorticity is suppressed by dropping the non-linear coupling terms that contribute to generate vortical components in the perturbed system. This will exclude errors related to the perturbed vorticity, deliberating the fact that it is not an important acoustic source at low Mach numbers. Through this modification, LPCE solutions can be independent of grid resolution and computational efficiency with the grid-splitting technique can be fully achieved. The present LPCE ensures grid-independent acoustic solutions by suppressing the generation of perturbed vorticity in the formulation.

The present paper is organized as follows. In Section 2, the perturbed compressible equations (PCE) and perturbed vorticity transport equations are revisited, and the linearized perturbed compressible equations (LPCE) are derived. In Section 3, the present method is applied to the prediction of turbulent edge-scattering noise to validate its accuracy. Finally, concluding remarks are summarized in Section 4.

2 THEORY OF LOW MACH NUMBER AERACOUSTICS

2.1 Perturbed Compressible Equations (PCE)

In the hydrodynamic/acoustic splitting method, the instantaneous total flow variables are decomposed into incompressible and perturbed compressible variables as

$$\begin{aligned} \rho(\vec{x},t) &= \rho_0 + \rho'(\vec{x},t) \\ \vec{u}(\vec{x},t) &= \vec{U}(\vec{x},t) + \vec{u'}(\vec{x},t) \\ p(\vec{x},t) &= P(\vec{x},t) + p'(\vec{x},t) \end{aligned} \tag{1}$$

The incompressible flow variables describe unsteady viscous flow, while acoustic fluctuations and other compressibility effects are represented by perturbed compressible variables. A hydrodynamic flow field is solved by the incompressible Navier-Stokes equations, while its compressibly perturbed field is calculated by the perturbed compressible equations (PCE).

The perturbed compressible equations are written as

$$\frac{\partial \rho'}{\partial t} + (\vec{u}\cdot\nabla)\rho' + \rho(\nabla\cdot\vec{u'}) = 0 \tag{2}$$

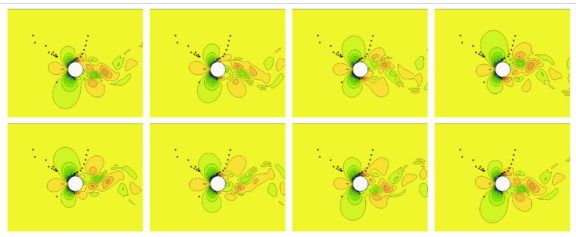
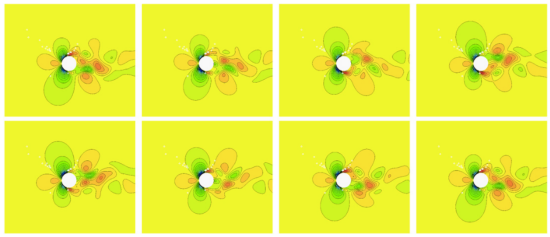
(a)  (b) 

Figure 2. (a) Instantaneous $\frac{1}{\rho}\frac{D\rho}{Dt}$ contours (compressible N–S eqs., $Re_D = 150, M = 0.2$), (b) instantaneous $\frac{1}{P}\frac{DP}{Dt}$ contours (incompressible N–S eqs., $Re_D = 150$)

$$\frac{\partial \vec{u'}}{\partial t} + (\vec{u}\cdot\nabla)\vec{u'} + (\vec{u'}\cdot\nabla)\vec{U} + \frac{1}{\rho}\nabla p' + \frac{\rho'}{\rho}\frac{D\vec{U}}{Dt} = \frac{1}{\rho}\vec{f'_{vis}} \tag{3}$$

$$\frac{\partial p'}{\partial t} + (\vec{u}\cdot\nabla)p' + \gamma p(\nabla\cdot\vec{u'}) + (\vec{u'}\cdot\nabla)P = -\frac{DP}{Dt} + (\gamma-1)(\Phi - \nabla\cdot\vec{q}) \tag{4}$$

where $D/Dt = \partial/\partial t + (\vec{U}\cdot\nabla)$, $\vec{f'_{vis}}$ is the perturbed viscous force vector, Φ and $\vec{q}$ represent thermal viscous dissipation and heat flux vector, respectively. At low Mach numbers, the perturbed viscous forces can be approximated as

$$f'_{vis,i} = \mu_0 \frac{\partial}{\partial x_j}\left(\frac{\partial u'_i}{\partial x_j} + \frac{\partial u'_j}{\partial x_i} - \frac{2}{3}\frac{\partial u'_k}{\partial x_k}\delta_{ij}\right) \tag{5}$$

by assuming viscosity $\mu \cong \mu_0$ (= constant), and Φ and $\vec{q}$ are expressed as

$$\Phi = \mu\left(\frac{\partial u_j}{\partial x_k} + \frac{\partial u_k}{\partial x_j} - \frac{2}{3}\frac{\partial u_l}{\partial x_l}\delta_{jk}\right)\frac{\partial u_k}{\partial x_k}, \tag{6}$$

$$q_j = -k\frac{\partial}{\partial x_j}\left(\frac{\gamma p}{\rho}\right) \tag{7}$$

More details of PCE derivation can be found in reference (1).

For low Mach number and non thermally-driven flows, the total derivative of the hydrodynamic pressure in the right hand side of Eq. (4) can be regarded as the only explicit acoustic source term. It is also interesting to note that Eq. (4) can be re-written as a 'dilatation rate equation',

$$D = -\frac{1}{\rho c^2}\left(\frac{dP}{dt} + \frac{dp'}{dt}\right) + T \tag{8}$$

where $D = \nabla\cdot\vec{u'}$ is the dilation rate, $d/dt = \partial/\partial t + (\vec{u}\cdot\nabla)$, $T = (\gamma-1)(\Phi - \nabla\cdot\vec{q})/(\rho c^2)$ is the thermal effect term, and relation of $\gamma p = \rho c^2$ is used. From Eq. (8), one can see that compressibility (or dilation rate) effect is related to a total derivative of the pressure (hydrodynamic and perturbed combined) (see Figure 2) (3).

2.2 Perturbed Voticity Transport Equations

Since perturbed variables in PCE are residuals of the total variables with incompressible components subtracted, they represent not only the acoustic fluctuations but also the other compressibility effects such as coupling effects between the hydrodynamic flow and the perturbed field. One particular component of the perturbed variables that concerns consistency of the acoustic solution is perturbed vorticity, $\vec{\omega}' = \nabla\times\vec{u'}$, a 'non-radiating' vortical component generated in the PCE system. This fluctuating quantity becomes unstable for various reasons

and generates unwanted errors in acoustic calculations. Here, attention is given to identify terms associated with production and diffusion of perturbed vorticity in its transport processes.

In order to derive the perturbed vorticity transport equation, the perturbed momentum equation, Eq. (3) is re-written as

$$\frac{\partial \vec{u}'}{\partial t} + \nabla(\vec{u}' \cdot \vec{U}) + \nabla(\frac{1}{2}\vec{u}' \cdot \vec{u}') + (\vec{\omega}' \times \vec{U}) + (\vec{\Omega} \times \vec{u}') + (\vec{\omega}' \times \vec{u}') + \frac{1}{\rho}\nabla p' = -\frac{\rho'}{\rho}\frac{DU}{Dt} + \frac{1}{\rho}\vec{f}'_{vis} \tag{9}$$

Taking a curl on the left hand side of Eq. (9) yields

$$\frac{\partial \vec{\omega}'}{\partial t} + (\vec{u} \cdot \nabla)\vec{\omega}' + \vec{\omega}'(\nabla \cdot \vec{u}') + (\vec{u}' \cdot \nabla)\vec{\Omega} + \vec{\Omega}(\nabla \cdot \vec{u}') - (\vec{\Omega} \cdot \nabla)\vec{u}' - (\vec{\omega}' \cdot \nabla)\vec{u} - \frac{1}{\rho^2}(\nabla\rho \times \nabla p').$$

With the incompressible Navier-Stokes equations, the right hand side of Eq. (9) can be re-written as

$$\frac{\rho'}{\rho_0 \rho}\nabla P - \frac{\rho'}{\rho}\nu_0 \nabla^2 \vec{U} + \frac{1}{\rho}\vec{f}'_{vis}, \tag{10}$$

and the curl of Eq. (10) yields

$$\frac{1}{\rho^2}(\nabla\rho \times \nabla P) + \nabla \times \left(\frac{1}{\rho}\vec{f}'_{vis} - \frac{\rho'}{\rho}\nu_0 \nabla^2 \vec{U}\right). \tag{11}$$

Combining Eq. (9) and (11) and dividing both sides by ρ, one obtains the perturbed vorticity transport equations.

$$\begin{aligned}\frac{\partial}{\partial t}\left(\frac{\vec{\omega}'}{\rho}\right) + (\vec{u} \cdot \nabla)\left(\frac{\vec{\omega}'}{\rho}\right) = \\ \underbrace{\underbrace{\tfrac{1}{\rho}[\underbrace{(\vec{\Omega} \cdot \nabla)\vec{u}'}_{I-a} + \underbrace{(\vec{\omega}' \cdot \nabla)\vec{u}}_{I-b}]}_{I} - \underbrace{\underbrace{\tfrac{1}{\rho}[\underbrace{(\vec{u}' \cdot \nabla)\vec{\Omega}}_{II-a} + \underbrace{\vec{\Omega}(\nabla \cdot \vec{u}')}_{II-b}]}_{II}}} \\ + \underbrace{\frac{1}{\rho^3}(\nabla\rho \times \nabla p)}_{III} + \underbrace{\frac{1}{\rho}\nabla \times \vec{F}_{vis}}_{IV},\end{aligned} \tag{12}$$

where $\vec{F}_{vis} = (\vec{f}'_{vis} - \rho'\nu_0\nabla^2\vec{U})/\rho$.

In Eq. (12), one can clearly see that perturbed vorticity is generated and diffused by source terms on the right hand side through: (i) coupling effects between the hydrodynamic vorticity and the perturbed velocities (terms I and II), (ii) entropy field (term III), and (iii) viscous force (term IV). Term I is related to a three-dimensional effect of vortex stretching: stretching of hydrodynamic vorticity by perturbed velocities (term I-a) and stretching of perturbed vorticity by total velocities (term I-b). Term II represents a more direct coupling between the hydrodynamic vorticity and the perturbed velocities. The convective effect of hydrodynamic vorticity by perturbed velocity is represented by term II-a, whereas term II-b is related to the dilatation rate effect. Term III is not so important for low Mach number, non thermally-driven flows and term IV only provides physical diffusion to the perturbed vorticity. In our previous study (1), it was shown that term II-a is the most dominant source term that generates perturbed vorticity and term II-b is considered less important at low Mach numbers.

It is interesting to note that perturbed vorticity is not a 'radiating' acoustic quantity but a 'convecting' hydrodynamic vortical. Its physical meaning represents modification of hydrodynamic vorticity through interactions between the hydrodynamic vorticity and the velocity fluctuations. At low Mach numbers, the magnitude of the perturbed vorticity is small but, if falsely resolved, it becomes self-excited and grows to affect the acoustic

solution. Since term II-a is related to the gradient of hydrodynamic vorticity Ω, perturbed vorticity ω' usually appears at the edge of the hydrodynamic vorticity and its length scale is similar to (or sometimes smaller than) the hydrodynamic vortical scale. Therefore, acoustic grid resolution must carefully be handled in PCE calculation. More details can be found in reference (1).

2.3 Linearized Perturbed Compressible Equations (LPCE)

The linearized perturbed compressible equations (LPCE) are proposed to secure a stable and grid-independent acoustic solution. Neglecting the second-order, non-linear terms such as $(\vec{u}'\cdot\nabla)\vec{u}'$, the original PCE, Eqs. (2)-(4) can be re-written as

$$\frac{\partial\rho'}{\partial t}+(\vec{U}\cdot\nabla)\rho'+\rho_0(\nabla\cdot\vec{u}')=0 \tag{13}$$

$$\frac{\partial\vec{u}'}{\partial t}+\nabla(\vec{u}'\cdot\vec{U})+\frac{1}{\rho_0}\nabla p'=-(\vec{\Omega}\times\vec{u}')-(\vec{\omega}'\times\vec{U})-\frac{\rho'}{\rho_0}\frac{D\vec{U}}{Dt}+\frac{1}{\rho_0}\vec{f}'_{vis} \tag{14}$$

$$\frac{\partial p'}{\partial t}+(\vec{U}\cdot\nabla)p'+\gamma P(\nabla\cdot\vec{u}')+(\vec{u}'\cdot\nabla)P=-\frac{DP}{Dt}+(\gamma-1)(\Phi-\nabla\cdot\vec{q}) \tag{15}$$

Since the left hand side of Eq. (14) does not generate any vortical component, only the right hand side terms are responsible for the generation of perturbed vorticity. The first two terms, $\vec{\Omega}\times\vec{u}'$ and $\vec{\omega}'\times\vec{U}$ correspond to the dominant source terms (terms I and II) in the perturbed vorticity transport equations and the last two terms are associated with the entropy and viscous effects (terms III and IV).

With the thermal terms neglected in the perturbed energy equation, a set of linearized perturbed compressible equations (LPCE) is written as

$$\frac{\partial\rho'}{\partial t}+(\vec{U}\cdot\nabla)\rho'+\rho_0(\nabla\cdot\vec{u}')=0 \tag{16}$$

$$\frac{\partial\vec{u}'}{\partial t}+\nabla(\vec{u}'\cdot\vec{U})+\frac{1}{\rho_0}\nabla p'=0 \tag{17}$$

$$\frac{\partial p'}{\partial t}+(\vec{U}\cdot\nabla)p'+\gamma P(\nabla\cdot\vec{u}')+(\vec{u}'\cdot\nabla)P=-\frac{DP}{Dt}. \tag{18}$$

Since the curl of the linearized perturbed momentum equations, Eq. (17) yields

$$\frac{\partial\vec{\omega}'}{\partial t}=0, \tag{19}$$

Thus, generation of perturbed vorticity is suppressed in the LPCE formulation: i.e. any further changes (generation, convection, and decaying) of perturbed vorticity in time are prevented. Now, one can use larger normal grid spacings near the wall because LPCE is an inviscid form. More details can be found in reference (2).

3 TURBULENT EDGE-SCATTERING NOISE

A flow ($U_o=20m/s$) over the flat plate at an angle of attack $\alpha=0$ is considered. The plate has a chord length $c=10cm$, thickness $h=0.03c$, span $L=3c$, and the plate edges have four corners cut with a radius of $0.5mm$ in order to smoothen the geometrical singularities. The Reynolds number based on the chord length, Re_c is 1.3×10^5 and the flow Mach number, M_o is 0.06. An incompressible large eddy simulation is performed for the computational domain shown in Figure 5. Flow periodicity is assumed in the spanwise direction for the simulated span, $L_S=0.03c$. An O-type grid is used with $657\times201\times21$ (about 2.8 millions) points in x,y, and z. The minimum grid spacing for x and y is $0.0005c$ (or $\Delta x^+_{min}=\Delta y^+_{min}=3$) and a uniform grid spacing of $0.0015c$ (or $\Delta z^+=15$) is used in the spanwise direction. More details can be found in reference (4).

Figure 3(a) shows the iso-surfaces of the second invariant property of the velocity gradients, $Q(=200)$ over the plate. A separation occurs at the leading-edge and the shear layer approximately reattaches at $x=-0.8c$.

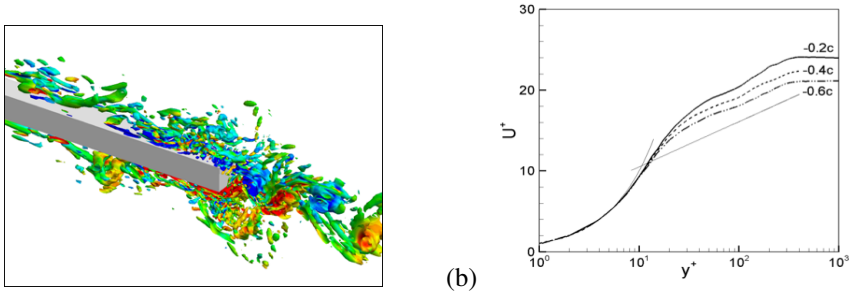


Figure 3. Instantaneous hydrodynamic flow field at $Re_c = 1.3 \times 10^5$ $(U_o = 20m/s)$; (a) iso-surfaces of Q (=200) non-dimensionalized by $(U_o/h)^2$, (b) turbulent boundary layer characteristics; boundary layer profiles (time-averaged) at $x = -0.2c$, $-0.4c$, and $-0.6c$

Then, it breaks off into eddies that are convected downstream along the plate surface. It also exhibits the expected von Kármán vortex shedding in the wake region. Figure 3(b) shows the boundary layer profiles over the plate, which are expected to be turbulent but with a pressure gradient effect imposed upon it. A boundary layer thickness, δ at $x = -0.2c$ (upstream from the trailing-edge) is $1.12h$ and the turbulent Reynolds number, Re_τ is 231.

Temporal variations of the wall pressure fluctuations at various stations over the plate (from A to I) are exemplified in Figure 4(a). First, one can identify that at station A, pressure fluctuations with a range of scales are monitored because it is close to the reattachment point of the shear layer ($x = -0.8c$). Small scale eddies are rapidly decaying but large-scale structures generated at very low frequency ($St = fh/Uo = 0.01$ or $67Hz$) seem to survive to the trailing-edge and influence the region close to the stations at H and I. Station H clearly shows the pressure fluctuations at the von Kármán vortex shedding frequency ($St = 0.2$ or $1333Hz$). At station I, pressure fluctuations at St=0.01 are only visible. A $x-t$ plot of the wall C_p presented in Figure 4(b) clearly indicates that large-scale pressure bursts 'originated' from the shear layer reattachment point have a non-dimensional time scale close to 100 (= tU_O/h), which corresponds to the frequency close to $St = 0.01$. It is also indicated that pressure bubbles are convected downstream with $U_C = 0.83U_O$.

The flat plate self-noise at $Re_C = 1.3 \times 10^5$ and $M_o = 0.06$ (for $\alpha = 0$) is computed by solving the linearized perturbed compressible equations (LPCE). The LPCE calculation is conducted in a two-dimensional compu-

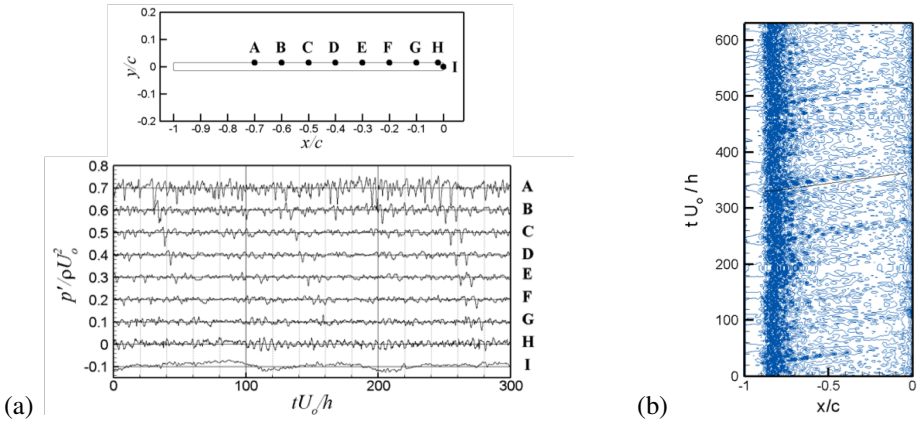


Figure 4. (a) Time history of surface pressure fluctuations at streamwise stations A, B, C, D, E, F, G, H, I; curves are separated by a vertical off set of 0.1 with the corresponding zero lines located at -0.1, 0, 0.1, 0.2,...,0.7, (b) $x-t$ plot of C_p (plate wall): exhibiting large-scale pressure fluctuations at $St = 0.01$ with a convection velocity, $U_c = 0.83U_o$

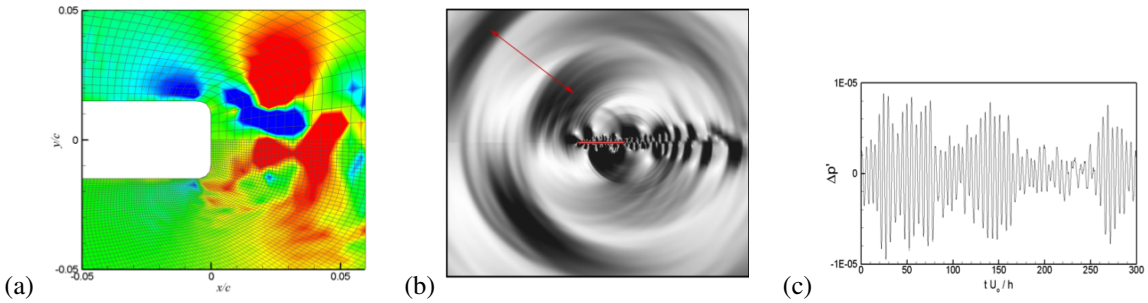


Figure 5. (a) Instantaneous DP/Dt field (spanwise-averaged) projected onto the acoustic grid (347×247: top) from the hydrodynamic grid (657×201×21: bottom), (b) instantaneous pressure fluctuation field ($\Delta p' = (\overline{P+p'}) - (P+p')$), (c) time history of pressure fluctuations at $r = 70h$ (or $2.1c$) vertically away from the trailing-edge; non-dimensionalized by $\rho_o {c_o}^2$

tational domain, where it is coupled with the 'spanwise-averaged' incompressible LES solution. An O-type acoustic grid is used with 347×247 points and a minimal normal spacing at the wall is five times larger than the hydrodynamic one. Figure 5(a) shows the grid details near the trailing-edge and the noise sources, i.e. the von Karman vortex shedding and the convected eddies in the boundary layer. The noise source, DP/Dt field is acquired from the LES solution and projected onto the coarse acoustic grid.

The instantaneous pressure fluctuation field ($\Delta p' = (\overline{P+p'}) - (P+p')$) computed by LPCE is presented in Figure 5(b). First, a dipole tone generated by the von Karman vortex shedding at the trailing-edge is clearly noticeable. The acoustic wavelength, λ/c is close to 2.5, which corresponds to the frequency, $St = 0.2$. Besides, one may note that the other higher frequency components superimposed in the near-field are being generated from the trailing-edge and the reattachment point of the shear layer. Due to the grid coarseness, however, acoustic waves with short wavelengths are expected to be numerically dissipated as propagating away from the plate. Figure 5(c) also shows the time history of the pressure fluctuations monitored at $r = 70h$ (or $2.1c$) vertically away from the trailing-edge.

Since the microphone is located 20c from the plate, the 2D acoustic field computed by LPCE within the domain of $10c$ needs to be extrapolated by the Kirchhoff method and also to be corrected to 3D spectral pressure by Oberai's method (*). Finally, the 3D spectral pressure in the far-field, which is radiated from span (h), needs to be corrected for the total span ($100h$ or $3c$) used in the experiment. In this procedure, we need information on the spanwise coherence function of the surface pressure , $\gamma(z)$ in the most dominant noise source region.

Figure 6(a) shows the $\gamma(z)$ function, which is computed by LES for h as well as measured for $3c$ (or $100h$). The spanwise coherence function rapidly drops in most frequencies, except for the tone at $St = 0.2$. The

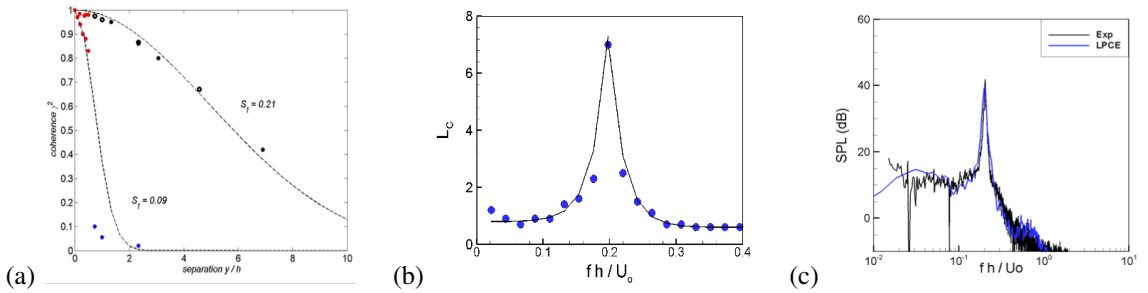


Figure 6. (a) Spanwise coherence; o: computations, (o, o): wind-tunnel measurements, (b) spanwise coherence length; data interpolated by a Gaussian law, $\gamma(z) = \exp(-(z/L_c)^2)$, (c) comparison of SPL spectrum at $r = 20c$ vertically away from the mid-chord of the plate; computation (blue), experiment (black)

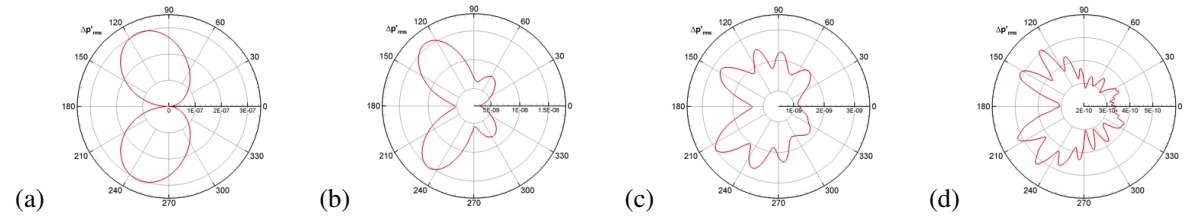


Figure 7. Directivity patterns of $\Delta p'_{rms}$ at $r = 20c$; (a) $St = 0.2\,(c/\lambda = 0.4)$, (b) $St = 0.4\,(c/\lambda = 0.8)$, (c) $St = 1\,(c/\lambda = 2)$, (d) $St = 2\,(c/\lambda = 4)$

spanwise coherence length of the surface pressure, L_C calculated by the Gaussian law, $\gamma(z) = \exp(-(z/L_c)^2$ is shown in Figure 6(b). The largest value of L_C is approximately 7h at St=0.2 but L_C is mostly under 2h at other frequencies. The far-field SPL predicted for the actual span is now compared in Figure 6(c) with the measured data at *Ecole Centrale Lyon*. The comparison is very good, except at low frequency ($St < 0.03$). The measured SPL spectrum indicates an increase of SPL as the Strouhal number decreases towards $St = 0.01$ but the prediction fails to show it. The discrepancy comes from the fact that for the tone at $St = 0.2$, the microphone location (at $20c$ vertically away from the mid-chord of the plate) is 8 times larger than the corresponding acoustic wavelength ($2.5c$) and one can say that the far-field approximation is quite valid. On the other hand, at $St = 0.01$, the acoustic wavelength is approximately $50c$ and the far-field assumption is not valid any more. As a reference, the acoustic wave generated at $St = 0.025$ has a wavelength comparable to the microphone location (i.e. $20c$).

Figure 7 shows the directivity patterns of $\Delta p'_{rms}$ at $r = 20c$ for various Strouhal numbers (or ratios of the plate chord length to the acoustic wavelength). At the von Kármán vortex shedding frequency ($St = 0.2$ or $c/\lambda = 0.4$), it clearly shows a dipolar pattern. The figure also shows that as Strouhal number increases (or acoustic wavelength becomes shorter than the chord length, the directivity pattern changes to a finger-like shape due to wave diffractions around the leading and trailing edges of the plate. Finally, one can see that the present computational methodologies for flow and acoustics reasonably capture the physical aspects of flat plate self-noise, i.e. the noise generation mechanism and its interactions with the flow and structure.

4 CONCLUSIONS

This paper reviews the perturbed compressible equations (PCE), the perturbed vorticity transport equation, and the linearized perturbed compressible equations (LPCE). The concept of perturbed vorticity is introduced and its importance in hydrodynamics/acoustics splitting methods is fully discussed. This paper successfully demonstrates that the present hybrid method using LES and LPCE was found to be accurate in predicting turbulent edge-scattering noise.

REFERENCES

[1] Seo, JH and Moon YJ. Perurbed compressible equations for aeroacoustic noise prediction at low Mach numbers. AIAA Journal. 2005;43(8).

[2] Seo, JH, and Moon, YJ. Linearized perturbed compressible equations for low Mach number aeroacoustics. Journal of Computational Physics. 2006;218.

[3] Moon, YJ. Sound of fluids at low Mach numbers. European Journal of Mechanics B/Fluids. 2013;40.

[4] Chang, KW, Seo, JH, Moon, YJ, and Roger, M. Prediction of Flat Plate Self-Noise. AIAA Paper 2006-2513. 2006.

PROCEEDINGS of the
24th International Congress on Acoustics

October 24 to 28, 2022, in Gyeongju, Korea

Extended abstract

ABS-0141

Novel formulation of semi-analytical finite element method for acoustic problems

Timur ZHARNIKOV[1]; Roman PONOMARENKO[2]; Denis SABITOV[2]; Christopher AYADIUNO[3]

[1] Aramco Research Center, Russia

[2] Aramco Research Center, Russia

[3] Saudi Aramco, Saudi Arabia

ABSTRACT

In this work, novel formulation of the SAFE approach is presented. It is based on the spectral element method (SEM) variant of the finite element method and offers high order of accuracy. Also, model geometry description with the curvilinear elements is developed and implemented. Proposed SEM-SAFE formulation has the potential to improve the spectrum estimation and the dispersion curve computation by offering more accurate description of the interfaces with less elements and higher degree of approximation. Mass and stiffness matrix computation is simplified by using SEM formulation. This approach is exemplified by computing the spectrum of fluid-filled waveguides in anisotropic medium. Better quality of the eigenfunctions approximation is observed.

Keywords: SAFE, dispersion, anisotropy

1. INTRODUCTION

The semi-analytical finite element method (SAFE) is a powerful tool to compute the spectrum and the dispersion curves of complex waveguide structures. Such problems attract attention and have many applications, especially in the situations when no analytical solution is available. Of note are the non-destructive testing and geophysics (references (1,2)). The latter deals with the acoustics of boreholes in rock formations, which are often anisotropic. In addition, the computations have to be fast and accurate. It stimulates the interest to evaluate SAFE techniques with improved characteristics.

Spectral element method (SEM) is a version of the finite element method with specially designed nodal basis functions (references (3,4)). Their hallmark is the property of discrete orthogonality, which results in block diagonal mass matrix. In addition, it allows for high orders of approximation and for the possibility to use the curvilinear mesh elements. Therefore, the number of elements required for the description of the borehole, can be significantly reduced.

In this work we present the formulation of SAFE approach using SEM version of the finite element method. The methodology and the examples are outlined in below Sections.

2. METHOD

SAFE method formulation is well developed (see references (1,2) and references therein). It is based on the finite element discretization of the virtual work principle. Assuming translational invariance of the waveguide and the absence of cross-terms with respect to the frequency, the displacement field can be discretized as:

$$\boldsymbol{u}(x,y,k,\omega) = \boldsymbol{N}(x,y)\boldsymbol{u}(k,\omega)e^{i(kz-\omega t)} \quad (1)$$

where $\boldsymbol{N}(x,y)$ is the matrix of the basis functions and $\boldsymbol{u}(k,\omega)$ are the displacement field values in the nodes in the $(k-\omega)$ domain. Substituting such an approximation into the variational principle results in the generalized eigenvalue problem of the form

$$(\mathbf{K}_1 + ik\mathbf{K}_2 + k^2\mathbf{K}_3 - \omega^2\mathbf{M} + i\omega\boldsymbol{P})\mathbf{U} = \mathbf{0} \quad (2)$$

[1] timur.zharnikov@aramcoinnovations.com

Saudi Aramco: Public

Here, the matrices are computed as the combinations of blocks of the matrix integrals of the form (references (1,2))

$$\mathbf{K}_1^e = \int_V^{(e)} \mathbf{B}_1^* \mathbf{C} \mathbf{B}_1 dV \qquad \mathbf{M} = \int_V^{(e)} \mathbf{N}^* \rho \mathbf{N} dV \tag{3}$$

and the like. The integrands in these expressions involve the density of the medium, stiffness tensor, basis functions and their derivatives, etc.

The key difference of the developed approach from the standard formulation of the SAFE method is that here spectral element basis functions $N_{ij}(x, y)$ are used (references (3,4)). They are taken as Lagrange functions: each function equals to 1 at the specific node and to zero at all other nodes as shown in Figure 1. The nodes are distributed inside the cell as the nodes of Gauss-Lobatto-Lagrange (GLL) quadrature. Such a choice is made to simplify numerical integration described further.

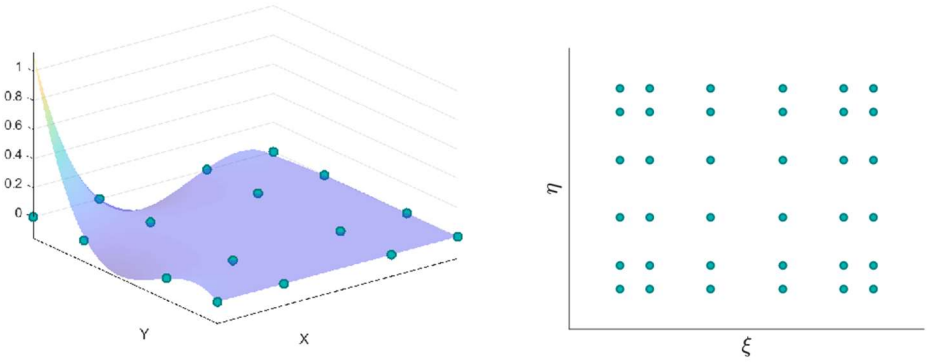


Figure 1 – Example of basis function and distribution of nodes in the physical cell (left) and reference coordinate system (right)

The calculation of mass and stiffness matrices is a cumbersome operation. Integration with GLL quadrature for structured grid is easy. In the unstructured curvilinear grid, each element is deformed in a unique way, transformation from the reference coordinate system to the physical element is non-linear. Hence, the matrices should be computed for each cell separately. Transformation from the reference coordinates to the coordinates in physical space can be obtained by considering the mapping function in the following form:

$$\begin{cases} x = a_x + b_x\xi + c_x\eta + d_x\xi\eta + e_x\xi^2 + f_x\eta^2 + g_x\xi^2\eta + h_x\eta^2\xi \\ y = a_y + b_y\xi + c_y\eta + d_y\xi\eta + e_y\xi^2 + f_y\eta^2 + g_y\xi^2\eta + h_y\eta^2\xi \end{cases} \tag{4}$$

The mass, stiffness, and other matrices appearing in SAFE, can be calculated by integration over the reference element as

$$M_{ij} = \int N_i(x,y) N_j(x,y) dxdy = \int N_i(\xi,\eta) N_j(\xi,\eta) J d\xi d\eta \tag{5}$$

using the Jacobi matrix of the mapping function (4):

$$J = \begin{vmatrix} \partial x/\partial\xi & \partial x/\partial\eta \\ \partial y/\partial\xi & \partial y/\partial\eta \end{vmatrix} \tag{6}$$

Once the matrix coefficients of generalized eigenvalue problem (2) are computed and assembled, the latter can be solved by standard algorithms. Doing so for a series of frequencies, the dispersion curves of the modes can be obtained.

3. RESULTS AND DISCUSSION

To illustrate the capabilities of the developed approach, we considered the waveguide in the homogeneous horizontal transverse isotropy (HTI) medium. The parameters of the corresponding vertical transverse isotropy (VTI) medium were as follows: density $\rho = 2230\ kg/m^3$; elastic moduli

Saudi Aramco: Public

of corresponding VTI medium are $C_{11} = 40.9\ GPa$, $C_{13} = 8.5\ GPa$, $C_{33} = 26.9\ GPa$, $C_{44} = 10.5\ GPa$, $C_{66} = 15.3\ GPa$. The waveguide is filled with water with the density $\rho = 1000\ kg/m^3$ and the bulk modulus $K = 2.25\ GPa$, its radius is R=0.1016 m. The method was tested by calculating the eigenfunctions for several frequencies and constructing the dispersion curves.

In line with the SAFE-SEM formulation introduced above, the computational domain was discretized using the curvilinear elements (see Figure 2). Implemented algorithm supports high order basis functions. For simplicity's sake, the second order basis functions were used in this case. As a result, coarser grid can be used to approximate the problem.

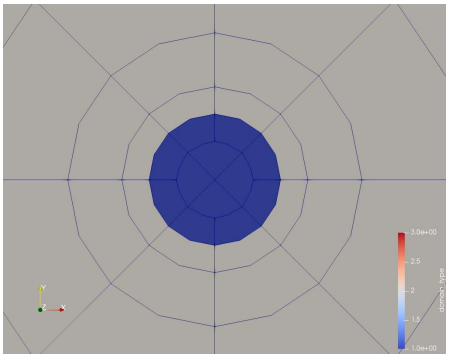


Figure 2 – Example of curvilinear mesh used for the computation

Solving the generalized eigenvalue problem (2) allowed the construction of the dispersion curves. The examples of the latter for the ground mode (known as the Stoneley mode in geophysical applications) and for the dipole modes are presented in Figure 3. Black dots correspond to the Stoneley mode, red and blue dots denote fast and slow dipole modes, respectively. The examples of the eigenfunctions' shape for another model are shown in Figure 4. Good quality of the eigenfunction approximation can be observed.

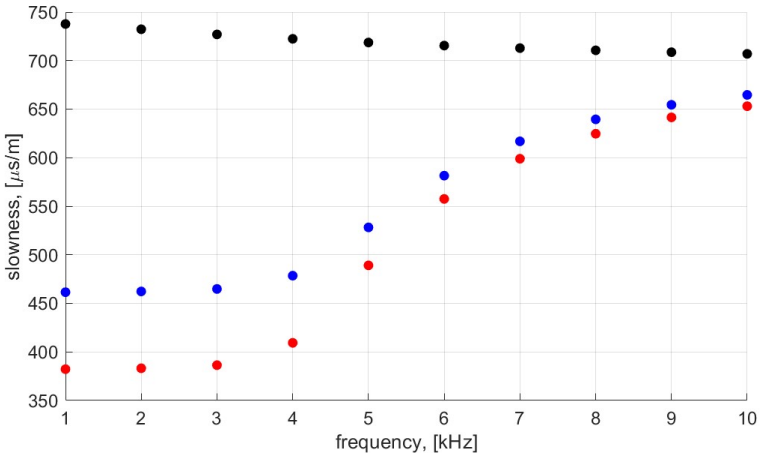


Figure 3 – Example of computed dispersion curves

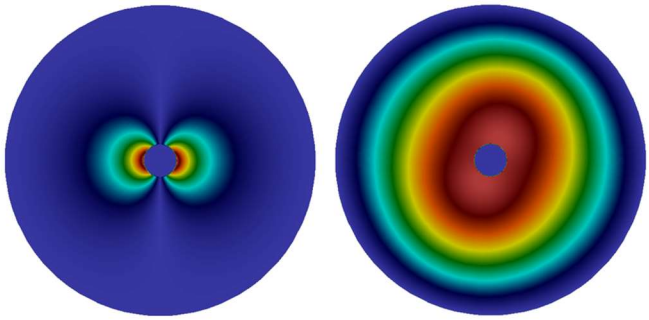


Figure 4 – Example of eigenfunctions computed for another model

In addition, the comparison of the eigenfunctions and the dispersion curves with those obtained by

Saudi Aramco: Public

the standard SAFE approach and previously developed pseudospectral method demonstrated good agreement. It confirms that developed approach can be considered as viable alternative to the traditional SAFE formulation.

CONCLUSION

The formulation of the SAFE approach using the spectral element (SEM) version of the finite element technique is presented. The advantage of developed approach is the possibility to use high order basis functions and the curvilinear elements. It results in significant reduction of the elements without sacrificing the accuracy. The numerical example of computing the dispersion curves for the anisotropic medium demonstrates and confirms the capabilities of SAFE-SEM formulation.

REFERENCES

1. Ellefsen KJ, Cheng CH, Toksoz MN. Effects of anisotropy upon the normal modes in a borehole. J Acoust Soc Am. 1991;89:2597–2616.
2. Zharnikov T, Syresin D. Repulsion of dispersion curves of quasidipole modes of anisotropic waveguides studied by finite element method. J Acoust Soc Am. 2015;137(6):EL402.
3. Komatitsch D, Vilotte J-P. The spectral element method: An efficient tool to simulate the seismic response of 2D and 3D geological structures. Bulletin of the Seismological Society of America. 1998;88(2):368–392.
4. Charara M, Sabitov D. Efficient and accurate 3D sonic logging modeling in anisotropic viscoelastic media. Society of Exploration Geophysicists. Global Meeting Abstracts. 2020;33–36.

Saudi Aramco: Public

ICA 2022
24th INTERNATIONAL CONGRESS ON ACOUSTICS
October 24(Mon) - 28(Fri), 2022 Gyeongju, Korea

PROCEEDINGS of the
24th International Congress on Acoustics

October 24 to 28, 2022 in Gyeongju, Korea

Extended abstract

ABS-0229

Spectral estimation for nonstationary audio signals: Beyond the uncertainty principle

Adrien MEYNARD[1]; Bruno TORRÉSANI[2]

[1]ENSL,CNRS, Laboratoire de physique, Lyon, France
[2]Aix Marseille Univ, CNRS, I2M, Marseille, France

ABSTRACT
Spectral analysis aims to determine the frequency content of stationary signals. However, the stationarity assumption is too strong a restriction for modeling audio signals, whose statistical properties intrinsically vary over time. To address this challenge, we have proposed a spectral estimation method that takes into account several physical sources of nonstationarity in acoustics, such as intensity variations, or the Doppler effect. The signal's model is formed of a stationary signal deformed by a stationarity-breaking operator (namely, a combination of amplitude modulation and time warping). The resulting algorithm provides simultaneous estimates for the underlying spectrum and the deformation operator. The approximation relation the algorithm is based on is only valid for slowly varying deformations. To overcome these limitations, we developed a Bayesian approach that allows us to include sharpness priors on the spectrum's shape, and hence concurrently improve the estimation quality and the time-scale signal's representation.

Keywords: Nonstationarity, Wavelet transform, Time-scale synthesis, Time warping

1 INTRODUCTION

Spectral analysis consists in the determination of the frequency content of stationary signals. Among other techniques, Welch's method [13] has been widely used to perform spectral estimation of stationary signals. Whatever the method used, the stationary assumption is necessary to give sense to the estimated quantity, called *power spectrum* [11].

Stationarity is a mathematical notion that guarantees the independence in time of the statistical properties of a random process. A signal is said to be stationary when it is modeled as a realization of a stationary random process. Most audio signals cannot be satisfactorily modeled as stationary. Indeed, the physical sources that generate these sounds are inherently varying over time. For example, when a rotating engine accelerates, the pitch of the sound produced increases with the speed of the engine. Other phenomena, such as the Doppler effect or intensity variations are sources of non-stationarity.

Several extensions of spectral analysis to classes of nonstationary signals have been proposed [10]. In our work, we have considered nonstationary signals modeled as stemming from stationary signals deformed by stationarity-breaking operators. We considered a physically relevant deformation, namely a combination of amplitude modulation and time warping. We then developed JEFAS [6], an algorithm for the simultaneous estimation of the stationarity-breaking operator and the power spectrum of the underlying stationary signal. Based on an idea introduced by Clerc and Mallat [2] and developed by Omer [8], our approach approximates the effect of the deformation in the wavelet domain as a mere displacement of coefficients in the time-scale plane. The estimation procedure proposed in JEFAS is thus performed in the wavelet domain.

We have also developed and studied an alternative approach, called the *synthesis approach*, inspired by a model developed by Turner & Sahani [12], which interprets time-frequency transform in terms of probabilistic inference. The Turner-Sahani was applied to various time-frequency problems. Our model expresses nonstationary signals as the result of a time-scale synthesis from a random time-scale representation, governed by a

prescribed prior distribution, which involves the time warping model. We study the corresponding model, and compute the posterior distribution which is used to construct an estimator for the model parameters. This approach, called JEFAS-S (where the "S" stands for "synthesis"), also outputs an adapted time-scale representation from which signal synthesis is possible. Remarkably enough, JEFAS-S is able to handle time warping models in situations where the time warping function can have much faster variations. In addition, JEFAS-S can also yield time-frequency representations which are much sharper than conventional transforms.

In this article, we describe the nonstationary signals involved. We then successively present the *analysis approach* that gave rise to JEFAS and the *synthesis approach* used to develop JEFAS-S. Finally, we present numerical results where we put a particular emphasis on the pros and cons of both approaches. This paper is an extended abstract of our full paper [7], currently under peer review.

2 NON-STATIONARITY MODEL

Amplitude modulated and time warped (AM-TW) signals are defined as realizations of nonstationary processes taking the form

$$Y = \mathscr{M}_\alpha \mathscr{D}_\gamma X, \tag{1}$$

where $\mathscr{M}_\alpha$ is the amplitude modulation operator (pointwise multiplication with the positive valued function α), and $\mathscr{D}_\gamma$ is the time warping operator (composition with the monotone function γ, assumed to be differentiable and strictly increasing):

$$\mathscr{M}_\alpha x(t) = \alpha(t)x(t)\ , \qquad \mathscr{D}_\gamma x(t) = \sqrt{\gamma'(t)}x(\gamma(t))\ . \tag{2}$$

Here, X is a second order wide-sense stationary random process, with zero mean. Its power spectrum is denoted by $\mathscr{S}_X$.

In analogy with the spectral estimation of stationary random processes (estimate the power spectrum from one or several realizations of the process), spectral analysis of AM-TW signals is defined as the problem of the joint estimation of the functions α, γ and the underlying power spectrum $\mathscr{S}_X$ from one realization of the nonstationary process Y.

3 JEFAS: AN ANALYSIS APPROACH

3.1 Wavelet transform

Under certain existence conditions [4], the wavelet transform $\mathscr{W}_x$ of a signal x is defined by:

$$\mathscr{W}_x(s,\tau) = \int_{\mathbb{R}} x(t)\overline{\psi_s}(t-\tau)\,dt\,, \tag{3}$$

where ψ is the analysis wavelet, and ψ_s are the scaled wavelets defined by

$$\psi_s(t) = 2^{-s/2}\psi\left(2^{-s}t\right), \quad s \in \mathbb{R}.$$

We will focus here on the so-called sharp wavelet, introduced in [6]. Using such wavelet, the synthesis formula reads (for a suitably chosen normalization of ψ)

$$x(t) = \Re\left(\int_{-\infty}^{\infty}\int_{-\infty}^{\infty}\psi_s(t-\tau)\mathscr{W}_x(s,\tau)d\tau\frac{ds}{s}\right). \tag{4}$$

3.2 Approximation result

In that framework, it can be shown [6] that the respective wavelet transforms $\mathscr{W}_y$ and $\mathscr{W}_x$ of y and x (realizations of the processes defined in (1)) are approximately related by

$$\mathscr{W}_y(s,\tau) \approx \mathscr{W}_x(s+\log_2(\gamma'(\tau)),\gamma(\tau))\ . \tag{5}$$

In the setting of random processes, under Gaussian assumption, it can be shown [8, 6] that the approximation error is unbiased and its variance can be controlled thanks to the decay properties of the wavelet ψ, and the variations of γ'.

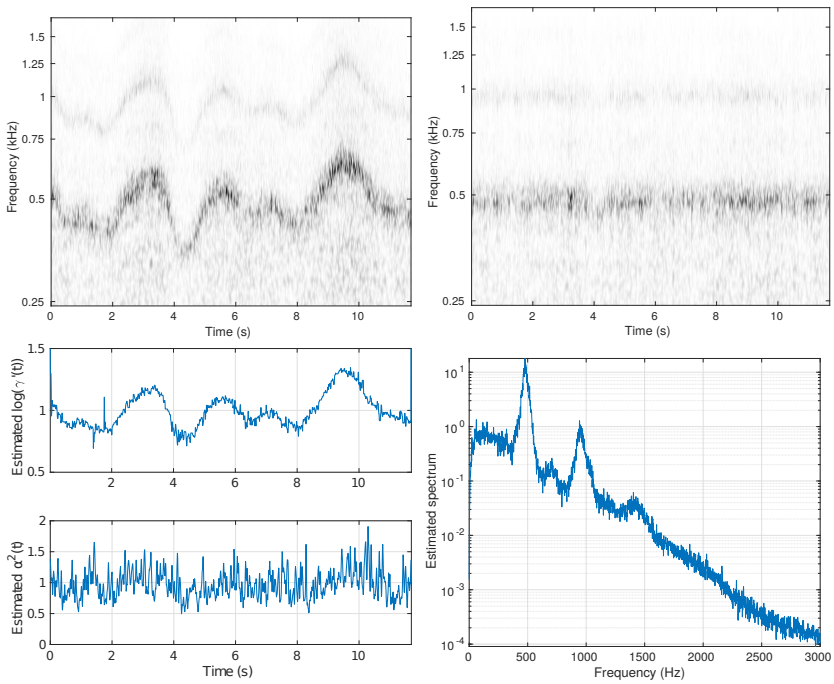


Figure 1. Spectral analysis of a wind sound with JEFAS. Top left: wavelet transform (absolute value) of the original signal. Bottom left: estimates of TW an AM functions. Top right: wavelet transform (absolute value) of the estimated underlying stationary signal. Bottom right: estimated power spectrum.

3.3 JEFAS

JEFAS relies on the approximated behavior (5). Indeed, we proposed an algorithm which performs alternate estimations of the non-stationarity functions α and γ, and the underlying power spectrum $\mathscr{S}_X$. The estimations of α and γ are performed in the wavelet domain, and consist in resolving a maximum likelihood problem.

JEFAS has been implemented and tested on various audio signals such as: recording of a racing car passing by (non-stationarity caused by the Doppler effect), wind blowing through a window, or dolphins vocalizations. The output of JEFAS applied to a sound recording produced by wind blowing is displayed in Fig. 1. One must note that nonstationarity caused by speed variations (i.e. time warping) is well estimated, while amplitude modulation is badly handled. The theoretical study of the performance of JEFAS—in particular the Cramér-Rao bound on the variance of the estimators—explains that behavior [6].

JEFAS is a highly effective method for estimating TW deformation of nonstationary signals. It is however limited by the intrinsic properties of the wavelet transform. In particular the uncertainty principle limits the capability to estimate fast varying time warping functions.

4 JEFAS-S: A SYNTHESIS APPROACH

4.1 Synthesis model

Instead of starting from the wavelet transform, the approach is based on a synthesis model. The nonstationary random discretized signal $\mathbf{y}$ is modeled as stemming from a random time-scale representation, in the form of the inversion formula (4), namely

$$\mathbf{y} = \Re\left(\mathbf{DW}\right) + \varepsilon \ , \tag{6}$$

where ε is a zero mean, Gaussian white noise, $\mathbf{D}$ is a wavelet dictionary. $\mathbf{W}$ is a random time-scale matrix, with prescribed prior probability distribution, which will implement the time warping model. Based on the latter, the goal is to estimate $\mathbf{W}$ from the realization $\mathbf{y}$.

We now introduce the time-scale warping prior model on $\mathbf{W}$. This prior model is designed so as to mimic the behavior of wavelet transform of time warped stationary processes, and involve the following elements

1. Columns of $\mathbf{W}$ are assumed independently distributed, according to a circular complex Gaussian law (this was an approximation in JEFAS, and is now a prior model in JEFAS-S). We refer to e.g. [9] for an extended description of multivariate complex Gaussian distributions.

2. The natural choice for the covariance matrix of a given column of $\mathbf{W}$ is given by JEFAS, and the approximation result (5). However, we will also investigate other choices that provide sharper time-scale representations.

Unlike JEFAS, amplitude modulation is not included in JEFAS-S. Nevertheless, there is no theoretical obstruction to the inclusion of amplitude modulation in the model if necessary.

4.2 JEFAS-S

In a Bayesian framework, the posterior distribution of the time-scale representation is derived in [7]. It is a zero-mean complex Gaussian multivariate random variable, whose covariance and relation matrices depend on the nonstationarity parameters, i.e. $\mathscr{S}_X$ and the TW function.

in this paradigm, the Expectation-Maximization (EM) strategy [3] leads to an estimation algorithm for the simultaneous estimation of the nonstationarity parameters and the time-scale representation. The update rules are detailed in [5, 7], together with some numerical considerations (e.g. initialization, dimension reduction).

5 Numerical results

The numerical results presented in the current section are reproducible. The MATLAB code is available online at https://github.com/AdMeynard/JEFAS.

We illustrate here the ability of JEFAS-S to handle non-stationary TW signals with fast varying spectral content. To this end, a nonstationary signal is synthesized from a stationary signal $\mathbf{x}$ comprised of two sine waves with close frequencies. We have

$$\mathbf{x}[n] = \cos\left(2\pi f_1 \frac{n}{N_\tau} + \varphi_1\right) + 2\cos\left(2\pi f_2 \frac{n}{N_\tau} + \varphi_2\right) \ , \tag{7}$$

where $N_\tau = 1024$, $f_1 = 184$ and $f_2 = 154$. The phases φ_1 and φ_2 are independent random scalars drawn from a uniform distribution in the interval $[0, 2\pi)$. We then apply the time warping operator. The warping function γ is derived from the electrocardiogram of a patient with irregular heartbeat. Its derivative is obtained evaluating the R-peak to R-peak intervals, followed by a cubic spline interpolation. This fast varying function is shown in Fig. 2 (dotted line). Eventually, a Gaussian white noise of variance $\sigma^2 = 2.5 \times 10^{-3}$ is added to the observations. The wavelet transform of the TW signal, shown in the top left panel of Fig. 3, is highly disturbed by interference between the two components. Indeed, on the one hand, the ability to discriminate two close sine waves requires the analysis wavelet to be sharply localized in frequency, but then interference appears along the time axis. On the other hand, the fast variations of the warping function are only discernible if the wavelet is sharp in time, but interference then appears along the scale axis. The impossibility to avoid interference is a consequence of the uncertainty principle. Hence, the approximated behavior of the wavelet transform JEFAS is based on is not valid. On this example JEFAS turns out to converge in 3 iterations, but the algorithm does not converge satisfactorily towards the ground truth warping function. This is shown in the left panel of Fig. 2. The rapid variations of γ' are strongly smoothed by the JEFAS estimate.

JEFAS-S converges in 111 iterations. The estimated γ' function is represented in the right panel of Fig. 2. The rapid variations are now accurately reproduced. The accuracy of the estimate is markedly improved: the mean square error goes from 0.0261 for JEFAS to 0.0069 for JEFAS-S. The time-scale representation estimated with JEFAS-S is depicted in the top right panel of Fig. 3. Although the presence of two components is not visible, we clearly visualize the rapid variations of the time warping function. Unlike the wavelet transform, interference is absent here.

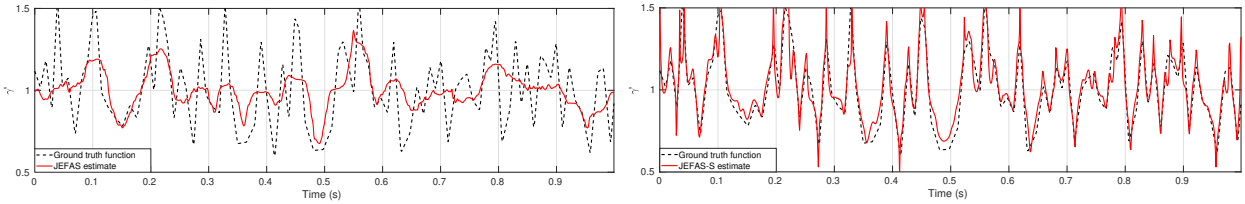


Figure 2. Derivative of the warping function, derived from real heartbeat measurements (dotted lines). The resulting JEFAS (left) and JEFAS-S (right) estimates are superimposed in red.

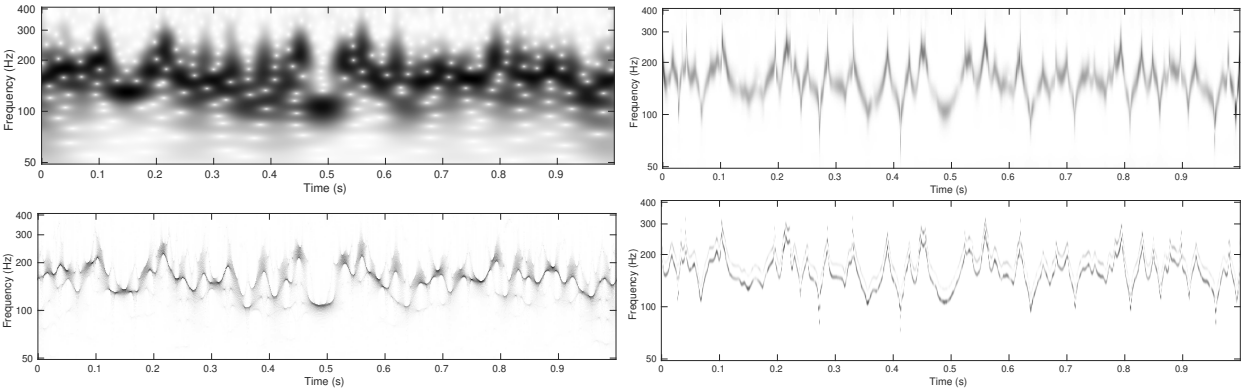


Figure 3. Wavelet transform of the TW signal (top left). JEFAS-S time-scale representation (top right), and its sharpened version (bottom right). The synchrosqueezed wavelet transform is shown for comparison (bottom left).

Once the parameters of the model have been estimated, we can take advantage of the Bayesian framework to adapt the form of the time-scale representation to new a priori constraints. To do this, we simply modify the expression of the covariance template, i.e. the shape of the prior covariance matrix. We choose here to take into account the knowledge of the sparse structure of the power spectrum to modify the covariance prior so that the estimated power spectrum is of the form

$$\tilde{\mathscr{S}}_{X,\mathrm{sp}}(\xi) \stackrel{\Delta}{=} \sum_{k=1}^{K} \tilde{a}_k^2 \delta(\xi - \tilde{\xi}_k),$$

where $\tilde{a}_k$ and $\tilde{\xi}_k$ are the estimates of the amplitudes and frequencies of the stationary signal. These estimates are obtained using the local maxima of the spectrum estimated by JEFAS-S. In this example w find $\tilde{\xi}_1 = 155$ and $\tilde{\xi}_2 = 184$. The resulting time-scale transform is shown in the middle Fig. 3, and as expected turns out to be much sharper than the time-scale representation given on the top image. In addition, the two components forming the signal appear quite distinctly, the synthesis was indeed able to separate these two components.

Besides, the comparison with the synchrosqueezed wavelet transform [1], depicted in the bottom left of Fig. 3, shows that our sharpened representation presents a much better concentration of the time-scale coefficients along the instantaneous frequencies, and does not suffer from the smoothing effect which is visible on the synchrosqueezed scalogram.

6 CONCLUSION

We have presented two approaches for spectral estimation of a class of nonstationary signals.

JEFAS is an analysis approach that relies of the approximate behavior of the wavelet transform of AM-TW signals. It is a fast algorithm, which has been applied to diverse audio signals. The main limitation of JEFAS is its inaccuracy when the TW function varies rapidly.

JEFAS-S is a new synthesis approach for time-scale representation, which is able to handle fast varying non-stationarities. In comparison with existing approaches, a main originality is that JEFAS-S is based upon explicit probabilistic modeling of a time-scale synthesis representation, which allows to bypass (to a certain extent) constraints due to uncertainty principles. JEFAS-S can handle both locally broadband and narrowband signals. In the latter case, i.e. for signals generated by time warping of sums of sine waves, JEFAS-S is also able to yield extremely sharp time-scale representations. Since JEFAS-S is a synthesis approach, we also point out that the signal can be synthesized from the sharpened representation (as well as a stationary signal constructed from a corrected time-scale transform). The approach is limited so far to non-stationarities generated by time warping, but could be extended to other types, for example by adding amplitude modulation, or introducing frequency modulation or more general frequency nonlinear transformation. JEFAS-S also suffers from a longer computation time compared to JEFAS.

REFERENCES

[1] F. Auger, P. Flandrin, Y.-T. Lin, S. Mclaughlin, S. Meignen, T. Oberlin, and H.-T. Wu. Time-frequency reassignment and synchrosqueezing: An overview. *IEEE Signal Processing Magazine*, 30(6):32–41, 2013.

[2] M. Clerc and S. Mallat. Estimating deformations of stationary processes. *Ann. Statist.*, 31(6):1772–1821, Dec. 2003.

[3] A. P. Dempster, N. M. Laird, and D. B. Rubin. Maximum likelihood from incomplete data via the EM algorithm. *Journal of the Royal Statistical Society. Series B (Methodological)*, 39(1):1–38, 1977.

[4] S. Mallat. *A Wavelet tour of signal processing*. Elsevier/Academic Press, 1998.

[5] A. Meynard. *Stationnarités brisées : approches à l'analyse et à la synthèse*. Theses, Aix-Marseille Université, Oct. 2019.

[6] A. Meynard and B. Torrésani. Spectral Analysis for Nonstationary Audio. *IEEE/ACM Transactions on Audio, Speech and Language Processing*, 26(12):2371 – 2380, Dec. 2018.

[7] A. Meynard and B. Torrésani. Synthesis-based time-scale transforms for non-stationary signals. preprint, May 2022.

[8] H. Omer and B. Torrésani. Time-frequency and time-scale analysis of deformed stationary processes, with application to non-stationary sound modeling. *Applied and Computational Harmonic Analysis*, 43(1):1 – 22, 2017.

[9] B. Picinbono. Second-order complex random vectors and normal distributions. *IEEE Transactions on Signal Processing*, 44(10):2637–2640, 1996.

[10] M. B. Priestley. *Non-linear and non-stationary time series analysis*. Academic Press, 1988.

[11] P. Stoica and R. L. Moses. *Introduction to Spectral Analysis*. Prentice Hall, 1997.

[12] R. E. Turner and M. Sahani. Time-frequency analysis as probabilistic inference. *IEEE Transactions on Signal Processing*, 62(23):6171–6183, Dec. 2014.

[13] P. D. Welch. The use of fast Fourier transform for the estimation of power spectra: A method based on time averaging over short, modified periodograms. *IEEE Transactions on Audio and Electroacoustics*, 15(2):70–73, June 1967.

PROCEEDINGS of the
24th International Congress on Acoustics

October 24 to 28, 2022 in Gyeongju, Korea

ABS-0234

Local time-frequency fading

Marina KRÉMÉ[1]; Bruno TORRÉSANI[2]; Antoine DELEFORGE[3]

[1,3]Université de Lorraine, CNRS, Inria, Loria, F-54000 Nancy, France
[2]Aix-Marseille Univ, CNRS, I2M, Marseille, France

ABSTRACT

For efficient analysis of non-stationary signals, such as radar, sonar, speech, music, or general audio, time-frequency (TF) representations are required. They allow performing non-stationary filtering, ie extracting non-stationary "components" in signals. However, ad-hoc procedures are frequently used, whose accuracy is difficult to assess and control. In this contribution, we are interested in such time-frequency filtering, which we define as follows: the attenuation of a given, small region Ω in the time-frequency plane. This problem, addressed in a recent publication, is referred to as time-frequency fading (TFF).
We address a local version of TFF, called LTFF, that only exploits a neighborhood $\overline{\Omega}$ of the time-frequency region of interest Ω, which is supposed to be much smaller than the full time-frequency domain. This problem will be referred to as local time-frequency fading. We propose a method for determining such a neighborhood $\overline{\Omega}$. The local TFF problem is then solved using a variational approach, that minimizes a suitable quadratic objective function. Thus, there is a closed-form solution involving Gabor multipliers.

Keywords: Time-Frequency Fading, Local time-frequency fading, Gabor transforms, Gabor multipliers

1 INTRODUCTION

Filtering is one of the fundamental techniques in signal processing. By filtering one often means linear time invariant (LTI) filtering, which has a simple characterization in time and/or frequency domains. We refer to [1] for an in-depth description, in view of audio applications. Sticking to linear filters, time varying (LTV) filtering is also fundamental, as most devices actually feature time variations. LTV filters form a much wider class than LTI filters, and may be represented in several different ways, for example as matrices as described in [1] for digital signals, or pseudo-differential operators in the mathematical literature [2] in the analog case. Among LTV filters, filters that can be efficiently represented in a joint time-frequency domain have received significant interest in the last two decades. These include filters whose spectral characteristics (frequency response) vary slowly as a function of time, or filters designed to enhance, attenuate or cancel out components which possess specific localization properties in joint time-frequency domain (e.g., chirps with prescribed or parameterized frequency modulation laws, transient oscillatory waves). Several formulations for non-stationary Wiener filtering have been proposed, that rely on time-frequency representations such as the spectrogram [3] or Wigner distribution [4, 5, 6]. These generally rely on pointwise multiplication in the time-frequency domain prior to inversion, very much in the spirit of classical LTI filtering. Filtering in the time-frequency domain has been used for a wide range of applications including decision, detection, or time-frequency segmentation.

Time-frequency filtering exploits the ability of some time-frequency representations to efficiently represent signals of interest. Limited to linear transforms, usual choices are Gabor transform [7] or Short Time Fourier Transform [8], on which we will focus in the present paper, or wavelet transform, constant Q transform or S transform, the choice often depending on the application domain.

In this paper, we discuss a local version of time-frequency fading (TFF) [9], which is a type of time-frequency filter design. Time-frequency fading is the process of restoring a signal that has been degraded by an additive disturbance, in the case where the latter is well localized in a specific region of the time-frequency domain. We previously investigated and proposed a rigorous formulation of TFF in our previous paper [9]. We

[1] ama-marina.kreme@inria.fr
[2] bruno.torresani@univ-amu.fr
[3] antoine.deleforge@inria.fr

solved it and proposed several algorithms that make use of random projection techniques to enable numerical scaling. TFF, on the other hand, formulates the problem in the signal dimension. As a result, despite the fact that dimension reduction methods have been used to approximate the solution, TFF remains difficult to apply to long signals, such as those sampled at 44100 Hz. Here, we rely on the formulation proposed in and take advantage of the support reduction. In section 2 we briefly recall the time-frequency fading problem, and we introduce and formulate local TFF. In section 3, we illustrate LTFF on an example of signal mixing. Section 4 presents the ongoing work. An extended version of this work is under preparation.

2 GLOBAL AND LOCAL TIME-FREQUENCY FADING

2.1 TFF and notations

The Time-Frequency Fading (TFF) problem introduced in [9] may be seen as a time-frequency analogue of a stop-band filter design problem, where one tries to attenuate a set of prescribed regions $\Omega_p \subset \Lambda$ of the time-frequency plane Λ, with prescribed gains. This is achieved via a variational formulation, of the form

$$\mathbf{x}^* = \underset{\mathbf{x}\in\mathbb{C}^L}{\arg\min} \quad \|\mathscr{V}_{\boldsymbol{g}}\mathbf{x} - \mathscr{V}_{\boldsymbol{g}}\boldsymbol{z}\|^2_{\overline{\Omega}} + \sum_{p=1}^{P} \lambda_p \|\mathscr{V}_{\boldsymbol{g}}\mathbf{x}\|^2_{\Omega_p} \ , \tag{1}$$

where $\boldsymbol{z} \in \mathbb{C}^L$ is the input signal, $\mathscr{V}_{\boldsymbol{g}} : \mathbb{C}^L \to \Lambda$ is a linear time-frequency transform (see below for notations), $\Omega_p \subset \Lambda$, $p = 1, \dots P$ are the regions of interest in the time-frequency plane Λ, and the $\lambda_p \in \mathbb{R}^*_+$ are parameters that control the tradeoff between the various terms in (1). $\|\cdot\|$ is the usual Frobenius norm on the time-frequency space Λ, and $\|\cdot\|_\Omega$ denotes its restriction to a given region Ω.

The quadratic nature of the objective function naturally leads to a linear system, whose closed-form solution reads (see [9] for details)

$$\mathbf{x}^* = \boldsymbol{z} - \left(\mathrm{I} + \sum_{p=1}^{P} (1-\lambda_p) \mathfrak{M}_{\Omega_p} \right)^{-1} \sum_{p=1}^{p} \lambda_p \mathfrak{M}_{\Omega_p} \boldsymbol{z} \ , \tag{2}$$

which can involve high dimensional linear system for large signals. In [9], dimension reduction techniques were proposed to handle the problem and use a spectral approach that exploits time-frequency localization properties. However, the formulation of [9] involves a L-dimensional problem, which may involve regions of the time-frequency plane quite far away from Ω and do not significantly influence the solution.

The approach can be developed for any linear time-frequency transform, but in the present paper we will limit to the discrete Gabor transform (DGT) defined as follows (we refer to [9] for more details and notations, and to [10, 11] for numerical implementations we use in this work). Let a, b be two divisors of L, and set $M = L/b$ and $N = L/a$. The discrete time-frequency space is denoted by $\Lambda = \mathbb{Z}_M \times Z_N$. For any $\mathbf{x} \in \mathbb{C}^L$, its DGT $\mathscr{V}_{\boldsymbol{g}} \in \ell^2(\Lambda) = \mathbb{C}^{M\times N}$ is defined by

$$\mathscr{V}_{\boldsymbol{g}}\mathbf{x}[m,n] = \langle \mathbf{x}, \boldsymbol{g}_{mn} \rangle = \sum_{\ell=0}^{L-1} \mathbf{x}[\ell] \overline{\boldsymbol{g}}[\ell - na] e^{-2i\pi m\ell/M} \quad , \quad (m,n) \in \Lambda \ , \tag{3}$$

where the $\boldsymbol{g}_{mn} \in \mathbb{C}^L$, called Gabor atoms, are obtained from $\boldsymbol{g}$ by time-frequency translations, i.e. $\boldsymbol{g}_{mn}[\ell] = e^{2i\pi m\ell/M} \boldsymbol{g}[\ell - na]$. For convenience we introduce the time-frequency shift operators π_{mn} such that $\boldsymbol{g}_{mn} = \pi_{mn}\boldsymbol{g}$. These operators satisfy the composition rule $\pi_{mn}\pi_{m'n'} = e^{-2i\pi m'na/M} \pi_{m+m' \ n+n'}$, and the adjoint operator reads $\pi^*_{mn} = e^{-2i\pi mna/M} \pi_{-m \ -n}$.

Given $\mathbf{M} \in \mathbb{C}^{M\times N}$, the corresponding *Gabor multiplier* is the linear operator $\mathfrak{M}_{\mathbf{M}} : \mathbb{C}^L \to \mathbb{C}^L$ given by

$$\mathfrak{M}_{\mathbf{M}} = \mathscr{V}^*_{\boldsymbol{g}} \mathbf{M} \mathscr{V}_{\boldsymbol{g}} \ , \tag{4}$$

where by abuse of notation we have denoted by $\mathbf{M}$ the operator of pointwise multiplication with $\mathbf{M}$. $\mathbf{M}$ is called time-frequency mask, or upper symbol, of $\mathfrak{M}_{\mathbf{M}}$. When $\mathbf{M}$ is the indicator function of a subset $\Omega \subset \Lambda$ we will use the notation $\mathfrak{M}_\Omega$. Elementary properties of Gabor multipliers can be found in [12]. Among these, the approach of [9] relies strongly on the fact that for real valued masks, corresponding Gabor multipliers are self-adjoint, and their spectrum can be controlled under suitable assumptions on the window $\boldsymbol{g}$.

The closed form solution of the problem (1) can be expressed in terms of Gabor multipliers, and will appear as a special case of the solution given below, we thus refrain to reproduce it in this section.

2.2 Local TFF

In this section, we are interested in the estimation of a part of a locally degraded signal. We define an envelope around the masked region, and formulate LTFF from the newly defined regions.

2.2.1 Determination of the time-frequency regions of interest

Let $\varepsilon > 0$ be a fixed tolerance parameter. For each sub-region Ω_p, we define the *influence envelope* Ω_p^ε of Ω_p as follows:

$$\Omega_p^\varepsilon = \left\{ (m,n) \in \Lambda : \exists\, (m',n') \in \Omega_p, |\langle \boldsymbol{g}_{mn}, \boldsymbol{g}_{m'n'} \rangle|^2 \geq \varepsilon \right\} \tag{5}$$

The set Ω_p^ε consists in the time-frequency points where the corresponding atoms "communicate" with those in the masked region Ω_p, and therefore depends on the window $\boldsymbol{g}$ and the sampling parameters. Notice that

$$\langle \boldsymbol{g}_{mn}, \boldsymbol{g}_{m'n'} \rangle = \langle \pi_{m'n'}^* \pi_{mn} \boldsymbol{g}, \boldsymbol{g} \rangle = e^{2i\pi(m-m')n'a/M} \langle \pi_{m-m'\ n-n'} \boldsymbol{g}, \boldsymbol{g} \rangle = e^{2i\pi(m-m')n'a/M} \mathscr{A}_{\boldsymbol{g}}[m-m', n-n'] \ , \tag{6}$$

$\mathscr{A}_{\boldsymbol{g}}$ being the ambiguity function of the window $\boldsymbol{g}$: $\mathscr{A}_{\boldsymbol{g}}[m,n] = \langle \pi_{mn} \boldsymbol{g}, \boldsymbol{g} \rangle$. Therefore the ambiguity function of the analysis window $\boldsymbol{g}$ is used as the selection criterion. We also denote by

$$\Delta_p = \Omega_p^\varepsilon \backslash \Omega_p \ , \qquad \Delta = \bigcup_p \Delta_p \ , \qquad \Gamma = \overline{\Omega} \backslash \Delta \tag{7}$$

respectively the complementary region of Ω_p in Ω_p^ε, the union of these complementary regions and the complementary region of Δ in $\overline{\Omega}$, and $\overline{\Omega} = \Lambda \setminus \left(\bigcup_p \Omega_p \right)$.

We will also need the projection of the envelope Ω_p^ε onto the time domain, which is the interval obtained as follows:

$$I_p = [a n_{\min}(p), a n_{\max}(p)], \tag{8}$$

where $n_{\min}(p) = \min \left\{ n \mid \exists m \, , (m,n) \in \Omega_p^\varepsilon \right\}$ and $n_{\max}(p) = \max \left\{ n \mid \exists m \, , (m,n) \in \Omega_p^\varepsilon \right\}$ are respectively the minimum and maximum time indices in the time-frequency envelope Ω_p^ε (we recall that a is the time sampling step, i.e. the hop size).

2.2.2 Local TFF formulation

Similarly to TFF, and using the above notations, we formulate local TFF as follows:

$$\mathbf{x}^* = \underset{\mathbf{x} \in \mathbb{C}^L}{\arg\min} \quad \sum_{p=1}^{P} \| \mathscr{V}_{\boldsymbol{g}} \mathbf{x} - \mathscr{V}_{\boldsymbol{g}} \boldsymbol{z} \|_{\Delta_p}^2 + \sum_{p=1}^{P} \lambda_p \| \mathscr{V}_{\boldsymbol{g}} \mathbf{x} \|_{\Omega_p}^2 + \| \mathscr{V}_{\boldsymbol{g}} \mathbf{x} - \mathscr{V}_{\boldsymbol{g}} \boldsymbol{z} \|_{\Gamma}^2 \ , \tag{9}$$

In this formulation, we keep the part of the signal that is not masked (terms 1 and 3) and control the energy within each sub-region Ω_p (term 2) Note that, at this point, the reconstructed signal has length L. The following resolution will make the concept of "local" more clear. By setting the gradient of the objective function in (1) equal to zero, we obtain the following linear system:

$$\left[\mathfrak{M}_\Gamma + \sum_{p=1}^{P} \left(\mathfrak{M}_{\Delta_p} + \lambda_p \mathfrak{M}_{\Omega_p} \right) \right] \mathbf{x} = \left[\mathfrak{M}_\Gamma + \sum_{p=1}^{P} \mathfrak{M}_{\Delta_p} \right] \boldsymbol{z} \ , \tag{10}$$

which we now approximate as a family of smaller dimensional problems.

For all $q = 1, \ldots P$, denote by 1_q the indicator function of I_q. Assuming that the intervals I_q are disjoint $\cap_{q=1}^P I_q = \emptyset$, we have

$$\mathbf{x} = \sum_{q=1}^{P} 1_q \mathbf{x} + 1_J \mathbf{x}, \tag{11}$$

where 1_J the complementary of $\cup_{q=1}^{P} I_q$. The linear system becomes (10):

$$\left[\sum_p \sum_q \left(\mathfrak{M}_{\Delta_p} + \lambda_p \mathfrak{M}_{\Omega_p}\right) 1_q + \sum_q \mathfrak{M}_\Gamma 1_q\right] \mathbf{x} = \left[\sum_p \sum_q \mathfrak{M}_{\Omega_p} 1_q + \sum_q \mathfrak{M}_\Gamma 1_q\right] \boldsymbol{z}$$

Assuming that the non-diagonal terms in the sums can be neglected, i.e. that

$$\left\| \left(\mathfrak{M}_{\Delta_p} + \lambda_p \mathfrak{M}_{\Omega_p}\right) 1_q \right\|, \quad \left\| \mathfrak{M}_{\Omega_p} 1_q \right\|$$

are small enough for all $q \neq p$, and

$$\left\| \mathfrak{M}_\Gamma 1_q \right\|$$

are small enough for all q, we end up with

$$\left[\mathfrak{M}_{\Delta_p} + \lambda_p \mathfrak{M}_{\Omega_p}\right] \mathbf{x}_p = \mathfrak{M}_{\Omega_p} \boldsymbol{z}_p \ , \tag{12}$$

where we have set $\mathbf{x}_p = 1_p \mathbf{x}$. The operator $\mathfrak{M}_{\Delta_p} + \lambda_p \mathfrak{M}_{\Omega_p}$ is in fact a Gabor multiplier associated to a constant mask $\mathbf{M} = 1_{\Delta_p} + \lambda_p 1_{\Omega_p}$, where 1_{Δ_p} (respectively 1_{Ω_p}) is the indicator function of the subregion Ω_p (respectively Δ_p). If $\lambda_p > 0$ for all p, then the smallest value of the mask $\mathbf{M}$ is strictly positive, so the mask is said to be semi-normalized [1], which implies invertibility (see Proposition 3.7 in [13]). From now on, we assume that $\lambda_p > 0$ for all p. The solution (12) is then written :

$$\mathbf{x}_p = \left[\mathfrak{M}_{\Delta_p} + \lambda_p \mathfrak{M}_{\Omega_p}\right]^{-1} \mathfrak{M}_{\Omega_p} \boldsymbol{z}_p \tag{13}$$

Thus, for each sub-region p, the masked time domain signal is reconstructed. In this formula we have reduced the dimension of the problem. From a Gabor multiplier, initially of dimension L, we pass to a multiplier in the dimension of the masked region which is much smaller.

3 Experiments

We illustrate the approach on a (single) synthetic mixture of two real audio signals.We first describe the signals, but we do not recall the actions of Gabor multipliers already widely discussed in [9]. We also consider the case where $P = 1$, i.e. a single masked region.

3.1 Experimental setting

We consider two audio signals sampled at 8 kHz of length 16384 (about 2 seconds). The signal of interest is a car engine noise and the perturbation signal is the song of a bird. As mentioned in the previous sections, the signal of interest has a broadband spectrogram (i.e., with energy spread all over the time-frequency plane), while the perturbation signal has its energy well localized in the time-frequency plane. The Gabor transform for each of these signals is calculated with a Gauss window of length 256, the time-frequency lattice parameters are set to $a = 32$ and $b = 512$, generating a 513×256 time-frequency matrix. The observation is a linear combinations of these two signals, as shown in Fig 1 (left). The corresponding binary mask is on the right. The goal is to filter the bird song from the mixture. We construct the Ω_p^ε region as described in section 2.2.1. The value of ε here is 10^{-6}. The Fig 2 shows the masked Ω_p region (in dark yellow) as well as the Ω_p^ε region (in light yellow). The corresponding time interval is $I_p = [47\ 127]$.

We then restrict the frequency time plane of dimension of size 513×256 to 513×80. We solve TFF from this reduced time-frequency plane. The time domain signal to be reconstructed corresponds only to the time domain signal which is in the Ω_p region and and is of length 1600 here. The closed-form solution (12) depends on the regularization parameter $\lambda_p = \lambda > 0$ which is adjusted using the strategy presented in [14]: the optimal value of λ is chosen as the one for which the energy of the reconstructed signal in the region Ω_p corresponds to a given target energy E. Here, the energy E was chosen roughly by hand. In this example, the optimal value of λ is 10^{-3}.

[1] A sequence $\mathbf{M} = (\mathbf{M}[n])_{n>1}$ is said to be semi-normalized if there exist a and b such that $0 < a \leq |\mathbf{M}[n]| \leq b < \infty$ for all $n \in \mathbb{N}$.

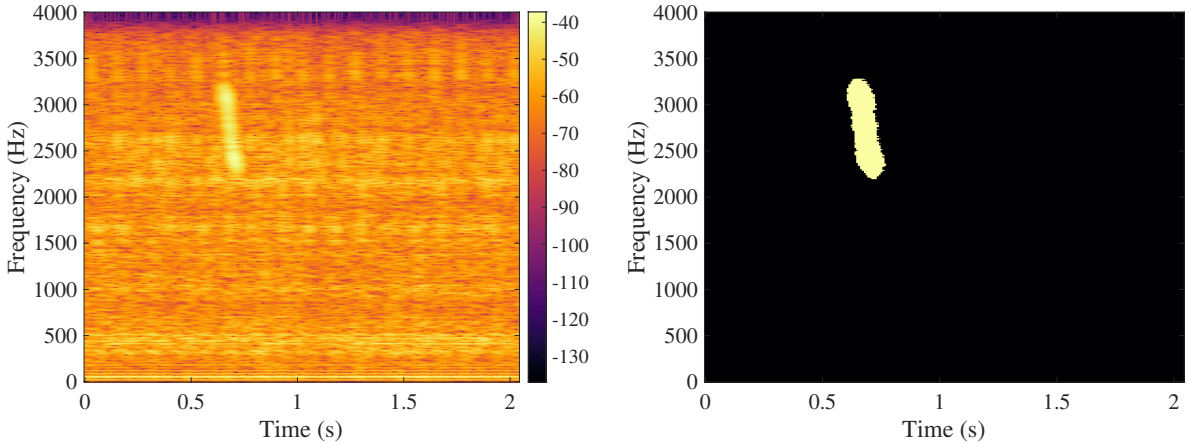


Figure 1. Left: Spectrogram of the mixture of the engine noise of a car (energy spread everywhere in the time-frequency plane) and of a bird "cuicui" (energy well localized - dark yellow area). Right: binary mask constructed from the spectrogram of two sources as in [9]

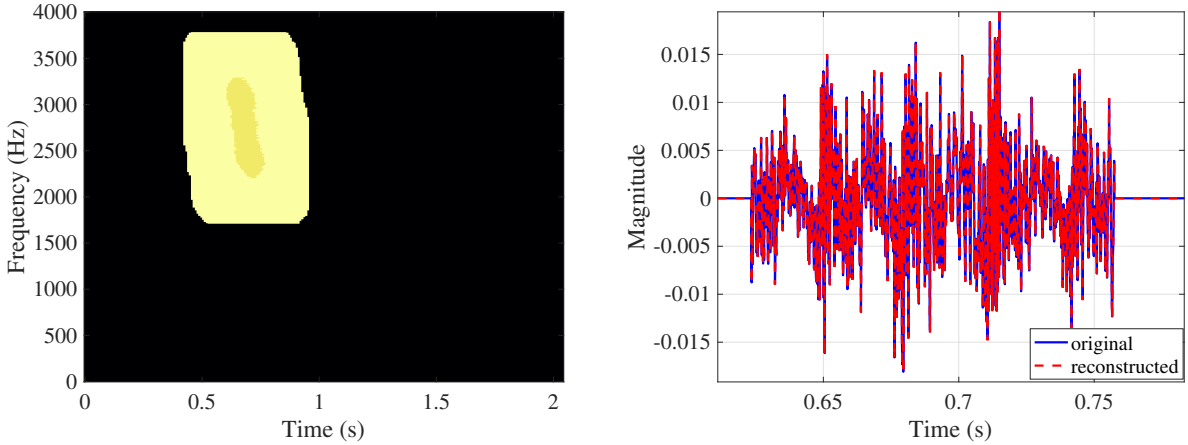


Figure 2. Left: Illustration of Ω_p and Ω_p^ε regions in the case of a single region. The value of e is 10^{-6}. Right: a zoom on reconstruction of the part of the signal of interest masked by the bird song.

We quantitatively evaluate the quality of the reconstruction, via the source-to-distortion ratio (SDR) [15] expressed in decibel by

$$\mathrm{SDR}\left(\mathbf{x}_p, \mathbf{x}_p^{ref}\right) = 20\log_{10}\left(\frac{\|\mathbf{x}_p^{ref}\|}{\|\mathbf{x}_p - \mathbf{x}_p^{ref}\|}\right), \tag{14}$$

where $\mathbf{x}_p^{ref}$ is the reference signal. The right panel of Figure 2 shows the reconstruction of the part of the car engine noise signal masked by the bird song in red. We can see that on this simple example, LTFF reconstructs almost perfectly the missing part of the signal with SDR $= 40$ dB. This experiment shows that LTFF could lead to satisfactory reconstruction results in the case of several regions P >1. Moreover, LTFF could solve such problems in high dimension since it has fast computation time.

4 Ongoing work

We present a novel method for performing local time-frequency fading in this paper. Because it is limited to a neighborhood of the masked region, this method can handle longer signals. However, the obtained theoretical

results are based on assumptions concerning a control on the norm of the sum of the two Gabor multipliers that we have not presented here. As part of this work, we will establish more rigorous proof results. From an experimental point of view, we have presented one example to illustrate the idea of our work. In the rest of our work, we will extend these experiments to the case where we have $P > 1$ regions and also to signals sampled at 44.1 kHz. We will also compare the results of reconstructions obtained with TFF as well as the computation times. The experiments will then be extended to a larger class of signals by automating the code. Finally, the combination of TFF and LTFF may result in a novel source separation method.

References

[1] J. O. Smith, *Introduction to Digital Filters: With Audio Applications*, ser. Music signal processing series. W3K, 2007. [Online]. Available: https://books.google.fr/books?id=pC1iCQUAsHEC

[2] G. F. Margrave, P. C. Gibson, J. P. Grossman, D. C. Henley, V. Iliescu, and M. P. Lamoureux, "The Gabor transform, pseudodifferential operators, and seismic deconvolution," vol. 12, pp. 43–55, 2005.

[3] P. Lander and E. J. Berbari, "Enhanced ensemble averaging using the time-frequency plane," in *IEEE-SP Proc. Int. Symp. on Time-Freq. and Time-Scale Analysis*, 1994, pp. 241–243.

[4] G. F. Boudreaux-Bartels and T. W. Parks, "Time-varying filtering and signal estimation using Wigner distribution synthesis techniques," vol. 34, no. 3, pp. 442–451, 1986.

[5] F. Hlawatsch, G. Matz, H. Kirchauer, and W. Kozek, "Time-frequency formulation, design, and implementation of time-varying optimal filters for signal estimation," vol. 48, no. 5, pp. 1417–1432, 2000.

[6] L. Stankovic, "On the time-frequency analysis based filtering," vol. 55, no. 5, pp. 216–225, May 2000. [Online]. Available: https://doi.org/10.1007/BF02994785

[7] D. Gabor, "Theory of communication. part 1: The analysis of information," *Journal of the Institution of Electrical Engineers - Part III: Radio and Communication Engineering*, vol. 93, no. 26, pp. 429–441, Nov. 1946.

[8] M. R. Portnoff, "Time-frequency representation of digital signals and systems based on short-time Fourier analysis," vol. 28, no. 1, pp. 55–69, 1980.

[9] A. M. Krémé, V. Emiya, C. Chaux, and B. Torrésani, "Time-frequency fading algorithms based on Gabor multipliers," *IEEE Journal of Selected Topics in Signal Processing*, vol. 15, no. 1, pp. 65–77, Jan 2021.

[10] P. Soendergaard, B. Torrésani, and P. Balazs, "The linear time frequency analysis toolbox," *International Journal of Wavelets and Multiresolution Information Processing*, vol. 10, no. 4, pp. 1 250 032–1 – 1 250 032–27, 2012.

[11] Z. Průša, P. L. Søndergaard, N. Holighaus, C. Wiesmeyr, and P. Balazs, "The Large Time-Frequency Analysis Toolbox 2.0," in *Sound, Music, and Motion*, ser. LNCS. Springer International Publishing, 2014, pp. 419–442.

[12] H. G. Feichtinger and K. Nowak, "A first survey of Gabor multipliers," in *Advances in Gabor Analysis*, H. G. Feichtinger and T. Strohmer, Eds. Birkhaüser, 2002, pp. 99–128.

[13] D. T. Stoeva and P. Balazs, "A survey on the unconditional convergence and the invertibility of multipliers with implementation," in *Sampling – Theory and Applications (A Centennial Celebration of Claude Shannon)*, M. R. S. Casey, K. Okoudjou and B. Sadler, Eds. Springer, 2020, to appear, preprint arXiv:1803.00415.

[14] A. M. Krémé, V. Emiya, C. Chaux, and B. Torrésani, "Filtering out time-frequency areas using Gabor multipliers," 2020, pp. 5790–5794.

[15] E. Vincent, R. Gribonval, and C. Févotte, "Performance measurement in blind audio source separation," vol. 14, no. 4, pp. 1462–1469, Jul. 2006.

ICA 2022
24th INTERNATIONAL CONGRESS ON ACOUSTICS
October 24(Mon) - 28(Fri), 2022 Gyeongju, Korea

PROCEEDINGS of the
24th International Congress on Acoustics

October 24 to 28, 2022 in Gyeongju, Korea

ABS-0380

Scattering at the angles of polyhedral rooms: Application to stress-energy tensor conservation in Riemannian spaces

Jean-Dominique POLACK[(1)], Aidan MEACHAM[(2)], Roland BADEAU[(3)], Jean-Christophe VALIERE[(4)]

[(1)]Institut D'Alembert, Sorbonne Université, France, jean-dominique.polack@sorbonne-universite.fr

[(2)]Institut D'Alembert, Sorbonne Université, France, aidan@lam.jussieu.fr

[(3)]LTCI, TelecomParis, France, roland.badeau@telecom-paris.fr

[(4)]Institut PPrime, Université de Poitiers, France, jean.christophe.valiere@univ-poitiers.fr

ABSTRACT

Riemannian spaces with negative curvature constitute the proper setting for the distribution of images created by irregular polyhedral rooms with obtuse angles. The crucial parameter is the excess angle that arises around specific edges, called hinges, when first and second order images are considered, as it pilots the metric tensor of the space and all its geometrical properties. With the use of these geometrical properties, and complementing them with the uncertainty principle, we describe the scattering of wave packets around dihedral angles: it is proportional to the excess angle, and is best described in terms of the conservation of the stress-energy tensor. The basic elements for computing the scattering are given.

Keywords: Riemannian geometry, Polyhedral rooms, Scattering, Stress-energy tensor

1 INTRODUCTION

In a previous paper [1], we showed that the same mirroring technique as known for rectangular rooms can be applied to polygonal and polyhedral rooms of arbitrary shapes, leading to the tessellation of a Riemannian space with negative curvature. We were then able to show that the number of image sources increases exponentially with layer order, building a bridge between rooms with flat walls and generic mixing rooms with partially curved walls.

In the present paper, we take a further look at the implications of this tessellation, introducing the wave nature of the sound field in a room and the conservation of its energy and intensity, in order to explain scattering at corner and edges, while keeping mathematical complexity at minimum.

2 SCATTERING ON NON RECTANGULAR DIHEDRAL ANGLES

The proper setting for computing scattering on non rectangular dihedral angles is Riemannian geometry. We therefore first expose the basic principles of this geometry.

2.1 Riemannian geometry

We consider an n-dimensional space with its positive-definite metric tensor g_{ij} and the volume element $dV = \sqrt{g}dx^1 \dots dx^n$, where $g = \det g_{ij}$ is positive [2]. The infinitesimal distance element is given by:

$$ds^2 = g_{ij}dx^i dx^j \tag{1}$$

and we note g^{ij} the inverse matrix of g_{ij}. ∇_i is the covariant derivation with respect to x^i, which differs from the usual partial derivation ∂_i in a way that depends on the tensor rank. For example, for a function Φ:

$$\nabla_j \Phi = \partial_j \Phi = \Phi_j \tag{2}$$

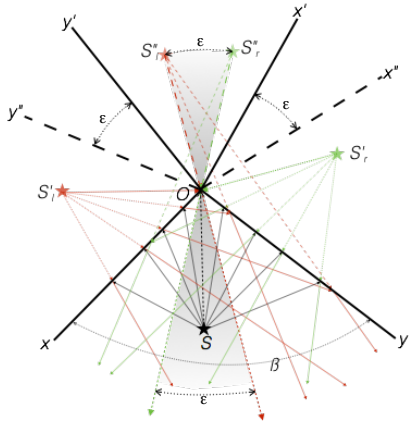


Figure 1. Reflection and scattering of sound rays on obtuse angle β. ε is the excess angle, since second order image angles overlap by ε.

but $\nabla_j \Phi_i = \partial_j \Phi_i - \Gamma^k_{ji} \Phi_k$ and $\nabla_j X^i = \partial_j X^i + \Gamma^i_{jk} X^k$, where X^i are the (contravariant) components of vector X and Γ^k_{ji} the Christoffel symbols linked to the derivatives of the elements of the metric tensor g_{ij}:

$$\Gamma^k_{ji} = \frac{1}{2} g^{kl} \left(\partial_j g_{il} + \partial_i g_{lj} - \partial_l g_{ji} \right) \tag{3}$$

Note that, unlike ordinary differentiations, covariant derivations do not commute.

2.2 Images rooms and obtuse angles

We consider the obtuse angle β of Figure 1 in a 2-dimensional Euclidean space. A sound source S (black star) emitting inside the angle emits rays in all directions. Some rays impinge on the left arm Ox of the angle and are reflected (red arrows). As the position of impact moves clockwise toward the apex, the reflected ray gradually moves upwards and eventually hits the right arm on which it is reflected once more. Finally, the ray impacts the apex of the angle (black upwards broken-line arrow).

In a similar fashion, some rays will impinge on the right arm Oy and be reflected (green arrows). As the position of impact moves anticlockwise toward the apex, the reflected ray gradually moves upwards and eventually hits the left arm on which it is reflected once more. Despite the continuity of the impinging rays around the apex, there is no continuity of the reflected rays, and this creates scattering.

In order to visualise the scattering, one needs to consider the images of the sound source by reflection on the two arms of the angle. Let's call S'_l the image of the source on the left arm (red star), and S'_r the image on the right arm (green star); S''_l the left-most second order image (dim red star), and S''_r the right-most second order image (dim green star). Reflected rays on the arms of the angle are first emitted from the first order image sources S'_l and S'_r, then from the second order sources S''_l and S''_r when the reflected rays hit the opposite arm, until the rays emitted from the first-order image sources reach the apex (red and green dotted-line arrows). In that position, the rays emitted from the second order image sources do not coincide in direction, since they are emitted from two different image sources at angle ε with respect to the apex. Scattering therefore comes in to *fill the gap* between these two directions, and in fact beyond them. In other words, one must consider a continuum of image sources along the sector between S''_l and S''_r (grey sector), that is, one must rotate the second order image angle by ε from position $y''0x'$ to position $y'0x''$.

In fact, when rays rotate *clockwise* around the original source S, the reflected rays rotate *anticlockwise* around the first order source S''_l, and *clockwise* around the second order source S''_r. So, when the secondary source moves *clockwise* from S''_l to S''_r on Figure 1, the diffracted rays rotate *clockwise* around the apex, thus filling the grey sector with continuity of rotations at its boundaries.

In order to make the second order images coincide, one needs to embed Figure 1 in a 3-dimensional space

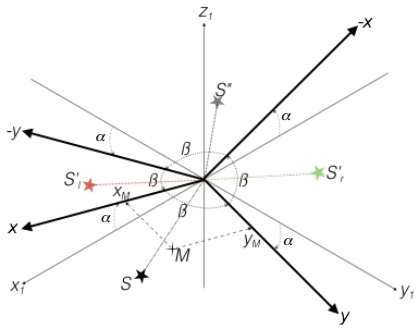


Figure 2. Embedding scattering on obtuse angle in 3-dimensional space. Angles α are vertical and measure deviations of angle arms from horizontal plane. Note that the two second order image sources coalesce in one single image source.

as in Figure 2. We call x_1, y_1, and z_1 the three Cartesian coordinates, and keep notations Ox and Oy for the arms of the original flat angular sector, which is now slanted so that angle β exactly projects on a right angle. As a consequence, Ox is elevated by angle α above Ox_1 and Oy is lowered by angle α below Oy_1; similarly, $O(-x)$ is elevated by angle α above $O(-x_1)$ and $O(-y)$ is lowered by angle α below $O(-y_1)$, so that the apex angle remains equal to β. In such a way, we obtain a *locally flat* space where rays are free to cross the borders between subsequent angular sectors without changing their direction.

2.3 Metric for obtuse angles

When the angle α is not null in Figure 2, that is, when $\beta > \pi/2$, the position of any point M in the system is given by its coordinates x and y, that are no longer orthogonal. In order to compute the corresponding infinitesimal distance element, one must project coordinates x and y on the Ox_1y_1 plane, then compute the vertical coordinate with equation:

$$z_1 = \tan\alpha(|\,x_1\,| - |\,y_1\,|) \tag{4}$$

valid for the four sectors of the system. With the convention $\mathrm{sgn}(0) = 0$, one obtains everywhere, even on the arms of the angles:

$$\begin{aligned} ds^2 &= dx_1^2 + dy_1^2 + dz_1^2 \\ &= (1+\tan^2\alpha)dx_1^2 + (1+\tan^2\alpha)dy_1^2 - 2\mathrm{sgn}(x)\mathrm{sgn}(y)\tan^2\alpha dx_1 dy_1 \end{aligned} \tag{5}$$

with $dx = \sqrt{1+\tan^2\alpha}dx_1$ and $dy = \sqrt{1+\tan^2\alpha}dy_1$, that is:

$$\begin{aligned} ds^2 &= dx^2 + dy^2 - 2\mathrm{sgn}(x)\mathrm{sgn}(y)\tfrac{\tan^2\alpha}{1+\tan^2\alpha}dxdy \\ &= dx^2 + dy^2 - 2\mathrm{sgn}(x)\mathrm{sgn}(y)\sin^2\alpha\, dxdy \end{aligned} \tag{6}$$

Simple projection on the plane Ox_1y_1 shows that $-\sin^2\alpha = \cos\beta$. Note that $\cos\beta < 0$ since $\pi/2 < \beta < \pi$ for obtuse angles. The last equation can therefore be written as:

$$ds^2 = dx^2 + dy^2 + 2\mathrm{sgn}(x)\mathrm{sgn}(y)\cos\beta\, dxdy \tag{7}$$

Using the embedding in the 3-dimensional space, distance elements ds are obviously continuous along a line that crosses one of the arms, implying that dx and dy are modified when the line crosses the arms. From the expression of ds^2, it is easy to deduce the metric tensor, its inverse, and its determinant:

$$g_{ij} = \begin{pmatrix} 1 & \mathrm{sgn}(x)\mathrm{sgn}(y)\cos\beta \\ \mathrm{sgn}(x)\mathrm{sgn}(y)\cos\beta & 1 \end{pmatrix} \tag{8}$$

$$g^{ij} = \frac{1}{\sin^2\beta}\begin{pmatrix} 1 & -\mathrm{sgn}(x)\mathrm{sgn}(y)\cos\beta \\ -\mathrm{sgn}(x)\mathrm{sgn}(y)\cos\beta & 1 \end{pmatrix} \tag{9}$$

$$g = \sin^2\beta \tag{10}$$

Note that g_{ij} and g^{ij} reduce to the identity matrix on the arms ($x = 0$ or $y = 0$) because of the convention $\mathrm{sgn}(0) = 0$, with $g = 1$.

Equation (3) then leads to the Christoffel symbols, that are all equal to 0, but for:

$$\begin{aligned} \Gamma^y_{xx} &= g^{yy}\partial_x g_{xy} = 2\delta(x)\mathrm{sgn}(y)\cos\beta \\ \Gamma^x_{yy} &= g^{xx}\partial_y g_{xy} = 2\mathrm{sgn}(x)\delta(y)\cos\beta \end{aligned} \tag{11}$$

where δ is the Dirac distribution, and where we have used the form for g^{xy} valid on the arms because $\delta(x)$, resp. $\delta(y)$, is null everywhere except on the arms $x = 0$, resp. $y = 0$;

It can further be shown [3] that the space has negative curvature at the apex O where it tends toward $4(\pi/2-\beta)$ for small values of $\pi/2-\beta$. Indeed, Regge [4] has shown that the curvature is equal to the total deficit angle at the apex $-\varepsilon = 2\pi - 4\beta$.

For a 3-dimensional obtuse dihedral angle, Fig 1 represents a projection of the rays on a plane perpendicular to the apical edge. But no equivalent of Fig 2 can be drawn, as the embedding takes place in a 4-dimensional space. Full computation shows that the local curvature remains null everywhere - flat space - except on the apical edge that Regge [4] calls *hinge*. Note that hinges are subspaces of co-dimension 2 where excess angle is non null.

3 SCATTERING

3.1 Time-space metric

In this Section, we now consider a 4-dimensional time-space with its metric tensor g_{ij} and the volume element $dV = \sqrt{|g|}dx^0\ldots dx^3$, where $g = \det g_{ij}$ [2]. Here, g is *negative* as the first eigenvalue of the metric tensor is negative and equal to $-c^2$, where c is the speed of sound: its eigenvector corresponds to the time direction dx^0. The infinitesimal distance element is still given by equation (1):

$$ds^2 = g_{ij}dx^i dx^j \tag{12}$$

Therefore, covariant derivations and Christoffel symbols are still defined as in Sec. 2.3. More precisely, we have:

$$g_{ij} = \begin{pmatrix} -c^2 & 0 & 0 & 0 \\ 0 & 1 & \mathrm{sgn}(x^1)\mathrm{sgn}(x^2)\cos\beta & 0 \\ 0 & \mathrm{sgn}(x^1)\mathrm{sgn}(x^2)\cos\beta & 1 & 0 \\ 0 & 0 & 0 & 1 \end{pmatrix} \tag{13}$$

$$g^{ij} = \begin{pmatrix} -c^{-2} & 0 & 0 & 0 \\ 0 & \frac{1}{\sin^2\beta} & -\frac{\mathrm{sgn}(x^1)\mathrm{sgn}(x^2)\cos\beta}{\sin^2\beta} & 0 \\ 0 & -\frac{\mathrm{sgn}(x^1)\mathrm{sgn}(x^2)\cos\beta}{\sin^2\beta} & \frac{1}{\sin^2\beta} & 0 \\ 0 & 0 & 0 & 1 \end{pmatrix} \tag{14}$$

where β is one fourth of the total dihedral angle around the hinge, and with determinant $g = -c^2\sin^2\beta < 0$. g_{ij} and g^{ij} reduce to diagonal matrices on the arms, now denoted ($x^1 = 0$ and $x^2 = 0$), with all diagonal elements equal to 1 except $g_{00} = -c^2$ and $g^{00} = -c^{-2}$, and with $g = -c^2$. As for the Christoffel symbols, they are all

equal to 0, but for $\Gamma^2_{11} = 2\delta(x^1)\mathrm{sgn}(x^2)\cos\beta$ and $\Gamma^1_{22} = 2\mathrm{sgn}(x^1)\delta(x^2)\cos\beta$ (eq 11). It can be shown [3] that the time-space remains flat everywhere, except on the hinges, now given by the apical edges extended by the time laps.

3.2 Conservation of stress-energy tensor

The stress-energy tensor formalism was introduced into Acoustics by Morse and Ingard [5] in order to extend the wave equation by a set of conservation equations that are sum-upped in the conservation of the stress-energy tensor T^{ij}:

$$T^{ij} = \begin{pmatrix} T^{tt} & T^{tx} & T^{ty} & T^{tz} \\ T^{tx} & T^{xx} & T^{xy} & T^{xz} \\ T^{ty} & T^{xy} & T^{yy} & T^{yz} \\ T^{tz} & T^{xz} & T^{yz} & T^{zz} \end{pmatrix} \tag{15}$$

where T^{tt} is the total energy density; T^{tx}, T^{ty} and T^{tz} the sound intensity vector; and the remnant terms represent the spatial distribution of kinetic energy. Note that the stress-energy tensor is symmetrical.

The conservation of the stress-energy tensor can be written in terms of the covariant derivative of the stress-energy tensor as:

$$\nabla_i T^{ij} = \partial_i T^{ij} + \Gamma^i_{ik} T^{kj} + \Gamma^j_{ik} T^{ik} = 0 \tag{16}$$

that is ([2] p.54):

$$\frac{1}{\sqrt{|g|}} \partial_i (\sqrt{|g|} T^{ij}) + \Gamma^j_{ik} T^{ik} = 0 \tag{17}$$

or, after integration on a small 4-dimensional volume V with border ∂V:

$$\int_{\partial V} n_i T^{ij} dS + \int_V \Gamma^j_{ik} T^{ik} dV = 0 \tag{18}$$

In the last equation, n_i is the outgoing normal covector to the boundary, normalized by $n_i g^{ij} n_j = \pm 1$, with a negative sign for time boundaries.

With the form chosen for the metric tensor, the conservation of the stress-energy tensor reduces to:

$$\begin{aligned} \textstyle\int_{\partial V} n_i T^{i0} dS &= 0 \\ \textstyle\int_{\partial V} n_i T^{i1} dS &= -2\cos\beta \textstyle\int_V \mathrm{sgn}(x^1)\delta(x^2) T^{22} \sqrt{|g|} dx^0 dx^1 dx^2 dx^3 \\ \textstyle\int_{\partial V} n_i T^{i2} dS &= -2\cos\beta \textstyle\int_V \delta(x^1)\mathrm{sgn}(x^2) T^{11} \sqrt{|g|} dx^0 dx^1 dx^2 dx^3 \\ \textstyle\int_{\partial V} n_i T^{i3} dS &= 0 \end{aligned} \tag{19}$$

Note that the first line simply corresponds to the conservation of the total energy. For the two next lines, since $\cos\beta < 0$, when the stress-energy tensor crosses the arm Ox^2 of the angle, it receives a positive acceleration proportional to T^{22} in the x^1 direction; and when it crosses the arm Ox^1 of the angle, it receives a positive acceleration proportional to T^{11} in the x^2 direction; no acceleration occurs in the x^3 direction. The accelerations along the x^1 and x^2 directions, however, do not correspond to deviations of the direction of propagation since the space is flat everywhere but on the hinge. It only takes into account the change of coordinates across the arms of the angle.

3.3 Wave packets

Any ray issued from a sound source will have some thickness. This is simply due to the uncertainty principle (see for example [6]), which states that positions and directions cannot be both determined with infinite precision. Note that this is not the case with the geometrical constructions of the previous Sections, where positions and directions are simultaneously defined with infinite precision.

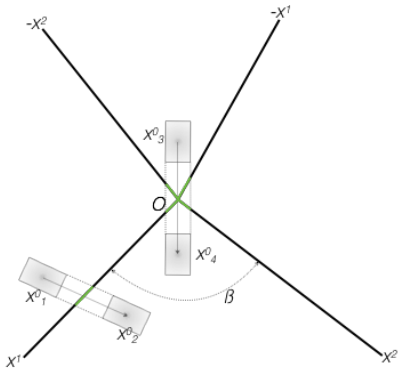


Figure 3. Wave packets crossing angle arms. Packet on the left crosses arm Ox^1 between x_1^0 and x_2^0; packet in the middle symmetrically crosses the two arms. Green lines mark the areas where deviations occur.

We now consider a wave packet, that is, a wave of finite extension, both along the direction of propagation and laterally, and we apply the stress-energy conservation equations (19) to it. We choose for integration a time interval over which the wave packet moves from one side of the angle arms to the other. Two cases are depicted in Figure 3.

The first wave packet is located in sector $(-x^2)Ox^1$ at time x_1^0. It is here defined by the projection of its distribution on the plane of Figure 3, where it is represented by a rectangle area with levels of grey proportional to the probability of presence of the wave packet. The size of the rectangle is chosen such that the components of the stress-energy tensor are negligible on its boundaries. As time increases, the wave packet moves at angle θ with respect to direction x^2 toward sector x^1Ox^2 in which it is located at time x_2^0. It crosses arm Ox^1 ($x^2=0$) in-between times x_1^0 and x_2^0, where it is deviated according to the second line of equation (19). In other words, the components of T^{ij} do not change, but for component T^{01}. Complete computation of the field [3] shows that the corresponding impulse exactly compensates for the change of coordinates, so that the wave packet keeps on travelling in its initial direction.

This is not the case for the second wave packet, located in sector $(-x^1)O(-x^2)$ at time x_3^0 and moving to sector x^1Ox^2 at time x_4^0. It symmetrically crosses the arms $x^1=0$ and $x^2=0$ on its way. Since the function sgn changes sign around the origin O, the negative deviation compensates for the positive one on each axis, and no deviations occurs. However, if a larger part of the packet passes on one side of the origin, some deviation occurs in proportion to the offset. This case is not represented in Figure 3.

In both cases, direct calculation shows that T^{00} does not change when crossing arm Ox^1, as expected for energy conservation.

3.4 Ray scattering

Instead of thickening the rays by considering wave packets, an alternative is to thicken the hinges by low-pass filtering the Christoffel symbols on the arms (equation 3), and to look at the geodesics in the vicinity of the hinges. Indeed, differential geometry is a high-frequency theory, that does not account for wave-like phenomena. As a consequence, rays have infinitesimal thickness and are not deviated by hinges, unless they cross them.

We therefore propose to replace, in the Christoffel symbols of equations (11), $\delta(x)$ by the approximation $\sin kx/\pi x$, the weak limit of which is known to be the Dirac delta function when the wave number k tends towards infinity; and the function $\mathrm{sgn}(x)$ by the integral $-1+\int_{-\infty}^{x}(\sin ku/\pi u)du$. We thus obtain:

$$\begin{aligned}\Gamma^y_{xx} &= \tfrac{\sin kx}{\pi x}\left[-1+2\int_{-\infty}^{x}\tfrac{\sin ku}{\pi u}du\right]\cos\beta\\ \Gamma^x_{yy} &= \left[-1+2\int_{-\infty}^{x}\tfrac{\sin ku}{\pi u}du\right]\tfrac{\sin ky}{\pi y}\cos\beta\end{aligned} \tag{20}$$

The crucial change introduced by these low-pass versions of the Christoffel symbols is the smooth and gradual transition from -1 to $+1$ that occurs across a hinge.

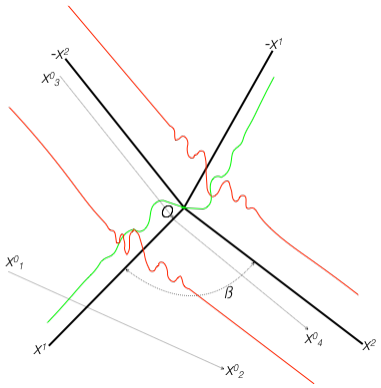


Figure 4. Ergodesics crossing angle arms. Geodesic x_1^0-x_2^0 crosses arm Ox^1 away from the apex and remains straight; geodesic x_3^0-x_4^0 crosses arm Ox^1 near the apex and is deflected. Green curve corresponds to low-pass sign function; red curves correspond to low-pass delta function.

In a Riemannian time-space, the equations of the geodesics are given by [2]:

$$\frac{dv^k}{d\tau} = -\Gamma^k_{ij} v^i v^j \tag{21}$$

where τ is the proper time, $v^i = dx^i/d\tau$ the velocity vector in direction x^i, and where $dv^k/d\tau$ is the acceleration in direction x^k In the present case, the only non-zero accelerations are therefore along x^1 when crossing the arm $x^2 = 0$, and along x^2 when crossing the arm $x^1 = 0$. We therefore obtain:

$$\begin{array}{ll} \frac{dv^1}{d\tau} & = -\cos\beta \frac{\sin kx}{\pi x} \left[-1 + 2\int_{-\infty}^{x} \frac{\sin ku}{\pi u} du\right] \left[v^2\right]^2 \\ \frac{dv^2}{d\tau} & = -\cos\beta \left[-1 + 2\int_{-\infty}^{x} \frac{\sin ku}{\pi u} du\right] \frac{\sin ky}{\pi y} \left[v^1\right]^2 \end{array} \tag{22}$$

As a consequence, a ray that crosses one of the arms far from the hinge carries on in its original direction - ray x_1^0-x_2^0 in Figure 4 - since the integral of the sinc-function is equal to 1: the total impulse in the neighbourhood of the arm just compensates for the coordinate changes. But a ray that crosses one of the arms near the hinge, at a distance less than π/k - ray x_3^0-x_4^0 in Figure 4 -, undergoes an impulse that does not fully compensate for the coordinate change, with less compensation the nearer it comes to the hinge. In the limit case where the ray crosses at the hinge, the impulse vanishes and the ray is deviated by half the excess angle.

4 CONCLUSIONS

We have presented a geometrical theory that naturally accounts for scattering on the boundaries of a room. It introduces Riemannian spaces with negative curvature, which constitute the proper setting for the distribution of images created by non-rectangular rooms with obtuse angles, that is, created by irregular polyhedra with a large enough number of faces. The crucial factor is the excess angle that arises around specific edges, called hinges, when first and second order images are considered, as it pilots the metric tensor of the space and all its geometrical properties, including its curvature.

Using the uncertainty principle, we were able to describe the scattering of wave packets around dihedral angles. The scattering is proportional to the excess angle, and can be described in terms of the stress-energy tensor, that is, in terms of energy conservation.

The present theory must now be developed to derive scattering coefficients from the distribution of hinges around a room. The excess angles are the main factors, complemented by the lengths of the hinges. But as shown in Sections 3.4, wave length also plays a rôle. Proper definition of scattering coefficients has long been missing for the application of the diffusion equation in Room Acoustics [7], despite some recent attempts [8].

There remains to introduce absorption in the present theory. Due to its geometrical nature, it cannot account for losses in its present form. The classical way to introduce absorption, which consider intensity flows inside the boundaries, cannot be used here without some adaptation. But accounting for losses should not proove difficult since absorption is easily described with the stress-energy tensor used in Sections 3.2 and 3.3, as shown in [9, 10].

REFERENCES

[1] Polack JD, Meacham A, Badeau R, Valière JC. Riemannian space tessellation with polyhedral room images. Proc 16th CFA; 11-15 April 2022; Marseille, France, 2022.

[2] Linet B. Notes de cours de relativité générale. Paris; 2004-5.

[3] Polack JD, Meacham A, Badeau R, Valière JC. Riemannian space tessellation with polyhedral room images. hal-03598258; 2022.

[4] Regge T. General Relativity without Coordinates. Nuovo Cimento. 1961;XIX:558-571.

[5] Morse PM, Ingard KU. Theoretical Acoustics. New York, USA; McGraw-Hill; 1968.

[6] Stephenson UM. An energetic Approach for the Simulation of Diffraction within Ray Tracing Based on the Uncertainty Relation. Acta Acust united Ac. 2010;96:516-535.

[7] Picaut J, Simon L, Polack JD. A mathematical model of diffuse sound field based on a diffusion equation. Acta Acust united Ac. 1997;83(4):614-621.

[8] Gül ZS. Exploration of room acoustics coupling in Hagia Sophia of Istanbul for its different states. J Acoust Soc Am., 2021;149(1):320-339.

[9] Dujourdy H, Pialot B, Toulemonde T, Polack JD. Energetic wave equation for modelling diffuse sound field - Applications to corridors. Acta Acust united Ac. 2017;103(3):480-491.

[10] Dujourdy H, Pialot B, Toulemonde T, Polack JD. Energetic wave equation for modelling diffuse sound field - Applications to open offices. Wave Motion. 2019;87:193-212.

ICA 2022
24th INTERNATIONAL CONGRESS ON ACOUSTICS
October 24(Mon) - 28(Fri), 2022 Gyeongju, Korea

PROCEEDINGS of the
24th International Congress on Acoustics

October 24 to 28, 2022 in Gyeongju, Korea

ABS-0565

Room shape reconstruction using acoustic super-resolution

Tom SPRUNCK[1,2], Yannick PRiVAT[1], Cédric FOY[3] and Antoine DELEFORGE[2]

[1]Université de Lorraine, CNRS, Inria, LORIA, F-54000 Nancy, France (firstname.name@inria.fr)

[2]IRMA, Université de Strasbourg, CNRS UMR 7501, 67084 Strasbourg, France (yannick.privat@unistra.fr)

[3]UMRAE, Cerema, Univ. Gustave Eiffel, Ifsttar, Strasbourg, 67035, France (cedric.foy@cerema.fr)

ABSTRACT

Room geometry reconstruction methods based on the image source model and room impulse response (RIR) measurements are still underdeveloped. Indeed, determining the 3D locations of the image sources is a difficult non-linear inverse problem in acoustics. The method presented here relies on super-resolution, a framework from the signal processing community. The fundamental objective is to reconstruct the locations and amplitudes of a linear combination of Dirac masses by using linear measurements. We consider here the linear operator mapping a weighted sum of 3D Dirac measures – modeling the image sources – to the corresponding discrete RIR. The reconstruction can be achieved by solving a relaxed convex problem in the space of Radon measures called BLASSO. Usual reconstruction guarantees do not directly apply here due to the singularity of the operator at each microphone position. We adapt and apply the Sliding Frank-Wolfe algorithm, which allows for an efficient numerical resolution of this problem. Experimental results on noisy synthetic data demonstrate the ability of the method to find the locations of hundreds of image sources in a variety of room configurations.

Keywords: Acoustic reflectors, room shape, sound field, super-resolution, convex optimization

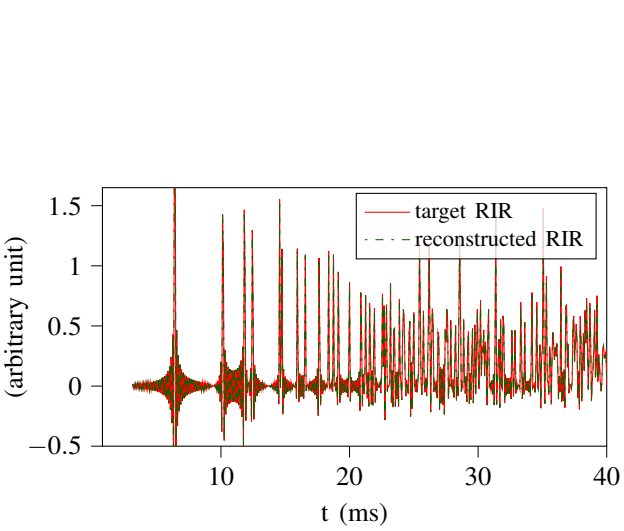
1 INTRODUCTION

The pressure field $p : \mathbb{R}^3 \times [0,\infty) \to \mathbb{R}$ resulting from a perfect omni-directional point source placed at a location $\boldsymbol{r}_0^{\text{src}} \in \mathbb{R}^3$ inside an empty room and emitting a perfect impulse obeys an inhomogeneous wave equation with complex boundary conditions. However, Allen and Berkley [1] showed that in the case of a rectangular room with rigid, perfectly specular walls this pair of partial differential equations is equivalent to the following free field wave equation:

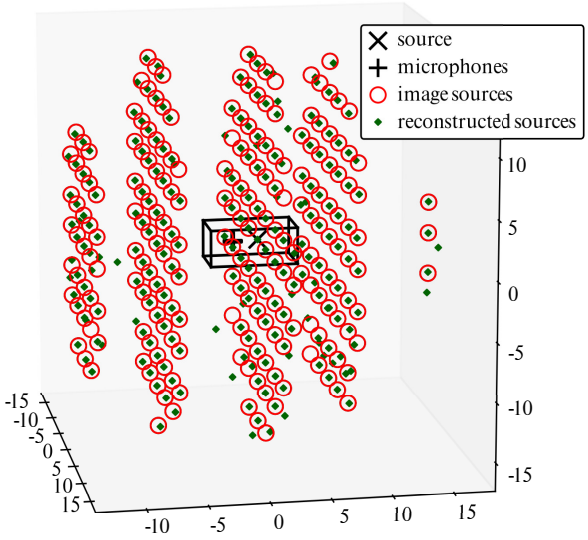
$$\frac{1}{c^2}\frac{\partial^2 p}{\partial t^2}(\boldsymbol{r},t) - \Delta p(\boldsymbol{r},t) = \sum_{k=0}^{+\infty} a_k \delta_{\boldsymbol{r}_k^{\text{src}}}(\boldsymbol{r})\,\delta_0(t). \tag{1}$$

The boundary conditions are removed by considering instead a source term composed by a sum of *image sources* $\delta_{\boldsymbol{r}_k^{\text{src}}}$ that simultaneously emit an impulse at the initial time $t = 0$. Each image source models a specular reflection path of the original impulse with regards to the walls of the room. Technically this equivalence only holds for perfectly reflective surfaces and $a_k = 1$, although it can be generalized by weighing images sources with coefficients $a_k \in [0,1]$ to account for a proportion of sound energy absorbed by the walls.

The image sources are constructed iteratively by applying to the original source a sequence of symmetries with respect to the walls of the room, thus the 3D locations of image sources contain the information necessary to find the dimensions of the room. However, reconstructing the locations $\boldsymbol{r}_k^{\text{src}}$ from punctual and discrete-time measurements of the sound field p (*i.e* a Room Impulse Response or RIR) remains a difficult inverse problem.



(a) Part of a RIR at one microphone



(b) 3D plot of the target and reconstructed sources

Figure 1. Simulated experiment: 32-channel spherical microphone array with diameter 16.8 cm, $f_s = 16$ kHz, $T_{max} = 50$ ms and no noise.

2 INVERSE PROBLEM

Equation (1) can be further generalized to an arbitrary source mass distribution ψ, yielding

$$\frac{1}{c^2}\frac{\partial^2}{\partial t^2}p(\boldsymbol{r},t) - \Delta p(\boldsymbol{r},t) = \psi(\boldsymbol{r})\delta_0(t), \tag{2}$$

where ψ belongs to the space $\mathscr{M}(\mathbb{R}^3)$ of *Radon measures*. Following a classical development, the general solution of equation (1) is given by a spatial convolution with a well known Green function:

$$p(\boldsymbol{r},t) = (G(\cdot,t) * \psi)(\boldsymbol{r}) = \int_{\boldsymbol{r}'\in\mathbb{R}^3} \frac{\delta(t - \|\boldsymbol{r}-\boldsymbol{r}'\|_2/c)}{4\pi\|\boldsymbol{r}-\boldsymbol{r}'\|_2}\psi(\boldsymbol{r}')d\boldsymbol{r}'. \tag{3}$$

The discrete multichannel RIR measured by M microphones placed at locations $\{\boldsymbol{r}_m^{\text{mic}}\}_{m\in[\![1,M]\!]}$ inside the room can then be expressed as

$$x_m[n] = (\kappa_m * p(\boldsymbol{r}_m^{\text{mic}},\cdot))(n/f_s),\ n \in [\![0,N-1]\!]. \tag{4}$$

Here $*$ denotes time-domain convolution, f_s is the microphones' sampling frequency and $\kappa_m : \mathbb{R} \to \mathbb{R}$ are time-domain filters that model the response of the source and the microphones. By combining this relation with equation (3) we obtain the complete expression of the discrete observation vector $\boldsymbol{x} \in \mathbb{R}^{MN}$ resulting from a source distribution ψ:

$$x_m[n] = \int_{\boldsymbol{r}\in\mathbb{R}^3} \gamma_{m,n}(\boldsymbol{r})d\psi(\boldsymbol{r}) = \langle \gamma_{m,n}, \psi\rangle \quad \text{where } \gamma_{m,n}(\boldsymbol{r}) \overset{\text{def}}{=} \frac{\kappa\left(n/f_s - \left\|\boldsymbol{r}_m^{\text{mic}} - \boldsymbol{r}\right\|_2/c\right)}{4\pi\left\|\boldsymbol{r}_m^{\text{mic}} - \boldsymbol{r}\right\|_2}. \tag{5}$$

This allows us to define a linear observation operator $\boldsymbol{\Gamma} : \mathscr{M}(\mathbb{R}^3) \to \mathbb{R}^{MN}$ that maps a source distribution ψ to its corresponding observation vector $\boldsymbol{x}$. We now can particularize (5) to the discrete image sources distribution $\psi_{\boldsymbol{a},\boldsymbol{r}^{\text{src}}}(\boldsymbol{r}) \overset{\text{def}}{=} \sum_{k=0}^{K} a_k \delta_{\boldsymbol{r}_k^{\text{src}}}(\boldsymbol{r})$ to get the measured RIR:

$$\boldsymbol{x} = \boldsymbol{\Gamma}\psi_{\boldsymbol{a},\boldsymbol{r}^{\text{src}}} = \sum_{k=0}^{K} a_k \boldsymbol{\gamma}(\boldsymbol{r}_k^{\text{src}}) = \left(\sum_{k=0}^{K} a_k \frac{\kappa_m\left(n/f_s - \left\|\boldsymbol{r}_m^{\text{mic}} - \boldsymbol{r}_k^{\text{src}}\right\|_2/c\right)}{4\pi\left\|\boldsymbol{r}_m^{\text{mic}} - \boldsymbol{r}_k^{\text{src}}\right\|_2}\right)_{m,n} \in \mathbb{R}^{MN}. \tag{6}$$

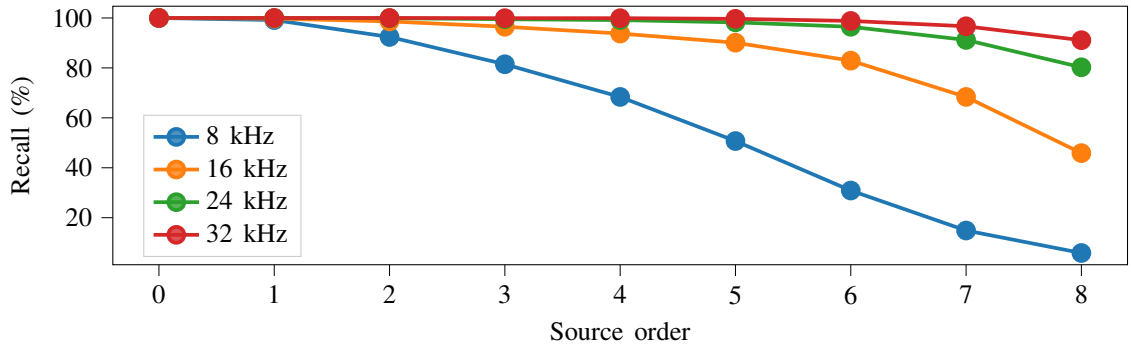


Figure 2. Recall in function of source order for varying sampling frequency for a 32-channel spherical microphone array with diameter 16.8 cm and no noise

Note that the infinite image source distribution can be accurately approximated by a finite number K of image sources as higher order image sources have a negligible impact on the measured RIR, due to repeated absorptions and increasing source-microphone distances.

Let $\mathscr{M}_+(\mathbb{R}^3) \subset \mathscr{M}(\mathbb{R}^3)$ denote the subset of sparse Radon measures of the form $\psi_{\boldsymbol{a},\boldsymbol{r}^{\text{src}}}$ with $K \in \mathbb{N}$, $\boldsymbol{a} \in \mathbb{R}_+^{K+1}$ and $\boldsymbol{r}^{\text{src}} \in (\mathbb{R}^3)^{K+1}$, *i.e.* measures that are finite positive combinations of spikes. The inverse problem of recovering the amplitudes and positions of these spikes given noisy observations $\boldsymbol{x}$ belongs to a general class of problems where the goal is to recover the continuous locations of a set of spikes given discrete linear observations over their measure [2, 4, 3, 5].

Rather than solving a non-convex optimization problem on the amplitudes and positions of the image sources, we follow the approach in [3] and consider a convex relaxation to the whole space of Radon measures (BLASSO):

$$\underset{\psi \in \mathscr{M}(\mathbb{R}^3)}{\operatorname{argmin}} \frac{1}{2} \|\boldsymbol{x} - \boldsymbol{\Gamma}\psi\|_2^2 + \lambda \|\psi\|_{\text{TV}}, \tag{7}$$

where $\lambda > 0$ is a regularization parameter.

Strictly speaking, $\boldsymbol{\Gamma}$ is not well defined because $\boldsymbol{\gamma}$ is singular at each microphone position. These singularities can be ignored by changing the integration domain in (5) to $\mathbb{R}^3_\varepsilon \overset{\text{def}}{=} \mathbb{R}^3 \setminus \cup_{m=1}^M B(\boldsymbol{r}_m^{\text{mic}}, \varepsilon)$ for a fixed $\varepsilon > 0$ and by only considering measures $\psi \in \mathscr{M}(\mathbb{R}^3_\varepsilon)$, without altering the convexity of the optimization problem.

3 NUMERICAL RESOLUTION AND RESULTS

In order to solve (7) numerically, we adapt the Sliding Frank-Wolfe algorithm proposed in [3], which is briefly reviewed below.

Let us denote by $\boldsymbol{a}^{(i)} \in \mathbb{R}_+^{Q_i}$ and $\boldsymbol{r}^{(i)} \in (\mathbb{R}^3)^{Q_i}$ the lists of Q_i spike amplitudes and positions estimated at iteration i, with $\boldsymbol{a}^{(0)} = \boldsymbol{r}^{(0)} = \emptyset$. At iteration $i+1$, the following four steps are performed:

- **Step 1:** A new spike location $\boldsymbol{r}_{Q_i+1}$ is first added to $\boldsymbol{r}^{(i+1)}$ by maximizing the following *dual*, non-convex objective based on the current residual $\boldsymbol{y}^{(i)} \overset{\text{def}}{=} \boldsymbol{x} - \boldsymbol{\Gamma}\psi_{\boldsymbol{a}^{(i)},\boldsymbol{r}^{(i)}}$:

$$\max_{\boldsymbol{r} \in \mathbb{R}^3} \eta^{(i)}(\boldsymbol{r}) \overset{\text{def}}{=} \left[\boldsymbol{\Gamma}^*(\boldsymbol{y}^{(i)})\right](\boldsymbol{r}) = \sum_{m,n} y_m^{(i)}[n] \gamma_{m,n}(\boldsymbol{r}) \tag{8}$$

  where $\boldsymbol{\Gamma}^*$ denotes the *Hermitian adjoint* of $\boldsymbol{\Gamma}$.

- **Step 2:** The whole list of amplitudes $\boldsymbol{a}^{(i+1)}$ is updated by minimizing the cost function in (7) over $\boldsymbol{a}$ only. This amounts to a classical non-negative LASSO convex optimization problem for which efficient solvers are available.

- **Step 3** (*Sliding*): The value of the cost function in (7) is further decreased by jointly refining all the values in $\boldsymbol{a}^{(i+1)}$ and $\boldsymbol{r}^{(i+1)}$ through non-convex local search.

• **Step 4:** The spikes whose amplitudes are lower than a threshold $\alpha_{\min}$ are removed from $\boldsymbol{a}^{(i+1)}$ and $\boldsymbol{r}^{(i+1)}$.

The main modification applied to the original algorithm concerns the first step, spike finding. Solving this maximization problem requires choosing an accurate initial guess for the optimization algorithm (BFGS). This is usually achieved by first solving the problem over a discrete grid covering the entire 3D search space, which is computationally intractable here. We instead use the time signals to compute an approximate time of arrival at each microphone. This allows us to reduce the search space to spheres centered around the microphones, which are consequently meshed with a finite grid. Step 3 is also only applied once at the end of the algorithm, as the large number of spikes to recover makes it computationally intensive.

We apply this algorithm to a set of 200 randomly generated rectangular rooms. We consider here a compact spherical array of 32 omni-directional microphones that all carry the same response, an ideal low-pass filter with cutting frequency $f_s/2$, *i.e* $\kappa_m = \kappa : t \mapsto \mathrm{sinc}(\pi f_s t)$. The source and array are randomly located in each room, with a minimum separating distance of 1 m from each other and to the walls. We apply operator $\boldsymbol{\Gamma}$ to the theoretical image sources distribution to generate the target RIR and add white Gaussian noise. All the RIRs are finally cut to last 50 ms. The code used to run the experiments is available at `https://github.com/Sprunckt/acoustic-sfw`.

Figure 2 shows an example of simulated RIR, the image sources found by the algorithm and the corresponding time signal for a given microphone. We perform an experimental study of the impact of noise, microphone array diameter and sampling frequency on the accuracy of the reconstruction. We observe that for a great enough sampling frequency and array diameter we recover over 90% of the observable image sources with an angular error lower than 2 °. All of the 200 original sources were correctly located, and nearly every first order source.

4 CONCLUSIONS

We introduced a new method to recover the continuous 3D positions and amplitudes of all audible image sources given the early part of a discrete-time multichannel room impulse response from a compact microphone array. Although there is room for improvement on the algorithmic side, simulated experiments suggest that under idealized conditions, namely, no noise, omni-directional point source and microphones with known responses and perfectly specular room boundaries the inverse problem is essentially solved. Further theoretical investigations are needed to understand the conditions under which existence, uniqueness and stability guarantees can be established for problem (7).

ACKNOWLEDGEMENTS

This work was made with the support of the French National Research Agency through project DENISE (ANR-20-CE48-0013).

REFERENCES

[1] J. B. Allen and D. A. Berkley. Image method for efficiently simulating small-room acoustics. *Journal of the Acoustical Society of America*, 65:943–950, 1976.

[2] E. J. Candès and C. Fernandez-Granda. Towards a mathematical theory of super-resolution. *Communications on pure and applied Mathematics*, 67(6):906–956, 2014.

[3] Q. Denoyelle, V. Duval, G. Peyré, and E. Soubies. The Sliding Frank-Wolfe Algorithm and its Application to Super-Resolution Microscopy. *Inverse Problems*, 2019.

[4] V. Duval and G. Peyré. Exact Support Recovery for Sparse Spikes Deconvolution. *Foundations of Computational Mathematics*, 15(5):1315–1355, 2015.

[5] Y. Traonmilin and J.-F. Aujol. The basins of attraction of the global minimizers of the non-convex sparse spike estimation problem. *Inverse Problems*, 36(4):045003, 2020.

ICA 2022
24th INTERNATIONAL CONGRESS ON ACOUSTICS
October 24(Mon) - 28(Fri), 2022 Gyeongju, Korea

PROCEEDINGS of the
24th International Congress on Acoustics

October 24 to 28, 2022 in Gyeongju, Korea

ABS-0567

Audio Inpainting

Peter BALAZS[(1)], Georg TAUBÖCK[(2)], Shristi RAJBAMSHI, Nicki HOLIGHAUS[(1)]

[(1)]Acoustics Research Institute, Austrian Academy of Sciences, Austria

[(2)]Institute of Telecommunications, TU Wien, Austria

ABSTRACT

The objective of audio inpainting is to conceal missing or heavily distorted segments in an audio signal. This is ideally done by reconstructing the original signal or, at least, by inferring a meaningful surrogate signal. We present here a novel approach applying sparse modeling in the time-frequency (TF) domain which was recently published.

In particular, we devise a dictionary learning technique which learns the dictionary from reliable parts around the gap with the goal to obtain a signal representation with improved TF sparsity. The presented method is based on a basis optimization technique that deforms a given Gabor frame such that the sparsity of the analysis coefficients of the resulting frame is maximized (with respect to a certain sparsity measure). Furthermore, we modify the SParse Audio INpainter (SPAIN) such that it is able to exploit the improved TF sparsity and—in turn—benefits from dictionary learning. As an alternative, we combine dictionary learning with weighted ℓ_1-minimization adapted for audio inpainting to compensate for the loss of energy within the gap after restoration. Our experiments demonstrate that the developed methods achieve significant gains in terms of signal-to-distortion ratio (SDR) and objective difference grade (ODG) compared with several state-of-the-art audio inpainting techniques.

Keywords: Audio inpainting, time-frequcny, Gabor dichtionary, compressive sensing, basis optimization, convex optimization, Alternating Direction Method of Multipliers (ADMM)

1 INTRODUCTION

Audio Inpainting [1] is a technique that fills missing or disturbed information in an audio signal. Usually, consecutive samples are considered - a "hole" or gap. Such techniques were first used in image processing - hence the name - and later were also applied to audio signals. Early methods exploiting sparsity in the time-frequency domain were only able to cover short holes, approximately up to 10 ms. Here, due to the quasi-stationary nature of sound, one can expect that an "interpolation" of the conditions before and after the gap will give very satisfying results. Hence, it is reasonable that the original signal can be recovered. We note that the LPC method from [2] has been applied successfully to this scenario.

For long gaps, above 100 ms, reconstruction of the true original signal is by no means feasible. The distribution of audio parameters will, most likely, change drastically in this period. Thus, one has to aim at a "decent" inpainting - meaning a perceptual or information-related reasonable fitting. Here let us mention the approach in [3], where a similarity graph - comparing the parts around the gaps to other parts of the signal - is used, or [4], based on generative neural networks.

In this contribution we focus on the intermediate case, i.e gaps between 10 and 100 ms, not covered by the methods mentioned above. We present the methodology introduced in [5] and [6]. The key ideas are the following: First, a time-frequency dictionary - a Gabor frame - is used with an optimization approach. Here, sparsity is not promoted in both directions, but rather only in the frequency domain, while simultaneously controlling the maximal values in the time domain. Optimization is performed using an Alternating Direction Method of Multipliers (ADMM) [7] solver. Alternatively, we perform weighted ℓ_1-minimization applying the Chambolle-Pock (CP) algorithm [8]. Both approaches avoid or at least reduce the energy loss problem. Secondly, we use

Gabor Parameters	Used Value
window g	*Hann* window
window length w_g	2800 samples ($\sim$64 ms)
hop size a	700 samples
number of modulations M	2800

Table 1. Gabor Parameters

a basis optimization technique to adapt the dictionary to our signal. Discussions with other researchers lead us to believe that the usage of perturbed Gabor atoms - instead of a completely "free", i.e unstructured, learned dictionary - seems to be the crucial step that facilitates the mehotd's success.

We will present the results of our algorithms. But, in the spirit of the special session "mathematical methods in acoustics", we further elaborate on some of the mathematical details.

2 SIMULATION AND RESULTS

In this section, we compare the audio inpainting performance of modified SPAIN combined with dictionary learning, (A-SPAIN-LEARNED. [5]), and weighted ℓ_1-minimization combined with dictionary learning, (CP-LEARNED, [6]), with the original methods A-SPAIN and CP, presented in [9] and [10], respectively. We also compare our approaches with other audio inpainting techniques such as A-SPAIN-MOD [5], i.e., modified SPAIN without dictionary learning, and JANSSEN [2]. The letter 'A-' indicates that an algorithms optimizes *analysis sparsity*[11, 12]. Note that A-SPAIN uses a frame-wise DFT dictionary, whereas A-SPAIN-LEARNED and A-SPAIN-MOD use a (deformed) Gabor dictionary. Following common practice in time-frequency audio processing, the dictionary is four times overcomplete in either case. JANSSEN uses an auto-regressive model with the same parameters as in [5, 6, 10].

As a means to compare the performance, we use the signal-to-distortion ratio (SDR) [1] defined as,

$$\mathrm{SDR}(x_{\mathrm{orig}}, x_{\mathrm{inp}}) = 10 \log_{10} \frac{\|x_{\mathrm{orig}}\|_2^2}{\|x_{\mathrm{orig}} - x_{\mathrm{inp}}\|_2^2} \quad [\mathrm{dB}],$$

where x_{orig} and x_{inp} denote original and inpainted signal within the gaps, respectively. Note that higher SDR values imply better signal restoration.

For our experiments, we used the same ten music signals from the EBU SQAM dataset [13] as in [5, 6, 10], in order to allow for a valid and comparable assessment. All considered signals were sampled at 44.1 kHz and represent different levels of sparsity with respect to the original Gabor dictionary. In each test instance, the input was a signal with 5 gaps at random positions. The lengths of these gaps ranged from 5 ms up to 85 ms. For fixed lengths, the results over all ten signals containing the 5 gaps were averaged.

Furthermore, we also calculated the PEMO-Q values [14], which utilize a human auditory system model to assess the quality of the restored signal. Thus, the PEMO-Q criterion is closer to the subjective evaluation than the SDR. The PEMO-Q model provides two quantities quantifying overall perceptual similarity: *perceptual similarity measure* (PSM) and the more commonly used *objective difference grade* (ODG). For simplicity, we restrict to ODG in this contribution. ODG quantifies the perceptual impact of audio artifacts in the restored signal and its value ranges from -4 (very annoying) up to 0 (imperceptible). Hence, ODG can be interpreted as the degree of perceptual similarity of x_{orig} and x_{inp}.

Throughout our experiments, we used the fast implementation of Gabor transforms available in the LTFAT toolbox [15, 16], and adopted its time-frequency conventions. The Gabor parameters used in our experiment are summarized in Table 1. For the remaining parameters, we refer the reader to [6].

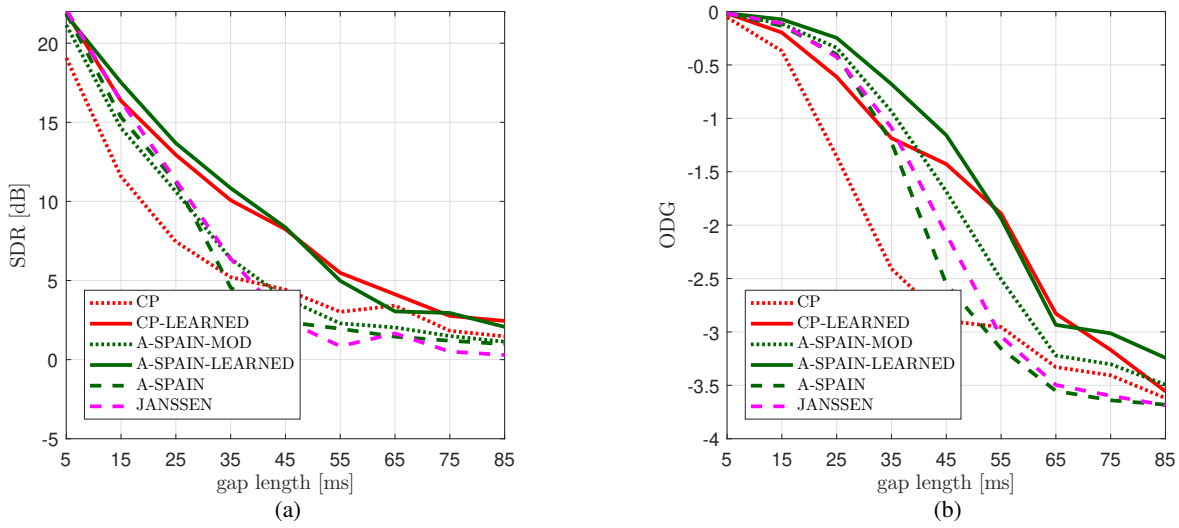


Figure 1. Performance comparison of different audio inpainting algorithms in terms of (a) SDR and (b) ODG for varying gap lengths.

Fig. 1(a) shows the inpainting performance in terms of SDR of all tested algorithms. We can observe that CP-LEARNED performs significantly better than CP, i.e., the original weighted ℓ_1-minimization method. Even more, it beats all other methods except A-SPAIN-LEARNED, which is slightly superior for gap lengths below 45 ms. Remarkably, CP-LEARNED even outperforms the otherwise best performing A-SPAIN-LEARNED algorithm for longer gaps ($\geq$ 45 ms) although the observed improvements are minor.

Fig. 1(b) shows the overall inpainting performance in terms of ODG. For smaller gap lengths ($\leq$ 35 ms), the performance of CP-LEARNED is superior to CP and a bit worse compared to other competing methods, whereas for longer gap lengths ($\geq$ 45 ms), CP-LEARNED's performance relative to the other methods improves, exceeding all the other methods except A-SPAIN-LEARNED for gap lengths above 65 ms.

ACKNOWLEDGEMENTS

This work was supported by Vienna Science and Technology Fund (WWTF) grant MA16-53 (INSIGHT) as well as by the Austrian Science Fund (FWF) projects I 3067-N30 (MERLIN), P 34624 (LoFT), and P 34922 (NoMASP).

REFERENCES

[1] A. Adler, V. Emiya, M. Jafari, M. Elad, R. Gribonval, and M. Plumbley, "Audio inpainting," *IEEE Trans. Audio, Speech, and Language Processing*, vol. 20, pp. 922–932, March 2012.

[2] A. Janssen, R. Veldhuis, and L. Vries, "Adaptive interpolation of discrete-time signals that can be modeled as autoregressive processes," *IEEE Trans. Ac., Sp., Sign. Proc.*, vol. 34, no. 2, pp. 317–330, 1986.

[3] N. Perraudin, N. Holighaus, P. Majdak, and P. Balazs, "Inpainting of long audio segments with similarity graphs," *IEEE Transactions on Audio, Speech and Language Processing*, vol. 26, no. 6, pp. 1079–1090, 2018.

[4] A. Marafioti, P. Majdak, N. Holighaus, and N. Perraudin, "Gacela: A generative adversarial context encoder for long audio inpainting of music," *IEEE Journal of Selected Topics in Signal Processing*, vol. 15, no. 1, pp. 120–131, 2020.

[5] G. Tauböck, S. Rajbamshi, and P. Balazs, "Dictionary learning for sparse audio inpainting," *Journal of Selected Topics in Signal Processing*, vol. 15, no. 1, pp. 104–119.

[6] S. Rajbamshi, G. Tauböck, N. Holighaus, and P. Balazs, "Audio inpainting via ℓ_1-minimization and dictionary learning," in *2021 29th European Signal Processing Conference (EUSIPCO)*, pp. 2149–2153, 2021.

[7] S. Boyd, N. Parikh, E. Chu, B. Peleato, J. Eckstein, *et al.*, "Distributed optimization and statistical learning via the alternating direction method of multipliers," *Foundations and Trends® in Machine learning*, vol. 3, no. 1, pp. 1–122, 2011.

[8] A. Chambolle and T. Pock, "A first-order primal-dual algorithm for convex problems with applications to imaging," *Journal of mathematical imaging and vision*, vol. 40, no. 1, pp. 120–145, 2011.

[9] O. Mokrỳ, P. Záviška, P. Rajmic, and V. Veselỳ, "Introducing SPAIN (SParse Audio INpainter)," in *2019 27th European Signal Processing Conference (EUSIPCO)*, pp. 1–5, IEEE, 2019.

[10] O. Mokrý and P. Rajmic, "Audio inpainting: Revisited and reweighted," *IEEE/ACM Transactions on Audio, Speech, and Language Processing*, vol. 28, pp. 2906–2918, 2020.

[11] M. Elad, P. Milanfar, and R. Rubinstein, "Analysis versus synthesis in signal priors," *Inverse problems*, vol. 23, no. 3, p. 947, 2007.

[12] S. Kitić, N. Bertin, and R. Gribonval, "Sparsity and cosparsity for audio declipping: a flexible non-convex approach," in *International Conference on Latent Variable Analysis and Signal Separation*, pp. 243–250, Springer, 2015.

[13] EBU, "EBU SQAM CD: Sound quality assessment material recordings for subjective tests."

[14] R. Huber and B. Kollmeier, "PEMO-Q–A new method for objective audio quality assessment using a model of auditory perception," *IEEE Transactions on Audio, Speech, and Language Processing*, vol. 14, no. 6, pp. 1902–1911, 2006.

[15] P. L. Søndergaard, B. Torrésani, and P. Balazs, "The linear time frequency analysis toolbox," *Int. J. Wavel., Multires. a. Inf. Process.*, vol. 10, no. 04, p. 1250032, 2012.

[16] Z. Průša, P. L. Søndergaard, N. Holighaus, C. Wiesmeyr, and P. Balazs, "The Large Time-Frequency Analysis Toolbox 2.0," in *Sound, Music, and Motion* (M. Aramaki, O. Derrien, R. Kronland-Martinet, and S. Ystad, eds.), Lecture Notes in Computer Science, pp. 419–442, Springer International Publishing, 2014.

ICA 2022
24th INTERNATIONAL CONGRESS ON ACOUSTICS
October 24(Mon) - 28(Fri), 2022 Gyeongju, Korea

PROCEEDINGS of the
24th International Congress on Acoustics

October 24 to 28, 2022 in Gyeongju, Korea

ABS-0587

Active subspace realization for accelerated training of parametric reduced-order models in vibroacoustics

Harikrishnan K. SREEKUMAR[(1)], Yannik HÜPEL[(1)], Sabine C. LANGER[(1)]

[(1)]Technische Universität Braunschweig, Institute for Acoustics, Germany, hk.sreekumar@tu-braunschweig.de

ABSTRACT

Parametric model order reduction techniques have seen significant applications in the field of multi-query problems like uncertainty quantification, optimization and sensitivity analysis to yield faster evaluation of large-scale models. However, capturing parametric effects of a large number of parameters is still challenging owing to the curse of dimensionality. This is the case for practical vibroacoustic models where for instance a range of material parameters have to be considered. As a consequence, the offline or the training phase in a parametric model order reduction algorithm becomes computationally demanding due to the large training set. In this contribution, we investigate and present the results of reducing the high-dimensional parameter domain from vibroacoustic models to a low-dimensional subspace by applying the method of active subspaces. The method identifies a set of parameters in the low-dimensional subspace which primarily influence the system's response. We present the existence of such active subspaces for classical vibroacoustic problems reduced in a desired parametric domain. Finally, the training in such active subspaces has shown to yield a significant reduction in search space and training cost.

Keywords: Parametric model order reduction, Active subspaces, Vibroacoustics

1 INTRODUCTION

At an early design phase, simulation of vibroacoustic systems delivers insights to optimizing design parameters with the aim of improving their acoustic characteristics among other properties. However, every simulation at a new parameter setting is computationally demanding. One way to circumvent the high computational cost is to approximate the frequency response functions (FRF) of such large-scale models using model order reduction (MOR) methods to yield a frequency-domain reduced-order model (fROM) valid for a desired frequency region. Krylov-subspace projection techniques have shown an efficient reduction of such large-scale models in the frequency domain. In addition, one can include parametric effects to the reduction framework with the help of parametric model order reduction (PMOR) methods [2]. As a result, parametric computations can be efficiently performed with a PMOR generated surrogate model.

The offline or training phase of PMOR utilizes adaptive algorithms, such as the greedy algorithm, to obtain an accurate parametric reduced-order model (pROM). In the context of projection-based MOR techniques, a range of options are available to finally yield an accurate pROM spanning a desired parametric domain. The global basis approach resulting in a single projection basis is less reliable for high-dimensional problems. Consequently, local basis approaches became popular where the system's response at a desired parametric point is obtained using information from a number of local fROMs with interpolation or regression techniques. The most popular interpolation techniques include interpolating underlying subspaces [1], reduced-order model matrices, output responses or transfer functions and pole-matching [13, 10]. In this contribution, we choose this local approach by interpolating multiple FRFs obtained from locally generated fROMs.

The cost of training is an important factor when it comes to practical high-dimensional parametric problems. In the context of parametric computations and surrogate modelling, the problem of the curse of dimensionality is infamous, which makes it infeasible to consider a large number of parametric variations thereby increasing the training cost exponentially. A classical full grid computation is possible only for a small number of parameters

($n_p < 3$). For a higher number of parameters ($n_p \geq 3$), there are various approaches to circumvent the curse of dimensionality; with the method of sparse grids [4, 15] being one popular among them. A sub-sampling strategy to reduce the computational cost for large parameter time-dependent problems can be referred to [5]. Altogether, the requirement to deal with high-dimensional problems is of great demand and is an active field of research.

Another approach is to perform dimensionality reduction, where the number of parameters is reduced by exploiting the hidden anisotropy of a high dimensional parametric problem. With the sensitivity analysis one can identify parameters which have the strongest influence on the system's response. As a result, it is possible to train a pROM by finding the most important and contributing fROMs along the direction of highly ranked parameters based on their sensitivity measures. A disadvantage of such an approach is that they reveal the prominent parametric (univariate-)directions which are only aligned with the natural parameter coordinate direction. On the other hand, the active subspace method (ASM) [7, 6] identifies the prominent directions which may not be aligned with the parametric dimension or in other words oriented multi-dimensionally. The main idea is to establish a rotated coordinate system, where the parametric surface variation is now aligned to (1) vary the most along certain new rotated coordinates called the *active* parameter coordinates and (2) vary the least or invariant along the *inactive* parameter coordinates. The rotated coordinates enable one to define a low-dimensional subspace called the *active subspaces* constructed with only the active parameters. As a result, it is now possible to investigate the parametric computations within this low-dimensional parameter space. The method so far has shown significant advantages in many applications for instance [17, 18].

In the context of PMOR, this means that the reduced dimensionality with active subspaces has greater potential to lower the cost of PMOR training and narrow the search space to this low-dimensional active subspace to find the most contributing fROMs characterizing the entire parametric domain of interest; thereby offering a promising method to approach the curse of dimensionality. In this contribution, we present results and insights which imply the existence of a low-dimensional active subspace for vibroacoustic problems and their advantages in performing a PMOR training phase with reduced computational cost.

The paper is structured to firstly introduce the considered vibroacoustic problem in Section 2 and the essential mathematical concepts of PMOR in Section 3. The theory of active subspaces based on gradient evaluations is detailed in Section 4. Postliminary, Section 5 elaborates on the methodology and algorithms for performing PMOR training in active subspaces which are the main contribution of the paper. The advantages and robustness of the method are then examined by application to a generic vibroacoustic model of a coupled plate-fluid cavity presented in Section 6. Finally in Section 7, we present our conclusions and final remarks.

2 VIBROACOUSTIC PROBLEM DEFINITION

In this paper, we deal with typical vibroacoustic problems for modelling structure-borne and air-borne sound wave propagation. The basic system of equations is obtained from the finite element method (FEM), approximating the system behaviour of large and complex domains. The core problem in consideration showcases a classical vibroacoustic problem, a strongly coupled fluid-structure system. The system represents a range of practical examples where one is interested to estimate the sound radiating from a vibrating structure such as the estimation of noise in a room due to vibration of surrounding walls. A more complex example is an aircraft cabin subjected to external loading on the fuselage exterior in order to assess the cabin noise [3]. The resulting FEM system of equations of the coupled problem can be expressed as:

$$\left(-\omega^2\begin{bmatrix} M_s & 0 \\ K_c^T & M_f \end{bmatrix} + i\omega\begin{bmatrix} D_s & 0 \\ 0 & D_f \end{bmatrix} + \begin{bmatrix} K_s & -K_c \\ 0 & K_f \end{bmatrix}\right)\begin{bmatrix} x_s \\ x_f \end{bmatrix} = \begin{bmatrix} F_s \\ 0 \end{bmatrix} \Rightarrow \left(-\omega^2 M + i\omega D + K\right)x = F, \tag{1}$$

where $M, D, K \in \mathbb{C}^{n\times n}$ are the mass, damping and stiffness matrix respectively. The system matrices and vectors with subscripts s and f denote the structural and fluid domain. Excitation is considered for the vibrating structure with the load F_s. In our case, the corresponding state or modelled degrees of freedom in x_s and x_f account to the deflection and rotation of the structural nodes and acoustic pressure for the nodes in the fluid medium. In addition, the term K_c denotes the coupling matrix accounting for the strong coupling between the two domains. Finally, $\omega = 2\pi f$ denote the angular frequency in radians per second with f the frequency in Hertz (Hz).

3 PARAMETRIC MODEL ORDER REDUCTION

The basic system of equations presented in (1) is often computationally demanding to solve especially for system evaluations at higher frequencies owing to the wave resolving nature of FEM. This system of equations is considered as the large-scale model in upcoming discussions, which is subjected to MOR procedure to yield faster system evaluations.

Consider the essential parameter variables represented as $p \in \mathscr{P}^{n_p}$, where $p = [p_1, p_2, \cdots, p_{n_p}]$ contains the various parameters and the parameter space $\mathscr{P}$ is, for our problems, a bounded domain normalized to $[-1,1]$. The parametric system of equations for the dynamic steady-state analysis in the frequency domain can be then expressed as:

$$\begin{aligned} \left(-\omega^2 M(p) + i\omega D(p) + K(p)\right) x(\omega, p) &= F \\ y(\omega, p) &= C x(\omega, p). \end{aligned} \tag{2}$$

Equation (2) is similar to the dynamic system of equations presented in (1) with the parameter list p containing the underlying material and design parameters. For the numerical examples considered in this paper, the material parameters include the variables occurring from a viscoelastic isotropic material behaviour assignment for the structural domain and a damped Helmholtz domain for the fluid-cavity. We discuss the parameters in detail within Section 6. For simplicity, we consider a single-input-single-output configuration where $F \in \mathbb{C}^{n\times 1}$ is the input or loaded excitation to the system, $y(\omega, p) = Cx(\omega, p)$ is the output FRF with $C \in \mathbb{C}^{1\times n}$ and $x(\omega, p)$ is the state vector. The superscript T denotes the hermitian transpose. An extension towards the practical multiple-input-multiple-output configuration for the presented work in this paper is straight forward. The output FRF of the above parametric system reads:

$$y(\omega, p) = C(-\omega^2 M(p) + i\omega D(p) + K(p))^{-1} F.$$

With projection-based techniques, dynamic systems in the frequency domain can be approximated with a projection basis $V(p) \in \mathbb{C}^{n\times r}$ and the resulting FRF yielded from the reduced system reads:

$$y_R(\omega, p) = C_R(-\omega^2 M_R(p) + i\omega D_R(p) + K_R(p))^{-1} F_R$$

where the reduced-order matrices obtained after Galerkin projection can be expressed as $[\cdot]_R = V(p)^T [\cdot] V(p)$ with $[\cdot] = \{M(p), D(p), K(p)\}$, $C_R = CV(p)$, $F_R = V(p)^T F(p)$. The projection basis V is orthogonal as a result of iterative Arnoldi algorithm with Gram-Schmidt orthogonalization [16]. Consequently, the computations are performed faster with reduced systems $M_R(p), D_R(p), K_R(p) \in \mathbb{C}^{r\times r}$, $F_R, C_R \in \mathbb{C}^{1\times r}$ where $r \ll n$.

Using global PMOR approaches, one tends to find a single $V(p)$ to span the desired parametric domain. On the contrary, with local PMOR approaches, there are multiple local projection basis $V(p_1), V(p_2), \cdots, V(p_n)$ at various parameter points and computes $V(p)$ at any desired parameter point by interpolation or regression. We refer to [2] for more background on PMOR and [8] for projection-based MOR with Krylov subspaces.

In this contribution, we use the state-of-the-art second-order Krylov subspaces expressed as:

$$V \in \text{colspan}\left(-\tilde{K}^{-1}\tilde{D}, -\tilde{K}^{-1}\tilde{M}, -\tilde{K}^{-1}F\right)$$

and multi-point Padé approximation to yield accurate fROMs within the desired frequency range where $\tilde{K} = -\omega^2 M + i\omega D + K$, $\tilde{D} = 2i\omega M + D$ and $\tilde{M} = M$. A detailed discussion on the same for vibroacoustics can be found in [16].

A range of adaptive algorithms are available to yield an accurate pROM. Following the conventional terms of *offline* and *online* phases in PMOR, in this paper, we refer to the offline phase also as the training procedure. During the training procedure, we apply suitable adaptive algorithms like the greedy algorithm to actively identify a small set of local fROMs which, in turn, can be used to describe the parametric response. On the other hand, the online phase refers to the faster response evaluation procedure at any desired parametric point with the trained pROM using interpolation or regression.

The adaptive algorithms use a suitable error estimator or an error indicator to observe the convergence of the yielded pROM and to choose new local fROM(s) in further iterations. We use a relatively computationally cheap

error estimate of normalized relative frequency difference (NRFD) to access the convergence of interpolated pROM by comparing the natural frequencies of the respective FRFs. The maximum NRFD error is chosen for the frequency domain of interest, expressed as:

$$\varepsilon_{\text{NRFD}} = \max_i \left| \frac{\omega_{r,i} - \hat{\omega}_{r,i}}{\omega_{r,i}} \right| \tag{3}$$

where $\omega_{r,i}$ represents the reference natural frequencies obtained from a direct fROM evaluated FRF y_R and $\hat{\omega}_{r,i}$ represents the compared natural frequencies obtained from the pROM online evaluated FRF $\hat{y}_R$ for a given parametric point. The success of using this error estimate is presented later in Section 6. While NRFD checks the quality of a pROM with the occurrence of resonances in the FRFs, we use absolute error norms to evaluate the quality of generated fROMs and consequently the FRF itself.

4 ACTIVE SUBSPACE METHOD USING THE GRADIENT BASED APPROACH

The ASM, introduced in [7], is an efficient mathematical tool to perform dimensionality reduction of high-dimensional parametric problems. The method is highly suitable for problems where the output varies predominantly in certain parametric directions. Moreover, we present later in Section 6, that the sensitivity indices for the considered vibroacoustic models support the existence of strong anisotropy from the parameters. However, strong variability along multi-direction is hard to realize when using sensitivity indices to rank the input parameters according to the strongest influence. The ASM reorients coordinate directions by rotation so as to align the strongest and the weakest variations to the new rotated coordinates. The rotated subspace can be then approximated with a set of prominent active subspace parameters thereby constructing the low-dimensional subspace called the active subspace.

A gradient-based approach is used to construct the active subspace which can then reveal a set of active and inactive parameters. The active parameters are now the coordinates in the active subspace capturing the strongest influence. On the other hand, the inactive parameters constitute coordinate directions where the output response is almost invariant. Such a separation of parameters into active and inactive is enabled with mainly three steps: (1) computing the gradient response of the system, (2) construction and factorization of a covariance-style matrix using the computed gradients and (3) segregation of active parameters and computing the approximated low-dimensional or active subspace. Below we briefly describe these three steps.

The gradient can be used to capture the variability of the model response. Let $f(p)$ represent the output response function for input parameters $p \in \mathscr{P}^{n_p}$ and $\nabla_p f(p) = \left[\frac{\partial f}{\partial p_1}, \frac{\partial f}{\partial p_2}, \cdots, \frac{\partial f}{\partial p_{n_p}}\right]$ is the corresponding gradient. To compute the gradient for the whole parametric domain, a Monte-Carlo (MC) integration is performed as suggested in [7], which reads for m MC samples in the parameter space $\mathscr{P}^{n_p}$:

$$\nabla_p f_j = \nabla_p f(p_j) \; \forall p_j \in \mathscr{P}^{n_p}, j = 1, \cdots, m.$$

A suitable method can be used to compute the gradient at each sampled point. In this contribution, we use the computationally expensive method of finite differences for gradient computation. The number of samples considered for the MC integration is commented on later in Section 5.

As a second step, the computed gradient enables the building of a covariance-style matrix $C \in \mathbb{C}^{n_p \times n_p}$ or termed as the active subspace matrix reads:

$$C = \mathbb{E}\left[(\nabla_p f)(\nabla_p f)^T\right] = \int (\nabla_p f)(\nabla_p f)^T \rho(p)\, \mathrm{d}p \Rightarrow C \approx \tilde{C} = GG^T = \frac{1}{m} \Sigma_{j=1}^{m} (\nabla_p f_j)(\nabla_p f_j)^T, \tag{4}$$

where $G = \frac{1}{\sqrt{m}}\left[\nabla_p f_1, \nabla_p f_2, \cdots, \nabla_p f_{n_p}\right]$. The active subspace matrix in (4) is expressed first in a probabilistic setting with an underlying density function $\rho(p)$ and then expressed using evaluation with MC integration.

Now, an eigenvalue decomposition is performed on the matrix $\tilde{C}$, such that $\tilde{C} = \tilde{W}\tilde{\Lambda}\tilde{W}^T$, to yield a set of eigenvalues Λ and corresponding eigenvectors W, which are then partitioned suitably to form:

$$\Lambda = \begin{bmatrix} \Lambda_1 & \\ & \Lambda_2 \end{bmatrix}, \text{ and } W = \begin{bmatrix} W_1 & W_2 \end{bmatrix}.$$

Alternatively, a singular value decomposition (SVD) can be performed on the matrix G yielding $G = \tilde{W}\sqrt{\tilde{\Lambda}}V^T$. For the algorithm used in this paper, we follow this procedure with a SVD.

Thirdly, the huge gaps between the eigenvalues obtained from an SVD can be used to perform dimensionality reduction where a partition is done based on arranging the eigenvalues in descending order of their magnitudes and observing the most dominant eigenvalues. This strongly relates to the principal component analysis [11] which can be used to discover active subspaces by preserving the components with high variability. Or in other words, eigenvalues which are almost of zero magnitude can be discarded or be considered inactive. As a result, $\mathrm{diag}(\Lambda_1) \in \mathbb{C}^{l_p}$ and $W_1 \in \mathbb{C}^{n_p \times l_p}$ contain the most important eigenvalues and eigenvectors where the number of active parameters $l_p < n_p$. The eigenvectors W_1 define the rotation of the coordinates corresponding to the most prominent variation. The respective transformation of original parameter coordinates p to the rotated coordinates can be achieved with:

$$\phi = W_1^T p, \ \psi = W_2^T p. \tag{5}$$

As a result, we have now obtained a set of active and inactive parameters. Using these active parameters and the transformations in (5), one can perform the parametric training procedure within this low-dimensional active subspace with less numbers of parameters. Finally, the goal of approximating the system response is to approximate an n_p-variate function with an l_p-variate function. Hence, the response function in the original parametric domain is approximated with the dominant l_p number of variables. For this approximation in the original parametric domain, firstly we perform k functional evaluations in the active subspace expressed as:

$$G(\phi_i) \approx f(p_i) \ \text{ for } \ p_i = W_1\phi_i + W_2\psi_i \approx W_1\phi_i \ \text{ and } \ i = 1, \cdots, k. \tag{6}$$

Then, we compute the interpolated or regression response over the original parametric domain of interest using the above k functional evaluations expressed as:

$$f(p) \approx \hat{G}(\phi)$$

where $\hat{G}(\phi)$ is the interpolated or regression surface constructed with k data points in active subspace $(\phi_i, f(p_i))$. The preference for interpolation and regression techniques in context of PMOR is commented in Section 5.

In (6), the grid transformation from the active subspace to the physical space is approximated with contribution from only the active parameters. Also, the transformation from ϕ to p is ill-posed [6]. The approximation introduces an error when the eigenvalues corresponding to the inactive parameters Λ_2 are not zero. Hence, the influence of the approximation on the overall subspace approximation is fully dependent on the nature of the problem. In our investigations, this influence is negligible as the eigenvalues $\lambda_{l_p+1}, \cdots, \lambda_{n_p}$ are small.

5 PROPOSED TRAINING STRATEGY WITH ACTIVE SUBSPACES

The major computational cost in PMOR accounts for the training procedure. A suitable test grid, which is often a fine grid, is chosen to evaluate the error evolving in each iteration of an adaptive algorithm. For a large number of parameters, we, therefore, need a very large test grid adding to the curse of dimensionality, making it impossible to train for high-dimensional parametric problems. In this section, we describe the combined approach of ASM presented in Section 4 within a PMOR framework presented in Section 3. Firstly, an outline of the computational pipeline is presented. This is followed by the algorithms for computing the active subspaces and the overall PMOR training using ASM. Finally, we comment on the computational cost.

5.1 Computational pipeline

To illustrate the role of active subspaces in the PMOR training phase, a typical pipeline comparing the conventional training and training in the active subspace is depicted in Figure 1.

A conventional training pipeline with greedy algorithm, marked in Figure 1, involves an iterative procedure of interpolating a set of fROMs, also known as the interpolated grid $\Xi_{\text{interpolated}}$, which essentially forms the pROM. A test or training grid Ξ_{train} is chosen to check the convergence of the produced pROM in each greedy iteration. An error measure is computed for Ξ_{train} and the convergence of pROM is then checked against a

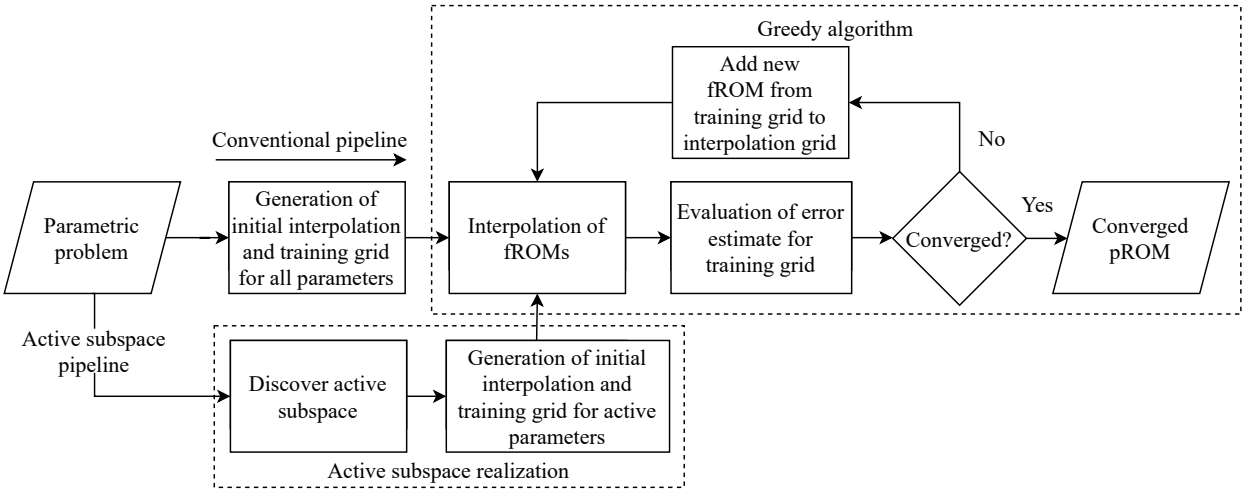


Figure 1. Flow chart representing both the conventional PMOR training pipeline and PMOR training pipeline with active subspace

suitable error tolerance. The interpolated grid continues to grow and contain more fROMs from the training grid until the pROM converges. This training procedure is marked as the conventional pipeline in Figure 1.

In general, the interpolation grid is initially a coarse grid and the training grid accounts for a finer grid. Using suitable sampling techniques, one can generate a fitting number of parameter points for $\Xi_{\text{interpolated}}$ and Ξ_{train}. However, $\Xi_{\text{interpolated}}$ and Ξ_{train} can be huge when the number of parameters are high owing to the curse of dimensionality. Next, we present the pipeline for training with active subspaces to circumvent this problem.

For a PMOR training pipeline with active subspaces, also marked in Figure 1, the aim is to find a low-dimensional active subspace where the parametric response variations are dominant. As a result, training in such an active subspace reduces the number of parameters and also reduces the search space. As a first step in the pipeline, we construct the active subspace using the gradient-based approach mentioned in Section 4 so as to yield a low-dimensional subspace of active parameters. Consequently, $\Xi_{\text{interpolated}}$ and Ξ_{train} are defined on the active subspace domain with reduced parameters. It is often observed that for problems with strong anisotropy of considered parameters, the active subspace is constructed with very few (one or two) parameters. We observe this later for the considered vibroacoustic example in Section 6. Considering such a small number of parameters, it is now affordable to just use the full-grid sampling to proceed with the training. Therefore, in this paper, we consider full-grid sampling which delivers converging pROMs. However, the usage of sparse grids on the active parameter grid is still possible for better performance and is interesting for future research. As depicted in Figure 1, the consequent part of the pipeline is the greedy procedure to finally yield a converged pROM trained in the active subspace. As a result, one can integrate the active subspace training into a conventional PMOR algorithm with less effort. The algorithms for this active subspace pipeline are detailed further in Section 5.2.

Commenting on the online evaluations in the parametric domain, we choose two different approaches for (1) while in training procedure and (2) while in post-training evaluations. While in training procedure, we prefer interpolation techniques over regression for better convergence of the greedy algorithm. As already mentioned in Section 4, the ASM rotates the parametric domain and aligns to a reduced set of active parameters. Training in such an active subspace evaluates a narrow parametric domain where the response variations are dominant. The resulting pROM is still valid and accurate for the entire parameter domain of interest, which includes the less dominant regions. As a result, we require a fitted response surface using regression for a global evaluation of the response functions outside the active subspace interpolated grid $\Xi_{\text{interpolated}}$. Hence after a successful training procedure with the interpolation grid $\Xi_{\text{interpolated}}$, a regression surface is computed with the converged $\Xi_{\text{interpolated}}$ as the data points. In this paper, a response surface for global evaluation is constructed using Gaussian process regression (GPR) using an exponential kernel. For the response functions presented in this contribution, we use

the `GaussianProcessRegressor` from `scikit-learn` [14]. Details on the construction of response surfaces with kriging in the context of ASM can be referred to [7].

5.2 Algorithm

With an understanding of the theory of active subspaces from Section 4 and the pipeline explained in the previous section, we present the underlying major algorithms in the form of pseudocodes in Algorithm 1 and Algorithm 2.

Algorithm 1 Algorithm to perform PMOR training procedure based on a greedy approach with active subspace

function PERFORMPMORTRAININGGREEDYASM(Parametrized full system Σ, frequency range $\omega = [\omega_{\min} : \omega_{\max}]$, parameter domain $\mathscr{P} \in [-1,1]$, error tolerance σ_{tol})
  Φ = CONSTRUCTACTIVESUBSPACE(Σ, m, $\mathscr{P}$, $\sigma_{\text{tol,AS}}$) ▷ See Algorithm 2
  Ξ_{train} = GENERATESAMPLES(n_{train}, Φ, 'full-grid') ▷ Generates n_{train} samples
  $\Xi_{\text{interpolation}}$ = GENERATESAMPLES($n_{\text{interpolation}}$, Φ, 'full-grid') ▷ Generates $n_{\text{interpolation}}$ samples
  do ▷ Greedy iteration
    /* Compute interpolated function with current $\Xi_{\text{interpolation}}$ */
    $y_R(\omega, p)$ = COMPUTELOCALROMSANDINTERPOLATERESPONSEFUNCTIONS(Σ, $\Xi_{\text{interpolation}}$)
    $\varepsilon = []$
    for all $p_i \in \Xi_{\text{train}}$ **do** ▷ Computing error over test grid
      /* Compute FRF using the interpolated function */
      $\hat{y}_{R,i}(\omega, p_i) = y_R(\omega, p_i)$
      /* Compute FRF by building new local ROM */
      $\tilde{y}_{R,i}(\omega, p_i)$ = COMPUTELOCALROMANDGENERATERESPONSEFUNCTIONS(Σ, p_i, ω)
      ε_i = COMPUTEERRORNRFD($\tilde{y}_{R,i}(\omega, p_i)$, $\hat{y}_{R,i}(\omega, p_i)$)
      if $\varepsilon_i < \sigma_{\text{tol}}$ **then** ▷ Check for local convergence
        Ξ_{train} = REMOVEPOINTFROMGRID(Ξ_{train}, p_i) ▷ Converged points are removed from grid
      end if
    end for
    $\varepsilon_{\max}, p_{\text{new}} = \text{argmax}(\varepsilon)$ ▷ Maximum error point is chosen for interpolation in next greedy iteration
    $\Xi_{\text{interpolation}}$ = ADDMAXIMUMERRORPOINTTOGRID($\Xi_{\text{interpolation}}$, p_{new})
  while $\varepsilon_{\max} > \sigma_{\text{tol}}$ ▷ Check for convergence in entire training grid
  return Converged interpolated grid $\Xi_{\text{interpolated}}$
end function

Algorithm 1 highlights the major steps in a PMOR training procedure for the proposed approach using ASM. The ASM training routine includes the construction of the covariance matrix with function CONSTRUCTACTIVESUBSPACE detailed in Algorithm 2. The inputs to the algorithm are (1) the parametric problem $\Sigma(p)$ - which are the parametrized FEM system evaluations from an in-house FEM software in our case, (2) the frequency domain of interest $\omega = [\omega_{\min} : \omega_{\max}]$, (3) the parameter domain $\mathscr{P}$ normalized to scale $[-1,1]$, and (4) the error tolerance for the greedy algorithm σ_{tol}. In every greedy iteration, new local fROMs are added to $\Xi_{\text{interpolated}}$ from Ξ_{train} that correspond to the maximum error estimate expressed in (3). Each local fROM in $\Xi_{\text{interpolated}}$ and Ξ_{train}, computed with function COMPUTELOCALROMSANDINTERPOLATERESPONSEFUNCTIONS, is produced using Krylov-based MOR techniques. For sake of brevity, the algorithm for fROM generation is not elaborated. The authors advise to refer to the classical MOR and PMOR literature for more details. While in ASM training, it is worth mentioning that the samples are drawn from the constructed active subspace Φ. Also with regards to the interpolation of FRFs in $\Xi_{\text{interpolated}}$, we use the linear n-dimensional interpolation capability of `interpolate.griddata` function from `scipy` in Python.

The function CONSTRUCTACTIVESUBSPACE to construct the active subspace is further detailed in Algorithm 2. The algorithm performs an evaluation of the parametric functional response gradient using finite differences and builds the covariance matrix G. Using SVD, the matrix is factorized into eigenvalues and eigenvectors which are then sorted accordingly to construct the active subspace Φ which are essentially the dominant eigen-

values Λ_1 and eigenvectors W_1.

Algorithm 2 Algorithm to construct the low-dimensional active subspace

function CONSTRUCTACTIVESUBSPACE(Parametrized full system Σ, number of gradient evaluations m, parameter domain $\mathscr{P} \in [-1,1]$, tolerance for grouping eigenvalues $\sigma_{\text{tol,AS}}$)
  Ξ_{MC} = GENERATESAMPLES(m, $\mathscr{P}$, 'random-uniform') ▷ Generates m samples for MC integration
  for all $p_i \in \Xi_{\text{MC}}$ **do** ▷ Computing gradient
    $\nabla_p f_i$ = COMPUTEGRADIENT(Σ, p_i) ▷ Here with a finite difference scheme
  end for
  $G = \frac{1}{\sqrt{m}} \left[\nabla_p f_1, \nabla_p f_2, \cdots, \nabla_p f_{n_p}\right]$ ▷ Compute covariance matrix
  W, Σ, V^T = SINGULARVALUEDECOMPOSITION(G) ▷ Factorization
  /* Grouping into active and inactive */
  $\Lambda = \Sigma^2$
  Λ, W = SORTPAIRDESCENDING(Λ, W)
  $\Lambda_1, \Lambda_2, W_1, W_1 = [\,]$
  for all $\Lambda_i \in \Lambda$ and $W_{:,i} \in W$ **do**
    if $\Lambda_i / \Lambda_0 > \sigma_{\text{tol,AS}}$ **then**
      $\Lambda_1 = \begin{bmatrix}\Lambda_1 & \Lambda_i\end{bmatrix}$; $W_1 = \begin{bmatrix}W_1 & W_{:,i}\end{bmatrix}$
    else
      $\Lambda_2 = \begin{bmatrix}\Lambda_2 & \Lambda_i\end{bmatrix}$; $W_2 = \begin{bmatrix}W_2 & W_{:,i}\end{bmatrix}$
    end if
  end for
  return $\Phi : \{\Lambda_1, W_1\}$
end function

5.3 Computational cost

Commenting on the computational cost, the extra cost for the proposed algorithm 1 is the construction of the essential active subspace. The major costs incur from the number of MC samples m used to establish the covariance matrix in (4), which includes the evaluation of gradients of the original function $f(p)$. We use the finite-differences method, which adds to the computational cost. However, more affordable gradient computation methods, such as the adjoint method, are suggested when available. A multi-fidelity approach is presented in [12] to approximate the covariance matrix with both low and high-fidelity gradient functions, thereby reducing the cost of realizing the active subspaces. However, for the considered example in Section 6, we observe a requirement of a few sample evaluations - around 100 samples - to sufficiently capture the dominant eigenpairs. The usage of the above mentioned efficient methods for gradient computation and further optimization regarding the required number of samples is proposed for further investigations. Regardless, the cost of training with the original grid outweighs the cost incurred with active subspaces.

6 NUMERICAL EXAMPLE

In this section, we present the results of PMOR training with ASM discussed in Section 5 applied to a generic vibroacoustic model. The study is focused on an evaluation in the frequency region of $100-400$ Hz for every 1 Hz frequency step and to a single-input-single-output configuration for simplicity. The response evaluations for generated fROMs and gradient computations correspond to the fROMs yielded from respective FEM models using an in-house vibroacoustic solver coded in C++ for high-performance parallel computing.

The coupled plate-cavity example represents a typical vibroacoustic problem with the respective FEM discretised system mentioned in Section 2. The discretised FE model is illustrated in Figure 2. The model essentially includes a two-dimensional plate with dimensions $1\text{m} \times 0.7\text{m}$ strongly coupled to a three-dimensional acoustic cavity with dimensions $1\text{m} \times 0.7\text{m} \times 1.3\text{m}$. The plate is modelled with the Reissner-Mindlin plate formulation and viscoelastic material properties. Whereas, the acoustic medium is a Helmholtz domain modelling acoustic

wave propagation through a stationary, ideal and compressible fluid. The plate and fluid domain are discretised with respective quadratic elements and strongly coupled with conforming meshes yielding a full-order system dimension of 10395. In total, the parametric response can be described using 9 parameters which are: (a) 5 parameters from the plate domain - Young's modulus (E), Poisson's ratio (ν), density (ρ), thickness (t) and damping loss factor (η), and (b) 4 parameters from the fluid domain - the real and imaginary part of speed of sound $c_{\text{f,real}}, c_{\text{f,imag}}$ and fluid density $\rho_{\text{f,real}}, \rho_{\text{f,imag}}$. The imaginary part for the fluid parameters is accounted to consider numerical damping in the fluid domain. The nominal values and considered variations of each parameter are described in Table 1.

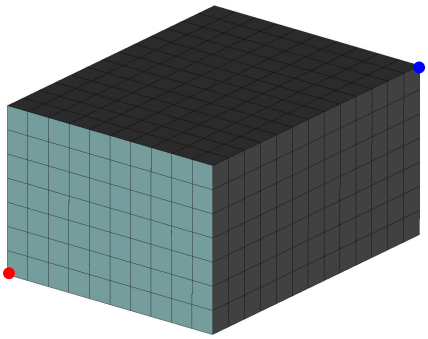


Figure 2. Discretised plate-cavity model with plate domain shaded in cyan and fluid-cavity domain shaded in grey. Also, the input node is marked as red • and output node marked as blue • points.

Table 1. Parameter variations considered for the coupled plate-cavity model. The individual parameter bounds and nominal values presented in the table are later normalized to scale $[-1,1]$ for the active-subspace algorithms dealing with general domains.

Domain	Material	Parameter	Units	Nominal value	Variation	Bound	NRFD
Plate	Aluminium	E	N/m^2	$7 \cdot 10^{10}$	10%	$[6.65, 7.35] \cdot 10^{10}$	$6.26 \cdot 10^{-3}$
		η	.	0.05	10%	$[0.0475, 0.0525]$	$3.98 \cdot 10^{-3}$
		ν	.	0.3	10%	$[0.285, 0.315]$	$5.45 \cdot 10^{-3}$
		ρ	kg/m^3	2700	10%	$[2565, 2835]$	$9.79 \cdot 10^{-3}$
		t	m	0.003	10%	$[0.00285, 0.00315]$	$8.45 \cdot 10^{-3}$
Cavity	Air	$c_{\text{f,real}}$	m/s	343.11	10%	$[325.95, 360.26]$	$7.31 \cdot 10^{-3}$
		$c_{\text{f,imag}}$	m/s	8.572	10%	$[8.144, 9.001]$	$8.07 \cdot 10^{-3}$
		$\rho_{\text{f,real}}$	kg/m^3	1.21	10%	$[1.15, 1.27]$	$6.25 \cdot 10^{-3}$
		$\rho_{\text{f,imag}}$	kg/m^3	0.0302	10%	$[0.029, 0.032]$	$3.98 \cdot 10^{-3}$

The input to the model is a node at $(0.,0.,0.)$ in plate for excitation perpendicular to the plate surface and output is observed at a node at $(1.,0.7,1.3)$ at the end of the fluid domain also depicted in Figure 2. Therefore, the MOR procedure for this model yields a FRF consisting of the acoustic pressure response for the output node. The aim is to perform accurate PMOR training by interpolating the least number of FRFs obtained from the respective local fROMs. For the nominal parametric setting, an accurate local fROM of size $r = 90$ and absolute error norm $1.3 \cdot 10^{-10}$ is generated with expansion points $\omega_{\text{EP}} = 2\pi\{100, 400\}$ rad·s^{-1} using Krylov-based MOR techniques presented in Section 3.

For the current parametric problem involving 9 parameters, we deploy Algorithm 1 and thereby Algorithm 2 to perform PMOR training using ASM. In Figure 3, the eigenvalues corresponding to the covariance matrix evaluated using 100 Monte Carlo integration samples are plotted. It is evident from the figure that for the

current model, there is a single parameter direction in the active subspace where the system response is largely varying. To further support this, we also performed a Sobol sensitivity analysis with 12000 Saltelli samples and respective fROM evaluations using the `SALib` python library [9]. The first order Sobol indices are plotted for each of the parameters over frequency in Figure 4 and are in close accordance with the results in [15]. It is evident that the speed of sound $c_{\text{f,real}}$ has a significant influence on the system response for the entire frequency domain. In summary, the few dominant active parameters exposed with ASM and the sensitivity measures from the parameter study support hidden anisotropy within vibroacoustic parametric problems which can be leveraged to achieve significant dimensionality reduction of high-dimensional problems. As a result, we expect ASM to perform efficiently with the found reduced low-dimensional active subspace. For further training, we build the active subspace with the first two eigenpairs or active parameters. Considering full-grid sampling in the constructed active subspace using (5), the initial interpolation grid is chosen to contain $8 \times 8 = 64$ fROMs and the training grid with $30 \times 30 = 900$ fROMs. For a given NRFD error tolerance $\sigma_{\text{tol}} = 10^{-2}$, the greedy algorithm converges with 303 fROMs in $\Xi_{\text{interpolated}}$ for a final maximum NRFD error of $7.99 \cdot 10^{-3}$.

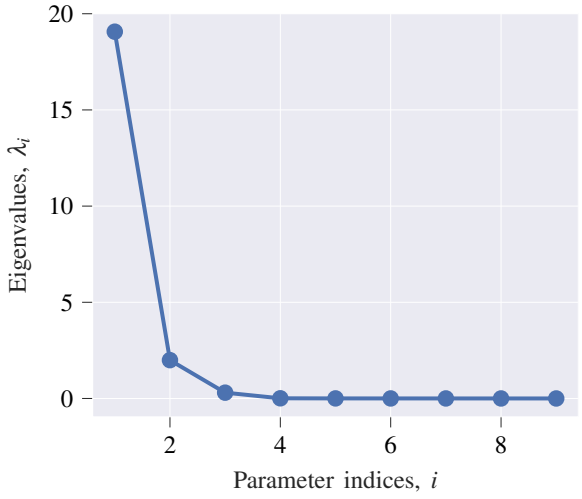


Figure 3. Plate-cavity model eigenvalue decay plot evaluated for 100 gradient evaluations based on high-fidelity solution response obtained from respective fROMs. Dominant eigenvalues are visible.

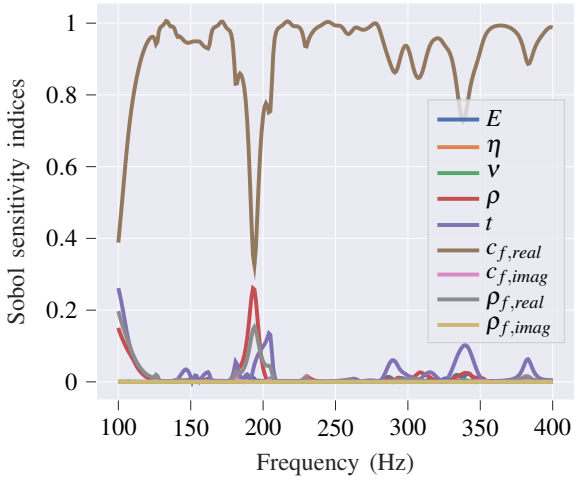


Figure 4. First order Sobol sensitivity indices obtained from Monte-Carlo simulation and pROM online computation for each parameters computed with 12000 Saltelli samples.

We present the efficiency of the proposed training method using the parametric surface plots for the most dominant and least dominant parameters along with their NRFD error values. The response plot obtained from PMOR online phase for pROM obtained with training in ASM is compared with the response plot obtained with direct full-order model expensive computation. The response plots are computed by varying the parameter of interest for the entire desired parametric domain and other parameter values corresponding to their nominal values as per Table 1. As a result, the response plots for the PMOR online phase are essentially the FRFs which are interpolated from the respective pROM. We obtain a maximum NRFD error of $7.31 \cdot 10^{-3}$ for the dominant parameter $c_{\text{f,real}}$ with respective response plots in Figure 5. Similarly, Figure 6 shows the response plots obtained for the least dominant parameter ν with a maximum NRFD error of $5.45 \cdot 10^{-3}$. Observing both of the response plots along with their NRFD error, we see the response obtained from PMOR online phase accurately approximating the direct response. The maximum NRDF error for other parameters, see Table 1, are also within tolerable limits. Hence, using NRFD error for our PMOR-ASM framework has shown to provide accurate and converging pROM thereby sufficiently capturing the dynamics of the system response.

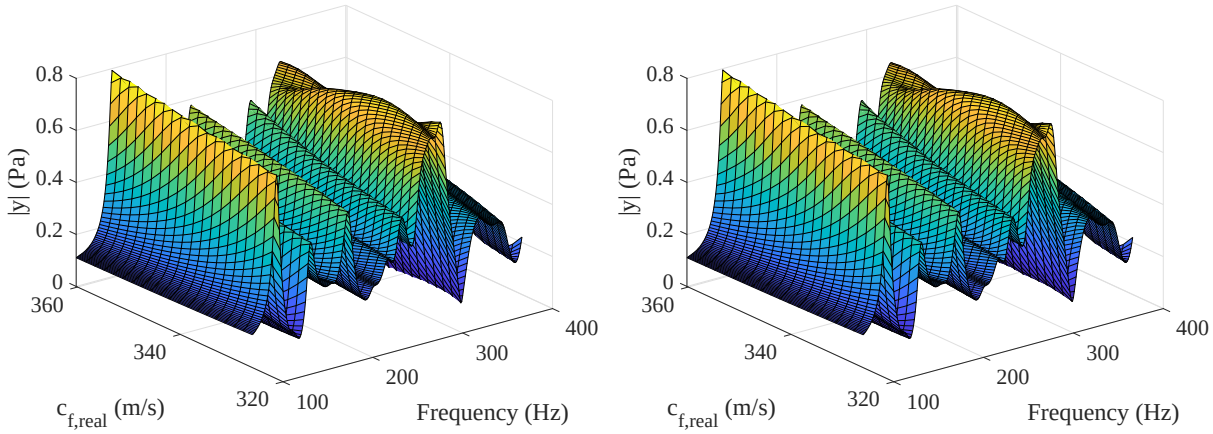


Figure 5. Pressure response of the coupled plate-cavity system by varying the most dominant parameter - real part of speed of sound $c_{\mathrm{f,real}}$, obtained from PMOR online phase (left) and full-order model computation (right) with corresponding maximum NRFD error $7.31 \cdot 10^{-3}$.

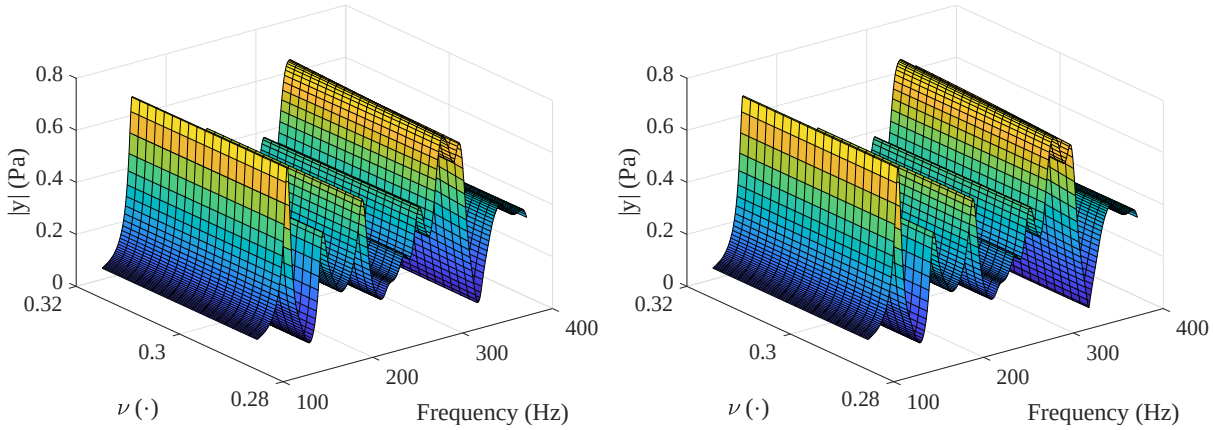


Figure 6. Pressure response of the coupled plate-cavity system by varying the least dominant parameter - the Poisson's ratio ν, obtained from PMOR online phase (left) and full-order model computation (right) with corresponding maximum NRFD error $5.45 \cdot 10^{-3}$.

7 CONCLUSIONS

In this paper, we presented a strategy along with algorithms for accelerating a PMOR training procedure using low-dimensional active subspaces. Using such an approach, we have shown the potential of such a method to address the curse of dimensionality by dimensionality reduction using gradient-based active subspace realization. For the representative vibroacoustic problem presented in this paper, the active subspace method reduces the number of parameters to a few number of active parameters - just two in our case. The advantage of using an active subspace for the training phase of a PMOR algorithm is significant and has yielded an accurate approximation of parametric response for the entire desired space. Furthermore, we see the requirement for efficient gradient evaluations of systems involving high dynamics, especially in the higher frequency domain with high modal density. Also, efficient optimization of presented PMOR algorithms with suitable interpolation or regression techniques to support large-scale practical applications are interesting for future research.

References

[1] D. Amsallem and C. Farhat. Interpolation method for adapting reduced-order models and application to aeroelasticity. *AIAA Journal*, 46(7):1803–1813, 2008.

[2] P. Benner, S. Gugercin, and K. Willcox. A survey of projection-based model reduction methods for parametric dynamical systems. *SIAM Review*, 57(4):483–531, 2015.

[3] C. Blech, C. K. Appel, R. Ewert, J. W. Delfs, and S. C. Langer. Numerical prediction of passenger cabin noise due to jet noise by an ultra–high–bypass ratio engine. *Journal of Sound and Vibration*, 464:114960, 2020.

[4] H.-J. Bungartz and M. Griebel. Sparse grids. *Acta Numerica*, 13:147–269, 2004.

[5] S. Chellappa, L. Feng, and P. Benner. A training set subsampling strategy for the reduced basis method. *Journal of Scientific Computing*, 89(3):63, 2021.

[6] P. G. Constantine. *Active subspaces: Emerging ideas for dimension reduction in parameter studies*, volume 2 of *SIAM spotlights*. Society for Industrial and Applied Mathematics, Philadelphia, 2015.

[7] P. G. Constantine, E. Dow, and Q. Wang. Active subspace methods in theory and practice: applications to kriging surfaces. *SIAM Journal on Scientific Computing*, 36(4):A1500–A1524, 2014.

[8] E. J. Grimme. *Krylov Projection Methods for Model Reduction*. PhD thesis, 1997.

[9] J. Herman and W. Usher. SALib: An open-source python library for sensitivity analysis. *The Journal of Open Source Software*, 2(9), 2017.

[10] Y. Hüpel, H. K. Sreekumar, and S. C. Langer. Pole-matching technique for parametric model order reduction of second order vibroacoustic systems. In *Proceedings of the DAGA Conference*, Vienna, Austria, 2021.

[11] I. T. Jolliffe and J. Cadima. Principal component analysis: a review and recent developments. *Philosophical Transactions of the Royal Society A: Mathematical, Physical and Engineering Sciences*, 374(2065):20150202, 2016.

[12] R. R. Lam, O. Zahm, Y. M. Marzouk, and K. E. Willcox. Multifidelity dimension reduction via active subspaces. *SIAM Journal on Scientific Computing*, 42(2):A929–A956, 2020.

[13] F. Nobile and D. Pradovera. Non-intrusive double-greedy parametric model reduction by interpolation of frequency-domain rational surrogates. *ESAIM: M2AN*, 55(5):1895–1920, 2021.

[14] F. Pedregosa, G. Varoquaux, A. Gramfort, V. Michel, B. Thirion, O. Grisel, M. Blondel, P. Prettenhofer, R. Weiss, V. Dubourg, J. Vanderplas, A. Passos, D. Cournapeau, M. Brucher, M. Perrot, and E. Duchesnay. Scikit-learn: Machine learning in Python. *Journal of Machine Learning Research*, 12:2825–2830, 2011.

[15] U. Römer, M. Bollhöfer, H. K. Sreekumar, C. Blech, and S. C. Langer. An adaptive sparse grid rational arnoldi method for uncertainty quantification of dynamical systems in the frequency domain. *International Journal for Numerical Methods in Engineering*, 122(20):5487–5511, 2021.

[16] H. K. Sreekumar, R. Ullmann, S. Sicklinger, and S. C. Langer. *Efficient Krylov Subspace Techniques for Model Order Reduction of Automotive Structures in Vibroacoustic Applications*, pages 259–282. Springer International Publishing, Cham, 2021.

[17] M. Tezzele, F. Ballarin, and G. Rozza. *Combined Parameter and Model Reduction of Cardiovascular Problems by Means of Active Subspaces and POD-Galerkin Methods*, pages 185–207. Springer International Publishing, Cham, 2018.

[18] M. Vohra, A. Alexanderian, H. Guy, and S. Mahadevan. Active subspace-based dimension reduction for chemical kinetics applications with epistemic uncertainty. *Combustion and Flame*, 204:152–161, 2019.

ICA 2022
24th INTERNATIONAL CONGRESS ON ACOUSTICS
October 24(Mon) - 28(Fri), 2022 Gyeongju, Korea

PROCEEDINGS of the
24th International Congress on Acoustics

October 24 to 28, 2022 in Gyeongju, Korea

ABS-0637

Random time-varying filtering with subsampling

Georg TAUBÖCK[(1)], Shristi RAJBAMSHI, Peter BALAZS[(2)]

[(1)]Institute of Telecommunications, TU Wien, Austria, georg.tauboeck@tuwien.ac.at

[(2)]Acoustics Research Institute, Austrian Academy of Sciences, Austria, peter.balazs@oeaw.ac.at

ABSTRACT

Time-varying filtering is of crucial importance in many areas of signal processing and, in particular, in audio processing. From a mathematical point of view, time-varying filters correspond to so-called "frame multipliers". Here, the audio signal is first transformed into another signal domain, typically by means of a time-frequency transformation; then, the resulting transformed signal coefficients are multiplied with a "symbol"; and, finally, an audio signal is re-synthesized. Depending on the choice of the symbol, a frame multiplier allows to amplify certain audio components and/or to suppress others. In this contribution, we consider frame multipliers, whose symbols are chosen at random with an additional subsampling step of the output signal. We show that the corresponding subsampled random time-varying filters satisfy remarkable mathematical properties. Moreover, we demonstrate that they are highly efficient for signal compression. Our analysis is based on the recent mathematical methodology "compressive sensing".

Keywords: Frames, Compressive Sensing, Frame Multiplier, Random Symbol Vector

1 INTRODUCTION

In audio and acoustics, time-dependent signal representation and processing techniques are highly relevant for various applications. A mathematical theory which is particularly suited to serve as framework for the development and analysis of such methods is *frame theory*. Frames provide the following general properties: *perfect reconstruction*, *stability*, *redundancy*, and a *signal-independent, linear inversion procedure*.

1.1 Frames and frame multipliers

A (finite) *frame* Ψ over $\mathbb{C}^N$ with frame bounds $0 < A \leq B < \infty$ is a family of Q vectors $\Psi = \{\psi_0, \ldots, \psi_{Q-1}\}$, $\psi_q \in \mathbb{C}^N$, such that

$$A\|\mathrm{x}\|_2^2 \leq \sum_{q=0}^{Q-1} \left|\langle \mathrm{x}, \psi_q \rangle\right|^2 \leq B\|\mathrm{x}\|_2^2, \qquad \forall \mathrm{x} \in \mathbb{C}^N.$$

The *synthesis operator* of a frame Ψ is defined as the operator[1] $\mathrm{T}_\Psi \colon \mathbb{C}^Q \to \mathbb{C}^N$, $\mathrm{a} = [a_0, \ldots, a_{Q-1}]^\mathsf{T} \mapsto \mathrm{T}_\Psi \mathrm{a} = \sum_{q=0}^{Q-1} a_q \psi_q$, and is (equivalently) represented via the $N \times Q$ synthesis operator matrix

$$\mathrm{T}_\Psi = \begin{bmatrix} \psi_0 & \psi_1 & \cdots & \psi_{Q-1} \end{bmatrix}.$$

A frame $\Psi = \{\psi_0, \ldots, \psi_{Q-1}\}$ over $\mathbb{C}^N$ is denoted as *full spark frame*, if *any* subfamily of N vectors $\{\psi_{q_0}, \ldots, \psi_{q_{N-1}}\}$ is linearly independent [1]. Accordingly, a matrix is called *full spark*, if the set of its column vectors constitutes a full spark frame.

[1]The superscripts $^\mathsf{T}$ and $^\mathsf{H}$ represent transposition and Hermitian transposition, respectively.

Suppose next that we are given two frames $\Psi = \{\psi_0, \ldots, \psi_{Q-1}\}$ over $\mathbb{C}^N$ and $\Phi = \{\phi_0, \ldots, \phi_{Q-1}\}$ over $\mathbb{C}^L$ with the same cardinality Q, respectively. The operator $\mathrm{M}_{\mathrm{m},\Phi,\Psi} \colon \mathbb{C}^N \to \mathbb{C}^L$ defined as[2]

$$\mathrm{x} \;\mapsto\; \mathrm{M}_{\mathrm{m},\Phi,\Psi}\mathrm{x} = \sum_{q=0}^{Q-1} m_q \langle \mathrm{x}, \psi_q \rangle \phi_q \tag{1}$$

is called *frame multiplier* with associated *symbol* (vector) $\mathrm{m} = [m_0, \ldots, \mathrm{m}_{Q-1}]^{\mathsf{T}} \in \mathbb{C}^Q$ [2]. Note that the corresponding frame multiplier matrix can be represented by the matrix product

$$\mathrm{M}_{\mathrm{m},\Phi,\Psi} = \mathrm{T}_\Phi \operatorname{diag}(\mathrm{m})\, \mathrm{T}_\Psi^{\mathsf{H}} = \begin{bmatrix} \phi_0 & \cdots & \phi_{Q-1} \end{bmatrix} \begin{bmatrix} m_0 & & 0 \\ & \ddots & \\ 0 & & m_{Q-1} \end{bmatrix} \begin{bmatrix} \psi_0^{\mathsf{H}} \\ \vdots \\ \psi_{Q-1}^{\mathsf{H}} \end{bmatrix}, \tag{2}$$

where $\operatorname{diag}(\mathrm{m})$ denotes the diagonal matrix with symbol vector m on its main diagonal.

1.2 Gabor systems

Let us define the following two linear operators on $\mathbb{C}^N$: the *cyclic shift* or *translation* operator $\mathrm{T} \colon \mathbb{C}^N \to \mathbb{C}^N$, which is given by

$$\mathrm{x} = [x_0, x_1, \ldots, x_{N-1}]^{\mathsf{T}} \;\mapsto\; \mathrm{Tx} = [x_{N-1}, x_0, x_1, \ldots, x_{N-2}]^{\mathsf{T}}$$

and the *modulation* or *frequency shift* operator $\mathrm{E} : \mathbb{C}^N \to \mathbb{C}^N$, which is given by

$$\mathrm{x} = [x_0, x_1, \ldots, x_{N-1}]^{\mathsf{T}} \;\mapsto\; \mathrm{Ex} = [x_0, \omega x_1, \ldots, \omega^{N-1} x_{N-1}]^{\mathsf{T}},$$

where $\omega = e^{2\pi \mathrm{i}/N}$. The operators $\pi(\lambda) = \mathrm{E}^j \mathrm{T}^k$, $\lambda = (k, j)$, are called *time-frequency shift* operators and the collection of vectors

$$(\mathrm{g}, \Lambda) = \{\pi(\lambda)\mathrm{g} : \lambda \in \Lambda\}, \qquad \text{where } \Lambda \subseteq \mathbb{Z}_N \times \mathbb{Z}_N$$

with $\mathbb{Z}_N = \{0, 1, \ldots, N-1\}$, is denoted as *Gabor system with window* g. If $\Lambda = \mathbb{Z}_N \times \mathbb{Z}_N$, (g, Λ) is called *full* Gabor system with window g. The number $R = \operatorname{card}(\Lambda)/N$ is referred to as *redundancy* of the Gabor system.

Gabor systems exhibit very rich structural properties. The following theorem was first proven in [3] for N prime and later generlized to all positve integers $N \in \mathbb{N}$ in [4].

Theorem 1. *For every positive integer N, there is some window* $\mathrm{g} \in \mathbb{C}^N$*, such that for all* $\Lambda \subseteq \mathbb{Z}_N \times \mathbb{Z}_N$ *with* $\operatorname{card}(\Lambda) \geq N$ *the Gabor system* $\Psi = (\mathrm{g}, \Lambda)$ *is a full spark frame. Morever, the set of such windows* g *is of full measure, i.e., its complement has N-dimensional Lebesgue measure zero.*

Obviously, one can consider multipliers for which Ψ and(/or) Φ are Gabor systems. A typical application scenario of such *Gabor multipliers* is to enhance, reduce, suppress, or even completely remove time-frequency (TF) components of a given signal according to a predefined TF mask (represented by the symbol m) [5, 6].

1.3 Linear time-invariant (LTI) and time-varying (LTV) filters

Let us consider a finite-dimensional LTI filter. It is described by a circulant matrix H, for which

$$\mathrm{H} = \begin{bmatrix} h_0 & h_{N-1} & \cdots & h_1 \\ h_1 & h_0 & & h_2 \\ \vdots & & \ddots & \vdots \\ h_{N-1} & h_{N-2} & \cdots & h_0 \end{bmatrix} = \mathrm{F}_N \operatorname{diag}(\mathrm{m})\, \mathrm{F}_N^{\mathsf{H}}, \tag{3}$$

where F_N denotes the unitary $N \times N$ discrete Fourier transform (DFT) matrix and $[h_0, \ldots, h_{N-1}]^{\mathsf{T}} = \frac{1}{\sqrt{N}} \mathrm{F}_N \mathrm{m}$.

[2] $\langle \cdot, \cdot \rangle$ denotes the conventional Euclidean inner product.

Comparing (3) with (2), we see that an LTI filter is a special case of frame multiplier with frame vectors given by the columns of F_N.

Furthermore, let us consider a finite-dimensional LTV filter. It can be represented by a general matrix H, for which the singular value decomposition is given by

$$\mathrm{H} = \mathrm{U}\,\mathrm{diag}(\mathrm{m})\,\mathrm{V}^{\mathsf{H}}. \tag{4}$$

Again, cf. (4) and (2), we conclude that any LTV filter can be rewritten as a frame multiplier.

2 COMPRESSIVE SENSING

Compressive sensing (CS) has been one of the major developments in applied mathematics in the past 15 years [7–9]. It considers the recovery of (approximately) sparse vectors from incomplete and possibly perturbed linear measurements via efficient algorithms such as ℓ_1-minimization.

In general, reconstruction of $\mathrm{x} = [x_0, \ldots, x_{N-1}]^{\mathsf{T}} \in \mathbb{C}^N$ from measurements

$$\mathrm{y} = \mathrm{Ax}, \tag{5}$$

where $\mathrm{A} \in \mathbb{C}^{M\times N}$ and $M \ll N$, is impossible without substantial *a priori* information about x. In compressive sensing (CS), the assumption that x is S-sparse, that is, $\|\mathrm{x}\|_0 = \mathrm{card}(\mathrm{supp}(\mathrm{x})) \leq S$ for some $S \ll N$ is introduced to guarantee uniqueness and efficient recoverability of x. An estimate $\hat{\mathrm{x}}$ of the sparse vector x can be obtained by means of solving the ℓ_0-minimization problem,

$$\text{(P0)} \qquad \hat{\mathrm{x}} = \arg\min_{z} \|\mathrm{z}\|_0 \qquad \text{subject to} \qquad \mathrm{y} = \mathrm{Az}.$$

In words, we search for the sparsest vector consistent with the measured data $\mathrm{y} = \mathrm{Ax}$. Unfortunately, ℓ_0-minimization is NP-hard in general. Consequently, a number of alternatives, for example, greedy algorithms [10], have been proposed in the literature. The most popular approach utilizes ℓ_1–minimization [7, 8, 11], that is, the convex program

$$\text{(P1)} \qquad \hat{\mathrm{x}} = \arg\min_{z} \|\mathrm{z}\|_1 \qquad \text{subject to} \qquad \mathrm{y} = \mathrm{Az}$$

is solved, where $\|\mathrm{z}\|_1 = |z_0| + |z_1| + \ldots + |z_{N-1}|$ denotes the usual ℓ_1 vector norm.

Whether the estimate $\hat{\mathrm{x}}$ obtained by programs (P0) or (P1) coincides with the true solution x in (5), depends on the properties of the so-called measurement matrix A. It is rather elementary to show [9] that $\hat{\mathrm{x}}$ obtained by (P0) satisfies $\hat{\mathrm{x}} = \mathrm{x}$ for all S-sparse x, if every set of $2S$ columns of A is linearly independent. Hence, it is desirable if A is full spark, since then any S-sparse signal x with $S \leq M/2$ is necessarily the unique sparsest solution to $\mathrm{y} = \mathrm{Ax}$.

To guarantee recoverability of the sparse vector x in (5) by means of program (P1) and greedy algorithms, it suffices to establish the restricted isometry property (RIP) of A [9]: define the restricted isometry constant δ_S of an $M \times N$ matrix A to be the smallest positive number that satisfies

$$(1-\delta_S)\|\mathrm{x}\|_2^2 \leq \|\mathrm{Ax}\|_2^2 \leq (1+\delta_S)\|\mathrm{x}\|_2^2 \qquad \text{for all x with } \|\mathrm{x}\|_0 \leq S. \tag{6}$$

In words, the statement (6) requires that all column submatrices of A with at most S columns are well-conditioned. Informally, A is said to satisfy the RIP with order S when δ_S is "small". Now, if the matrix A obeys (6) with $\delta_{\kappa S} < \delta^*$ for suitable constants $\kappa \geq 1$ and $\delta^* < 1$, then many algorithms precisely recover any S-sparse vectors x from the measurements $\mathrm{y} = \mathrm{Ax}$. Moreover, the RIP usually implies robustness w.r.t. noise and ensures that the algorithms produce reliable results not only for perfectly sparse but also for approximately sparse *(compressible)* vectors x [9].

It is worth mentioning the difference between matrices satisfying the RIP and full spark matrices. While the submatrices of full spark matrices are invertible, they may not be well-conditioned as required for the RIP to

hold. Unfortunately, for deterministic matrices, it is difficult to determine the conditioning of every submatrix; to date, no deterministic RIP matrix is known to perform optimally [12], whereas deterministic constructions of full spark matrices are known [1].

A natural generalization of the CS framework mentioned above is the situation when x is assumed to be sparse w.r.t. a given dictionary D, i.e., $\mathrm{x} = \mathrm{D}\mathrm{s}$ with $\|\mathrm{s}\|_0 \leq S \ll N$, where D is allowed to differ from the identity matrix. A straightforward (though maybe not necessarily optimum) way to address this generalization is to consider the composite measurement matrix $\mathrm{A}' \triangleq \mathrm{A}\mathrm{D}$ and solve programs (P0) or (P1) using A' instead of A to obtain an estimate $\hat{\mathrm{s}}$ of the coefficient vector s; an estimate of x is then obtained via $\hat{\mathrm{x}} = \mathrm{D}\hat{\mathrm{s}}$.

3 TIME-VARYING FILTERS AS CS MEASUREMENTS

We now investigate the applicability of time-varying filters or, equivalently, of frame multipliers, cf. Subsection 1.3, as CS measurements (see also [13, 14] for an approach without subsampling). Let us first recall the key assumption in CS that the number of measurements is (much) smaller than the ambient dimension of the unknown vector x, i.e., $M \ll N$. Although our definition of a frame multiplier (1) allows for different dimensions N and L, we note that many frame multipliers used in practice restrict to the special case $N = L$. Therefore, to ensure "compatibility" with the CS framework for these practically relevant frame multipliers as well, we incorporate the necessary dimensionality reduction via an additional subsampling step. More formally, for a subset $\mathscr{M} \subseteq \{0, \ldots, L-1\}$ of cardinality M, let $\mathrm{P}_{\mathscr{M}} : \mathbb{C}^L \to \mathbb{C}^M$, $\mathrm{x} \mapsto \mathrm{x}_{\mathscr{M}}$ be the operator that restricts a vector to the entries indexed by $\mathscr{M}$. The main question we would like to address is if measurement matrices of the form

$$\mathrm{A} = \mathrm{P}_{\mathscr{M}} \mathrm{M}_{\mathrm{m},\Phi,\Psi} \in \mathbb{C}^{M \times N} \tag{7}$$

are suitable for CS reconstruction.

In the following, we assume that Ψ and Φ are full spark frames. This encompasses the important cases, where Ψ and Φ are harmonic frames [15], i.e., frames whose synthesis operator matrix consists of the first N rows of the $Q \times Q$ DFT matrix, as well as where Ψ and Φ are Gabor systems for almost all choices of windows according to Theorem 1. Thus, in fact, both subsampled Fourier and Gabor multipliers are covered by our framework, or, equivalently stated (see Subsection 1.3), subsampled time-invariant and time-varying systems, respectively, are investigated as measurement procedures.

Furthermore, let $Q = \mathrm{card}(\Psi) = \mathrm{card}(\Phi) \geq N + L - 1$. We have (see next theorem for its formal statement) that there exists a symbol $\mathrm{m} \in \mathbb{C}^Q$ such that the $\mathrm{card}(\mathscr{M}) \times N$ measurement matrix A defined in (7) is full spark for all $\mathscr{M} \subseteq \{0, \ldots, L-1\}$. Moreover, this holds for almost all symbols.

Theorem 2. *Let Ψ and Φ are full spark frames over $\mathbb{C}^N$ and $\mathbb{C}^L$ with same cardinality $Q = \mathrm{card}(\Psi) = \mathrm{card}(\Phi)$. Provided that $Q \geq N + L - 1$, the symbol* m *can be chosen in a way such that the subsampled frame multiplier matrix $\mathrm{P}_{\mathscr{M}} \mathrm{M}_{\mathrm{m},\Phi,\Psi}$ is full spark for all subsets $\mathscr{M} \subseteq \{0, \ldots, L-1\}$, $\mathscr{M} \neq \emptyset$. Moreover, the set of such symbols is of full measure, i.e., its complement has Q-dimensional Lebesgue measure zero.*

Note that this theorem can be generalized to the situation when x is assumed to be sparse w.r.t. a given dictionary D (cf. Section 2).

Theorem 3. *Let Ψ and Φ are full spark frames over $\mathbb{C}^N$ and $\mathbb{C}^L$ with same cardinality $Q = \mathrm{card}(\Psi) = \mathrm{card}(\Phi)$, respectively. Provided that $Q \geq N + L - 1$, the symbol* m *can be chosen in a way such that a vector* x *which is S-sparse ($S \leq L/2$) w.r.t. a given dictionary* D *is necessarily the unique sparsest solution (w.r.t.* D*) to the reconstruction problem*

$$\mathrm{y} = \mathrm{P}_{\mathscr{M}} \mathrm{M}_{\mathrm{m},\Phi,\Psi} \mathrm{x}$$

for all subsets $\mathscr{M} \subseteq \{0, \ldots, L-1\}$ with $\mathrm{card}(\mathscr{M}) \geq 2S$. Moreover, the set of such symbols is of full measure, i.e., its complement has Q-dimensional Lebesgue measure zero.

Therefore, time-varying filtering with subsampling constitutes an effective CS measurement procedure provided that the assumptions of the Theorems 2 and 3 are met. The proofs of Theorems 2 and 3 can be found in [16].

4 AUDIO SIGNAL COMPRESSION

We now assess the compression capabilities of time-varying filtering with subsampling for real-world audio signals. To that end, we choose the signal "a16_clarinet" from the EBU SQAM dataset [17] as our input audio signal x. This signal is sampled at 22.05 kHz and consists of 131072 samples. Since it is real-valued, we set $\mathrm{x} = \mathrm{D}\mathrm{s}$, where D corresponds to a Gabor synthesis matrix that only takes into account positive frequencies (real discrete Gabor transform). More specifically, we use a Gabor system with rectangular grid $\Lambda = \{0, a, \ldots, (N/a-1)a\} \times \{0, b, \ldots, (N/b-1)b\}$, where $a = 512$ and $b = 64$, and with a periodized and normalized Gaussian window. Hence, the dimension of D is 131072 $\times$ 262400. As shown in Fig. 1, this signal is approximately sparse in the TF domain. The measurement vector y is obtained via $\mathrm{y} = \mathrm{P}_{\mathscr{M}}\mathrm{M}_{\mathrm{m},\Phi,\Psi}\mathrm{x}$, where $\Phi = \Psi$ are again Gabor systems with rectangular grid $\Lambda = \{0, a, \ldots, (N/a-1)a\} \times \{0, b, \ldots, (N/(b)-1)b\}$; however, with parameters $a = 16$ and $b = 4096$ (redundancy $R = 2$). We choose the Gabor window at random (standard normal distributed; canonical tight window), as this will yield a full spark frame with probability 1 according to Theorem 1. Similarly, the symbol is a realization of a zero-mean proper complex Gaussian random vector with identity covariance matrix, so that the assumptions of Theorems 2 and 3 are met with probability 1. Moreover, we subsample every third element, i.e., $\mathscr{M} = \{0, 3, 6 \ldots, 131070\}$, achieving a compression ratio of 1:3. Since this is a large scale problem, we employ the SPGL1 software [18, 19] to recover TF coefficients $\hat{\mathrm{s}}$ and apply $\hat{\mathrm{x}} = \mathrm{D}\hat{\mathrm{s}}$ to reconstruct the original audio signal. It can be seen from Fig. 1 that the difference between original and reconstructed signal is relatively small.

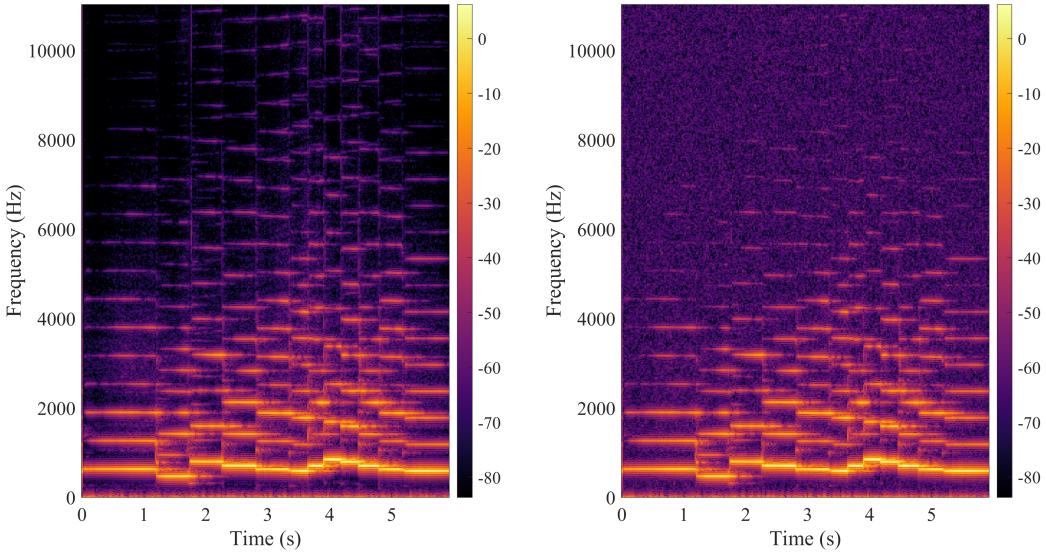


Figure 1. Real discrete Gabor transform magnitude of the audio signal "a16_clarinet": original signal (left), reconstructed signal (right).

5 CONCLUSIONS

We demonstrated that random time-varying filtering with subsampling can be efficiently used for compressive sampling of signals that are sparse with respect to a given dictionary. We showed excellent compression performance not only for ideally sparse but also for approximately sparse (compressible) signals. This is important because real-world signals such as audio signals are rarely ideally sparse. Our experiments indicated that for audio signals a compression ratio of 1:3 is easily possible without notable differences. Therefore, we believe that random time-varying filters, or equivalently, random frame multipliers, will be a very useful tool for present and future audio applications.

ACKNOWLEDGEMENTS

This work was supported by WWTF grant INSIGHT (MA16-53).

REFERENCES

[1] B. Alexeev, J. Cahill, and D. G. Mixon, "Full spark frames," *Journal of Fourier Analysis and Applications*, vol. 18, pp. 1167–1194, Dec. 2012.

[2] P. Balazs, "Basic definition and properties of Bessel multipliers," *Journal of Mathematical Analysis and Applications*, vol. 325, no. 1, pp. 571–585, 2007.

[3] J. Lawrence, G. E. Pfander, and D. Walnut, "Linear independence of Gabor systems in finite dimensional vector spaces," *Journal of Fourier Analysis and Applications*, vol. 11, no. 6, pp. 715–726, 2005.

[4] R.-D. Malikiosis, "A note on Gabor frames in finite dimensions," *Applied and Computational Harmonic Analysis*, vol. 38, no. 2, pp. 318–330, 2015.

[5] H. G. Feichtinger and K. Nowak, "A first survey of Gabor multipliers," in *Advances in Gabor analysis*, pp. 99–128, Springer, 2003.

[6] P. Balazs, B. Laback, G. Eckel, and W. A. Deutsch, "Time–frequency sparsity by removing perceptually irrelevant components using a simple model of simultaneous masking," *IEEE Transactions on Audio, Speech, and Language Processing*, vol. 18, no. 1, pp. 34–49, 2010.

[7] E. J. Candès, J. Romberg, and T. Tao, "Robust uncertainty principles: Exact signal reconstruction from highly incomplete frequency information," *IEEE Trans. Inf. Theory*, vol. 52, no. 2, pp. 489–509, 2006.

[8] D. L. Donoho, "Compressed sensing," *IEEE Transactions on Information Theory*, vol. 52, pp. 1289–1306, Apr. 2006.

[9] S. Foucart and H. Rauhut, *A Mathematical Introduction to Compressive Sensing*. Applied and Numerical Harmonic Analysis, Basel: Birkhäuser, 2013.

[10] J. A. Tropp, "Greed is good: Algorithmic results for sparse approximation," *IEEE Trans. Inf. Theory*, vol. 50, pp. 2231–2242, Oct. 2004.

[11] S. S. Chen, D. L. Donoho, and M. A. Saunders, "Atomic decomposition by basis pursuit," *SIAM review*, vol. 43, no. 1, pp. 129–159, 2001.

[12] A. S. Bandeira, M. Fickus, D. G. Mixon, and P. Wong, "The road to deterministic matrices with the restricted isometry property," *Journal of Fourier Analysis and Applications*, vol. 19, no. 6, pp. 1123–1149, 2013.

[13] G. Tauböck, S. Rajbamshi, P. Balazs, and L. D. Abreu, "Random Gabor multipliers and compressive sensing," in *13th International conference on Sampling Theory and Applications (SampTA)*, pp. 1–4, 2019.

[14] S. Rajbamshi, G. Tauböck, P. Balazs, and L. D. Abreu, "Random Gabor multipliers for compressive sensing: A simulation study," in *27th European Signal Processing Conference (EUSIPCO)*, pp. 1–5, 2019.

[15] O. Christensen *et al.*, *An introduction to frames and Riesz bases*. Springer, 2016.

[16] G. Tauböck, S. Rajbamshi, and P. Balazs, "Frame multipliers and compressive sensing," *preprint*, 2022.

[17] EBU, "EBU SQAM CD: Sound quality assessment material recordings for subjective tests."

[18] E. van den Berg and M. P. Friedlander, "SPGL1: A solver for large-scale sparse reconstruction," Dec. 2019. https://friedlander.io/spgl1.

[19] E. van den Berg and M. P. Friedlander, "Probing the pareto frontier for basis pursuit solutions," *SIAM Journal on Scientific Computing*, vol. 31, no. 2, pp. 890–912, 2008.

ICA 2022
24th INTERNATIONAL CONGRESS ON ACOUSTICS
October 24(Mon) - 28(Fri), 2022 Gyeongju, Korea

PROCEEDINGS of the
24th International Congress on Acoustics

October 24 to 28, 2022 in Gyeongju, Korea

ABS-0794

Grid-like wavelet sampling for audio processing applications

Clara HOLLOMEY*, Nicki HOLIGHAUS, Günther KOLIANDER

Acoustics Research Institute, Academy of Sciences, Austria

*clara.hollomey@oeaw.ac.at

ABSTRACT

We present a novel sampling strategy that enables the use of wavelet transforms with audio processing algorithms that rely on a time-frequency matrix structure as present in the short-time Fourier transform (STFT). We apply the proposed scheme to a blind source separation task based on non-negative matrix factorization and give practical guidance on the usage of the transform for audio applications. Comparable results to those achieved via the STFT demonstrate the potential of the method. Wavelet transforms exhibit a constant center frequency to bandwidth ratio (Q-factor) and are thus particularly useful for representing audio data, but prior, non-uniform sampling strategies do not lend themselves well to audio processing. Specifically, the sampling interval classically decreases with the wavelets' center frequency, and the resulting coefficients have no time-frequency matrix structure. By introducing quasi-random delays, we construct invertible wavelet transforms with linearly spaced center frequencies and a fixed sampling interval. Interpreting the resulting coefficients as a time-frequency matrix provides access to processing schemes that are normally not readily usable with wavelet transforms.

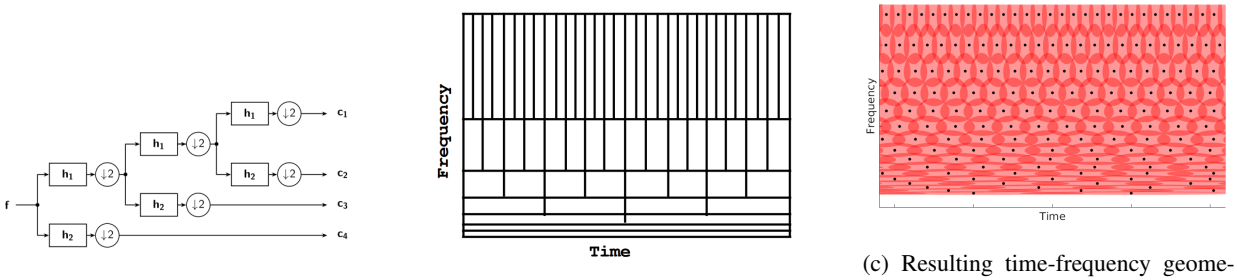
Keywords: Wavelets, Sampling, Audio analysis

1 INTRODUCTION

Constructed by scaling a fixed *mother wavelet*, wavelet filters are functions that exhibit a fixed number of oscillations, usually designed for simultaneously localizing a signal in time and frequency [2]. Due to the scaling, their bandwidth increases linearly with frequency, such that wavelets favor signal representations on logarithmic frequency axes that give rise to efficient invertible filter bank implementations, most notably [11]. As a consequence, wavelet transforms can offer a worthwhile alternative to the Fourier transform, particularly for the processing of signals with frequencies spanning several orders of magnitude, such as audio.

However, precisely their constant center frequency to bandwidth ratio forms an impediment to the application of the wavelet transform in practice. The efficient approaches for constructing invertible wavelet bases mentioned above rely on the dyadic splitting of the time-frequency plane, which restricts the bandwidth of the frequency channels, potentially yielding undesirably low frequency resolution [4]. Approaches that provide more flexibility [3], on the other hand, usually yield highly redundant time-frequency coefficients [14], and are thus less efficient. Moreover, in addition to flexibility in the choice of frequency scaling and the invertibility of the time-frequency coefficients, many audio processing algorithms (e.g. [6, 15, 9]) require the alignment of time-frequency coefficients over frequency. For the short-time Fourier transform (STFT), those requirements are easily fulfilled when its downsampling factor which is usually the same for all frequency channels, is chosen such that the invertibility of the resulting coefficients is ensured. For wavelets, choosing the same downsampling factor for all frequency channels and imposing invertibility of the transform implies excessive redundancy and therefore often impairs its practical usefulness.

In [8], we introduced a sampling scheme mitigating those trade-offs, and exemplified its suitability for audio processing applications. Here, we summarize that approach and describe the implementation and usage of the resulting filter bank.

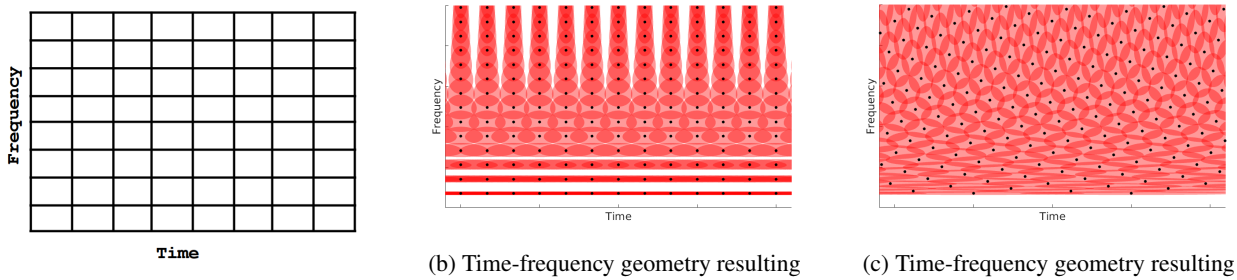


(a) Mallat's algorithm, from [1]

(b) Resulting sampling grid

(c) Resulting time-frequency geometry, from [8]

Figure 1. A typical filter bank structure for implementing the fast dyadic wavelet transform, also termed Mallat's algorithm. The resulting sampling grid yields a time-frequency geometry that covers the time-frequency plane evenly.



(a) Uniform sampling grid

(b) Time-frequency geometry resulting from equidistant sampling, from [8]

(c) Time-frequency geometry resulting from grid-like sampling, from [8]

Figure 2. A uniform time-frequency sampling grid; the resulting time-frequency geometry does not cover the time-frequency plane well. The proposed grid-like sampling provides even coverage.

2 GRID-LIKE WAVELET SAMPLING

Classical approaches to the wavelet transform, such as Mallat's algorithm depicted in Figure 1(a) achieve spectral coverage by tieing the downsampling factor to the channel number per tree level. The consequential time-frequency sampling grid is not equidistantly spaced, as schematically depicted in Figure 1(b), but achieves even coverage of the time-frequency plane, see Figure 1(c). Uniform sampling on a grid, on the other hand, does not lead to similarly even coverage of the time-frequency plane, as depicted in Figure 2(b).

Intuitively, to obtain a matrix-like time-frequency structure of samples and invertibility at the same time, a sampling scheme for wavelets should thus, on the one hand, be equidistributed on the time-frequency plane to ensure that one sampling value lies within each tile of the grid depicted in Figure 2(a). On the other hand, it should permit sufficient variation in the spacing of sampling points to achieve even coverage of the time-frequency plane.

A sequence in the domain $[0,1)^d$ is called equidistributed, if, asymptotically, the number of points in every subset of the domain is approximately proportional to the size of the subset. Random and pseudorandom processes yield such equidistributed sequences, but do not satisfy a counterpart of equidistribution for finite sequences. Thus, although in discrete scenarios, equidistribution of a sequence may arise empirically, it is not guaranteed, and may only do so for subsequences that are prohibitively long in a sampling context. Low discrepancy sequences [5] exhibit characteristics of random and pseudorandom sequences, but are constructed according to deterministic principles to achieve a specific type of equidistribution on specified intervals even for finite subsequences of almost arbitrary length. Many low discrepancy sequences are designed such that they guarantee a certain order of convergence in their prime application, numeric integration via the quasi-Monte

Carlo method [12]. As we demonstrate, they can be used equally well to ensure even coverage of the time-frequency plane by wavelet atoms.

We use low discrepancy sequences for generating a small delay that is applied to each filter in the wavelet transform to achieve the even coverage of the time-frequency plane depicted in Figure 2(c). More specifically, for a given mother wavelet ψ, wavelet filters are generated via dilation by $s_j = \left(\frac{1}{b} + \frac{j}{q}\right)^{-1} > 0$ and translation by $d(l+\delta_j)$

$$\psi_{l,j}[n] = \frac{1}{\sqrt{s_j}} \psi \left[\frac{n - d(l+\delta_j)}{s_j} \right] \tag{1}$$

where $d, b, q > 0$ and δ_j corresponds to the delay and is generated by a low discrepancy sequence $(\delta_0, \delta_1, \delta_2, \ldots)$.

3 IMPLEMENTATION AND USAGE

The grid-like sampled wavelet transform is implemented in MATLAB/GNU Octave as part of the filter bank framework of the Large Time-Frequency Analysis Toolbox (LTFAT) 2.5 [13]. It comprises `waveletfilters`, a function that derives the wavelets along with their associated downsampling factors and center frequencies, and the actual `filterbank` function, that, based on the output of `waveletfilters`, computes the time-frequency coefficients for a specific input signal.

`waveletfilters` is a general purpose tool for generating wavelet functions that cover a specified filter bank length and frequency range. In its default configuration, besides the filter bank length to be covered, `waveletfilters` accepts a vector of nearly arbitrary scales as input arguments. A mother wavelet is then generated, and the downsampling factors are derived therefrom according to the input scales. The mother wavelet is specified in the frequency domain, with a Cauchy wavelet as the default and centered at a relative frequency of $f_{CW} = 0.1$, i.e., a scale of 1 always corresponds to a wavelet with relative center frequency 0.1. In compliance with LTFAT's conventions for relative frequency that standardize the Nyquist frequency f_{NL} to one, the minimum scale s_N (and corresponding relative center frequency f_N) accepted by `waveletfilters` is thus limited by its internal Nyquist frequency

$$f_N = \frac{f_{NL}}{f_{CW}} = \frac{1}{0.1} = 10, \tag{2}$$

to $s_N \geq \frac{1}{f_N} = 0.1$. Alternatively to providing the scales directly, linear frequency spacing across the range of interest can be achieved by specifying a desired minimal and maximal frequency, as well as the desired number of wavelet channels M. For our proposed grid-like sampling scheme, the desired sequence of delays is additionally passed to `waveletfilters` as an optional parameter, either as a vector or as an anonymous function, describing e.g. a low discrepancy sequence, such as a Kronecker [10] or the van der Corput sequence [16].
Since the bandwidth of a wavelet increases proportional to its center frequency, the lower frequency regions of the transform may, as depicted in Figures 1(c) and 2(c), be insufficiently covered for allowing stable inversion. To mitigate this issue the `waveletfilters` implementation adds one lowpass filter by default to cover the frequency range from zero to the lowest wavelet center frequency specified. For greater flexibility, it is also possible to parametrize `waveletfilters` such that this frequency range is covered by several frequency-shifted copies of that wavelet.

An example for the usage of a wavelet filter bank in a uniform filter bank setting is given in Listing 1. The synthesis of the time domain signal can be achieved efficiently by calculating the dual window via the function `filterbankrealdual` and making use of the filter bank inversion routine `ifilterbank`, which are readily available in LTFAT. `ifilterbank` generally outputs complex signals. Energy-preserving recovery of real signals, such as audio, thus necessitates the multiplication by a factor of two, as indicated in lines 33 and 34 of the listing.

Listing 1: GNU Octave usage example for grid-like wavelet sampling in a uniform filter bank setting

```
% access the audio file and its sampling frequency
[x,fs] = audioread('inputsignal.wav');
%the filter bank length corresponds to the length of the audio file
Ls = length(x);

% delays via a golden Kronecker sequence
alpha = 1-2/(1+sqrt(5)); % 1-1/(goldenratio)
delays = @(n,a) a*(mod(n*alpha+.5,1)-.5);

% parameters of the wavelet transform
redundancy = 2;
M = 1021; %number of frequency channels minus the lowpass filter
start_index = 3; % number of channels to be covered by copies
                 % of the lowest frequency wavelet

% derive the scales
fmax = 10; % 10=Nyquist frequency
freq_step = fmax/M; % steps in frequency
fmin = freq_step*start_index; % center frequency of the minimum wavelet channel
scales = 1./linspace(fmin,fmax,M-start_index+1);

% generate grid-like sampled wavelet filters with a redundancy of two
% for the usage in a filter bank with uniform downsampling factors
[g, a, fc, L, info] = waveletfilters(Ls,scales,'delay',delays, 'redtar', redundancy,...
'uniform', 'repeat');

% compute the time-frequency coefficients via a uniform filter bank
X = ufilterbank(x,g,a);

% synthesize the time-domain signal via an inverse filter bank
% calculate the dual windows
gd = filterbankrealdual(g,a,L);
%set flag 'real' to implicitly multiply by two and take the real part of the output
y=ifilterbank(X, gd, a, Ls,'real');
```

4 AUDIO PROCESSING APPLICATIONS

Grid-like wavelet sampling can be used as a plug-and-play alternative to the STFT. In [6], Févotte et al. used nonnegative matrix factorization (NMF)—a dimension-reduction technique for non-negative data, optimized with regards to the Itakura-Saito divergence—for the decomposition of audio signals. They obtained a meaningful factorization of spectrograms S as $S = W \cdot H$, with component and activation matrices W and H, respectively. Adapting the code from [6], we achieved similar results in [8] when replacing the spectrogram with the time-frequency coefficients obtained from the grid-like sampled wavelet transform. In [8], we chose the parameters of the wavelet transform according to frame theoretic considerations. Here, we take a more practical angle, using the STFT as a baseline to outline necessary considerations when applying the grid-like wavelet transform as its substitute.

As an input signal, we consider a piano recording, a sequence of six chords and use the NMF algorithm to split them into eight components. The smoothing prior introduced in [6] was not used, i.e., its weight was set to 0. For both transforms, $M = 1024$ frequency channels were used, with $M = 1018$ wavelet channels and 6 lowpass channels of the wavelet transform matching the $M = 1024$ uniform channels of the STFT used in [6]. Similarly, the total oversampling rate of the wavelet transform was set to 2, matching [6]. The delays δ_i were

generated via a Kronecker sequence [10]. A Cauchy wavelet with hyperparameter $\alpha = 1200$ and a sinebell window were used, respectively. This resulted, after truncation for numeric reasons, in a wavelet transform where the frequency support of the middle scales (i.e. those around 5.5kHz for the audio signal used in this setup) had a similar frequency support to the window of the STFT. Nonetheless, the bandwidth of the STFT filters remains fixed across frequency, whereas the wavelet filters have a constant center frequency to bandwidth ratio, such that there is no direct correspondence between both representations.

The results, depicted in Figures 3 and 4, were sorted in decreasing order of variance of their temporal components and analyzed via a constant-Q transform [7] for better display of the characteristic patterns. Overall, the audio tracks are similar. In both cases, tracks 1-4 (counted from highest to lowest variance of the temporal components) represent the various notes of the chord, with the wavelets providing slightly less separation across frequency, while the last two components appear to capture low-intensity, residual sound. The main differences lie in tracks 5 and 6. From visual inspection and informal listening, it appears that the audio captured in track 5 by the STFT-NMF has been split into two tracks, track 5 and 6, by the wavelet-NMF.

5 FURTHER RESOURCES

The code for the grid-like sampled wavelet transform can be freely downloaded as part of the Large Time-Frequency Analysis Toolbox (LTFAT) 2.5 under the General Public License version 3. LTFAT, supplemental code and additional material comprising experimental results and audio examples are available from `http://ltfat.org`.

ACKNOWLEDGEMENTS

We would like to thank Cédric Févotte for kindly providing their code for Itakura-Saito NMF and some guidance on its use. We further thank Georg Tauböck for fruitful discussion on potential applications of the proposed method.

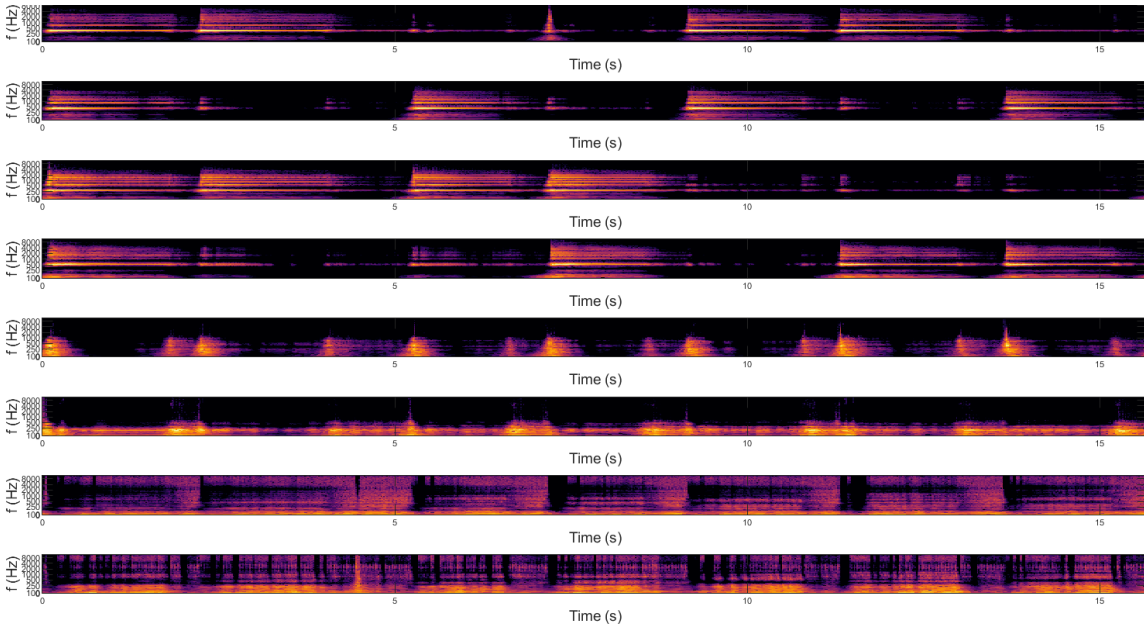


Figure 3. Audio components obtained from the NMF based on the grid-like sampled wavelet transform, sorted in order of descending variance of their temporal components, plots were normalized to equal magnitude for better display

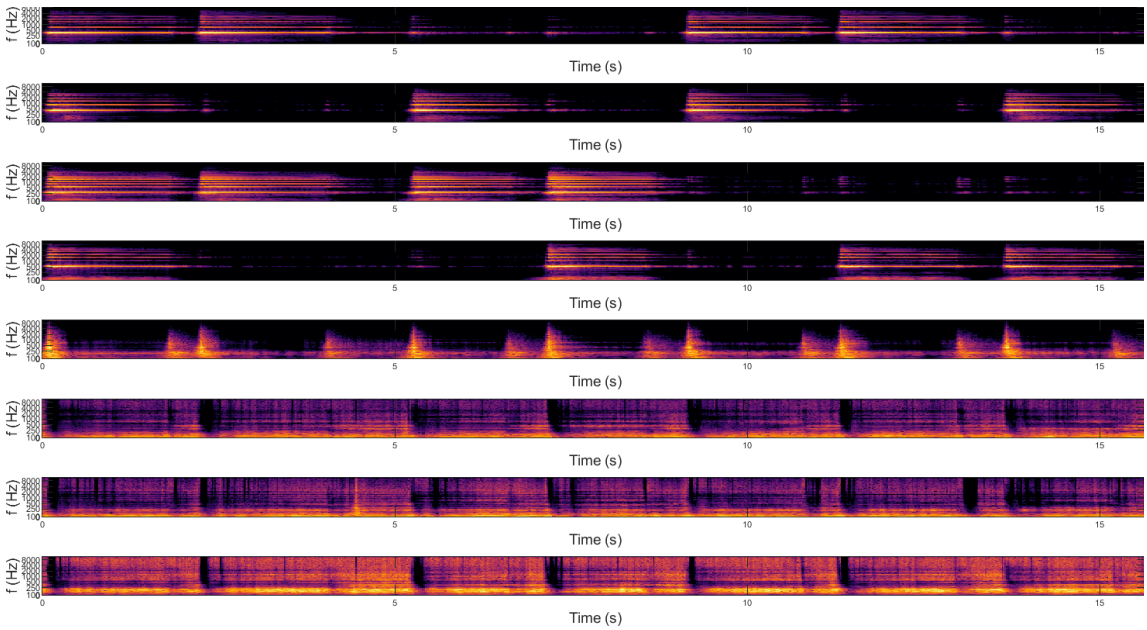


Figure 4. Audio components obtained from the NMF based on the STFT, sorted in order of descending variance of their temporal components; plots were normalized to equal magnitude for better display

References

[1] Homepage of the Large Time-Frequency Analysis Toolbox. `ltfat.org`. Accessed: 2022-08-04.

[2] C. Burrus, R. Gopinath, and H. Guo. Introduction to Wavelets and Wavelet Transform—A Primer. *Recherche*, 67, 01 1998.

[3] R. Coifman and M. Wickerhauser. Entropy-based algorithms for best basis selection. *IEEE Transactions on Information Theory*, 38(2):713–718, 1992.

[4] I. Daubechies. Orthonormal bases of compactly supported wavelets. *Communications on Pure and Applied Mathematics*, 41(7):909–996, 1988.

[5] J. Dick and F. Pillichshammer. *Digital Nets and Sequences: Discrepancy Theory and Quasi–Monte Carlo Integration*. Cambridge University Press, 2010.

[6] C. Févotte. Majorization-minimization algorithm for smooth Itakura-Saito nonnegative matrix factorization. In *2011 IEEE International Conference on Acoustics, Speech and Signal Processing (ICASSP)*, pages 1980–1983, 2011.

[7] N. Holighaus, M. Dörfler, G. A. Velasco, and T. Grill. A framework for invertible, real-time constant-Q transforms. *IEEE Transactions on Audio, Speech, and Language Processing*, 21(4):775–785, 2012.

[8] N. Holighaus, G. Koliander, C. Hollomey, and F. Pillichshammer. Grid-based Decimation for Invertible Wavelet Transforms in Audio Processing. *submitted*, 2022. `https://ltfat.org/notes/ltfatnote057.pdf`.

[9] F. Jaillet and B. Torrésani. Time-Frequency Jigsaw Puzzle: adaptive multiwindow and multilayered Gabor expansions. *International Journal of Wavelets, Multiresolution and Information Processing*, 05, 03 2007.

[10] L. Kuipers and H. Niederreiter. *Uniform Distribution of Sequences*. John Wiley, 1974.

[11] S. Mallat. A theory for multiresolution signal decomposition: the wavelet representation. *IEEE Transactions on Pattern Analysis and Machine Intelligence*, 11(7):674–693, 1989.

[12] H. Niederreiter. *Random Number Generation and Quasi-Monte Carlo Methods*. CBMS-NSF Regional Conference Series in Applied Mathematics. Society for Industrial and Applied Mathematics, 1992.

[13] Z. Průša, P. L. Søndergaard, N. Holighaus, C. Wiesmeyr, and P. Balazs. The Large Time-Frequency Analysis Toolbox 2.0. In M. Aramaki, O. Derrien, R. Kronland-Martinet, and S. Ystad, editors, *Sound, Music, and Motion*, pages 419–442. Springer, Cham, Switzerland, 2014.

[14] Z. Průša, P. L. Søndergaard, and P. Rajmic. Discrete Wavelet Transforms in the Large Time-Frequency Analysis Toolbox for Matlab/GNU Octave. *ACM Trans. Math. Softw.*, 42(4):32:1–32:23, June 2016.

[15] G. Tauböck, S. Rajbamshi, and P. Balazs. Dictionary Learning for Sparse Audio Inpainting. *IEEE Journal of Selected Topics in Signal Processing*, 15(1):104–119, 2021.

[16] J. G. van der Corput. Verteilungsfunktionen I-II. *Proc. Akad. Wet. Amsterdam*, 38:813–821, 1058–1066, 1935.

ICA 2022
24th INTERNATIONAL CONGRESS ON ACOUSTICS
October 24(Mon) - 28(Fri), 2022 Gyeongju, Korea

PROCEEDINGS of the
24th International Congress on Acoustics

October 24 to 28, 2022 in Gyeongju, Korea

ABS-0930

Differentiable Dictionary Search: Integrating Linear Mixing with Deep Non-linear Modelling for Audio Source Separation

Lukáš Samuel Marták, Rainer Kelz, Gerhard Widmer

[1]Institute of Computational Perception & LIT AI Lab, Johannes Kepler University Linz, Austria, lukas.martak@jku.at

ABSTRACT

This paper describes several improvements to a new method for signal decomposition that we recently formulated under the name of Differentiable Dictionary Search (DDS). The fundamental idea of DDS is to exploit a class of powerful deep invertible density estimators called normalizing flows, to model the dictionary in a linear decomposition method such as NMF, effectively creating a bijection between the space of dictionary elements and the associated probability space, allowing a differentiable search through the dictionary space, guided by the estimated densities. As the initial formulation was a proof of concept with some practical limitations, we will present several steps towards making it scalable, hoping to improve both the computational complexity of the method and its signal decomposition capabilities. As a testbed for experimental evaluation, we choose the task of frame-level piano transcription, where the signal is to be decomposed into sources whose activity is attributed to individual piano notes. To highlight the impact of improved non-linear modelling of sources, we compare variants of our method to a linear overcomplete NMF baseline. Experimental results will show that even in the absence of additional constraints, our models produce increasingly sparse and precise decompositions, according to two pertinent evaluation measures.

Keywords: differentiable dictionary search, non-negative matrix factorization, normalizing flows, invertible neural networks, audio signal decomposition.

1 INTRODUCTION

Decomposing a signal that was produced as a mixture of source signals is an essential task in signal analysis, with applications in audio source separation, automatic speech recognition, audio de-noising, musical instrument recognition, musical audio de-mixing, harmonic-percussive source separation, musical melody extraction, polyphonic music transcription, and many more. In different domains, various assumptions are made about the nature of what is to be considered an elementary source signal, and different artifacts of decomposition are desirable, dictated by the respective objectives.

This has led to a multitude of conceptually different approaches to signal mixture decomposition. *Linear methods* such as Non-negative Matrix Factorization (NMF) have been widely extended, adjusted and customized with various constraints, to incorporate assumptions and inductive biases accommodating specificities of particular problems. In contrast, more general and highly flexible *non-linear models* such as, specifically, deep end-to-end neural networks have been successfully trained to perform mixture decomposition. While the linear methods have inherent performance limitations relating to their modeling capacity, they seem to have an edge at both the interpretability of inference, and robustness of performance in the face of distribution shift between training and inference, when compared to these deep non-linear models.

In this work, we aim to advance an ongoing effort in integrating the strengths of these contrasting approaches. The assumption of approximately linear mixing of sources is reflected in our use of additive source re-composition of NMF. This can be seen as a strong inductive bias on the algorithm searching for optimal signal decomposition, since it significantly constrains the size of available hypothesis space, as opposed to a non-linear mixing model. However, the constituent sources often arise as a result of some complex non-linear

physics. To address this, we assume non-linear sound producing processes for constituent sources, and train deep non-linear models to represent them.

We present a new method for signal decomposition based on the concept of *Differentiable Dictionary Search (DDS)*, which was originally introduced in [15]. The general idea of DDS is to use a trained explicit-likelihood density model to impose a distance measure on the semantically structured space of spectral activity that the relevant sound sources exhibit, and use it to constrain the optimization process guiding the decomposition of an audio mixture. This combines the efficiency of dictionary sharing across time inherited from the non-negative matrix factorization framework, with improved modelling capacity of deep normalizing flows used to express the acoustic diversity of individual sound sources.

The initial DDS formulation [15] was mainly a proof of concept, still exhibiting a number of severe limitations. In particular, lack of dictionary sharing and parameter reuse in source modelling resulted in scalability issues with respect to growing input size and number of sources. In this paper, we present several extensions of the original model with the goal to further increase parameter reuse and data efficiency. We address this by choosing to model all sources together with a *single conditional density model*, with the source identity expressed by the variable being conditioned on, which we hope also leads to better generalization. These adjustments are aimed at reducing time and space complexity of the decomposition algorithm, while improving performance at the task of source attribution.

We use audio recordings of polyphonic piano music with temporally aligned labels to evaluate the decomposition quality by assessing the precision of spectral activity attribution to the sources. We compare variants of our method to an overcomplete NMF baseline, providing all of the compared methods with equivalent data for training (i.e. initialization), and iteration budget for inference (i.e. decomposition), ensuring that the conditions for comparison are fair, and that differences in performance can be attributed purely to differences in the methods' mechanics. To highlight these differences, we assess the memory and computation requirements as a function of the size of training data. Our experiments will show systematic improvement, in terms of source attribution, along the axis of method adjustments introduced by our advanced formulations. We will also see that the adjustments lead to increasingly sparse decompositions, according to a standard sparsity measure.

2 RELATED WORK

The model class used for modeling the spectral content of individual sources is called "normalizing flows", which have been introduced in [6]. We used deep parametric density model architectures *RealNVP* [3] and *Glow* [11]. Adaptive dictionaries, or generative models, have been used for audio decomposition before. Examples using Generative Adverserial Networks include [18, 13], examples using (variational) autoencoders are [17, 9]. All these approaches have a shortcoming in their lack of explicit access to the likelihood of their samples. It is therefore somewhat difficult to prevent the generative models from producing samples "too far away" from the training data manifold. Although Variational Autoencoders can provide the likelihood of samples they generate, Monte Carlo methods need to be used to approximate an expectation of a lower bound on the likelihood [1]. A very interesting line of research is discussed in [16, 14, 5], where Gaussian Processes are used for source separation. These models are adaptive, well grounded in probability theory, and even have an accessible, explicit likelihood, but are unfortunately extremely computationally demanding.

3 METHOD

The idea at the core of the DDS approach is to take the NMF framework $\mathbf{S} \approx \mathbf{W} \cdot \mathbf{H}$ and replace the dictionary $\mathbf{W}$ in a specific way. A dictionary entry corresponding to a particular source represents the spectral profile of that source by using a deep generative density model. The spectrogram $\mathbf{S}$ is decomposed into linear combinations of samples (likely spectral profiles) that are generated by these non-linear source density models. Those samples are allowed to adapt to the input that is being decomposed. The normalizing flow establishes a bijective differentiable mapping between the data space and a latent space, and allows explicit access to the likelihood of a sample as well. This enables to (softly) constrain the likelihoods of samples in a natural way, which in turn (softly) constrains how far the samples can deviate from the training distribution. The direction in which the samples should adapt is indirectly given by the gradient of the reconstruction error with respect to the latent

code that produced a sample. We are able to do this because the mapping between data space and latent space is fully differentiable.

To put it differently: by fitting generative density models to the training samples of isolated sources, we fit a parametrized function to estimate the data generating distribution. Since the model class we chose is a smooth, differentiable and invertible mapping between two manifolds (a so called *diffeomorphism*), we can *travel* on the data manifold by taking small steps in arbitrary directions of the high-likelihood region of the latent space to which the data manifold has been mapped. This enables us to *search* through this *differentiable dictionary* in any direction in data space we desire — thus the name *"Differentiable Dictionary Search"*. Several benefits of this approach have been demonstrated in [15], through a set of highly controlled experiments.

In the following, we describe three different formulations of the DDS method, along with a semi-supervised NMF baseline, all of which will be evaluated in Section 5. These three variants of DDS represent the iterative process towards improving both scalability and performance of the method.

3.1 The Linear Baseline: NMF

We will denote the log-magnitude spectrogram of an audio snippet as $\mathbf{S} \in \mathbb{R}_+^{D \times T}$, with D the spectral resolution (number of frequency bins) and T the length of the input (number of time frames). The NMF approximation is given as $\hat{\mathbf{S}} = \mathbf{W} \cdot \mathbf{H}$, where $\mathbf{W} \in \mathbb{R}_+^{D \times M}$ is the dictionary matrix, and $\mathbf{H} \in \mathbb{R}_+^{M \times T}$ is the activation matrix.

The inner dimension M of the NMF matrix multiplication corresponds to the number of components of the decomposition, and gives the number of columns in $\mathbf{W}$ ("dictionary entries") as well as the number of rows in $\mathbf{H}$ ("component activations"). In an unsupervised NMF, M would be a free parameter of the method. In our experiments, M will correspond to the total number of all samples (spectral frames of isolated notes) from both training and validation sets combined, that are otherwise used for training (and selection) of the dictionary model(s) in our variants of the DDS method. We simply store all of these samples in the dictionary $\mathbf{W}$ to initialize the method, and keep it fixed during the decomposition. This is what makes our baseline a semi-supervised and over-complete variant of the NMF method. The motivation is to enable fair comparison conditions by keeping the access to raw training data equal among the methods.

We will denote the number of sources (e.g. notes in the case of piano recordings) modeled by each method as K. After decomposition, the M "component activations" (rows in $\mathbf{H}$) are collapsed into the K rows of "source activations" by summing components according to their source identity.

3.2 The Unconstrained Formulation: DDS-1

This is the original formulation of the DDS method, as proposed in [15]. The primary deviation of the DDS-1 formulation from NMF (as well as the other two formulations) stems from the independent treatment of time frames in the decomposed spectrogram $\mathbf{S}$. Each time frame is modeled separately as a linear combination of K different dictionary entries. Each of the K possible sources is modeled with a separate density model using the RealNVP architecture, structure and configuration following [15].

The dictionary for the k-th source $\mathbf{W}_k \in \mathbb{R}_+^{D \times T}$ is generated by the corresponding density model F_{θ_k}. Please note, that each F_{θ_k} has its own set of parameters θ_k. Transforming the corresponding set of latent codes $\mathbf{Z}_k \in \mathbb{R}^{D \times T}$ as $F_{\theta_k}^{-1}(\mathbf{Z}_k^\top)^\top = \mathbf{W}_k$ for each source makes the full dictionary $\mathbf{W}$ of shape $(D \times T \times K)$ large. The activation matrix $\mathbf{H} \in \mathbb{R}_+^{K \times T}$ then contains one scalar for scaling each dictionary entry. With the row vector $\mathbf{h}_k$ denoting k-th source activations in $\mathbf{H}$, the input approximation is given as $\hat{\mathbf{S}} = \sum_{k=1}^{K} \mathbf{W}_k \odot \mathbf{h}_k$.

This specific setup was meaningful for the evaluation of the proof of concept implementation, where we treated the monophonic test samples independently in the highly controlled experiment of [15], and had only 12 sources (1 octave) in the exemplary semantic decomposition at the end. However, it is also the source of computational bottleneck when applying this variant to larger scale problems.

3.3 Constraining the Dictionary Size: DDS-2

As a first step to improve scalability, we re-introduce the sharing of dictionary entries across time from the NMF framework, such that the input approximation is given by the product of the dictionary and activation matrices $\hat{\mathbf{S}} = \mathbf{W} \cdot \mathbf{H}$.

We introduce a new free parameter N denoting "number of *components per source*", which specifies how many dictionary entries (columns in $\mathbf{W}$) will be used to explain activity of each source. This yields a new structure of the dictionary $\mathbf{W} \in \mathbb{R}_+^{D \times KN}$ and activation $\mathbf{H} \in \mathbb{R}_+^{KN \times T}$ matrices, with each of the K sources represented by N components. After decomposition, the N "component activations" (rows in $\mathbf{H}$) of each source are combined by summation, to make the $K \times T$ activation matrix $\mathbf{H}$. Dictionary entries for each source are generated by a separate, source-specific density model F_{θ_k} using the RealNVP architecture, following DDS-1. With the N dictionary latent codes $\mathbf{Z}_k \in \mathbb{R}^{D \times N}$ generating a subset of the dictionary as $\mathbf{W}_k = F_{\theta_k}^{-1}(\mathbf{Z}_k^\top)^\top$ for each of the K sources, the full dictionary is constructed by concatenating the generated entries of all source models: $\mathbf{W} = [\mathbf{W}_1, \mathbf{W}_2, \cdots, \mathbf{W}_K]$.

This imposes another regularization on the adaptation of dictionary entries (other than the likelihood penalty that is fundamental to the general DDS approach), as the entries now need to be re-usable across multiple spectrogram frames of the polyphonic mixture. As a result, computational efficiency is increased along with performance, due to the reduction in potential for "overfitting" any particular frame.

3.4 Unifying the Dictionary Model: DDS-3

This formulation builds on the previous one (DDS-2) by additionally regularizing the source modeling for the differentiable dictionary. Instead of a set of multiple source models, a single model F_θ (with a unique set of parameters θ), is now trained as a *conditional* density model — allowing sampling $x \sim p_{model}(x|y)$ conditioned on the source class label y — used to model the full set of dictionary entries for all K sources. To accomplish this, we choose to use an adaptation of the architecture described in [8], which allows for the class conditioning to be expressed explicitly in the latent mapping $\mathbf{z}$ by splitting it into a *semantic* part $\mathbf{z}_s \in \mathbb{R}^K$, and a *nuisance* part $\mathbf{z}_n \in \mathbb{R}^{D-K}$. The source identity is expressed by a 1-hot vector in the semantic part $\mathbf{z}_s$, while most of the intra-class variance of the source should manifest in the nuisance part $\mathbf{z}_n$. To train the conditional generative density model, we follow the training procedure from [8] up to a small change in the independence cross-entropy (*iCE*) objective: we replace the softmax cross-entropy on the semantic dimensions $\mathbf{z}_s$ with a mean squared error against the 1-hot class labels. Because the softmax has no explicit inverse, the conditional generation of dictionary entries using our model's explicit inverse F_θ^{-1} would become difficult. The full dictionary $\mathbf{W} \in \mathbb{R}_+^{D \times KN}$ is then generated form the corresponding set of latent codes $\mathbf{Z} \in \mathbb{R}^{D \times KN}$ by the multi-source dictionary model as $\mathbf{W} = F_\theta^{-1}(\mathbf{Z}^\top)^\top$, and the decomposition is given by $\hat{\mathbf{S}} = \mathbf{W} \cdot \mathbf{H}$, following DDS-2.

By having a single model jointly express probability densities of all sources, the set of parameters θ, albeit larger than that of any individual source model in the prior DDS variants, is now optimized using all of the available training samples combined. The ratio of $\frac{\text{\# trainable parameters}}{\text{\# training data}}$ thus goes down drastically, increasing both data efficiency, and utilization of parameters.

All of the DDS variants obtain decomposition by minimizing the reconstruction error $\|\mathbf{S} - \hat{\mathbf{S}}\|_2$ jointly with $-\log p(\mathbf{z})$ — the negative log-likelihoods on the dictionary entries — amounting to a maximum likelihood estimation (MLE) term, which is further weighted by relative contributions of dictionary entries to the full activation matrix. This objective is minimized via gradient descent by alternating updates of dictionary latent codes $\mathbf{Z}$ and the activations $\mathbf{H}$. In the specific case of DDS-3, only the nuisance parts of the latent code $\mathbf{z}_n$ are updated, as semantics $\mathbf{z}_s$ are held fixed.

3.5 Computational Complexity

To highlight how the methods that we will evaluate compare in terms of asymptotic computational complexity, we provide a rough assessment of their respective costs in an analysis with several simplifying assumptions.

Since training of the NMF method corresponds to simple storage of data samples into the dictionary, it has virtually no computational cost, as opposed to the DDS method variants, where one or many instances of a source model need to be trained.

All compared decomposition methods proceed iteratively, and the cost of one iteration stays constant, hence giving the runtime complexity of one iteration is sufficient to compare the four different approaches. Furthermore, since the gradient-based parameter update has a cost that is a constant factor of the forward pass cost — the inference of $\hat{\mathbf{S}}$ from these parameters — we limit our assessment in Table 1 to reporting on two major components of single iteration: (i) the reconstruction of input $\hat{\mathbf{S}}$ from $\mathbf{W}$ and $\mathbf{H}$, and (ii) the construction of

Table 1. Comparing Methods by Computational Complexity of Single Iteration

type	component	method			
		NMF	DDS-1	DDS-2	DDS-3
time	$\hat{\mathbf{S}} \leftarrow f(\mathbf{W},\mathbf{H})$	$\Theta(DTM)$	$\Theta(DTK)$	$\Theta(DTKN)$	$\Theta(DTKN)$
	$\mathbf{W} \leftarrow f(\mathbf{Z},\theta)$	—	$\Theta(TD^2)\cdot KUV$	$\Theta(ND^2)\cdot KUV$	$\Theta(KND^2)\cdot UV$
space	$\hat{\mathbf{S}} \leftarrow f(\mathbf{W},\mathbf{H})$	$\Theta(DM+MT+DT)$	$\Theta(DTK+TK+DT)$	$\Theta(DKN+KNT+DT)$	$\Theta(DKN+KNT+DT)$
	$\mathbf{W} \leftarrow f(\mathbf{Z},\theta)$	—	$\Theta(TD+D^2)\cdot KUV$	$\Theta(ND+D^2)\cdot KUV$	$\Theta(KND+D^2)\cdot UV$

dictionary $\mathbf{W}$ from $\mathbf{Z}$, using a set of parameters θ; computed by each method as described above, omitting the associated costs of the gradient computation and gradient-based parameter update.

As inference of the dictionary $\mathbf{W}$ corresponds to passing a specific batch of data ($\mathbf{Z}$) through a (set of) normalizing flow(s), we assess this by recounting the number of matrix multiplications involved, leaving out other operations of cost proportional to the input size via constant factor, which is negligible. We denote the number of flow steps in a normalizing flow model by U, and the number of matrix multiplication operations involved in a single flow step[1] by V. Further assumption that those matrix multiplications are on the order of the data dimension D, which approximately holds for all of our DDS variants parametrizations among our experiments, yields us the estimates in Table 1.

First, the NMF baseline has no cost of dictionary inference, as that is fixed to the training data, but this advantage comes at the cost of *linear* time and space complexity of NMF with respect to the *size* of training data M, as opposed to the *constant* complexity of the DDS variants. This is one of the many benefits of dictionary modeling, as typically $M \gg KN$ for most practical scenarios, such as decomposition of piano recordings. On the other hand, the cost of dictionary modeling grows *quadratically* with the spectral resolution D in both time and space for all DDS methods, as opposed to merely *linear* growth in NMF.

The computational bottleneck of the initial DDS-1 formulation can now easily be pinpointed to the obviously *linear* growth of already D-quadratic dictionary modeling costs in terms of temporal length T of the input, which is the ultimate, fastest growing parameter in any practical scenario. The dictionary sharing with an adjustable parameter N introduced in DDS-2 (and DDS-3) purposefully eliminates this linear cost. Ultimately, the step from DDS-2 to DDS-3 – consolidating the dictionary into a single model – does not save much time in the big picture, but improves the space complexity by eliminating the K-factor from the D-quadratic cost[2], which definitely makes a difference with higher spectral resolutions D and larger sets of sources K.

4 EXPERIMENTAL SETUP

4.1 Data and Basic Audio Signal Processing

To assess the relevant aspects of performance with respect to varying degrees of task complexity (such as number of concurrently sounding notes, or variance in note intensities), we use the MAPS (MIDI-Aligned Piano Sounds) dataset [4], as its large variety of systematically structured examples allows us to study certain aspects of our method formulations in better isolation. We will use the ISOL subset of MAPS — samples of isolated notes — for training. To evaluate the decomposition performance, we will use the RAND subset of MAPS, which contains samples of randomly generated note combinations (chords) drawn from a specific range of notes, with varying degrees of polyphony and intensity (loudness). The MAPS dataset also allows to control for timbral variance in terms of the used instrument model and its recording conditions. We evaluate

[1] Such as the dimension shuffling operation, or the densely connected layers of the Multi-Layer Perceptron (MLP) networks used to learn the coupling functions.

[2] After multiplying by K in DDS-2, the inference of $\mathbf{W}$ costs $\Theta(KND+KD^2)\cdot UV$ as opposed to $\Theta(KND+D^2)\cdot UV$ in DDS-3, making it a difference of $(K-1)D^2\cdot UV$.

behavior of the tested systems in presence of timbral distribution shift, by carefully selecting subsets of samples for training and evaluation with no overlap along the timbre-determining axes. In the following experiments, we train all systems on samples of synthetic, sample-based instruments, excluding only the Disklavier(`ENSTDk*`) samples from training. We randomly split this set into 80% training and 20% validation samples. Evaluation is done on samples from the Disklavier instrument in "Close" recording setting — code (`ENSTDkCl`) in [4].

The MAPS audio samples are encoded as 44.1 [kHz] stereo WAV files with the temporally aligned ground truth in the form of MIDI files. Before computing spectrograms, we downsample the recordings to 16 [kHz] mono waveforms, preserving spectral activity in the frequency range of $[0;8]$ [kHz]. We analyze the audio at spectral resolution of 512 frequency bins, given by DFT window size of 1024, using the Hann window function, and a hop size of 512 samples. The temporal resolution, as determined by the combination of sampling rate and hop size, is then used to quantize the MIDI ground truth into a piano-roll with a shape matching that of the activation matrix produced by the decomposition. After spectral analysis of different sample audio files, silent frames are discarded based on the ground truth annotations.

4.2 Parametrization of Methods (1): Training

We choose to evaluate on a portion of RAND subset of MAPS that uses the pitch range of the centered 5 octaves, marked by `M36-95` in [4], corresponding to 60 notes between and including C2 and B6, that the evaluated methods need to model as individual sources. This range is commonly used to evaluate multi-pitch algorithms. Note that this is a 5-fold increase from the single octave (12 notes) modelled by DDS-1 in [15].

NMF. The dictionary $\mathbf{W}$ in NMF is initialized by loading all of the samples, which are otherwise also used for both *training* and *validating* the normalizing flows used in our DDS method formulations, and storing them directly in the dictionary, giving this method a slight edge in terms of training data volume.

DDS. The differentiable dictionaries in both the DDS-1 and DDS-2 formulations, are initialized by training a set of unconditional density models (parametrized by a modified single-scale 1-dimensional RealNVP architecture, as per Section 3), one for each note. We follow [15] closely in regard to the model architecture and hyperparameters. In particular, the 16 flow steps are realized via affine coupling blocks [2] with their coupling functions approximated using MLPs with 4 dense layers of 128 units with SELU [12] activations. The shuffling of dimensions between the coupling blocks is realized via randomly initialized, fixed permutation layers, which are easily invertible via transposition.

The differentiable dictionary in DDS-3 formulation is initialized by training a single conditional density model (parameterized by a modified single-scale 1-dimensional Glow architecture with semantic conditioning, as per Section 3). Specifically, following the Glow architecture [11], each of the 32 flow steps has (i) an ActNorm layer, (ii) a trainable mixing layer parameterized in its LU-decomposition, and (iii) an affine coupling parameterized as MLP with 3 dense layers of 1024 units and Leaky ReLU [19] activations.

All density models were trained with the Adam optimizer [10] for up to 2500 epochs using mini-batch size of 512, and learning rate of $1 \cdot 10^{-3}$ with the single-source models (DDS-1 and DDS-2) and $1 \cdot 10^{-5}$ with the multi-source model (DDS-3). After each training epoch, the model was evaluated on the validation data for subsequent model selection.

4.3 Parametrization of Methods (2): Inference

For all methods, the decomposition is run for a maximum of 1000 update steps, each of which allows for two independent updates of the dictionary, and activation matrix, respectively, following the procedure of alternating updates. NMF uses a step size of $1 \cdot 10^{-2}$, the DDS variants use $5 \cdot 10^{-3}$. The remaining parameters and aspects of decomposition, such as learning rate reduction upon loss plateau detection or the early stopping condition, are set equally for all methods, and follow the experimental setup outlined in [15] identically.

Initial Conditions for the NMF method. Let M denote total number of samples used for training and validation, and thus also the number of entries forming the dictionary $\mathbf{W}$ in NMF. Then, the activation matrix $\mathbf{H}$ is initialized with $\frac{1}{M}$ everywhere.[3]

[3]This by no means implies that NMF is allowed twice as many updates of $\mathbf{H}$ (due to having $\mathbf{W}$ fixed) as the DDS methods. The maximum number of updates for each parameter is equal for all methods. A single update step allows for exactly one update of $\mathbf{H}$ and one update of $\mathbf{W}$.

Initial Conditions for DDS variants. In all variants of the DDS method, the latent space mapping vectors $\mathbf{Z}$ of the differentiable dictionaries are initialized to $\mathbf{0}$ vectors. The activation matrix $\mathbf{H}$ is initialized to small, random numbers drawn from a uniform distribution $h_i \sim \mathscr{U}(0,1)$, re-scaled to a factor of $\frac{E}{\sqrt{K}}$ for DDS-1 and $\frac{E}{\sqrt{K \cdot N}}$ for DDS-2 and DDS-3, where E is the average energy of the input magnitude spectrogram $\mathbf{S}$, K is number of sources, and N is number of components per source.

4.4 Post-processing

Once the inference of activations $\mathbf{H}$ via the decomposition of input spectrogram $\mathbf{S}$ is finished, yet before calculating any performance quantifiers, we re-scale each scalar value in $\mathbf{H}$ by the norm of its associated dictionary vector from $\mathbf{W}$, the one that is "activated" by it. This works slightly differently for each of the methods, and for NMF, DDS-2 and DDS-3, it is followed by aggregating the activity of sources over the components that represent them. Nonetheless, the principle is the same, and this step has an equally positive effect on the performance of all methods. The basic idea is that normalizing the dictionary entries to equal-length vectors will put the values of $\mathbf{H}$ on a rather more "comparable" scale of activity contribution, without burdening the optimization process of decomposition with enforcing equal norms of vectors that are being searched over. As a result, this is a cheap way to express the activation values in $\mathbf{H}$ on a consistent, $\mathbf{W}$-independent scale.

4.5 Evaluation Metrics

To quantify performance of the inspected methods for a relative comparison of their properties, we calculate and report two pertinent evaluation measures, defined as follows.

Decomposition Correctness. In order to measure the quality of decomposition, we define a metric that we call *Precision of Source Attribution* (PSA). As per the Eq. 1, both the activation matrix $\mathbf{H}$ and the thresholded, binary labels $\mathbf{Y}$ have the shape $[K \times T]$. The numerator in Eq. 1 quantifies the amount of activity attributed *correctly*, while the denominator quantifies all of the activity attributed *in total*.

$$\mathrm{PSA} = \frac{\sum_{k,t} \mathbf{H} \odot \mathbf{Y}}{\sum_{k,t} \mathbf{H}} \tag{1}$$

Intuitively, PSA quantifies the fraction of activity in the activation matrix $\mathbf{H}$ that is attributed to those sources that are active according to the ground truth annotations. Combined with the post-processing of $\mathbf{H}$ described above, it helps capture how well the activity in magnitude spectra is explained by the dictionary elements associated with those sources that are truly active.

Decomposition Sparsity. To quantify the sparsity of the activation matrices produced, we will report a simple measure of sparsity based on L^0_ε [7]. The standard L^0-sparsity simply computes fraction of the count of zeros to the total number of elements in the matrix. The L^0_ε-sparsity also includes small, non-zero elements into that count, if they are below some ε threshold. We use $\varepsilon = 5 \cdot 10^{-2}$ to correct for noisy activity in $\mathbf{H}$, which our NMF baseline is more prone to generate due to its excessive dictionary size.

5 RESULTS

To examine the general trends of task difficulty and method performance on different problem configurations, we executed multiple audio decomposition experiments using audio snippets created using various parametrizations. To highlight the relative performance of the tested methods, we first report a detailed result on a single such configuration, picked at random. Nonetheless, the observed trends in relative performance of the compared methods seem to hold consistently across varying test configurations.

5.1 Method Comparison

The numbers reported in Table 2 were obtained by running decompositions on a test snippet constructed by concatenating only segments with actual note content, excluding all silence. The segments were selected to fulfill the following criteria: (i) notes have an intensity range `I32-96` representing the more complex scenario of higher dynamic range, (ii) there are only two notes sounding at any given time. The number of individual dictionary components used for each source was set to $N = 64$ for both DDS-2 and DDS-3.

Table 2. Improving attribution correctness.

	NMF	DDS-1	DDS-2	DDS-3
PSA	0.3568	0.2760	0.4323	0.6475
L_ε^0	0.6824	0.7039	0.8121	0.9367

As our measure of decomposition quality PSA (Eq. 1) indicates, each of the adjustments introduced to our formulation of the DDS approach led to an improvement in performance, ultimately outperforming the linear baseline by a large margin. In particular, the introduction of dictionary sharing into DDS-2 seems to be responsible for a 56.7% relative improvement against DDS-1, while the additional introduction of parameter sharing in the parameterization of source model in DDS-3 seems to have improved the decomposition quality by another 49.8% with respect to DDS-2. The under-performance of DDS-1 compared to the NMF baseline points towards its inefficient scaling, as discussed in 3.5.

Moreover, all of the considered variants of DDS appear to be producing increasingly sparse decompositions, demonstrating increasing suitability to the problem domain of audio decomposition, in which mixtures are typically composed of small subsets of all potential sources. However, we observed this as an unintended positive side effect of the adjustments introduced, having designed none of them with the specific goal of encouraging sparse decompositions in mind. Using any of these methods, sparsity can still be additionally incentivized through an explicit regularization term in the decomposition objective.

5.2 General Trends

In broader set of experiments, we varied different problem parameters and method arguments, such as spectral resolution of the input, polyphony level and dynamics range of the test samples, and the method flexibility for DDS-2 and DDS-3 controlled via the dictionary size argument N (components per source). While the trend of relative performance gains reported in 5.1 appeared quite consistently, we observed several additional trends.

In general, all methods — including the baseline — usually achieve slightly better decomposition metrics at a larger spectral resolution of 1024, albeit at higher computational cost. Most of the trends we observe, appear to be more pronounced at the higher spectral resolution of 1024. In terms of both the decomposition and reconstruction quality measures, the samples with a higher dynamic range (`I32-96`) were generally representing a harder task than those of lower dynamic range (`I60-68`), as all methods had consistently better metrics on the samples with low dynamic range. The problem difficulty also seems to grow almost linearly with the level of polyphony, at least between `P2` and `P7`, for which we have measurements from the MAPS dataset. When tweaking the method capacity parameter N, higher values in DDS-2 produced generally smaller reconstruction error, but not necessarily more precise decomposition. On the contrary, lower N seemed to produce more accurate decompositions. In contrast, with growing N, DDS-3 seemed to be producing either equally good, or better decompositions than for lower values of N, in both decomposition quality and reconstruction error. This can be interpreted as evidence for a difference between properties of the "bag of models" approach to dictionary modeling of DDS-2, and the "one conditional model for all sources" approach of DDS-3, considering all other aspects being equal. We conjecture that the extra regularization of the single dictionary model in DDS-3 markedly reduced the potential to "misuse" the spare capacity at higher N, as contrasted with DDS-2 and its many less regularized models.

6 CONCLUSION

We presented several adjustments to a recently proposed method for audio decomposition, improving its computation and memory costs, as well as quality of the decompositions in terms of precision of source attribution. As a positive side effect, these improvements also incentivize sparser decompositions. An investigation into these dictionary models' dynamics could reveal promising directions for further improvements.

REFERENCES

[1] Y. Bando, M. Mimura, K. Itoyama, K. Yoshii, and T. Kawahara. Statistical speech enhancement based on probabilistic integration of variational autoencoder and non-negative matrix factorization. In *2018 IEEE Int. Conf. on Acoustics, Speech and Signal Processing, ICASSP 2018, Calgary, AB, Canada*.

[2] L. Dinh, D. Krueger, and Y. Bengio. Nice: Non-linear independent components estimation. *arXiv preprint arXiv:1410.8516*, 2014.

[3] L. Dinh, J. Sohl-Dickstein, and S. Bengio. Density estimation using Real NVP. In *5th International Conference on Learning Representations, ICLR 2017, Toulon, France*.

[4] V. Emiya, R. Badeau, and B. David. Multipitch estimation of piano sounds using a new probabilistic spectral smoothness principle. *IEEE Transactions on Audio, Speech, and Language Processing*, 18(6):1643–1654, 2009.

[5] D. G. Fantinato, L. T. Duarte, B. Rivet, B. Ehsandoust, R. Attux, and C. Jutten. Gaussian processes for source separation in overdetermined bilinear mixtures. In *Latent Variable Analysis and Signal Separation - 13th International Conference, LVA/ICA 2017, Grenoble, France*, volume 10169, pages 300–309, 2017.

[6] E. G. Tabak and E. Vanden-Eijnden. Density estimation by dual ascent of the log-likelihood. *Communications in Mathematical Sciences - COMMUN MATH SCI*, 8, 03 2010.

[7] N. Hurley and S. Rickard. Comparing measures of sparsity. *IEEE Transactions on Information Theory*, 55(10):4723–4741, 2009.

[8] J.-H. Jacobsen, J. Behrmann, R. Zemel, and M. Bethge. Excessive invariance causes adversarial vulnerability. *arXiv preprint arXiv:1811.00401*, 2018.

[9] E. Karamatli, A. T. Cemgil, and S. Kirbiz. Audio source separation using variational autoencoders and weak class supervision. *IEEE Signal Process. Lett.*, 26(9):1349–1353, 2019.

[10] D. P. Kingma and J. Ba. Adam: A method for stochastic optimization. In *3rd International Conference on Learning Representations, ICLR 2015, San Diego, CA, USA*.

[11] D. P. Kingma and P. Dhariwal. Glow: Generative flow with invertible 1x1 convolutions. *Advances in neural information processing systems*, 31, 2018.

[12] G. Klambauer, T. Unterthiner, A. Mayr, and S. Hochreiter. Self-normalizing neural networks. In *Advances in Neural Information Processing Systems 30: Annual Conference on Neural Information Processing Systems 2017, Long Beach, CA, USA*, pages 971–980.

[13] L. Li, H. Kameoka, and S. Makino. Determined audio source separation with multichannel star generative adversarial network. In *30th IEEE Int. Workshop on Machine Learning for Signal Processing*. IEEE, 2020.

[14] A. Liutkus, R. Badeau, and G. Richard. Gaussian processes for underdetermined source separation. *IEEE Trans. Signal Process.*, 59(7):3155–3167, 2011.

[15] L. S. Marták, R. Kelz, and G. Widmer. Probabilistic Modelling of Signal Mixtures with Differentiable Dictionaries. *Proceedings of European Signal Processing Conference*, pages 441–445, 2021.

[16] S. Park and S. Choi. Gaussian processes for source separation. In *Proceedings of the IEEE Int. Conf. on Acoustics, Speech, and Signal Processing, ICASSP 2008, Caesars Palace, Las Vegas, Nevada, USA*. IEEE.

[17] S. Squires, A. Prügel-Bennett, and M. Niranjan. A variational autoencoder for probabilistic non-negative matrix factorisation. *CoRR*, abs/1906.05912, 2019.

[18] Y. C. Sübakan and P. Smaragdis. Generative adversarial source separation. In *2018 IEEE Int. Conf. on Acoustics, Speech and Signal Processing, ICASSP 2018, Calgary, AB, Canada*, pages 26–30. IEEE, 2018.

[19] B. Xu, N. Wang, T. Chen, and M. Li. Empirical evaluation of rectified activations in convolutional network. *arXiv preprint arXiv:1505.00853*, 2015.